NASA Conference Publication 2493

Turbine Engine Hot Section Technology 1987

Proceedings of a conference sponsored
by NASA Lewis Research Center
Cleveland, Ohio
October 20 and 21, 1987

National Aeronautics
and Space Administration

Scientific and Technical
Information Division

1987

FOREWORD

As I have noted in previous HOST conference publications, the NASA Hot Section Technology (HOST) Project addresses advanced turbine engine durability needs. The project has involved representatives from six engineering disciplines who are spread across three work sectors.

To address more fully the technology needs resulting from durability challenges, we encouraged researchers from the technical disciplines of instrumentation, combustion, turbine heat transfer, structural analysis, fatigue and fracture, and surface protection to work together, often for the first time. Additionally, we wanted to prompt both basic and applications-oriented research within each of the six disciplines. This induced us to involve scientists and engineers from three work sectors - academia, where significant basic research is usually performed; industry, where research as well as applications work is addressed; and NASA, which supports both basic and applications research and has the resources to link the other two sectors.

To provide a vehicle for improved dialogue among these numerous and diverse groups - six disciplines and three sectors, NASA's Lewis Research Center sponsored a technical workshop annually from 1982 to 1987.

During this past year, we learned that funding for the HOST Project would end with Fiscal Year 1987. Thus, the HOST Sixth Annual Workshop, held October 20-21, 1987, was the last in the series. This publication contains the papers presented at the workshop.

Daniel E. Sokolowski
Manager, HOST Project

CONTENTS

TURBINE HEAT TRANSFER

STRUCTURAL ANALYSIS

SURFACE PROTECTION

FATIGUE AND FRACTURE

TURBINE ENGINE HOT SECTION TECHNOLOGY (HOST) PROJECT

Daniel E. Sokolowski and C. Robert Ensign
NASA Lewis Research Center
Cleveland, Ohio

This publication is a record of the presentations made at the Sixth Annual Workshop for the Hot Section Technology (HOST) Project. Since the project began - officially in October, 1980, we have seen significant advances in turbine engine hot section technology, many of which were made possible through HOST Project funding and research efforts. For example, before 1980, most engine developers adhered to the "build 'em and bust 'em" approach. HOST Project work has spearheaded the change from this traditional approach to engine development. The currently evolving approach stresses using mathematical models and computer codes, suppported by broad experimental databases. These models and codes allow researchers to make analytical predictions before they build hardware for confirmation testing.

This new approach has already prompted improved and more durable engine designs. Additionally, it has increased technical understanding of hot section behavior and is leading to reduced development time and cost. As more researchers use these models and codes, we expect this trend on benefits to become even more significant.

We at the NASA Lewis Research Center are also proud of the HOST Project legacy to the Center's research facilities. HOST funding has supported the development of several state-of-the-art laboratories. These include a world-class high-temperature fatigue and structures laboratory, the high-temperature instrumentation research laboratory, and a unique cyclic high-temperature structural component response test facility.

Annual attendance at the six workshops has averaged over 250. At least forty-five papers have been presented each year. Representatives from more than a dozen government agencies, more than 40 companies, and 21 universities have attended annually. Agencies included the Air Force Aeropropulsion Laboratory, Argonne National Laboratory, and Oak Ridge National Laboratory. From industry the obvious companies, such as Pratt & Whitney, General Electric, Allison, and Garrett sent scientists and engineers. In addition, though, researchers from General Motors research labs, Electric Power Research Institute, Kentron, and Chromalloy attended, along with others. There were also university faculty and researchers from all over the country, including the University of California, Purdue University, the University of Akron, and Yale University.

Many of the leading experts in hot section technology presented papers. Professor Daniel Rosner (Yale University) spoke about turbine airfoil deposition models. Dr. Robert Dring (UTRC) talked about gas-side heat transfer with rotation. Professor Robert Moffat (Stanford University) gave a presentation on heat transfer with very high free-stream turbulence and streamwise vortices. Dr. Eric Jordan (University of Connecticut) and Dr. Kevin Walker (Engineering Science Software,

Inc.) delivered a progress report on constitutive modeling of a single crystal and directionally solidified superalloys.

During these six workshops, we have provided what participants tell us has been an unusually fertile opportunity to learn from colleagues in disciplines and sectors that generally do not talk much with one another. This forum has offered the latest technical information about durability issues through formal paper presentations. Participants also report that the exchanges between presentations, at meals and breaks, and in the evenings have also been singularly rich. For these comments we are grateful. It is quite clear that these positive experiences have been possible only because outstanding and dedicated researchers took the time to attend the workshop and to participate with striking enthusiasm.

As HOST winds down, we look to the future, which we believe includes higher-temperature turbine engine environments. These produce special challenges, such as being able to withstand temperatures approaching 4000 °F in the hot section and the need to introduce higher-temperature, lighter-weight materials and structures.

Since the HOST Project is winding down, we are working on three wrap-up publications that may interest participants and followers of the project:

1. **Bibliography.** In the HOST Fifth Annual Workshop Publication and in this present one, we include a bibliography of HOST research publications. We have planned a more complete and annotated bibliography of HOST publications that NASA Lewis Research Center will publish during 1988 as an independent Technical Memorandum.

2. **ASME Aeroengine Congress Preprint.** The ASME has invited us to conduct a double session on recent hot section technology - at the 1988 International Gas Turbine and Aeroengine Congress and Exposition (July 5-9, 1988, in Amsterdam, The Netherlands). The invited participants will review and assess HOST Project achievements. Authors will include both NASA and industry representatives. Plans are being formulated to publish the session papers in a bound ASME volume of preprints.

3. **HOST book.** The HOST project has made several unique contributions to durability needs - particularly with respect to changes in how engineers analyze turbine engine designs using models and codes. To document these developments, we have commissioned a book about the HOST Project that NASA Headquarters will publish in 1988.

HOST INSTRUMENTATION R&D PROGRAM OVERVIEW

David R. Englund
NASA Lewis Research Center
Cleveland, Ohio

The goal of the HOST Instrumentation R&D program over the last five years has been to develop improved instrumentation for measuring the environment within the hot section of turbine engines and for measuring the response of hot-section components to that imposed environment. The program has included work on a dynamic gas-temperature measuring system, on total heat flux sensors, on a system for viewing the interior of a combustor during operation, on laser anemometry, and on high-temperature strain-measuring systems including strain gages and strain gage materials, and a remote optical strain measuring system. Most of this work has been completed and reported on at earlier meetings and in written form. Work which is still active includes strain gage development and application activities, application of laser anemometry to high-temperature flow streams, and an experiment on turbulence measurement.

The HOST Instrumentation R&D program for the period 1984 through 1987 is shown in figure 1. Each entry on this figure represents a contract, grant, or in-house project, and the goal of each effort is listed in the right column. The completed projects shown here cover gas temperature, optical strain measurement, and heat flux sensors. The turbine blade and vane static strain gage is a contract effort which should be completed in fiscal year 1988. This contact effort developed the palladium-chromium strain gage alloy and is now working to develop a thin-film strain gage system based on this alloy. The work on high-temperature strain gage materials is a research grant to Northwestern University which is scheduled to end in 1988. One of the promising materials being studied in this grant is boron-carbide, on which a gage factor of 190 was measured at 1000 °C. The other active project in the strain measurement area is the development of an in-house high-temperature strain gage capability; this work is emphasizing both wire and thin-film gages using the palladium-chromium alloy. The work listed under turbulence is an experiment to compare methods for measuring turbulence in the exhaust stream of an atmospheric burner in which there is appreciable temperature fluctuation. The fringe laser anemometer and the dynamic gas-temperature measuring system are being used in this experiment to compare turbulence in terms of the fluctuation in velocity with turbulence in terms of the fluctuation in the density-velocity product. The final project listed is the work to apply laser anemometry to hot-section components; the main product of this effort will be to operate a two-axis laser anemometer on the warm turbine rig at Lewis Research Center.

HOST INSTRUMENTATION R&D PROGRAM

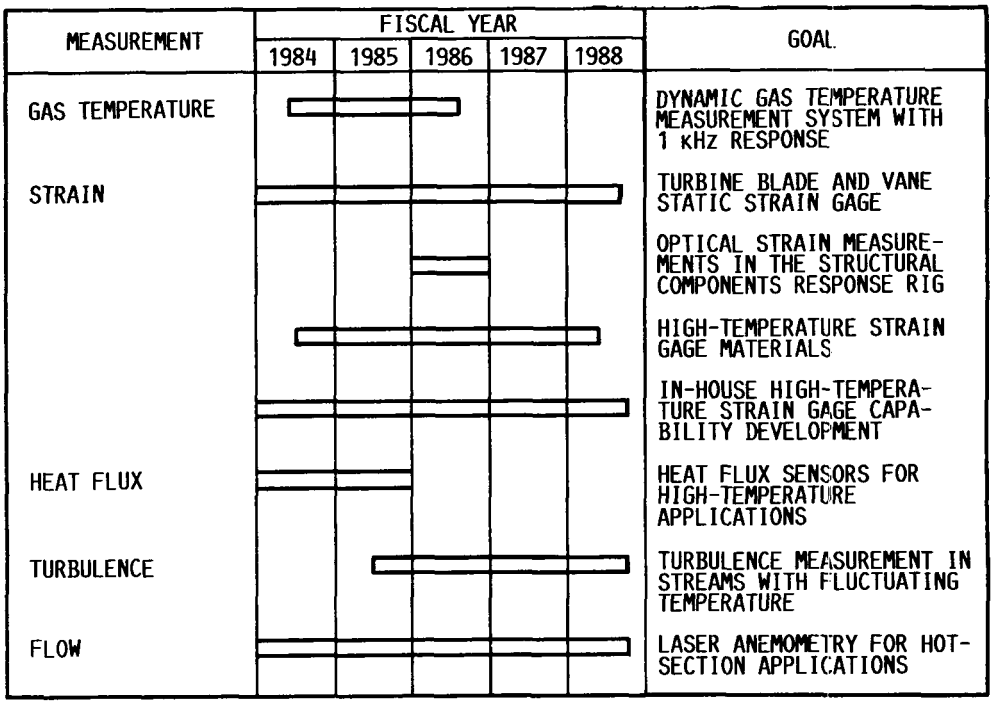

CD-87-29031

Figure 1

HOST COMBUSTION R&T OVERVIEW

Raymond E. Gaugler
NASA Lewis Research Center
Cleveland, Ohio

The overall objective of the Turbine Engine Hot-Section Technology Combustion Project is to develop and verify improved and more accurate numerical analysis methods for increasing the ability to design with confidence combustion systems for advanced aircraft gas turbine engines.

The objective is being approached from two directions: computational and experimental. On the computational side, the approach was to first assess and evaluate existing combustor aerothermal analysis models by means of a contracted effort initiated during fiscal year 1982. This effort has quantified the strengths and deficiencies of existing models. The results of this assessment were summarized at a previous HOST Workshop. Next, phase II contracts were let in fiscal 1984 to develop new and improved numerical methods for the analysis of turbulent viscous recirculating flows, with the prime objectives being improved accuracy and speed of convergence. Progress reports under one contract and a university grant will be presented at this workshop. The third part of the computational approach was to be tied very closely to the experiments. It was to consist of incorporating improved physical models into the computational codes. Unfortunately, the phase III work has been postponed due to funding cuts.

On the experimental side, three types of experiments can be identified: first, fundamental experiments directed toward improved understanding of the flow physics and chemistry; second, experiments run to provide data for the empirical modeling of complex phenomena; and third, benchmark experiments for computer code validation.

Four experimental efforts have been completed and reported on previously, and three are still under way, nearing completion. Progress reports will be presented on those three at this workshop.

The completed experimental programs were aimed primarily at obtaining a basic understanding of the flows and improving empirical models. Two programs that concentrated on the interaction of dilution jets and the main-stream flow field have added substantially to the understanding of such flows. A third experimental program examined in detail the mass and momentum transport in swirling and nonswirling coaxial jets. The fourth effort was an investigation of the radiative heat loading in an advanced, high-pressure gas turbine combustor.

The other three experimental programs are concentrating on the generation of benchmark-quality data for use in validating new computer codes and models.

COMBUSTOR FLOW PHENOMENA

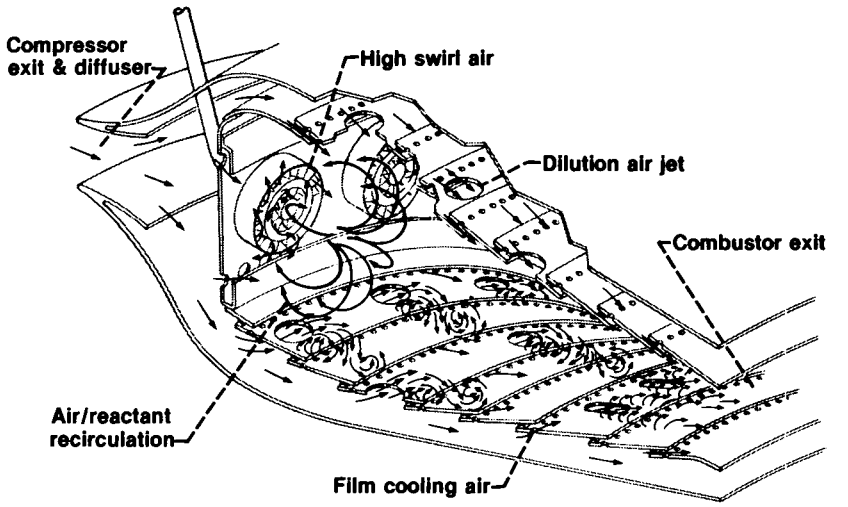

- FULLY 3-DIMENSIONAL FLOW
- CHEMICAL REACTION/HEAT RELEASE
- HIGH TURBULENCE LEVELS
- 2 PHASE WITH VAPORIZATION

CD-81-12820

Figure 1

COMBUSTION

PROGRAM ELEMENT	FISCAL YEAR 81	82	83	84	85	86	87	88	89	EXPECTED RESULT
AEROTHERMAL MODELING ASSESSMENT, PHASE I:										
GARRETT TURBINE ENGINE										IDENTIFY MODEL AND BENCHMARK DATA DEFICIENCIES
GENERAL ELECTRIC										
PRATT & WHITNEY										
LATERAL JET INJECTION (OKLAHOMA STATE U.)										THREE-DIMENSIONAL FLOW MEASUREMENTS
AEROTHERMAL MODEL DEVELOPMENT, PHASE II										
MASS & MOMENTUM TRANSFER (P&W)										NEW PHYSICAL MODEL AND COMPUTING METHODS
NUMERICAL METHODS (ALLISON, AVCO EVERETT)										
FLOW INTERACTION (ALLISON)										
FUEL SPRAY-FLOWFIELD INTERACTIONS (ALLISON, UTRC)										
NUMERICAL METHODS (U. MINNESOTA)										
MULTIPLE JET DILUTION MIXING (GARRETT)										EXIT TEMPERATURE PROFILE
FLAME RADIATION/HEAT FLUX										HIGH PRESSURE FLAME RADIATION
DILUTION JET ANALYSIS										JET MIXING MODEL
DIFFUSER STUDIES (GARRETT) (JOINT WITH AIR FORCE)										IMPROVED COMBUSTOR-DIFFUSER INTERACTION MODEL

CD-86-22159

Figure 2

HOST TURBINE HEAT TRANSFER PROGRAM OVERVIEW

Herbert J. Gladden
NASA Lewis Research Center
Cleveland, Ohio

Improved performance of aircraft gas turbine engines is typically accompanied by increased cycle pressure ratio and combustor exit gas temperature. Consequently, the hot-section components of these turbojet/turbofan engines are subjected to severe aerothermal loads during the mission flight profile. Meeting the design goals of high cycle efficiency, increased durability of the hot-section components, and lower operating cost requires an improved understanding of the flowfield physics and the heat transfer process in the turbine gas path.

The objectives of the turbine heat transfer program are to achieve more efficient and durable hot-section components through a combined experimental and analytical multiyear effort. This program effort is presented in figures 1 and 2.

The experimental part of the turbine heat transfer subproject consists of six large experiments, which will be highlighted in this overview, and three of somewhat more modest scope. Three of the large experiments were conducted in the stationary frame of reference and are essentially complete. One of the initial efforts was the stator airfoil heat transfer program conducted at Allison Gas Turbine Division. The non-film-cooled and the showerhead-film-cooled data have already been reported. Highlights of the data are shown in figure 3. The gill-region film-cooling experimental effort is also complete but not yet reported. The investigation of secondary flows in a 90° curved duct, conducted at the University of Tennessee Space Institute, has also been completed. The first phase examined flows with a relatively thin inlet boundary layer and low free-stream turbulence. The second phase studied a thicker inlet boundary layer and higher free-stream turbulence. A comparison of analytical and experimental cross-flow velocity vectors is shown for the 60° plane in figure 4. Two experiments were also conducted at Lewis in the high-pressure facility. One examined full-coverage film-cooled vanes, and the other, advanced instrumentation. Reports on these results have been published.

The other three large experimental efforts were conducted in a rotating reference frame. An experiment to obtain gas-path airfoil heat transfer coefficients in the large, low-speed turbine at United Technologies Research Center has been completed. Single-stage data with both high- and low-inlet turbulence were taken in phase I. The second phase examined a one and one-half stage turbine and focused on the second vane row. Under phase III aerodynamic quantities such as interrow time-averaged and rms values of velocity, flow angle, inlet turbulence, and surface pressure distribution were measured. All of these data have been published except the aerodynamic data. Results of upstream turbulence in the stator and rotor heat transfer are shown in figure 5.

Coolant passage heat-transfer data in a rotating frame are also being obtained at Pratt & Whitney/United Technologies Research Center. Experiments with smooth-wall serpentine passages and with skewed turbulators have been completed. Some results

of the effect of rotation and heat transfer are shown in figure 6 for the smooth-wall case. An experiment with turbulators normal to the flow has been started and will be completed in 1988.

The final large experiment will be conducted at Lewis in the warm-core turbine. This facility, which fully scales a modern turbine stage, is being modified for laser anemometry access to the vane and blade passages. Research will begin in 1988.

The three smaller and somewhat more fundamental experiments are directed at important mechanisms. Two are being conducted by Arizona State University. The first, on impingement cooling, is complete; the second, on tip region heat transfer simulation, is providing excellent data. An experiment on the heat transfer effects of large-scale, high-intensity turbulence, similar to that found at combustor exits, is also underway at Stanford University.

The analytic efforts in the turbine heat transfer subproject are characterized by efforts to adapt existing codes and analyses to turbine heat transfer. In general these codes and analyses were well established before HOST became involved; however, the applications were not for turbine heat transfer, and extensive revision has often been required. In some cases the analytic and experimental work were part of the same contract.

The well-known STAN5 boundary-layer code was modified by Allison Gas Turbine Division to define starting points and transition to turbulent flow to accommodate their data, with and without film cooling, as well as data in the literature.

United Technologies Research Center assessed its three-dimensional boundary layer code and modified it to allow for easier application of turbine type inviscid edge conditions. The same code is being modified for use as a two-dimensional unsteady code in order to analyze the rotor-stator interaction data.

The also well-known three-dimensional Navier-Stokes TEACH code has been modified by Pratt & Whitney for application to internal passages and to incorporate rotational terms. The modified code has been delivered to NASA Lewis and tested on some simple geometric cases.

A fully elliptic three-dimensional Navier-Stokes code has been under development at Scientific Research Associates (SRA) for many years. It was primarily directed at inlets and nozzles. SRA, first as a subcontractor to Allison Gas Turbine Division and now as a prime contractor, has been modifying the code for turbine applications. This includes grid work for turbine airfoils, adding an energy equation and turbulence modeling, and improved user friendliness. The code has been installed on the Lewis Cray XMP, and a first report on its use for turbine heat transfer has been published. A comparison with the Allison nonrotating experimental data is shown in figure 7.

Finally, a fundamental study on numerical turbulence modeling, directed specifically at the airfoil in the turbine environment, was conducted at the University of Minnesota. A comparison with the Allison airfoil data is shown in figure 8.

TURBINE HEAT TRANSFER SUBPROJECT (1)

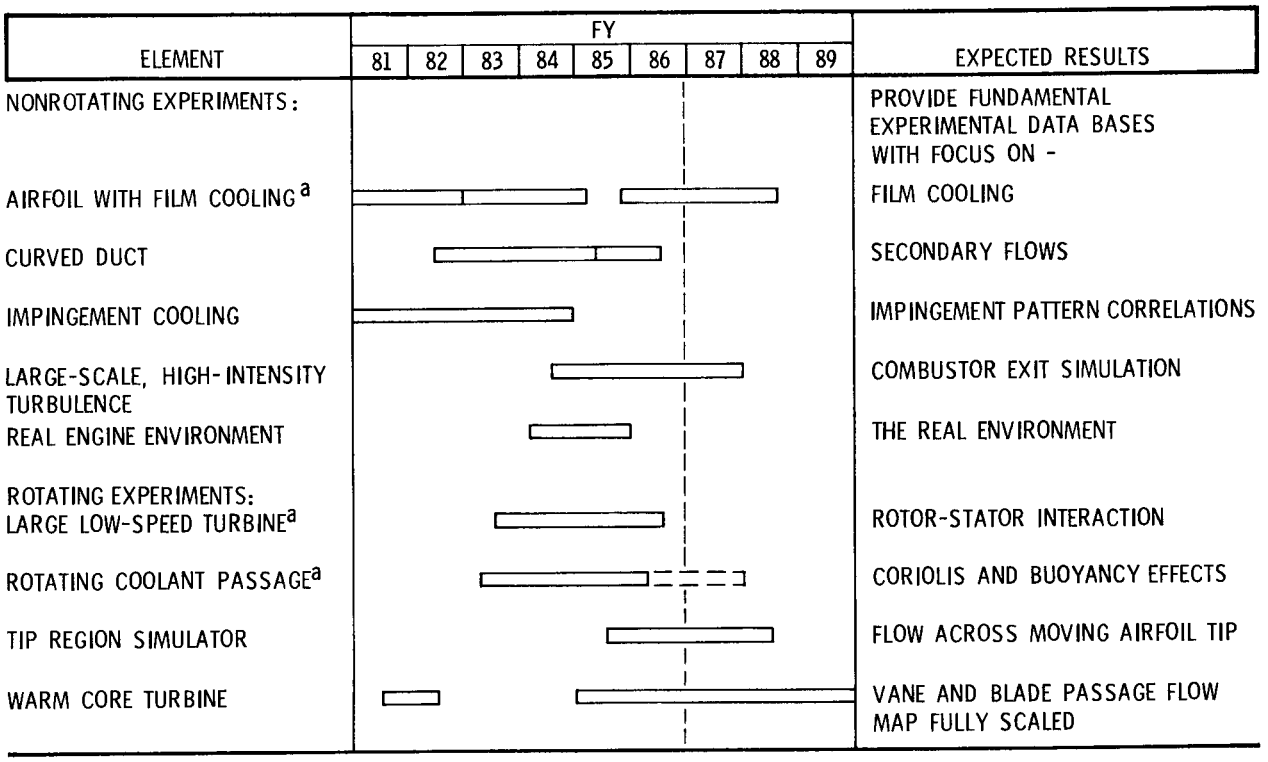

[a]EXPERIMENT AND ANALYSIS IN THE SAME CONTRACT

CD-86-21830

Figure 1

TURBINE HEAT-TRANSFER SUBPROJECT (2)

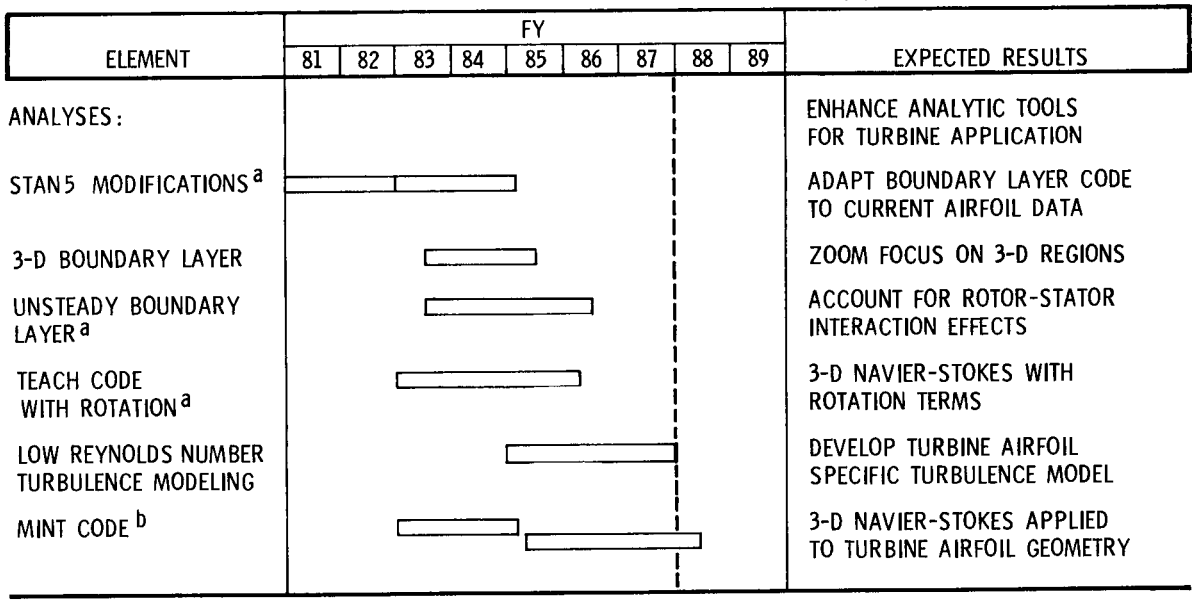

[a]EXPERIMENT AND ANALYSIS IN THE SAME CONTRACT

[b]WORK DONE UNDER TWO SEPARATE CONTRACTS

CD-86-21828

Figure 2

GAS-SIDE HEAT TRANSFER WITH LEADING EDGE FILM COOLING

NOMINAL RUN CONDITIONS
M_2 = 0.90
T_W/T_G = 0.70
Tu = 6.5

DATA	STAN5	EXIT REYNOLDS NUMBER
◆	— · —	2.49×10^6
+	- - - -	1.99×10^6
□	———	1.51×10^6

CASCADE TEST FACILITY

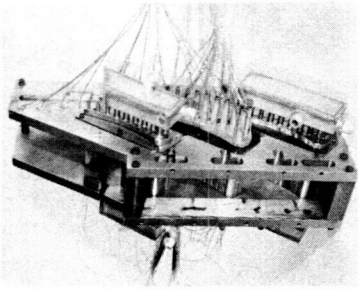

HEAT TRANSFER COEFFICIENT, H/H_0

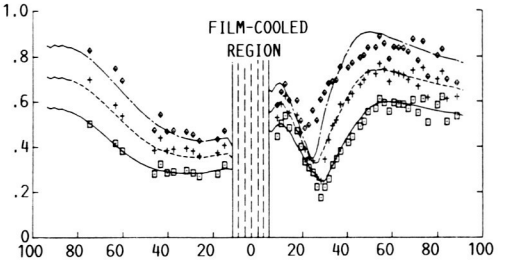

EXPERIMENTAL/ANALYTICAL COMPARISON WITHOUT FILM COOLING

STANTON NUMBER REDUCTION

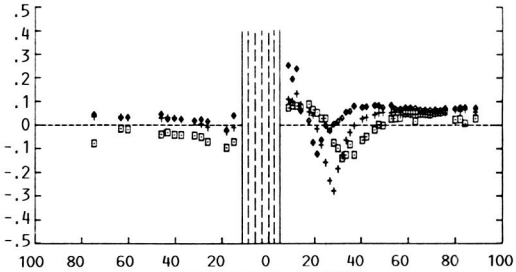

STANTON NUMBER REDUCTION WITH LEADING EDGE FILM COOLING

CD-86-21833

Figure 3

THREE-DIMENSIONAL FLOW FIELD SIMULATING TURBINE PASSAGES

CURVED-DUCT FACILITY

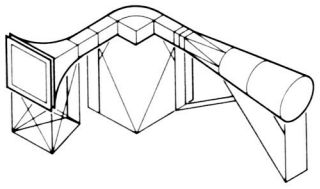

3-D LV OPTICAL SYSTEM

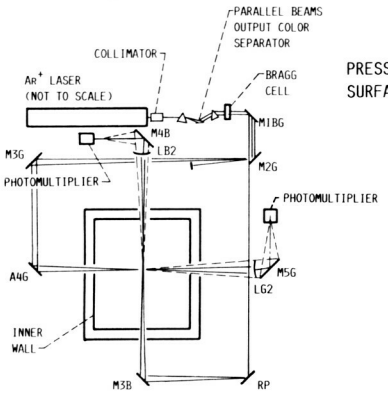

CROSSFLOW VELOCITY AT 60°

EXPERIMENTAL-ANALYTICAL COMPARISON

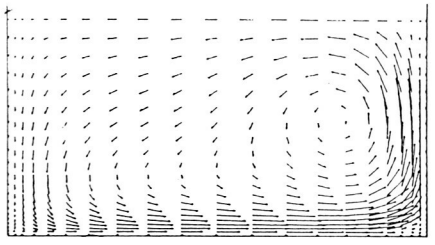

PRESSURE SURFACE

P.D. THOMAS CODE RESULTS

SUCTION SURFACE

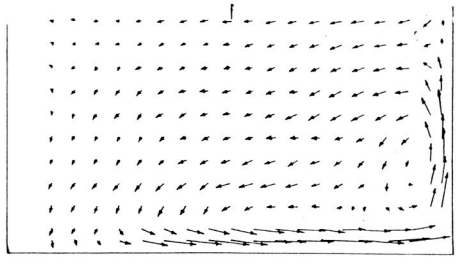

LOW REYNOLDS NUMBER DATA

CD-86-21829

Figure 4

FIRST STATOR AND ROTOR

HIGH REYNOLD's NUMBER; 65-PERCENT GAP; $C_x/U_m = 0.78$

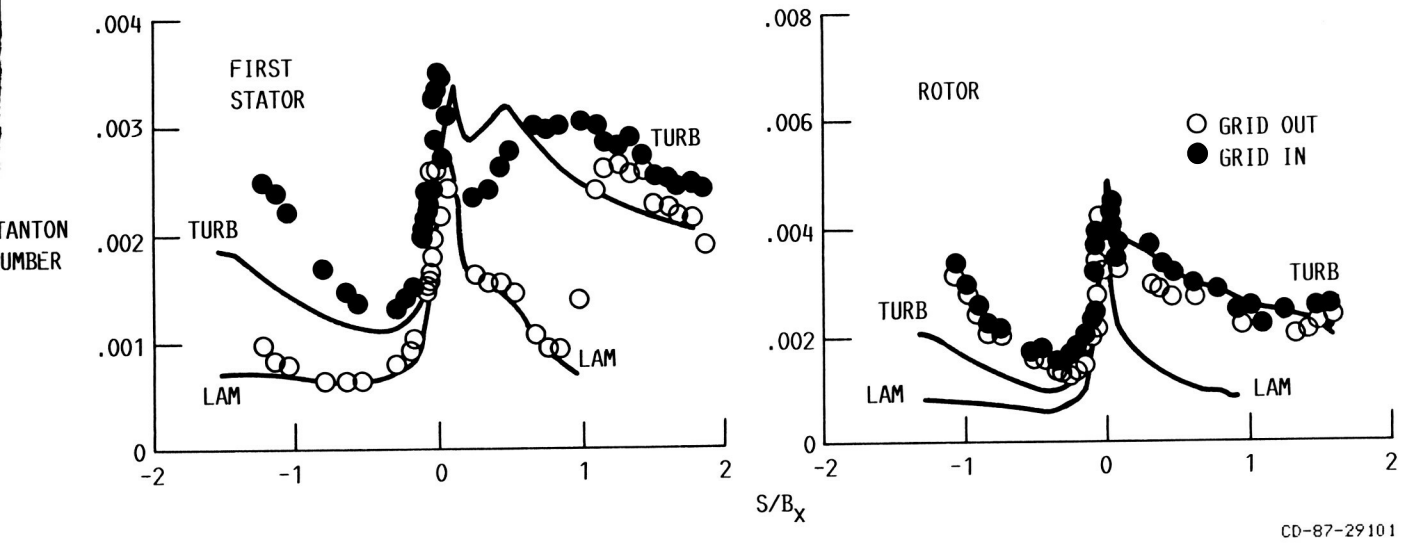

Figure 5

EFFECT OF ROTATION ON COOLANT PASSAGE HEAT TRANSFER

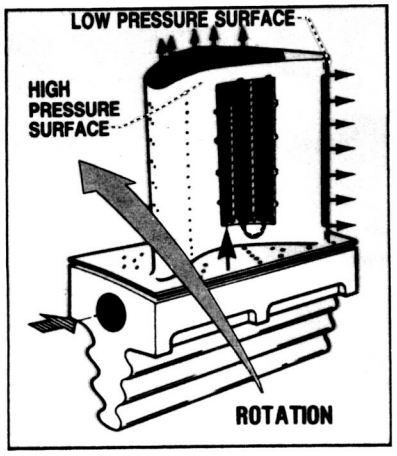

CD-86-21831

HEAT TRANSFER IN MULTIPASS GEOMETRIES IS ALREADY VERY COMPLEX. ROTATION INTRODUCES ADDITIONAL FIRST-ORDER EFFECTS WHICH MUST BE CORRECTLY UNDERSTOOD AND MODELED

HEAT TRANSFER IN SMOOTH-WALLED TEST MODEL

RADIALLY OUTWARD FLOW, FIRST LEG; Re ≈ 25,000; Δ T = 80°F

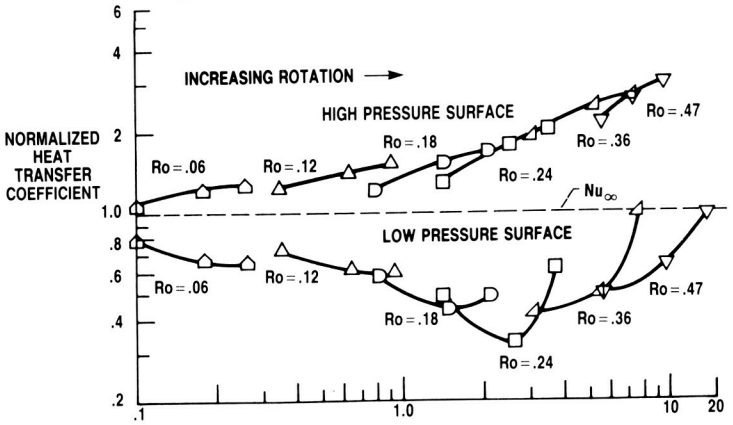

Figure 6

CALCULATION OF AIRFOIL HEAT TRANSFER USING A FULL NAVIER-STOKES CODE

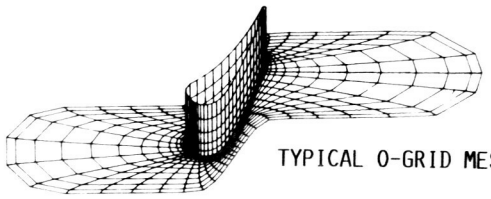

TYPICAL O-GRID MESH

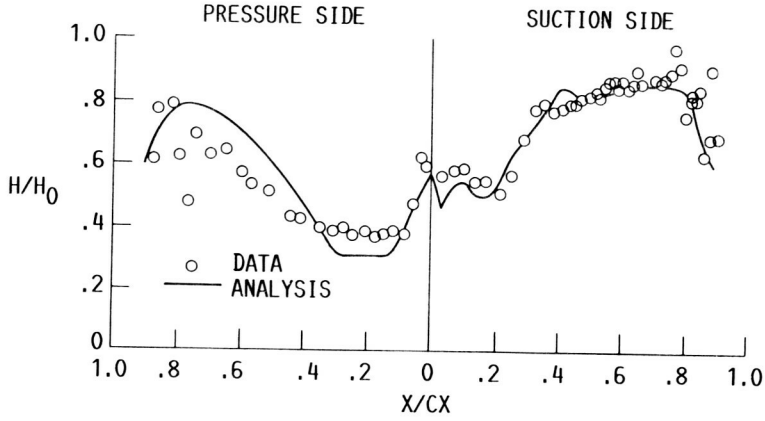

CD-86-21832

AIRFOIL HEAT TRANSFER

Figure 7

GAS-SIDE HEAT TRANSFER COEFFICIENT ANALYTICAL/EXPERIMENTAL

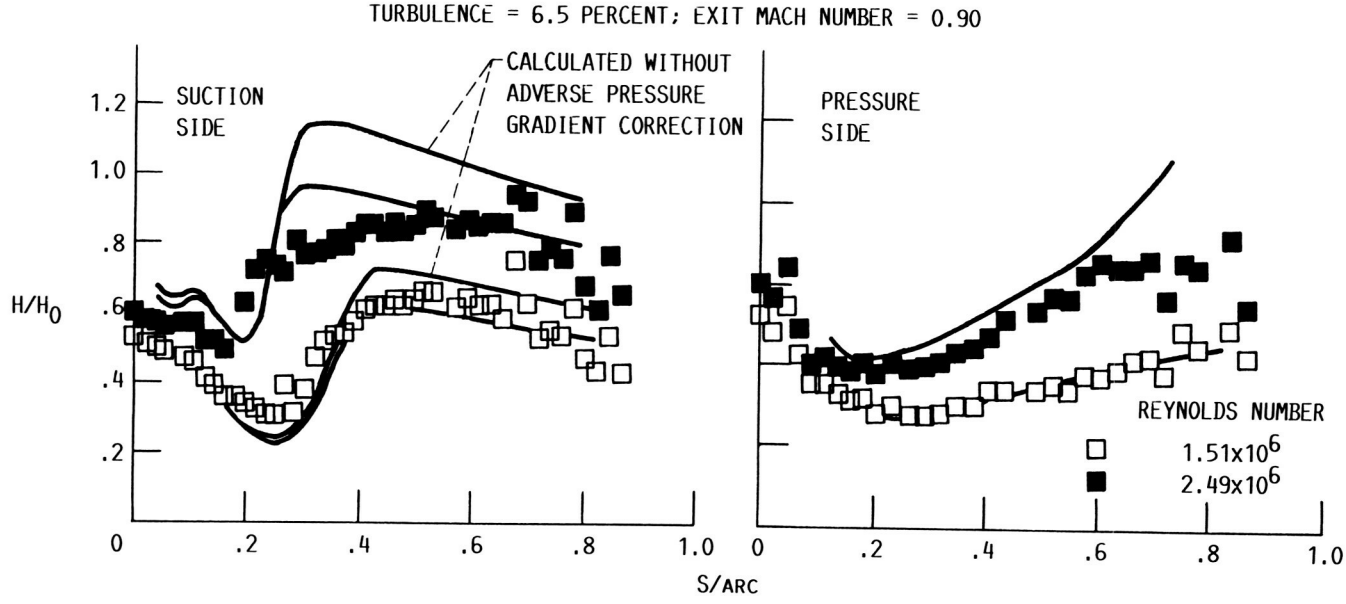

CD-87-29102

Figure 8

HOST STRUCTURAL ANALYSIS PROGRAM OVERVIEW

R.L. Thompson
NASA Lewis Research Center
Cleveland, Ohio

Hot-section components of aircraft gas-turbine engines are subjected to severe thermal-structural loading conditions, especially during the startup and takeoff portions of the engine cycle. The most severe and damaging stresses and strains are those induced by the steep thermal gradients induced during the startup transient. These transient stresses and strains are also the most difficult to predict, in part because the temperature gradient and distributions are not well known or readily predictable and, in part, because the cyclic elastic-viscoplastic behavior of the materials at these extremes of temperature and strain are not well known or readily predictable.

A broad spectrum of structures-related technology programs is underway at NASA Lewis to address these deficiencies at the basic as well as the applied level, with participation by industry and universities, as well as in-house. The three key elements in these programs are constitutive modeling, experiments, and computations. The program and its elements are shown in figures 1 and 2. Figure 3 shows the hot-section components to be analyzed.

The first element of the structures program is the development of constitutive models and their implementations in structural analysis codes. Viscoplastic constitutive modeling methods are being developed for both isotropic and anisotropic materials to improve the stress-strain prediction of material subjected to thermomechanical loads. The models are incorporated in nonlinear, finite-element structural analysis computer programs for analysis of combustor liners and turbine blades and vanes. Research programs in this element are summarized in figures 4 to 7.

The second element of the structures program is experimentation for calibration and verification purposes. Experimental facilities to aid in developing and verifying theories and models as well as to aid in evaluating advanced instrumentation have been constructed at Lewis. These include the high-temperature structures laboratory for testing tubular specimens and structural component response test facility for testing plates, cylinders, and combustor liner segments. Large quality data bases have been generated in both test facilities. Advanced strain measurement systems have also been evaluated. Research programs in this element are summarized in figures 8 to 16.

Computations are the third element of the structures program. This effort focuses on the developing improved time-varying thermal-mechanical load models for the entire engine mission cycle from startup to shutdown. The thermal model refinements are consistent with those required by the structural code, including considerations of mesh-point density, strain concentrations, and thermal gradients. Models have been developed for the engine hot-section components namely, the burner liner, turbine vane, and turbine blade. An automated component-specific geometric modeling capability, which will produce three-dimensional finite-element models of the components, is another part of this element. Self-adaptive solution strategies

have been developed and included to facilitate the selection of appropriate elements, mesh sizes, etc. The development of new and improved, nonlinear, three-dimensional finite elements and associated structural analysis programs, including the development of temporal elements with time-dependent properties to account for creep effects in the materials and components, is another major part of this element. Figure 17 to 23 summarize the programs in this element.

Further explanation and details about three elements in the structures program mentioned above are given in the Structural Analysis section of this publication.

STRUCTURAL ANALYSIS...IT'S ROLE IN HOST

GOAL:

TO DEVELOP AND VALIDATE TIME-VARYING INTEGRATED TIME-VARYING THERMAL/MECHANICAL LOAD MODELS, COMPONENT-SPECIFIC AUTOMATED GEOMETRIC MODELING AND SOLUTION STRATEGY CAPABILITIES, AND ADVANCED INELASTIC ANALYSIS METHODS AND CONSTITUTIVE MODELS, INCLUDING PLASTICITY AND CREEP EFFECTS, FOR NONLINEAR, ANISOTROPIC, FINITE-ELEMENT STRUCTURAL ANALYSIS AND DESIGN COMPUTER CODES.

PROGRAM INTEGRATION

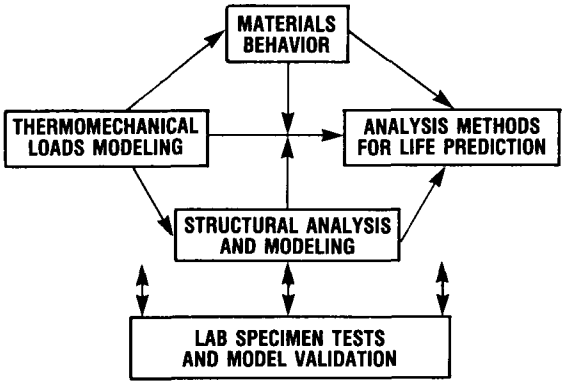

PROGRAM ELEMENTS

- **CONSTITUTIVE MODELING**
- **EXPERIMENTATION:**
  - **STRUCTURAL COMPONENT REPONSE RIG**
  - **HIGH-TEMPERATURE STRUCTURES LABORATORY**
- **COMPUTATIONS:**
  - **THERMAL/STRUCTURAL DATA TRANSFER MODULE**
  - **THERMAL/MECHANICAL LOAD/MISSION AND COMPONENT-SPECIFIC STRUCTURAL MODELS**
  - **THREE-DIMENSIONAL INELASTIC ANALYSIS METHODS**

CD-87-29215

Figure 1

STRUCTURAL ANALYSIS

PROGRAM ELEMENT	FISCAL YEAR 82	83	84	85	86	87	EXPECTED RESULT
THERMAL DATA TRANSFER	(C)						COMPUTER MODULE LINKING THERMAL AND STRUCTURAL ANALYSES
COMPONENT SPECIFIC MODELING		(C)			▼		COMPONENT-RELATED, TIME VARYING, THERMAL-MECHANICAL LOAD HISTORY AND GEOMETRIC MODELS
THREE-DIMENSIONAL INELASTIC ANALYSIS		(C)		▼			ADVANCED THREE-DIMENSIONAL INELASTIC STRUCTURAL STRESS ANALYSIS METHODS AND SOLUTION STRATEGIES
ISOTROPIC MODEL DEVELOPMENT		(C)					CYCLIC STRUCTURAL ANALYSIS
STRUCTURAL COMPONENT RESPONSE		(IH)					BURNER STRUCTURAL LIFE EXPERIMENTS
HIGH-TEMPERATURE STRUCTURES LAB			(IH)				INTEGRATED EXPERIMENTAL AND ANALYTICAL RESEARCH
MATERIAL BEHAVIOR TECHNOLOGY		(IH and G)					CONSTITUTIVE THEORY AND MODELING METHODS

CD-87-29221

Figure 2

HOT-SECTION COMPONENTS REQUIRING THREE-DIMENSIONAL INELASTIC ANALYSIS

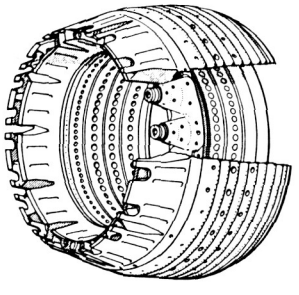

COMBUSTOR LINER

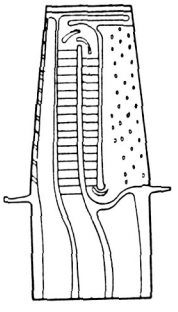

TURBINE BLADE

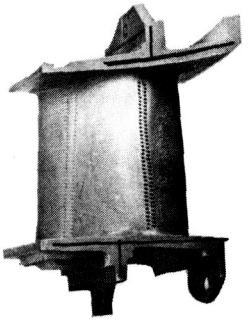

TURBINE VANE

CD-87-29209

Figure 3

BIAXIAL CONSTITUTIVE EQUATION DEVELOPMENT FOR SINGLE CRYSTALS

OBJECTIVE:
DEVELOP AND VERIFY NEW TYPES OF CONSTITUTIVE MODELS IN MULTIAXIAL FORM FOR A REALISTIC AIRCRAFT ENGINE SINGLE CRYSTAL ALLOY.

GRANT (LEWIS/WPAFB):
UNIVERSITY OF CONNECTICUT (NAG3-512).

ACCOMPLISHMENTS:
ANISOTROPIC CONSTITUTIVE MODELS FOR PWA 1480 HAVE BEEN DEVELOPED AND INCORPORATED IN A FINITE-ELEMENT CODE.

A HIGH-TEMPERATURE BIAXIAL COMPUTER CONTROLLED TEST CAPABILITY EXISTS AT THE UNIVERSITY OF CONNECTICUT.

A DATA BASE ON PWA 1480 HAS BEEN GENERATED.

HIGH-TEMPERATURE BIAXIAL VERIFICATION TESTS ARE CONTINUING.

CD-87-29218

Figure 4

CONSTITUTIVE MODELING OF INELASTIC ANISOTROPIC MATERIAL RESPONSES

OBJECTVE:
DEVELOP A WORKABLE CONSTITUTIVE MODEL THAT PREDICTS THE INELASTIC STRUCTURAL RESPONSES OF SINGLE-CRYSTAL ALLOYS USED IN GAS TURBINE ENGINE BLADES AND VANES.

GRANT (LEWIS/WPAFB):
UNIVERSITY OF CINCINNATI (NAG3-511).

ACCOMPLISHMENTS:
- AN ANISOTROPIC CONSTITUTIVE MODEL FOR RENÉ N4 HAS BEEN DEVELOPED AND INCORPORATED IN A FINITE-ELEMENT CODE.
- A CODE TO DETERMINE THE MATERIAL CONSTANTS FROM EXPERIMENTAL DATA HAS BEEN DEVELOPED.
- A HIGH-TEMPERATURE UNIAXIAL COMPUTER CONTROLLED TEST CAPABILITY EXISTS AT THE UNIVERSITY OF CINCINNATI.
- A LARGE QUALITY DATA BASE FOR RENÉ N4 AT TEMPERATURES OF 1400, 1600, AND 1800 °F HAS BEEN GENERATED.
- A CONSTITUTIVE MODEL CODE HAS BEEN DELIVERED TO LEWIS.

CD-87-29216

Figure 5

CONTINUUM DEFORMATION THEORY FOR METAL-MATRIX COMPOSITES AT HIGH TEMPERATURE

OBJECTIVE:
DEVELOP A CONTINUUM THEORY THAT REPRESENTS THE HIGH-TEMPERATURE, TIME-DEPENDENT, HEREDITARY DEFORMATION BEHAVIOR OF METALLIC COMPOSITES USED IN GAS TURBINE ENGINE APPLICATIONS.

GRANT:
UNIVERSITY OF AKRON (NAG3-3179).

ACCOMPLISHMENTS:

- **DEVELOPED A CONSTITUTIVE MODEL BASED ON A DISSIPATION POTENTIAL FOR A TWO-CONSTITUENT (FIBER/MATRIX), PSUEDOHOMOGENEOUS COMPOSITE MATERIAL.**
- **IMPLEMENTED THEORY IN TWO FINITE-ELEMENT STRUCTURAL ANALYSIS CODES.**

CD-87-29214

Figure 6

CONSTITUTIVE MODELING FOR ISOTROPIC MATERIALS

OBJECTIVE:
TO DEVELOP A UNIFIED CONSTITUTIVE MODEL FOR FINITE-ELEMENT STRUCTURAL ANALYSES OF TURBINE-ENGINE HOT-SECTION COMPONENTS, PARTICULARLY CAST NICKEL-BASE ALLOYS FOR AIR-COOLED TURBINE BLADES AND VANES.

CONTRACTOR:
SOUTHWEST RESEARCH INSTITUTE (NAS3-23925).

ACCOMPLISHMENTS:

- DATA BASES OF CYCLIC UNIAXIAL AND MULTIAXIAL BEHAVIOR HAVE BEEN OBTAINED FOR A BASE MATERIAL (B-1900) AND AN ALTERNATE MATERIAL (MAR M247).
- EFFICIENT METHODS FOR OBTAINING MODEL CONSTANTS HAVE BEEN DEVELOPED.
- UPDATED VERSIONS OF THE BODNER AND WALKER MODELS, WITH COMPATIBLE NUMERICAL INTEGRATION SCHEMES WERE INCORPORATED IN THE MARC CODE.
- THESE WERE EXERCISED IN SIMULATIONS OF A LARGE NUMBER OF CYCLIC TESTS WITH GENERALLY GOOD RESULTS.

CD-87-29206

Figure 7

MULTIAXIAL TEST PROGRAM TO DETERMINE SURFACES OF CONSTANT INELASTIC STRAIN RATE AT ELEVATED TEMPERATURE

OBJECTIVE:
PROVIDE HIGH-TEMPERATURE BIAXIAL EXPERIMENTAL DATA TO ASSIST IN THE FORMULATION OF NONLINEAR CONSTITUTIVE MODELS FOR STRUCTURAL ALLOYS USED IN TURBINE ENGINE HOT-SECTION COMPONENTS.

INTERAGENCY AGREEMENT:
OAK RIDGE NATIONAL LABORATORY.

ACCOMPLISHMENTS:

- COMPUTER-CONTROLLED BIAXIAL (TENSION/TORSION) TESTS AT A TEMPERATURE OF 650 ^{0}C ON A REFERENCE HEAT OF TYPE 316 STAINLESS STEEL HAVE BEEN CONDUCTED.
- SURFACES OF CONSTANT INELASTIC STRAIN RATE HAVE BEEN GENERATED.
- SOFTWARE FOR STORAGE, TRANSFER, REDUCTION, AND ANALYSIS OF DATA HAS BEEN DEVELOPED.

CD-87-29217

Figure 8

HIGH-TEMPERATURE STRUCTURES LABORATORY

OBJECTIVE:

PROVIDE HIGH-TEMPERATURE UNIAXIAL AND BIAXIAL EXPERIMENTAL DATA ON CYLINDRICAL SPECIMENS TO ASSIST IN THE FORMULATION, DEVELOPMENT, AND VERIFICATION OF NEW AND IMPROVED ISOTROPIC AND ANISOTROPIC CONSTITUTIVE MODELS, AND TO EVALUATE ADVANCED INSTRUMENTATION.

IN HOUSE

ACCOMPLISHMENTS:

- LARGE QUALITY UNIAXIAL DATA BASE FOR HASTELLOY-X UNDER BOTH CYCLIC ISOTHERMAL AND NONISOTHERMAL TEST CONDITIONS HAS BEEN GENERATED.
- SOFTWARE FOR DETAILED ANALYSIS OF DATA HAS BEEN DEVELOPED.
- COMPUTER-CONTROLLED UNIAXIAL TEST MACHINES FOR HIGH-TEMPERATURE TESTING ARE OPERATIONAL.
- THERMOMECHANICAL DATA BASE FOR HAYNES-188 HAS BEEN GENERATED.
- A FY88 CoF FOR LAB ADDITION HAS BEEN APPROVED

CD-87-29201

Figure 9

HIGH-TEMPERATURE FATIGUE & STRUCTURES LABORATORY

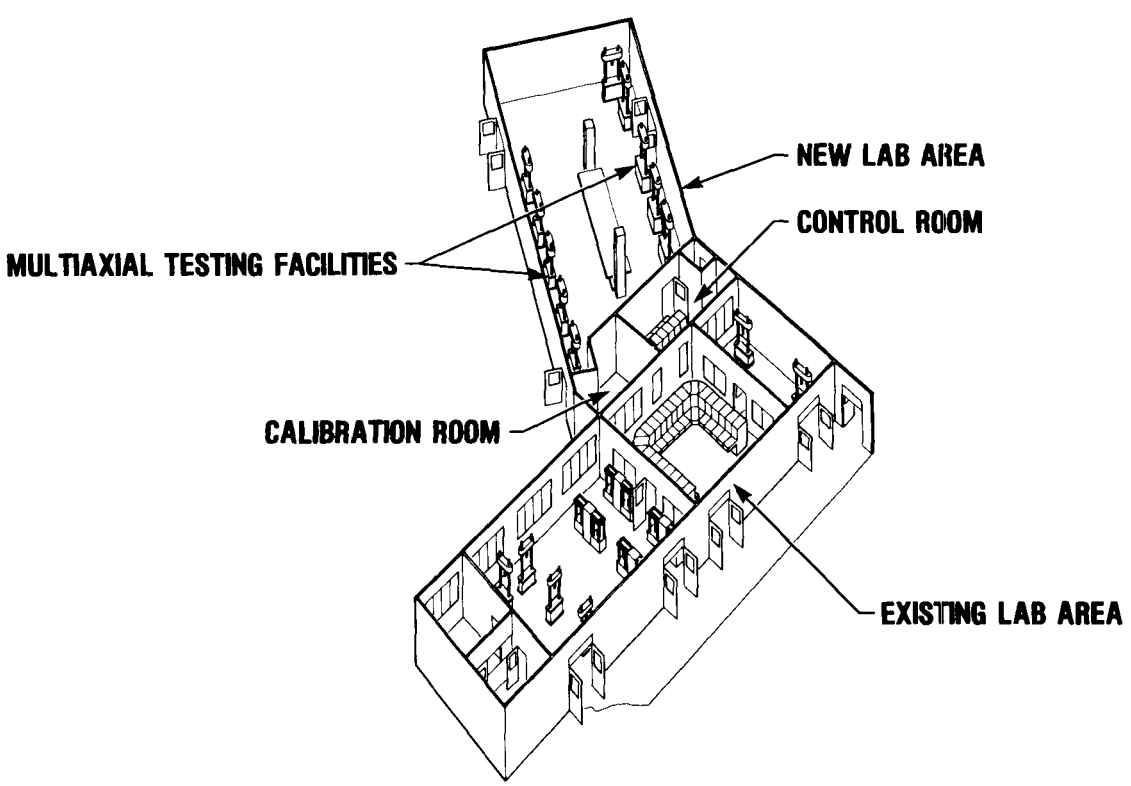

CD-87-29220

Figure 10

BENCH-TOP RIG

OBJECTIVE:

PROVIDE HIGH-TEMPERATURE EXPERIMENTAL DATA ON FLAT PLATES TO ASSIST IN THE DEVELOPMENT AND VERIFICATION OF NEW AND IMPROVED STRUCTURAL ANALYSIS AND LIFE-PREDICTION TOOLS AND TO EVALUATE ADVANCED INSTRUMENTATION.

IN HOUSE

ACCOMPLISHMENTS:

- TEST RIG IS A VIABLE STRUCTURAL COMPONENT EXPERIMENTAL TOOL.
- INFRARED THERMOVISION SYSTEM HAS PROVIDED TEMPERATURE MAPS OF COOL SURFACE OF TEST PLATE.
- A UTRC LASER SPECKLEGRAM SYSTEM TO MEASURE STRAINS WAS EVALUATED. A HIGH-RESOLUTION CAMERA SYSTEM TO MEASURE DISPLACEMENTS WAS EVALUATED.
- THERMAL/STRUCTURAL ANALYSES OF PLATES HAVE BEEN PERFORMED.
- AN AUTOMATED DATA ACQUISITION SYSTEM TO STORE, REDUCE, AND DISPLAY THE DATA WAS DEVELOPED.

CD-87-29202

Figure 11

BENCH-TOP RIG

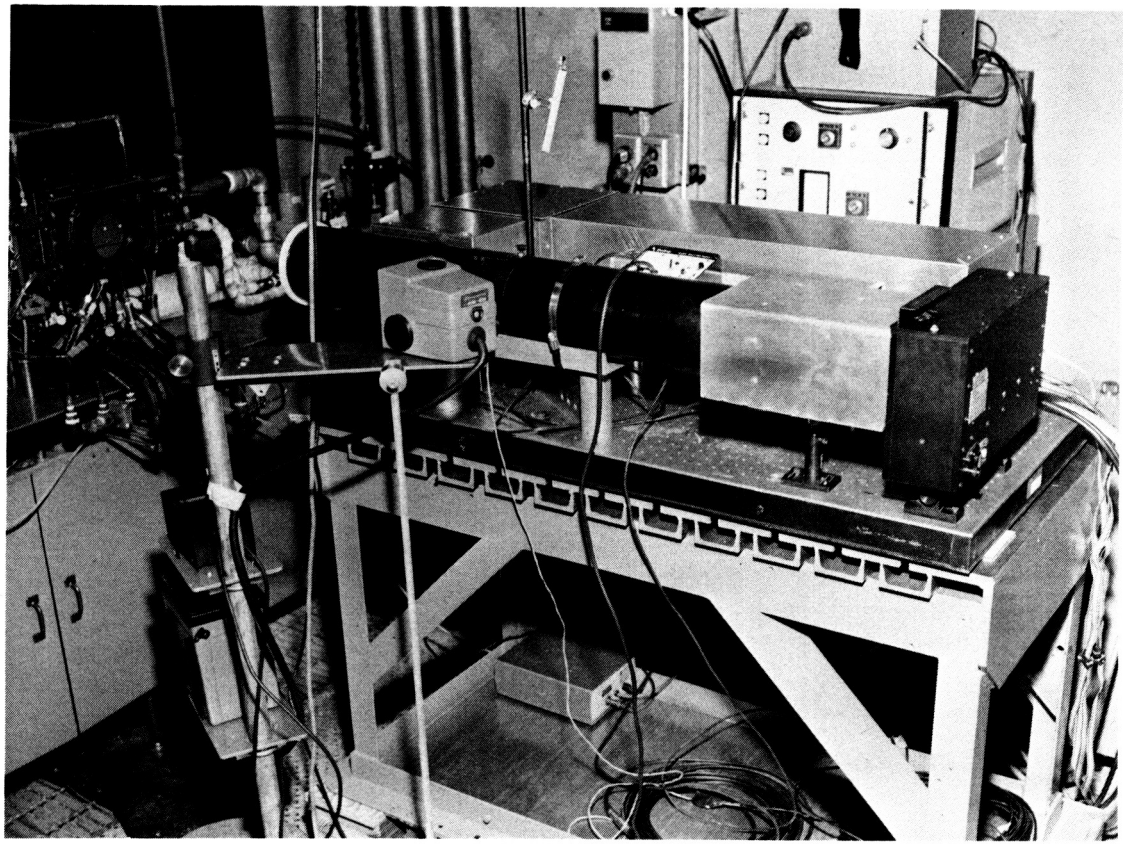

CD-87-29211

Figure 12

STRUCTURAL COMPONENT RESPONSE RIG

OBJECTIVE:

PROVIDE HIGH-TEMPERATURE EXPERIMENTAL DATA ON COMBUSTOR LINER SEGMENTS TO ASSIST IN THE DEVELOPMENT AND VERIFICATION OF NEW AND IMPROVED STRUCTURAL ANALYSIS AND LIFE-PREDICTION TOOLS, AND TO EVALUATE ADVANCED INSTRUMENTATION.

COOPERATIVE NASA LEWIS AND PRATT & WHITNEY EFFORT.

ACCOMPLISHMENTS:

- TEST RIG IS A VIABLE STRUCTURAL COMPONENT EXPERIMENTAL TOOL.
- COMPLETED TESTING OF A CONVENTIONAL COMBUSTOR LINER SEGMENT.

RESULTS:

- CONVENTIONAL LINER
  - LINER CRACKING AT A SEAM WELD WAS OBSERVED AFTER 1600 THERMAL CYCLES.
  - TESTING WAS STOPPED AFTER 1800 THERMAL CYCLES DUE TO LINER DISTORTION.
  - INCREASING MAXIMUM TEMPERATURE BY 100 ^{0}F ACCELERATED LINER DAMAGE.
  - LINER TEMPERATURES WERE REPEATABLE FROM CYCLE TO CYCLE.
  - LARGE QUALITY DATA BASE INCLUDING TEMPERATURE DISPLACEMENT MEASUREMENTS WAS OBTAINED.
  - PERFORMED THREE-DIMENSIONAL THERMAL/STRUCTURAL ANALYSIS OF THE LINER.
- ADVANCED LINER
  - INITIATED TESTING OF AN ADVANCED (PANELED) COMBUSTOR LINER CONCEPT.
  - INITIATED THREE-DIMENSIONAL THERMAL/STRUCTURAL ANALYSIS OF PANELED LINER.
  - DEVELOPED AN AUTOMATED DATA ACQUISITION SYSTEM TO STORE, REDUCE AND DISPLAY THE DATA.

Figure 13

STRUCTURAL COMPONENT REPONSE RIG

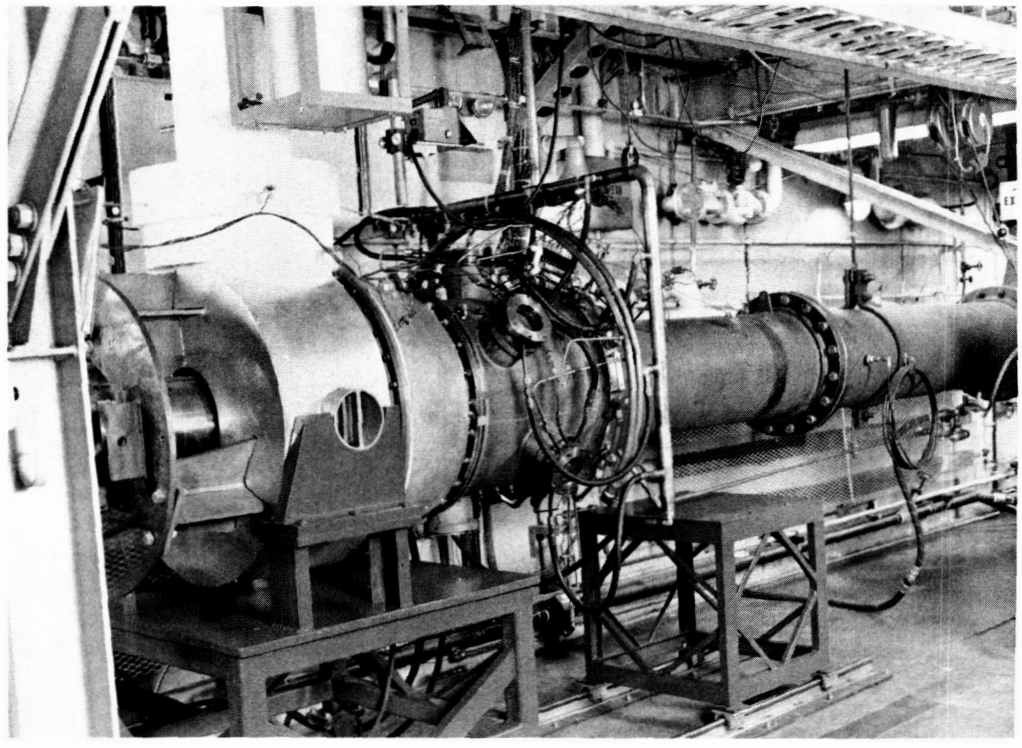

CO-87-29213

Figure 14

CONVENTIONAL COMBUSTOR TEST LINER AFTER 1280 THERMAL CYCLES

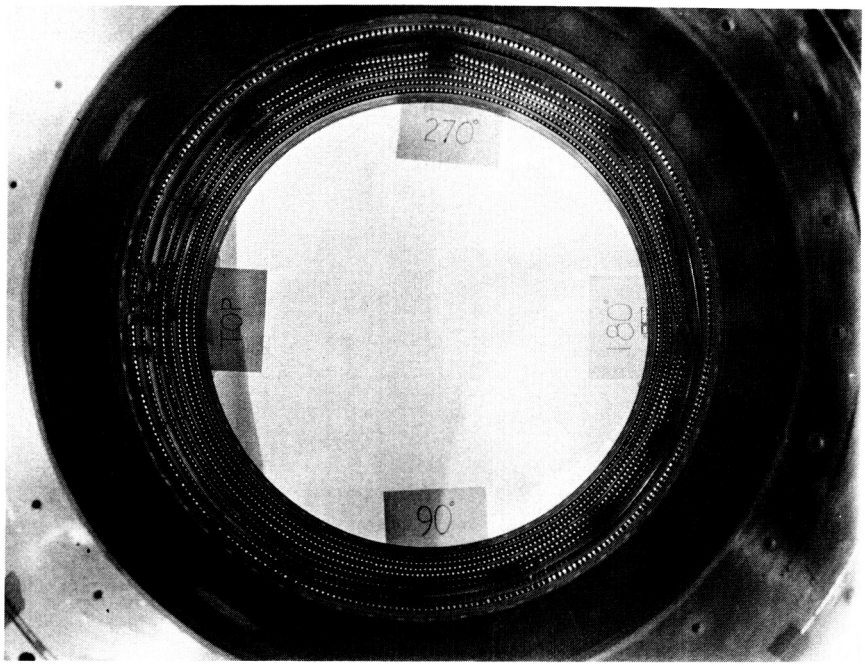

CD-87-29210

Figure 15

ADVANCED (PANELED) COMBUSTOR TEST LINER AFTER 10 THERMAL CYCLES

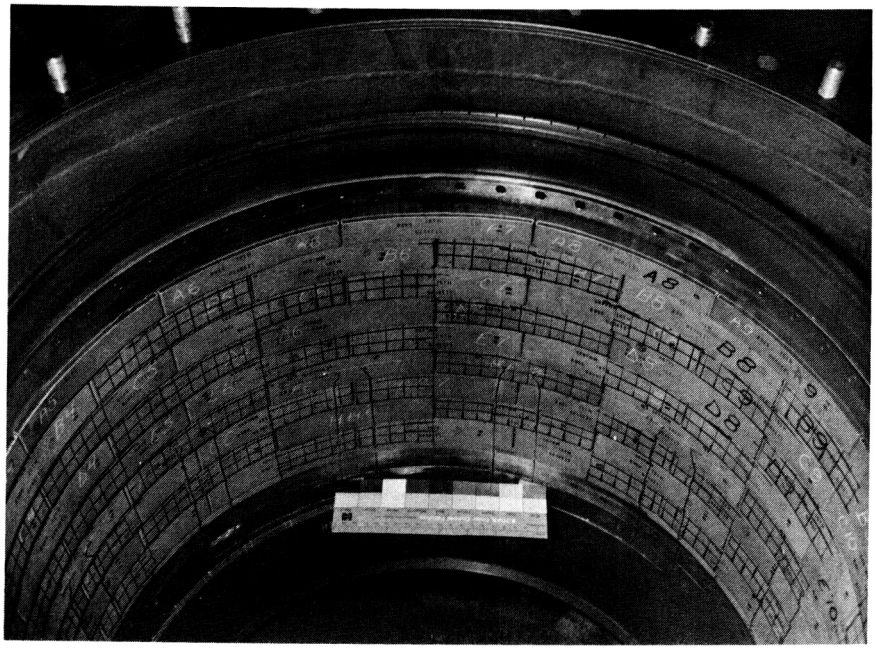

CD-87-29212

Figure 16

THERMAL/STRUCTURAL DATA TRANSFER MODULE

OBJECTIVE:

DEVELOP AN AUTOMATED PROCEDURE FOR EFFICIENT AND ACCURATE TRANSFER OF TEMPERATURES FROM A HEAT TRANSFER CODE TO A STRUCTURAL ANALYSIS CODE.

CONTRACT:

GENERAL ELECTRIC (NAS3-23272).

ACCOMPLISHMENTS:

- FEATURES AND CAPABILITIES OF CODE ARE
  MODULAR, USER FRIENDLY, DIFFERENT THREE-DIMENSIONAL MESH DENSITIES, BOTH FINITE-ELEMENT AND FINITE-DIFFERENCE HEAT TRANSFER CODES, EFFICIENT THREE-DIMENSIONAL SEARCH AND WEIGHTING ROUTINES, HARD-WIRED THERMAL AND STRUCTURAL CODES, FILES TO EASILY ACCESS OTHER CODES WINDOWING, ALIGNMENT OF HEAT TRANSFER AND STRESS MODES, EXTERIOR STRESS POINT BY AN OUTSIDE HEAT TRANSFER MODEL, AND ABILITY TO SELECT A TIME SLIP FROM A LARGE TRANSIENT THERMAL ANALYSIS.
- OVER 30 USERS HAVE A COPY OF THE CODE.
- CODE HAS BEEN SENT TO COSMIC.

CD-87-29204

Figure 17

PROGRAM SCHEMATIC FOR THREE-DIMENSIONAL TRANCITS

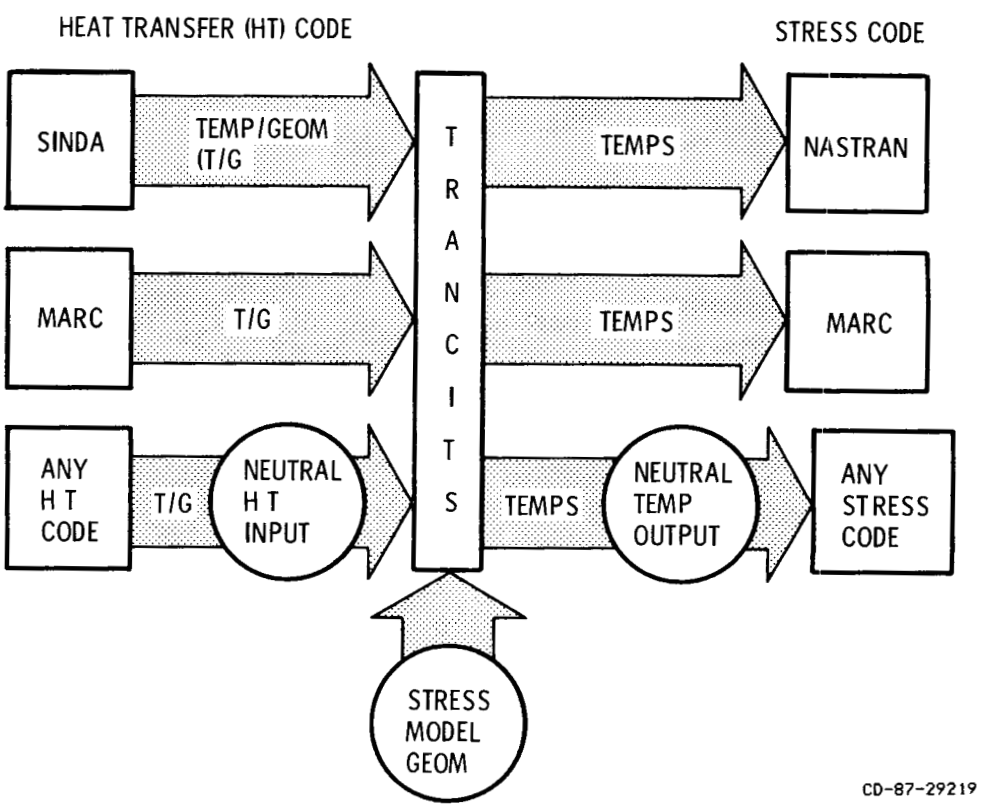

CD-87-29219

Figure 18

COMPONENT—SPECIFIC MODELING (COSMO)

OBJECTIVE:
DEVELOP/VERIFY INTERDISCIPLINARY MODELING ANALYSIS METHODS AND REQUISITE COMPUTER CODES STREAMLINED FOR THREE HOT-SECTION COMPONENTS.

CONTRACTOR:
GENERAL ELECTRIC BUSINESS GROUP (NAS3-23687).

ACCOMPLISHMENTS:
- AVAILABLE METHODS FOR GAS DYNAMICS, HEAT TRANSFER, AND THREE-DIMENSIONAL INELASTIC MATERIAL BEHAVIOR INCORPORATED IN CODE.
- MODIFIED ANALYSES AND MODELING TECHNIQUES REQUIRED TO COMPUTATIONALLY VALIDATE HOT-SECTION COMPONENT DESIGNS.
- EXTENDED AND INTEGRATED ANALYSES AND TECHNIQUES IN A MODULAR COMPUTER CODE (COSMO).
- THERMODYNAMIC, THERMOCHEMICAL LOAD TRANSFER, AND EXECUTIVE MODULES ARE OPERATIONAL ON THE LEWIS CRAY COMPUTER.

CD-87-29205

Figure 19

COMPONENT—SPECIFIC MODELING (HOST)

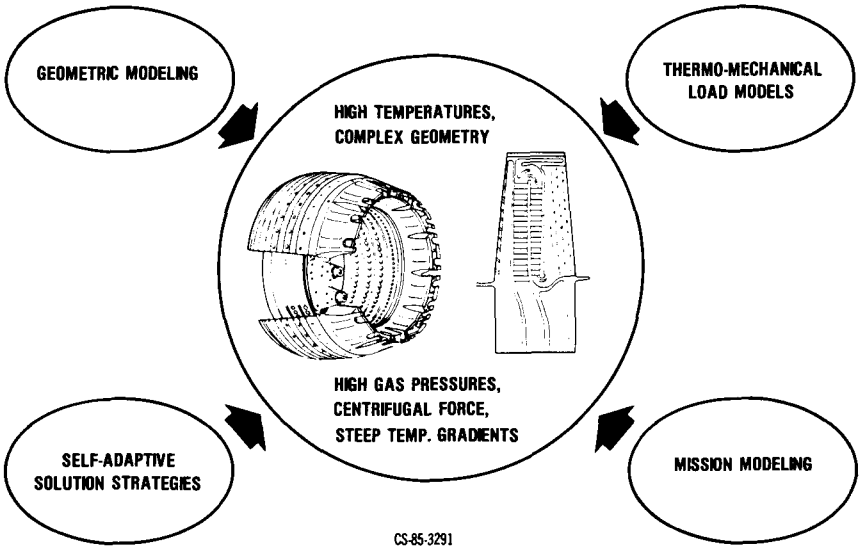

Figure 20

THREE-DIMENSIONAL INELASTIC ANALYSIS METHODS FOR HOT-SECTION COMPONENTS–I

OBJECTIVE:
DEVELOP NEW ANALYTICAL METHODS THAT PERMIT MORE ACCURATE AND EFFICIENT STRUCTURAL ANALYSIS FOR COMBUSTER LINERS, TURBINE BLADES AND VANES.

CONTRACTOR:
PRATT & WHITNEY.

ACCOMPLISHMENTS:
DEVELOPED A SERIES OF NEW COMPUTER CODES THAT EMBODY PROGRESSIVELY MORE SOPHISTICATED ANALYSIS CAPABILITIES BASED ON
- AN APPROXIMATE MECHANICS OF MATERIALS FORMULATION (MOMM)
- A STATE-OF-THE-ART, SPECIAL FINITE-ELEMENT FORMULATION (MHOST)
- AN ADVANCED TECHNOLOGY BOUNDARY-ELEMENT FORMULATION (BEST3D)

CD-87-29207

Figure 21

3-D INELASTIC ANALYSIS (HOST)

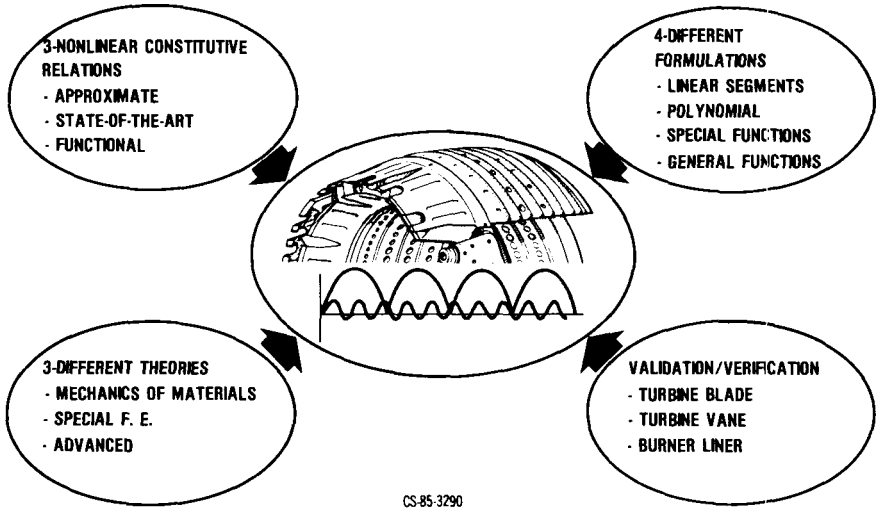

Figure 22

THREE-DIMENSIONAL INELASTIC ANALYSIS METHODS FOR HOT SECTION COMPONENTS-II

OBJECTIVE:

DEVELOP IMPROVED ANALYSIS TOOLS THAT ALLOW MORE ACCURATE AND EFFICIENT CHARACTERIZATION OF THE CYCLIC TIME-DEPENDENT PLASTICITY OCCURRING IN HOT-SECTION COMPONENTS.

CONTRACTOR:

GENERAL ELECTRIC.

DEVELOPED A MATRIX OF FINITE-ELEMENT-BASED CODES WITH VARYING SOPHISITICATION RELATIVE TO

- ELEMENT TYPE FORMULATION
- MATERIAL CONSTITUTIVE MODEL REPRESENTATION SHARING A COMMON EMPHASIS ON EFFICIENT SOLUTION ALGORITHMS

CD-87-29208

Figure 23

FATIGUE AND FRACTURE OVERVIEW

Gary R. Halford
NASA Lewis Research Center
Cleveland, Ohio

The programs in the fatigue and fracture area of the HOST Project have produced numerous accomplishments. I will point out the major accomplishments, mention the ongoing work, and make note of any unfinished efforts. A list of the programs most recently supported under fatigue and fracture is shown in table I. There are three contractual efforts, one grant, and an in-house activity. The latter two have concluded quite successfully in the past year. The grant effort at Syracuse University with Professor Liu as principal investigator has produced 14 technical papers that have added significantly to the literature on crystallographic slip and oxidation mechanisms of high-temperature crack growth; and the world-class high-temperature fatigue and structures laboratory at Lewis is now operational, and in fact has grown to the point of requiring additional floor space.

Figure 1 summarizes the recent activities under the isotropic creep-fatigue crack initiation life-prediction program. This program has been handled by Pratt & Whitney under the able management of Mr. Richard Nelson. To date, a quite sizeable creep-fatigue crack initiation data base has been generated on the nickel-base superalloy B-1900 + Hf. A companion constitutive modeling program has generated extensive cyclic stress-strain data bases on the same heat of material. Two unified constitutive models have resulted from that work. The crack initiation results generated by Nelson have formed the basis of a new model for creep-fatigue life prediction. The term CDA (Cyclic Damage Accumulation) has been coined for the method, which is being evaluated under isothermal conditions, uniaxial conditions, multiaxial conditions, nonsteady cumulative fatigue damage loading, mean stresses, mean strains, and thermomechanical fatigue loading. Coatings and environmental conditions have also been evaluated in supporting the development of the modularly constructed CDA model. This work is described in greater depth in the Fatigue and Fracture Session by Mr. Nelson.

Figure 2 lists the modules that remain unfinished at this time. These modules eventually will be integrated into the master life-prediction model and a computer code will be written and made available to potential users. Final verification of the completed model is being accomplished through use of an alternative alloy, Inconel 718.

The isotropic high-temperature crack growth program at the General Electric Company, under the guidance of Dr. J.H. Laflen, has been relatively inactive over the past year due to funding limitations brought about by the scaling back of the HOST Project. The program is now back up to speed, and critical experiments are being conducted to test the applicability of the proposed path-independent integrals (fig. 3) for thermomechanical cycling with thermal gradients. Dr. Laflen will be making the presentation of the most recent findings. Unfinished work includes the codification of the computer analysis for predicting cyclic crack propagation under general high-temperature thermomechanical loadings.

Figure 4 summarizes the major accomplishments under the anisotropic cyclic crack initiation and constitutive modeling program at Pratt & Whitney under the direction of Mr. G.A. Swanson. Work has concentrated on developing cyclic constitutive models applicable to material response prior to crack initiation. Two workable constitutive models for single-crystal alloys have been developed and integrated into computer codes. One is based on the classical Schmid law for critical resolved shear stress and the other on the unified constitutive modeling theory of Dr. K. Walker. The anisotropic constitutive models have proven themselves to be powerful tools for the analysis of high-temperature components such as turbine blades. Verification of the models has been achieved at the laboratory specimen level. A composite computer-generated plot of a cyclic stress-strain hysteresis loop of single crystal PWA 1480 and of its PWA 286 overlay coating is shown in figure 4. Note the nominally elastic response of the PWA 1480 and the elasto-plastic-creep response of the much weaker ductile coating. Evaluation of the aluminide diffusion coating constitutive properties is proving to be a delicate experimental task. Modeling is in progress.

Currently, the crack initiation data base is being generated upon which the life-prediction method will be built. Both isothermal, low-cycle fatigue and thermo-mechanical fatigue experiments are being conducted.

A particularly striking result has been that all of the thermomechanical fatigue tests of coated PWA 1480 initiate cracks at sites where coating cracking had occurred. Four different crystal orientations are included in this data base. This cracking response is consistent with turbine airfoil experience. By contrast, many isothermally tested, non-⟨001⟩ oriented substrate specimens initiated subsurface cracks, either in the PWA 1480 or in the interfacial region between substrate and coating. This observation clearly points out the limitation of isothermal fatigue testing of complex materials systems such as coated anisotropic alloys or other composite material systems.

The life models being developed will feed into the total life equations shown in figure 5. Here, the total life is the sum of the component lives: coating cracking life N_c, the substrate crack initiation life N_{sc}, the substrate crack initiation life without coating N_{si}, and the substrate propagation life N_{sp}.

A tensile hysteretic model for computing N_c for overlay coatings is being pursued. This model is an extension of Ostergren's approach. A total strain range correlation with N_c appears to work best for the aluminide coating. Several existing life models are being explored for N_{si} and N_{sp}.

The root attachment area of single-crystal turbine blades (fig. 6) poses additional complexities that are to be addressed later in the program.

In summary, I would like to emphasize the significant accomplishments that we have enjoyed in the fatigue and fracture arena through the atmosphere created by the HOST Project. We are now much better able to deal with durability enhancement in the aeronautical proulsion industry through theoretical, analytical, and experimental approaches. Given the ability to complete the tasks we have started, we expect to reap even greater rewards in the near future.

TABLE I

FATIGUE AND FRACTURE PROGRAMS

- NAS3-23288, PRATT & WHITNEY (R.S. NELSON), LEWIS (G.R. HALFORD)
  CREEP-FATIGUE CRACK INITIATION—ISOTROPIC
- NAS3-23940, GENERAL ELECTRIC (J.H. LAFLEN), LEWIS (T.W. ORANGE)
  ELEVATED TEMPERATURE CRACK GROWTH—ISOTROPIC
- NAS3-23939, PRATT & WHITNEY (G.A. SWANSON), LEWIS (G.R. HALFORD)
  LIFE PREDICTION/CONSTITUTIVE MODELING—ANISOTROPIC
- NAG3-348, SYRACUSE UNIVERSITY (H.W. LIU), LEWIS (I.J. TELESMAN)
  CRACK GROWTH MECHANISMS—ISOTROPIC
- LEWIS,(M.A. McGAW)
  HIGH-TEMPERATURE FATIGUE AND STRUCTURES LABORATORY

} COMPLETED

CD-86-21861

CREEP-FATIGUE CRACK INITIATION—ISOTROPIC
CURRENT ACTIVITIES

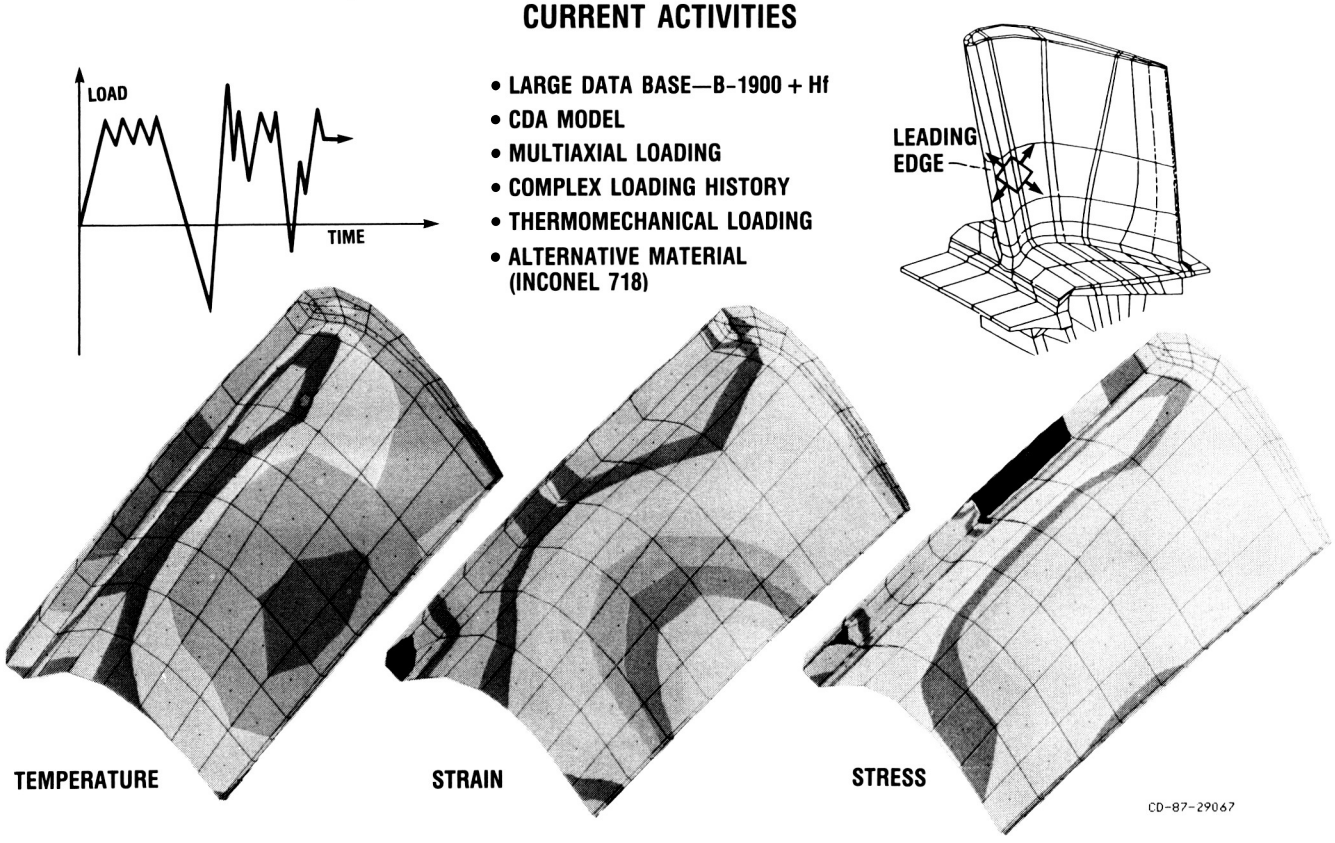

Figure 1

CREEP-FATIGUE CRACK INITIATION—ISOTROPIC
TO BE COMPLETED

- ENVIRONMENTAL MODULE
- COATINGS MODULE
- MEAN STRESS MODULE
- MODULES INTEGRATED INTO MODEL
- ALTERNATIVE ALLOY VERIFICATION
- COMPUTER CODE

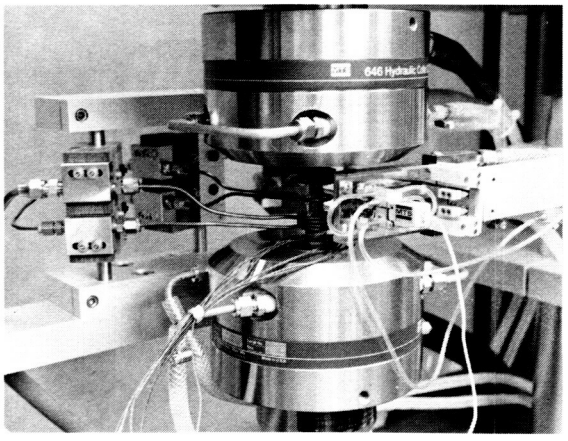

CD-87-29066

Figure 2

CYCLIC CRACK GROWTH—ISOTROPIC
CURRENT ACTIVITIES

- PATH-INDEPENDENT INTEGRALS (J_x) IDENTIFIED
- NONISOTHERMAL VERIFICATION

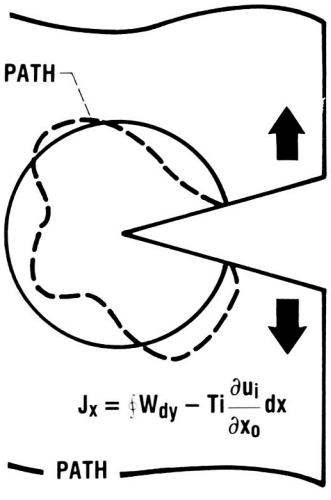

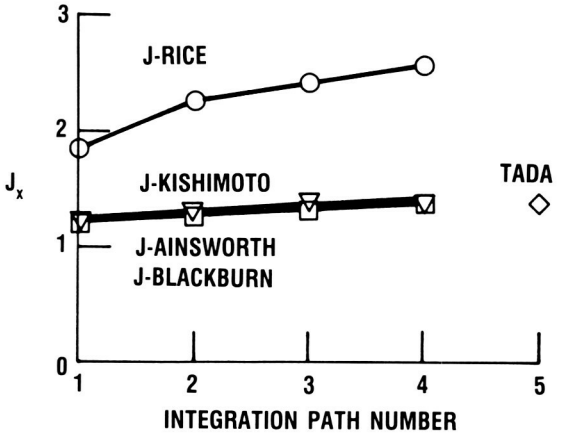

CD-87-29068

Figure 3

CONSTITUTIVE MODELING—ANISOTROPIC CURRENT ACTIVITIES

- SINGLE-CRYSTAL CONSTITUTIVE MODEL (PWA 1480)
  - — SCHMID LAW (MICROSCOPIC-CRYSTALLOGRAPHIC SLIP)
  - — WALKER THEORY (MACROSCOPIC UNIFIED MODEL)
- OVERLAY COATING CONSTITUTIVE MODEL (PWA 286)
  - — WALKER THEORY (MACROSCOPIC)
- ALUMINIDE DIFFUSION COATING (PWA 273)
  - — DELICATE EXPERIMENTS
  - — MODELING IN PROGRESS

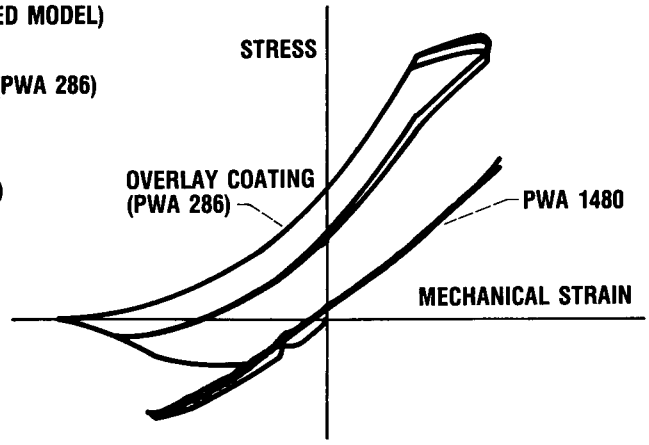

CD-86-21869

Figure 4

FATIGUE LIFE PREDICTION MODELING—ANISOTROPIC CURRENT ACTIVITIES

- PRELIMINARY LIFE MODELS

$$N_f = N_c + N_{sc} + N_{sp}$$

or $N_f = N_{si} + N_{sp}$

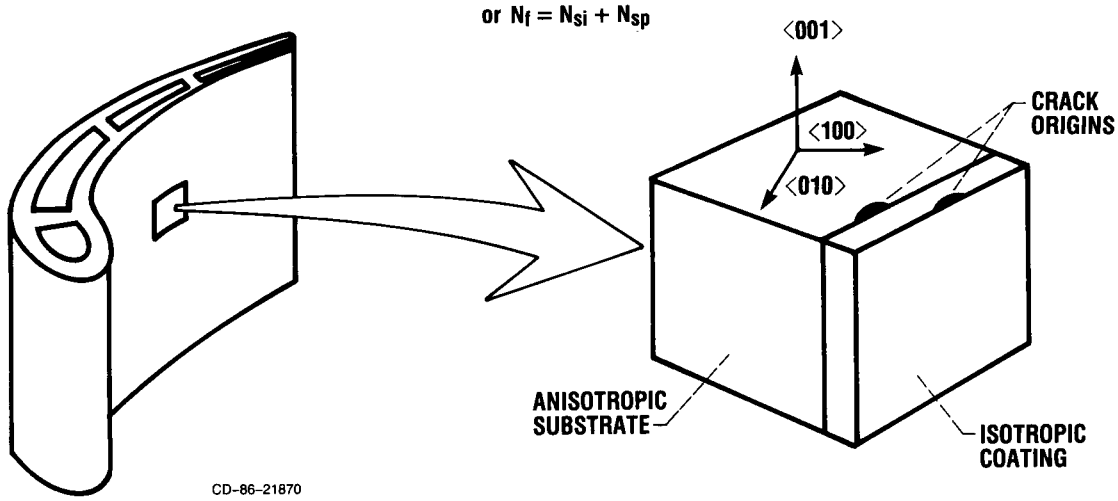

CD-86-21870

Figure 5

FATIGUE AND CONSTITUTIVE MODELING—ANISOTROPIC TO BE COMPLETED

- BLADE ATTACHMENT
- INTEGRATED LIFE MODELS

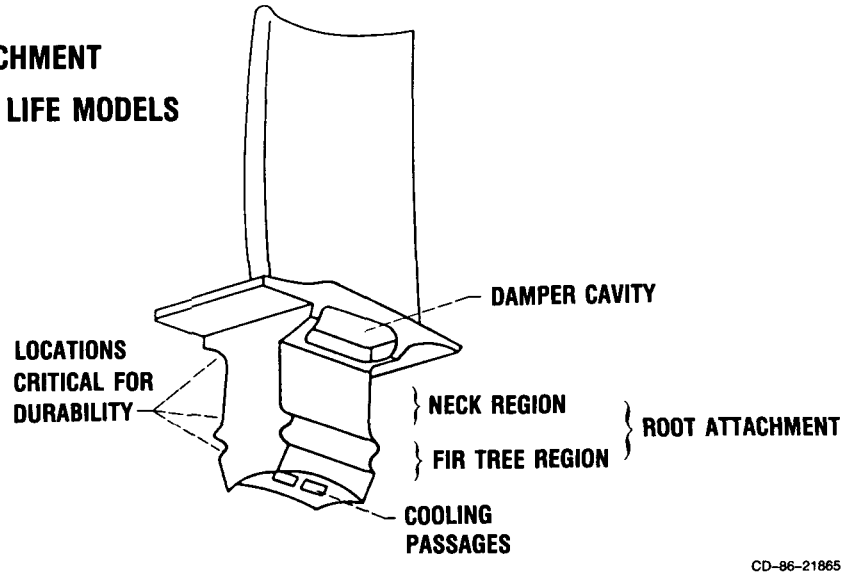

Figure 6

HOST SURFACE PROTECTION R&T OVERVIEW

Robert A. Miller
NASA Lewis Research Center
Cleveland, Ohio

Phase I of all three HOST-sponsored thermal barrier coating (TBC) life-prediction contracts was brought to a successful conclusion in the past year. This work resulted in three quite different approaches to TBC life modeling. The work also yielded improved understanding of failure mechanisms, the measurement of thermomechanical properties, and new approaches to finite element modeling. The three prime contractors involved in phase I were the General Electric Company, the Garrett Turbine Engine Company, and Pratt & Whitney Aircraft.

Phase II has been awarded to Pratt & Whitney and a grant for complimentary modeling and properties measurement has been awarded to the Southwest Research Institute. Southwest Research Institute served as a subcontractor to Pratt & Whitney during phase I. Phase II will be devoted to understanding and modeling physical vapor-deposited thermal barrier coatings. The detailed finite element stress analyses which are being conducted at Cleveland State University (CSU) will not receive further HOST support but will continue under another funding source. The CSU work has emphasized finite element analyses that are more detailed than those generally used in industry.

The HOST TBC life-prediction program was set up to emphasize failure mechanism understanding, thermomechanical properties measurement, finite element stress-strain analyses, and design-capable life model development. This program was patterned after an earlier in-house program which emphasized understanding and life modeling.

These pre-HOST and HOST programs have led to several observations regarding coating failure. It is now believed that coatings fail as a result of near-interfacial cracking in the ceramic followed eventually by delamination. The stresses and strains leading to failure are thought to result primarily from thermal expansion mismatch between the ceramic and metallic layers - although these stresses are strongly influenced by time-at-temperature effects such as bond-coat oxidation. Finite element analyses of the stresses which develop in the ceramic were conducted by all three contractors and CSU. Although the CSU efforts were less mission oriented than the contractor efforts they did include the effects of bond-coat roughness. These calculations showed that high radial tensile stresses accompanied by compressive hoop and axial stresses develop in the ceramic just above the tips of the interfacial asperities. High tensile stresses are cause for concern because the measured tensile strength was low compared with the high compressive strain tolerance. It was also shown that the ceramic exhibits fatigue, slow crack growth, and creep.

The initial life model developed at NASA treated only oxidation and thermal expansion mismatch strains with either of two assumed relationships between oxidation and strain. The mathematical form of the model was that of a four-term

summation expression. Model parameters were either inferred from the experiment or adjusted to fit the life data. This approach was used successfully to model laboratory test lives.

The model developed by Pratt & Whitney and their subcontractor Southwest Research Institute built on and extended the NASA model. It employed an assumption of oxidation-induced strength degradation and used finite element analyses to calculate an inelastic strain range. The resulting model was able to predict the life of a bill-of-material coating system to plus or minus a factor of 3, which was considered adequate.

The Garrett approach considered three independent failure rates - for failure due to mechanical, oxidation, and salt-deposition effects. Their model includes terms for heating-cycle length, oxidation life, zirconia densification, and hot salt damage. A significant difference between the predictions from the Garrett and NASA models occurred at very low temperatures where much greater lives were predicted by the NASA model.

The General Electric approach relied on finite element analysis of the shear and normal strain ranges and then correlated these strain ranges to life. This approach was the only one to include shearing stresses. The stress exponent derived from the log strain versus log life plot was about -1.4. Interestingly, this differed greatly from the presumably related fatigue exponent measured by Pratt & Whitney and Southwest Research Institute, which was about -50.

Phase II of the HOST program will focus on electron beam - physical vapor deposited (EB-PVD) thermal barrier coatings. These coatings have a columnar rather than a splat structure and they are believed to be promising candidates for future aeronautical applications. Therefore a HOST-type of program may help to accelerate their development.

One of the primary concerns about EB-PVD coatings is that while their open structure imparts excellent strain tolerance it also allows for rapid bond-coat oxidation and, under certain conditions, hot corrosion. A columnar structure is theoretically expected to have a higher thermal conductivity than a splat structure. However, the initial conductivity value reported under phase I by Garrett has not supported this concern. These issues will be further addressed in phase II.

Although phase I has been highly successful - especially from a design point of view - an array of questions remain unanswered. Most of the questions are, in fact, very fundamental. Among these is the question of whether a plot of log life versus log temperature is concave upward, downward, or even s-shaped. An s-shaped curve would be rationalized in terms of log lives at low temperatures due to decreased oxidation and strain and downward curving at very high temperatures as new failure modes became important.

The effects of creep and inelasticity of both the ceramic and bond-coat layers are also poorly understood. In fact, there appears to be uncertainty as to whether such effects would be harmful or beneficial. In addition, the magnitude of the fatigue exponent is uncertain, and the role of shearing stresses is not well understood.

Another area of uncertainty is the mechanism by which bond-coat oxidation controls coating system life. Since oxidation is a very important step in the

overall TBC failure mechanism, our finite element analyses and life models are necessarily flawed. Furthermore, it is not known whether or not the assumption of a smooth interface, commonly employed to simplify finite element analyses, can lead to inaccurate or even misleading results. Other areas of controversy are the importance of sintering at high temperatures and of hot corrosion at relatively low temperatures.

Despite many remaining uncertainties, our knowledge of coating behavior and our ability to apply this knowledge to the design of coated components has benefited greatly from the HOST TBC efforts. Further benefits are expected from the additional work to be completed under HOST.

HOST SURFACE PROTECTION FY87 ACCOMPLISHMENTS

- COMPLETION OF PHASE-I TBC LIFE-PREDICTION PROGRAMS
  - THREE DIFFERENT LIFE MODELS
  - LIFE DATA BASE ESTABLISHED
- FAILURE MECHANISMS ELUCIDATED
  - THERMOMECHANICAL PROPERTIES MEASURED
  - FINITE ELEMENT σ/ϵ ANALYSES PERFORMED
- PHASE-II TBC LIFE PREDICTION INITIATED
- CSU/NASA DETAILED FINITE ELEMENT MODELING CONTINUES TO YIELD INSIGHTS

CD-87-29051

Figure 1

HOST TBC LIFE PREDICTION

NASA
C. STEARNS
R. MILLER
J. NESBITT
S. LEVINE
J. MERUTKA

GE
R. HILLERY
B. PILSNER
R. McKNIGHT

PRATT & WHITNEY
K. SHEFFLER
J. DeMASI
S. MANNING
M. ORTIZ

SOUTHWEST RESEARCH INSTITUTE
T. CRUSE
A. NAGY

GARRETT TURBINE ENGINE CO.
T. STRANGMAN
J. NEUMAN
A. LIU

CSU
G. CHANG
W. PHUCHAROEN

CD-87-29053

Figure 2

APPROACH TO TBC LIFE MODEL DEVELOPMENT

- INITIAL LABORATORY MODEL (NASA)
  - UNDERSTAND FAILURE MECHANISMS
  - FORMULATE MECHANISM MATHEMATICALLY
  - COLLECT LABORATORY LIFE DATA
  - FIT MODEL TO LIVES
- ENGINE CAPABLE MODELS (PWA, GTEC, GE CONTRACTS)
  - FURTHER UNDERSTANDING
  - FORMULATE MATHEMATICALLY
  - COLLECT LIFE DATA OVER MANY CONDITIONS ON BOM SYSTEM
  - MEASURE MATERIALS PROPERTIES
  - FIT MODEL TO LIVES
  - EXTRAPOLATE TO ENGINE MISSIONS
- DETAILED FINITE ELEMENT σ/ϵ ANALYSIS (CSU, NASA)

CD-87-29050

Figure 3

TYPICAL AEROTHERMAL BARRIER COATING

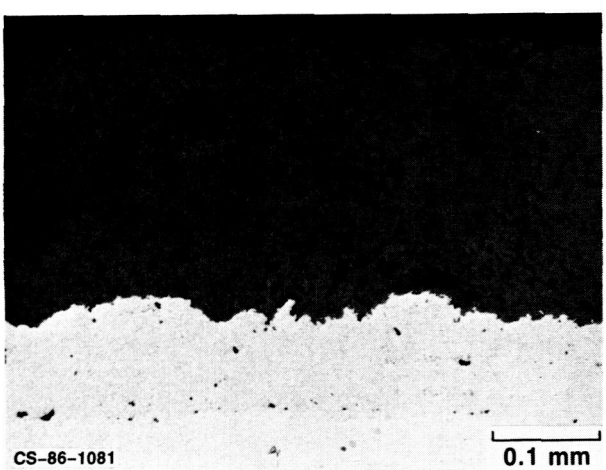

ZrO_2-(6 TO 8%)-Y_2O_3
AIR PLASMA SPRAYED
POROUS AND MICROCRACKED

MCrAlY BOND COAT
LOW-PRESSURE PLASMA SPRAYED
HIGH DENSITY

SUPERALLOY SUBSTRATE

CD-87-29060

Figure 4

UNDERSTANDING OF FAILURE MECHANISMS SUFFICIENT TO ALLOW MODELING

FAILURE BY CRACKING/DELAMINATION IN CERAMIC NEAR INTERFACE

- PROGRESSIVE CRACKING OBSERVED
- σ,ϵ MODELED

EMPIRICAL OBSERVATIONS

CYCLIC COMPONENT TO FAILURE

- THERMAL EXPANSION MISMATCH[a]
- HEATING TRANSIENTS

TIME-AT-TEMPERATURE COMPONENT

- OXIDATION[a]
- PHASE CHANGES
- SINTERING
- DIFFUSION
- CREEP

[a]KEY FACTORS INCLUDED IN PRELIMINARY NASA MODEL.

CD-87-29052

Figure 5

DETAILED FINITE ELEMENT STRESS ANALYSIS YIELDS INSIGHTS INTO TBC BEHAVIOR

700 °C (STRESS FREE)–600 °C

HIGH TENSILE RADIAL STRESS IN CERAMIC NEAR INTERFACE

LOWER σ_r THROUGH LOWER

- $E_{CERAMIC}$
- $\alpha_{CERAMIC} - \alpha_{BOND\ COAT}$
- YIELD STRENGTH OF CERAMIC
- ROUGHNESS
- OXIDATION

WEAK EFFECT ON σ_r FROM

- $\alpha_{SUBSTRATE}$
- $\mu_{BOND\ COAT}$
- $E_{BOND\ COAT}$

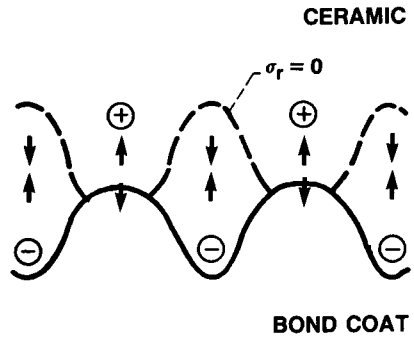

CD-87-29044

Figure 6

SPLAT STRUCTURE FOUND TO YIELD UNUSUAL THERMOMECHANICAL PROPERTIES

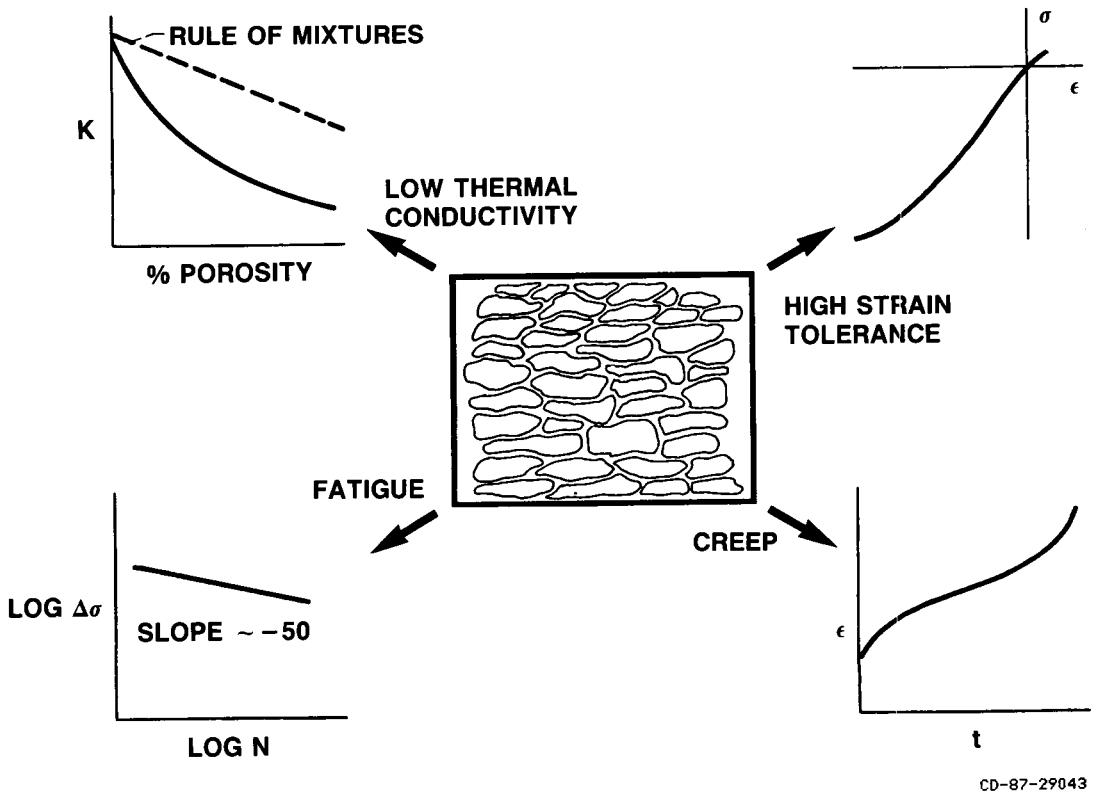

Figure 7

NASA PRELIMINARY TBC LIFE MODEL

- ONE COATING SYSTEM
- TIME-AT-TEMPERATURE EFFECT
  - OXIDATION ONLY, W_N
- CYCLE FREQUENCY EFFECT
  - SLOW CRACK GROWTH (MICROCRACK LINK UP IN CERAMIC

$$\frac{da}{dN} = A\epsilon_e^b a^c$$

(FATIGUE/MINER'S LAW APPROACH ALSO NOTED)

- ASSUMED RELATIONSHIP BETWEEN WEIGHT GAIN AND STRAIN

$$\epsilon_e = (\epsilon_f - \epsilon_r)\,(W_N/W_c)^m + \epsilon_r$$

Figure 8(a)

CD-87-29056

NASA PRELIMINARY TBC LIFE MODEL CONTINUED

- **RESULTING MODEL**

$$\sum_{N=1}^{N_f} \left[(1 - \epsilon_r/\epsilon_f)\ (W_N/W_c)^m + \epsilon_r/\epsilon_f \right]^b$$

- **ALTERNATIVE ASSUMPTION OF STRENGTH DEGRADATION FROM ϵ_{f_0} TO ϵ_r**

$$\epsilon_f/\epsilon_r = (1 - \epsilon_{f_0}/\epsilon_r)\ (W_N/W_c)^m + \epsilon_{f_0}/\epsilon_r$$

- **RESULTING ALTERNATIVE MODEL**

$$\sum_{N=1}^{N_f} \left[(1 - \epsilon_{f_0}/\epsilon_r)\ (W_N/W_c)^m + \epsilon_{f_0}/\epsilon_r \right]^{-b} = 1$$

Figure 8(b)

CD-87-29057

PRELIMINARY MODEL YIELDS GOOD AGREEMENT BETWEEN EXPERIMENTAL AND CALCULATED TBC LIVES

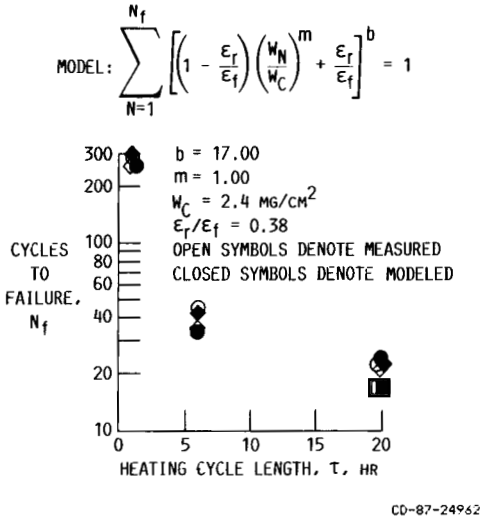

CD-87-24962

Figure 9

PWA/SwRI TBC LIFE MODEL

- BILL-OF-MATERIAL COATING SYSTEM
- TIME-AT-TEMPERATURE EFFECT
  - OXIDATION ONLY, δ
  - ARRHENIUS LAW
- CYCLE FREQUENCY EFFECT
  - INELASTIC FATIGUE MODEL

$$N_f = (\Delta\epsilon_i/\Delta\epsilon_f)^b$$

$$\Delta\epsilon_i = \Delta\alpha\ \Delta T + \Delta\epsilon_h + \Delta\epsilon_c - 2\frac{\sigma_{ys}}{E}$$

ASSUMED STRENGTH DEGRADATION DUE TO OXIDATION

$$\Delta\epsilon_f = \Delta\epsilon_{f_0}\ (1-\delta/\delta_c)^c + \Delta\epsilon_i\ (\delta/\delta_c)^d$$

- MINERS RULE

$$\sum_{N=1}^{N_f} \frac{1}{N} \geq 1$$

CD-87-29055

Figure 10

CORRELATION BETWEEN MEASURED AND MODELED LIVES (PRELIMINARY PRATT & WHITNEY DATA)

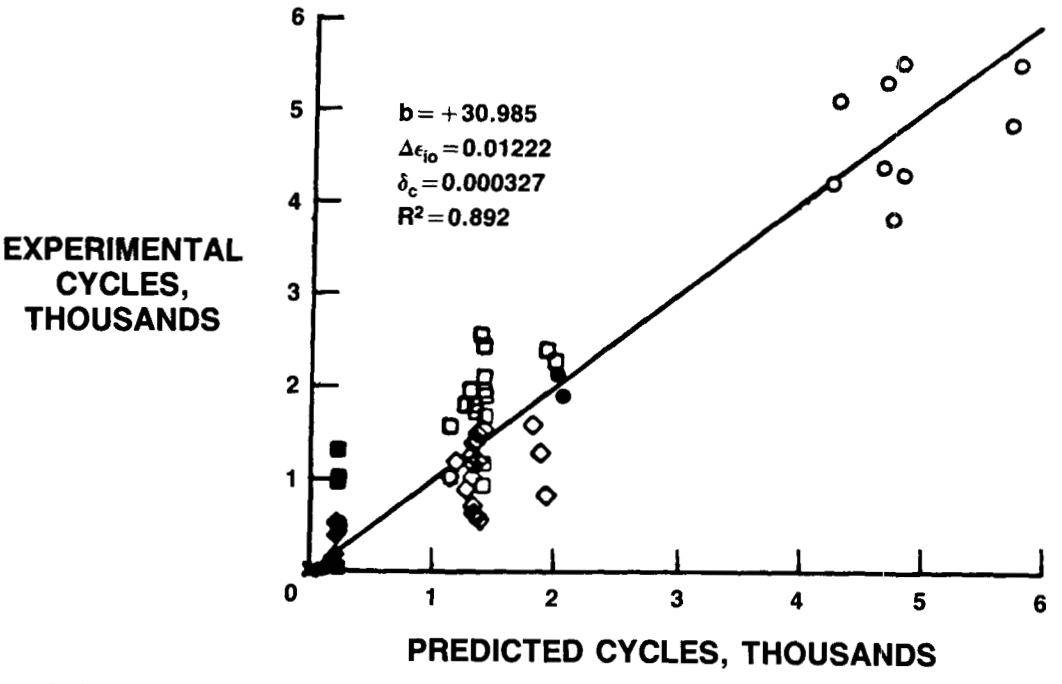

CD-87-24362

Figure 11

GARRETT TBC LIFE MODELING APPROACH

TBC DEGRADATION = RATE

F_1 (MECHANICAL)
- COATING STRESSES
- TEMPERATURE
- MATERIAL SYSTEM
  - K_{IC}
  - FLAW SIZE
  - ELASTIC MODULUS
  - SPALLING STRAIN

$+F_2$ (OXIDATION)
- TEMPERATURE
- TIME
- MATERIALS SYSTEM

$+F_3$ (SALT DEPOSITION)
- ALTITUDE (SALT INGESTION)
- TURBINE PRESSURE
- SALT EVAPORATION
- SALT SOLIDIFICATION
- TEMPERATURE
- GAS VELOCITY
- AIRCRAFT LOCATION
- MATERIALS SYSTEM

CD-87-24364

Figure 12

GARRETT TBC LIFE MODEL HAS THREE DEGRADATION MODES

$$\text{TBC LIFE} = \frac{1}{\left[\frac{\text{HEATING CYCLE LENGTH FACTOR}}{(\text{OXIDATION LIFE})^{-1} + \left(\frac{\text{ZIRCONIA DENSIFICATION}}{\text{PLUS OXIDATION LIFE}}\right)^{-1}}\right]^{-1} + \left[\text{SALT FILM DAMAGE LIFE}\right]^{-1}}$$

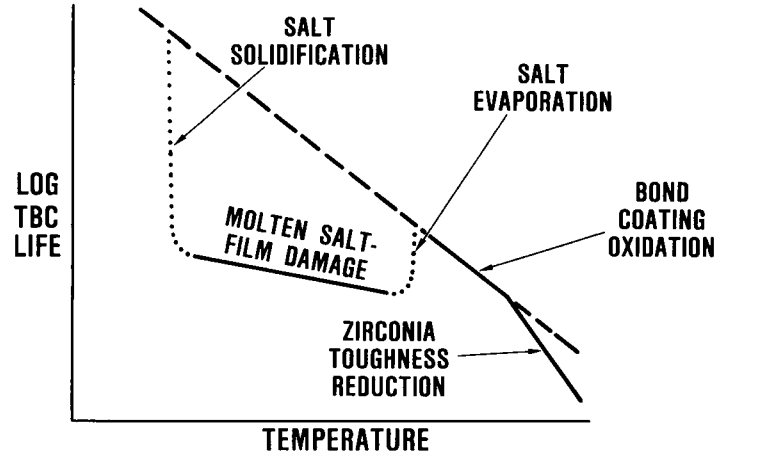

CD-87-29058

Figure 13

GARRETT TBC MODEL FIT THROUGH MINIMUM LIVES

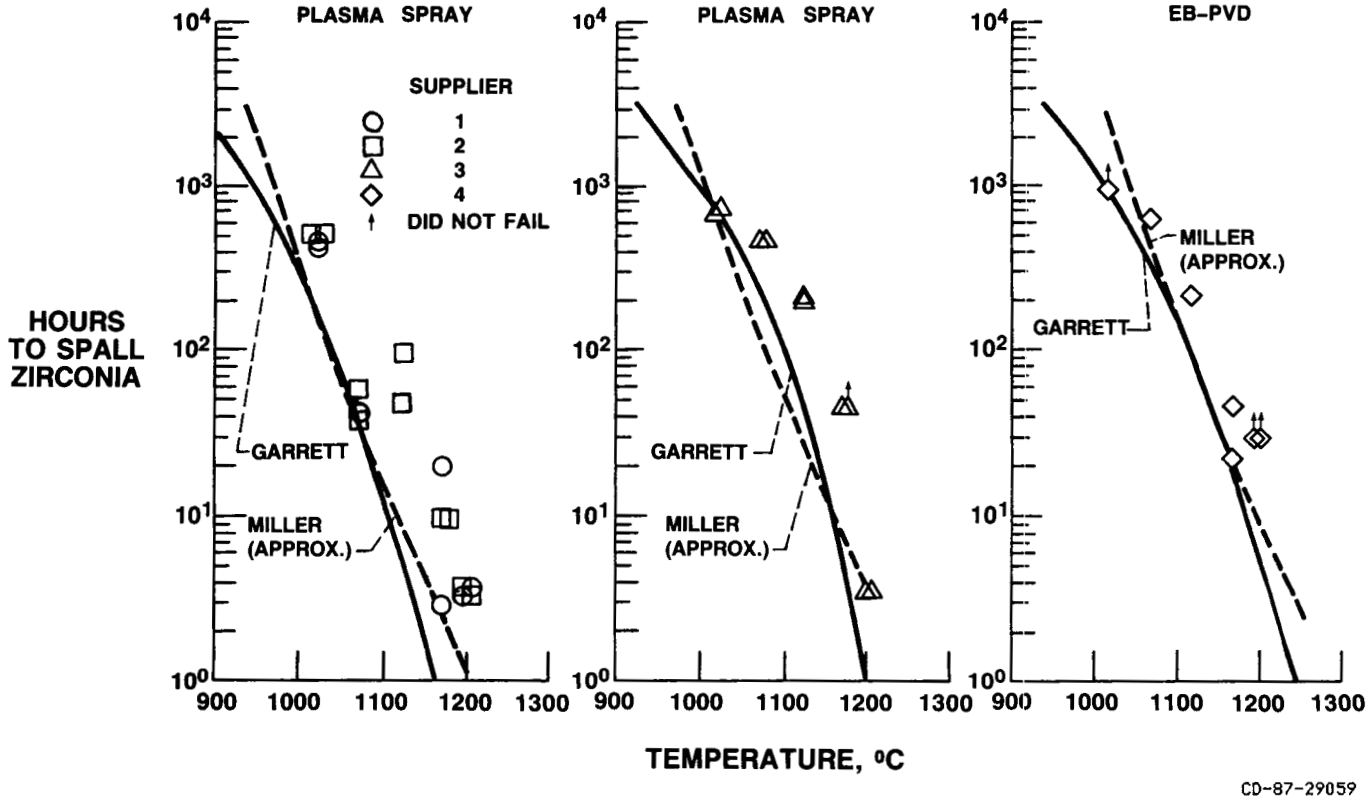

Figure 14

GENERAL ELECTRIC TBC LIFE MODELING APPROACH

- ANALYSIS—PREDICTS σ,ϵ UNDER VARIOUS TIME, TEMPERATURE CONDITIONS
- TESTING—DEFINES EFFECTS OF SPECIMEN HISTORY, LOADS (σ,ϵ), AND T ON TIME TO FAILURE
- EMPIRICALLY RELATED ANALYSIS AND TEST—INFERENCE
- GREATER NUMBER OF TEST CONDITIONS GIVES INCREASED INFERENCE AND CONFIDENCE CAPABILITY
- VERIFY AND MODIFY BY ADDITIONAL TESTS

CD-87-29045

Figure 15

GENERAL ELECTRIC TBC LIFE-PREDICTION MODEL

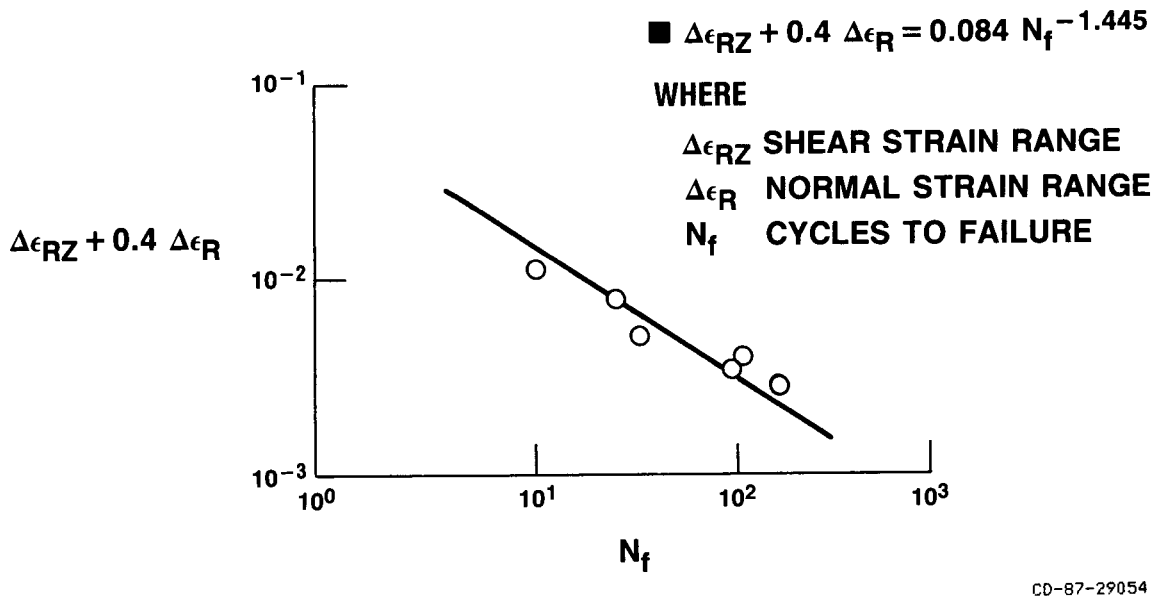

Figure 16

PHASE-I SUMMARY

- SUCCESSFUL PHASE-I TBC LIFE-PREDICTION PROGRAM
- FIRST COMPREHENSIVE STRUCTURES LOOK AT TBC's
- THREE DIFFERENT LIFE-PREDICTION APPROACHES DEVELOPED

Figure 17

PHASE-II PROGRAM GOALS

- EB-PVD FAILURE MECHANISM UNDERSTANDING
- EB-PVD LIFE-PREDICTION MODEL DEVELOPMENT

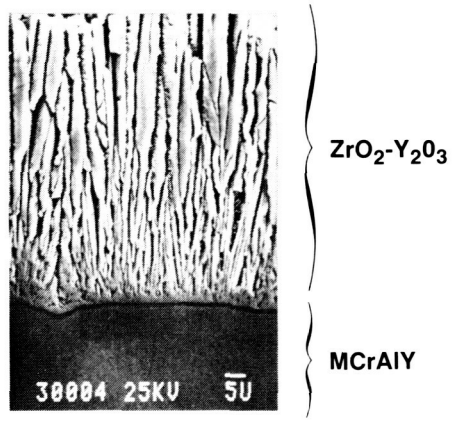

CD-87-29065

Figure 18

CONCLUDING REMARKS

HOST TBC LIFE-PREDICTION PROGRAM HAS BEEN VERY SUCCESSFUL, BUT MANY QUESTIONS REMAIN

- ☐ SHAPE OF ln N_f VERSUS ln T: ◺ , ◺ , OR ◺
- ☐ EFFECT OF INELASTICITY/CREEP IN BOTH LAYERS
- ☐ MAGNITUDE OF FATIGUE EXPONENT (−1.4 or −50)
- ☐ ROLE OF SHEARING STRESSES
- ☐ ADEQUACY OF SIMPLE FINITE ELEMENT ANALYSIS ON SMOOTH INTERFACES
- ☐ DETAILS OF HOW OXIDATION CONTROLS LIFE
  - ☐ BEST WAY TO FINITE ELEMENT MODEL
  - ☐ BEST WAY TO LIFE MODEL
- ☐ WHETHER OR NOT SINTERING IS IMPORTANT
- ☐ WHEN HOT SALT CORROSION IS IMPORTANT
- ☐ APPLICABILITY OF CURRENT APPROACH TO EB-PVD COATINGS
- ☐ SENSITIVITY OF EB-PVD COATINGS TO OXIDATION/HOT SALT CORROSION

CD-87-29046

Figure 19

DEVELOPMENT OF A HIGH TEMPERATURE THIN FILM STATIC STRAIN GAGE

Charles O. Hulse and Richard S. Bailey
United Technologies Research Center
East Hartford, Connecticut
and
Howard P. Grant and John S. Przybyszewski
Pratt & Whitney Division
East Hartford, Connecticut

The objective of this effort is to develop a new thin film resistance strain gage system which will be suitable for use inside gas turbine engines on blades or vanes at temperatures up to 1250 K. These gages are to be capable of making strain measurements to ±2000 microstrain with total errors of no more than ±10 percent during a 50 hour period. In addition to survival and stability in this hostile environment, attaining a low temperature coefficient of resistance, of the order of 20 ppm/K or less, is an important goal. This requirement arises from the presently unavoidable uncertainties in the measurement of exact temperatures inside gas turbine engines for use in making corrections for apparent strain.

SENSOR PROPERTIES

The most desirable material to select as a strain sensitive resistor would be a pure, precious metal which would have a high melting point and be inert to oxidation attack. Unfortunately, the resistances of pure metals all have high thermal sensitivities to temperature which is unacceptable in this application. Unacceptably large uncertainties in strain (errors) result when high coefficients of resistance are combined with the typical uncertainties in measurements of the temperature of gas turbine parts. This consideration is further complicated when the sensor must be used on a structure containing a high thermal gradient.

Alloying with other precious metals to form solid solutions can be used to introduce electron scattering centers whose concentrations and resistance effects are essentially independent of temperature. Unfortunately, the choices available do not result in alloys whose resistivities have sufficiently low thermal sensitivities to be

*Work done under NASA Contract NAS3-23722

useful. The optimum sensor composition developed in this and previous programs (refs. 1-4) is an alloy of Pd containing 13 weight percent Cr. This alloy is particularly desirable because, not only does the Cr act as effective scattering agent to increase the resistance and lower the thermal sensitivity of resistance of the alloy, but the Cr diffuses to the surface to form a coating of Cr_2O_3 which resists further oxidation of the Cr. Figure 1 shows the resistance versus temperature behavior of this alloy. The fact that the resistance is linear with temperature indicates that the Cr remains in complete solid solution over the full temperature range of interest and that no ordering effects occur.

Unfortunately, when this alloy is prepared as a sputtered film only 6.5 micrometers thick, the amount of Cr in the film is not sufficient to form a protective coating without almost completely depleting the remaining alloy of Cr. Figure 2 shows how the resistance of different thicknesses of the PdCr alloy changes with time when exposed to oxidation at 1250 K.

PROTECTIVE OVERCOATS

Efforts are currently underway to develop protective overcoat/top seal coatings to overcome this oxidation problem. Alumina has been selected as the primary overcoat material because of the general recognition that it forms the most oxidation resistant coatings for use on nickel-base superalloys. Unfortunately, sputtered films of alumina do not remain completely dense and inert upon firing to elevated temperature for various reasons: (a) the transformation from gamma to alpha or from amorphous to crystalline, (b) evolution of argon entrapped in the structure during sputtering, (c) oxidation to restore stoichiometry, and (d) accommodation of the strains caused by the differences in thermal expansion between the alumina and the superalloy substrate, which are typically of the order 7×10^{-6}/K. Table I presents a listing of the various top seal coats which are being evaluated in attempts to make the alumina impervious to oxygen.

Preliminary experiments are also underway to evaluate the potential advantages of sputtering the alumina films on a heated substrate. Because these films will be formed at a high temperature they should have a high stress free temperature and experience only moderate tensile stresses when heated to the highest temperature of use.

INSULATION COATINGS

Decreases in the measured resistances of strain gage circuits can also occur because of electrical leakages through the alumina insulation coating on the Hastelloy-X substrate. These create additional parallel paths for current to flow through the metal substrate. Figure 3 shows an example where shorting has developed at high temperatures which gradually became worse with time. Measure-

ments of the resistance between the gage and the substrate can be used to confirm the cause of this behavior.

Our investigations of this problem have focused on the importance of surface defects originally present on the highly polished metal surface and debris present on these surfaces during sputtering. These defects can result in abnormal growths in the sputtered films which tend to become detached during subsequent thermal cycling to form very fine pinholes. We have carried out careful examinations of all of our sputtered surface to ensure that these sources are removed, and we feel that our further results will confirm that most of this problem can be avoided by the use of these careful procedures.

TEMPERATURE COMPENSATION AND LEAD WIRE CONSIDERATIONS

Temperature Compensation Design

An analysis of temperature effects on static strain gage accuracy carried out by NASA and UTC during Task 1 and 2 of the program concluded that active temperature compensation would be needed in addition to corrections for residual apparent strain due to temperature. Active resistive temperature compensation can be accomplished by installing an additional temperature sensitive (relatively strain insensitive) element at the point of measurement, and combining the output signal from this element with the output signal from the strain gage element, as shown in Figure 4. Good thermal compensation can be expected over only a moderate temperature range because the thermal sensitivities of the gage and the compensating element typically vary differently with temperature. Note that the use of an adjustable resistor across the compensating arm of the bridge (the dashed lines in Figure 4) as a means of further adjusting the compensation, is not advisable because this shunt would also be across two of the three lead wire resistances, and therefore would defeat the lead wire cancellation provided by the 3-wire hookup.

Lead Resistance Effects

Once the strain gage bridge adjustments in Figure 4 have been set for initial balance, including the temperature compensation adjustments, subsequent changes in temperature distribution in the lead wires and lead films can produce apparent strain due to temperature at the bridge output in two ways: (a) common mode changes in all lead resistances, and (b) differential changes due to transverse temperature gradients. In order to reduce the common-mode error to an acceptable level, the temperature compensation element in the bridge of Figure 4 must have a resistance and temperature coefficient of resistance that produce the same total level of change in resistance with temperature as the strain element, within about 5%. Only if this is true can the bridge ratio be set close to 1:1 as required to minimize this type of error. The effects of temperature gradients can be minimized by routing the two critical leads as close together as possible.

Lead Wire Thermocouple Effects

For a gage factor of 2 and for a bridge voltage E_1 of 5 volts, the thermocouple effect in any arm of the bridge is about 1 microstrain for every 5 microvolts of stray thermocouple emf. The thermocouple emf generated in each lead wire, lead film, strain element, or compensating element is proportional to the temperature difference between the two ends of the element. Factors of proportionality (thermocouple emf per Kelvin, relative to platinum measuring leads) are listed in Table II for several candidate metals and alloys. These factors range from -15 μv/K to +32 μv/k so that careful attention must be used in choosing materials and layout.

Thermocouple effects can be reduced if the bridge voltage E_1 is increased, but E_1 must not be made so large that significant self-heating of the strain element occurs. Thermocouple effects may also be reduced by employing pulsed DC excitation to raise E_1 by an order of magnituide without producing self-heating. Capacitively and inductively coupled transient noise voltages are potential problems when pulsed excitation is employed. In principle, residual thermocouple effects on static strain measurements can also be completely suppressed by turning off the bridge excitation before each strain measurement and readjusting a bucking voltage to rebalance the bridge.

SUMMARY AND CONCLUSIONS

The Pd-13 Cr (weight percent) alloy developed in this program appears to meet the program goals of stability and reproducibility for use as a static strain gage up to 1250 K when prepared in bulk form. When prepared as a 6.5 micrometer thick sputtered strain gage, however, the naturally occurring protective coating of Cr_2O_3 is inadequate to prevent oxidation attack and a protective overcoat/seal coat system is required. An evaluation of these systems is currently underway as well as an examination of the use of sputtering at elevated temperature to reduce the problems caused by the differences in thermal expansion between the substrate and sputtered alumina layers.

The important factors and problems involved in the selection and use of lead wires with static strain gages have been reviewed. It is believed that problems with electrical leakage between the strain gage and the substrate can be overcome primarily by the use of extreme care in surface preparation before sputtering to eliminate surface defects which can cause defects to occur in the sputtered layers. This is also still being evaluated.

REFERENCES

1. Hulse, C. O.; Bailey, R. S.; and Lemkey, F. D.: High Temperature Static Strain Gage Alloy Development Program, NASA CR-174833, March 1985.

2. Hulse, C. O.; Bailey, R. S.; and Grant, H. P.: The Development of a High Temperature Static Strain Gage System. Turbine Engine Hot Section Technology, 1985. NASA CP-2405, pp. 45-49.

3. Hulse, C. O.; Bailey, R. S.; and Grant, H. P.: Development of a High Temperature Static Strain Sensor. Turbine Engine Hot Section Technology, 1986. NASA CP-2444, pp. 85-90.

4. Hulse, C. O.; Bailey, R. S.; Grant, H. P.; and Przybyszewski, J. S.: High Temperature Static Strain Gage Development Contract, NASA CR-180811, July 1987.

TABLE I. STRAIN GAGE OVERCOAT SYSTEMS

Type	Sensor	Sputtered					Transfer tape
	PdCr	Al_2O_3	FeCrAl	Pt	Glass	Al	Glass
1	X	X					
2	X	X	X				
3	X	X		X			
4	X	X			X		
5	X	X				X	
6	X	X					X

TABLE II. APPROXIMATE PROPERTIES OF SELECTED METALS AND ALLOYS

Material	Composition Weight Percent	TC EMF Relative To Platinum 273 K to 1250 K	Melting Point	Temp. Coeff. Lin. Exp. 273 K to 1250 K	Temp. Coef. of Resistance	Resistivity	Product	Gage Factor	Ratio	Lead Wire Resistance for 1 meter of .25 cm Wire
					α	ρ	$\alpha\rho$	G	α/G	R_w
		(μV/K)	(K)	x 10^6 (K^{-1})	(K^{-1})	(ohm-cm)	(ohm-cm-K^{-1})		(K^{-1})	$(.2\times10^6)\rho$ (ohms/meter)
Palladium	Pd	-15	1827K	12	.003800	10.8×10^{-6}	$.041\times10^{-6}$	6.6	.000576	2.2
Nickel	Ni	-12	1608K	13	.004800	10×10^{-6}	$.048\times10^{-6}$	2.0	.002400	2.0
Alumel	Ni-2Al-3Mn-1Si	- 9	1673K		.001900	29×10^{-6}	$.055\times10^{-6}$	2.0	.000950	5.8
Platinum	Pt	0	2046K	10	.003000	10.6×10^{-6}	$.032\times10^{-6}$	4.8	.000625	2.1
Gold	Au	+ 8	1336K	14	.003400	2.4×10^{-6}	$.008\times10^{-6}$	2.0	.001700	.48
Aluminum	Al	+ 9	933K	24	.004000	2.7×10^{-6}	$.011\times10^{-6}$			
Pd-13Cr	Pd-13Cr	+19*			.000170	100×10^{-6}	$.017\times10^{-6}$	1.8	.000094	20.0
Pt-10Rh	Pt-10Rh	+10	2100K		.001700	18×10^{-6}	$.031\times10^{-6}$	2.0	.000850	3.6
Pt-10Ni	Pt-10Ni	+15	1920K		.001400	30×10^{-6}	$.042\times10^{-6}$	2.0	.000700	6.0
Copper	Cu	+18	1356K	16	.003900	1.7×10^{-6}	$.007\times10^{-6}$	2.0	.001950	.34
Nichrome	Ni-20Cr	+23	1673K	14	.000100	108×10^{-6}	$.011\times10^{-6}$	2.0	.000050	21.6
Chromel P	Ni-10Cr	+32	1700K		.000320	70×10^{-6}	$.022\times10^{-6}$	2.0	.000160	14.0
Ni-30Cr	Ni-30Cr				.000100	150×10^{-6}	$.015\times10^{-6}$	2.0	.000050	30.0
Rhodium	Rh	+13.4	2239K	8		4.5×10^{-6}				.9

*NASA Pd-13Cr cast ribbon 10-17-86

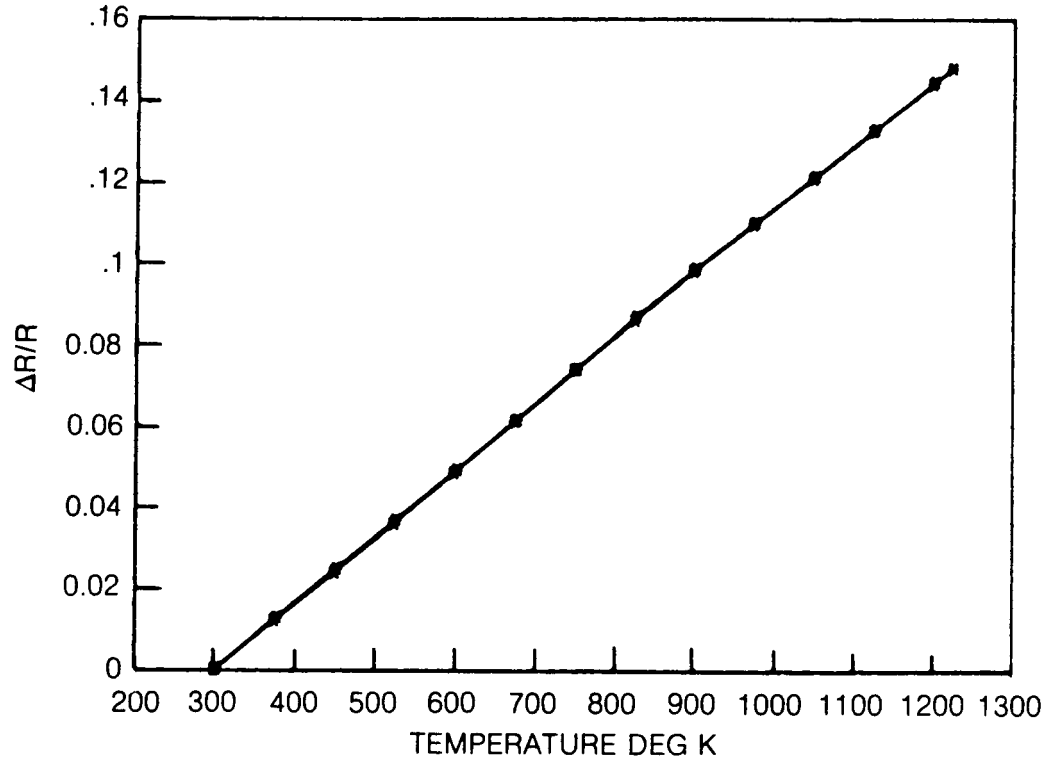

Figure 1. Resistance vs Temperature at 50 deg K/min (Pd-13 Wt % Cr)

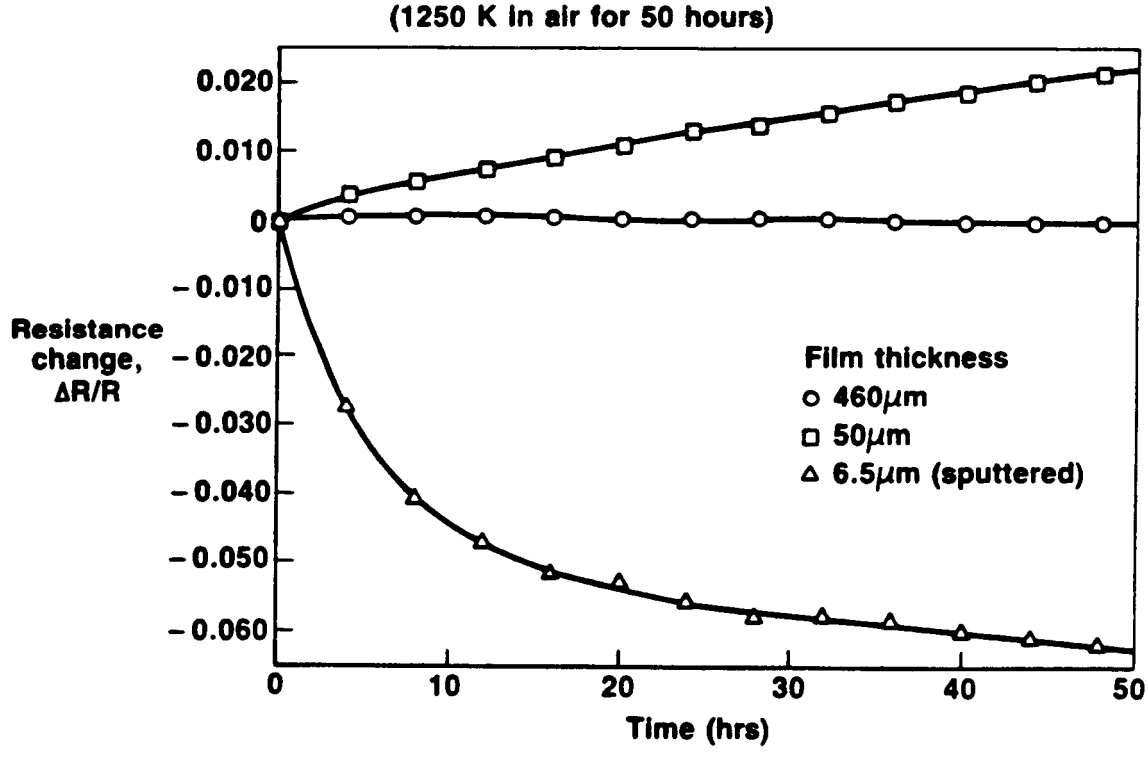

Figure 2. Effect of Film Thickness on Drift in Resistance of Pd-13 wt % Cr

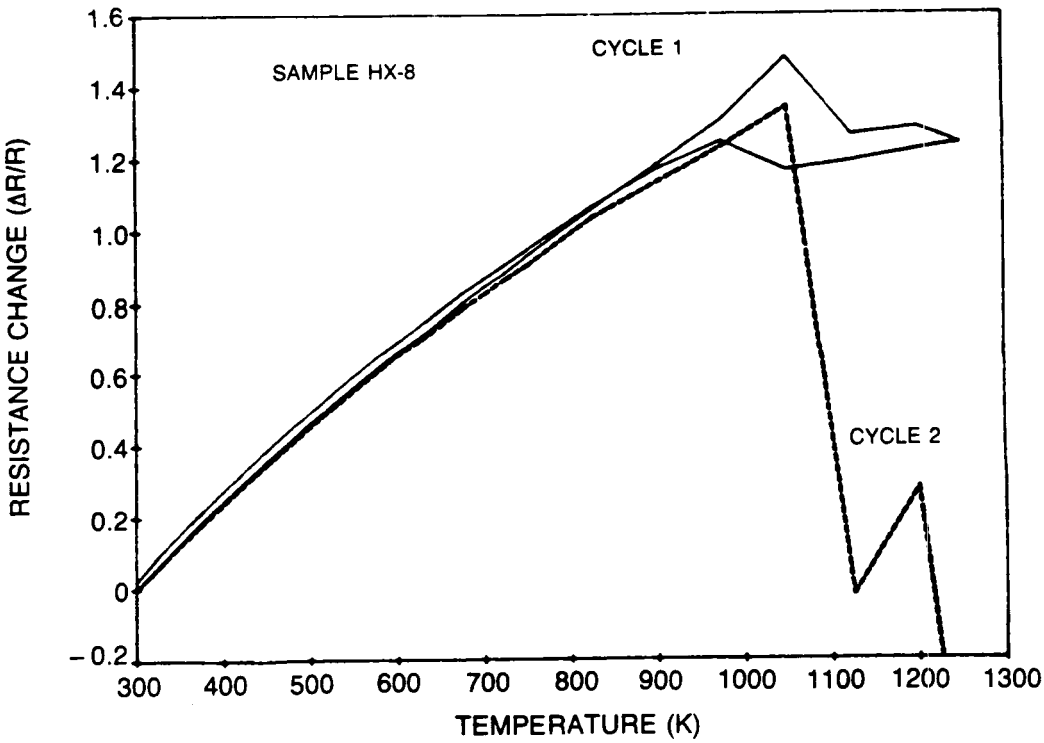

Figure 3. Resistance vs Temperature for Sputtered Pd-13Cr (wt%) Pretreated 10 hrs in Air at 1370 K

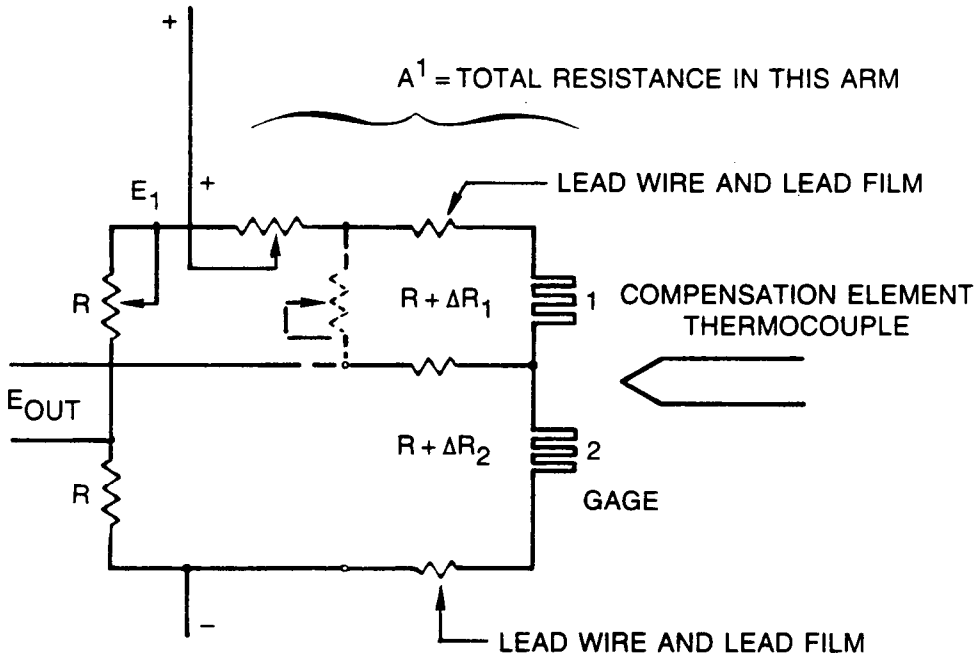

Figure 4. Temperature Compensation Arrangements

ELEVATED TEMPERATURE STRAIN GAGES

J.F. Lei, M. Shaarbaf, and J.O. Brittain
Northwestern University
Evanston, Illinois

The objective of this research is to study the electrical resistance of materials that are potentially useful as resistance strain gages at 1000°C. A set of criteria (1) were set and used to select strain gage candidate materials that are electrically stable and reproducible at all temperatures up to 1000°C. For the experimental phase of this research the electrical resistance change with temperature of three groups of materials (solid solution alloys, transition metal carbides and nitrides, and semiconductors) were studied with the intention of identifying materials with low temperature coefficient of resistance (TCR) and low resistance drift rate (DR) at 1000°C. A preliminary study of gage factor on one of the best candidates materials, B_4C, was also undertaken. The results of the investigation on these materials are presented in this report.

I. INTRODUCTION

A. Solid Solution Alloys

In previous report (1) a number of binary alloys were reported to have desirable electrical properties. These included alloys from Ag-Pd, Al-V, and Mo-Re systems. Since then the addition of third elements to these alloys has been made with the goal of decreasing TCR and DR at 1000°C. The third element(s) for each system was selected based upon Hume-Rothery's criteria for ideal solid solution (similar atomic radii, valance, and electronegativity) to avoid segregation or clustering which could have negative effects on electrical properties. The concentration ranges of these elements were selected by considering their solubility limits in the parent elements in each alloy in order to avoid formation of new phases.

B. Transition Metal Compounds

The refractory carbides and nitrides of the transition metals comprise a class of compounds with many scientifically interesting and useful properties such as: high melting temperatures ($\simeq$ 3000°C), high electrical conductivity, great hardness, wide homogeneity range, and excellent chemical stability. The transition metals in these compounds are from groups IV (Ti, Zr, Hf), V (V, Nb, Ta), and VI (Cr, Mo, W) of the periodic table. However, not all the carbides and nitrides of these elements seemed to be suitable for high temperature resistance strain gage application. Among these materials, nitrides of group VI were excluded from list of potential compounds because they dissociate rapidly at high temperatures. VN, NbN, MoC and WC were also excluded due to their complex phase diagrams and narrow ranges of homogeneity.

A wide homogeneity range is characteristic of the cubic transition metal compounds. For all rocksalt structured transition metal carbides, nonstoichiometry is due to carbon vacancies only and the metallic sublattice remains completely occupied, as shown by precise density measurements (2). Some mononitrides such as TiN_x are reported to be nonstoichiometry with x values larger than 1. These compounds are characterized as containing metal vacancies whose concentration increases with an increase in x, that is for a nitrogen concentration > 1 (4). The presence of a large concentration of vacancies would be expected to affect various physical properties. In this research the effect of vacancy concentration on the electrical properties of these transition metal compounds was also investigated in order to select the proper strain gage candidates among them.

C. Semiconducting Materials

Traditional semiconductor resistance strain gages are made of silicon or germanium, which have band gaps of 1.11 and 0.67 eV, respectively. In order to extend the working temperature of the strain gages to higher temperatures, semiconducting materials with band gaps larger than 1.11 eV are therefore needed. α-SiC, β-SiC and B_4C with band gaps of 2.86, 2.3 and 2.5 eV, respectively, were chosen for this study. Their intrinsic conduction occurs at temperatures above 1000°C.

II. MATERIALS PREPARATION, PROCESSING AND EXPERIMENTAL TECHNIQUE

The alloys listed in Table I were prepared by arc melting and remelting (about 5 times) charges of about 5 grams under purified argon atmosphere. The ingots were then cut by electrical discharge mechining into rectangular samples of 8x3x1 mm for electrical resistance measurements.

The specimens of transition metal compounds and β-SiC were prepared as thin films on Al_2O_3 substrates by several different evaporation or sputtering techniques, listed in Table II. All films were cut into samples about 15 mm long by 1.5 mm wide via a diamond blade. Boron carbide and α-silicon carbide bulk samples prepared by hot pressing were thinned by slicing into 15x1.5x1 mm specimens via a diamond cut-off wheel.

Specimens for electrical resistance measurements were chemically cleaned to remove any debris and contaminations. These samples were then encapsulated in quartz tubings under vacuum and were subsequently annealed for one day at slightly above 1000°C followed by furnace cooling to room temperature. The electrical resistance (ER) of two or three specimens were measured simultaneously via a four probe technique as described in previous report (1) in the temperature range of 23-1000°C under vacuum ($2x10^{-5}$ torr). The ER of boron carbide in air was also measured.

A device which consisted of a constant strain cantilever beam designed first by McClintock (3) was adopted and modified (Fig. 1) to measure the gage factor of materials. Samples were attached to the surface of the cantilever

beam by means of a high temperature ceramic adhesive (AREMCO products). The stepped, sliding block which is in contact with the free end of the beam via a screw was accurately machined so that the difference in height between any two steps represents a known deflection of the free end of the beam, and consequently a known strain at the beam surface (Fig. 2). The sliding block, beam, frame and screws were all made of the same material (Aremcolox high temperature low thermal expansion machinable ceramics) to minimize relative dimensional changes of these parts resulting from the thermal expansion.

III. RESULTS — Solid Solution Alloys

Additions of third elements to the alloys of the following systems resulted in similar ER-T curves as their parent binary alloys. A metallographic examination indicated that these elements did not result in the formation of any new phases in these alloys.

A. Palladium-Silver System

Experimental results on Pd-Ag alloys (1) showed an increase in Ag content from 4.1 to 15.5 st.% reduced the TCR from 774 to 250 ppm/^{o}C without a significant change in reproducibility. This is in agreement with the published data for Pd-Ag alloys (4). Based on these observations the Pd-12 wt.% Ag alloys was selected to be doped by small additions of Ni to verify the effects of Ni on the electrical properties of these alloys. Fig. 3 shows the ER-T data for Pd-12 wt.% Ag-7 Ni alloy. Addition of Ni as a third element had a positive effect on TCR and DR of these alloys, Table 1. Figure 4 shows that an increase in Ni content resulted in systematic decrease in TCR.

B. Aluminum-Vanadium System

The experimental results of the investigated binary Al-V alloys (1) indicated that these alloys generally have low TCR values but undesirable drifts in ER at high temperatures. However, Al-79.3 wt.% V containing a small amount of Si had a very low TCR (-22 ppm/C) and drift (50 ppm/hr) at 1000^{o}C. This prompted an investigation of the effect of additions of third elements to these alloys. In this work the effects of Mo and Cr as third elements on electrical properties of Al-79.3 wt.% were investigated. Figures 5 and 6 show ER-T data for Al-79.3 wt.% V-4.25 wt.% Mo alloy and the effect of Mo content on TCR of these alloys. An increase in Mo content had a beneficial effect in these alloys as it resulted in lower TCR and drift values (Table I). On the other hand Cr is not a suitable ternary element for this system. Increasing the Cr content in Al-79.3 wt.% V-Cr alloys resulted in larger negative TCR values with no significant change in drift (Table I) in electrical resistance at high temperatures. Figures 7 and 8 show the ER-T data for Al-79.3 wt.% V-1.75 wt.% Cr alloy along with TCR vs Cr content of these alloys, respectively.

C. Niobium-Vanadium System

In previous report Nb-5.2 wt.% alloy was investigated based on its reported good oxidation resistance (5) but its rather large TCR (550 ppm/k) and drift (550 ppm/hr) values were less than desirable. Despite these observations this system was selected as a good candidate for further studies and Mo was selected as the ternary element for this system. Figure 9 shows the ER-T data for Nb-8 wt.% V-7 Mo alloy. Nb-V-Mo alloys studied all showed good reproducibility (low drift). However, Mo additions resulted in increase in TCR values for these alloys (Fig. 10).

IV. SUMMARY — Solid Solution Alloys

It was intended to study the general effects of selected ternary elements on the electrical properties of a number of alloy systems which in terms of low TCR (< 300 ppm/C) values seemed promising. The objective was to identify the most desirable third element for a specific alloy and the best concentration of the third element in that alloy.

In the case of Pd-Ag alloys, Ni has been found to be a suitable third element and addition of this element to Pd-Ag alloys with higher Ag contents (> 12 wt.%) may result in practically low TCR values.

All of the Al-V-Mo alloys meet the TCR requirements of < 300 ppm/C. The alloys with higher Mo content had lower drift values, in particular, Al-79.3 wt.% V-4.25 wt.% Mo had the best TCR (-19 ppm/C) and drift (103 ppm/hr) combination. Further study on this system with higher Mo content is planned. Because of the negative effects of Cr on Al-V alloys no further work is planned for this system incorporating Cr.

Addition of Mo resulted in negative effect on the electrical properties of Nb-V alloys. However, further work is underway on effect of other third elements on these alloys as well as the Mo-Re alloys.

V. RESULTS — Refractory Compounds

A. Transition Metal Compounds

The results of change in its ER with change in temperatures for two TiN_x, two TaN_x, three ZrN_x, two TiC_x and ZrN_x films with different x's were presented in last report (1). The ER-T curves for ZrC is shown in figure 11, and the comparison between results of three TaN_x and four ZrN_x films are shown in the figures 12 and 13, respectively. The compositions of these transition metal compound films were characterized by means of x-ray, SEM, and Auger electron spectroscopy. The experimental results of these transition metal compounds are summarized in Table III, including TCR (at 1000°C), DR (at 1000°C), resistivity (at room temperature), composition and the partial pressure of nitrogen (carbon) during preparation. From these results it is suggested that:

(1) TCR and DR of the stoichiometric carbides were lower than those of their corresponding stoichiometric nitrides, e.g., TCR of TiC was lower than that of TiN and TCR of ZrC was lower than that of ZrN, as shown in figure 14.

(2) TCR of stoichiometric ZrN was lower than that of TiN and TCR of ZrC is lower than that of TiC, also shown in figure 14. These results indicate that the TCR of transition metal nitrides and carbides with transition metals in the same column of the period table decreased as quantum number of the transition metal increased.

(3) The resistivities of these compounds increased while their TCC decreased with increasing the vacancy concentration, as shown in Table III and figure 12.

(4) As shown in figure 15 the TCR of these transition metal compounds decreased as the resistivities of the compounds increased. Extrapolation of the data in figure 15 suggests that TCR passed through zero at resistivity of about 800-1000 microohm-cm.

(5) High temperature resistance saturations were observed in the Zr-C and ZrN systems. These two samples had larger resistivities (in the range of 180 and 560 microohm-cm) that resulted from stronger vacancy scatterings among all of the specimens studied except $TiN_{0.9}$ which had a resistivity of 1130 microohm-cm and a negative TCR. The ER-T behaviors of ZrN and ZrC fitted a "parallel resistor" formula (6)

$$1/R(T) = 1/R(\text{ideal}) + 1/R_{max}$$

where $R(\text{ideal}) = R_o + bT$, R_o is the residual resistance, b is fitting parameter and R_{max} is the apparent saturation value of the resistance at high temperatures. Plots of $(R_{max} \times R)/(R_{max} - R)$ versus temperature for ZrN and ZrC were made and shown in figures 16 and 17, respectively, where R_{max} corresponded to a resistivity of 1000 microohm-cm. The value of this saturation resistivity (1000 microohm-cm) was about the same as that when TCR vs resistivity curve (Fig. 15) passes through zero TCR.

(6) The presence of both a small TCR and a small DR value seemed to be mutually exclusive. However, the source of the high temperature resistance drift for the materials investigated was not ascertained. Note that pure platinum also displayed a high DR ($\simeq$ 0.2 %/hr).

B. Semiconductors

Table IV summarized the experimental results for the B_4C, β-SiC and α-SiC. The ER-T curves of B_4C, β-SiC-1 and α-SiC tested in a vacuum were presented in previous report (1). Since B_4C looked promising, it was therefore also tested in the air, its ER-T curve shown in Fig. 18. β-SiC-2 which had some N_2 dopants was also tested (in the vacuum) to study the doping effect, this is shown in Fig. 19. The results of these semiconductors can be summarized as follows:

(1) The change in resistance of B_4C with temperature followed a form of $R=AT \exp (E_A/kT)$, with activation energy (E_A) of about 0.14±0.005 eV, shown in Fig. 20. The temperature dependence of resistance in B_4C is actually the temperature dependence of its mobility (7), and the activation energy was large so that its mobility had a weakly temperature dependent value and resulted in a small TCR value at high temperatures.

(2) β-SiC had a weaker temperature dependence of resistance compared with α-SiC, and it is a more promising strain gage material for use at high temperatures. The TCR of β-SiC was decreased by doping, however, the DR showed a slight increase.

C. Gage Factor Measurement

The gage factor measurement system was first calibrated with three commercial resistance strain gage (Micro-Measurements Co.) at room temperature. Then a hot pressed B_4C was attached to the cantilever beam with a ceramic adhesive and tested in the vacuumed furnace. The change in its resistance with temperature was compared to that of the resistance data from a sample without applying adhesive as shown in Fig. 21, the consistence between the two curves indicates the inertness of the adhesive.

Figure 22 illustrates the resistance versus strain characteristics for boron carbide at three different temperatures. A linear change in resistance with applied strain at strain levels of 306 microstrain was observed. The gage factor drift at 1000°C was found to be about 0.22 %/hr for a period of 6 hours.

Figure 23 is a plot of percentage change in gage factor from its room temperature value versus temperature for B_4C in the temperature range of 23°C to 1000°C. This figure shows that the gage factor of B_4C decreased with increasing temperature. The gage factor was about 196±1% at 1000°C and 455±2% at room temperature. It varied by about 57% from room temperature to 1000°C. The gage factor of Wu's Chinese gage (8) was 2.56 at room temperature and 1.9 at 700°C, a variation of about 26% in the temperature range from room temperature to 700°C. In the same temperature range the gage factor variation for B_4C was about 32%. Since no effort has been made to optimize the performance of B_4C, the comparison is rather favorable. The reproducibility of gage factor of B_4C and its gage factor behavior under higher strain are planned for further studies.

VI. SUMMARY — Refractory Compounds

The low values of TCR of transition metal compounds were associated with highly defective lattice structures. However, structures with high concentration of defects were often unstable at high temperatures. Therefore, the selection of the composition of these transition metal compounds depends on which one of the two factors is more dominate, lower TCR or better stability.

Based upon the data presented in Table III and IV which summarize the

experimental results, we conclude that TiC, ZrC, B_4C and β-SiC have the potential to be used in production of high temperature resistance strain gages due to their low TCR and good stability. However, further studies on the optimization of their electrical behaviors and protection of these materials from oxidation at high temperature is necessary before these materials could be utilized in strain gage.

REFERENCES

1. Brittain, J. O.; Geslin, D.; and Lei, J. F.: Elevated Temperature Strain Gages, Proceedings of a Conference on Turbine Engine Hot Section Technology 1986, NASA Conference Publication 2444.

2. Storms, E. K.: The Refractory Carbides, Academic Press, N.Y. and London, 1967.

3. McClintock, R. M.: Strain Gage Calibration Device for Extreme Temperature. The Review of Scientific Instruments, Vol. 30, no. 8, 1959, pp. 715-718.

4. Schroder, K.: Handbook of Electrical Resistivities of Binary Metallic Alloys, CRC Press, 1983.

5. Lazarev, E.; and Eklind, G. S.: (Moscos) Izv. Akad. Nauk. SSSR, Met. (4), 1979.

6. Dy, L. C.; and Williams, W. S.: Resistivity, Superconductivity, and Order-Disorder Transformations in Transition Metal Carbides and Hydrogen-Doped Carbides, J. Appl. Phys., vol. 53, no. 12, 1982, pp. 8915-8927.

7. Wood, C.; and Emin, D.: Conduction Mechanism in Boron Carbides, Phys. Rev., vol. B29, no. 8, 1984, pp. 4582-4597.

8. Hobart, H. F.: Evaluation Results of the 700°C Chinese Strain Gages, NASA Conference publication 2443, 1985, pp. 77-84.

TABLE I. SUMMARIZED RESULTS FOR ALLOYS

Alloy	wt.%	TCR (1000°C)(ppm/C) Cycle 2 Heating	Cooling	Drift (1000°C)(ppm/hr)
Pd-12Ag-Ni	1 Ni	407	424	5080
	3	392	415	3640
	5	390	380	1163
	7	375	394	1460
Al-79.3V-Mo	.25 Mo	-113	-129	687
	.75	- 57	- 49	837
	2.25	- 27	- 31	54
	4.25	- 20	- 13	103
Al-79.3V-Cr	.25 Cr	- 28	- 8	- 74
	.75	- 44	- 80	-176
	1.25	- 75	-106	130
	1.75	-107	- 95	170
	2.25	- 22	- 34	-140
	2.75	-114	-125	- 70
Nb-8V-Mo	1 Mo	436	450	360
	3	540	550	400
	5	523	487	484
	7	557	528	115

TABLE II. PREPARATION METHODS FOR CANDIDATE MATERIALS*

Specimen	Preparation Method	Remarks
TiN-1	HCD, Hollow Cathode Discharge	
-2	CVD, Chemical Vapor Deposition	
ZrN-1		P_{N_2} = 114 ppm-torr
-2	RFS, Radio Frequency Sputtering	= 108 ppm-torr
-3		= 96 ppm-torr
-4		= 990 ppm-torr
TaN-1		P_{N_2} = 330 ppm-torr
-2	Magnetron RFS	= 375 ppm-torr
-3		= 600 ppm-torr
CrN	HCD	
TiC-1	ARE, Activated Reactive Evaporation	
-2	CVD	
ZrC	ARE	
B_4C	Hot Pressed	Bulk
β-SiC-1	EBE, Electron Beam Evaporation	
-2	CVD	with N_2 dopant
α-SiC	Hot Pressed	Bulk

*all the specimens are prepared as thin films on the Al_2O_3 substrates except for B_4C, α-SiC and CVD prepared β-SiC on Si substrate.

TABLE III. SUMMARIZED RESULTS FOR TRANSITION METAL COMPOUND MX_x

Specimen	P_{N_2} (μtorr)	X/M	Resistivity (μohm-cm)	TCR* (ppm/°C)	DR* (%/hr)
TiN(HCD)		1	30.5	588	0.14
(CVD)		0.9 (V_N)	1130	143	0.22
ZrN-1	114	≈1 (V_N)	180	275	-0.26
-2	108	<1 ↓	211	228	-0.36
-3	96	<<1 +	255	184	1.6
-4	990	≈1.10 (V_{Zr})	393	212	-0.54
TaN-1	330	+	113	255	0.53
-2	375	↑	103	301	0.5
-3	600	(V_N)	165	438	-0.16
CrN			13.8	710	2%
TiC(ARE)		≈1	39.4	338	0.06
(CVD)		0.8 (V_C)	169	210	-0.5
ZrC		0.76 (V_C) or 0.9	560	180	-0.13

*TCR and DR values are based on the data of 1000°C and DR were measured after cycle two heating.

TABLE IV. SUMMARIZED RESULTS FOR SEMICONDUCTING CANDIDATE MATERIALS

Specimen	ρ (Ω-cm)	TCR (ppm/^{o}C)	DR (%/hr)	Remarks
B_4C	0.24	-200	0.095	tested in vacuum
		-250	0.9	tested in air
				hot pressed bulk
β-SiC-1	0.01	-330	-0.32	"pure" 0.25 μm thick, prepared by EBE
-2	0.2	-223	-0.53	with N_2 dopants 7 μm thick prepared by CVD
α-SiC	10.1	-2100	0.04	hot pressed bulk

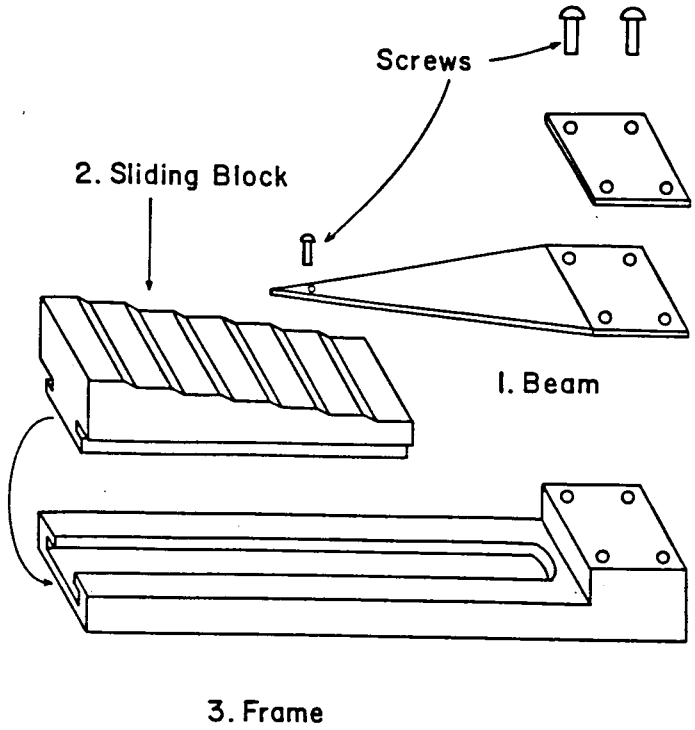

Fig. 1. Schematic diagram of the apparatus for gage factor measurements.

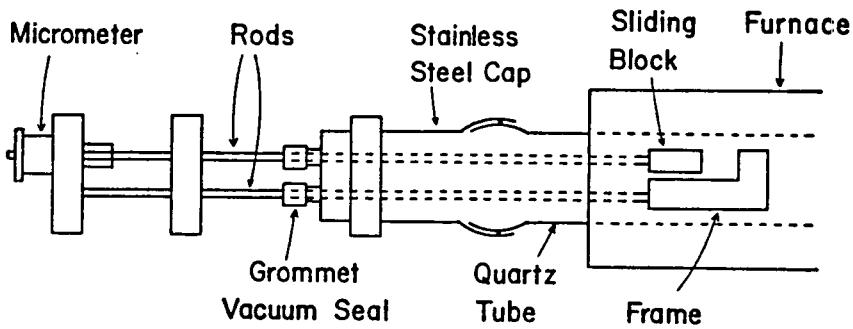

Fig. 2. Schematic diagram of the arrangement for actuating the sliding block to apply a strain to the specimen.

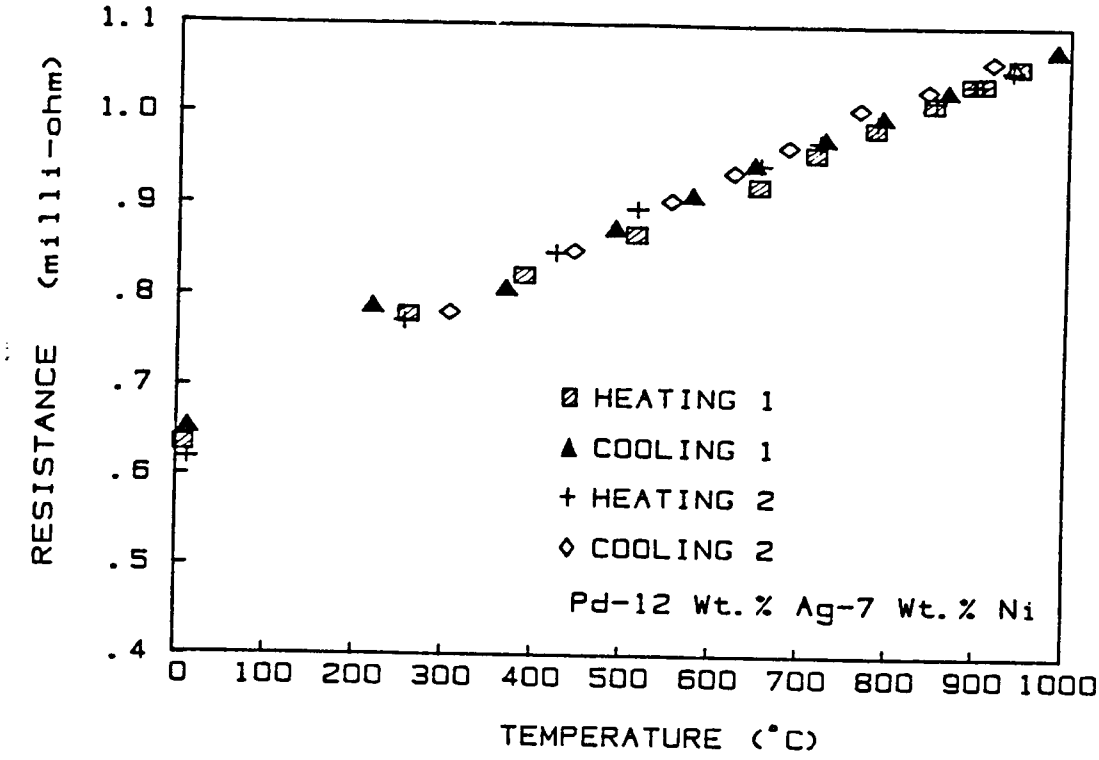

Fig. 3 RESISTANCE vs. TEMPERATURE

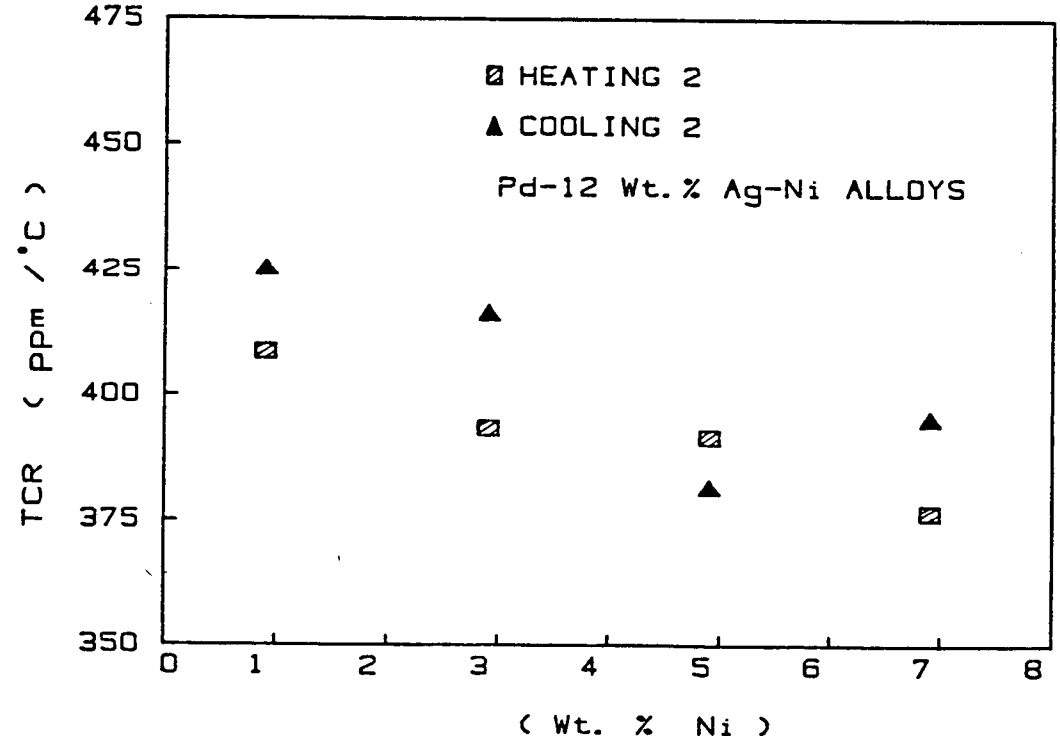

Fig. 4 TCR (1000°C) vs. Wt.% Ni

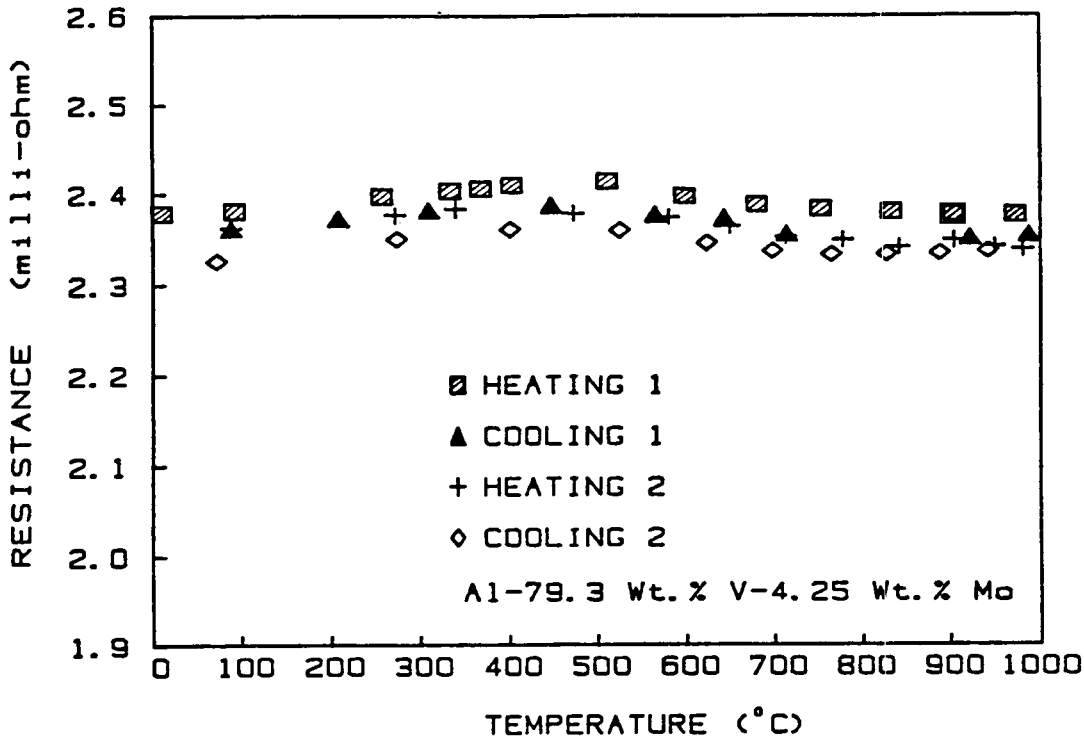

Fig. 5 RESISTANCE vs. TEMPERATURE

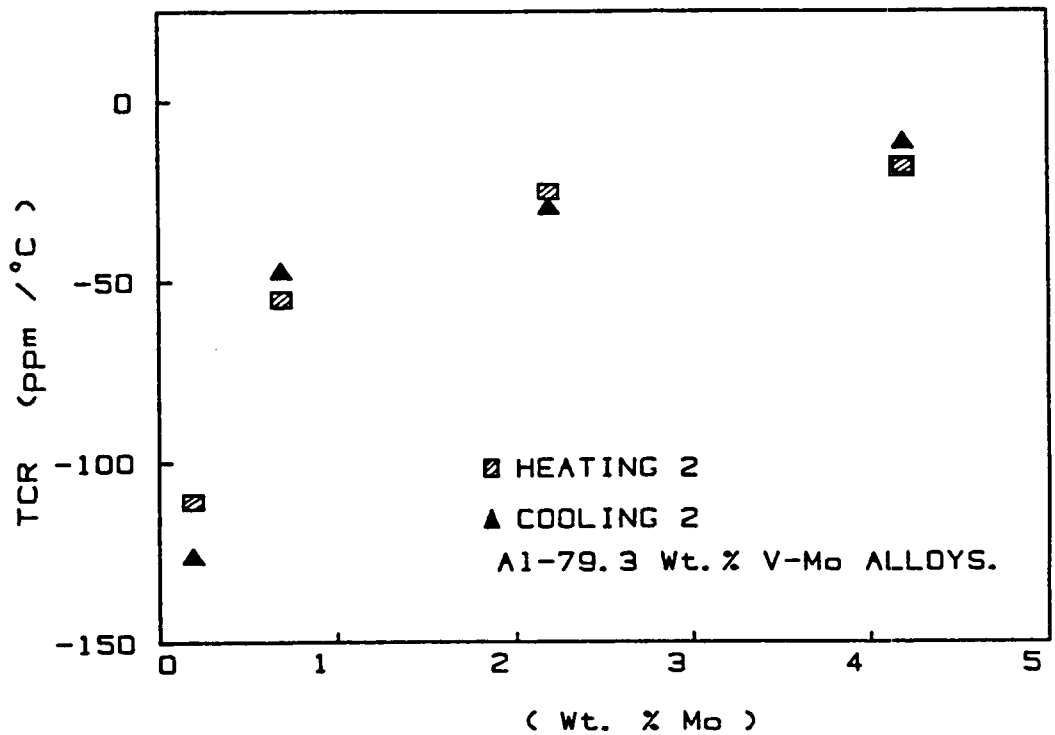

Fig. 6 TCR (1000°C) vs. Wt.% Mo

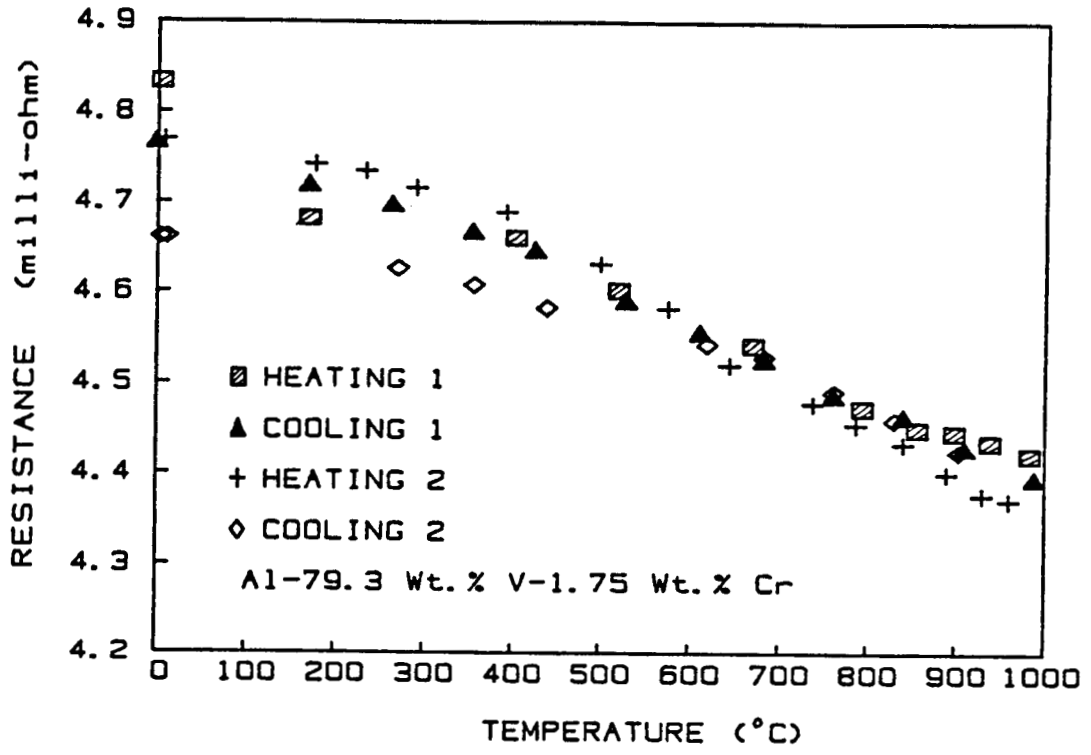

Fig. 7 RESISTANCE vs. TEMPERATURE

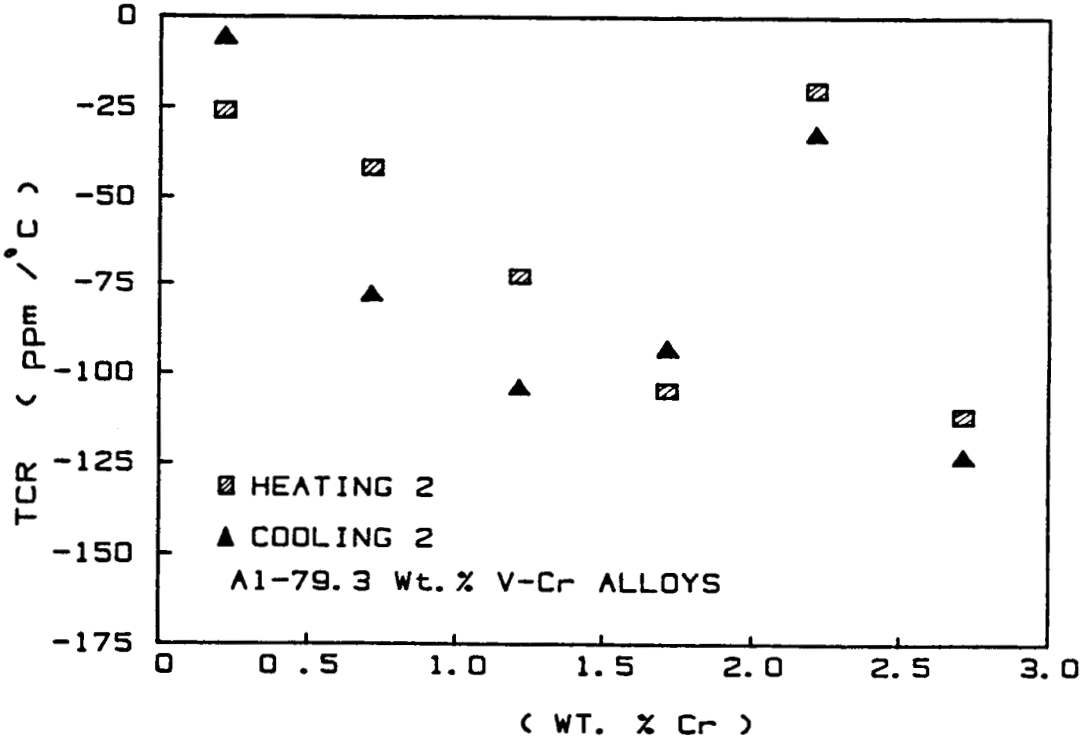

Fig. 8 TCR (1000 °C) vs. Wt.% Cr

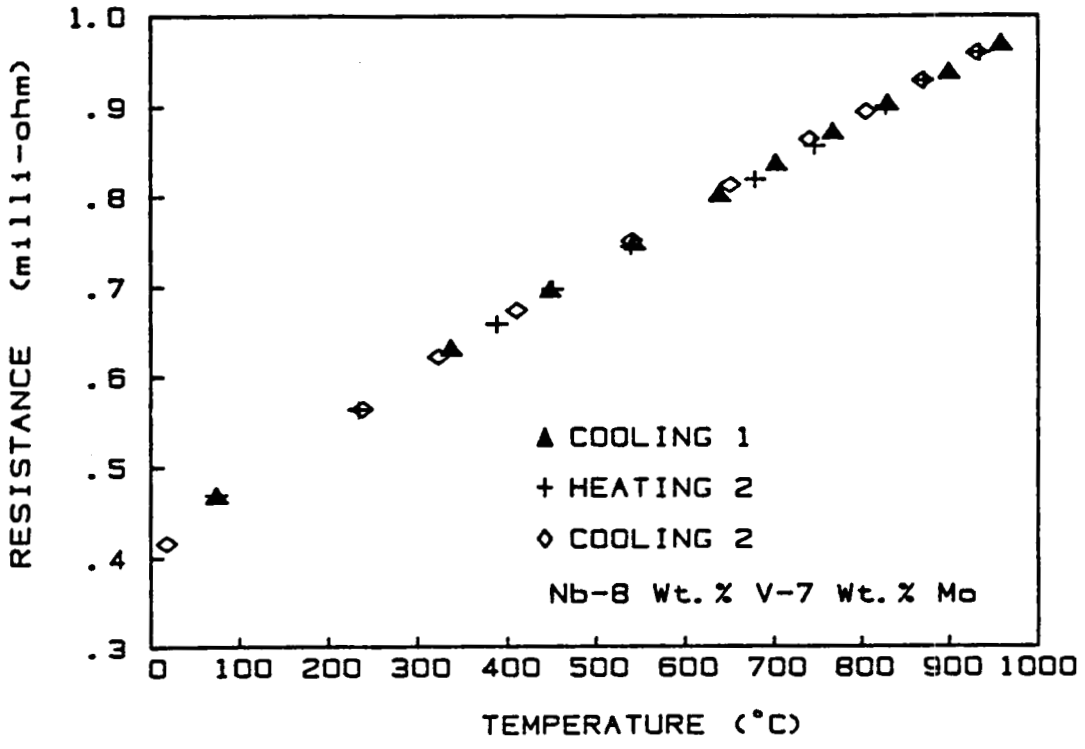

Fig. 9 RESISTANCE vs. TEMPERATURE

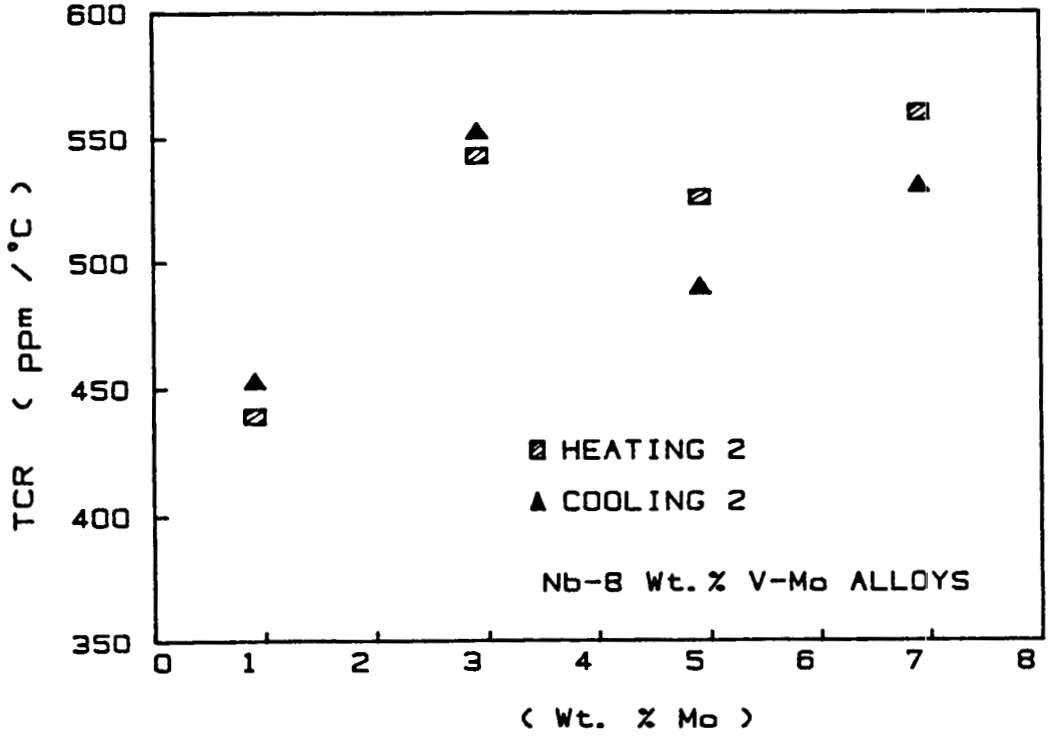

Fig. 10 TCR (1000°C) vs. Wt.% Mo

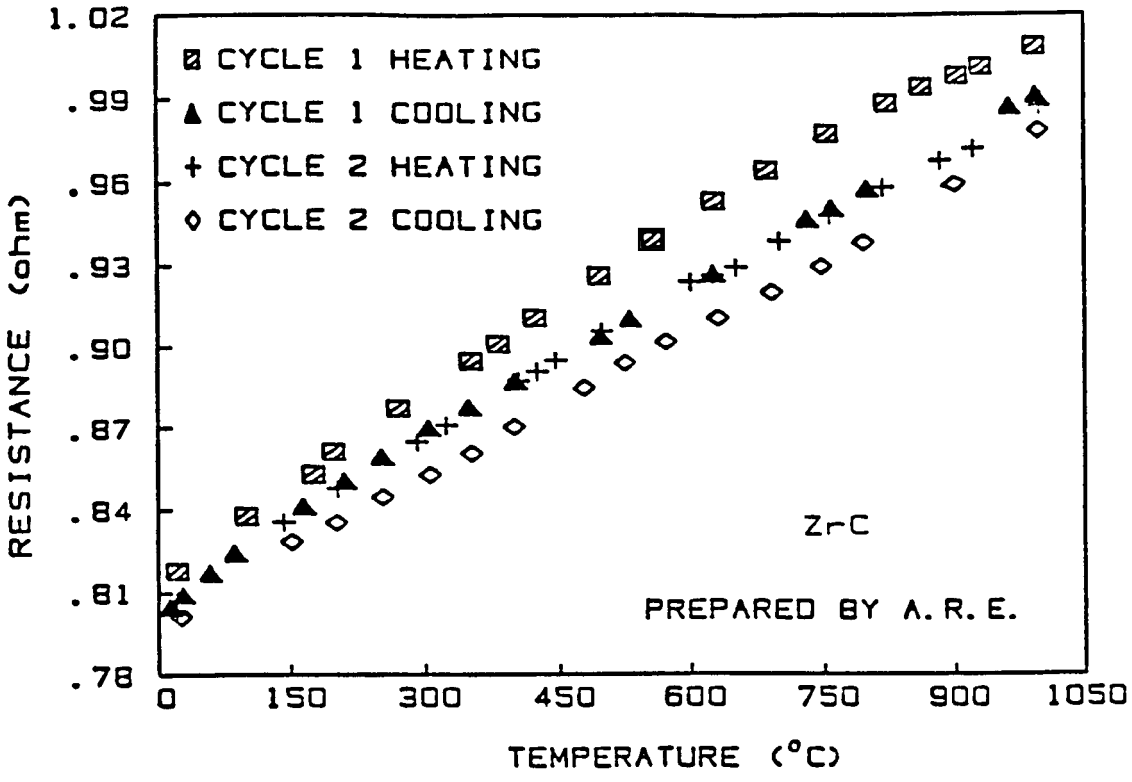

Fig. 11. Resistance vs. temperature of zirconium carbide.

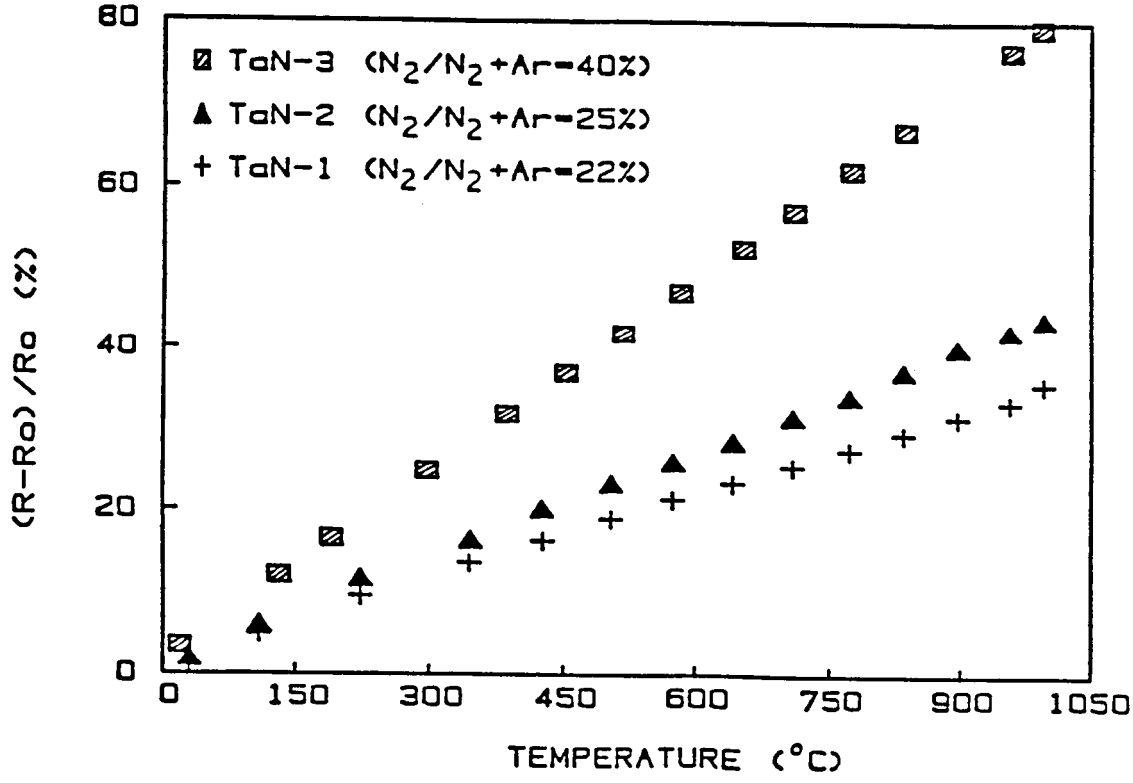

Fig. 12. Comparison the change in resistance with temperature for three tantalum nitrides.

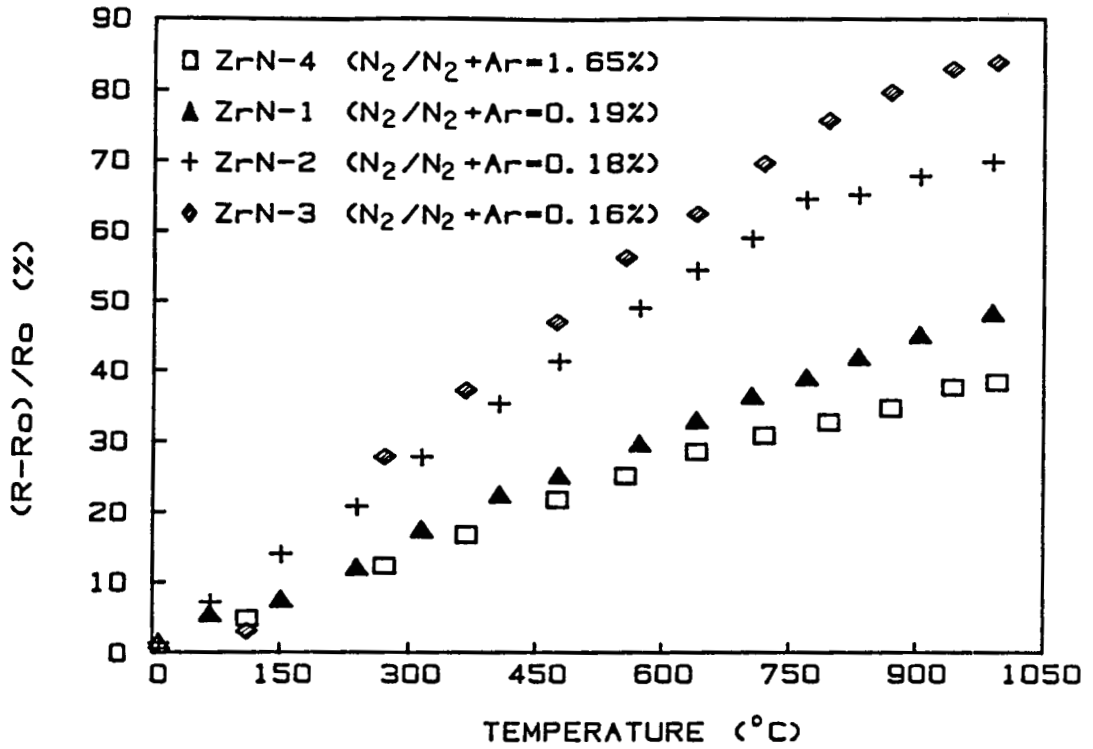

Fig. 13. Comparison the change in resistance with temperature for four zirconium nitrides.

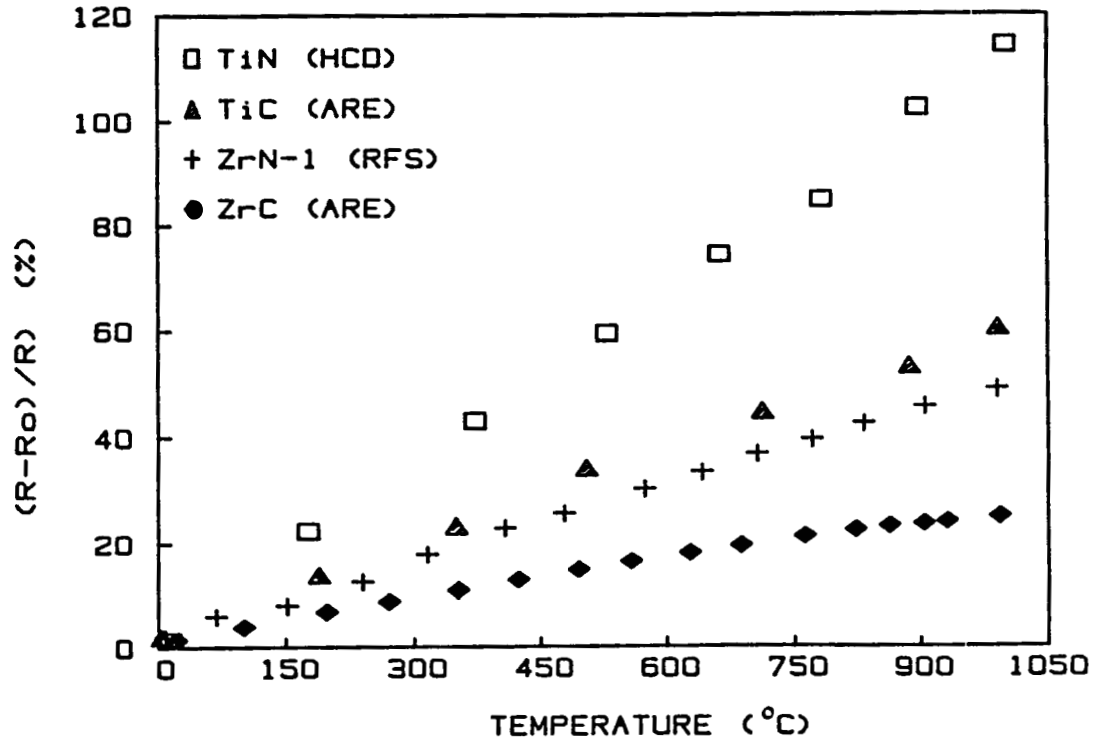

Fig. 14. Comparison the resistance change with temperature for TiC and TiN; ZrC and ZrN.

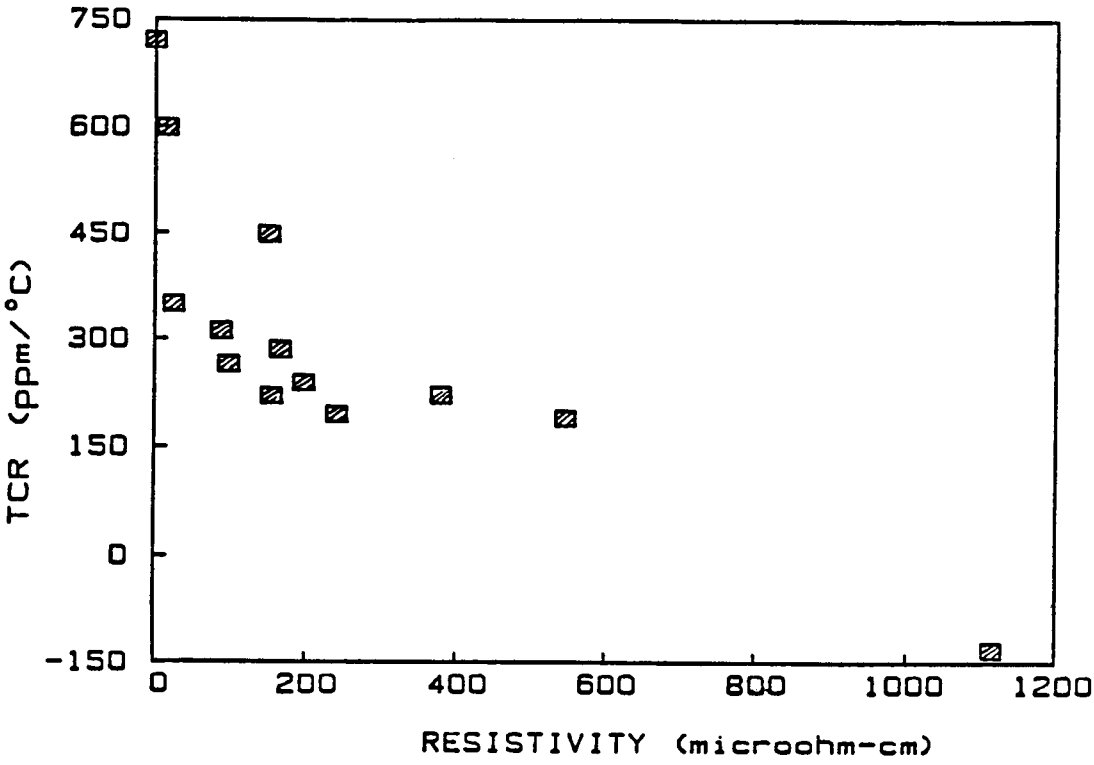

Fig. 15. TCR vs. resistivity for transition metal compounds.

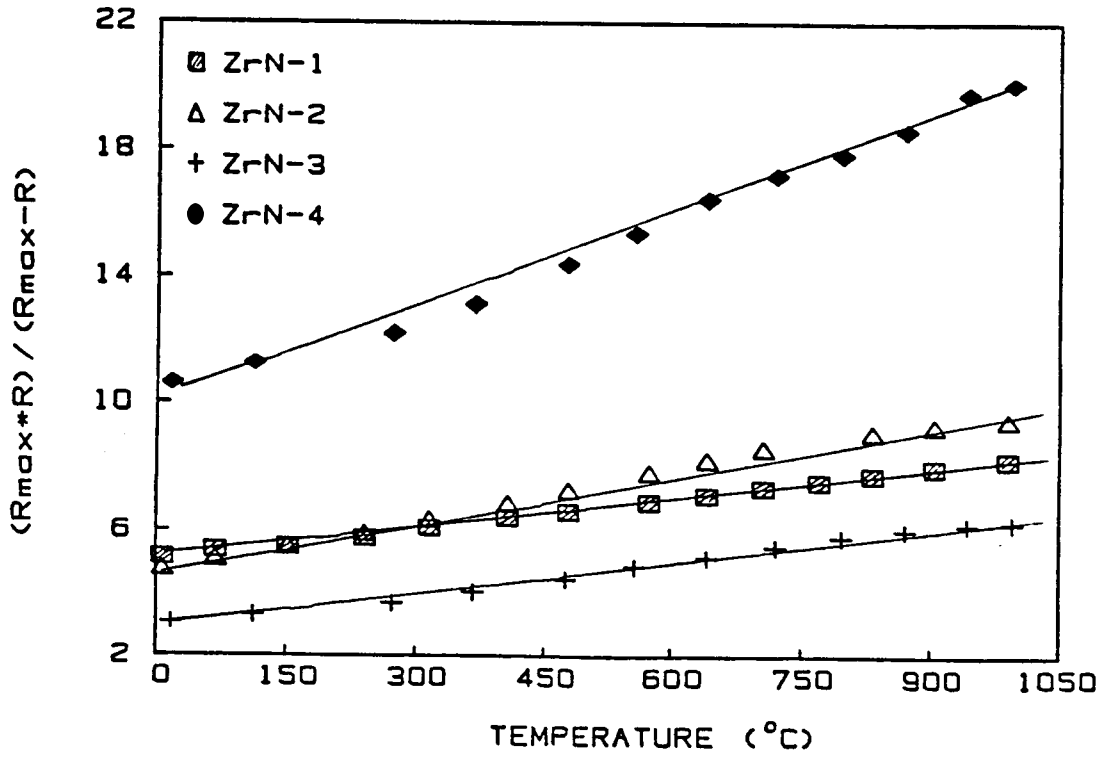

Fig. 16. (Rmax x R) / (Rmax-R) vs. temperature for four ZrN. Rmax correspondes to ρ_{max} = 1000 microohm-cm.

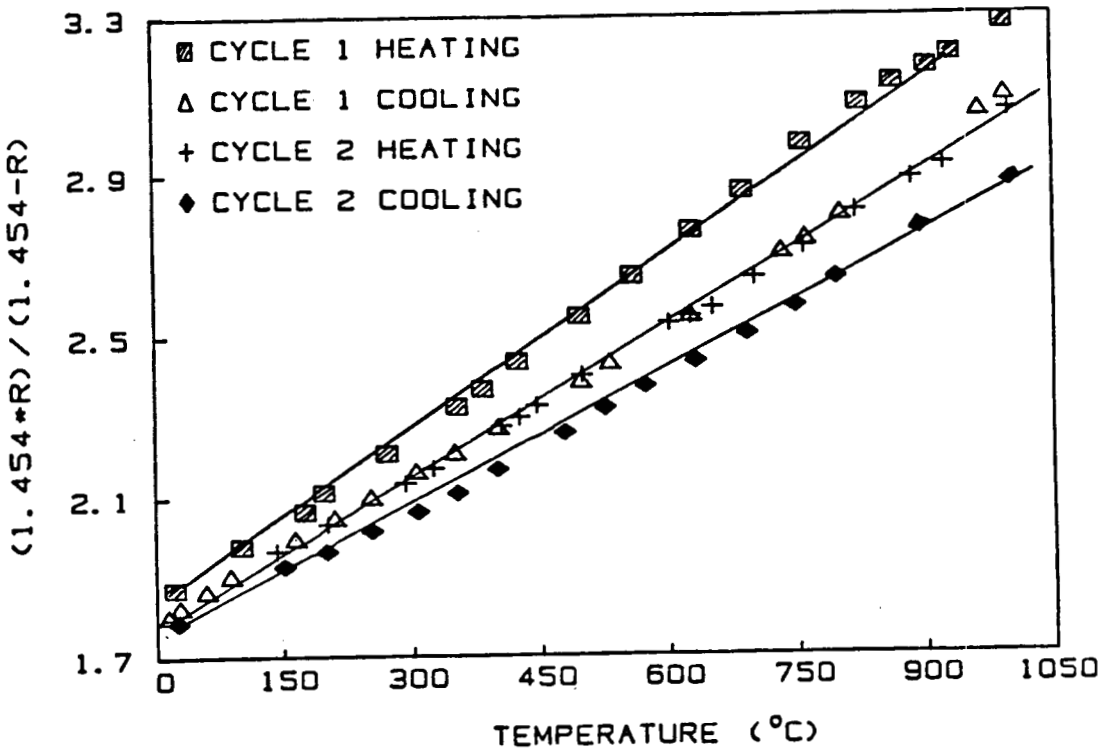

Fig. 17. (Rmax x R) / (Rmax-R) vs. temperature for ZrC.
Rmax=1.454 ohm correspondes to max = 1000 microohm-cm.

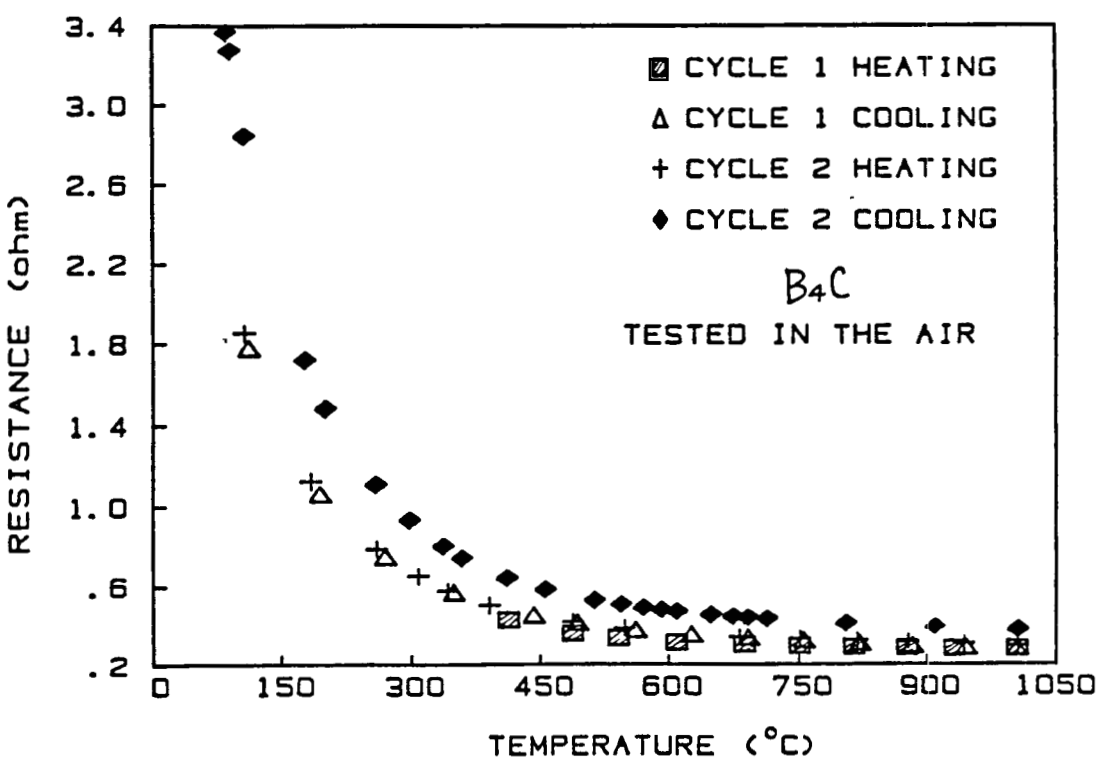

Fig. 18. Resistance vs. temperature for boron carbide tested in the air

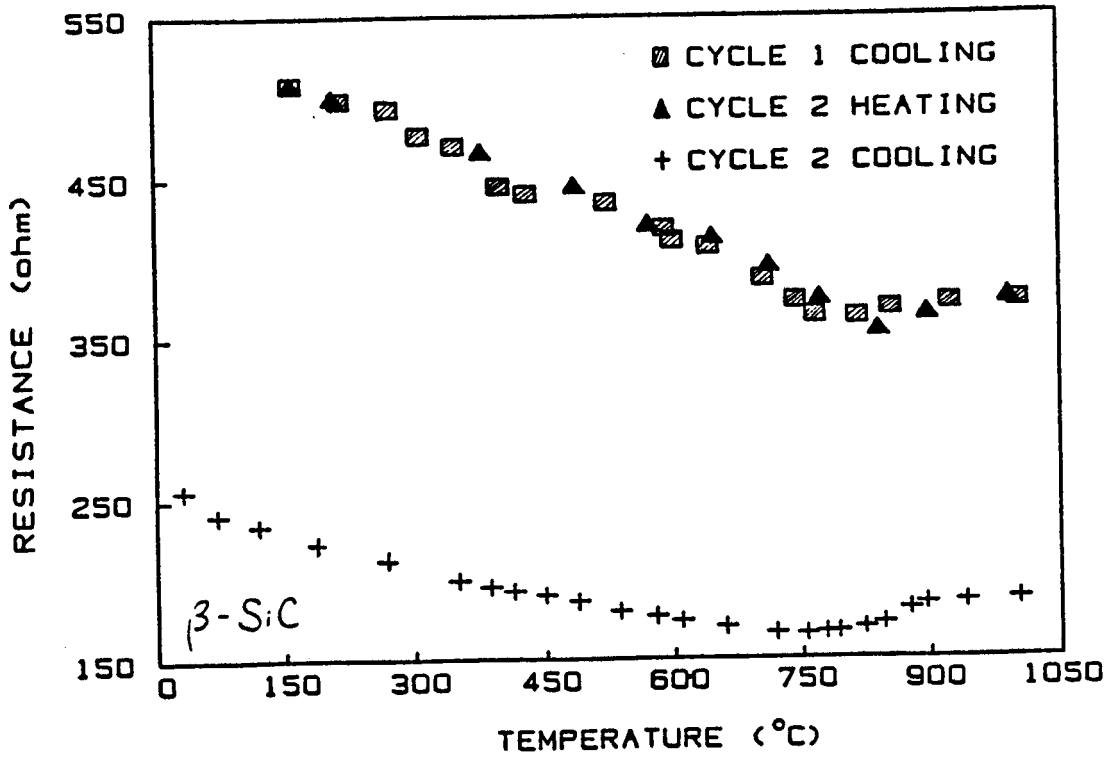

Fig. 19. Resistance vs. temperature for β-SiC film on the Al_2O_3 substrate. Film was porpared by CVD method.

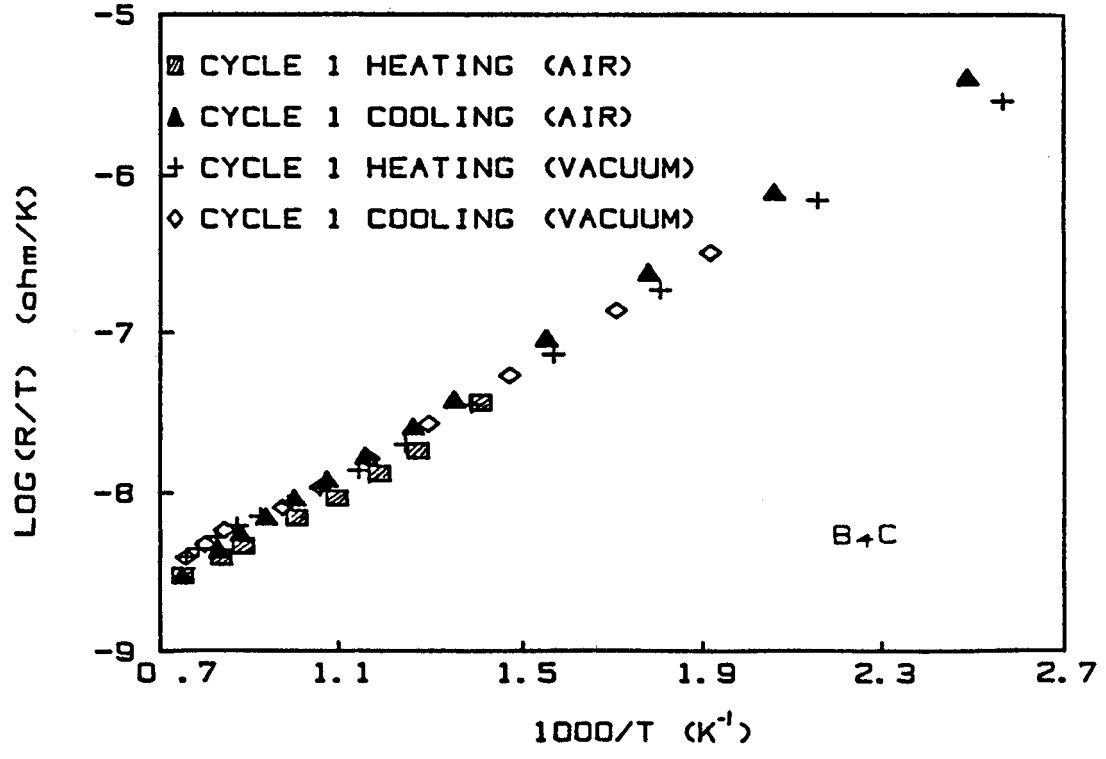

Fig. 20. Log(R/T) vs. 1/T for B_4C tested in air and in vacuum. Data are from the first cycle of heating and cooling.

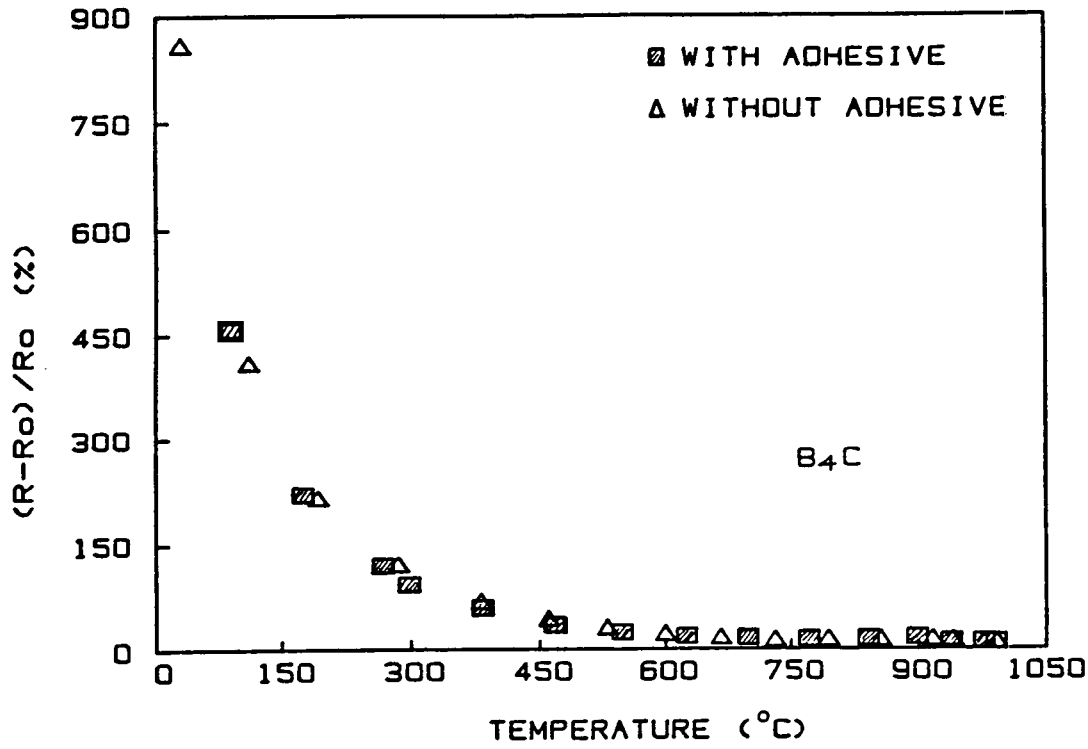

Fig. 21. Comparison the change in resistance with temperature of two B_4C: one with adhesive and one without

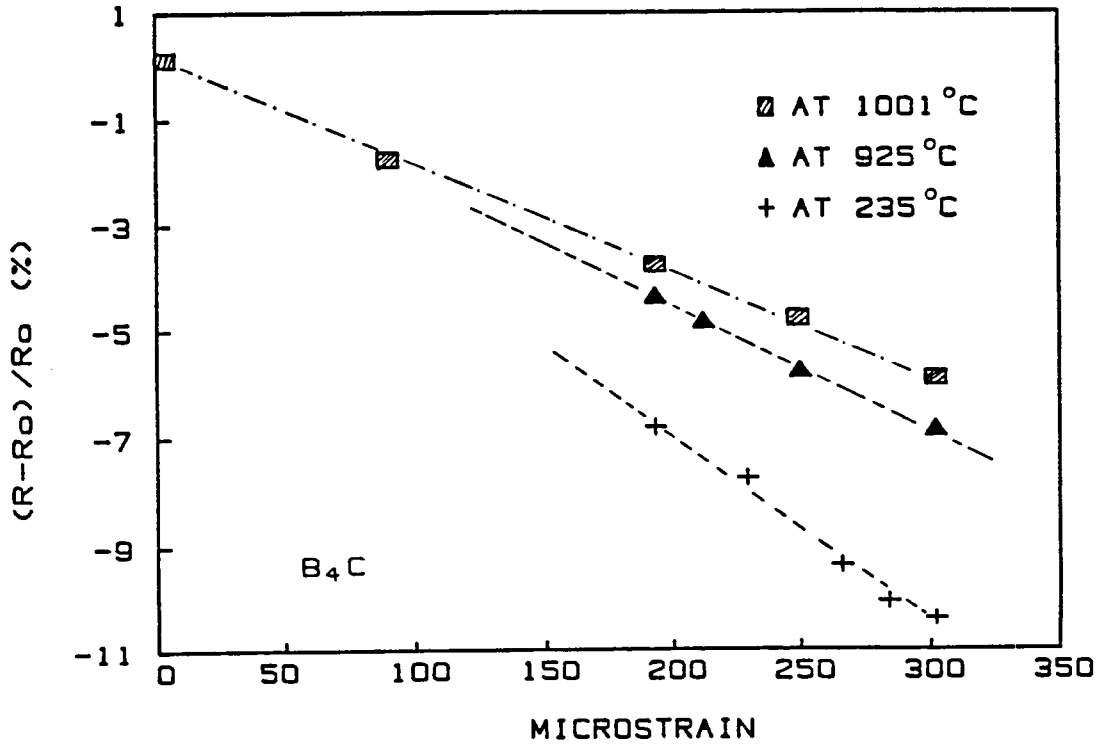

Fig. 22. Resistance vs. strain at three temperatures for B_4C. Resistance is normalized to its value under no strain.

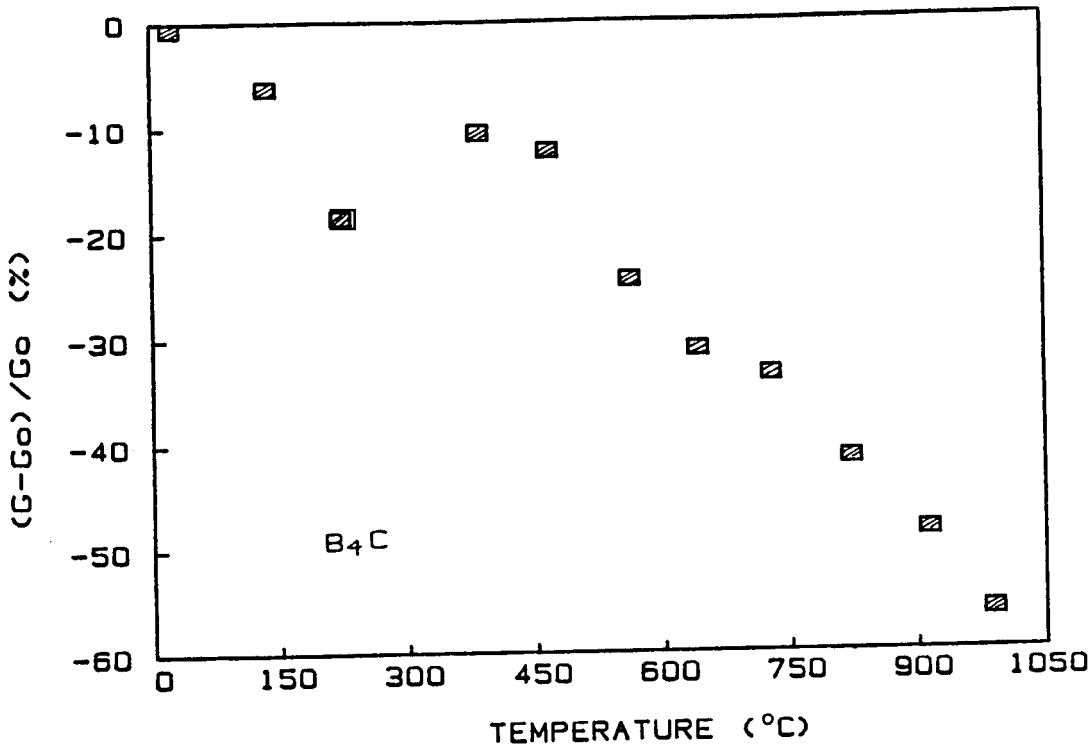

Fig. 23. Gage factor vs. temperature for boron carbide.

PROGRESS ON A PdCr WIRE STRAIN GAGE

David R. Englund
NASA Lewis Research Center
Cleveland, Ohio

The principal activity under the HOST effort to improve the state-of-the-art in high-temperature static strain measurement has been a contract under which a palladium-chromium (PdCr) alloy was developed. The contract effort is continuing with the goal of developing a thin-film high-temperature static strain gage system. In addition to this effort, we have contracted with Battelle-Columbus Laboratories to draw the PdCr alloy into wire and have been working here at Lewis to gain experience with this alloy as a wire strain gage. The progress of this work is reported herein.

THE PALLADIUM-CHROMIUM WIRE STRAIN GAGE SYSTEM

The plans for the strain gage system have been shaped by the known characteristics of the PdCr alloy. The specific characteristics that have had the greatest influence to date on these plans are the relatively high temperature coefficient of resistance (TCR) and the tendency for chromium to oxidize out of the alloy, causing the TCR to increase and the resistivity to decrease. Because of the oxidation problem, we will start working with rather large diameter wire (45 μm) and test its capability at temperatures up to 1250 K before we attempt to work with wire sizes in the range of 25 μm diameter. In addition, because of the relatively high TCR (175 ppm/K), a temperature compensation system will be used.

The temperature compensation technique chosen for this application uses a temperature-sensitive resistor in an adjacent leg of the bridge circuit. This technique has been used previously, especially with platinum-tungsten (PtW) gages, and has been described in texts on experimental stress analysis (e.g., ref. 1). The circuit, along with the nomenclature used here, is shown in figure 1. It can be shown that, if the effective temperature coefficient of the uncompensated strain gage is given by α_G, the effective temperature coefficient of the compensated circuit is given by

$$\left(1 - \frac{R_c}{R_c + R_B}\frac{\alpha_c}{\alpha_G}\right)\alpha_G$$

Temperature compensation is achieved by making

$$\left(1 - \frac{R_c}{R_c + R_B}\frac{\alpha_c}{\alpha_G}\right) = 0$$

The price one pays for this compensation is a reduced sensitivity to strain. The reduction in gage factor is given by

$$\left(1 - \frac{R_C}{R_C + R_B} \frac{G_C}{G_G}\right)$$

Optimum compensation is achieved by choosing a compensating resistor material with a very high TCR compared with that of the strain gage.

Preliminary Tests

Some preliminary tests were made to get experience with this technique; these were done using PtW strain gages mounted with ceramic cement to a constant strain beam which had been coated with flame-sprayed NiCrAlY and alumina. A 25-μm-diameter platinum (Pt) wire was used for the compensating resistor. The installed gages were soaked for 16 hr at 770 K before testing. Measurements of the effective temperature coefficients yielded 2990 ppm/K for the compensating resistor and 294 ppm/K for the strain gage. These values compare with handbook TCR values of 3940 and 240 ppm/K, respectively. The differences are due to differential thermal expansion (which should be a small effect), self-heating of the wires, and, in the strain gage, oxidation of the tungsten in the PtW alloy. The self-heating effect seems to be the major effect for the compensating resistor; therefore, measurement of temperature coefficient should be done with the same level of current that will be used in the bridge circuit.

A compensated bridge was set up based on the measured temperature coefficients. The resulting apparent strain over the temperature range to 770 K was within ±750 microstrain. The uncompensated apparent strain for this strain gage would have been approximately 140 000 microstrain at 770 K.

Tests on Palladium-Chromium Wire

Compensated strain gages have been made with the 45-μm-diameter PdCr wire. The strain gage shown in figure 2 is 8.2 mm long and 10.6 mm wide and has a nominal resistance of 81 Ω. The compensating resistor is Pt wire 25 μm in diameter, and the grid is 7.1 mm long and 3 mm wide. This gage is larger in size and lower in resistance than might be desirable because of the diameter of the wire used.

The test plan for these gages emphasizes testing for thermal stability and temperature compensation. Measurements of gage factor, strain range, etc., will be delayed until the temperature range over which we have acceptable repeatability is established. For this testing, the strain gages with Pt compensating elements are mounted on Hastelloy-X plates using Bean-H cement over flame-sprayed alumina (a base coat of flame-sprayed NiCrAlY is used under the alumina). An alternative mounting procedure will use plasma-sprayed alumina for both the insulating layer and for mounting the strain gage (i.e., no ceramic cement). The sequence of testing will start with a heat soak for stress relief followed by thermal cycles to permit measurement of the installed temperature coefficients and their repeatability. A temperature-compensated bridge will be established using the installed temperature coefficients, and a series of apparent strain and no-load drift tests will be run. For tests in which the gages are mechanically loaded, the gages will be mounted on Inconel 718 constant strain beam.

Test results to date indicate that the installed temperature coefficients after a 3-hr soak at 1230 K in air are 224 ppm/K for the strain gage and 1620 ppm/K for the platinum compensating resistor.

REFERENCES

1. Dove, R.C.; and Adams, P.H.: Experimental Stress Analysis and Motion Measurements. C.E. Merrill Books Inc., Columbus, OH, 1964.

TEMPERATURE COMPENSATED STRAIN GAGE BRIDGE CIRCUIT AND NOMENCLATURE USED IN CIRCUIT EQUATIONS

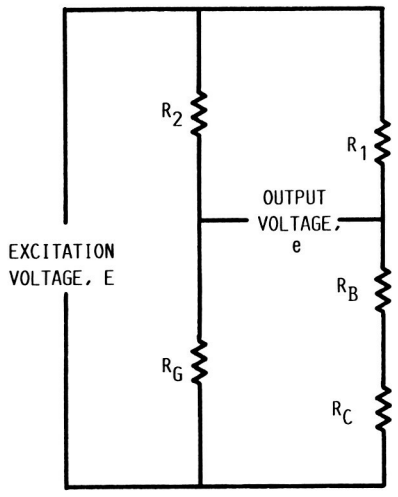

R_G	STRAIN GAGE $\Delta R_G/R_G = [(TCR)_G + G_G(\Delta TEC)_G]\Delta T + G_G\varepsilon = \alpha_G \Delta T + G_G\varepsilon$
R_C	RESISTANCE THERMOMETER $\Delta R_C/R_C = [(TCR)_C + G_C(\Delta TEC)_C] \Delta T + G_C\varepsilon = \alpha_C\Delta T + G_C\varepsilon$
R_B	FIXED BALLAST RESISTOR
R_1, R_2	BRIDGE COMPLETION RESISTORS
TCR	TEMPERATURE COEFFICIENT OF RESISTANCE
ΔTEC	DIFFERENCE IN THERMAL EXPANSION COEFFICIENTS BETWEEN RESISTOR AND SUBSTRATE
G	GAGE FACTOR
α	EFFECTIVE TEMPERATURE COEFFICIENT, [(TCR) + G(ΔTEC)]
ε	STRAIN

CD-87-29042

Figure 1

WIRE STRAIN GAGE MADE FROM 45-μm-DIAM PdCr WIRE WITH 25-μm-DIAM Pt WIRE COMPENSATING RESISTOR

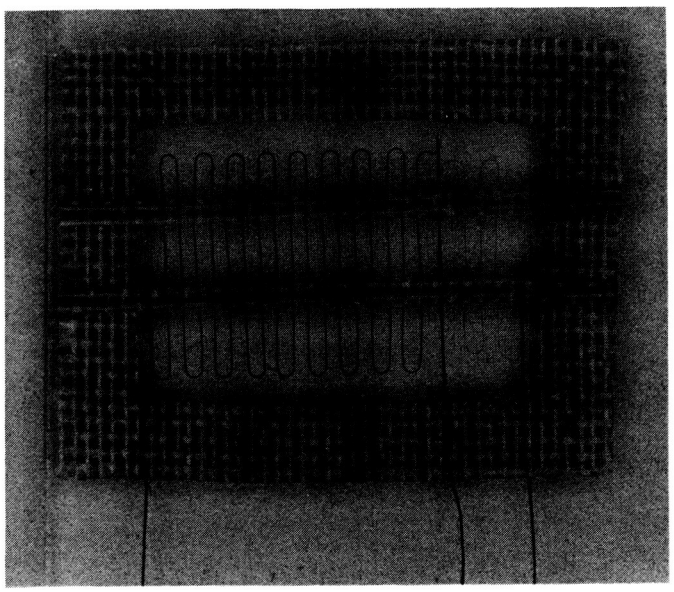

CD-87-29041

Figure 2

A COMPARISON OF TURBULENCE MEASUREMENT METHODS

Gustave C. Fralick
NASA Lewis Research Center
Cleveland, Ohio

Laser doppler anemometers are by now widely used to measure the turbulence properties of moving fluids. Their nonintrusive nature makes their use very attractive. By the nature of the measurement process, the turbulence parameters such as turbulence intensity and turbulence scale are based strictly on velocity measurements. However, if one is interested in convective heat transfer and if the gas stream has appreciable density fluctuations (which are equivalent to temperature fluctuations if the static pressure is constant), the turbulence should probably be based on the density-velocity product. Hot-wire anemometers, for instance, give results based on the product of density and velocity, and the operation of a hot-wire anemometer depends on the flow of heat away from the wire. Hot-wire anemometry, though, is not practical in high-temperature or high velocity flows.

In the experiment described herein, temperature (density) and velocity are measured separately but simultaneously as functions of time so that it is possible to determine the relationships among velocity, density, and the product of density and velocity.

DESCRIPTION OF EXPERIMENT

An atmospheric burner rig was used to provide the flow for this experiment. Data were taken at various flow conditions, at mean temperatures ranging from 850 to 1598 °F, at Mach numbers from 0.19 to 0.22, and at values of Reynolds number divided by characteristic length in the range 25 000 to 51 000 $in.^{-1}$. Probe location was varied from 2 to 4 in. from the burner outlet and up to 1/2 in. from the centerline. Temperature fluctuations as great as ±500 °F were measured in a similar burner, so compensated temperature fluctuations are expected to be in this range. This level of temperature fluctuation implies a density fluctuation of approximately 17 percent; previous measurements of velocity fluctuation in this rig were in the range of 5 to 10 percent.

Temperatures were measured with a dual-wire thermocouple probe (fig. 1) which is part of the dynamic gas temperature measurement system (refs. 1 and 2). The probe consists of two platinum-rhodium thermocouples located in close proximity to each other. The wires are of different diameters, 3 and 10 mils, respectively, in this case. By comparing the signals from the two thermocouples at different frequencies, it is possible to generate a compensation spectrum and thus to determine temperature fluctuations at frequencies up to 1 kHz.

Velocity data were supplied by a fringe laser-doppler anemometer (ref. 3) with sampling volume location varied from 0.2 to 2.5 mm upstream of the thermocouples. Data rates varied from 6.2 kHz farther from the burner outlet to 45.2 kHz closer to the burner outlet.

Figure 2 shows the setup of the probe in the flow stream of the burner and the crossing laser beams which form the sampling volume just in front of the probe.

The signals from the thermocouples and the laser were recorded on FM magnetic tape for later processing. The quantities stores are the ac-coupled voltage from both thermocouples, which permits frequency compensation of the temperature data, the dc-coupled signal from the large thermocouple, which provides the mean temperature, and the laser doppler signal, from which both mean and instantaneous velocity can be extracted.

PRELIMINARY RESULTS

For turbulence measurements, the quantities of interest are $V_{rms}/\bar{V}$, $(\rho V)rms/(\overline{\rho V})$, and their autocorrelations, which provide a measure of turbulence intensity and turbulence scale. The cross correlations are also of interest; they will answer questions such as whether the velocity peaks are related to the hotter combustion products or to the cooler, denser filaments of dilution air. Figure 3 is the cross correlation of the velocity and compensated temperature signal from the 3-mil thermocouple. The probe was located on the burner axis 4 in. from the burner face. The flow conditions were $M = 0.325$, $Re/L = 41\ 000\ in.^{-1}$, and $T = 1436\ °F$. The sharp, central peak indicates either very high correlation between the temperature and velocity fluctuations or a noise problem. This is under investigation.

FUTURE EFFORTS

Future efforts will proceed in several areas. One will be a closer investigation of the cross correlation for smaller time delays. Cross correlations calculated using uncompensated temperature signals showed peaks for time delays of a few milliseconds (ref. 4). Data from the other probe locations will also be reduced, as the degree of correlation can be expected to decline as more room air is entrained in the flow. The density-velocity product as a function of time must also be generated; it will then be possible to compare turbulence intensity based on velocity with that based on the density-velocity product.

REFERENCES

1. Elmore, D.L.; Robinson, W.W.; and Watkins, W.B.: Dynamic Gas Temperature Measurement System. (PWA/GPD-FR-17145-VOL-1, Pratt and Whitney Aircraft; NASA Contract NAS3-23154) NASA CR-168267-VOL-1, 1983.

2. Elmore, D.L.; Robinson, W.W.; and Watkins, W.B.: Further Development of the Dynamic Gas Temperature Measurement System. (P/W/GPD-FR-19381-VOL-1,-2, Pratt and Whitney Aircraft; NASA Contract NAS3-24228) NASA CR-179513-VOL-1,-2, 1986.

3. Seasholtz, R.G.; Oberle, L.G.; and Weikle, D.H.: Laser Anemometry for Hot Section Applications. Turbine Engine Hot Section Technology - 1983, NASA CP-2289, 1983, pp. 57-67.

4. Fralick, G.C.: Correlation of Velocity and Velocity-Density Turbulence in the Exhaust of an Atmospheric Burner. Turbine Engine Hot Section Technology - 1985, NASA CP-2465, 1985, pp. 81-85.

DUAL WIRE THERMOCOUPLE PROBE

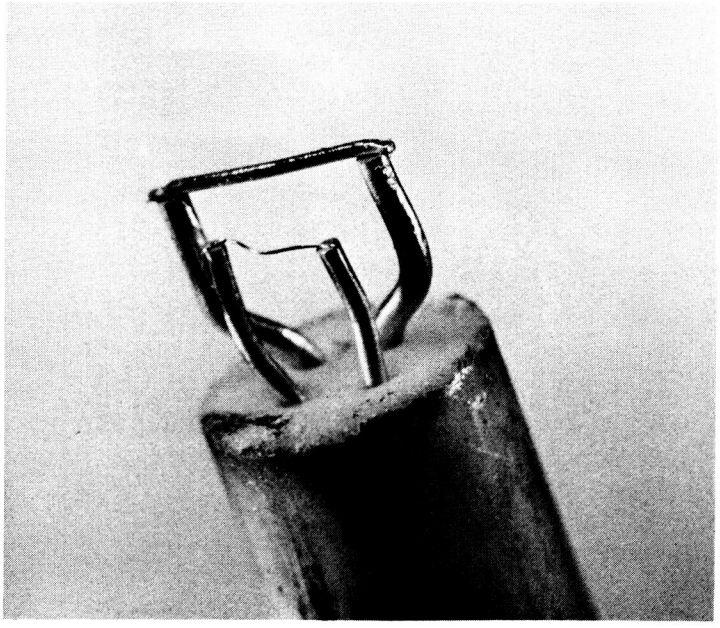

CS-85-3406

Figure 1

DUAL WIRE THERMOCOUPLE AND LDA SAMPLING VOLUME IN EXHAUST OF ATMOSPHERIC BURNER

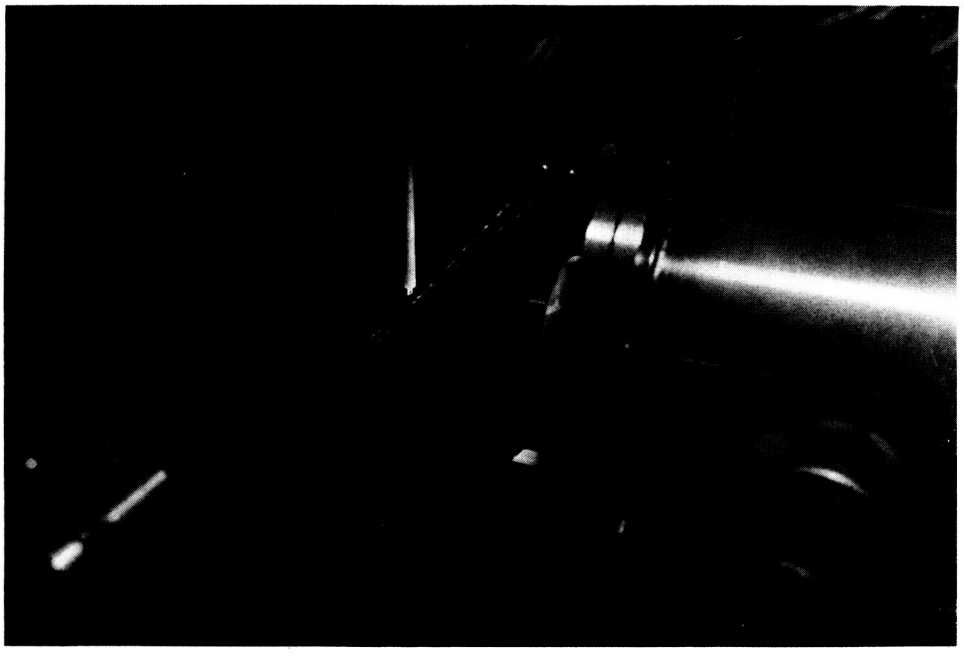

CS-85-3405

Figure 2

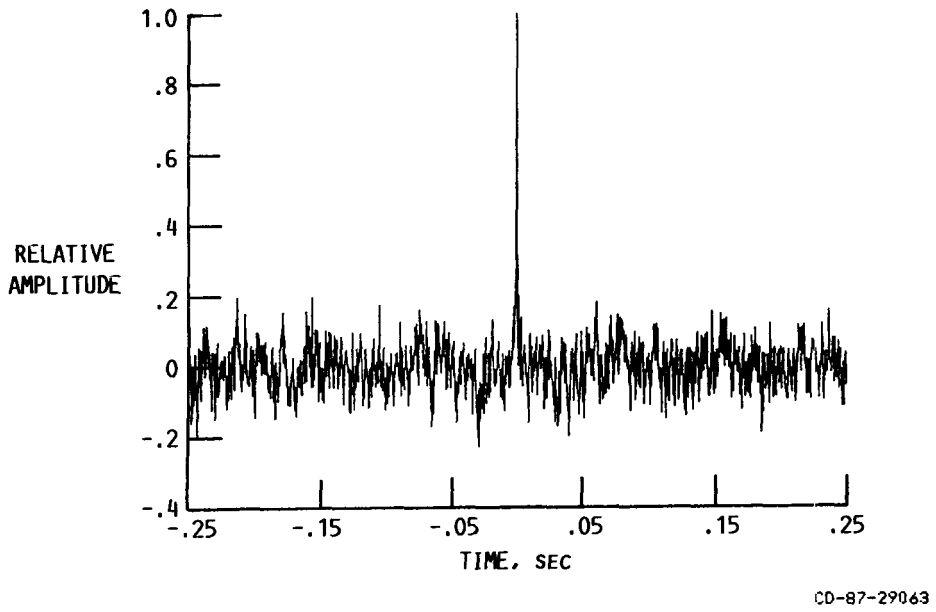
VELOCITY-TEMPERATURE CROSS CORRELATION
$\bar{V}$ =212 m/sec, $\bar{T}$ =1436 °F
RELATIVE AMPLITUDE
1.0
.8
.6
.4
.2
0
-.2
-.4
-.25
-.15
-.05
.05
.15
.25
TIME, SEC
CD-87-29063

Figure 3

AEROTHERMAL MODELING PROGRAM - PHASE II ELEMENT A: IMPROVED NUMERICAL METHODS FOR TURBULENT VISCOUS RECIRCULATING FLOWS

K.C. Karki, H.C. Mongia, S.V. Patankar*, and A.K. Runchal**
Allison Gas Turbine Division
General Motors Corporation
Indianapolis, Indiana

The objective of the NASA-sponsored Aerothermal Modeling Program, Phase II--Element A, is to develop improved numerical schemes for predicting combustor flow field. The effort consists of three technical tasks. Tasks 1 and 2 have been completed. Task 3 is in progress.

TASK 1--NUMERICAL METHOD SELECTION

Task 1 involved the evaluation of various candidate numerical schemes and selection of the promising schemes for detailed assessment under Task 2. The criteria for evaluation included accuracy, computational efficiency, stability, and ease of extension to multidimensions. The candidate schemes were assessed against a variety of simple one- and two-dimensional problems. These results led to the selection of the following schemes for further evaluation:

- o flux-spline schemes (linear and cubic)
- o Controlled Numerical Diffusion with Internal Feedback (CONDIF)

To improve the computational efficiency, a direct inversion technique was also selected for further testing. In this approach, the continuity and momentum equations are solved directly, rather than sequentially.

TASK 2--TECHNIQUE EVALUATION

Task 2 involved an in-depth evaluation of the numerical schemes selected in Task 1. The accuracy was judged by solving test problems for which reference solutions are available. The test cases included problems of scalar transport, laminar flows, and turbulent flows. These results indicated superior performance of the improved schemes. From scalar transport problems it was seen that the cubic flux-spline results were more accurate than those from the linear flux-spline. However, the cubic spline involved much more computational and programming effort and was not considered for fluid flow calculations.

For all the test problems, the linear flux-spline results were more accurate than the CONDIF results. The flux-spline scheme exhibited mild oscillations in the regions of steep gradient. However, it was felt that the presence of physical diffusion would tend to diminish these oscillations.

* University of Minnesota
**Analytic and Computational Research, Inc.

To improve the computational efficiency, the flux-spline (linear) was combined with a direct inversion technique using the Yale Sparse Matrix Package (YSMP) [ref 1]. Use of such a technique resulted in a factor of 2 to 3 reduction in the computational effort compared to the sequential solvers. A summary of the Task 2 effort is presented in references 2 and 3.

TASK 3-3D COMPUTATIONAL EVALUATION

Task 3, currently in progress, involves the incorporation of the flux-spline scheme and direct solution strategy in a computer program for 3D flows.

Due to the large storage requirement for the LU factorization, it is not possible to invert the continuity and momentum equations for the entire 3D field. Consequently, a plane-by-plane solution strategy was devised in which the cross stream (in-plane) velocities and pressure are solved in a coupled manner and the axial velocity is solved decoupled. However, the axial momentum and continuity equations are satisfied simultaneously. Such a procedure used in conjunction with the power-law scheme [ref 4] for convection-diffusion was found to be fast convergent and robust. Work is continuing on the use of the flux-spline scheme.

To demonstrate the accuracy of the flux-spline scheme for 3D flows, results are presented for the following two test cases:

- o radial heat conduction in a rotating hollow sphere
- o shear-driven laminar flow in a cubic cavity

Radial Heat Conduction in a Rotating Hollow Sphere

The problem is shown schematically in figure 1. A hollow sphere with its center located at the origin of a fixed Cartesian coordinate system rotates about the x-axis with a constant angular velocity $\omega = \omega \vec{e}_x$. The radius of the the inner surface is r_1, and is maintained at a uniform temperature T_1; r_2 is radius of the outer surface, which is at temperature T_2. For the case considered here, the radius ratio (r_2/r_1) is taken as 2.

With uniform properties under steady state, the temperature distribution is given by:

$$\theta = \frac{T - T_2}{T_1 - T_2} = \frac{2}{(r/r_1)} - 1 \qquad (1)$$

This problem, which is one-dimensional in the radial direction, appears three-dimensional if formulated in a Cartesian coordinate system. The calculation domain selected is shown as R in figure 1. The calculation domain is assumed to be fixed in space, so that the material within R has a steady velocity field given by:

$$\vec{V} = (\omega \vec{e}_x) X (x \vec{e}_x + y \vec{e}_y + z \vec{e}_z) \qquad (2)$$

The exact temperature distribution in Cartesian coordinates is obtained by transforming equation (1) to Cartesian coordinates:

$$\theta = \frac{2\, r_1}{\sqrt{x^2 + y^2 + z^2}} - 1 \qquad (3)$$

A uniform 11 x 11 x 11 grid was used to discretize the computational domain. Results were obtained for a range of Peclet numbers ($Pe = \rho\omega r_1^2/\Gamma$) and compared with the power-law scheme. Table I shows the error at the center point of the domain. The error has been defined as:

$$\varepsilon = \frac{|T_{computed} - T_{exact}|}{(T_{max} - T_{min})_{exact}} \times 100$$

Shear-Driven Laminar Flow in a Cubic Cavity

The flow situation under consideration is shown in figure 2. Due to symmetry considerations, the computational domain extended only half cavity width in the lateral (z) direction.

The flow Reynolds number is 400 and a uniform 22 x 22 x 12 (x, y, z) grid is employed for computations. The present results have been compared with the solution of Ku et al. [ref 5] obtained using a pseudospectral method (25 x 25 x 13 mode). This solution has been designated as "REFERENCE" in subsequent figures.

Figure 3 shows the velocity profiles of the u-component on the vertical centerline and the v-component on the horizontal centerline of the plane Z = 0.5. It is seen that for the same number of grid points the flux-spline solution is more accurate than the (lower-order) power-law solution.

Computations for turbulent flows are in progress.

REFERENCES

1. Eisenstat, M. C., Gursky, M. C., Shultz, M. H. and Sherman, A. H.; Yale Sparse Matrix Package, II, The Nonsymmetric Codes, Research Report No. 114, Yale University Department of Computer Sciences, 1977.
2. Patankar, S. V., Karki, K. C. and Mongia, H. C.; Development and Evaluation of Improved Numerical Schemes for Recirculating Flows, AIAA-87-0061.
3. Runchal, A. K., Anand, M. S. and Mongia H. C.; An Unconditionally-Stable Central Differencing Scheme for High Reynolds Number Flows, AIAA-87-0060.
4. Patankar, S. V.; Numerical Heat Transfer and Fluid Flow, Hemisphere, 1980.
5. Ku, H. C., Hirsch, R. S., and Taylor, T. D.; A Pseudospectral Method for Solution of the Three-Dimensional Incompressible Navier-Stokes Equations, Journal of Computational Physics, Vol 70, 1987, pp 439-462.

Table I.--ERROR AT THE CENTER POINT OF THE COMPUTATIONAL DOMAIN

	Pe = 1	10	100	1000
Error (ϵ) power-law	4.095×10^{-3}	1.439×10^{-2}	2.922×10^{-1}	2.756×10^{-1}
Error (ϵ) flux-spline	1.365×10^{-3}	4.445×10^{-3}	1.609×10^{-4}	1.177×10^{-2}

RADIAL HEAT CONDITIONS IN A ROTATING HOLLOW SPHERE: (a) PROBLEM SCHEMATIC; (b) DOMAIN DISCRETIZATION PATTERN ($x_1 = y_1 = z_1 = r_1/\sqrt{3}$; $x_2 = y_2 = z_2 = r_2/\sqrt{3}$).

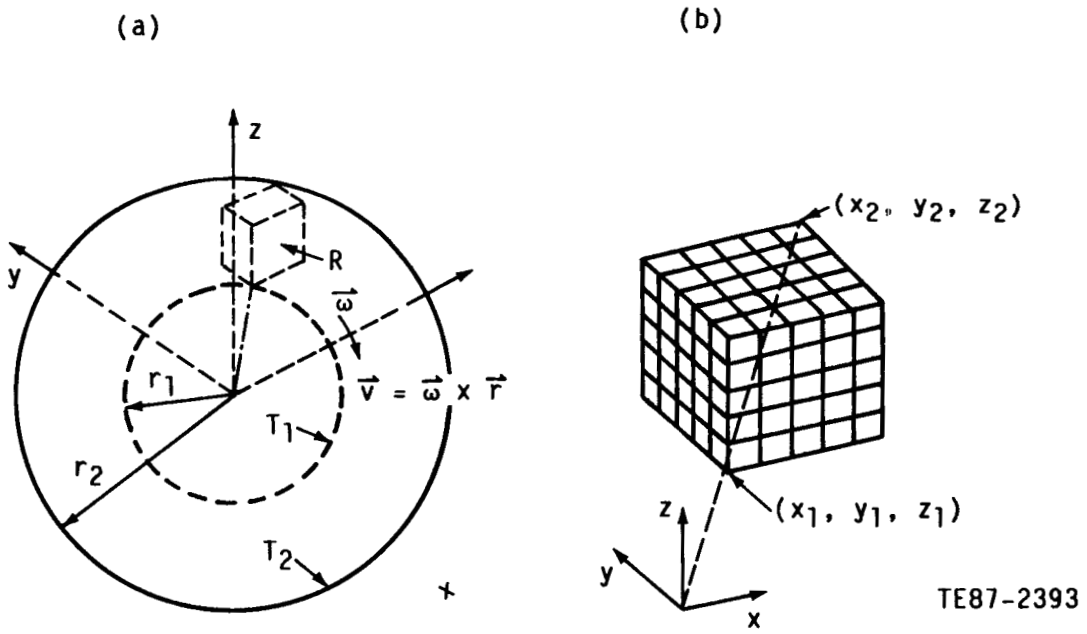

Figure 1

3D CAVITY FLOW CONFIGURATION

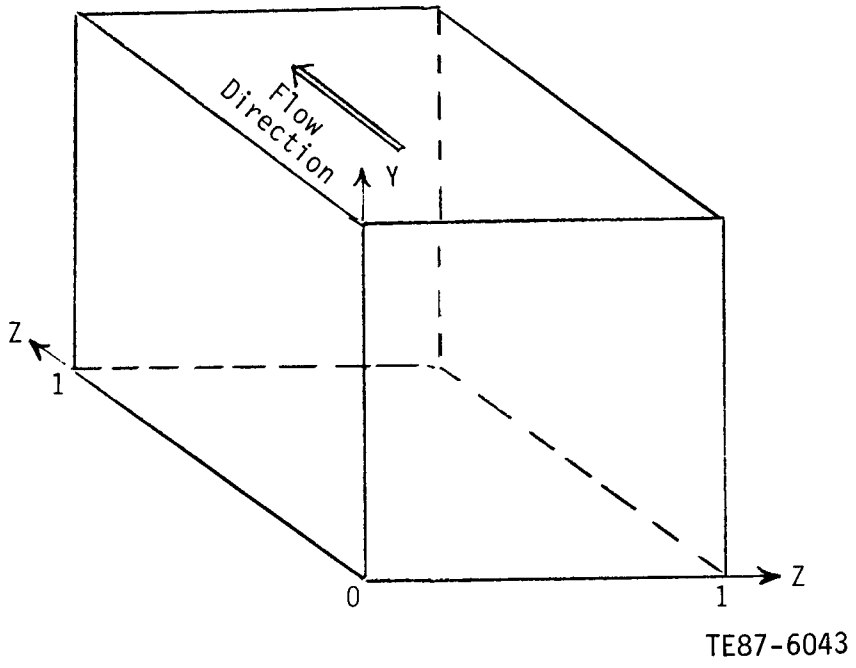

Figure 2

CUBIC CAVITY VELOCITY PROFILES FOR RE=400 ON (a) VERTICAL CENTERLINE;
(b) HORIZONTAL CENTERLINE

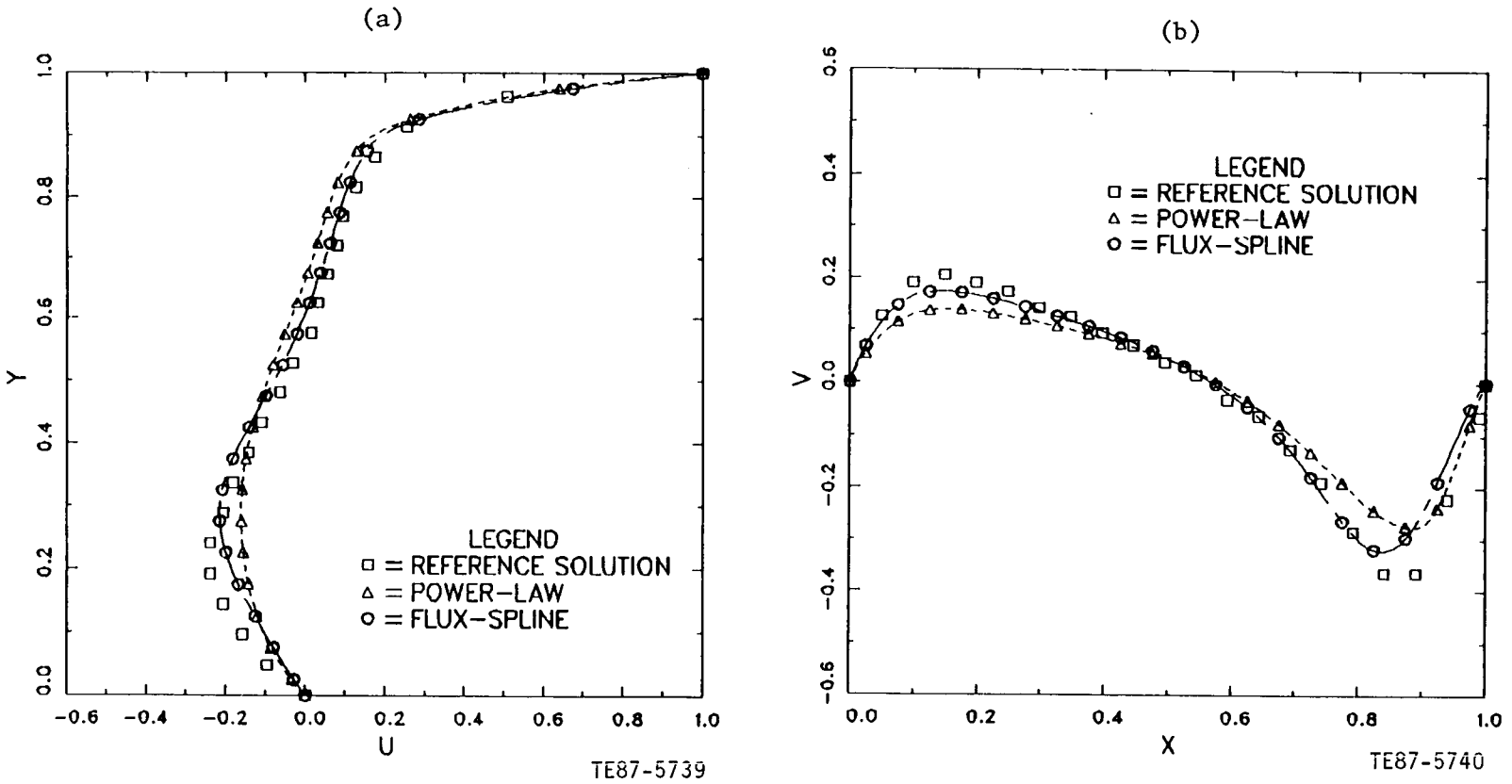

Figure 3

AEROTHERMAL MODELING PROGRAM - PHASE II* ELEMENT B: FLOW INTERACTION EXPERIMENT

M. Nikjooy, H.C. Mongia, S.N.B. Murthy†, and J.P. Sullivan†
Allison Gas Turbine Division
General Motors Corporation
Indianapolis, Indiana

NASA has instituted an extensive effort to improve the design process and data base for the hot section components of gas turbine engines. As part of this program, the purpose of Element B is to establish a benchmark quality data set that consists of measurements of the interaction of circular jets with swirling flow. Such flows are typical of those that occur in the primary zone of modern annular combustion liners. In addition to the detailed experimental effort, extensive computations of the swirling flows are to be compared with the measurements for the purpose of assessing the accuracy of current physical models used to predict such flows.

The Allison program for Element B has five major tasks:

1. Experimental Configuration
2. Modeling
3. Measurements
4. Results and Analysis
5. Model Improvement

EXPERIMENTAL CONFIGURATION

The flow to be investigated in the experiments consists of jets flowing into a confined swirling flow. The test section is a rectangular cross-section (381mm X 76.2mm) and extends to 10 duct heights (762mm) downstream from the headplate. A layout for the test section geometry is shown in Figure 1. The test section is constructed of glass and plexiglass to facilitate optical access for the Laser Doppler Velocimeter (LDV). Fluid enters the duct through five swirlers located at one end and through small jets located in the top and bottom. Experiments are done with both air and water as the flowing medium. The test section has been fabricated in such a way that two geometries could be investigated simultaneously--one using air for LDV measurements, and the other using water for flow visualization. The detailed test matrix for the Flow Interaction Program is given in Figure 2 and the corresponding flow configurations are shown in Figure 3. The configuration changes are made in both the air and water rigs with interchangeable upper and lower plates.

*Work done under NASA Contract NAS3-24350.
†Purdue University.

The variables to be investigated during this program are the following:

- o degree of swirl
- o distance of jets from the swirlers
- o ratio of mass flow through the jets to mass flow through the swirlers
- o jet locations with respect to the swirlers and each other

In all the measurements in air, the bulk velocity of the primary zone jets and of the fluid passing through the swirlers will be adjusted to 91m/sec and 45m/sec, respectively. The water experiments will require much lower velocities in order to avoid cavitation.

MODELING

This task involved simulation of different flow configurations using the current turbulence model (K-ε) for a preliminary study of the flow fields. The main importance of the task has been in highlighting different flow regions in the flow field that would be taken into account during measurements so as to resolve these regions of steep velocity gradient. Each flow configuration was computed using a 35X25X25 grid that was uniform in the Y-Z plane and nonuniform along the X-direction. There were several reasons for not using advanced turbulence models. Firstly, these are only used to help select the experimental configurations. Secondly, the results were obtained with a relatively course grid. Since these calculations are not grid independent, there is an excessive amount of numerical diffusion, thus obscuring the advantages offered by advanced models. The predicted results were qualitatively reasonable and the interaction of the jets and swirling flow was clearly seen.

MEASUREMENTS

An objective of the jet-swirl interaction experiments is to create a data base of benchmark quality on the fluid dynamic phenomena that occur in the primary zone of an annular gas turbine combustion chamber. The experiments include comprehensive measurements made at many points throughout the flow and completely document all boundary conditions. To be directly relevant to combustion.design, the basic configuration of swirlers, jets, and flow channel should be as close as possible to modern gas turbine configurations while at the same time permitting the flow conditions to be stable, repeatable, and easily controllable. Each of the flows in the test matrix will be investigated with flow visualization techniques to establish flow characteristics and define regions of interest for conducting detailed single-point measurements.
For the flow configuration identified in Task 1, measurements will be made to obtain the following:

- o detailed wall static pressure distribution
- o flow visualization
- o mean velocity and Reynolds stress components
- o fluctuating and mean concentration measurements
- o probability functions of velocity and concentration

Velocity measurements are made with a two-color, two-component LDV system which is mounted on a computer-controlled table that along with computer control of the field lens allows movement of the probe volume in three dimensions. The

data acquisition system consists of TSI counter type processors interfaced to a DEC 11/23 computer. The hardware interface contains a resettable 10-MHZ clock for measuring the time of arrival of a valid LDV signal. The simultaneous arrival of signals from the two components is determined in software by requiring that the respective clock signals are within 1-microsecond of each other. The DEC 11/23 also controls the X-Y-Z position of the probe volume through a stepper motor controller. The three beam optical arrangement allows measurements to be made close to a wall. By rotating the optics package about the optical axis, measurements near the end wall, top wall and bottom wall are possible.

RESULTS AND ANALYSIS

Measurements of velocity and concentration will be analyzed to determine the probability density function and auto- and cross-correlations.

The velocity distributions measured in the case of two on-line jets per swirler located at one duct height (3.0 in.) downstream of the swirler exit (Configuration A) for different axial locations are shown in Figures 4 through 7. These axial locations are at x = 1.0, 1.5, 2.0, 2.5, 3.5, 4.5, 6. in. from the swirler exit. The measurements are presented at different lateral locations (6.0 in.-7.4 in.). Here the strong swirling flow is clearly evident and the extent of the swirl can be seen clearly. The flow goes through some radical changes in the first duct height, after this flow profiles remain rather constant with minor decay of the magnitude of the velocities. The comparisons between the measurements and the calculations will be presented in the meeting.

MODEL IMPROVEMENT

Due to limited success with the standard K-ε model and its modifications, work must be continued in improving advanced turbulence and scalar transport models. Turbulent closure of the mean flow equations is obtained by adopting a non-equilibrium and an equilibrium model for the Reynolds stresses using different pressure-strain models (Reference 1). In addition, performance of a high and low Reynolds number model using Reynolds-stress closures is investigated. As for the turbulent scalar flux calculations, two different models are presented (Reference 2). One solves the algebraic equations for the scalar fluxes, while the other employes the transport equations for their respective scalar fluxes. The accuracy of the model is determined by comparing the results with measurements.

REFERENCES

1. Nikjooy, M. and So, R. M. C., "On the Modeling of Non-Reactive and Reactive Turbulent Combustor Flows," NASA CR-4041, 1987.
2. Nikjooy, M. and So, R.M.C., "On The Modeling of Scalar and Mass Transport in Turbulent Combustor Flows", 5th Int. Conf. of Numerical Methods of Thermal Problems, Montreal, Canada, June 29-July 3, 1987; also submitted to the Int. J. Numerical Methods in Engineering.

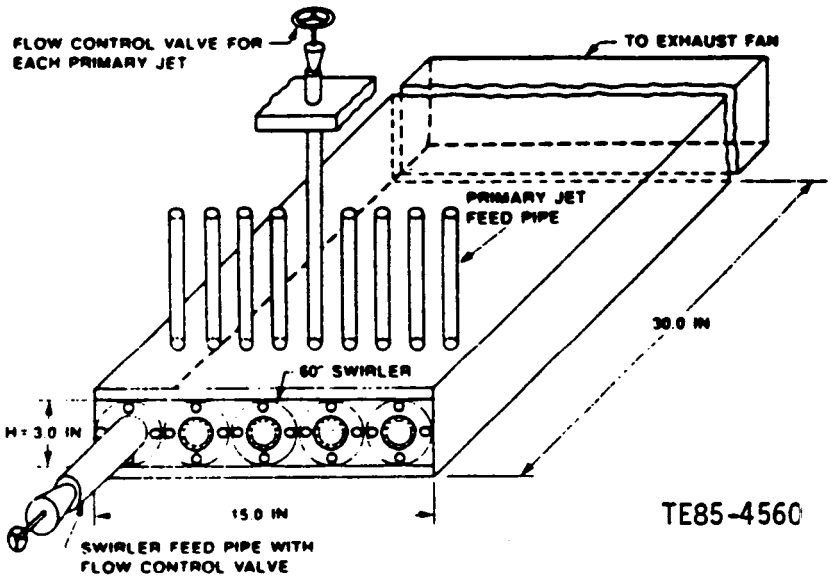

Figure 1. Test section geometry.

Test No.	Configuration	ℓ_j/H	X_j/H	M_j/M_s	Tracer	Jets/swirler
1	BC1	-	-	-	No	-
2	BC2	-	-	-	No	-
3	A	1.0	0.5	0.75	No	2
4	B	1.0	0.5	0.75	No	2
5	C	1.0	0.5	0.75	No	2
6	D	1.0	0.5	0.75	No	2
7	E	0.5	0.5	1.50	No	4
8	F	0.5	0.5	1.50	No	4
9	A	1.0	1.0	0.75	No	2
10	B	1.0	1.0	0.75	No	2
11	E	0.5	1.0	1.50	No	4
12	F	0.5	1.0	1.50	No	4
13	A	1.0	0.5	1.50	No	2
14	A	1.0	0.5	0.75	Yes	2
15	B	1.0	0.5	0.75	Yes	2
16	E	0.5	0.5	1.50	Yes	4
17	F	0.5	0.5	1.50	Yes	4

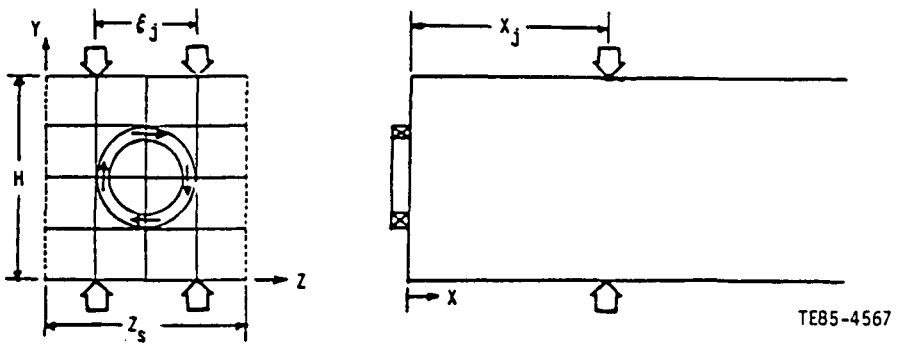

Figure 2. Test matrix.

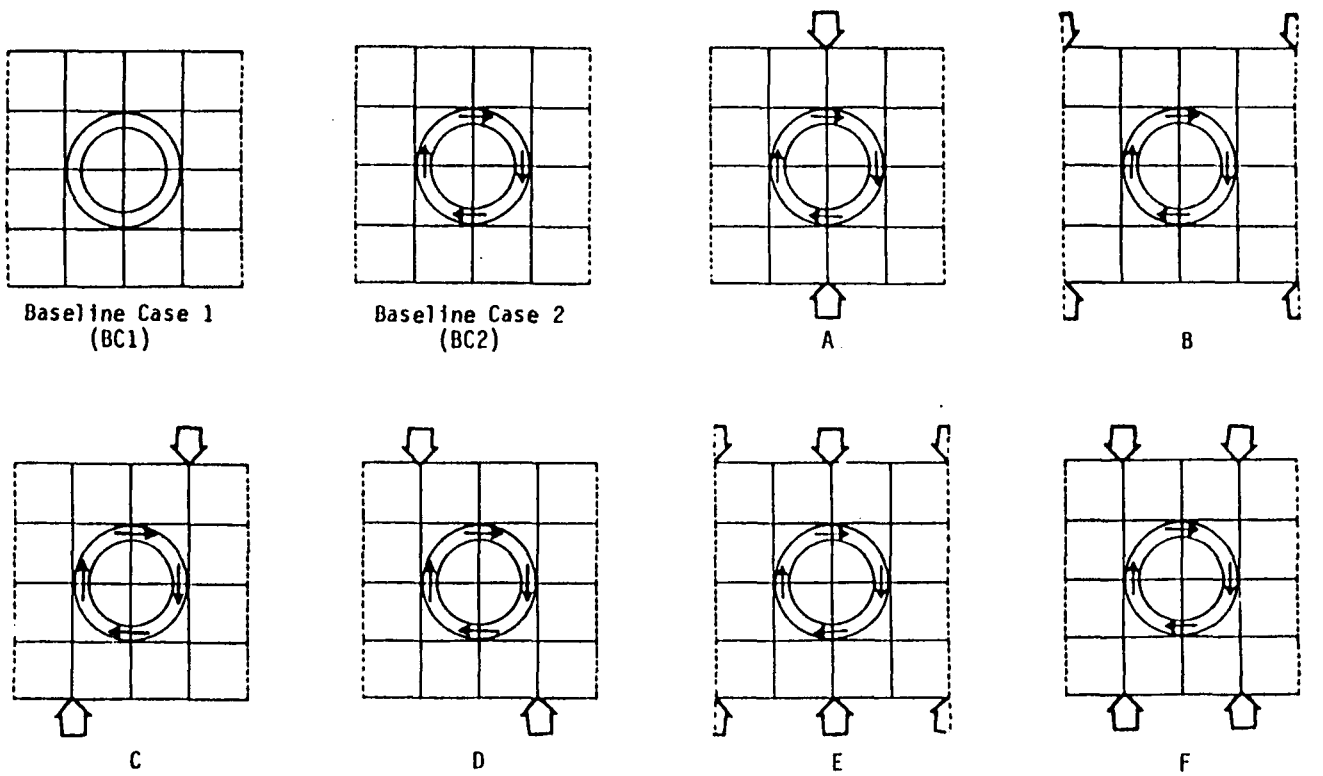

Figure 3. Basic flow configuration.

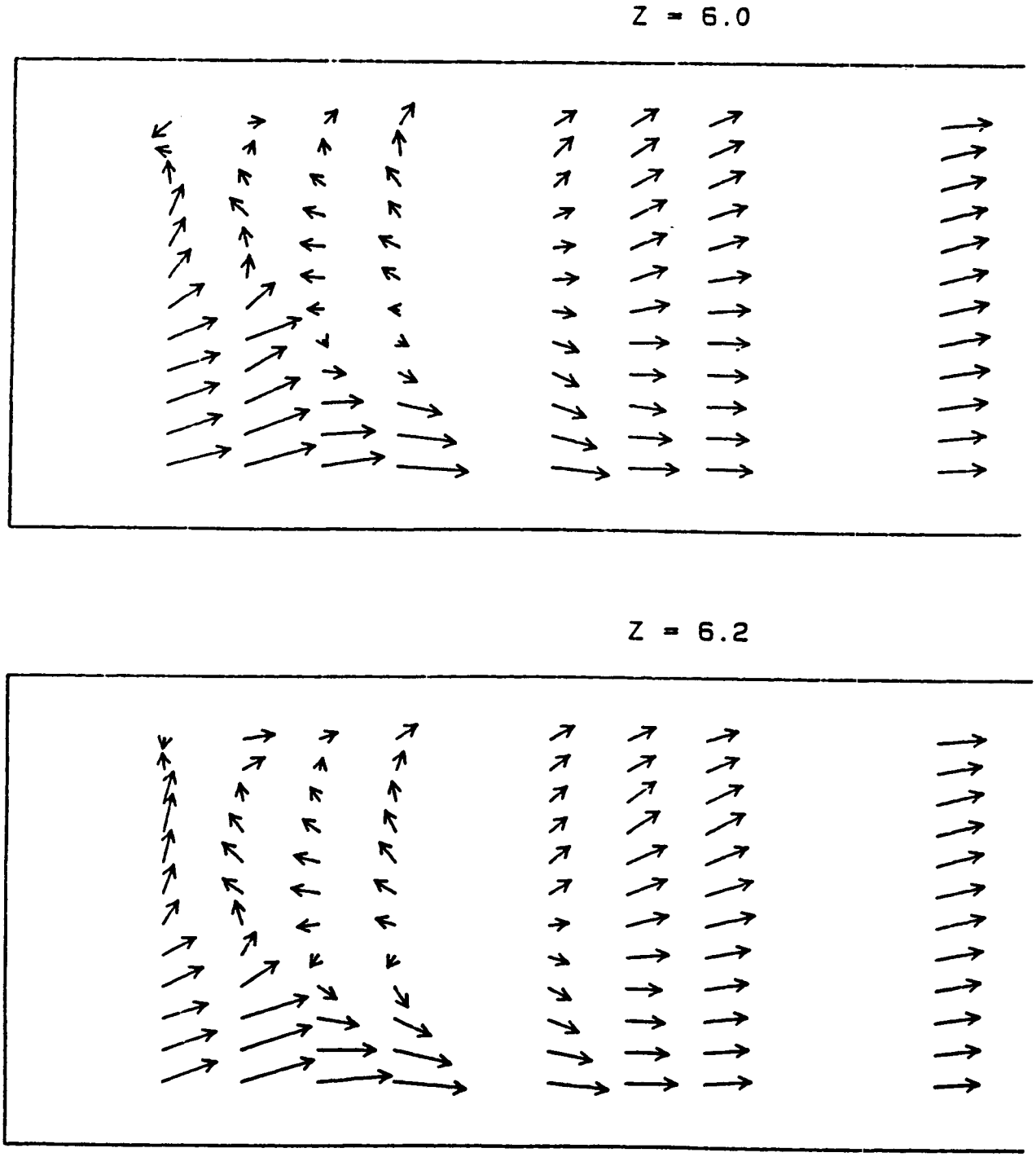

Figure 4. Longitudinal velocity vector plots for configuration with doubled primary jet flow.

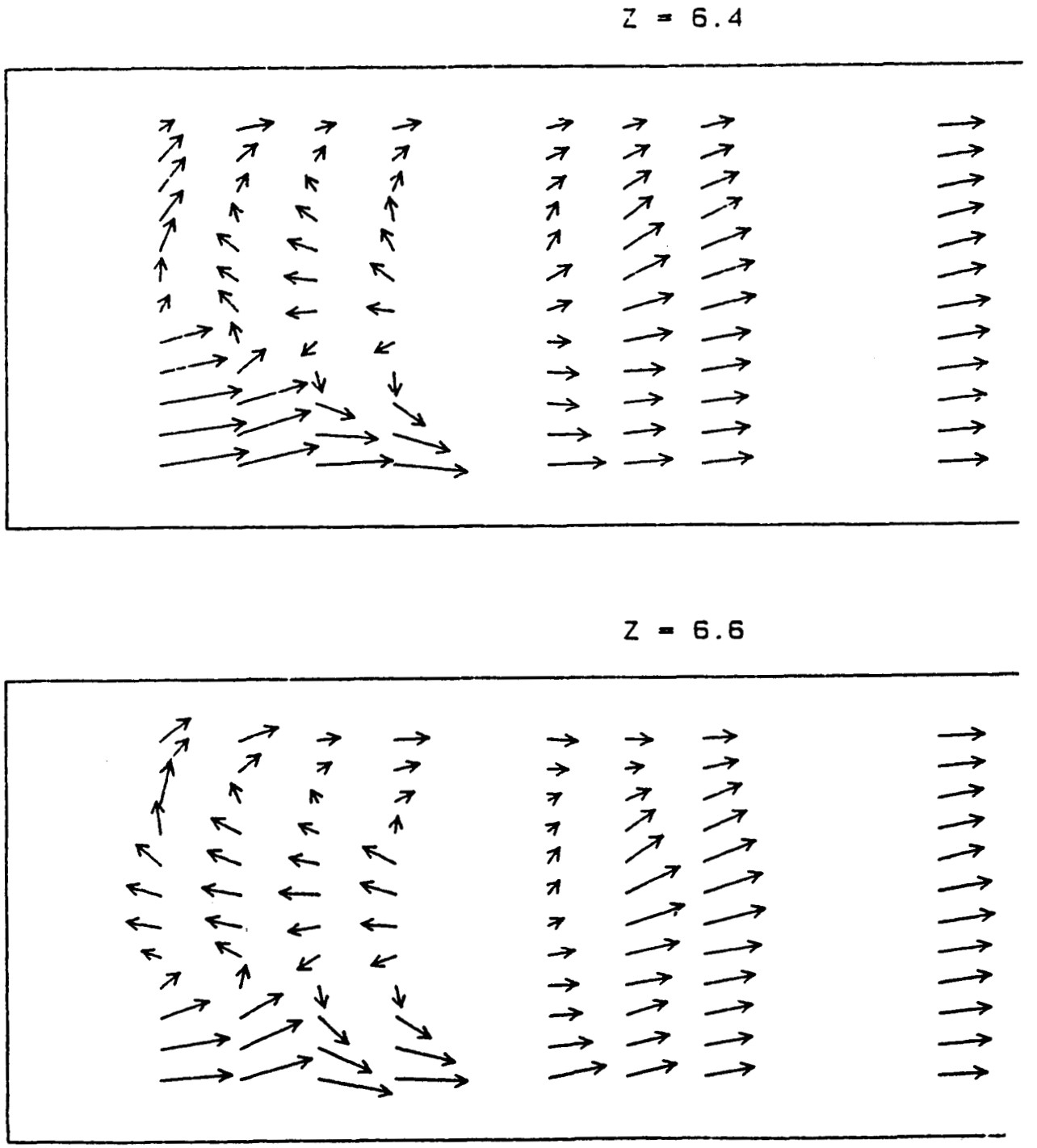

Figure 5. Longitudinal velocity vector plots for configuration with doubled primary jet flow.

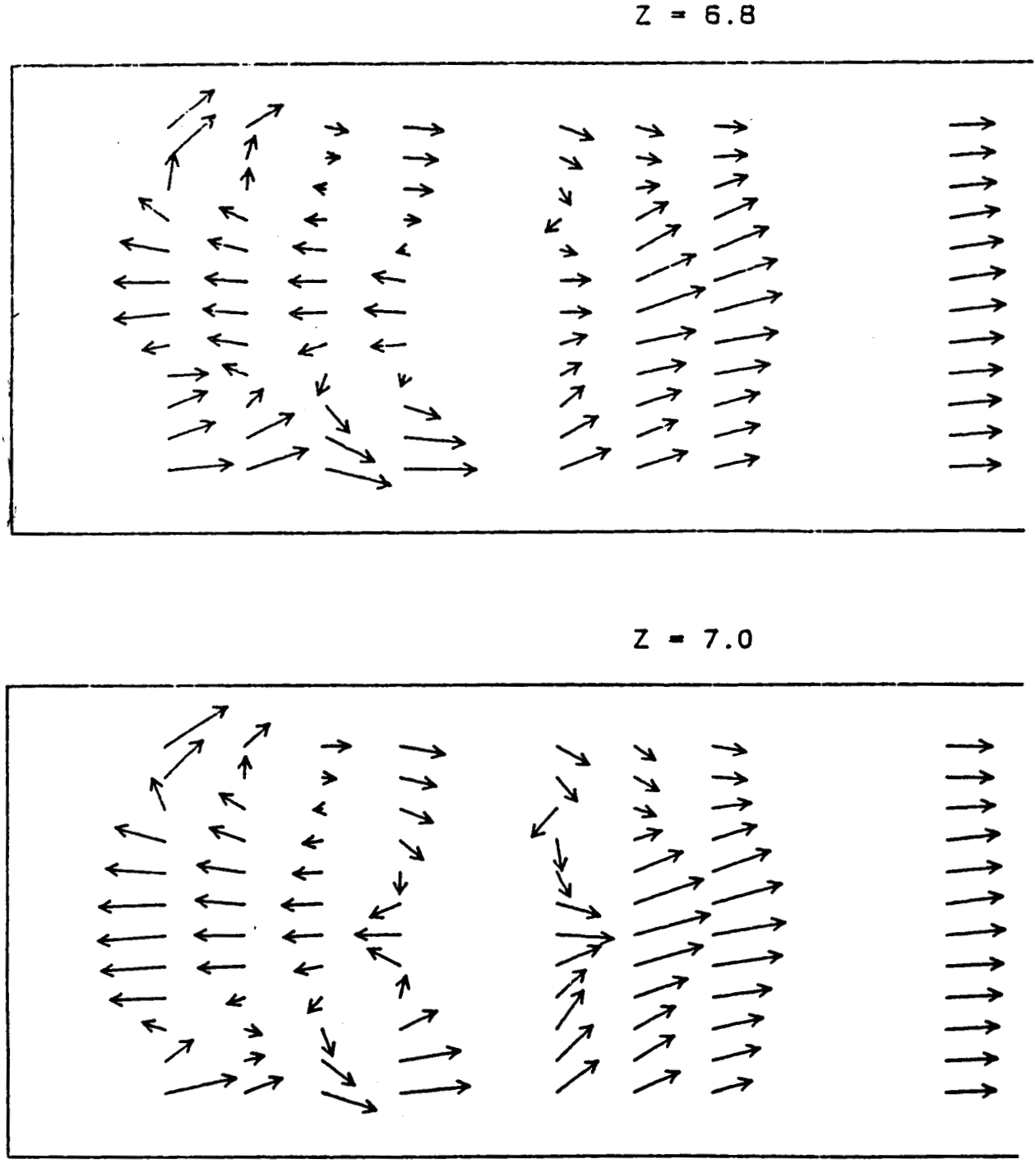

Figure 6. Longitudinal velocity vector plots for configuration with doubled primary jet flow.

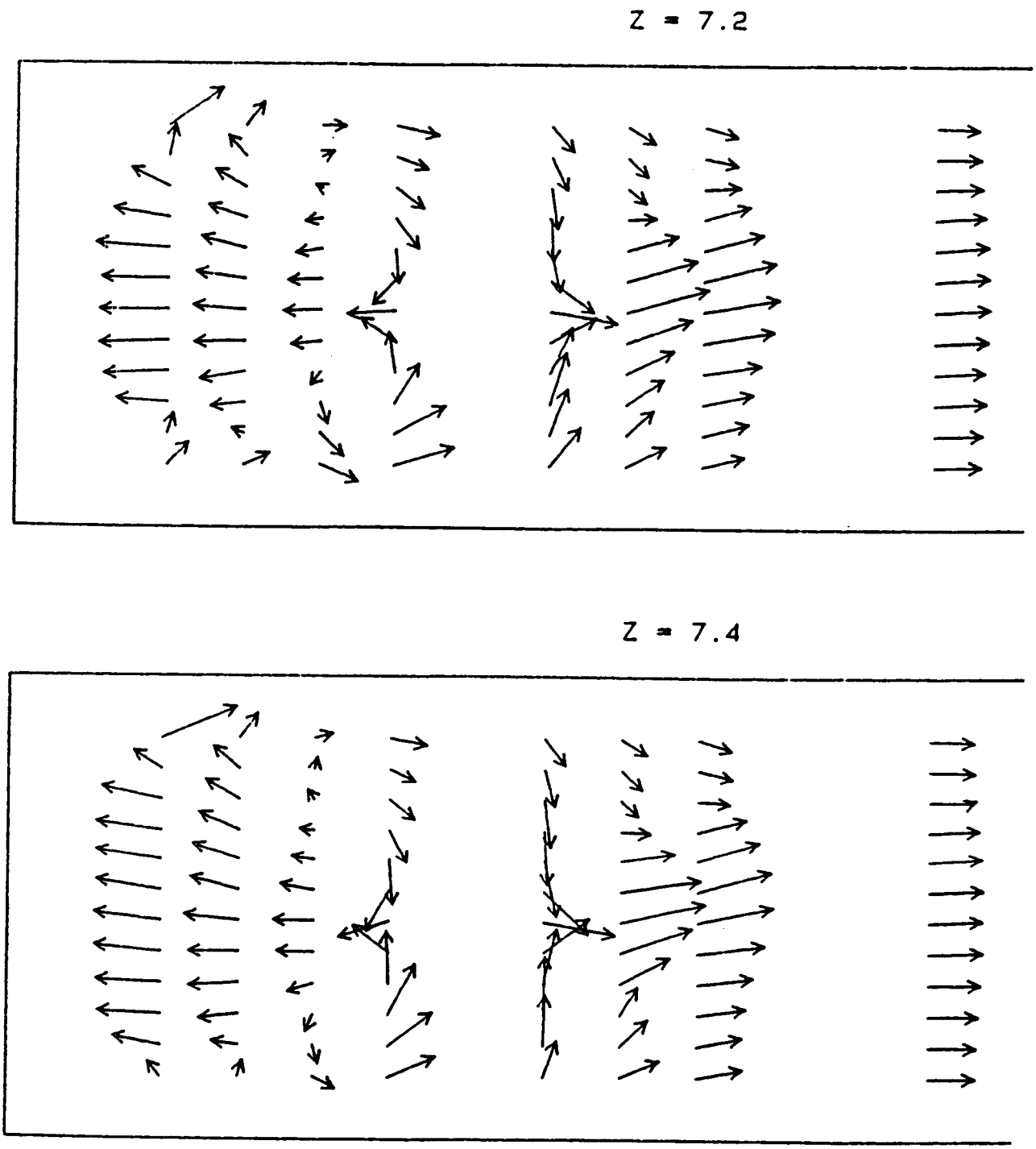

Figure 7. Longitudinal velocity vector plots for configuration with doubled primary jet flow.

N89-17305

AEROTHERMAL MODELING PROGRAM - PHASE II ELEMENT C: FUEL INJECTOR - AIR SWIRL CHARACTERIZATION

A.A. Mostafa, H.C. Mongia, V.G. McDonnel*, and G.S. Samuelsen*
Allison Gas Turbine Division
General Motors Corporation
Indianapolis, Indiana

The main objectives of the NASA-sponsored Aerothermal Modeling Program, Phase II Element C, are to collect benchmark quality data to quantify the fuel spray interaction with the turbulent swirling flows, and to validate current and advanced two-phase flow models. This effort consists of the following five technical tasks.

TASK 1--EXPERIMENTAL CONFIGURATION

A testing facility (Figure 1) was designed to characterize a wide variety of flows under isothermal conditions. The fuel nozzle and swirler combination is operated at both unconfined and confined conditions. The measurements include the following quantities: the three components of mean and root mean square (rms) gas velocity as well as Reynolds stresses, the three components of mean and rms droplet velocity, Sauter mean diameter, droplet size distribution, and cone angle.

All the test configurations (ref 1) are first operated free of injected particles, second with injected monodisperse solid particles (25-micron glass beads), then with two mixed particles (25- and 100-micron beads), and finally with a fuel spray through an airblast atomizer.

TASK 2--MODELING SENSITIVITY ANALYSIS

Computer codes were run to highlight different flow regimes that would be taken into account during data collection.

TASK 3--MEASUREMENTS

A two-component phase/Doppler system (Aerometrics, Inc., Model No. 2100-3) is being used to map out the flow field for both phases. The instrument simultaneously measures size and two orthogonal components of velocity for individual particles. The technique has been evaluated using both laser diffraction and laser visibility techniques in a series of studies (refs 2 and 3). Discrimination of phases or of different sized beads was inherent in the operation of the system. By sizing all particles, statistics are generated for both phases. Aluminum oxide (nominal 2.0 microns) was used to seed the gas phase and, when sized, provides a local peak in size scores substantially less than the local peak for the beads.

*University of California at Irvine

Data are tabulated, and the experiment is documented in Ref 4 following the format outlined in Ref 5. Details of test conditions are given in Ref 1, where the test cases are summarized in Table 1.

Results of cases (1, 2, 7, and 8) are presented below.

TASK 4--RESULTS AND ANALYSIS

Cases 1 and 2 relate to single phase axial and coaxial free jets, respectively; cases 7 and 8 are the corresponding two-phase flow cases with glass beads of 25 microns. The loading ratio (LR), defined as the ratio of particle-to-gas mass flow rate at the inlet plane for cases 7 and 8, are 1.0 and 0.2, respectively. More details for test conditions, data analysis, and model assessment of cases 1 and 7 are presented in Ref 6 while cases 2 and 8 are covered in Ref 7.

Figure 1 shows comparison between predicted and measured values of the mean and gas velocity for cases 1 and 7. It can be seen from Figure 1 that in the particle-laden jet, the gas velocity downstream of the nozzle exit is higher than the single-phase value. At z/D = 12.45, an increase of about 20% of the single-phase velocity is caused by the presence of the particles. This phenomenon is explained in detail by Mostafa and Mongia (ref 8) and can be attributed to two effects. One effect is the momentum transfer from the particles to the air since the particle velocity becomes greater than the gas velocity after a short distance downstream of the injector. The other effect is the modulation of the gas turbulence caused by the particles.

Figure 3 corresponds to measurements of the particle mean velocity and number density and shows the predictions with stochastic (ST) and deterministic (DT) treatments. It can be seen from Figure 3 that the ST provides good predictions compared with the experimental data, while the DT performs quite poorly. According to the latter, a particle moves radially due to its initial mean radial velocity and/or the mean radial gas velocity, both of which are small compared with the axial component.

Figures 4 and 5 correspond to Figures 2 and 3 but for coaxial jets and with LR = 0.2 instead of 1.0. Due to the small loading ratio, the effect of the particle on the gas mean velocity is very small (Figure 4). Figure 5 is consistent with Figure 3 in showing the superiority of the ST over DT in predicting particle properties.

TASK 5--MODEL IMPROVEMENT

A mathematical model for turbulent evaporating sprays based on the recent work in that area (ref 8) is being validated in this effort. Figure 6 relates to measurements of the gas kinetic energy and shear stress at LR = 1.0 and shows the predictions with the single-phase K-ε model and its version for two-phase flows. In the latter, the turbulence modulation is simulated by introducing extra terms in the turbulence kinetic energy and its dissipation rate equations. It can be seen from Figure 6 that the single-phase model does not

predict the turbulence modulation caused by the particles in the two cases. However, the two-phase flow model yields fairly good comparison with the data. This result confirms our previous findings (e.g., ref 9) that the interaction between the gas and particles is indeed due to both relative mean and fluctuating motion between the two phases, and the turbulence modulation caused by the particles is equally important to the particle's dispersion due to gas turbulence.

REFERENCES

1. A. A. Mostafa, H. C. Mongia, V. G. McDonell, and G. S. Samuelsen, "Aerothermal Modeling Program--Phase III, Element C: Fuel Injector-Air Swirl Characterization," NASA CP-2444.
2. T. A. Jackson and G. S. Samuelsen, "Droplet Sizing Interferometry: A Comparison of the Visibility and Phase Doppler Techniques," Applied Optics (in press), 1987.
3. V. G. McDonell, C. P. Wood, and G. S. Samuelsen, "A Comparison of Spatially-Resolved Drop Size and Drop Velocity Measurements in an Isothermal Chamber and Swirl-Stabilized Combustor," Twenty-First Symposium (International) on Combustion, The Combustion Institute (in press), 1987.
4. V. G. McDonell and G. S. Samuelsen, "Detailed Data Set: Two-Component Gas and Particle Velocity Statistics in a Particle-Laden Jet Flow," UCI Combustion Laboratory Report ARTR 87-1, Department of Mechanical Engineering, University of California, Irvine, CA, 1987.
5. G. M. Faeth and G. S. Samuelsen, "Fast Reaction Nonpremixed Combustion," Progress in Energy and Combustion Science, Vol 12, No. 4, 1987, pp 341-372.
6. A. A. Mostafa, H. C. Mongia, V. G. McDonell, and G. S. Samuelsen, "On the Evolution of Particle-Laden Jet Flows: A Theoretical and Experimental Study," AIAA 87-2181.
7. A. A. Mostafa, H. C. Mongia, V. G. McDonell, and G. S. Samuelsen, "On the Evolution of Particle-Laden Coaxial Jet Flows: A Theoretical and Experimental Study," AIAA 88.
8. A. A. Mostafa and H. C. Mongia, "On the Turbulence-Particles Interaction in Turbulent Two-Phase Flows," AIAA 86-215.
9. A. A. Mostafa and H. C. Mongia, "On the Modeling of Turbulent Evaporating Sprays: Eulerian Versus Langrangian Approach," Int J Heat Mass Transfer (in press), 1987.

TABLE 1 : TEST CASES

TEST CASE	NOZZLE "FLUID"				SWIRL		CONFINEMENT	
	NONE	PARTICLES		LIQUID	0^0	60^0	457 MM DUCT	152 MM DUCT
		MONO	MULTI	METHANOL				
AXIAL JET	△	△	▲		○ ○ ●	□ □ ■	1 2 3 7 8 9 13 14	4 5 6 10 11 12 15 16
FUEL INJECTOR	△			△	○ ○	□ □	17 18 19 23 24 25	20 21 22 26 27 28

- DATA SETS COLLECTED: 1 - 12
- PRELIMINARY DATA EVALUATION IS COMPLETED FOR CASES: 1, 2, 3, 7, 8, 9
- MODEL EVALUATION EFFORT
  - CASES COMPLETED: 1, 2, 7 & 8

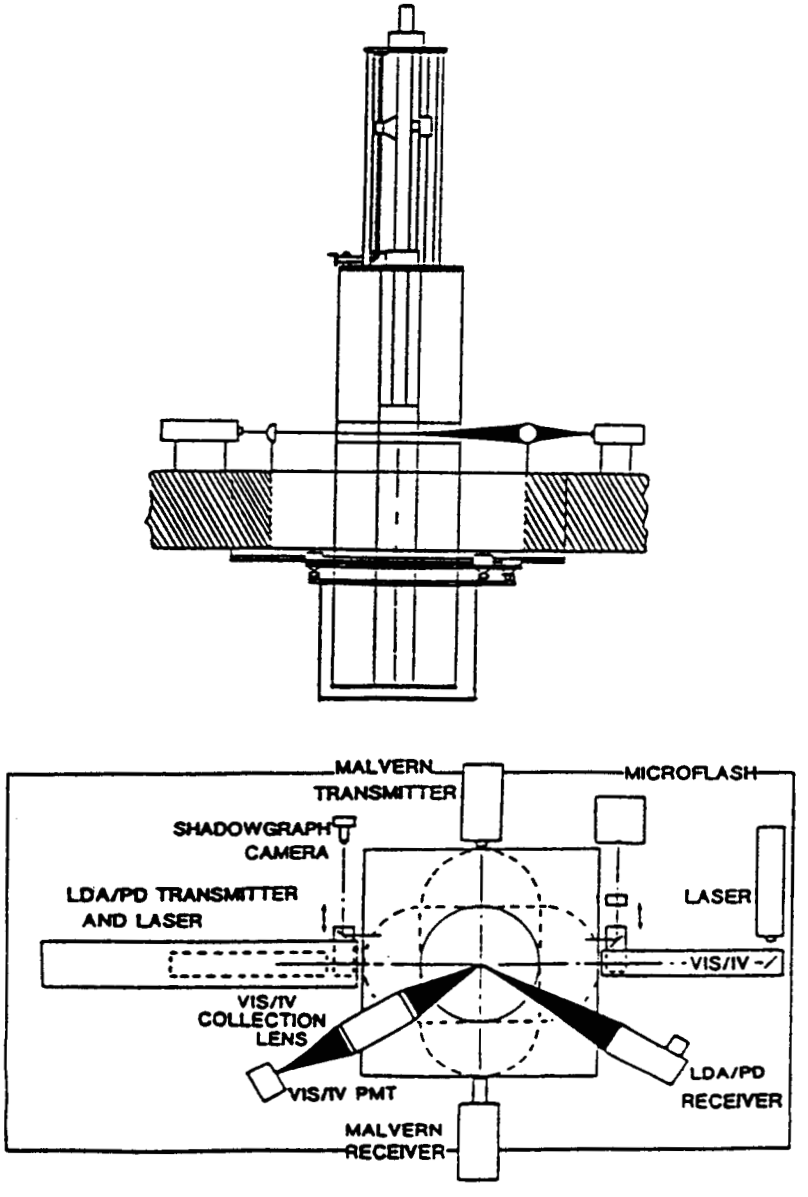

Figure 1. Flow facility and optical arrangement.

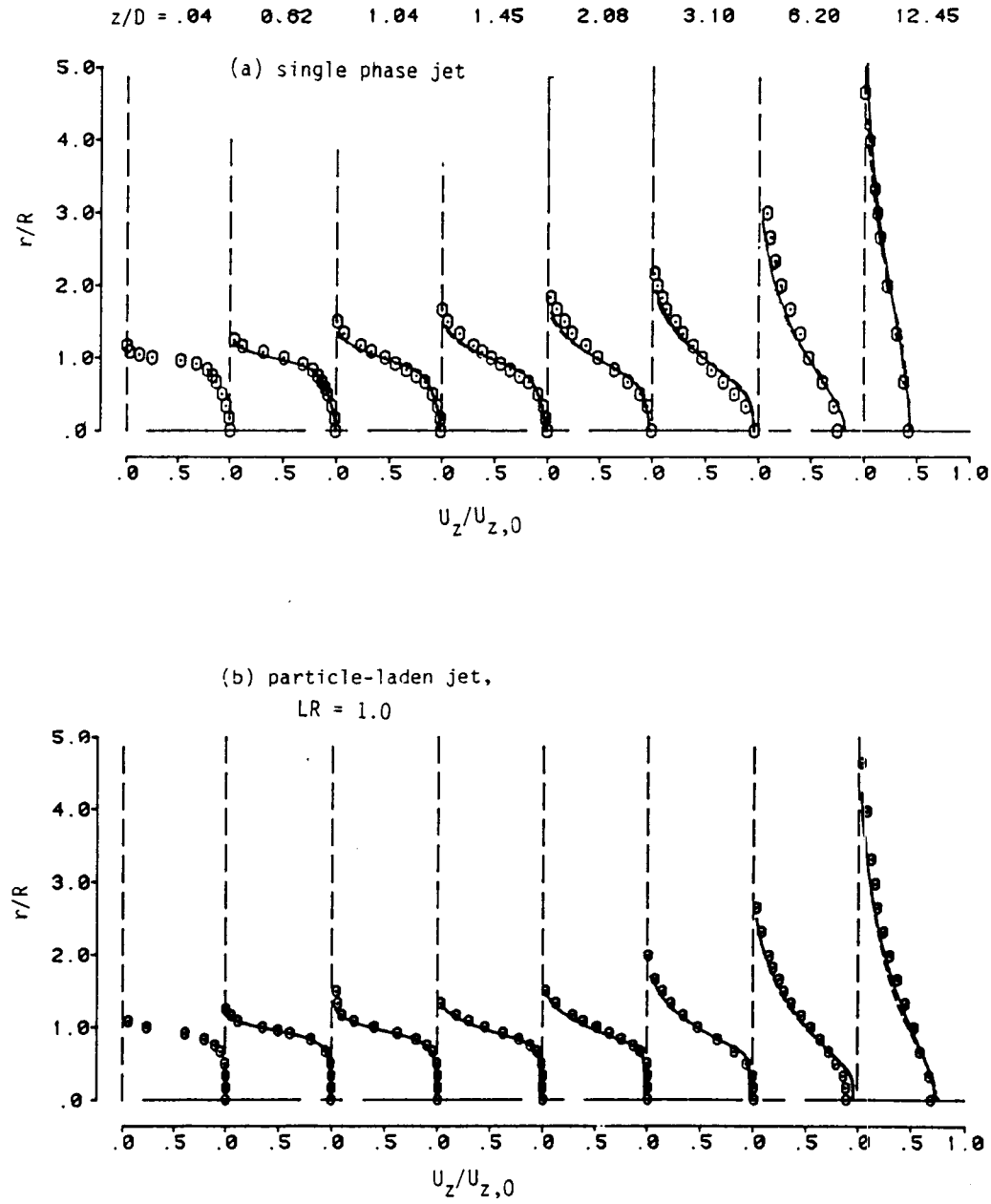

Figure 2. Radial profiles of normalized gas axial velocity for single-phase and particle-laden jet flows.

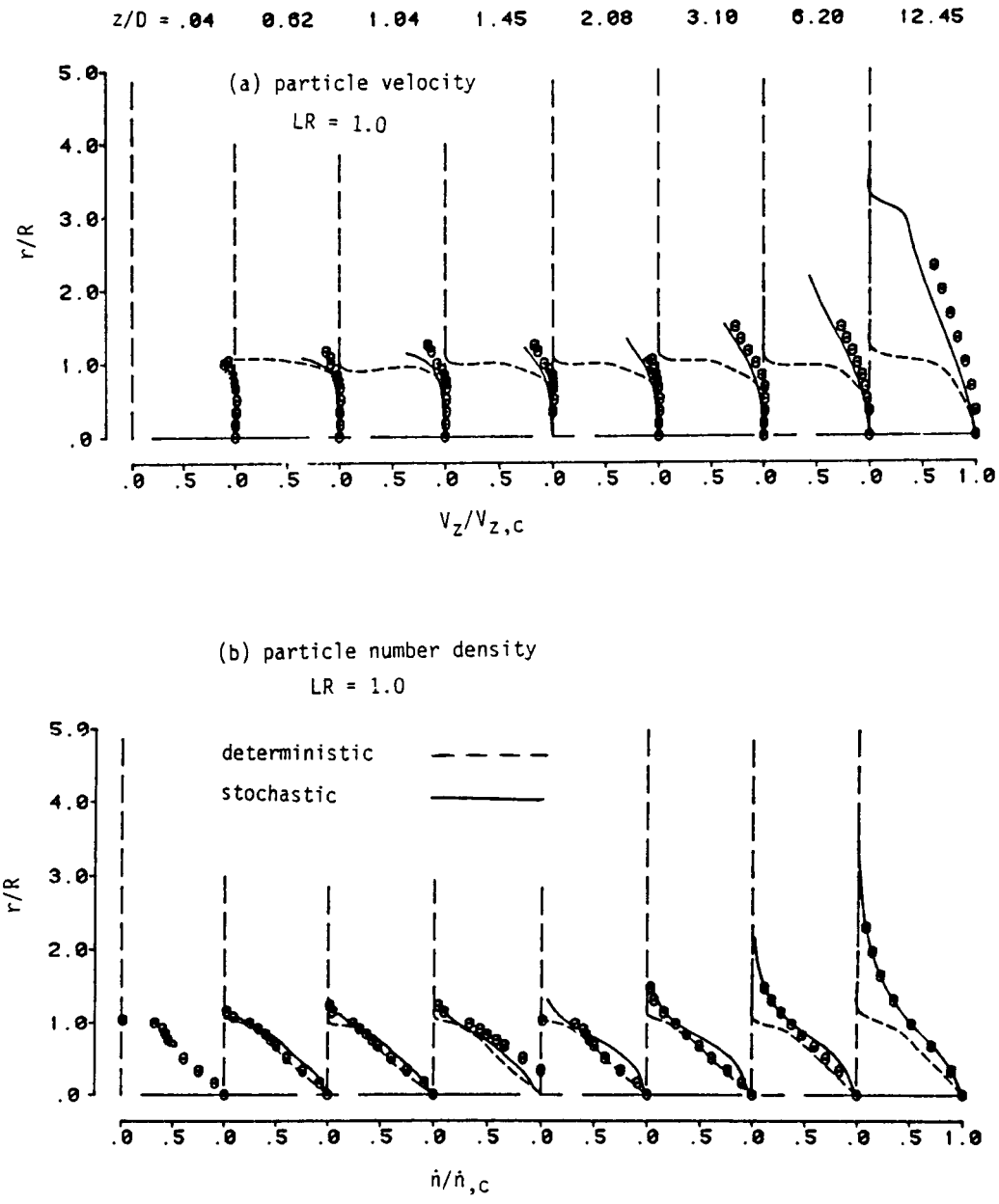

Figure 3. Radial profiles for normalized particle axial velocity and number density for particle-laden jet flows.

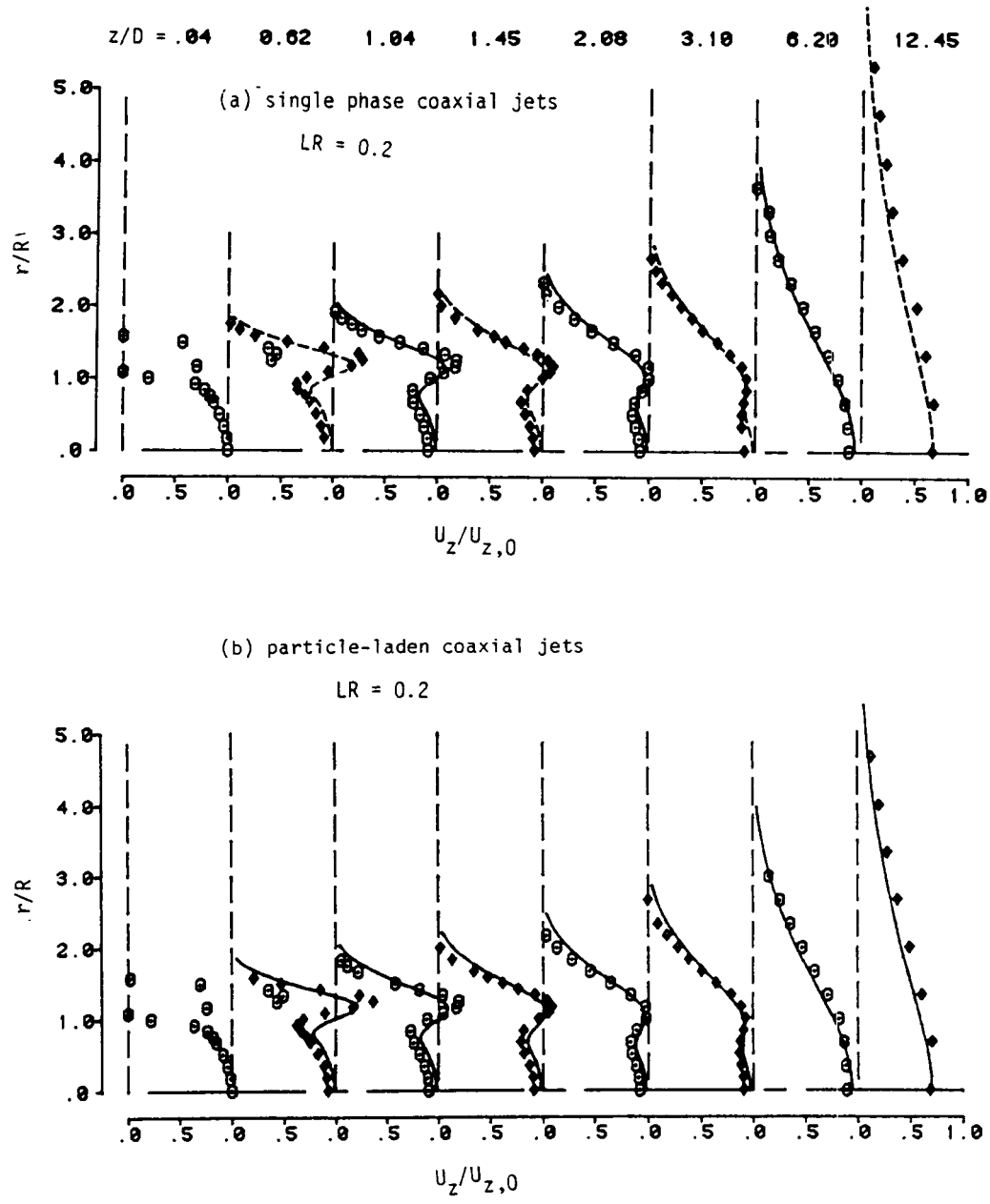

Figure 4. Radial profiles of normalized gas axial velocity for single-phase and particle-laden coaxial jet flows.

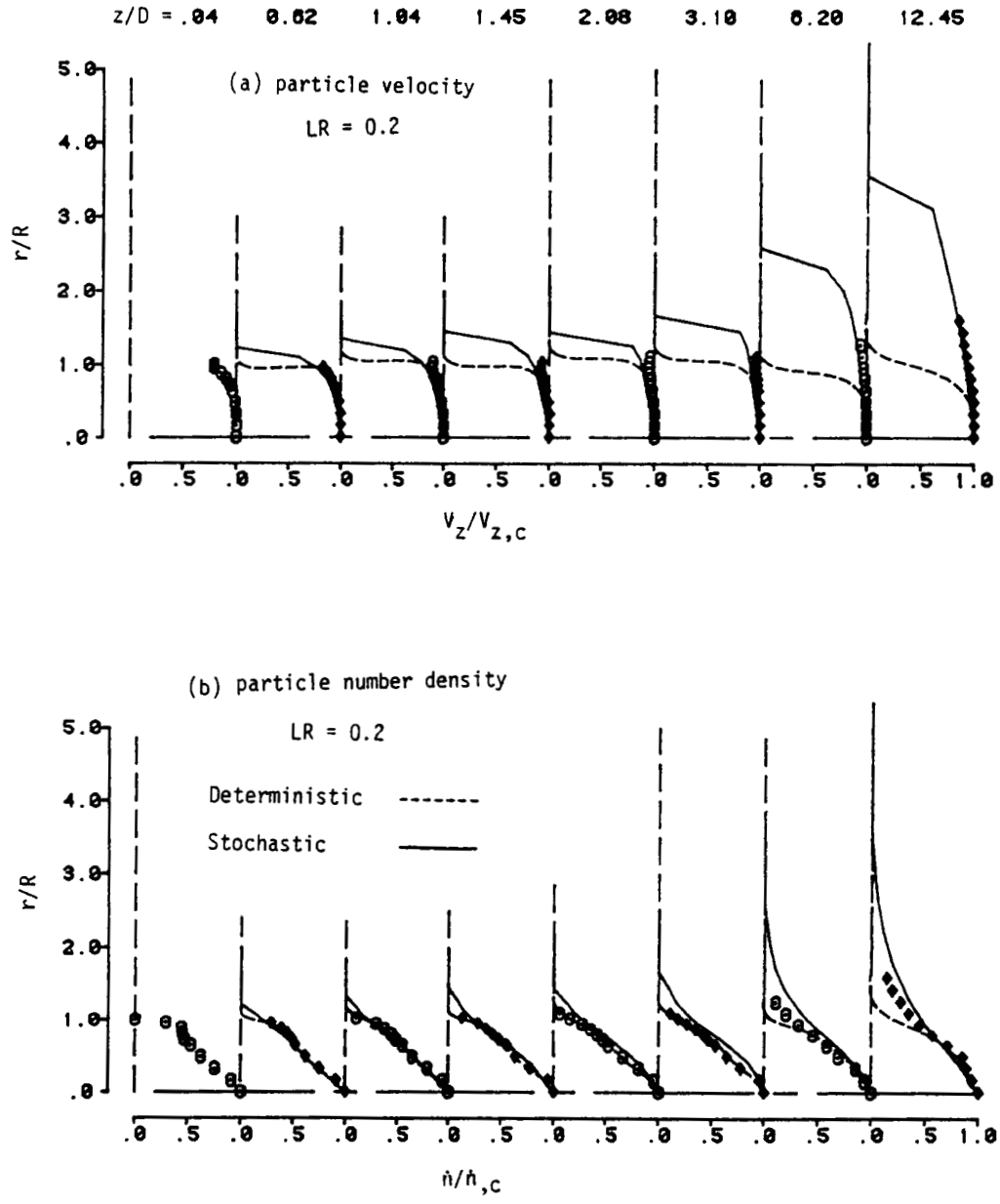

Figure 5. Radial profiles of normalized particle axial velocity and number density for particle-laden coaxial jet flows.

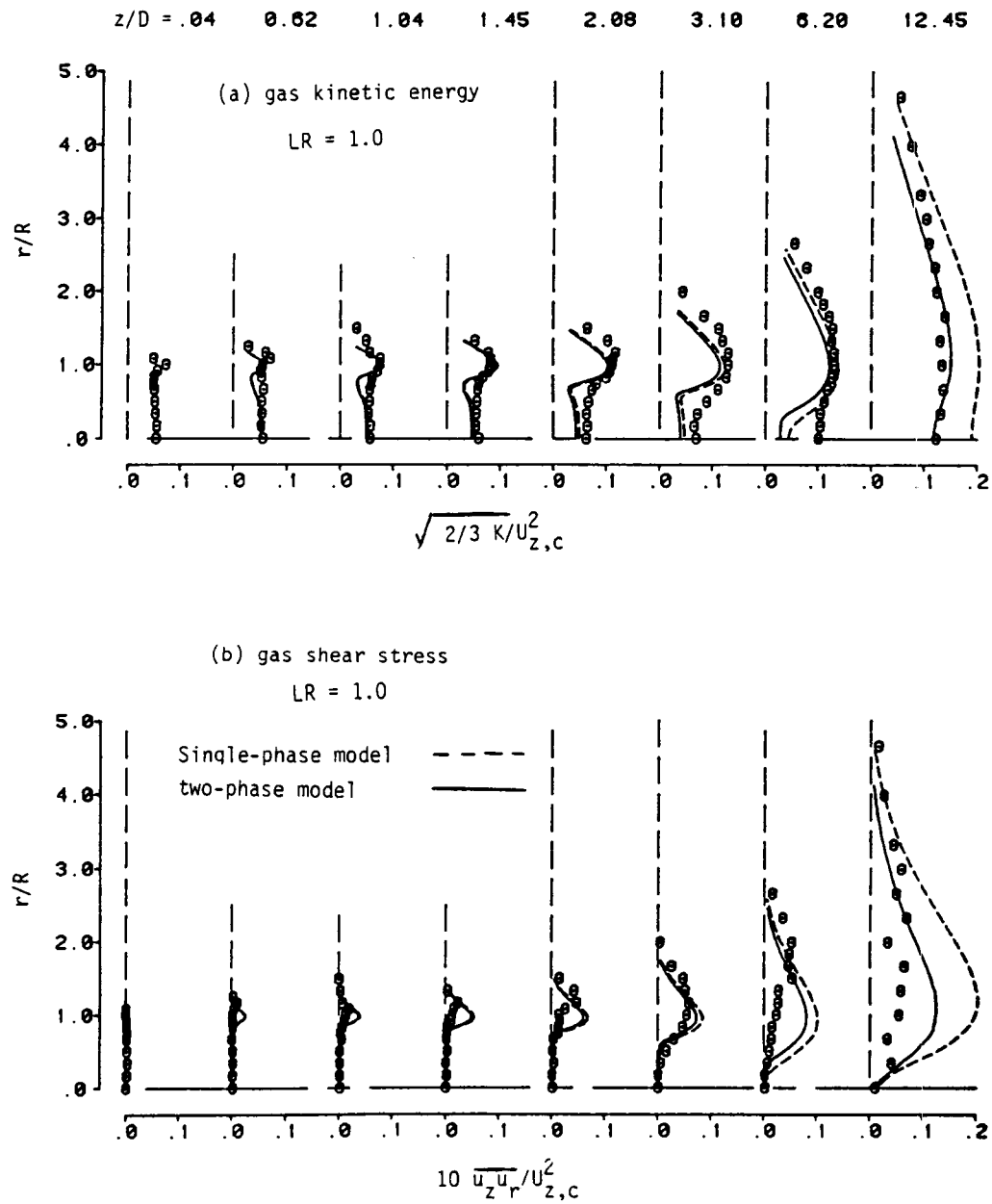

Figure 6. Effect of single-phase and two-phase turbulence models on gas turbulence kinetic energy and shear stress for particle-laden jet at loading ratio, L_R = 1.0.

APPLICATION OF ADVANCED DIAGNOSTICS TO AIRBLAST INJECTOR FLOWS*

John B. McVey, Jan B. Kennedy, and Sid Russell
United Technologies Research Center
East Hartford, Connecticut

The achievement of a predictable and satisfactory distribution of finely atomized fuel is of importance to the design of well-performing gas turbine engine combustion chambers. The development of non-intrusive laser diagnostics has offered the possibility of acquiring detailed point-resolved information on the gas and liquid-phase flow fields and on the droplet size distribution produced by fuel injectors. This effort is concerned with the application of both conventional laser velocimetry and phase-Doppler anemometry to the flow produced by an airblast nozzle. The emphasis is placed on the acquisition of data using actual engine injector/swirler components at (noncombusting) conditions simulating those encountered in an engine. The objective of the effort was to test the applicability of the instrumentation to real injector flows, to develop information on the behavior of injectors at high flow; and to provide data useful in the development of physical models of injector flows.

APPROACH

The airblast fuel nozzle employed in this study is typical of the designs employed in high-thrust advanced engines. Atomization is accomplished by concentric swirling airstreams which shear fluid from a filming lip. The nozzle selected was a model nozzle manufactured to within special tolerances in order to produce a closely-axisymmetric flow (Figs. 1 & 2).

The instrumentation employed includes a two-component TSI Model 9700-2 laser velocimeter (Fig. 3) used for measurement of the gas-phase flow velocity and a single-component Aerometrics Phase Doppler Particle Analyzer (Fig. 4) used for measurement of particle size and velocity. Also employed was a high-resolution fuel spray patternator which employs a physical probe array to acquire information on the spray mass flux distribution and a Malvern ST1800 spray analyzer used for determination of a path-mean droplet size.

For purposes of this study, the fuel nozzle was operated at a single atmospheric pressure condition. The simulation procedure used is to operate

* Work performed under Contract NAS3-24352

with a pressure drop across the injector/swirler assembly which produces the same air velocity as would be achieved under high power engine conditions, and with an injectant mass flow rate such that the liquid/gas momentum ratio present at engine conditions is preserved. For these tests, the peak gas velocities exceed 100 mps while the liquid flow rate is 70 Kg/hr.

RESULTS

The general characteristics of the flow produced by the nozzle are illustrated by the spray patternator results. Profiles illustrating the mass flux contours at stations 2.54, 3.81, 5.08, and 6.35 cm downstream of the nozzle exit are illustrated in Fig. 5. Water was used as the injectant in this test. Measures of the circumferential uniformity are provided by the patternation index (PI) and the Min/ Max ratio. These parameters are based on the mass flow passing through each of eight sectors shown superimposed on the contours and are the parameters generally used in the industry for acceptance testing of fuel nozzles. For an ideal nozzle, the value of PI (which is the sum of the [absolute] differences between the sector flow and that produced by a circumferentially uniform spray) would be zero. Real airblast fuel nozzles rarely exhibit values less than 10. The range of measured values from 5.5 to 7.4 indicate that this nozzle flow is highly uniform. This will permit the assumption of axisymmetry to be made with a high level of confidence when modelling this flow. The included angle (Alpha) formed by the spray boundary (defined by the radius of the cross section capturing 90% of flow) is shown to vary from 85 to 64 degrees. The measured magnitudes and manner of variation are typical of airblast nozzles. The Sauter mean diameter (SMD) measured using the Malvern ST1800 (a path measurement along a diameter) shows the indicated mean droplet size to range from 85 to 57 microns. This value is typical of values measured when airblast nozzles designed to operate with jet fuel are operated using water as the working fluid.

The results of tests performed using Jet A fuel are shown in Fig. 6. Again the circumferential uniformity is quite good. The spray angle is slightly smaller than the values measured using water. The SMD is substantially smaller and is in the 20-25 micron range generally indicated by the Malvern instruments for similar nozzles operating with jet fuel. Also shown on both figures is the collection efficiency of the patternation system which represents the ratio of the flow obtained by integration of the measured values and the metered flow rate. The collection efficiency is close to unity when operating with water but falls to 0.88 with Jet A indicating that there is some loss of mass captured in the case of the smaller diameter, more-volatile Jet A spray.

The character of the airflow produced by by the airblast nozzle is illustrated by the plots of axial velocity shown in Fig. 7. The diametral variation of velocity is shown for stations located from 0.11 to 10 cm downstream of the nozzle discharge plane. It is evident that the strongly swirled flow produces a central vortex having a centerline time mean velocity of 10 m/s or less (compared to a peak axial velocity of 70 m/s) for a distance

up to five cm from the nozzle face. The strength of this vortical flow is moderate in nature--some nozzle designs show no evidence of vortex breakdown when operated in an unconfined environment while others show a high, negative, time-mean centerline velocity.

Measurements of the radial distribution of the three components of velocity were performed at the nozzle discharge plane and of the axial variations of the three velocities at specified outer radii in order to provide boundary condition information for the modeling of the flow.

Typical results of the spatially-resolved measurements of spray droplet characteristics performed using a phase-doppler particle analyzer are shown in Fig. 8. Measurements of both the mean droplet velocity and the mean gas-phase velocity are shown. The designation "gas-phase" velocity pertains to the gas phase in the presence of the spray while the designation "gas-only" pertains to the axial velocity measurement obtained using the velocimeter and in the case when no spray was present. It is apparent that two flow regimes can be identified: a core region where the gas and liquid phase velocities are similar; and an outer region where the droplet velocity is significantly higher than the nearly-zero gas phase velocity.

Results of the droplet size measurements are shown in Fig. 2 where it is evident that the larger diameter droplets have been centrifuged to the outer region of the flow, as expected.

Information on the local mass flux is available and will be used to establish the relationship between metered liquid flow rate and that obtained by integration of the local flux.

These diametral surveys were successfully performed at downstream stations of 2.54, 3.81, 5.08 and 10.16 cm from the nozzle exit plane. Attempts to acquire data at a distance of 1.28 cm were unsuccessful due to the high density of the spray. It was entirely expected that the instrumentation would not yield valid data in these very dense upstream regions and certainly not at the exit plane where the atomization is not yet complete.

CONCLUDING REMARKS

The data obtained in this program provide information on the development of the two-phase flow field downstream of an air-blast nozzle. These data can be used to test the capability of existing fluid mechanic analyses for predicting the distribution of fuel within a combustion chamber. Determination of the adequacy of the several analyses being used by the technical community is important to establishing cost-effective design tools to be used in specifying the fuel nozzle characteristics which should lead to the tailored combustor exit temperature distributions required in high durability engines.

SCHEMATIC DIAGRAM OF MODEL NOZZLE

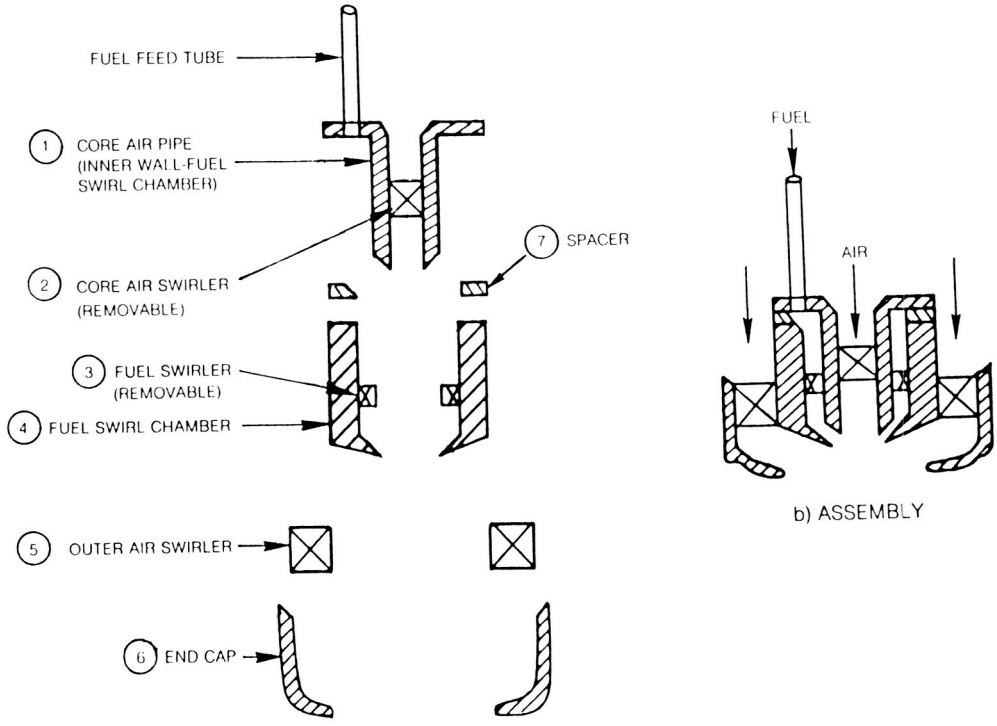

Figure 1

MODEL NOZZLE ASSEMBLY

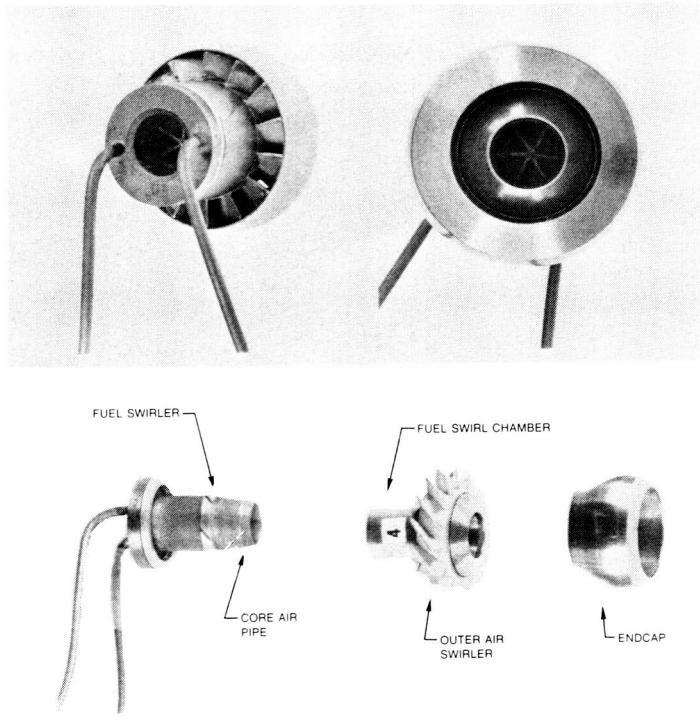

Figure 2

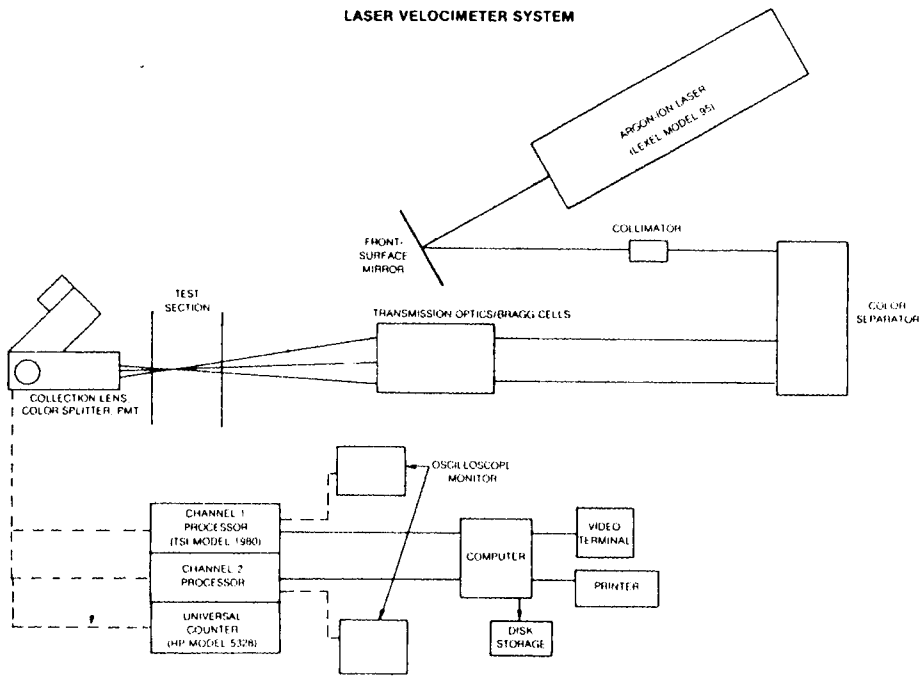

Figure 3

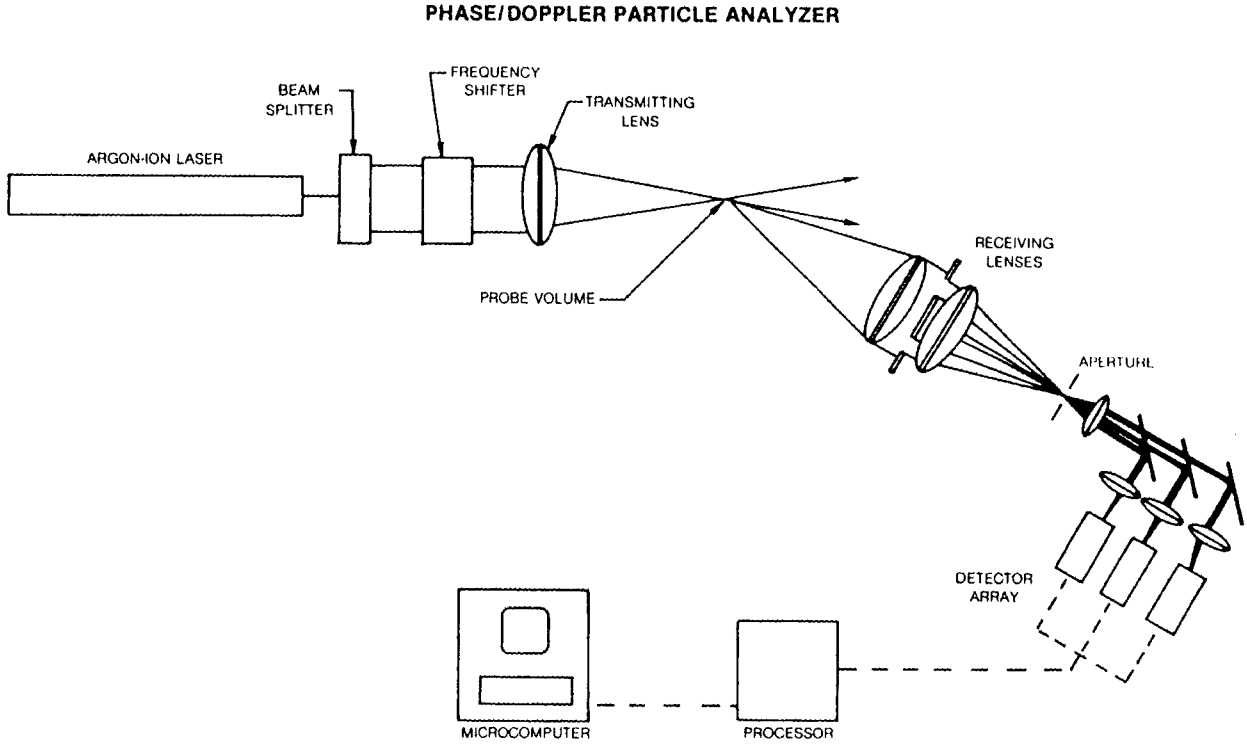

Figure 4

85-8-43-2

MASS FLUX DISTRIBUTION - WATER

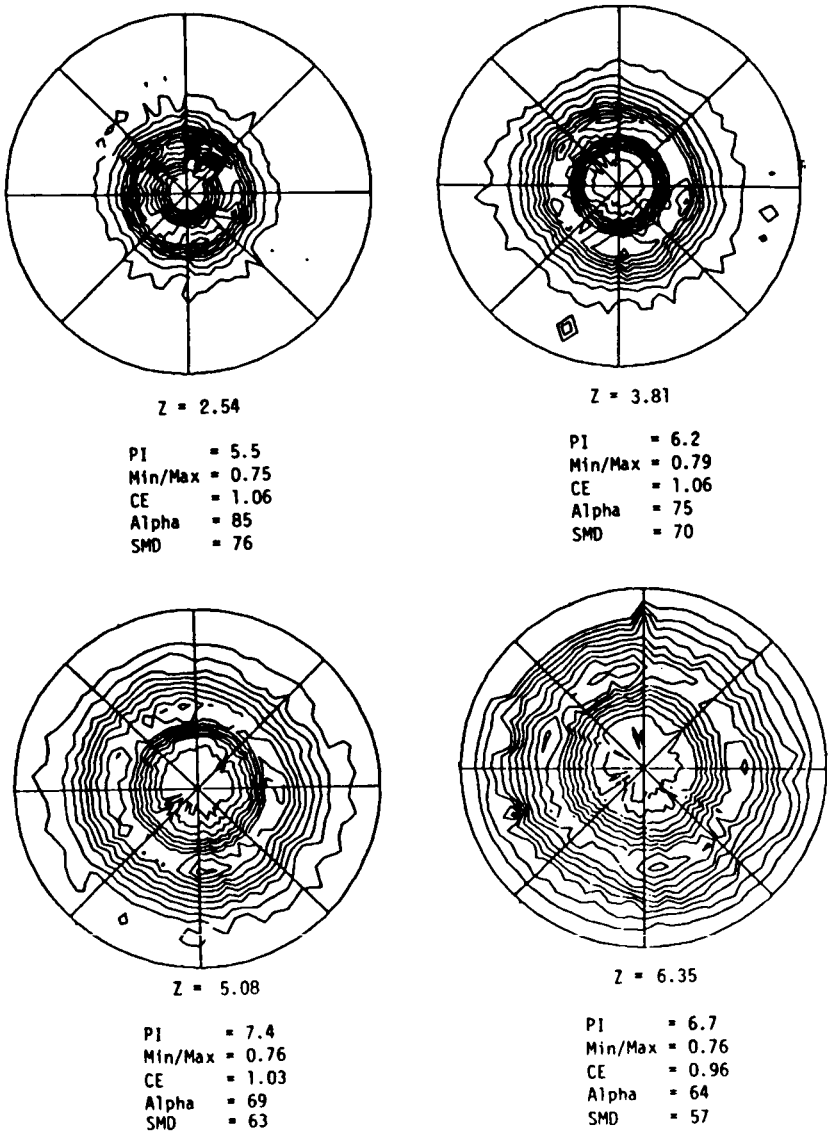

Figure 5

MASS FLUX DISTRIBUTION - JET A

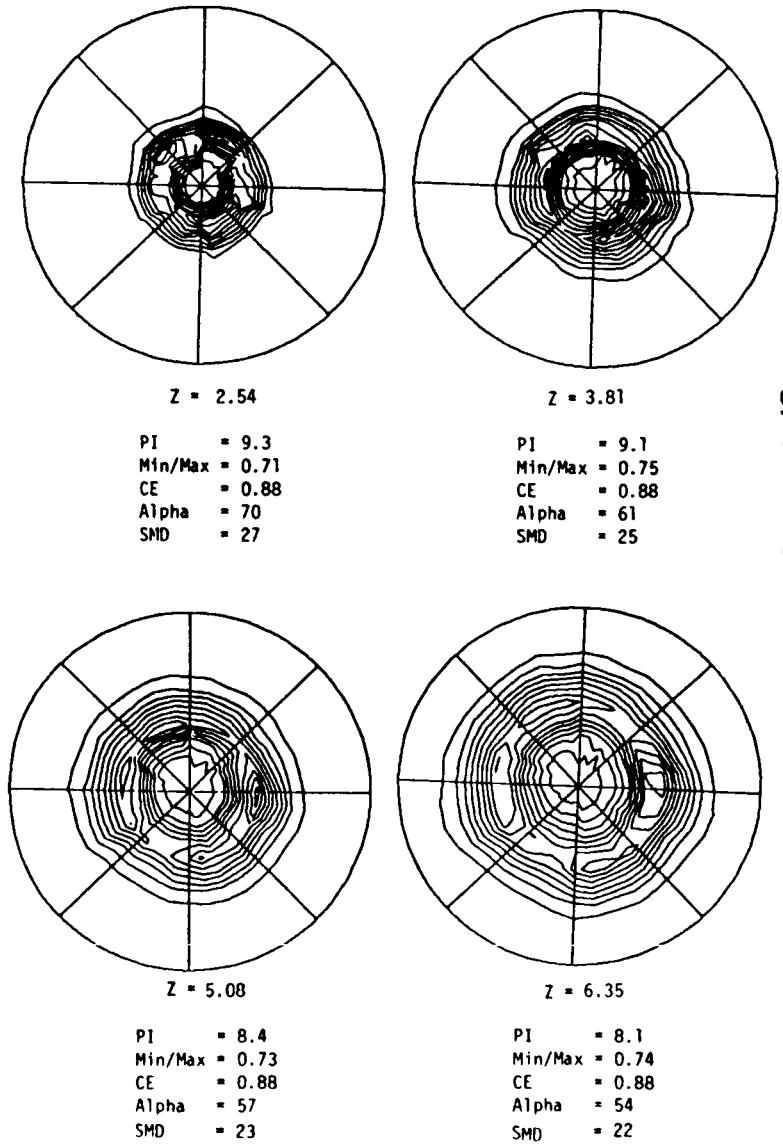

Figure 6

Mean Axial Velocity - Gas Phase Only

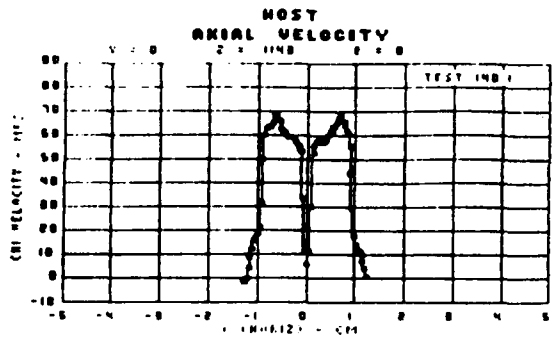

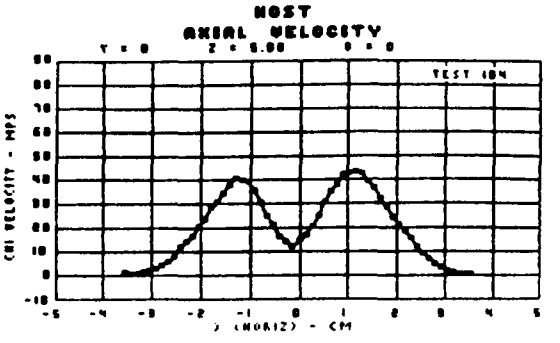

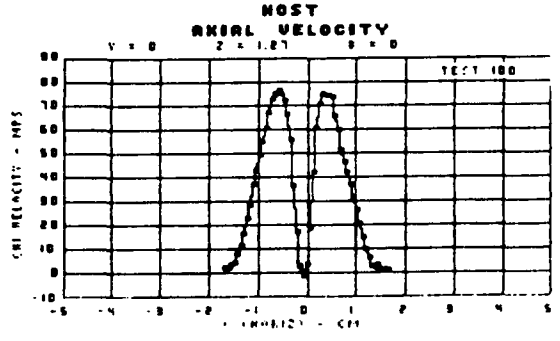

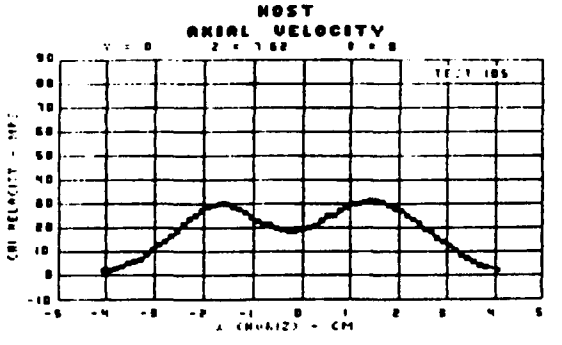

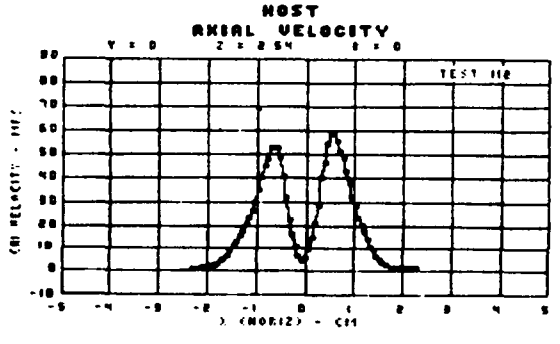

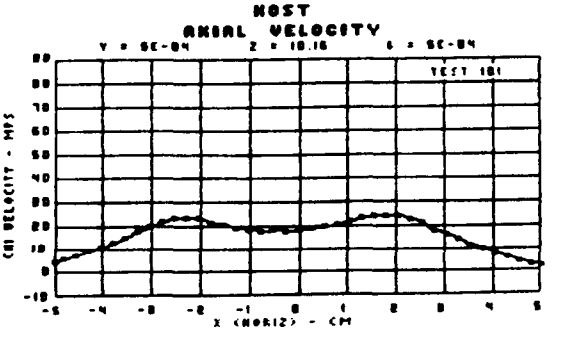

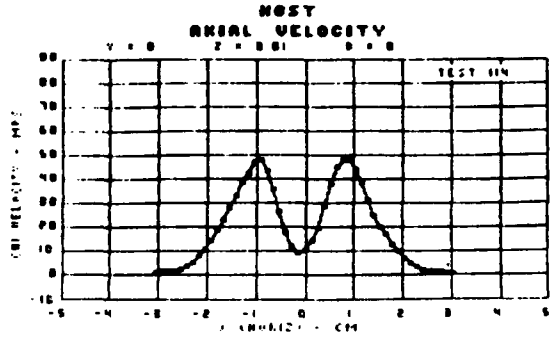

Figure 7

SPRAY AXIAL VELOCITY CHARACTERISTICS

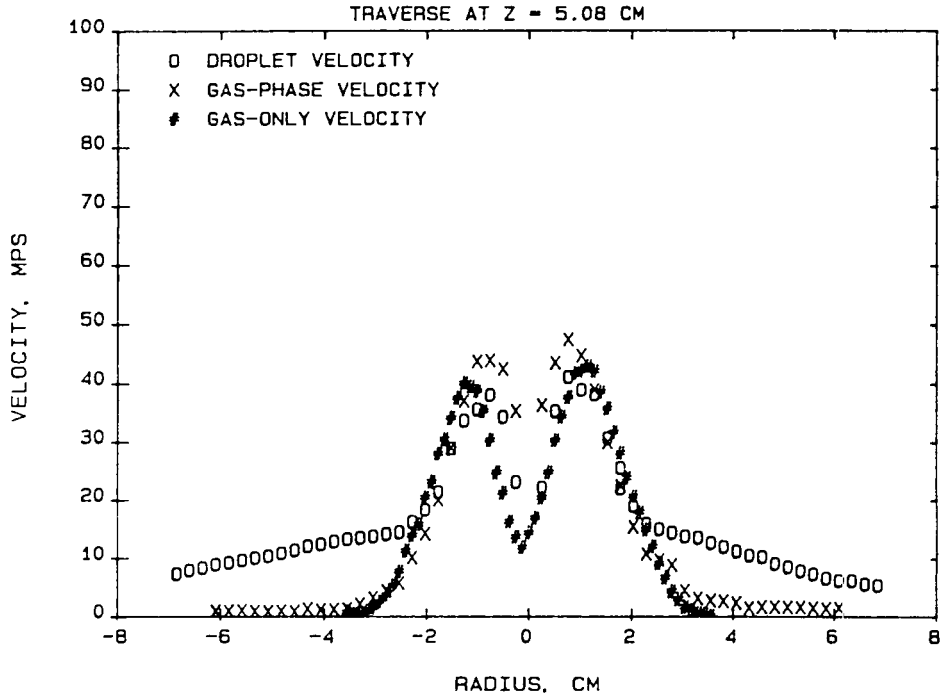

Figure 8

DROPLET SIZE CHARACTERISTICS

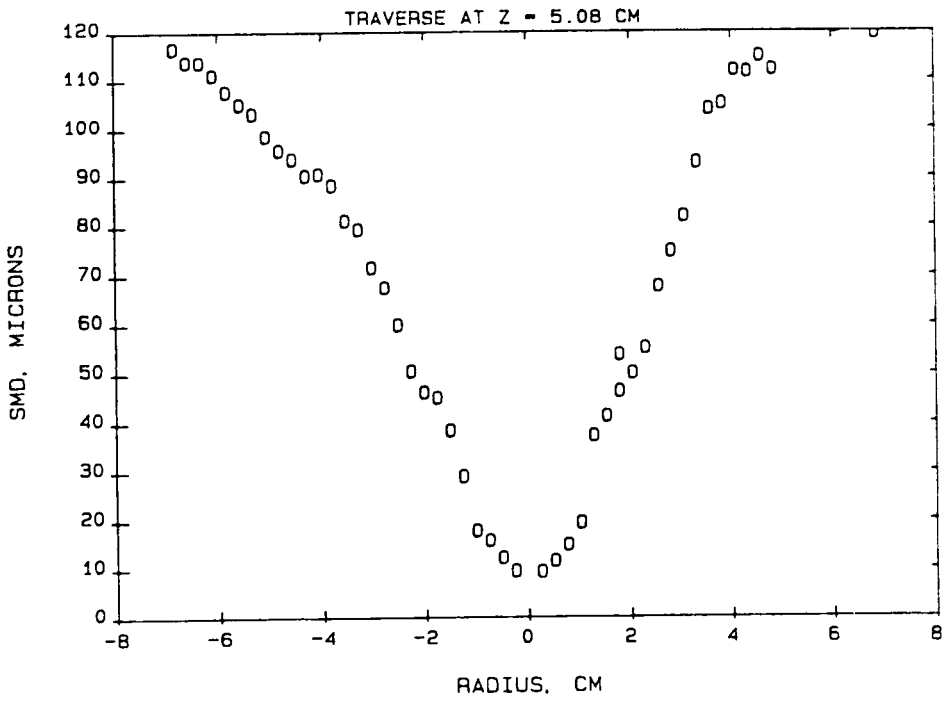

Figure 9

DEVELOPMENT OF GENERALIZED BLOCK CORRECTION PROCEDURES FOR THE SOLUTION OF DISCRETIZED NAVIER-STOKES EQUATIONS

Kanchan M. Kelkar and Suhas V. Patankar
University of Minnesota
Minneapolis, Minnesota

Computational methods are being increasingly used for the prediction of complex multidimensional flow phenomena. Although computations are far less expensive than full scale testing, costs of computational runs are still substantial. Therefore, considerable research effort is directed towards improving the accuracy and the efficiency of computational methods so that accurate predictions can be made at reasonable costs.

Computational methods involve discretization of the governing differential equations on a grid over the domain of interest. This generates a set of coupled nonlinear algebraic equations. Iterative methods are frequently used to solve these equations. However, iterative methods are prone to slow convergence or divergence and tend to be very sensitive to underrelaxation factors. Direct methods described in references [1], [2] and [3] do not suffer from these drawbacks. Accurate predictions of flow phenomena require use of fine grids. Direct methods cannot be used for such fine grid computations because of the excessive memory and cpu time requirements. In the present study, effort is directed towards developing a solution method which combines advantages of both the iterative and the direct methods. It involves iterative solution on the fine grid, convergence of which is enhanced by a direct solution for correction quantities on a coarse grid.

Nomenclature

$a^{p}_{i,j}$, $a^{nb}_{i,j}$, A	coefficients in the fine grid discretization equation at grid point (i,j)
$\bar{a}^{p}_{I,J}$, $\bar{a}^{nb}_{I,J}$, $\bar{A}$	coefficients in the block correction equation for block (I,J)
$b_{i,j}$	source term in the fine grid discretization equation at grid point (i,j)
$\bar{b}_{i,j}$	source term in the block correction equation for block (I,J)
$p_{i,j}$	pressure at grid point (i,j)
$\bar{p}_{I,J}$	uniform correction for pressure correction block (I,J)
$u_{i,j}$	u-velocity at grid point (i,j)
$\bar{u}_{I,J}$	uniform correction for u-velocity correction block (I,J)

Formulation of the Block Correction Procedure

The central feature in solving the discretization equations for flow prediction is the pressure-velocity coupling between the momentum and the continuity equations. Iterative methods solve the momentum and continuity equations in a sequential or an uncoupled manner. In addition, for iterative methods, the rate of propagation of the boundary information into the interior slows down as the grid fineness increases. Therefore, convergence of iterative methods is slow and it deteriorates as the grid fineness increases. In direct methods, all the equations are solved simultaneously so that the coupling between the continuity and the momentum equations is treated very effectively. The propagation of the boundary information into the interior is also instantaneous and iterations are performed only to account for the nonlinearity. Therefore, convergence for direct methods is fast and independent of the grid size. However, direct methods cannot be used for fine grids because of the excessive memory and cpu time requirements. The block correction technique described here has the low storage requirements of the iterative methods and the robustness of the direct methods. It uses iterative method to solve the equations on the grid on which the solution is sought, henceforth termed as fine grid. When the convergence of the iterative solution on the fine grid slows down, corrections to the existing solution are sought. The corrections are based on a coarse grid. The equations for correction quantities are solved directly so that the

correction quantities converge rapidly. In the following subsections, derivation of the block correction equations and the details of the solution algorithm are discussed.

Derivation of the block correction equations

Discretization equations on the fine grid are constructed using the power law scheme described in reference [4]. A staggered mesh arrangement is used to store the velocity components. Coarse grid corrections to the existing values of fine grid variables are sought when the convergence of the iterative solution on the fine slows down.

The coarse correction grid is composed of correction blocks. Correction blocks for each variable are obtained by grouping the fine grid control volumes for that variable. Thus, u-velocity correction blocks are obtained by grouping the u-momentum control volumes on the fine grid. Figure 1 illustrates the correction blocks for u-velocity, v-velocity and pressure. Since, u and v-momentum control volumes are staggered with respect to the control volumes for pressure(continuity), correction blocks for these variables also exhibit similar arrangement. For each variable, a uniform correction is assumed over each correction block and this uniform correction is added to the values of all the fine grid unknowns of that variable whose control volumes belong to the correction block under consideration. Then, for each variable, the equations for the block corrections are obtained by simply summing the corrected fine grid discretization equations over each of the individual correction blocks. For example, a typical discretized u-momentum equation on the fine grid for velocity $u_{i,j}$ is

$$a^{p}_{i,j}\, u_{i,j} = \sum a^{nb}_{i,j}\, u^{nb}_{i,j} + A(p_{i-1,j} - p_{i,j}) + b_{i,j} \qquad (1)$$

where $u^{nb}_{i,j}$ are the neighbor velocities of $u_{i,j}$. Now consider a u-velocity correction block (I,J), uniform correction on which is denoted by $\bar{u}_{I,J}$. The corrections on the adjacent staggered correction blocks for pressure are denoted by $\bar{p}_{I-1,J}$ and $\bar{p}_{I,J}$. The equation for this correction velocity is obtained by adding all the fine grid u-momentum equations which belong to this correction block and has the following form.

$$\bar{a}^{p}_{I,J}\,\bar{u}_{I,J} = \sum \bar{a}^{nb}_{I,J}\,\bar{u}^{nb}_{I,J} + \bar{A}(\bar{p}_{I-1,J} - \bar{p}_{I,J}) + \bar{b}_{i,j} \qquad (2)$$

The coefficients in the correction equation represent appropriate sums of the fine grid coefficients. In particular, the source term $\bar{b}_{i,j}$ is given by

$$\bar{b}_{i,j} = \sum_{\substack{\text{correction} \\ \text{block}}} [\sum a^{nb}_{i,j}\,u^{nb}_{i,j} + A(p_{i-1,j} - p_{i,j}) + b_{i,j} - a^{p}_{i,j}\,u_{i,j}] \qquad (3)$$

Thus, the source term is exactly equal to the algebraic sum of the residuals of all the u-momentum equations which belong to the correction block for u-velocity. Similar equations can be written for v-velocity block corrections. Equations for correction pressures are obtained by summing the corrected fine grid continuity equations over the correction blocks for pressure.

Equations for the velocity and pressure block corrections exhibit two important characteristics. Firstly, the form of the correction equations is exactly the same as that of the discretization equations on the fine grid. Secondly, all the correction equations are driven by the residuals on the fine grid. Thus, when the fine grid solution is converged, the corrections to the fine grid field become zero automatically.

The solution algorithm

The overall solution algorithm employed is very similar to the multigrid solution procedure of reference 5 with two grid levels and is shown in figure 2. Starting with an initial guess, coefficients for the fine grid discretization equations are computed. With these values of the fine grid coefficients, coeffients for the block correction equations are computed. The Yale Sparse Matrix Package, which uses LU factorization, is employed to solve the block correction equations directly and the values of the fine grid variables are corrected appropriately. To account for the nonlinearity, this procedure is repeated till the predicted corrections are small. Since, a direct solution method is employed to solve the correction equations, these iterations converge very rapidly. The corrected fine grid field satisfies integral balances of momentum and mass over the correction blocks. The

high frequency errors which now remain in the fine grid field are removed by solving the fine grid equations using the SIMPLER algorithm described in reference 4. When the rate of residue reduction per iteration on the fine grid drops below 0.5, coarse grid corrections are sought. This switching between the fine grid solution and coarse grid corrections is repeated till convergence.

Results and Discussion

The proposed block correction procedure has been applied to compute recirculating flow in a driven cavity. The flow in a driven cavity is strongly elliptic with significant nonlinearities at Re=2000 and it provides a good test for evaluating the performance of the block correction procedure. Figure 3 shows the variation of the fine grid residual with the number of iterations performed for a fine grid size of 62x62. Note that the iterations represent the repetitions of the SIMPLER algorithm on the fine grid irrespective of whether the block correction procedure is employed or not. It can be seen that the rate of residual reduction for SIMPLER alone is low and it decreases as the computation proceeds. However, when the block correction procedure is employed in conjunction with SIMPLER on the fine grid, the rate of residual reduction is substantially higher and is maintained at that high value till convergence. As the fineness of the block correction grid increases, the residue reduces at a faster rate, but with an associated increase the effort required for computing the corrections. Thus, for a given size of the fine grid, there is an optimum size of the correction grid for which the computational effort required to obtain the converged solution is minimized. Table 1 lists the number of fine grid iterations and the corresponding computational effort for two different fine grid sizes for SIMPLER with and without block corrections. Note that as the the main grid becomes finer, the number of iterations required for the SIMPLER algorithm increase substantially. But, when the block correction procedure is utilized, the number of fine grid iterations remain almost constant. Thus, although for a grid size of 20x20, the use of block correction procedure does not reduce the computational effort over that required for SIMPLER alone, substantial savings are obtained for the fine grid size of 62x62.

The proposed block correction procedure can also be effectively utilized to facilitate the convergence of subdomain methods. Subdomaining is often employed to minimize wasteful computations when the geometries for which the flow

computations are being made, include large passive areas. Boundary conditions on the internal boundaries of the subdomains are not known a priori and have to be adjusted iteratively. Convergence of the subdomain methods is dependent critically on the correctness of these boundary conditions. Coarse grid corrections spanning the entire domain can provide a good guess for the global solution and hence a good guess for the subdomain boundary conditions. Thus, the use of the block correction procedure can enhance the convergence of subdomain methods as well as remove the need for substantial overlapping among subdomains that is otherwise present. Work is currently in progress to verify the validity of this approach.

References

1. Braaten M. E. : Development and Evaluation of Iterative and Direct Methods for the Solution of the Equations Governing Recirculating Flows. Ph.D Thesis, University of Minnesota, 1985.
2. Vanka S. P., Leaf G. K. : Fully-Coupled Solution of Pressure-Linked Fluid Flow Equations. Argonne National Laboratory Report: ANL-83-73, 1983.
3. J. Ward MacArthur : Development and Implementation of Robust Direct Finite Difference Methods for the Solution of Strongly Coupled Elliptic Transport Equations. PhD Thesis, University of Minnesota, 1986.
4. Patankar S. V. : Numerical Heat Transfer and Fluid Flow. Hemisphere Publishing Corporation, 1980.
5. Brandt A. : Multi Level Adaptive Solutions to the Boundary Value Problems. Math. Comp., Vol. 31, 1980.

Table 1 - Number of iterations and the computational effort required for the solution of the driven cavity problem for Re = 2000 with and without block correction

Iterations(Computer Time*)

Driven Cavity (Re=2000)

Main Grid	SIMPLER	Correction grid	SIMPLER with block correction
20x20	42(1.1)	7x7	22(3.0)
62x62	250(51.0)	21x21	27(21.0)

* CPU seconds on CRAY-1 supercomputer

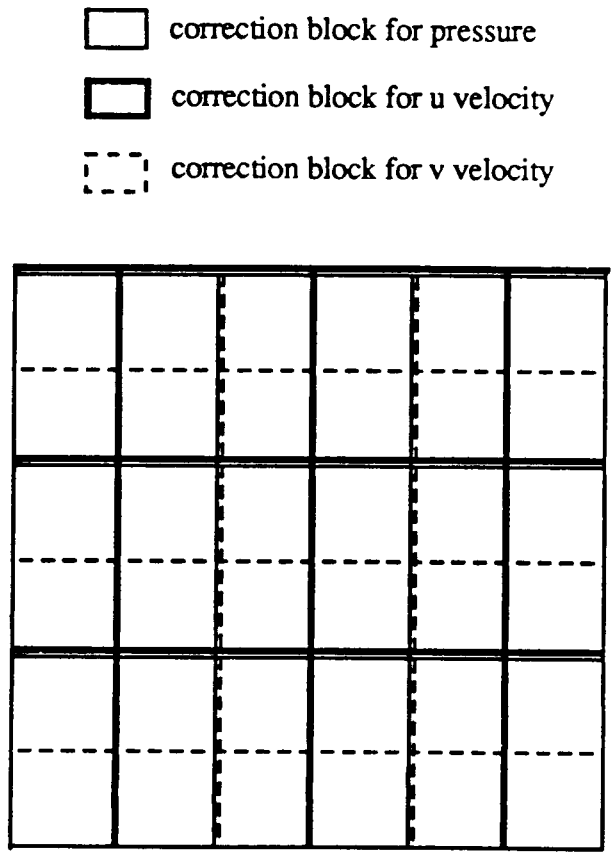

Figure 1 - Staggered arrangement of the correction blocks

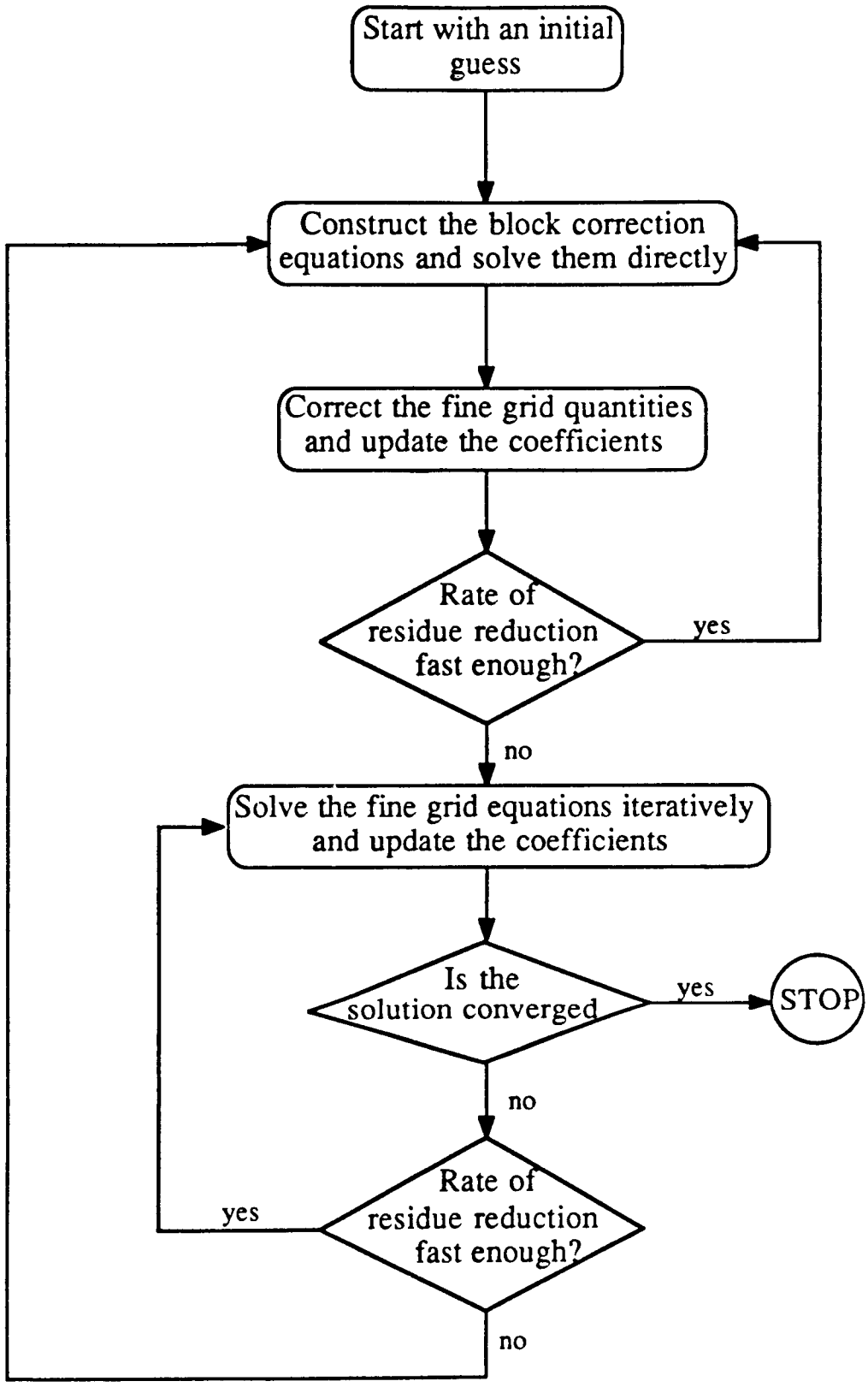

Figure 2 - The solution algorithm

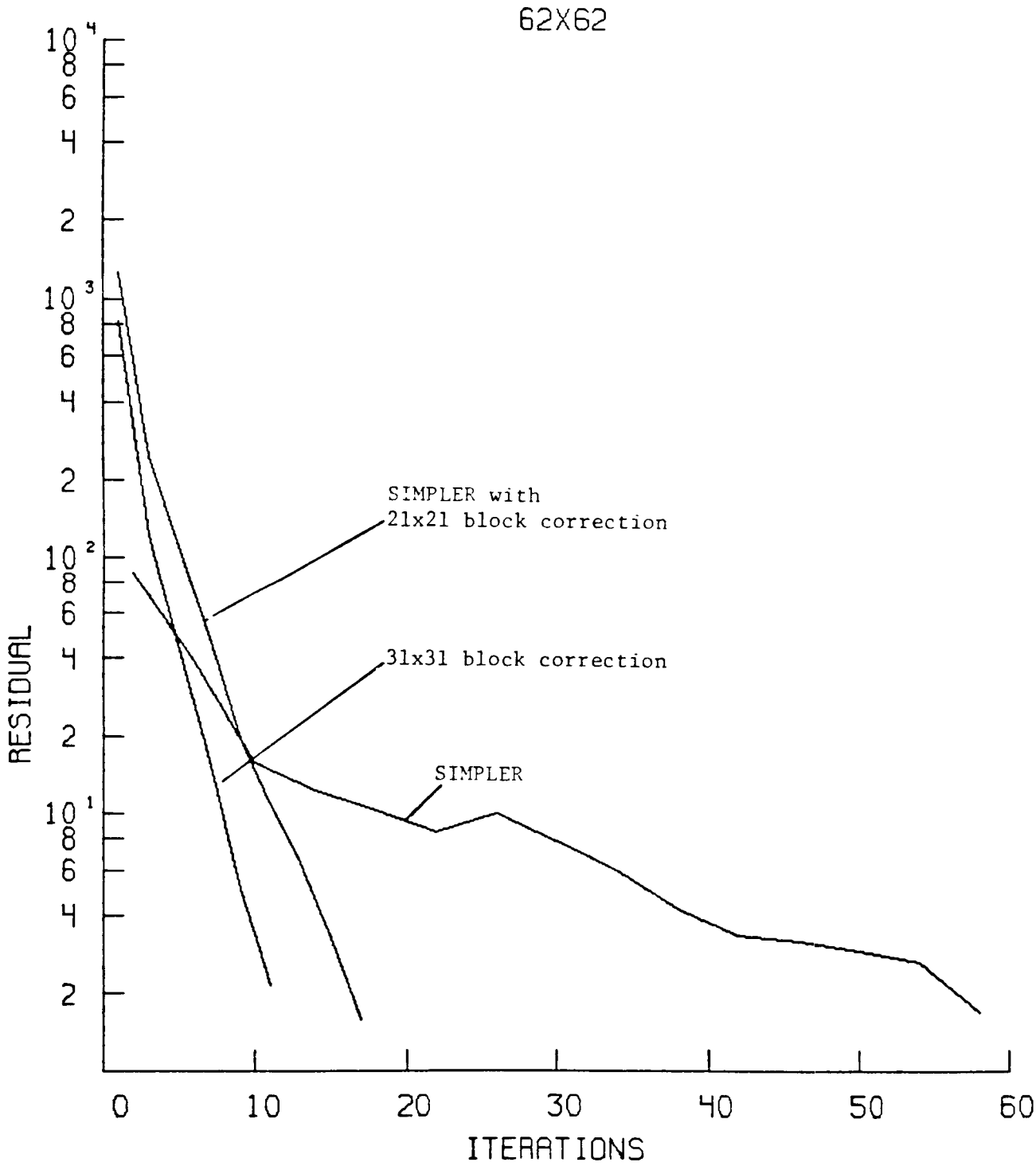

Figure 3 - Variation of the fine grid residual with the number of iterations on the fine grid for the driven cavity problem with Re = 2000

N89-17308

EVALUATION OF AEROTHERMAL MODELING COMPUTER PROGRAMS

K.C. Hsieh and S.T. Yu
Sverdrup Technology, Inc.
Lewis Research Center
Cleveland, Ohio

In the present research, various computer programs based upon the SIMPLE or SIMPLER (ref. 1) algorithm have been studied and compared for numerical accuracy, efficiency, and grid dependency. Four two-dimensional codes and one three-dimensional code originally developed by a number of research groups were considered. In general, the accuracy and the computational efficiency of these TEACH typed programs have been improved by modifying the differencing schemes and their solvers. A brief description of each program follows:

(a) Error Reduction Programs (ref. 2): a two-dimensional program and a three-dimensional program were developed by Pratt & Whitney and modified by Advanced Scientific Computing LTD. The modifications include (1) Stone's Strongly Implicit Procedure (SIP) for the solution of the pressure correction equation, (2) Incomplete Choleski (IC) for the solution of the pressure correction equation, (3) Additive Correction Multigrid (ACM) to accelerate the convergence of SIP and IC, (4) Block Correction (BC) to accelerate the convergence of IC with the option of further accelerating convergence by using ACM, and (5) incorporation of Linear Profile (LP) and Mass Weighted (MW) Skewed Upstream Differencing Schemes (SUDS).

(b) Two-Dimensional Flux Spline Programs (ref. 3): Two two-dimensional programs based on the flux spline method were developed by K.C. Karki in Allison Gas Turbine Corporation. The flux spline method assumes that the total flux across the boundaries of each numerical control volume varies in a piecewise linear manner as opposed to the lower-order methods, such as the hybrid scheme, which assumes that the total flux is uniform between two adjacent grid points. Thus, a more accurate solution can be obtained through the flux spline method. In this research, two versions of the flux spline programs were examined. The first program uses a traditional, line-by-line sequential solver. In the second version of the program, a sparse matrix package developed at Yale University was employed. The momentum equations and the pressure correction equation were solved simultaneously by this direct solver, and computational efficiency has been improved.

(c) Second Order Upwind Differencing Program (ref. 4): A computer program using Price's second order upwind difference scheme originally developed by S.P. Vanka was studied. The solution algorithm employed is based upon a coupled solution of nonlinear finite-difference equations using the multigrid technique.

The model problem for examining the three-dimensional program has been adopted as the subsonic jet in crossflow configuration. The code is efficient and the calculated results are compared with experimental data.

The test case for the four two-dimensional codes was chosen to be the developing entrance flow in a two-dimensional flat channel since the analytic solution is

available (ref. 5). All the programs will be examined based upon this configuration. The accuracy and computational efficiency of these programs are compared. The grid dependency of each code is also studied.

REFERENCES

1. Patankar, S.V.; "Numerical Heat Transfer and Fluid Flows," Series in Computational Method in Mechanics and Thermal Science. McGraw Hill Book Co., New York, 1980.

2. Syed, S.A.; Chiappetta, L.M.; and Gosman, A.D.: "Error Reduction Program," NASA Contractor Report 174776; January 11, 1985.

3. Patankar, S.V.; Karki, K.C.; and Mongia, H.C.: "Development and Evaluation of Improved Numerical Schemes for Recirculating Flows," AIAA paper 87-0061, 25th Aerospace Science Meeting, January 12 to 15, 1987, Reno, Nevada.

4. Vanka, S.V.: Study of Second Order Upwind Differencing in a Recirculating Flow," NASA Contractor Report 174939, June 1985.

5. VanDyke, M.: "Entry Flow in a Channel," J. Fluid Mechanics, vol. 44, part 4, pp. 813-823, 1970.

HEAT TRANSFER WITH VERY HIGH FREE-STREAM TURBULENCE AND HEAT TRANSFER WITH STREAMWISE VORTICES*

Robert J. Moffat, Paul Maciejewski,
John K. Eaton, and Wayne Pauley
Stanford University
Stanford, California

Two experimental programs are reviewed in this report, both related to augmentation of heat transfer by complex flow characteristics. The first program deals with very high turbulence (up to 63%) which has been shown to result in Stanton numbers as much as 5 times the expected values. Results from a large number of trials show that fixing the free stream velocity, x-Reynolds number, turbulence intensity and integral length scale does not fix the Stanton number. Two such cases have been found in which the Stanton number of one was 40% larger than the other. Mean velocity and mean temperature profiles are presented in this report, as well as profiles of turbulence intensity within the boundary layer. Two cases are displayed--one with high heat transfer augmentation (3/1) and the other with low (1.8/1). There are obvious, qualitative differences in the profiles

The second program deals with vortices originating at bluff bodies and traveling downstream embedded in the wall boundary layer. Velocity vector maps from the boundary layers and distributions of Stanton number on the wall are presented for three types of bodies: square, cylindrical, and teardrop.

The heat transfer and velocity maps do not show evidence of the expected "horseshoe vortices" but, instead, show a strong common-flow-up vortex pair. The fluid mechanic mechanism responsible for this secondary flow field has not yet been identified.

Foreword

Most heat transfer research is conducted in low-turbulence tunnels, that is, with less than 0.5% turbulence, in flows especially refined to be spanwise uniform and steady. These conditions produce a "low-limit" estimate of heat transfer for a given mean flow and geometry. Free stream turbulence, or unsteadiness, or streamwise vortices increase heat transfer.

* This work was performed under NASA NAG 3-522.

Free stream turbulence of 4 to 6% or larger may increase heat transfer even in fully turbulent regions [Blair, Ref. 1].

Gas turbines, on the other hand, run with turbulence up to 20-30%, which is probably highly anisotropic and well laced with large coherent structures coming downstream from the combustion chamber. Dils and Follansbee [Ref. 2] measured up to 16% in the discharge of a laboratory scale combustor in a bench test. They reported increases in heat transfer of over 50% on the stagnation line of a cylinder in that flow. Other recent observations (Rohde, [Ref. 3]) suggest 20 to 30% as a reasonable value for the relative turbulence near a typical first turbine nozzle ring.

The flow through a gas turbine may not look much like the flow most researchers have in mind when they think of "turbulence." It is not difficult to imagine, superimposed on the "normal" turbulent fluctuation, a whole family of flow disturbances whose spatial and temporal characteristics are determined by the engine configuration upstream of the point observation.

Among the phenomena which may be present (either intermittently or steadily) are:

(1) large scale, low frequency quasi-coherent structures,
(2) streamwise vortices,
(3) wakes from upstream vanes or blades,
(4) regions of high turbulent shear stress.

This paper describes recent results from two programs at Stanford, one concerning the effects on heat transfer of very high free-stream turbulence and the second concerning the effects of streamwise vortices.

The high turbulence has, so far, been created by placing the test plate in the margin of a large diameter free jet. This exposes the plate to a flow in which the local turbulence intensity can be as high as 70%. Putting the plate at different distances from the jet exit, and at different distances from the axis of the jet allows a certain degree of independence in choosing the mean velocity, turbulence intensity, and the integral length scale.

There is no assurance that this flow is like that which exists in a gas turbine, but it need not be the same to provide clear evidence that chaotic, unsteady, and highly Turbulent (with a capital T!) flows can result in heat transfer rates for higher than predicted by the usual correlations. One objective of this program is to demonstrate how high the "upper bound" of turbulent heat transfer can be pushed, at a given x-Reynolds number based on mean velocity. This will not prove where the upper bound is in a gas turbine, but will show at least where the lower limit of that upper limit might be. A second objective is to identify the turbulence descriptors which best relate to the increased heat transfer. This latter issue is critically important, since we must know what aspect of turbulence

best correlates with the increase in heat transfer before we can specify the measurements which must be made.

It would be very helpful to have a "good" description of the flow field in an engine, to guide the present experiments, but such data are not available. In fact, the present work has already raised some troubling questions about the sufficiency of the usual set of turbulence measures. The issue is, "What aspect of a turbulent flow field best correlates with the increase in heat transfer?" There is no assurance that measures of the mean velocity, turbulence intensity, and integral length scale will suffice to identify the heat transfer aspects of a flow. In fact, the work reported at HOST last year already contained evidence that fixing these three parameters did not fix the heat transfer. Until we know what aspect of the flow to measure, we cannot even enter a sensible request for "Engine Data."

The second program reported here concerns streamwise vortices, and their effect on heat transfer to turbulent boundary layers. This issue has attracted much attention over the last several years, chiefly with regard to the end-wall heat transfer. Several different vortical structures have been identified by flow visualization, but characterization of their effect on heat transfer has been slow in coming. This report describes some of the hydrodynamic features of a streamwise vortex pair which might relate to their effect on heat transfer. These results are described in the section entitled Phase II -- The Effects of the Streamwise Vortices.

Phase I: High Turbulence

This is an experimental program aimed at answering the following questions: (1) How much can free-stream turbulence raise convective heat transfer, all other factors remaining constant? (2) What measurable aspects of the turbulence form the "necessary and sufficient set" needed for predicting the augmentation? (3) How can the effects of turbulence be incorporated into current boundary layer heat transfer models?

Heat transfer experiments are being conducted with highly turbulent air flow over a smooth surface, with free-stream intensities from 15% to 65%. This covers a higher range than is believed to be present in gas turbines, by about a factor of two. These high turbulence levels are generated in the flow field of a large diameter (about 0.3 meter), low velocity (up to 5 meters/sec) free jet discharging into still air. The auto-correlation length scales can be large, up to 17 centimeters, but vary with distance from the nozzle so that different values can be found in the flow and the turbulence intensity varies both radially and axially. Different combinations of free-stream velocity, turbulence intensity, and integral length scale can be found by moving the leading edge of the plate to different locations within the jet. Using the known properties of a free jet and considering the jet initial velocity as a variable, one can plan sequences of trials in which the heat transfer can be measured at pairs of

different locations in the jet which have the same measurable flow properties (i.e., the same mean velocity, turbulence intensity, and integral length scale).

The general arrangement of the hardware is shown in Figure 1. The test surface is an Aluminum plate, 2 meters in length and about 0.5 meter wide, divided into 8 streamwise sections, each a separately instrumented heat transfer specimen. Two orientations are shown for the plate: parallel to the centerline of the jet and parallel to a ray. These result in slightly different distributions of mean velocity along the plate, one case corresponding to a flat plate, the other to a slightly accelerating flow. The free stream velocity and the turbulence intensity both drop off slightly with length along the test plate, but the variations are within +/- 10% of the mid-length values. Those are used to describe the flow. The effect of the radial distribution of velocity in the jet is still measurable near the outer edge of the plate boundary layer.

It was shown, in the 1985 HOST report, that the test plate was "qualified" in that it produced results within +/- 2% of the accepted flat plate correlation, when used in a low turbulence tunnel. It was also shown that the high turbulence flow field of the free jet produced a repeatable heat transfer situation, by a demonstration that two independent "build-ups", i.e., dismounting and re-mounting the plate into the same nominal location in the jet on consecutive days yielded the same data within +/- 2%. On the basis of those tests, it is felt that the results presented here are credible.

The first question, "How much can free-stream turbulence raise convective heat transfer, all other factors remaining constant?", is addressed in Figure 2 which shows that Stanton number augmentation by as much as a factor of 5 has been achieved. Previous work reported in the literature by many sources has shown that turbulence of less than 6% produced only small effects on heat transfer, with occasional reports of "no effect at all". The present results show that turbulence intensities from 20% to 60% can raise the Stanton number by factors of from 1.8 to 5.

The second question, "What measurable aspects of the turbulence form the 'necessary and sufficient set' needed for predicting the augmentation?" is also addressed in Figure 2. Four candidate descriptors are used in constructing this figure: free stream velocity, Re_x, turbulence intensity, and the integral length scale. No combination of these four constitutes a sufficient set, as can be seen by examining the combinations covered in this set of "paired comparison" runs. Numbering the runs from the top down, Runs 1 and 3 contain points at the same X-Reynolds number and turbulence intensity, yet the Stanton number augmentation differs by the ratio of 5 to 3, thus those two descriptors are not sufficient to uniquely define the augmentation. Runs 2 and 5 contain points at the same X-Reynolds number, free-stream velocity, turbulence intensity and integral length scale and yet their augmentation ratios are in the ratio 3 to 2.5 so even the set of four does not uniquely establish the augmentation to better than +/- 13%. Since the experiment has demonstrated repeatability to

within +2% it is evident that +13% is significant. Most current theories in the effects of turbulence describe the response of the boundary layer in terms simply of two (e.g. Reynolds number and turbulence intensity) or three parameters (Reynolds number, turbulence intensity, and length scale). The differences in the present data for the same values of these parameters strongly suggest that these theories cannot be reliable.

The experiments shown in Figure 2 have not yet identified the 'necessary and sufficient set' but have shown that no combination of the four tested are sufficient. No theory can be entirely correct which is based only on those four, since fixing all four does not uniquely determine the augmentation. The problem may be simpler at higher Reynolds numbers, and these four (or even fewer) may be sufficient in that regime but, for the present flow conditions, it seems clear that some additional descriptor must be found.

In the first series of experiments a single U-component hot-wire anemometer was used to estimate the mean velocity, turbulence intensity, integral length scale, even though its limitations were clearly recognized.

A single hot-wire probe cannot accurately describe the details of the free stream turbulence since it is sensitive to more than one component of the flow and yet does not accurately represent the total velocity. To investigate the magnitude of the error involved, an orthogonal triple-wire probe was used to measure the free stream turbulence properties. Its results confirmed the single-wire results within reasonable accuracy and, based on the findings already mentioned, we began to examine the details of the turbulence in two selected cases: High Augmentation and Low Augmentation.

Progress During the Past Year

Experiments during the past year were concentrated on obtaining more detailed turbulence measurements in the free stream and temperature and velocity profiles in the boundary layers. The objective in these profile measurements was to answer the following questions: (1) "How do the velocity and temperature distributions differ between the high augmentation and the low augmentation cases?", and (2) "How do the details of the free stream turbulence differ between the high and low augmentation cases?"

This question was addressed by using an orthogonal triple-hot-wire in the free stream, with analog processing capable of time-resolved measurements of the individual components of the Reynolds stress tensor and by two traversable probes for the boundary layer, a single-wire constant temperature anemometer for mean and fluctuating velocity measurements and a fine-wire thermocouple probe for mean temperature.

Within the boundary layers, the distributions of velocity and temperature were compared for the two cases -- high augmentation and low. The Stanton number data for the two cases are shown in Figure 3. These will be referred to in the following figures as the High Augmentation and the Low Augmentation cases not by their turbulence measure. Note that even in the "Low Augmentation" case, the Stanton number is higher than the usual flat plate value by a factor of 1.8, while the High case is up by a factor of 3.

Figure 4 presents the mean velocity distributions for both cases in $u^+ - y^+$ coordinates, at three locations along the test plate. The value of $C_f/2$ was assumed equal to the Stanton number. Experiments supporting this assumption were done last year. It was shown in those experiments that the turbulent shear stresses measured in the boundary layer using the triple-wire probe, if extrapolated to the wall, were in reasonable agreement with that assumption.

In one respect these data resemble rough-wall results: the log region is depressed proportionately more in the high augmentation (high turbulence) case than in the low. In addition, however, the log region for the high augmentation case displays a lower slope than the low augmentation case; evidently the mixing process in the boundary layer is significantly different in the two cases. There is no evidence of a wake region in either set of profiles.

These data appear somewhat irregular in the outer region, and one might wonder why. In fact, it is a non-trivial task to acquire representative data in the outer region of the boundary layer in this flow field -- there are some very long-period excursions in the flow. Figure 5 compares mean velocity profiles taken by two traversing strategies: 1000 measurements at each station, serially measured from the wall out to the free stream ("munching") and 30 measurements at each station, on each of 30 traverses, with the data then averaged ("looping"). The total time span of each acquisition was approximately 2.5 hours. Note that the "looping" strategy randomized the long period excursion of velocity which introduced the pathology in the "munching" profile. This long period excursion is believed to be due to meandering of the jet centerline, a large scale phenomenon which, if it is in fact present, would be scaled partly on the room dimensions, not only those of the jet. The turbulence profiles are less affected by the choice of traversing strategy since slow variations in the mean are not recorded. All of the data presented here were acquired by "looping" through the boundary layer and averaging the data sets.

Figure 6 compares the turbulence intensities deduced from the single-wire probe for the High and Low augmentation situations. In the High augmentation case, the turbulence intensity distribution resembles the mean velocity distribution itself, at least in its principal features. There appears to be a nearly-log region, and an inner region. Turbulence intensity is high throughout the inner region of the boundary layer, and there is no local "bulge" in the region usually associated with turbulence production in a normal boundary layer. The Low augmentation case does

show some evidence of a local increase, around y^+ of 20 to 30, but there is no pronounced bulge in that data either. In both situations the distributions of turbulence intensity are more like profiles of a conserved property than like the usual turbulence distributions.

Figure 7 shows that the mean temperature distributions at different x-locations are similar within each data set, (High and Low augmentation), but that the two flow fields produce different average profiles. There is one exception to this: the profile from the first segment of the low augmentation situation resembles more the high augmentation data than the low.

The RMS temperature fluctuations were measured for both cases and significantly higher values were found in the high augmentation case. The data are not shown, since no way could be found to deduce the level of fluctuations in the gas temperature from the recorded fluctuations in thermocouple temperature. With high turbulence and simultaneous velocity and temperature fluctuations, the usual time-constant compensation techniques cannot be justified.

Measurements in Highly Turbulent Flows

The work planned for this year involved a more detailed examination of the turbulence properties of the High and Low augmentation situations. In particular, we sought to measure the spectra and energy contents of each of several individual components of the Reynolds stress tensor. This requires accurate measurement of the individual components, which required a careful examination of the triple-wire response to high turbulence.

In the free stream, where turbulence intensities approach 65%, even the real-time-processes orthogonal-triple-wire data are subject to errors due to the instantaneous velocity vectors lying outside the measurable cone. Even if these errors only slightly affected the measurement of total turbulence intensity, they could seriously distort the measurements of the individual Reynolds stress tensor components. Thus, before detailed measurements in the high turbulence free-stream could be trusted, some means was needed for estimating the errors which might be present--in terms of the indicated data. The data acquisition was halted and attention turned to NRI development of a theory and method for estimating the errors. The results of this study are presented as a separate topic, in the next section of this report, but Figure 8, 9, and 10 show one way in which these errors affect the distribution of measured instantaneous velocities.

Figure 8 shows a histogram of 15,000 measurements from a single-wire probe in the free-stream flow of the Low Augmentation case where the turbulence intensity was about 17%. The dotted line represents the measurements while the dashed line is a normal distribution corresponding to the mean and variance of the set of 15,000 points. The agreement is

good, except very near the tails of the distribution. The turbulence is low enough, compared to the mean velocity, that the instantaneous effective velocity (for the hot wire) is dominated by the u-component. The fact that the observed distribution closely resembles the expected (normal) distribution also confirms that the flow field is a normally developing free jet flow.

The High Augmentation case is shown in Figure 9. The dotted line again shows a histogram of 15,000 measurements from a single-wire probe in the free stream flow. The dashed line is the normal distribution associated with the measured data, using Figure 11 (in the next section) as a guide to estimating the true mean and true intensity. Use of Figure 11 for a single-wire is an approximation since Figure 11 was derived for an orthogonal triple-wire. The pathology in the histogram (in the low and negative velocity region) reflects two mechanisms: (1) the probe cannot accurately measure velocity components which lie too close to the wire and, (2) the probe rectifies negative velocity components (those which approach from downstream) and "reports" them as positive. As a consequence, the hot-wire probe "folds" the velocity data across a value near zero, and puts spurious data into the low velocity part of the histogram.

To check that the interpretation proposed for the data in Figure 9 was correct, a computer experiment was performed to simulate the behavior of a triple wire. An artificial data set was generated consisting of 1024 individual realizations (u,v,w) calculated assuming an isotropic, joint-normal probability distribution for a specified mean velocity and turbulence intensity. Each triad was then processed through the response equations of the orthogonal triple-wire, assuming real-time data processing, as is used on the Stanford triple-wire system to eliminate the time-averaging ambiguity. The results of these calculations were then interpreted through the triple-wire velocity decomposition algorithm to yield 1024 values of the apparent u-component. These were then used to generate the histogram shown as the dotted line in Figure 10. This dotted line represents the histogram which would have been deduced from the triple wire if it had been in the hypothetical flow. The dashed line is the normal distribution associated with the hypothetical data set--the real u-components of the simulation set. All of the features of Figure 9 (from a single wire) are consistent with the present simulation of the triple-wire behavior. Figure 10 was generated assuming "critical reflection" at the wire angles, with accurate measurements everywhere within the cone and (except for sign) outside. There may not be a need for any more detailed response equations. The present predictions seem adequately accurate, at least for describing the u-component histogram.

The next section presents the theory of the proposed method for deducing the correct values of turbulence properties in a homogeneous, isotropic flow field from the output of an orthogonal, real-time hot wire system.

Estimating the Errors

An orthogonal triple-wire probe can provide accurate measurements of the mean velocities and the turbulence intensities up to levels of about 30% (Ref. 4). At higher turbulence levels, the probes will tend to overestimate the mean velocity and underestimate the turbulence intensity. Even at 30%, there is no assurance that the individual components of the Reynolds stress tensor are correctly measured.

Accurate measurement of the structure of high turbulence flows is becoming increasingly important. The objective of this portion of our research was to investigate means for extending the turbulence range of the orthogonal triple wire to include flows with up to 60% turbulence. The first goal was to demonstrate accurate measurements in a high turbulence, isotropic flow: the free flow of the present apparatus. This would permit accurate characterization of the individual components of turbulence and, possibly, lead to identifying which aspect of the turbulence most nearly correlated with the heat transfer augmentation.

Directional Ambiguity in Triple Wire Anemometry

The triple wire system involves the solution of the following set of equations:

$$\begin{matrix} X^2 \\ Y^2 \\ Z^2 \end{matrix} = [K]^{-1} \begin{matrix} U^2eff1 \\ U^2eff2 \\ U^2eff3 \end{matrix}$$

Because this system of equations involves the squares of the component velocities (X,Y, and Z in a coordinate system formed by the wires), it is impossible to distinguish a positive component velocity from a negative one. The common practice is to assume the instantaneous velocity vector falls in the first octant in X,Y,Z space even though there is a velocity vector in each of the other seven octants that could have produced the same combination of effective velocities on the three wires. This assumption is relatively safe as long as the turbulence is not more than moderately high (up to 30%) and where the probe axis is aligned with the mean flow direction. For higher levels of turbulence, or gross misalignment of the probe with the mean flow direction, the assumption that the instantaneous velocity vector falls inside the first octant fails. In these situations the actual instantaneous velocity vector cannot in general be determined unambiguously from the measured effective velocities.

The Nature of the Errors

To investigate these errors, a computer code was written to generate simulated velocity vector data for isotropic turbulence. The data are random samples from a tri-variate normal population with the three components having the same standard deviation specified as a fraction of the mean vector. These instantaneous velocity vectors were then "measured" using the equations of a triple wire aligned with the mean flow direction. The hot wire signal was calculated using the Jorgensen decomposition. With these equations the same effective velocity was assigned to all eight of the vector locations (quadrants 1-8) the "apparent" velocity (i.e. the velocity which would have been deduced from the hot wire output) was then calculated by mapping vectors falling in octants two through eight in X,Y,Z space into octant one. Figure 11 illustrates the relationship between the statistics of the simulated flow and those that would have been derived from the output of the triple wire. For small to moderately high levels of fluctuations relative to the mean, nearly all the velocity vectors do fall in the first octant and the agreement between the actual flow field statistics and the statistics of the triple wire output is excellent. For levels of turbulence greater than 30% the triple wire systematically overpredicts the mean and underpredicts the turbulence intensity.

Figure 11 can be used directly to correct the data taken with the triple wire in isotropic and nearly isotropic flows such as the free stream used in this study.

Figures 12 through 14 illustrate how Figure 11 was generated, showing the simulated triple wire data in the u-v plane. Each figure is a plot of 1024 data points generated from an isotropic tri-variate normal distribution. Figure 12 appears to contain fewer points than Figures 13 and 14, but that is only because the points are densely nested near the mean. For 20% turbulence substantially all the velocities do lie within the first octant of the triple wire system and the triple wire output is an accurate measure of the flow field. At 40% turbulence some of the vectors are folded into the first octant, as evidenced by the sharp boundary beginning to form at 45 degrees from the mean flow direction (this corresponds to the 54.7 degree orthogonal triple wire cone angle projected onto the u-v plane). For 60% turbulence, the data is even more distorted, demonstrating the shift the mean to a higher value and the reduction of the standard deviation, as seen in Figure 11.

For an arbitrary Reynolds' stress tensor with the probe misaligned with the mean flow direction the errors one will incur using a triple wire in a highly turbulent flow will be somewhat more complicated, but the trends in the errors are expected to be easy to recognize.

Improving the Accuracy

Figures 11 through 14 show that the triple wire system significantly distorts a cluster of velocity data for turbulence levels greater than 30%. The issue now becomes one of identifying the true population from the distorted cluster of data which was gathered. Figure 10 compares the u-component pdf calculated from the triple wire simulation in Figure 14 to the u-component distribution used in the simulation. Although the pdf is significantly distorted on the left-hand side, there is a region on the right-hand side that is not contaminated by the triple wire's mismapping of the flow field. This fact forms the basis for the present theory for dealing with high turbulence data from a triple wire.

The problem of using a triple in highly turbulent flows for the purpose of making mean velocity and Reynolds' stress measurements can be reduced to the problem of determining the actual probabilistic distribution of states of the velocity vector in complete X,Y,Z space given that all real vectors are mapped into the first octant by the measuring process. The triple wire data provides the distribution of states corresponding to the final states when the actual distribution of states is folded into itself to a degree set by the level of the turbulence measured and the degree to which the probe is misaligned from the mean flow direction. A method has been developed for inferring the actual velocity joint pdf from the "folded" data taken with a conventional triple wire, and is discussed next.

Figure 15 represents a bivariate normal joint pdf of u and v. Imagine an angle two theta such that the points falling outside two theta will be folded into the region inside two theta. The result of this folding will be another joint pdf of u and v which is uniquely related to the original joint pdf of u and v. This is the joint pdf of u and v seen through the triple wire. The next step is to construct a two dimensional histogram of triple wire data in the u-v plane. This histogram will contain a region into which little folding of data has occurred as well as a region including significant numbers of folded data points. If the joint pdf of u and v of the actual flow field were bivariate normal, level curves (equal probability lines) in the not-folded-into region of the histogram generated will be elliptical. If even one uncontaminated equal-probability ellipse can be identified, the actual joint pdf of u and v can be inferred.

Several alternative methods have been identified by which one might identify the "undisturbed pdf" given the "folded pdf". The choice of approach depends on the relative extent of the interference region.

The present proposal is to sample u,v,w triads and construct a high-density three dimensional histogram as an estimate of the u,v,w joint pdf seen through the triple wire. The equal-probability lines of this histogram will then be curve-fit to identify their shape and the u,v,w joint pdf of the actual flow. The present approach can, in principle, also be used in shear flows. It is not restricted to isotropic flows.

Verifying the Technique

We are currently developing the software and data acquisition strategy to implement the technique described above for using the triple wire in highly turbulent flow fields. The steps we propose to follow are: (1) simulate data acquisition from the triple wire probe by a computer experiment and determine whether or not the method is practical from a computational point of view, (2) transfer data acquisition to the actual triple wire to see if it demonstrates the same trends as the simulation, and (3) qualify quantitative measurements using the technique in the Stanford 2-D channel reference flow. The 2-D channel is a known flow field that can be accurately measured with the triple wire with the probe axis aligned with the axis of the channel (mean flow direction). Once the actual flow field has been measured and documented we can purposely misalign the probe in the flow field enough to cause any desired fraction of the instantaneous velocity vectors to fall outside the cone delimiting the first octant in X,Y,Z space. The data falling outside the cone will be folded into the cone. The joint pdf measured with the misaligned triple wire probe can then be compared directly to the known joint pdf for the flow in the channel.

If this technique for interpreting the triple wire output can predict the statistics of the flow in the 2-D channel we will then claim that the technique is ready for use with the triple wire to measure mean velocities and Reynolds stresses in highly turbulent flows.

Program for Next Year

The central problem still remains: "What measurable property of the turbulence predicts the augmentation of heat transfer?" The experiments conducted to date have shown that the four most likely candidates (U_∞, T_u, Re_x and λ) do not uniquely determine the augmentation. Proof that this set is not unique has been made by finding two locations in the flow where each of these four have the same value, and yet the heat transfer behavior is different. It follows that no function of these four can be adequate, however complex the form. What remains?

We plan to examine the spectrum and intensity of the individual components of the Reynolds stress test, in particular those dealing with velocity components normal to the wall.

The objective is to find some measurable attribute of the flow with which to complete the "necessary and sufficient" set. The missing attribute may be related to intensity or scale.

A small modelling effort will begin, using a 2-D time-averaged code (Stan6) with a mixing-length closure. The intent is to find out whether or

not the turbulent Prandtl number model recommended for low turbulence flows is valid at high turbulence. This can be done heuristically, by hypothesizing mixing length distributions, matching the experimental velocity profiles and then comparing predicted and measured temperature profiles.

Phase II: Streamwise Vortices

Our research program on embedded vortices has provided detailed data describing the perturbations in both the heat transfer and fluid mechanics behavior caused by various single vortices, vortex pairs, and vortex arrays. Most of the fundamental mechanisms responsible for heat transfer perturbations are now well understood as described in our two recent papers, Eibeck and Eaton, 1986, and Pauley and Eaton, 1987, (Ref. 5 and 6). The remaining question is: What type of embedded vortices are present in realistic flow geometries?

There has been a large amount of recent research examining the detailed heat transfer behavior in the vicinity of obstacles protruding through a boundary layer. These obstacles may represent either a turbine blade or an internal strut in an engine. The vortex wake trailing behind such obstacles has not been examined. The present facility was used to study the downstream perturbation in the boundary layer caused by various shapes of obstacles including circular, square, and teardrop shaped cross sections. The obstacles were installed in the two-dimensional boundary layer wind tunnel used for all of the previous embedded vortex work. The width of each obstacle was approximately equal to the boundary layer thickness and the height spanned the short dimension of the test section. Three-component mean velocity maps and the spatially resolved heat transfer coefficient were measured downstream of each type of obstacle.

The results were very surprising in view of previous assumptions about the vortex flow behind obstacles. Figure 16 shows the secondary flow in the wake behind a cylinder. A large common-flow-up vortex pair is evident in the mean flow. The diameter of the vortex is considerably larger than the boundary layer thickness, approximately 2 cm. A horseshoe vortex would appear as a common-flow-down vortex pair and would be embedded in the boundary layer. Clearly the present measurements are showing a different phenomenon. Figure 17 shows the heat transfer data behind the same circular cylinder. There is a very large perturbation in the heat transfer rate which can be explained in terms of the observed common-flow-up vortex pair.

Figure 18 provides a comparison between the secondary velocity plots for the wakes behind the three different shapes of obstacles. All three show a large common-flow-up pair but there are considerable differences in the details. There is no evidence of the classical horseshoe vortex in any of these flows. Heat transfer profiles at one axial station

(Figure 19) show that the square and cylindrical obstacles cause similar heat transfer perturbations. The teardrop shape causes a considerably weaker perturbation in general agreement with lower measured secondary flows.

The explanation for this unexpected behavior is not clear at this time. We believe that it has to do with the behavior of a Karman vortex street at an endwall. The vertical axis vorticity in the vortex street is rotated by the boundary layer shear at the endwall and results in longitudinal vortices. We cannot explain why this effect has not been observed previously. The parameters selected for the present experiment, in particular the ratio of the cylinder diameter to the boundary layer thickness may have a strong effect on the downstream flow.

References

1. Blair, M. F., "Influence of Free-Stream Turbulence on Turbulent Boundary Layer Heat Transfer and Mean Profile Development. Part I: Experimental Data," Journal of Heat Transfer, 105:33-41, February 1983.

2. Dills, R. R., and Follansbee, P. S., "Heat Transfer Coefficiency around Cylinders in Crossflow in Combustor Exhaust Gases," Jn. Eng. for Power, October 1977.

3. Rohde, J., "Personal Communication," 1984.

4. Frota, M. M., "Analysis of the Uncertainties in Velocity Measurements and Techniques for Turbulence Measurements in Complex Heated Flows with Multiple Hot Wires," Stanford University PhD Dissertation, Department of Mechanical Engineering, August 1982.

5. Eibeck, P.A. and Eaton, J.K. (1986) "The effects of longitudinal vortices embedded in a turbulent boundary layer of momentum and thermal transport," Proceedings of the Eighth Int'l Heat Transfer Conf., San Francisco, pp. 1115-1120.

6. Pauley, W.R. and Eaton, J.K. (1987) "The Effect of Embedded Longitudinal Vortex Pairs on Turbulent Boundary Layer Heat Transfer," to be presented at 2nd Int'l Symposium on Transport Phenomena in Turbulent Flows, Tokyo.

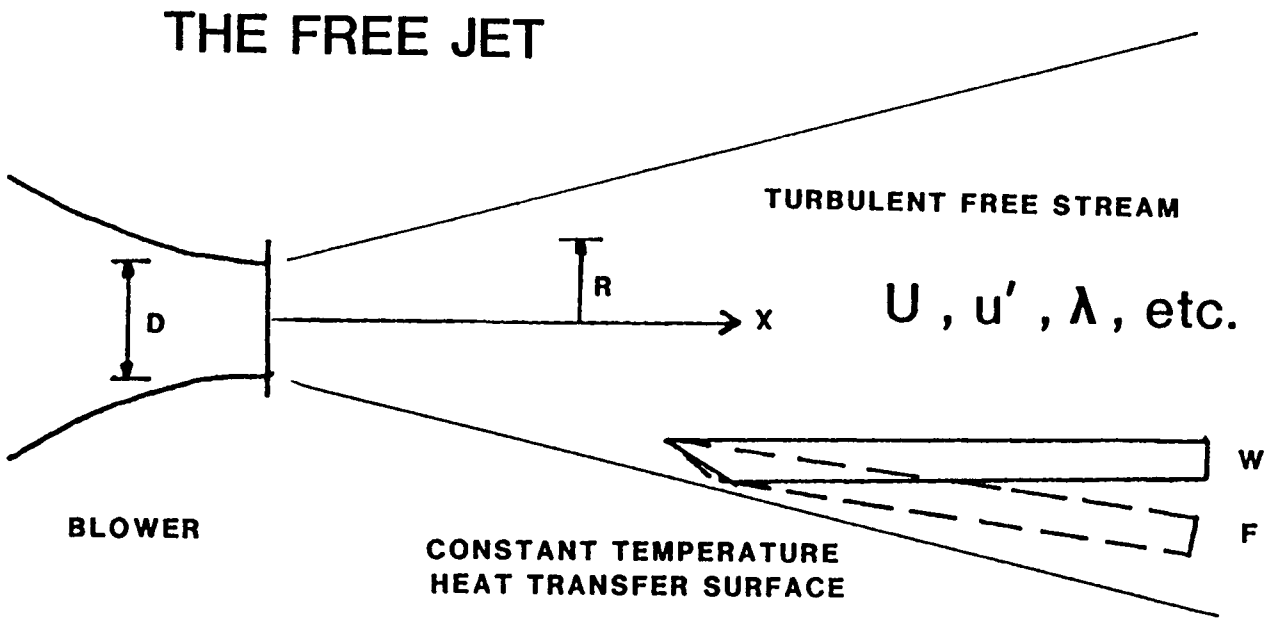

Figure 1 Schematic of the experiment on the effects of high turbulence on heat transfer.

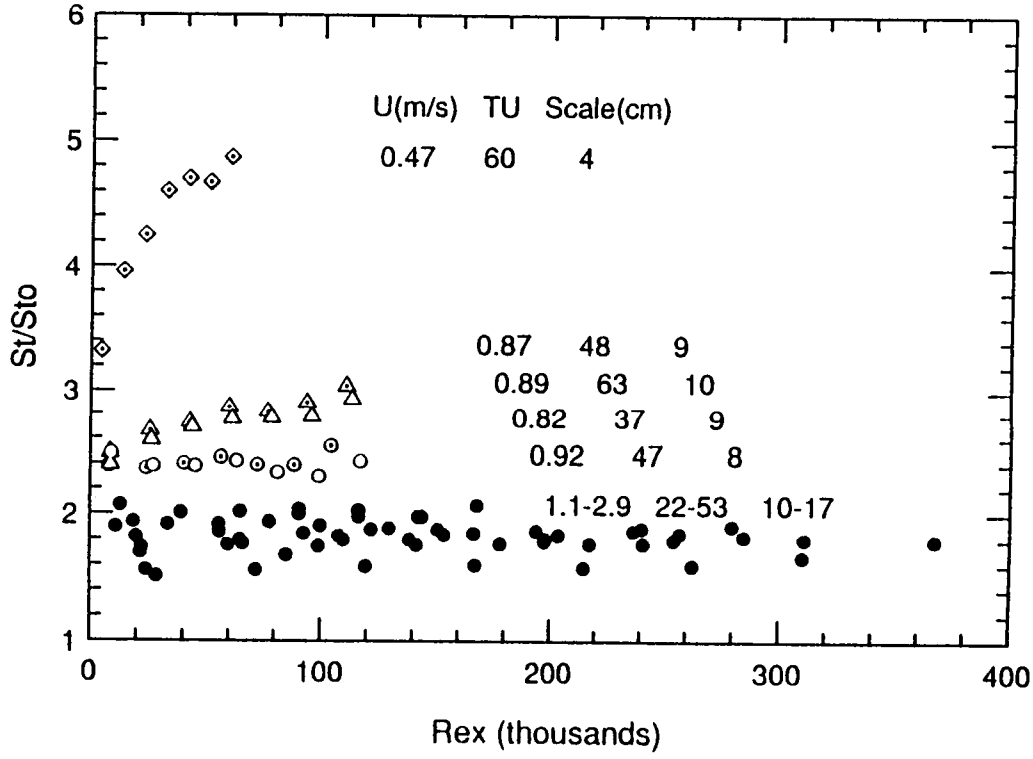

Figure 2 Comparison of hydrodynamic conditions associated with augmented heat transfer.

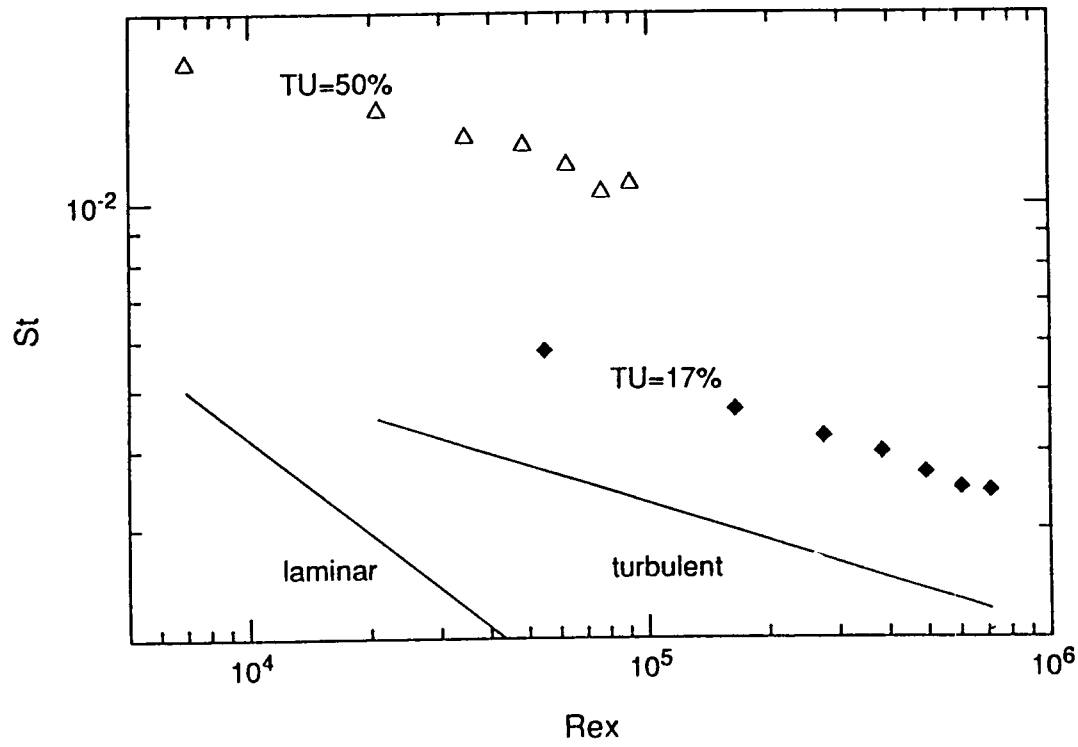

Figure 3 Heat transfer associated with data presented in Figures 4 through 9.

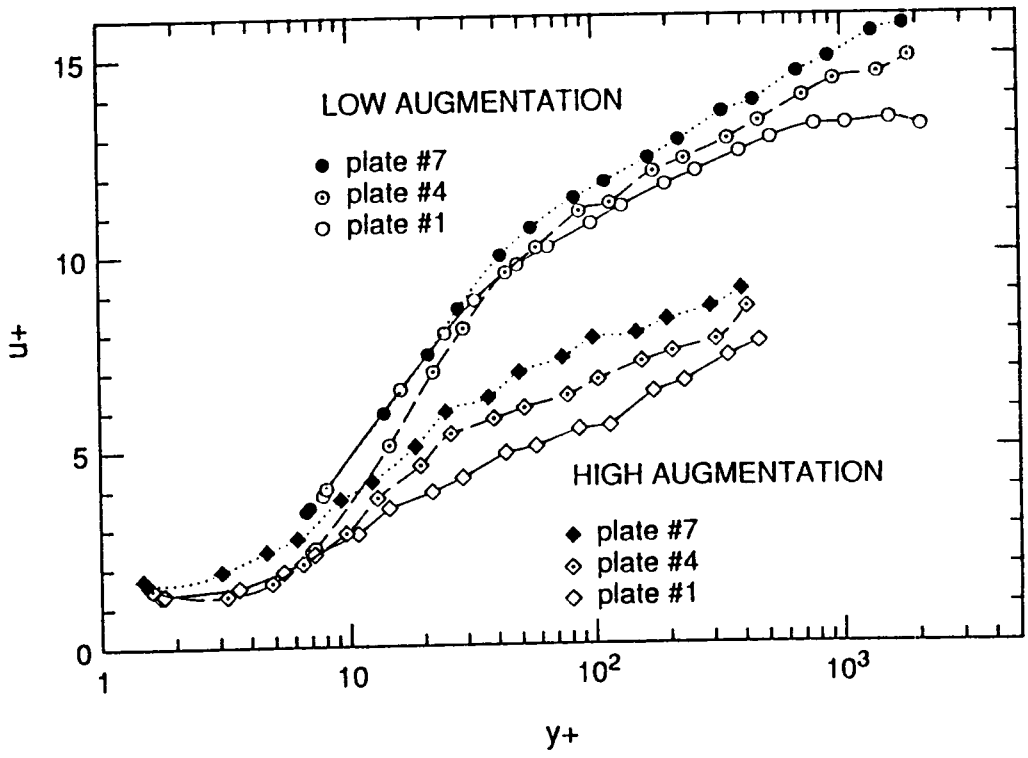

Figure 4 Mean velocity profiles.

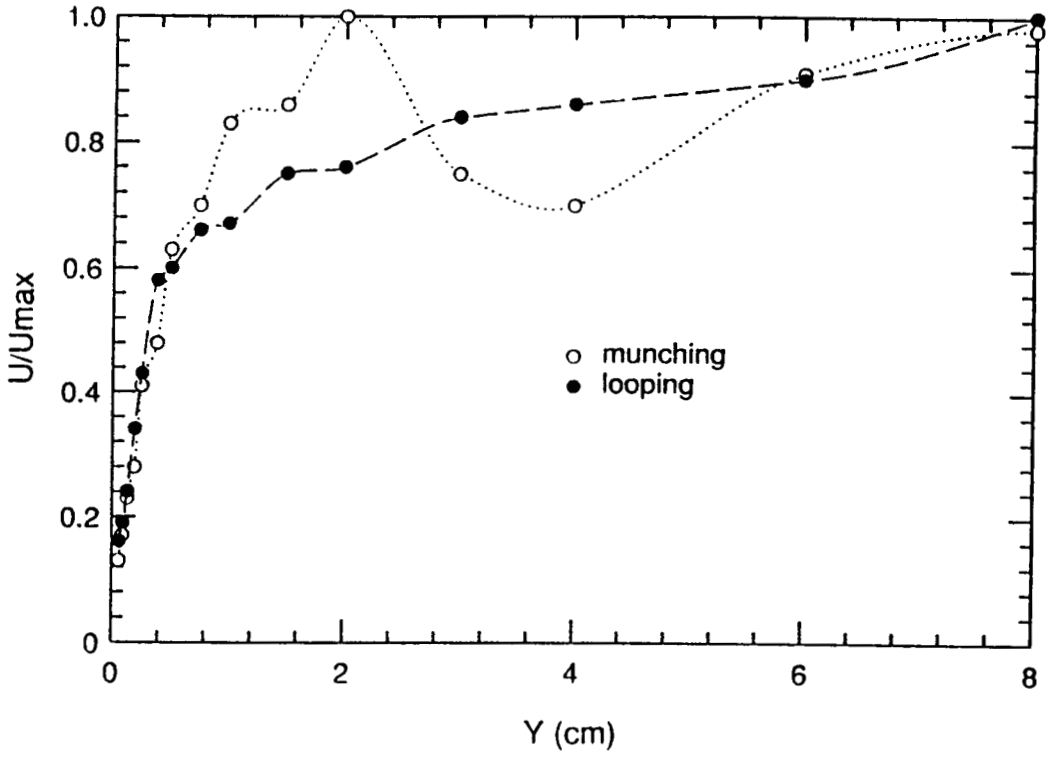

Figure 5 Velocity profiles using two traversing strategies.

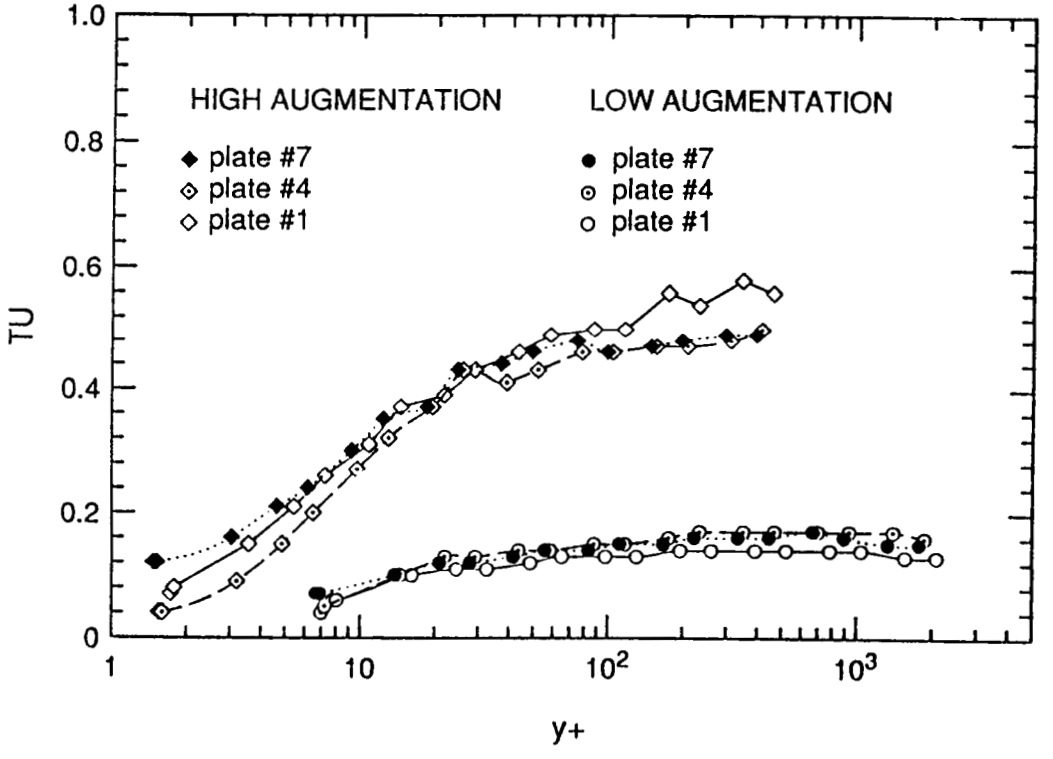

Figure 6 Turbulence intensity profiles.

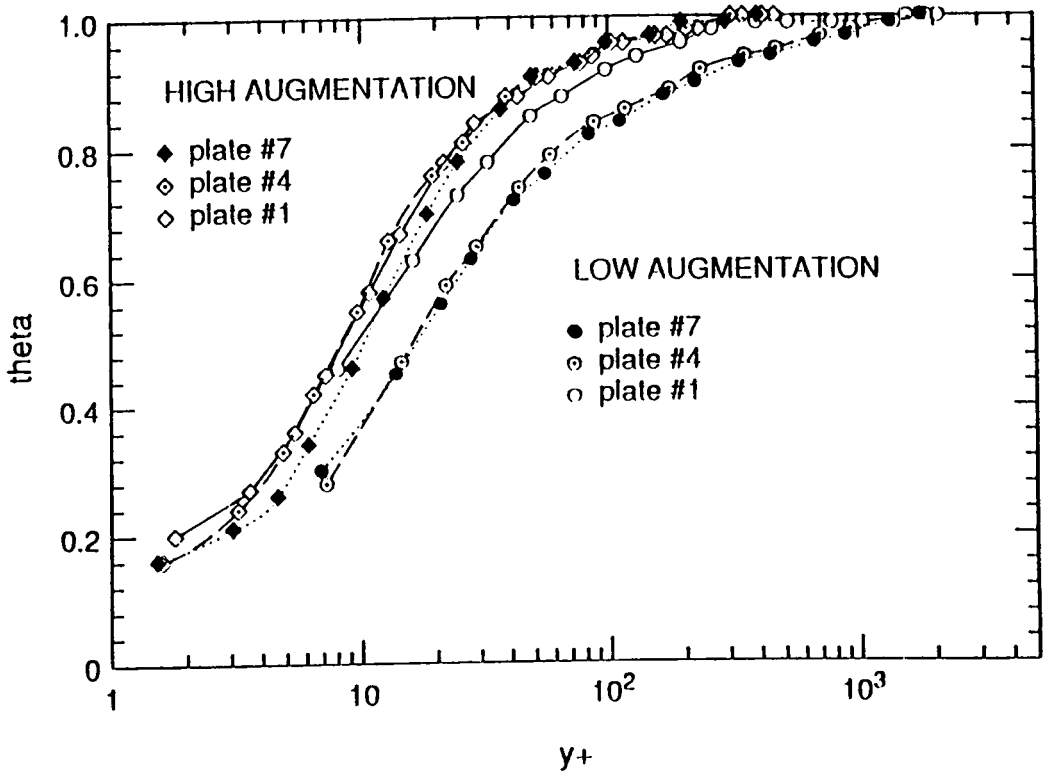

Figure 7 Mean temperature profiles.

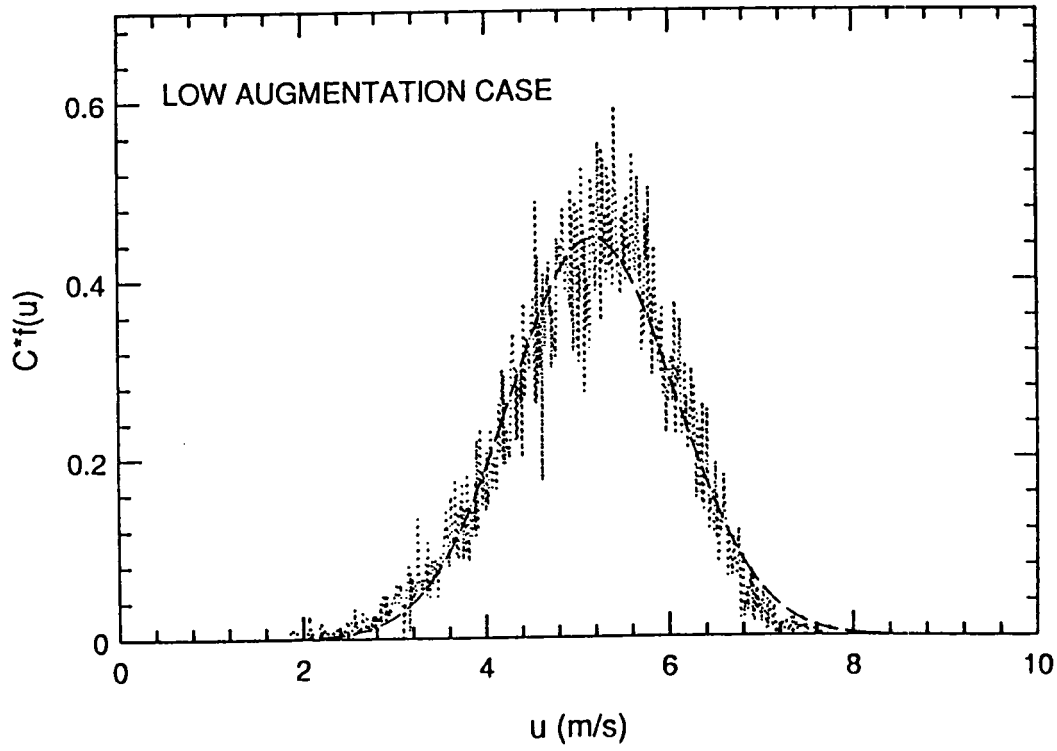

Figure 8 Free stream velocity pdf for low augmentation case.

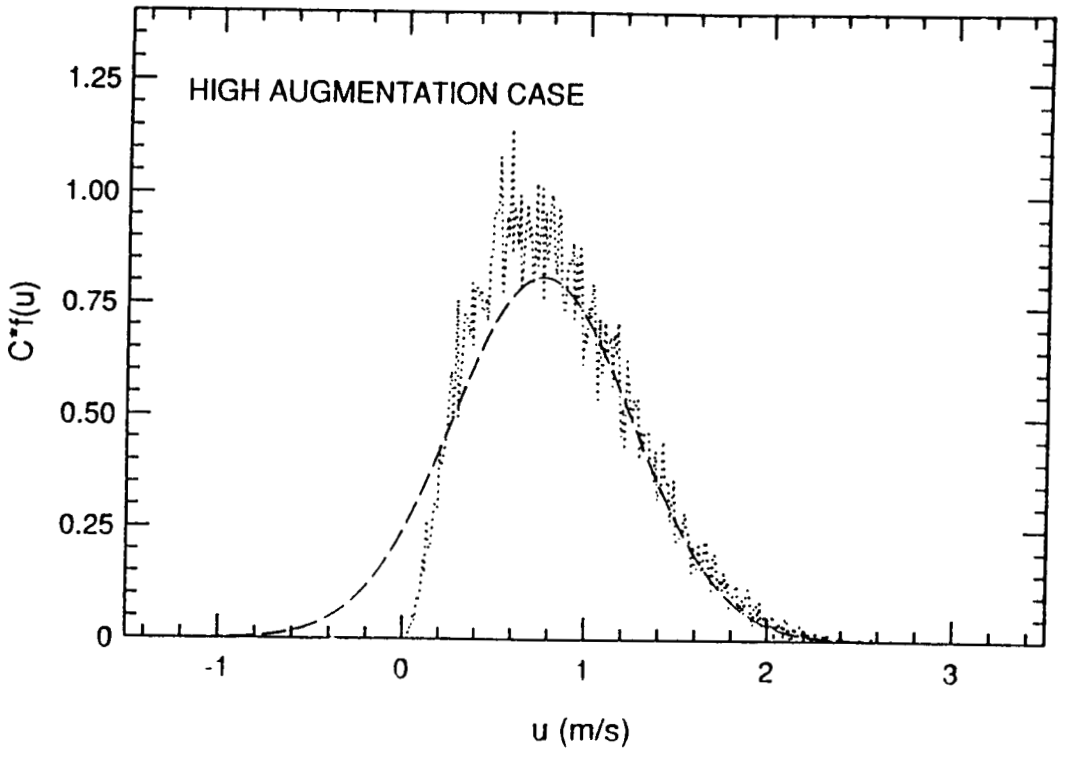

Figure 9 Free stream velocity pdf for high augmentation case.

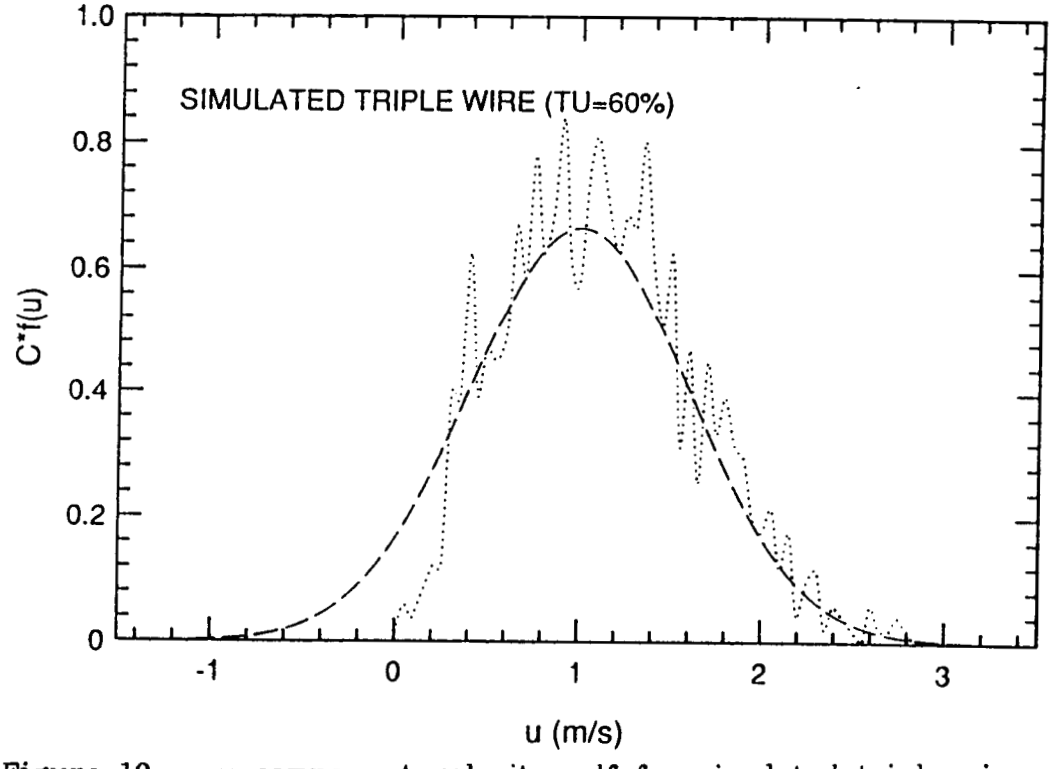

Figure 10 u-component velocity pdf for simulated triple wire.

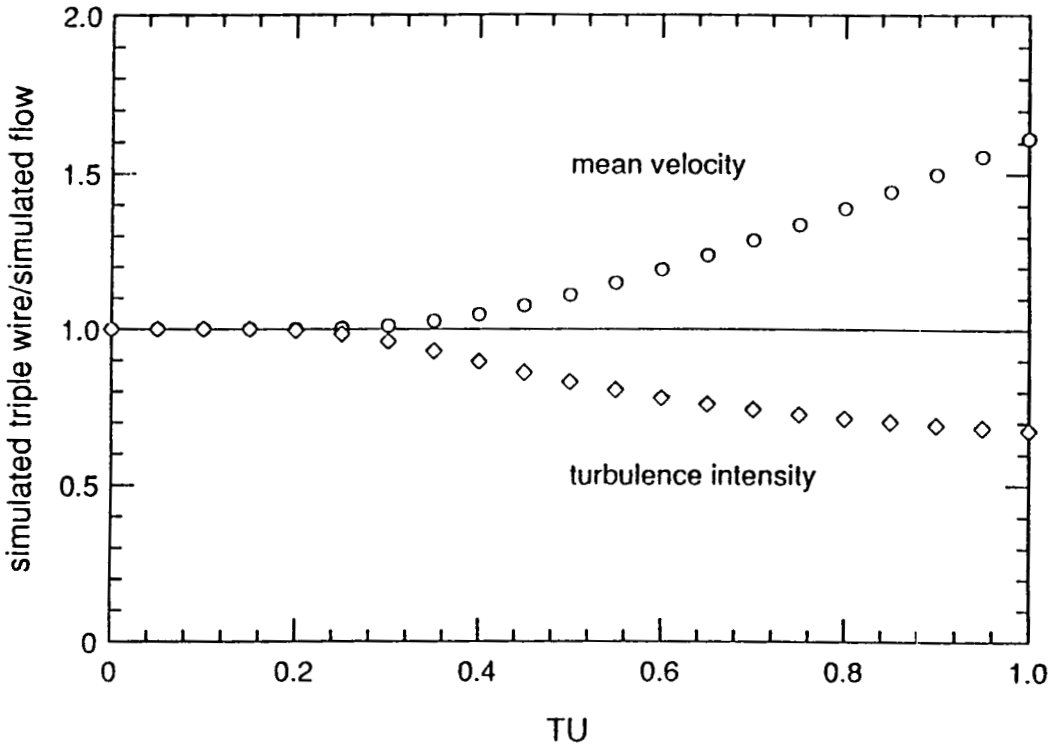

Figure 11 Effects of high turbulence on triple wire output.

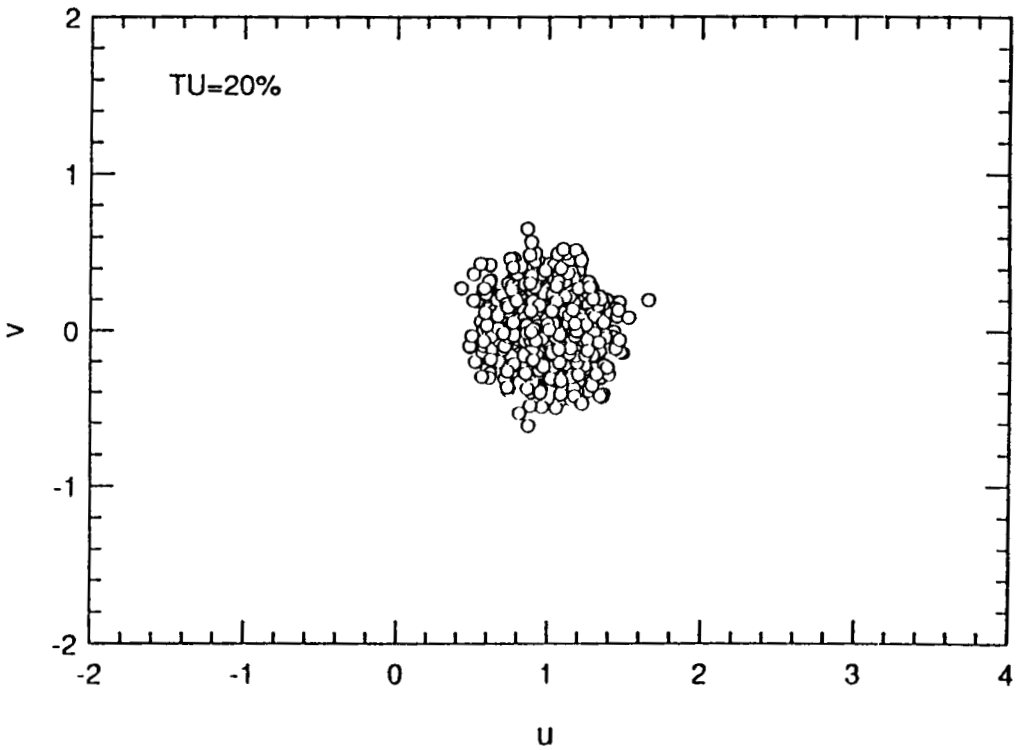

Figure 12 Simulated triple wire data in the u-v plane ror 20% isotropic turbulence.

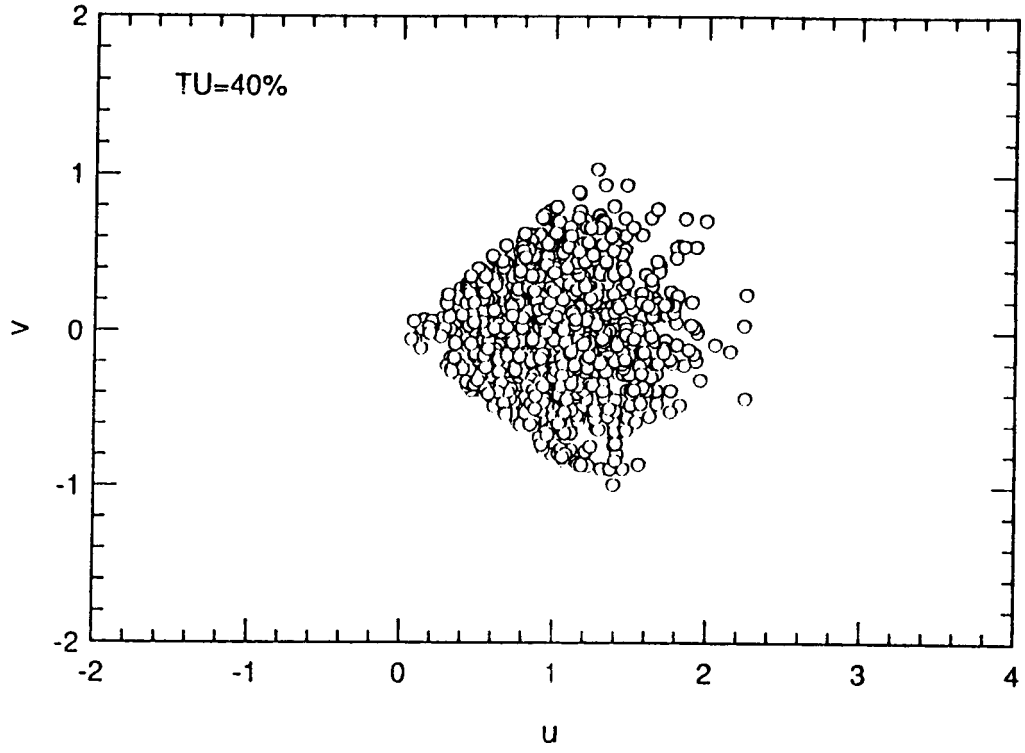

Figure 13 Simulated triple wire data in the u-v plane for 40% isotropic turbulence.

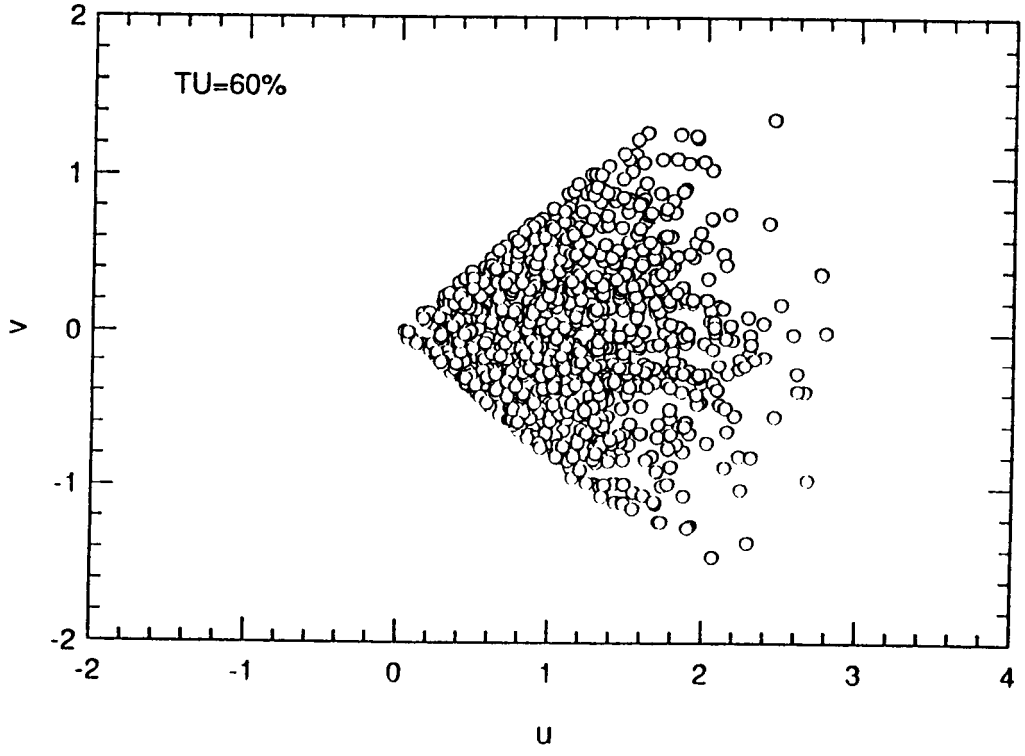

Figure 14 Simulated triple wire data in the u-v plane for 60% isotropic turbulence.

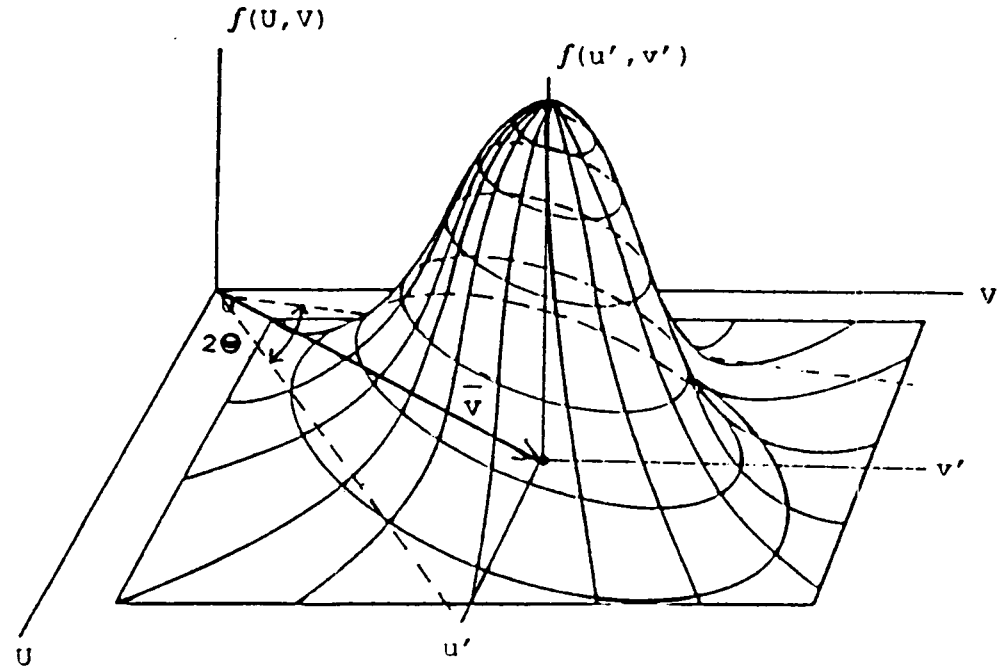

Figure 15 Bivariate normal u,v velocity joint pdf.

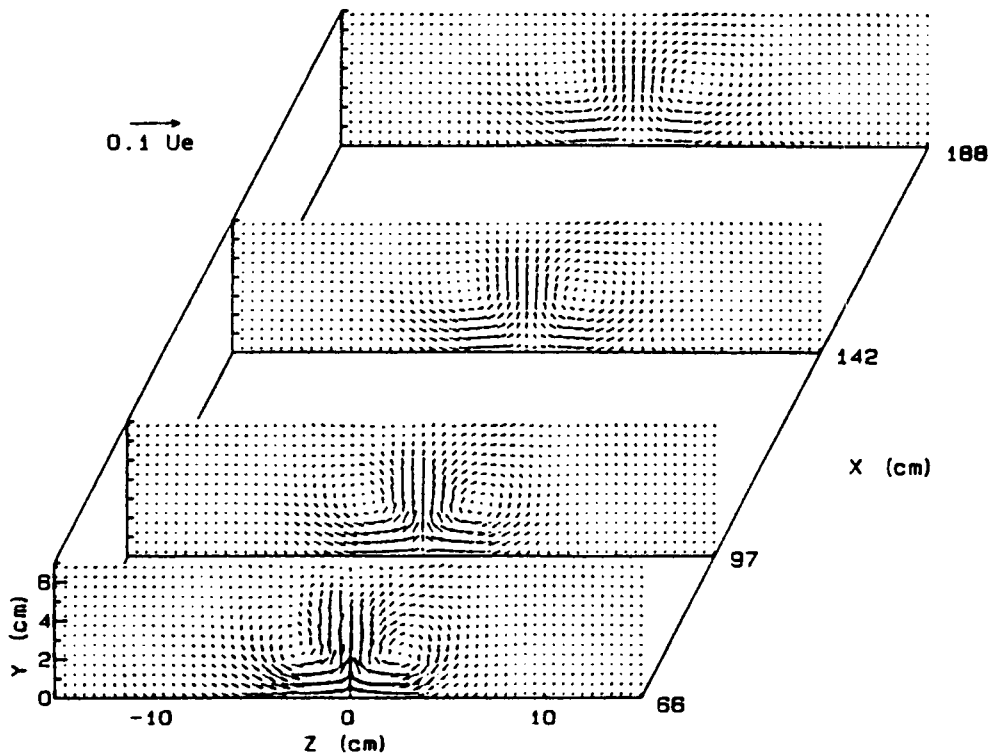

Figure 16 Secondary velocity vectors with cylinder.

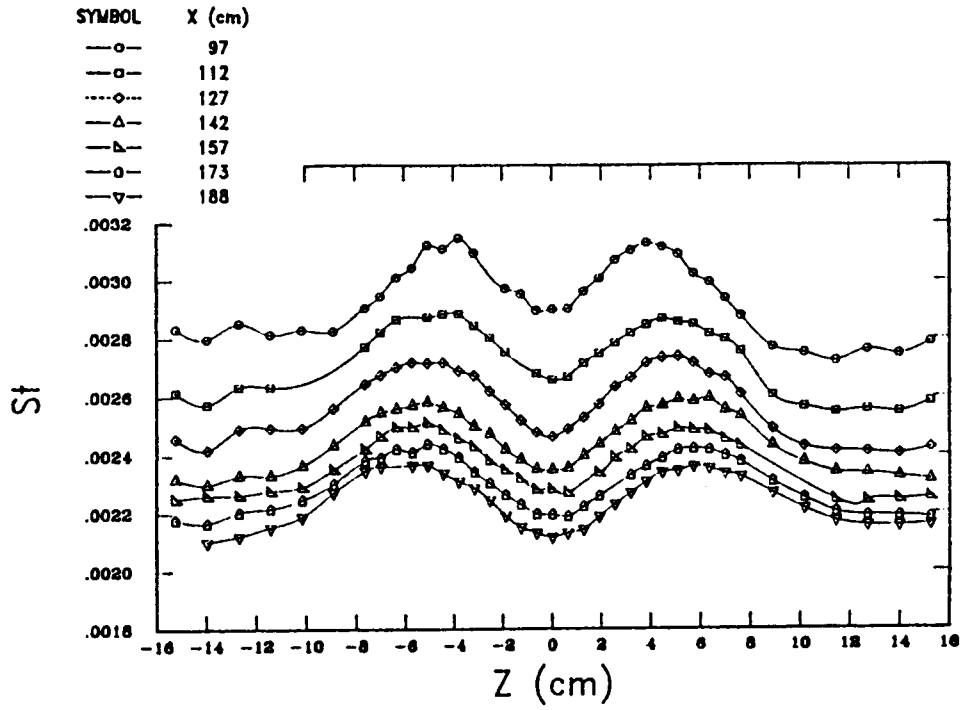

Figure 17 Spanwise distribution of Stanton number with 1 inch cylinder.

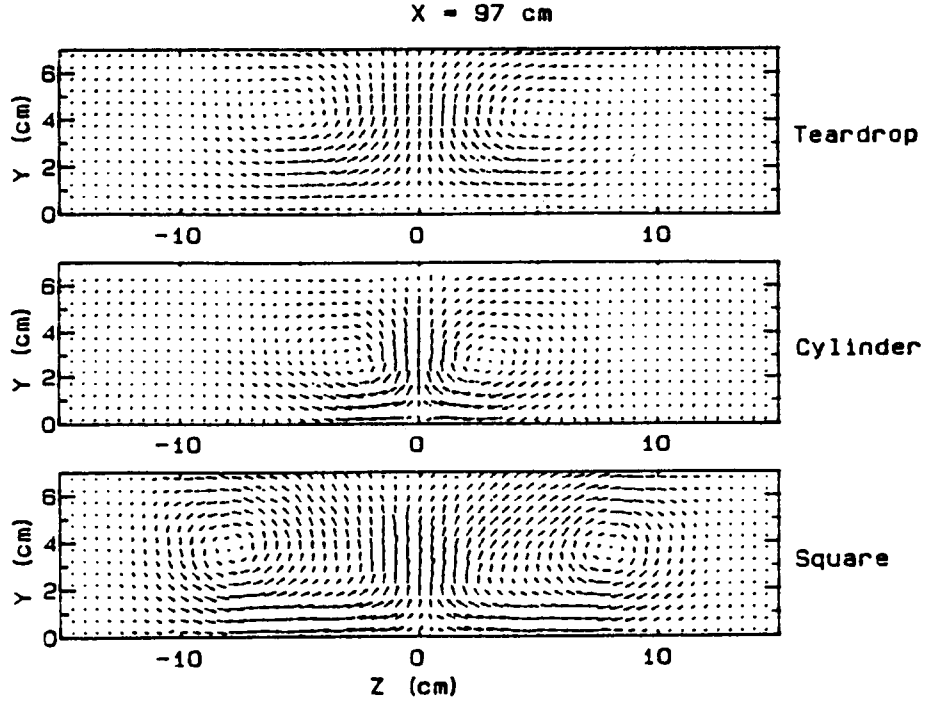

Figure 18 Secondary flow downstream of the three bodies extending from the wall.

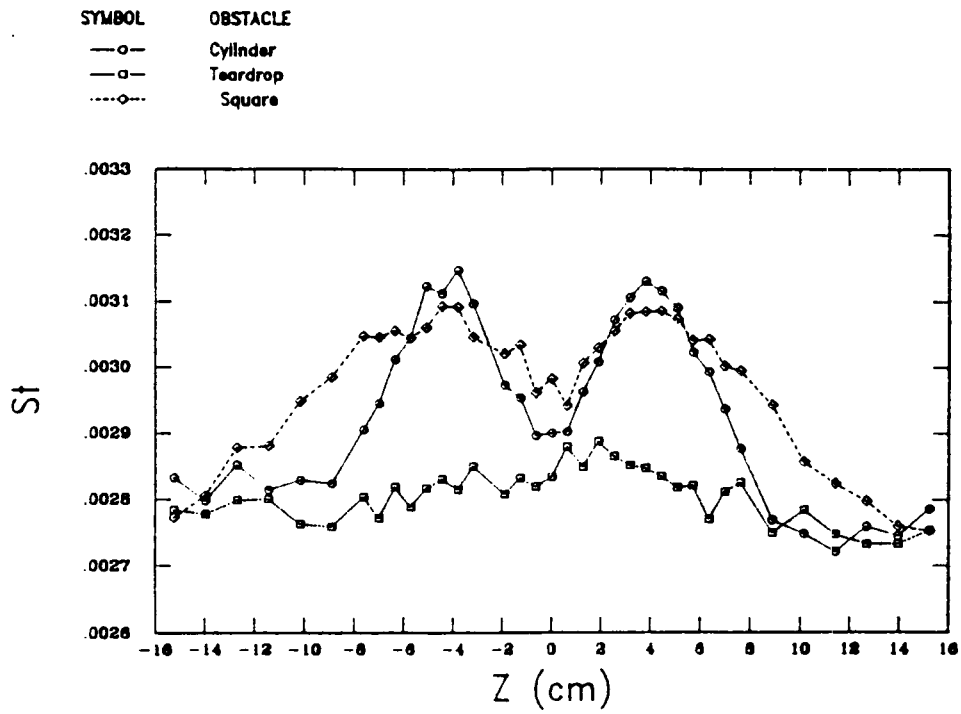

Figure 19 Spanwise distribution of Stanton number: comparison between types of obstacles at X=97 cm.

A LOW-REYNOLDS-NUMBER TWO-EQUATION TURBULENCE MODEL FOR PREDICTING HEAT TRANSFER ON TURBINE BLADES*

Suhas V. Patankar and Rodney C. Schmidt
University of Minnesota
Minneapolis, Minnesota

A modified form of the Lam-Bremhorst low-Reynolds-number k-ε turbulence model (ref. 1) has been developed for predicting transitional boundary layer flows under conditions characteristic of gas turbine blades. Since previously reported work (refs. 2,3) has outlined the basic form of the model and it's application to zero-pressure gradient flows with free-stream turbulence, this paper will primarily describe the application of the model to flows with pressure gradients, and will include tests against a number of turbine blade cascade data sets. Also, some additional refinements of the model made in recent months will be explained.

INTRODUCTION

The difficulty, and yet great importance, of accurately predicting external heat transfer on gas turbine blades has stimulated a large amount of research dedicated to understanding and modeling transitional boundary layer flows. The primary factors found to influence this phenomenon include Reynolds number, free-stream turbulence, pressure gradients and streamline curvature, all of which are present on a typical gas turbine blade. Although many approaches can and have been taken in modeling this process, our work has focused on exploring and developing the potential of low-Reynolds-number (hereafter abbreviated as "LRN") forms of the k-ε turbulence model for solving this type of problem.

A variety of different LRN modifications have been proposed in the literature for the purpose of extending the validity of two equation turbulence models through the viscous sublayer to the wall (see for example reference 4 for a good review). One attractive characteristic of this type of model is the seemingly natural process by which boundary layer transition from laminar to turbulent flow is simulated without requiring a separate model. However, although some of these models had already been used to predict heat transfer on gas turbine blade cascades prior to the initiation of our work (refs. 5,6,7), little had been reported documenting predictive capabilities for the less complex case of flat plate flow. As a result, our previously reported work began by evaluating two relatively popular LRN models with respect to the prediction of transition on flat plates under the influence of free-stream turbulence. This work showed that although these models do predict the qualitative aspects of transition correctly, the starting location and length over which it occurs is generally not well predicted.

*Work done under NASA Grant NAG-3-579

Subsequent to this evaluation a simple modification was proposed which could be applied within the framework of a LRN k-ε turbulence model, and which was designed to improve the prediction of boundary layer transition without affecting the fully turbulent model. The calibration of this model and application to flat plate zero pressure gradient flows, also reported earlier, proved to be fairly successful. Thus, this work has been pursued and the purpose of this paper is to report on the application of the model to predict experimental results of transitional flows with both free-stream turbulence and pressure gradients, and also to actual turbine blade cascade experiments.

NOMENCLATURE AND SYMBOLS

A, B	Empirical parameters in the proposed modification. Correlated as functions of Tu_e
$C_\mu, C_{\varepsilon 1}, C_{\varepsilon 2}$	Constants in the two-equation turbulence models.
f_μ, f_1, f_2	Low-Reynolds-number functions.
h, h'	Mean and fluctuating static enthalpy
H	Total enthalpy
k	Turbulent kinetic energy
K	Acceleration parameter $K=\upsilon/U^2\,(\partial U/\partial x)$
L	Turbulence length scale $L=k^{1.5}/\varepsilon$
P	Static pressure
P_k	Production term in the modeled k equation
Pr	Molecular and Turbulent Prandtl numbers
Re_θ	Reynolds number based on momentum thickness
$Re_{\theta,S}$	Momentum thickness Reynolds numbers at the start of transition
R_t,	Turbulence Reynolds number $R_t = k^2/(\upsilon\varepsilon)$
R_y	Wall Coordinate Turbulence Reynolds number $R_y = k^{.5}y/\upsilon$
St	Stanton number
Tu	Turbulence intensity, $Tu = \{1/3(\overline{u'^2}+ \overline{v'^2}+ \overline{w'^2})\}^{.5}/U$
U	Mean velocity in the x direction
u', v', w'	Fluctuating velocities in the x, y, z directions
x	Streamwise direction coordinate
y	Cross-stream coordinate
ρ	Fluid density
δ	Boundary layer thickness
θ	Momentum thickness of the boundary layer
Λ	Acceleration parameter $\Lambda=\delta^2(dU/dx)/\upsilon$
ε	Dissipation rate
μ	Molecular viscosity
μ_t	Eddy or turbulent viscosity
υ	Kinematic viscosity, $\upsilon = \mu/\rho$
σ_k, σ_ε	Empirical constants in the turbulence models.

Subscripts

c	denoting critical
e	denoting free-stream value
0	denoting value at x=0

BASIC EQUATIONS AND THE TURBULENCE MODEL

For the results presented in this work, the following forms of the time averaged continuity, momentum, and energy equations were solved.

$$\partial(\rho U)/\partial x + \partial(\rho V)/\partial y = 0 \tag{1}$$

$$\rho U[\partial U/\partial x] + \rho V[\partial U/\partial y] = \partial/\partial y[\mu \partial U/\partial y - \rho\overline{u'v'}] - dP/dx \tag{2}$$

$$\rho U[\partial H/\partial x] + \rho V[\partial H/\partial y] = \partial/\partial y[(\mu/Pr)\partial H/\partial y - \rho\overline{h'v'}] + \partial/\partial y\left\{ U[(1-1/Pr)\mu \partial U/\partial y - \rho\overline{u'v'}] \right\} \tag{3}$$

where $H=h+U^2/2$. Also the fluid is assumed to be a perfect gas with constant specific heat.
A LRN form of the k-ε turbulence model is used to determine the turbulent shear stress and turbulent heat flux by defining

$$-\rho\overline{u'v'} = \mu_t (\partial U/\partial y) \tag{4}$$

$$-\rho\overline{h'v'} = (\mu_t/Pr_t)\partial h/\partial y , \quad \text{with } Pr_t = 0.9 \tag{5}$$

and by solving the following two additional transport equations for k and ε.

$$\rho U[\partial k/\partial x] + \rho V[\partial k/\partial y] = \partial/\partial y[(\mu + \mu_t/\sigma_k)\partial k/\partial y] + \mu_t(\partial U/\partial y)^2 - \rho\varepsilon \tag{6}$$

$$\rho U[\partial \varepsilon/\partial x] + \rho V[\partial \varepsilon/\partial y] = \partial/\partial y[(\mu+\mu_t/\sigma_\varepsilon)\partial \varepsilon/\partial y] + C_{\varepsilon 1} f_1 (\varepsilon/k)\mu_t(\partial U/\partial y)^2 \tag{7}$$

where $$\mu_t = \rho C_\mu f_\mu (k^2/\varepsilon) \tag{8}$$

The constants C_μ, $C_{\varepsilon 1}$, $C_{\varepsilon 2}$, σ_k, and σ_ε, and the LRN functions f_1, f_2 are given in reference 8. The function f_μ has been slightly changed as compared to the Lam Bremhorst form to improve the predictions at very low Tu. Previous work had shown that the Lam-Bremhorst model did not predict transition for free-stream turbulence levels of lower than about 1% (refs. 2,7). Our investigation showed that this was due to the particular two parameter correlation for f_μ ($f_{\mu,LB}=f_\mu[R_t, R_y]$) chosen by Lam and Bremhorst which, under certain conditions predicted $f_\mu >> 1$. Since the function f_μ is intended to vary only from 0 to 1, this problem could be eliminated by simply restricting the magnitude of f_μ. The details of this are given in reference 8. For the calculations given here, f_μ was calculated as

$$f_\mu = \min(\ 1.,\ .5+.0025*R_t,\ f_{\mu,LB}) \tag{9}$$

The modification introduced to improve boundary layer transition predictions affects the so-called production term in the k equation, $P_k=\mu_t(\partial U/\partial y)^2$. (Note that the use of the words "production term" has been used rather loosely here to refer only to the quantity in the model, not a term in the exact form of the k equation.) This is done by limiting the magnitude of P_k before a specified stability limit ($R_{\theta,C}=125$), and then limiting the growth rate of P_k afterward. The details and the numerical implementation of this is given in reference 8. However, the basic relationship can be expressed as follows;

$$[\,\partial P_k/\partial t\,]_{max} = A\,{*}P_k + B \qquad (10)$$

The functions A and B have been correlated to the free-stream turbulence such that under flat-plate conditions the model predicts transition occurring at momentum thickness Reynolds numbers at the beginning and end of transition in according with the correlation of Abu-Ghannam and Shaw (ref. 9). It should be realized that the behavior shown in Figure 1 is unique to the LRN functions used in this model. Somewhat different values must be used with, for example, the Jones Launder model (ref. 10) to achieve similar results (see ref. 8). It also reflects somewhat different values then reported earlier in reference 2. This is a result of a reevaluation in the high Tu range, and also to the minor modification made to the f_μ function given in eq. (9).

COMPUTATIONAL PROCEDURE

Although details cannot be given here, a brief overview of some of the practical aspects of the computational procedure is appropriate. Before one can begin any computation, starting profiles and boundary conditions must be specified such that the actual problem of interest is solved. For a two equation turbulence model, this must include values for k and ε in addition to the velocity and enthalpy. For all of the results presented here the following procedure was followed.

Initial Starting Location: The method of Thwaites (see ref. 11, pg 315) was used to compute the momentum thickness Reynolds number variation from either the leading edge or the stagnation point. All calculations were then started at a streamwise location such that the momentum thickness Reynolds number was less than about 25. Our previous work showed that this minimized sensitivity to variations in initial profiles (ref. 2).

Velocity: Following the procedure of Rodi and Scheuerer (refs. 6,7), a Pohlhausen polynomial representation of the velocity profile was used. This requires an approximation for the local boundary layer thickness δ, and an acceleration parameter $\Lambda=\delta^2U'/\upsilon$. The details of this are given in reference 8. The local free-stream velocity and velocity gradient was determined from the experimental conditions.

Enthalpy: The total enthalpy in the free-stream was assumed to remain constant for all cases considered. For flat plate flows the starting enthalpy profile was derived from an approximate temperature-velocity profile relationship as per reference 6. For the turbine blade calculations, which were started near a stagnation point, this procedure was slightly modified to allow the thermal boundary layer δ_T, to be different than the velocity boundary layer. This was controlled by estimating the stagnation point heat transfer coefficient and relating this to δ_T. The details are given in reference 8.

k and ε: The free-stream values of k and ε were found by relating them to the experimentally reported values of the free-stream turbulence intensity. For isotropic turbulence, this implies that

$$k_e=1.5(Tu_eU_e)^2 \qquad (11)$$

The value of ε must be found such that the calculated decay in k with distance matches the data when the following two ordinary differential equations are solved.

$$U_e(dk_e/dx) = -\varepsilon_e \quad (12)$$

$$U_e(d\varepsilon_e/dx) = - C_{\varepsilon 2} (\varepsilon_e^2/k_e) \quad (13)$$

Documentation of these values for each case studied and the comparison with the experimental data is provided in reference 8. Since our previous work had shown the value of specifying k_e based on u' only, when possible this was always done.

When the experimental data is not sufficient to determine the dissipation length scale, such as is the case with much of the turbine blade cascade data, the calculations assume a small value of ε such that k remains essentially constant. Note that because of the relationship between k and Tu expressed in eq. (10), even if the value of k remains constant, Tu will vary with free-stream velocity.

For convenience, the initial profile specification of k and ε is similar to that of Rodi and Scheuerer (ref. 7) except that their parameter "a_1" was always assumed equal to unity. Details of this are also given in reference 8.

COMPARISON OF THE COMPUTATIONS TO EXPERIMENTS WITH FAVORABLE PRESSURE GRADIENTS

Taken together, the data sets of Blair (refs. 12,13), and of Rued and Wittig(refs. 14,15,16) provide a good variety of well documented experiments where the effects of both acceleration and free-stream turbulence on transition are represented. Both sets of data also provide the experimentally determined variation of Tu over the test sections, a key requirement for accurately modeling the transition process. Furthermore, the experiments of Rued have the additional attractive characteristic of representing wall to gas temperature ratios that are similar to those experienced on a gas turbine blade.

The experiments of Blair were set up so as to provide a flow with essentially constant acceleration, and two such levels of acceleration were explored. The magnitude of the acceleration parameter K corresponded to 0.2×10^{-6}, and $.75 \times 10^{-6}$. In figure 2, the Stanton number data found for the lowest acceleration case is shown for three different turbulence generating grids and compared to the computations. Although the Stanton number in the fully turbulent region is under-predicted, the location and extent of transition is reproduced fairly well. In Figure 3, results for the higher acceleration are shown. Here, the location of transition is reasonably reproduced at the higher turbulence level, but deviates somewhat in the lower turbulence case. Compared to the calculation, the experiments show the onset of transition to be further downstream, and the extent of the transition region to be longer. Furthermore, the extent to which the fully turbulent Stanton number is underpredicted has increased. The effect on transition is not unexpected, as we know that acceleration has a stabilizing effect on turbulence. However, it is not clear why the fully turbulent predictions were low. In our opinion, the most likely possibilities are an inadequate modeling of the turbulent heat flux (we used Pr_t=.9 = constant), and/or a problem in the dissipation equation in the near wall region during acceleration.

Figure 4 shows the variation over the test section of the acceleration parameter K for three of the test cases reported by Rued. Note that these achieve significantly higher values of K than the tests of Blair. Figures 5-7 show a comparison of our calculations with the reported Stanton number data for these flows at four different levels of free-stream turbulence each. The model is quite successful at

predicting the heat transfer for cases 6 and 12, except in the initial region after the unheated starting length. One of the important observations made by Rued and Wittig (ref. 13) about their work, was that the results did not show a lower limit on $Re_{\theta,S}$ of 163 as is used in the Correlation of Abu-Ghannam and Shaw for Tu>7%. This is reflected in these figures by our computations predicting the initial transition occurring too late at high Tu. For test case 10, grid two, the model indicates a relaminarization, whereas the experiments do not. Also, in grid 1, where transition occurs only after the acceleration has stopped, the transition length is underpredicted. In some ways this reminds us of the computation of Blair's data shown in figure 3, for grid 2.

COMPARISON OF THE COMPUTATIONS WITH TURBINE BLADE CASCADE DATA

Figures 7-10 provide a comparison of the models predictions with the data provided by Daniels and Browne (ref. 17), and Hylton et al.(ref. 18). Data at two different Reynolds numbers is shown for each blade on both the suction and the pressure side.

Since the turbulence intensity measurements reported by Daniels and Browne were taken somewhat upstream of the test section, figures 7 and 8 show the results of computations assuming Tu_0=3.5% and 3% for comparison purposes. As can be seen, the location and extent of transition, and the resulting heat transfer is very well predicted for these cases. The only significant variation between the data and the computation occurs at the higher Reynolds number in regions downstream of transition. On the suction side starting at S/L=.4-.5, the flow experiences a region of adverse pressure gradient. Previous research has documented the failure of 2-eq. LRN models such as that of Lam-Bremhorst to correctly calculate the near wall turbulence length scale in adverse pressure gradient flows, resulting in an over prediction of the skin friction and heat transfer (see ref. 19). For comparison, a computation is shown where the dissipation equation was modified in line with a suggestion of Launder (ref. 20) in the following manner.

$$C_{\varepsilon 1}=1.44*\max(\,1,\, L/L_{max})$$

where

$$L=k^{1.5}/\varepsilon\ , \qquad L_{max}=2.7y \tag{14}$$

The results of this additional modification show an improved prediction of the heat transfer on the suction side without influencing the transition predictions.

In figures 9 and 10, comparisons with the data of Hylton et al. are shown. These calculation show similar trends as was pointed out on the Daniels and Browne data, i.e., an excellent prediction of the lower Reynolds number data, but an over prediction of the heat transfer in the turbulent regions on both the suction and pressure sides for the higher Reynolds number case. Also, the modification given in eq. (14) is shown to reduce the predictions on the suction side down to match the data. However, there is a clear overshoot in the heat transfer predictions for run 145, which cannot be explained with reference to the dissipation equation correction. The reason for this difference may be related to the effects of curvature in the recovery region after the release of curvature. In the C3X blade the radius of curvature is small until about S/arc =.2.

CONCLUSIONS

Tests of the transition model proposed against a wide range of flows with pressure gradient have shown that even without additional modifications, the model is quite satisfactory for predicting much of the data. However, it appears that the computations might be improved in the future by considering the following;

(1) As the relationship between Re_θ and Tu at high Tu is clarified experimentally, improvements could be incorporated into the correlations for A and B, and possibly $Re_{\theta C}$.

(2) The length over which transition occurs during favorable pressure gradient conditions might be more accurately modeled by decreasing the value of A and/or B in some appropriate manner.

(3) Improvements in the LRN functions relative to the fully turbulent flows with pressure gradients.

(4) Appropriate incorporation of curvature effects into the transition modifications.

REFERENCES

1. Lam, C. K. G., and Bremhorst, K., "A Modified Form of the k-ε Model for predicting Wall Turbulence", J. of Fluids Engineering, Vol. 103, Sept. 1981, pp. 456-460
2. Schmidt, R. C., and Patankar, S. V., "Development of Low Reynolds Number Two Equation Turbulence Models for predicting External Heat Transfer on Turbine Blades" Proceedings of the 1986 Turbine Engine Hot section Technology Conference sponsored by the NASA Lewis Research Center, NASA Conference Publication 2444, Oct. 1986, pp. 219-232
3. Schmidt, R. C., and Patankar, S. V., "Prediction of Transition on a Flat Plate under the Influence of Free-Stream Turbulence using Low-Reynolds-Number Two-Equation Turbulence Models", ASME Paper 87-HT-32
4. Patel, V. C., Rodi, W., and Scheuerer, G., "A Review and Evaluation of Turbulence Models for Near Wall and Low Reynolds Number Flows", AIAA Journal, Vol. 23, 1985, p. 1308
5. Wang, J. H., Jen, H. F., and Hartel, E. O., "Airfoil Heat Transfer Using Low Reynolds Number Version of a Two Equation Turbulence Model.", J. of Engineering for Gas Turbines and Power, Vol. 107, No. 1, Jan. 1985, pp. 60-67
6. Rodi, W., and Scheuerer, G., "Calculation of Heat Transfer to Convection-Cooled Gas Turbine Blades", J. of Engineering for Gas Turbines and Power, Vol. 107, July 1985, pp. 620-627
7. Rodi, W., and Scheuerer, G., "Calculation of Laminar-Turbulent Boundary Layer Transition on Turbine Blades", AGARD-CPP-390
8. Schmidt, R. C. "Two-Equation Low-Reynolds-Number Turbulence Modeling of Transitional Boundary-Layer Flows Characteristic of Gas Turbine Blades", Ph. D. Thesis, Dept. of Mechanical Engineering, University of Minnesota, 1987
9. Abu-Ghannam, B. J., and Shaw, R., "Natural Transition of Boundary Layers -The Effects of Turbulence, Pressure Gradient, and Flow History", J. of Mech. Eng. Science, Vol. 22, No. 5, 1980, pp. 213-228
10. Jones, W. P., and Launder, B. E., "The Calculation of Low Reynolds Number Phenomena With a Two-Equation Model of Turbulence", Int. J. of Heat and Mass Transfer, Vol. 16, 1973, pp. 1119-113
11. White, F. M., Viscous Fluid Flow , McGraw-Hill, Inc. 1974

12.Blair, M. F., "Influence of Free-Stream Turbulence on Boundary Layer Transition in Favorable Pressure Gradients", ASME J. of Engineering for Power, Vol. 104, Oct. 1982, pp. 743-750
13.Blair, M. F., and Werle, M. J., "Combined Influence of Free-Stream Turbulence and Favorable Pressure Gradients on Boundary Layer Transition", UTRC Report R81-914388-17, Mar. 1981
14.Rued, K., and Wittig, S. "Free Stream Turbulence and Pressure Gradient Effects on Heat Transfer and Boundary Layer Development on Highly Cooled Surfaces", J. of Engineering for Gas Turbines and Power, Vol. 107, No. 1, Jan. 1985, pp. 54-59
15.Rued, K., and Wittig, S., "Laminar and Transitional Boundary Layer Structures in Accelerating Flow with Heat Transfer", ASME Paper No. 86-GT-97
16.Rued, K "Transitionale Grezschichten unter dem Einfluss hoher Freistromturbulenze, intensiver Wandkuehlung und starken Druckgradienten in Heissgasstroemungen", Thesis submitted at the University of Karsruhe, 1985
17.Daniels, L. D., Browne, W. B., "Calculation of Heat Transfer Rates to Gas Turbine Blades", Int. J. of Heat and Mass Transfer, Vol 24, No. 5, pp. 871-879, 1981
18.Hylton,L. D., Mihelc, M. S., Turner, E. R., Nealy, D. A., and York, R. E., "Analytical and Experimental Evaluation of the Heat Transfer Distribution Over the Surfaces of Turbine Vanes", NASA CR-168015, May 1983
19.Rodi, W., and Scheuerer, G., "Scrutinizing the k-ε Turbulence Model under Adverse Pressure Gradient Conditions", ASME J. of Fluids Eng., Vol 108, June 1986, pp 174-179
20.Launder, B. E., "Second Moment Closure: Methodology and Practice", Turbulence Models and Their Applications, Vol 2, Edition Eyrolles, Saint-Germain Paris, 1984

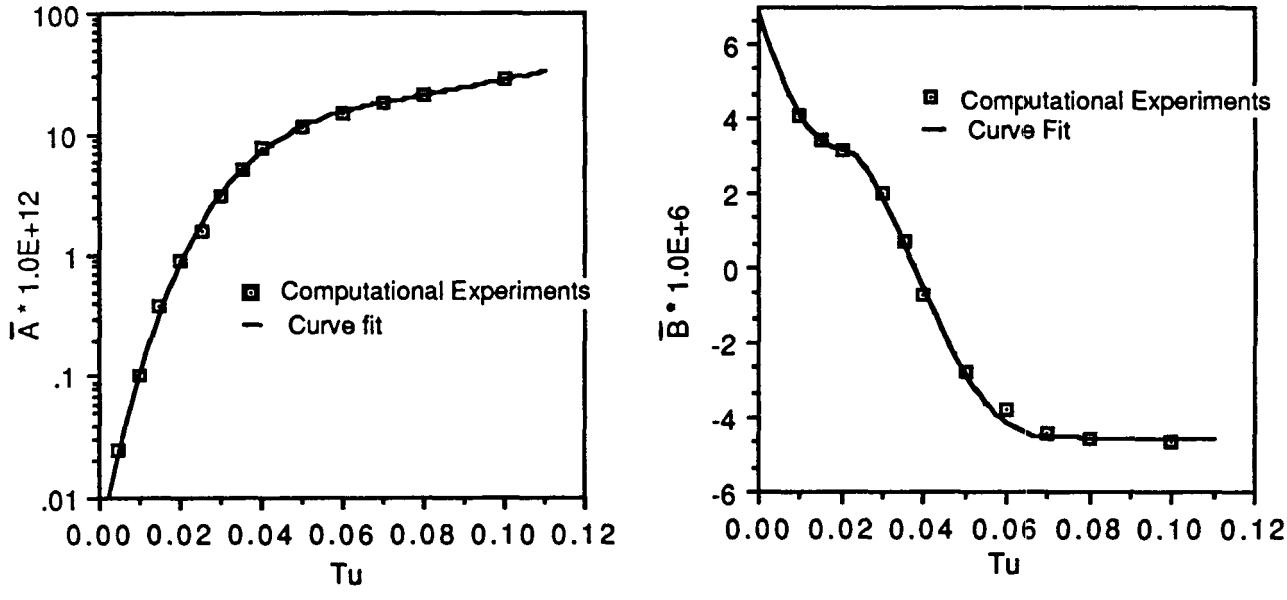

$\bar{A} = A\mu / (\rho U_e^2)$ $\qquad$ $\bar{B} = B\mu^2 / (\rho^3 U_e^4)$

FIGURE 1 Variation in "*A*" and "*B*" with free-stream turbulence intensity

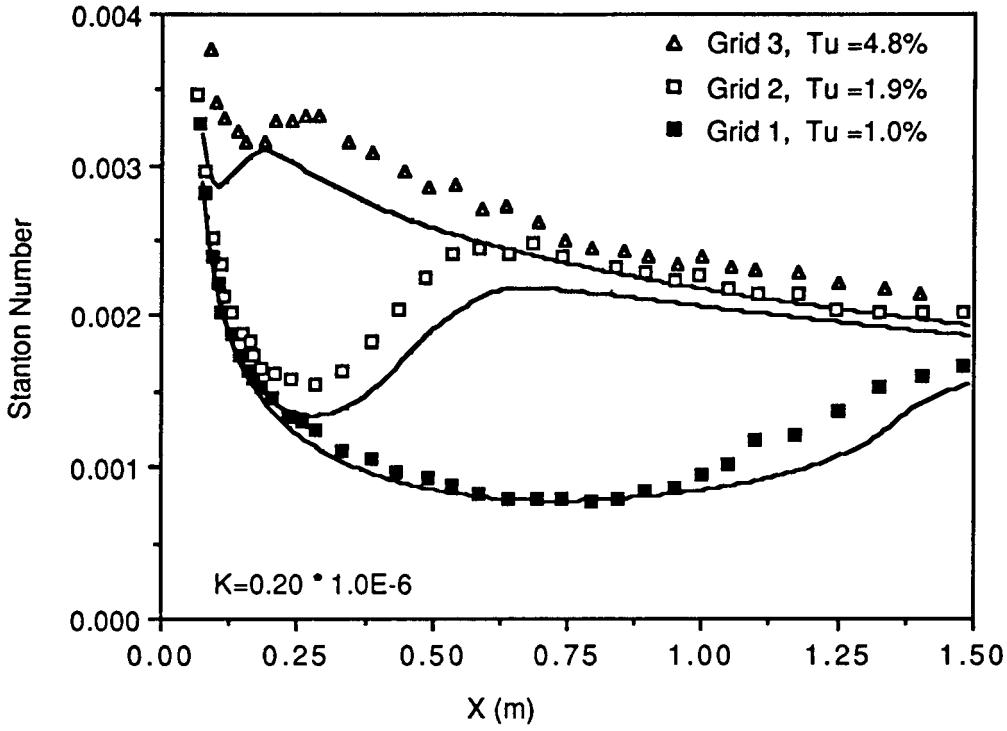

FIGURE 2 Comparison of the calculations with the lower acceleration test data of Blair

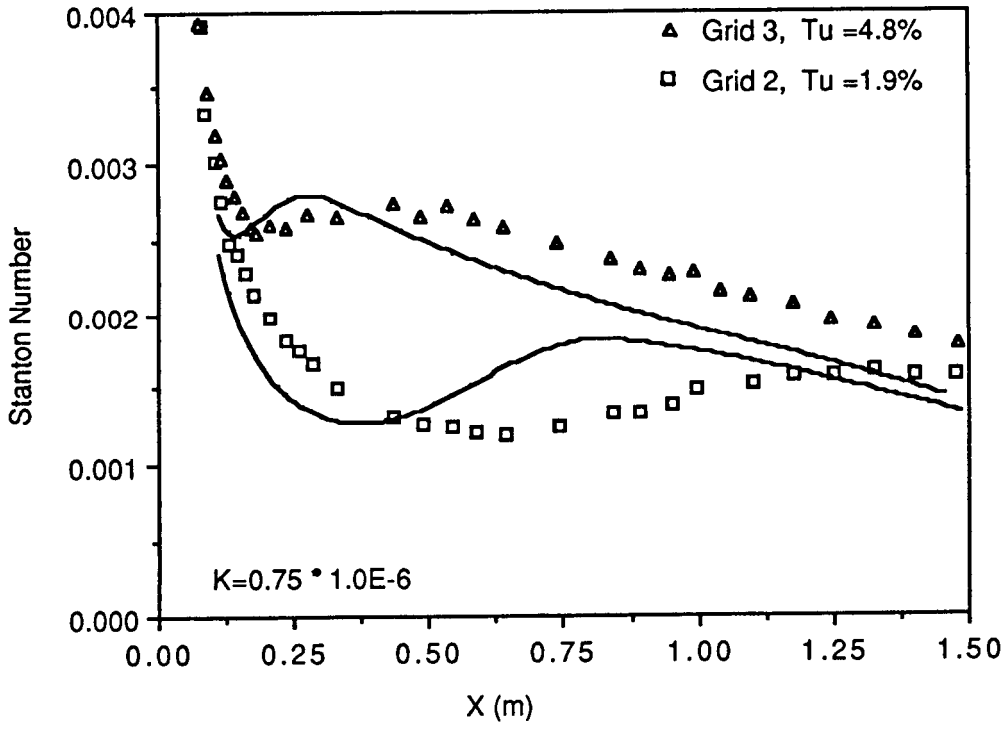

FIGURE 3 Comparison of the calculations with the higher acceleration test data of Blair

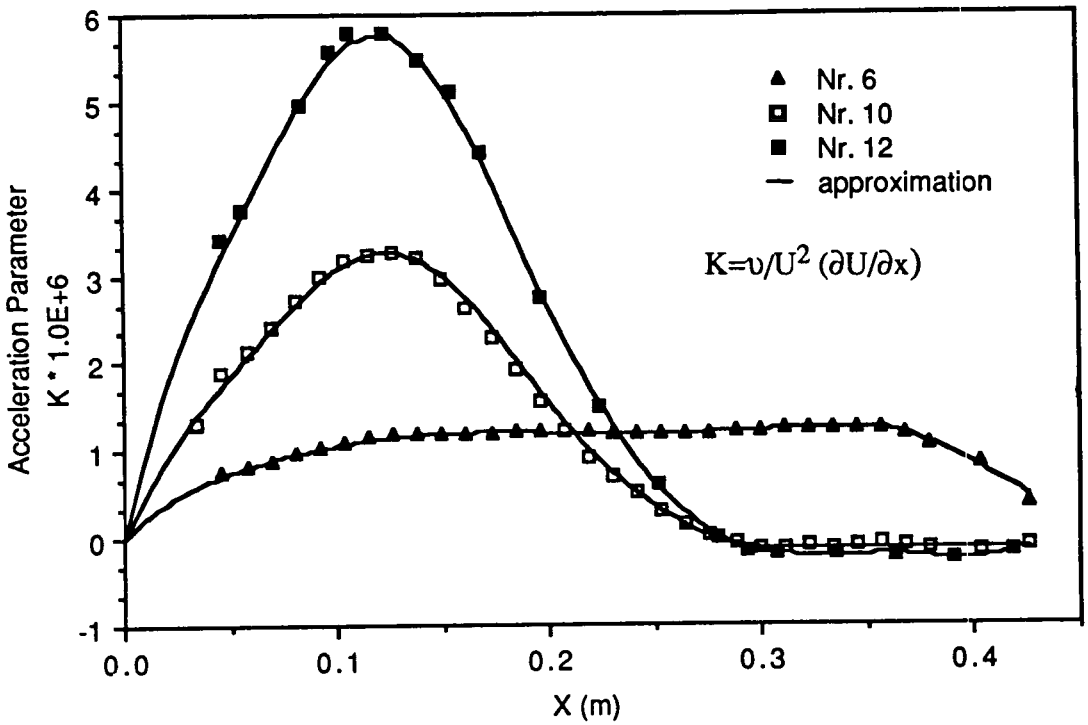

FIGURE 4 Variation in acceleration for three test cases of Rued

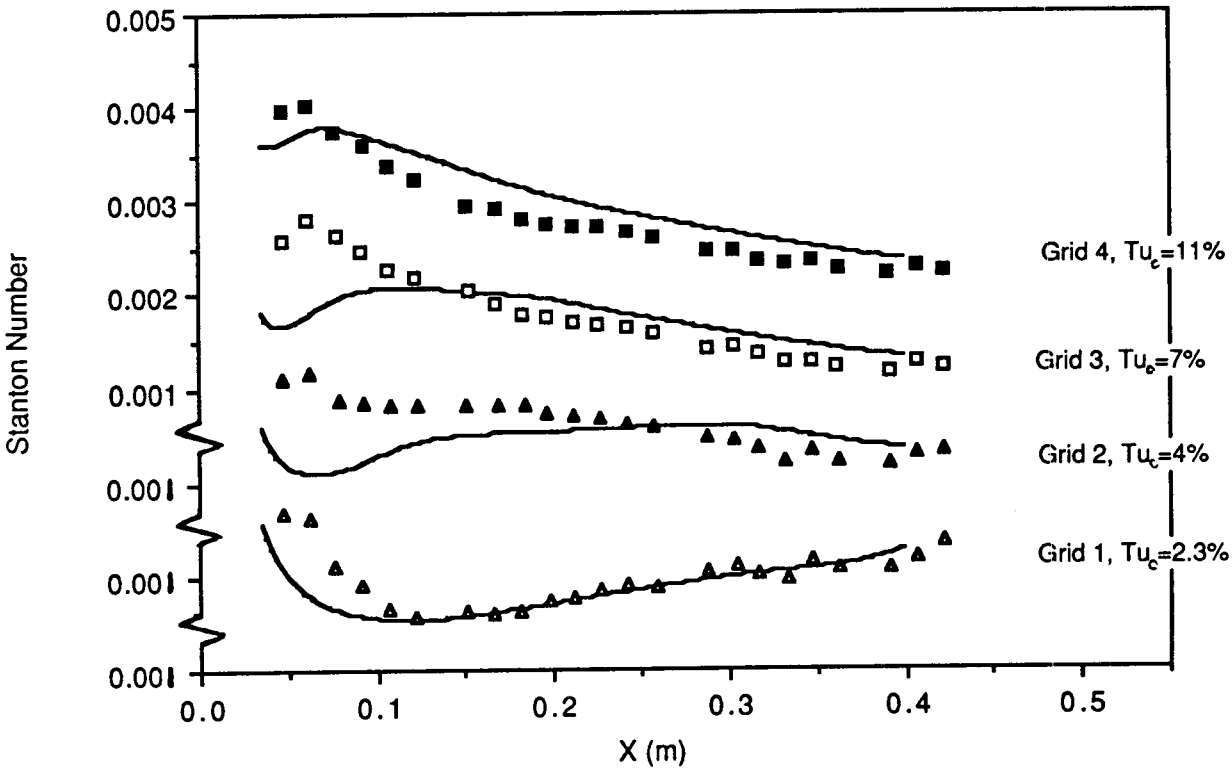

FIGURE 5 Comparison of the calculations with the data from case 6 of Rued

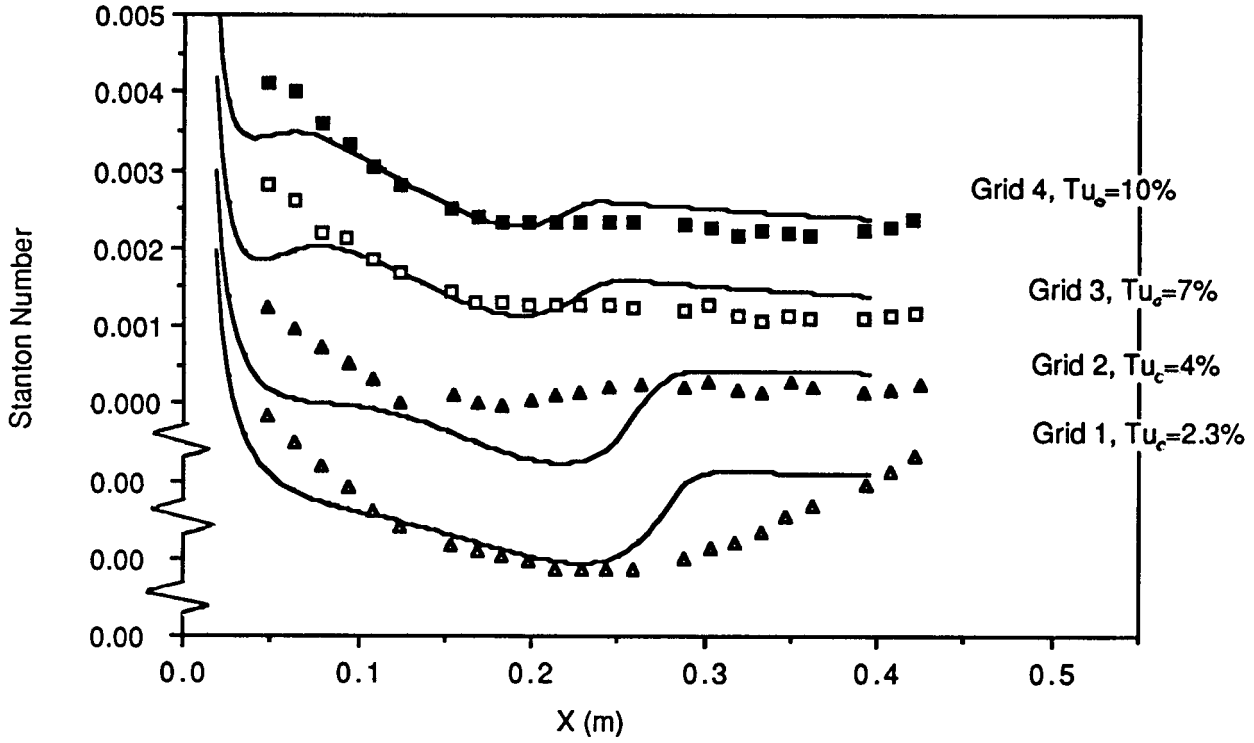

FIGURE 6 Comparison of the calculations with the data from case 10 of Rued

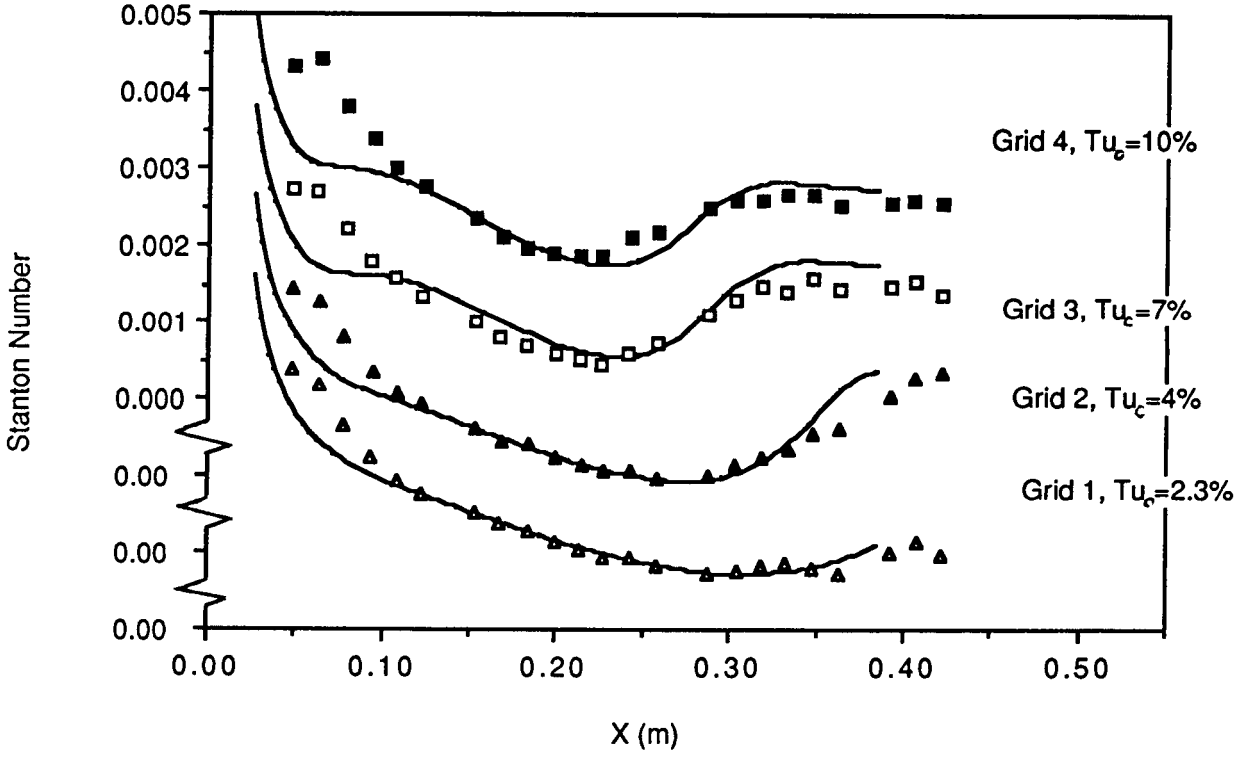

FIGURE 7 Comparison of the calculations with the data from case 12 of Rued

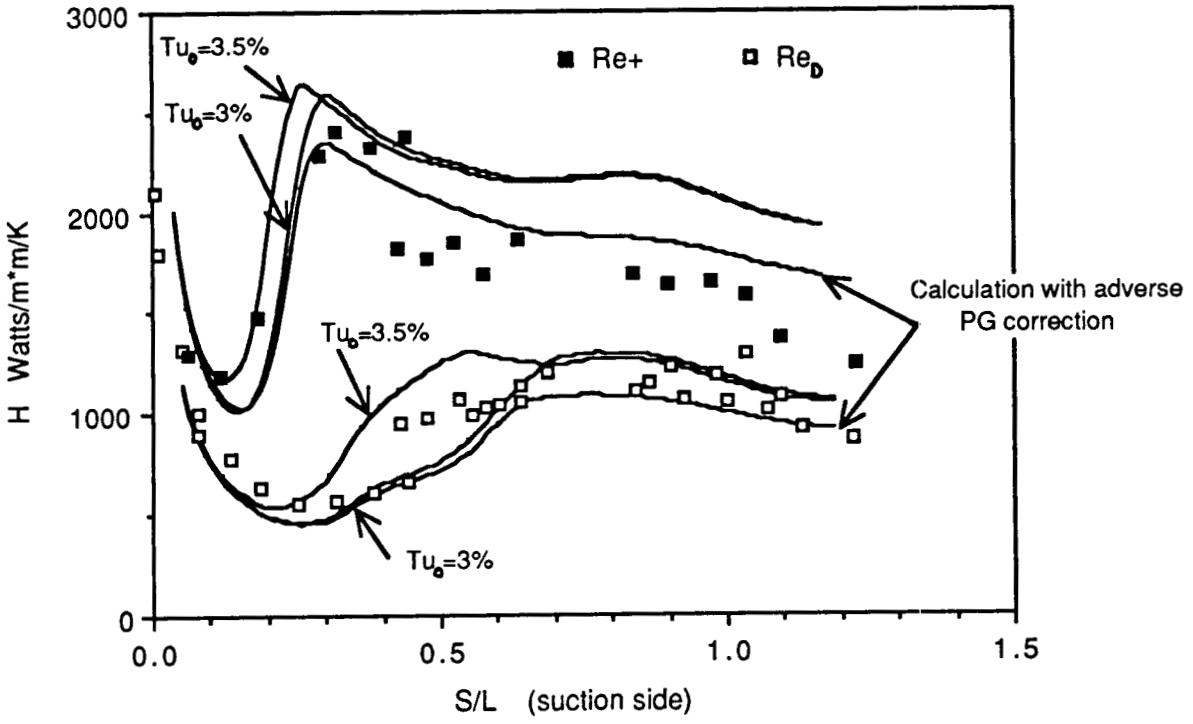

FIGURE 8 Comparison of the calculations with the data from Daniels and Browne on the suction side of the blade L=50.44 mm

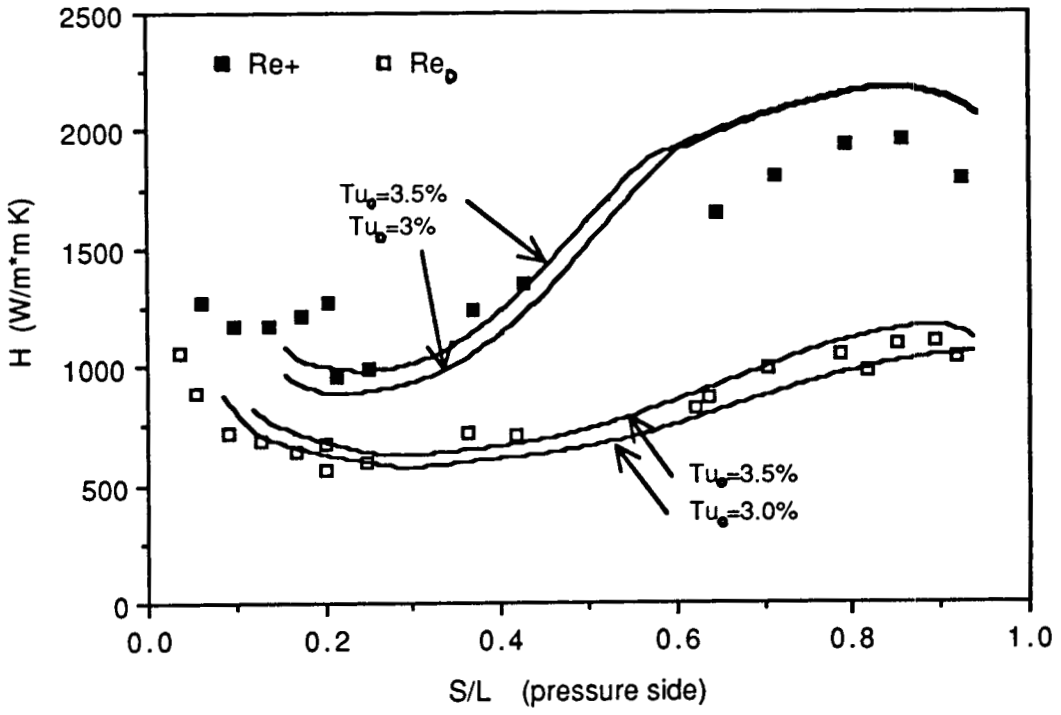

FIGURE 9 Comparison of the calculations with the data from Daniels and Browne on the pressure side of the blade L=50.44 mm

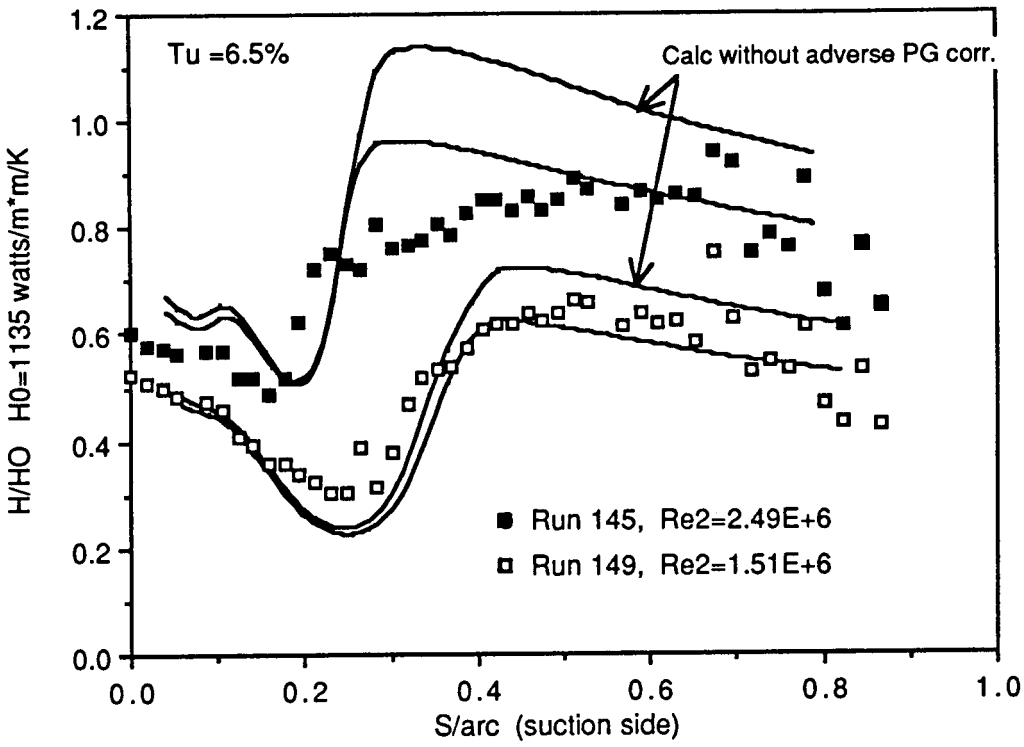

FIGURE 10 Comparison of the calculations with data on the suction side from runs 145 and 149 of the C3X blade of reference 18. arc=.18 m

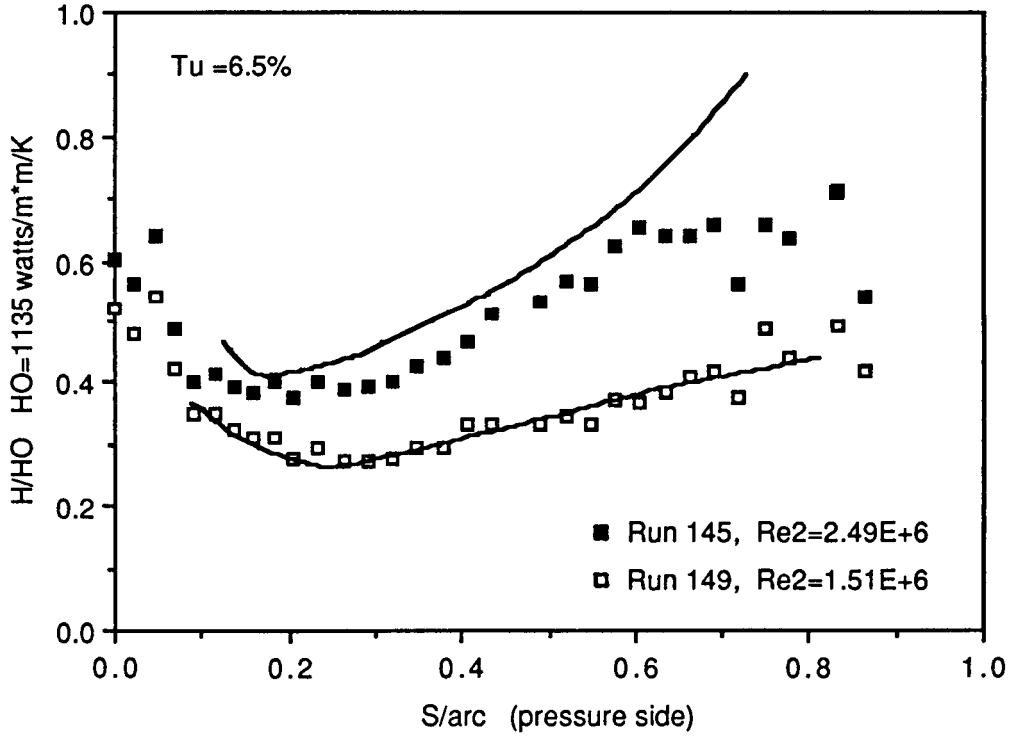

FIGURE 11 Comparison of the calculations with data on the pressure side from runs 145 and 149 of the C3X blade of reference 18. arc=.14 m

MEASUREMENT OF AIRFOIL HEAT TRANSFER COEFFICIENTS ON A TURBINE STAGE*

Robert P. Dring, Michael F. Blair, and H. David Joslyn
United Technologies Research Center
East Hartford, Connecticut

The Primary basis for heat transfer analysis of turbine airfoils is experimental data obtained in linear cascades. These data have been very valuable in identifying the major heat transfer and fluid flow features of a turbine airfoil. The question of major interest is how well all of these data translate to the rotating turbine stage. It is suggested from the work of Lokay and Trushin (ref. 1) that average heat transfer coefficients on the rotor may be as much as 40 percent above the values measured on the same blades nonrotating. Recent work by Dunn and Holt (ref. 2) supports the conclusion of reference 1. What is needed is a set of data from a rotating system which is of sufficient detail as to make careful local comparisons between static cascade and rotor blade heat transfer. In addition, data is needed in a rotating system in which there is sufficient documentation of the flow field to support the computer analyses being developed today. Other important questions include the impact of both random and periodic unsteadiness on both the rotor and stator airfoil heat transfer. The random unsteadiness arises from stage inlet turbulence and wake generated turbulence and the periodic unsteadiness arises from blade passing effects. A final question is the influence, if any, of the first stator row and first stator inlet turbulence on the heat transfer of the second stator row after the flow has been passed through the rotor.

OBJECTIVES

The first program objective is to obtain a detailed set of heat transfer coefficients along the midspan of a stator and a rotor in a rotating turbine stage. These data are to be such that the rotor data can be compared directly with data taken in a static cascade. The data are to be compared to some standard analysis of blade boundary layer heat transfer which is in use today. In addition to providing this all-important comparison between rotating and stationary data, this experiment should provide important insight to the more elaborate full three-dimensional programs being proposed for future research. A second program objective is to obtain a detailed set of heat transfer

*Work done under NASA Contract NAS3-23717.

coefficients along the midspan of a stator located in the wake of an upstream turbine stage. Particular focus here is on the relative circumferential location of the first and second stators. Both program objectives will be carried out at two levels of inlet turbulence. The low level will be on the order of 1 percent while the high level will be on the order of 10 percent which is more typical of combustor exit turbulence intensity. The final program objective is to improve the analytical capability to predict the experimental data.

DESCRIPTION OF EXPERIMENTAL EQUIPMENT AND TEST CONDITIONS

The experimental portion of this study was conducted in a large-scale (aproximately 5x engine), ambient temperature, rotating turbine model configured in both single-stage and stage-and-a-half arrangements. Heat transfer measurements were obtained using low-conductivity airfoils with miniature thermocouples welded to a thin, electrically heated surface skin. Heat transfer data were acquired for various combinations of low or high inlet turbulence intensity, flow coefficient, first-stator/rotor axial spacing, Reynolds number and relative circumferential position of the first and second stators. High levels of inlet turbulence were generated using a coarse biplane grid located 2 1/2 axial chords upstream of the first stator leading edge plane. With the grid out the midspan region turbulence intensity was slightly greater than 1/2% with much higher levels in the endwall boundary layers. With the grid in the midspan turbulence intensity averaged 9.8%. Spectral measurements of the grid generated turbulence indicated that it was in excellent agreement with the von Karman isotropic spectrum. Aerodynamic measurements obtained as part of the program include distributions of the mean and fluctuating velocities at the turbine inlet and, for each airfoil row, midspan airfoil surface pressures and circumferential distributions of the downstream steady state pressure and fluctuating velocities.

RESULTS

In-depth descriptions of the results of this program have already been presented at previous HOST contractor reviews. These descriptions have covered: (1) the heat transfer measurement technique, (2) both the turbulence and the time averaged nature of the flow entering the turbine model, (3) the effects of Reynolds number on the single-stage stator and rotor heat transfer, (4) the effects of inlet free-stream turbulence on the single-stage stator and rotor heat transfer, (5) the effects of stator/rotor axial spacing on the single-stage stator and rotor heat transfer, (6) the effects of extreme incidence variation on the rotor heat transfer, (7) the effect of the relative circumferential position of the first stator on the second stator heat transfer, (8) the nature of the heat transfer in the stagnation region of each airfoil, and (9) a comparison of the heat transfer for the rotor with the same airfoil midspan geometry in a plane cascade. The present discussion will focus on experimental/analytical comparisons for the first and second stators and for the rotor, and on the heat transfer trends from a surface averaged

point of view. Distributions of heat transfer along the various airfoil surfaces are presented as Stanton numbers based on exit conditions vs dimensionless surface distance. Included in figures 1, 2 and 3 are the specific flow coefficient and axial spacing for the data set and a note indicating whether the turbulence grid was IN or OUT.

The boundary layer analysis chosen for the present assessment is the "ABLE" code of Carter, Edwards and Werle (refs. 3 and 4). This is an efficient and versatile calculation that includes models for laminar, transitional, and turbulent flow. The ABLE code contains a number of options for the transition and turbulence models that are employed. In the present assessment two such models have been evaluated. The first was the algebraic turbulence model of Cebeci and Smith (ref. 5). The other model that will be evaluated is that of McDonald et al. (refs. 6 and 7). This analysis includes physical models for both transitional and turbulent flow, both of which are functions of the free-stream turbulence imposed. With this model the level of free-stream turbulence controls both the onset and the length of transition. It should be pointed out, however, that the turbulent Prandtl number profile used in the present comparison was not that of McDonald and Kreskovsky (ref. 7) but rather a profile based on the measurements of Blair (ref. 8) was used in its place. The effect of this modified turbulent Prandtl number profile was to increase the predicted Stanton numbers slightly beginning in the transitional region and through the turbulent region. The increase was typically 6% in the turbulent region.

The analytical/experimental comparisons for this assessment are shown in figures 1, 2, and 3 for the first stage stator, rotor, and the second stage stator respectively. The comparisons are all for the 0.78 flow coefficient. Comparisons were also made at 0.68 and 0.96 but the conclusions drawn were no different than those at 0.78. The comparisons are all for the data acquired in the 65% axial gap configuration. Changing the axial gap from 15% to 65% had little effect on the measured results. All of the comparisons are for the high Reynolds number cases, i.e. Reynolds numbers in the range of 600,000. Finally, the comparisons are with the data acquired both with the grid in and with the grid out. With the grid out the stage inlet turbulence was 0.5% and with the grid in it was typically 10%. Each of the figures includes a laminar prediction up to laminar separation indicated by "L", a fully turbulent prediction (using the Cebeci and Smith model, ref. 5) indicated by "T", and a family of transitional predictions (using the model of McDonald and Kreskovsky, ref. 7 with the turbulent Prandtl number profile of Blair, ref. 8) indicated by the level of the free-stream turbulence used in each calculation. On the pressure surfaces the transitional predictions for free-stream turbulences up to 10% were generally very close to the laminar predictions. On the suction surfaces increasing the free-stream turbulence produced a monotonic upstream movement of transition.

On the pressure surfaces of the three airfoils reasonable agreement between the measured and the computed results was only obtained on the first stator with the grid out. With the grid in the measured data were far above even the fully turbulent prediction. Similarly the pressure surface data for the rotor and the second stator were far above the fully turbulent predictions for the grid both in and out. It was previously observed that these high

pressure surface Stanton numbers occurred when the inlet unsteadiness was high (due to either turbulence or the passing of an upstream airfoil row) and when the Reynolds number was high. At lower Reynolds numbers the Stanton numbers reduced to near the fully turbulent level.

On the suction surfaces of the three airfoils the agreement between the measured and computed results was genrally unsatisfactory for both the cases with the grid in and with the grid out. The best agreement was obtained on the rotor for the case with the grid in. In this case after transition the data were in good agreement with the fully turbulent prediction. On the first stator the transition predictions were in poor agreement with the data in spite of the relatively benign inflow condition, i.e. without an upstream airfoil row. On the rotor the transition predictions were also poor. This may be related to the wakes of the upstream stator but recall that the rotor Stanton number distribution varied only slightly as the stator/rotor axial gap was changed from 15% to 65% with the grid both out and in. The analytical/experimental agreement for the second stator is poor but this is at least in part due to three dimensional effects present in the flow over the airfoil.

The results have also been examined in terms of the average Stanton number on the suction surface, on the pressure surface, and around the entire airfoil. These results are presented in figures 4 through 7 in terms of the variation of the average Stanton number with Reynolds number (based on axial chord and airfoil exit flow velocity). All of the averaged data shown here is for the case of the turbine operating at its design flow coefficient (C_x/U_m=0.78), and with the rotor/stator axial spacing equal to 15%.

Figure 4 illustrates the results for the first stator with the grid out. Suction (S) and pressure (P) surface data are shown as the symbols along with the fully turbulent (T) and laminar (L) predictions. The laminar prediction is shown only for the pressure surface. With the grid out the pressure surface is in good agreement with the laminar prediction. This could also be seen in figure 1. On the suction surface, however, because of the long region of laminar flow prior to transition (see fig. 1), the measured results are 30% below the fully turbulent prediction.

Figure 5 illustrates the results for the first stator with the grid in. These results are significantly different from those with the grid out (fig. 4). The data on both the suction and pressure surfaces are much closer to the fully turbulent predictions. The trends with Reynolds number, however, are particularly noteworthy. With the grid out (fig. 4) the Reynolds number trends were very similar to the laminar and turbulent predictions. With the grid in (fig. 5) there is a rising trend with increasing Reynolds number, especially on the pressure surface. At the highest Reynolds number the average pressure surface Stanton number is 40% greater than the fully turbulent prediction.

Figure 6 illustrates the results for the rotor with the grid both out and in. The suction and pressure surface data are shown in comparison with fully turbulent predictions and with the cascade data of Graziani et al. (ref. 9) for this same rotor midspan geometry. Several things are evident in this comparison. First, the difference between the grid in and grid out results is

much less than for the first stator due to the presence of the stator wakes passing over the rotor. Second, the trend of increasing Stanton number with increasing Reynolds number is even stronger on the rotor pressure surface than on the stator and it is occurring with the grid both in and out. At the highest Reynolds number with the grid in the average pressure surface Stanton number is 80% greater than the fully turbulent prediction (and 50% higher with the grid out). Finally, it can also be seen that the cascade results are consistent with the rotating rig results when the differences in Reynolds number and inlet turbulence (unsteadiness) are accounted for.

Figure 6 also illustrates the results for the rotor with the grid both out and in. The results shown here are for the average around the entire airfoil (suction and pressure surfaces). The figure includes the fully turbulent prediction, the cascade data of Graziani et al. (ref. 9), and the data of Lokay and Trushin (ref. 1, fig. 3). Several things are apparent. First, the differences in Reynolds number and inlet turbulence (unsteadiness) are sufficient to reconcile the present rotating rig results with the cascade results. Second, the typically 40% difference between the rotating and stationary results of Lokay and Trushin may also be due to inlet turbulence and unsteadiness. There is no evidence in the present results that this difference is in any way related to the effects of rotation (e.g. Coriolis or centrifugal effects). Some caution should be taken with regard to the data of Lokay and Trushin (ref. 1) due to the rather low Reynolds numbers at which they operated. Boundary layer separation may have been present.

CONCLUSIONS

A combined experimental and analytical program has been conducted to examine the impact of a number of variables on the midspan heat transfer coefficients of the three airfoil rows in a one and one-half stage large scale turbine model. These variables included:

- o stator 1/rotor axial spacing (15% and 65%)
- o Reynolds number (flow speed)
- o turbine inlet turbulence (0.5% and 10%)
- o flow coefficient (airfoil incidence)
- o relative stator 1/stator 2 circumferential position
- o rotation (rotor vs. cascade)

Heat transfer data were acquired on the suction and pressure surfaces of the three airfoils. High density data were also acquired in the leading edge stagnation regions. In addition to the heat transfer data, extensive documentation of the steady and unsteady aerodynamics was also acquired. Finally, the heat transfer data were compared with both a steady and an unsteady boundary layer analysis. Specific conclusions in each of these areas were as follows:

Steady Aerodynamics

It was observed that the airfoil midspan pressure distributions were in good agreement with two dimensional potential flow and that they were essentially unaffected by either the turbulence generating grid or the axial gaps between the airfoil rows. It was also observed that the turbulence generating grid had no significant impact on the circumferential distributions of flow speed downstream of each row of airfoils. The conclusion reached here was that the midspan aerodynamics in this experiment were well behaved and that the heat transfer results would be typical of those of a well-designed turbine.

Unsteady Aerodynamics

It was observed that the turbulence generating grid produced the desired level of turbine inlet turbulence (approximately 10%) and that the grid produced a large increase in total unsteadiness at the first stator exit. At the rotor exit and at the second stator exit, however, the change in unsteadiness level due to the grid was insignificant. The major conclusion reached here was that combustor-generated unsteadiness would strongly affect the flow over the first sttor of a turbine but that downsteam rows would be dominated by turbine-generated unsteadiness.

Heat Transfer

It was observed that a combination of unsteadiness, high Reynolds number and concave curvature could produce pressure surface heat transfer distributions well in excess of fully turbulent levels. It was shown that boundary layer separtion could also cause large increases in heat transfer. Finally, it was demonstrated that while turbine inlet turbulence can have a very strong impact on the first stator heat transfer, its impact on downstream rows is minimal. The major conclusion reached here was that pressure surface heat transfer could be well in excess of design predictions due to both combustor- and turbine-generated unsteadiness and that this is an area where additional research is sorely needed.

Steady Boundary Layer Analysis

The boundary layer transition and turbulence models examined in this assessment did not provide accurate predictions of either the transitional nature of the suction surface boundary layers or the very high heat transfer observed on the pressure surfaces. Although only one transition and turbulence model was assessed here the major conclusion is consistent with many previous assessments of other models. This conclusion is that these models are not yet capable of consistently predicting many of the important features of the heat transfer on turbine airfoils and that actual engine designs will probably have to rely, at least in part, on a correlative approach.

Unsteady Boundary Layer Analysis

An unsteady, compressible boundary layer analysis was developed to study the effects of rotor/stator interaction on the heat transfer rate at the blade surfaces. This analysis was applied to the present rotor/stator configuration using the measured pressure distributions as input to the boundary layer calculations. The conclusion drawn for these calculations was that the time averaged effect of unsteadiness on heat transfer was small since the time average of the unsteady heat transfer predictions differed only slightly from the heat transfer calculated for a steady prediction.

REFERENCES

1. Lokay, V. I., and Trushin, V. A.: Heat Transfer from the Gas and Flow-Passage Elements of a Rotating Gas Turbine. Heat Transfer-Soviet Research, Vol. 2, No. 4, July 1970.

2. Dunn, M. G., and Holt, J. L.: The Turbine Stage Heat Flux Measurements. Paper No. 82-1289, AIAA/ASME 18th Joint Propulsion Conference, Cleveland, Ohio, June 21-23, 1982.

3. Carter, J. E., Edwards, D. E. and Werle, M. J.: Coordinate Transformation for Laminar and Turbulent Boundary Layers, AIAA Journal, Vol. 20, No. 2, February 1982, pp. 282-284.

4. Edwards, D. E., Carter, J. E. and Werle, M. J.: Analysis of the Boundary Layer Equations Including a Coordinate Transformation--The ABLE Code, UTRC 81-30, 1981.

5. Cebeci, T. and Smith, A. M. O.: Analysis of Turbulent Boundary Layers, Academic Press, 1974.

6. McDonald, H. and Fish, R. W.: Practical Calculation of Transitional Boundary Layer. International Journal of Heat and Mass Transfer, Vol. 16, No. 9, 1973, pp. 1729-1744.

7. McDonald, H. and Kreskovsky: Effect of Free-Stream Turbulence on the Turbulent Boundary Layer, International Journal of Heat and Mass Transfer, Vol. 17, 1974.

8. Blair, M. F. and Edwards, D. E.: The Effects of Free-Stream Turbulence on the Turbulence Structure and Heat Transfer in Zero Pressure Gradient Boundary Layers, Final Report for AFOSR Contract No. F49620-81-C-0053, AFOSR TR-83-0149, Gov't Acc. No. ADA 126465, November 1982.

9. Graziani, R. A., M. F. Blair, J. R. Taylor and R. E. Mayle: An Experimental Study of Endwall and Airfoil Surface Heat Transfer in a Large Scale Turbine Blade Cascade, ASME Journal of Eng. for Power, Vol. 102, April 1980, pp. 257-267.

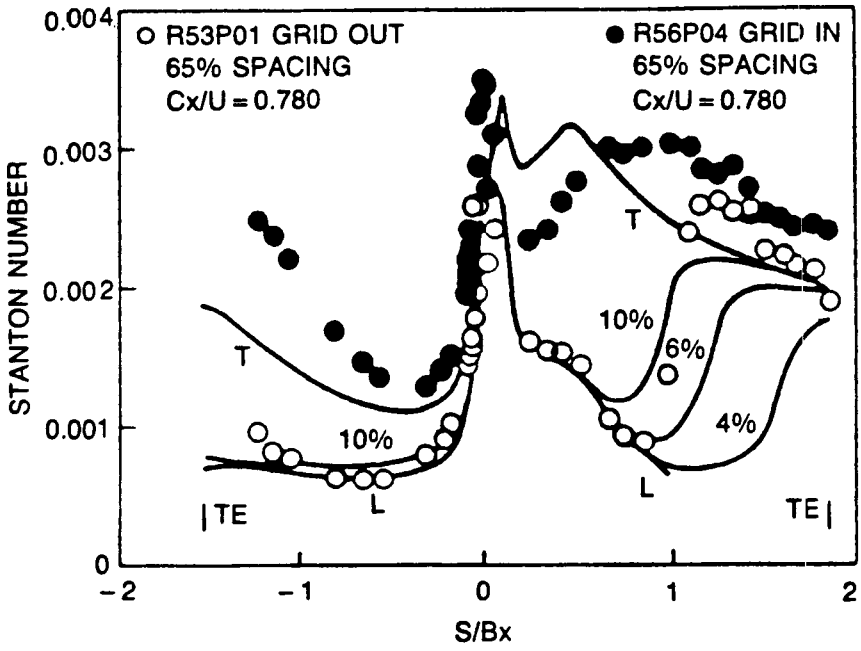

Fig. 1. Analytical/experimental comparisons for the first stage stator, Cx/U = 0.78.

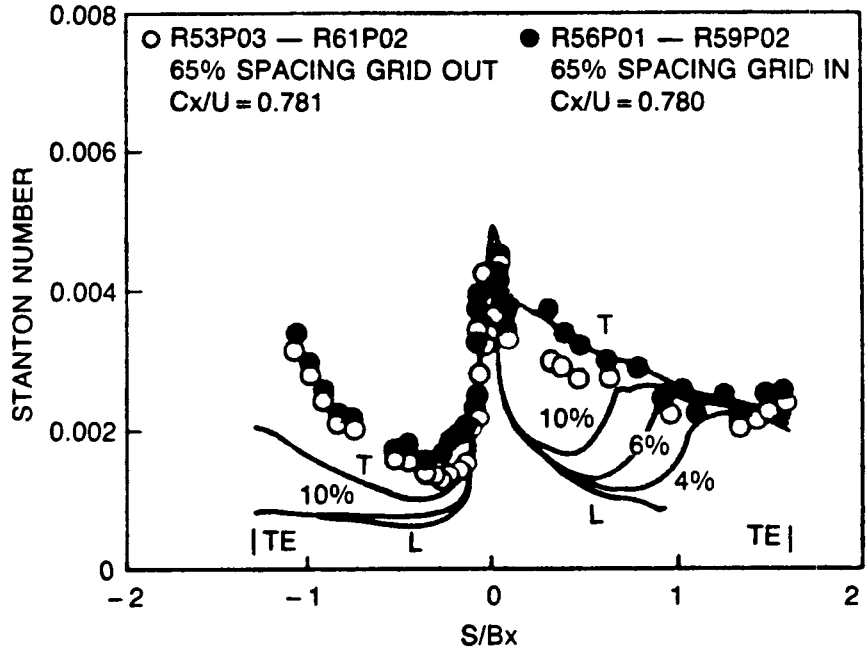

Fig. 2. Analytical/experimental comparisons for the first stage rotor, Cx/U = 0.78.

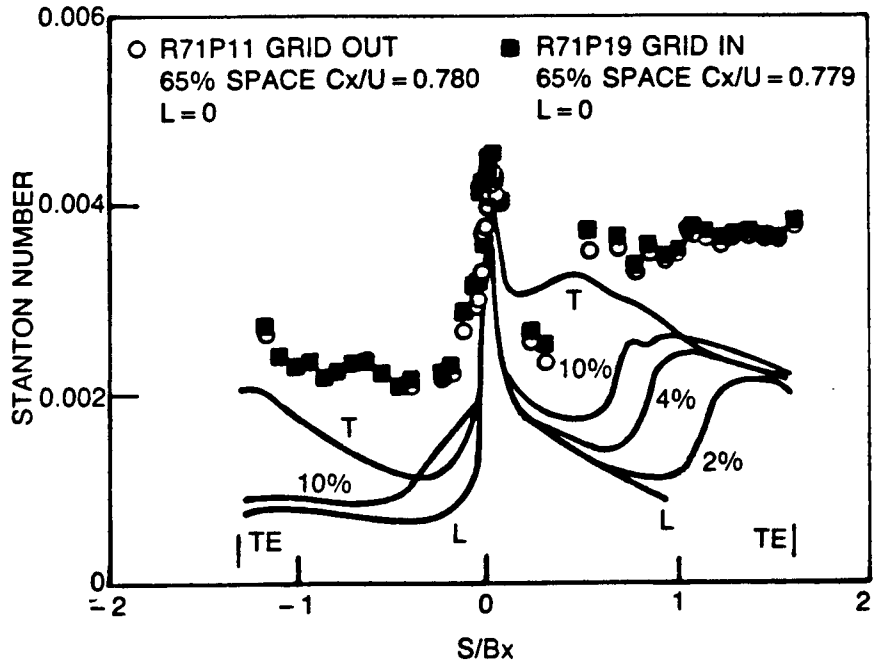

Fig. 3. Analytical/experimental comparisons for the second stage stator, Cx/U = 0.78.

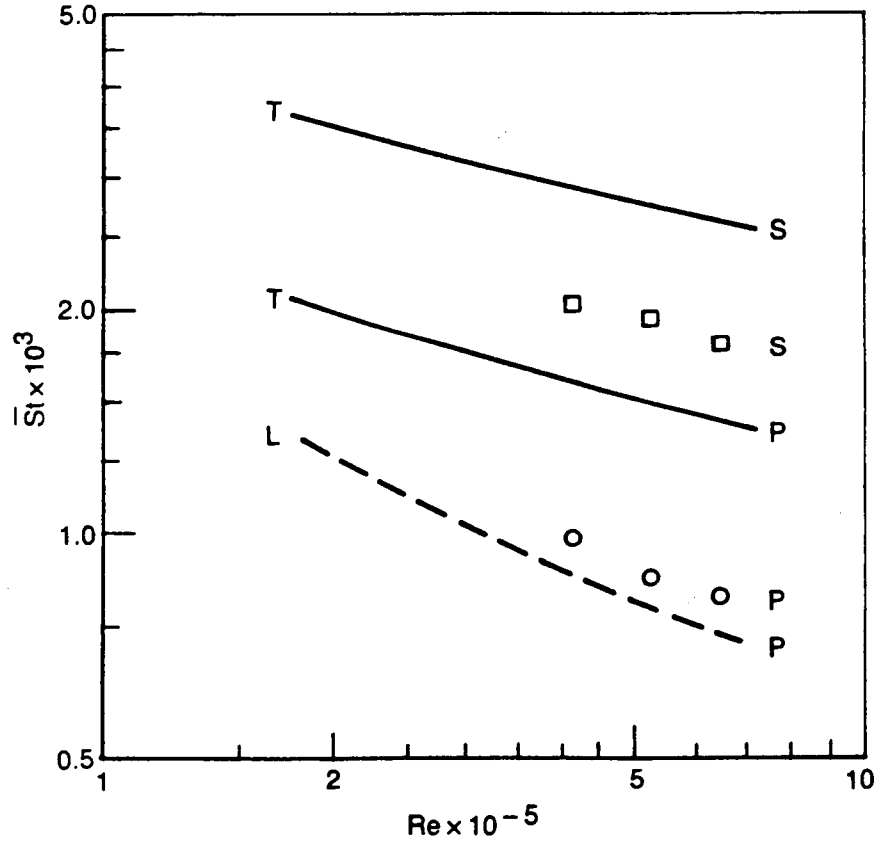

Fig. 4. First stator averaged suction (S) and pressure (P) surface heat transfer, $\phi = 0.78$, 15% gap, grid out.

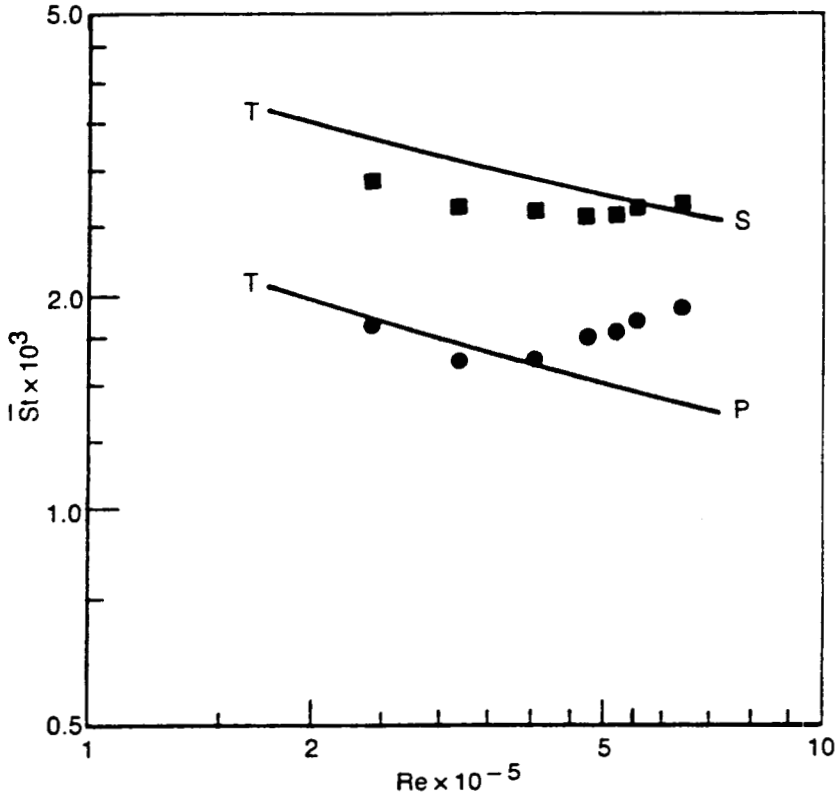

Fig. 5. First stator averaged suction (S) and pressure (P) surface heat transfer, $\phi = 0.78$, 15% gap, grid in.

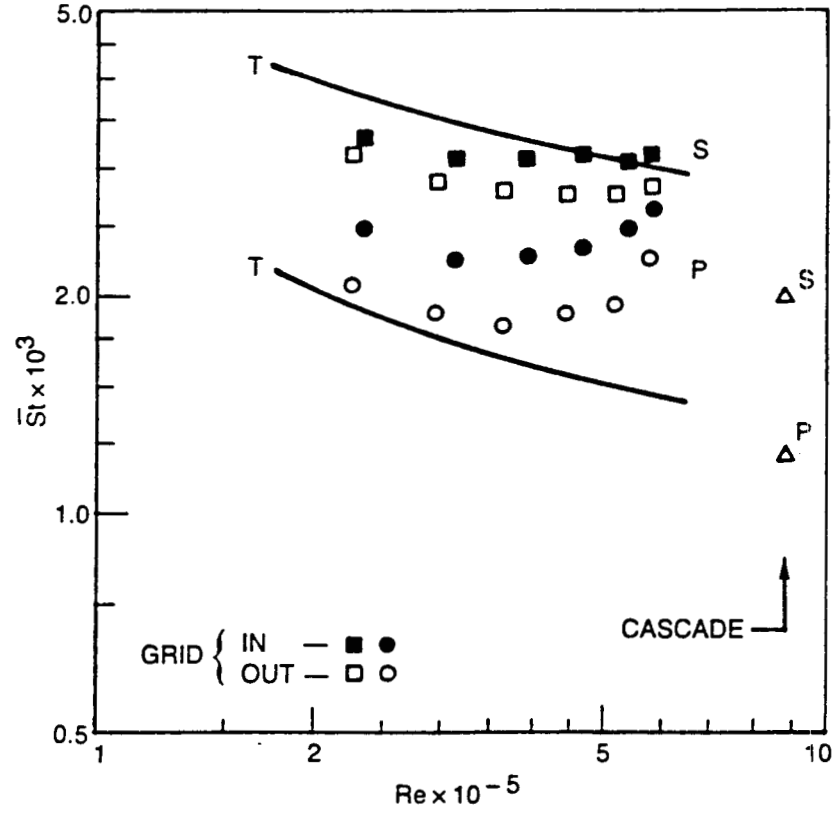

Fig. 6. Rotor averaged suction (S) and pressure (P) surface heat transfer, $\phi = 0.78$, 15% gap, grid in and out.

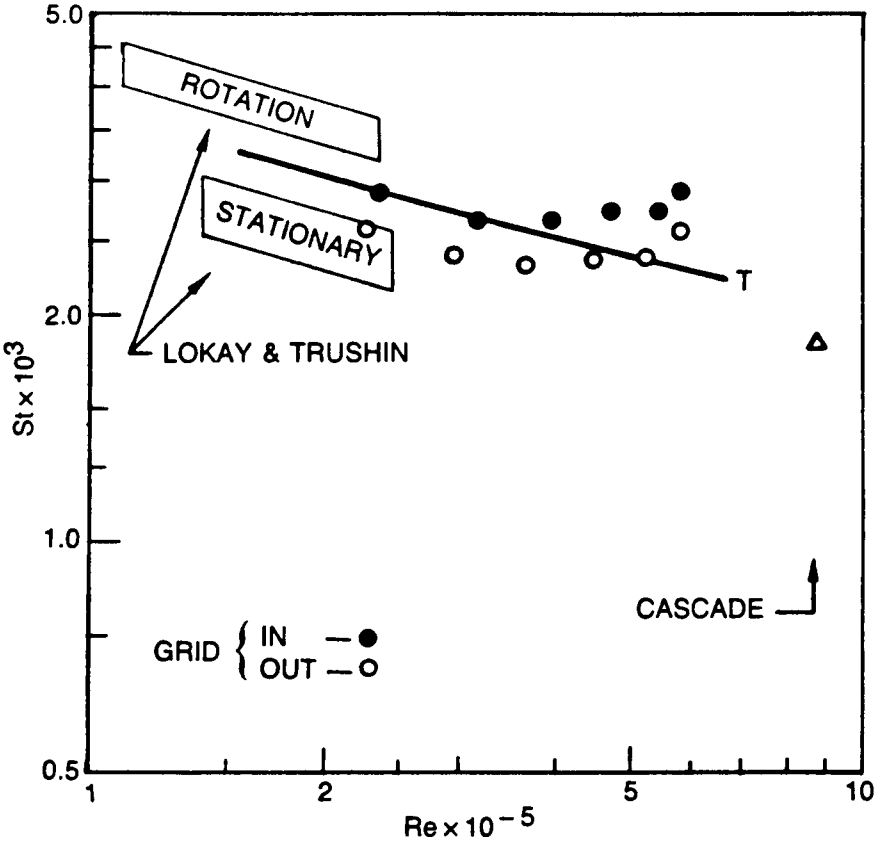

Fig. 7. Rotor averaged airfoil heat transfer, $\phi = 0.78$, 15% gap, grid in and out.

HEAT TRANSFER IN THE TIP REGION OF A ROTOR BLADE SIMULATOR*

M.K. Chyu† and D.E. Metzger
Arizona State University
Tempe, Arizona

The blades of axial turbine stages rotate in close proximity to a stationary peripheral wall (sometimes termed an outer ring or stationary shroud). Differential expansion of the turbine wheel, blades, and the shroud causes variations in the size of the clearance gap between the blade tip and stationary shroud. The necessity to tolerate this differential thermal expansion dictates that the clearance gap cannot be eliminated altogether, despite accurate engine machining [1]. This gap clearance provides a narrow flow passage between the pressure and suction sides of the blade and the resulting flow passing through the passage is often referred as the "tip leakage" flow.

The tip leakage flow is detrimental to engine performance and undesirable in practical design strategies. The primary detrimental effect of tip leakage flow is the reduction of turbine stage efficiency, but the convective heat transfer associated with the flow is an important secondary effect. The surface area at the blade tip in contact with the hot working gas represents an additional thermal loading on the blade which, together with heat transfer to the suction and pressure side surface area, must be removed by the blade internal cooling flows [2,3].

Very limited information on turbine tip heat transfer and fluid flow has been reported to date, and almost all of the published work dealing with clearance gap flows involves consideration only of plain flat blade tips. However, a strategy commonly employed to reduce tip flow and heat transfer is to groove a single rectangular cavity chordwise along the blade tip. The groove acts like the cell of a labyrinth seal to increase the pressure drop and thus reduce the flow for a given pressure differential across the tip. The reduction of the flow will also act to reduce heat transfer. A schematic diagram representing the geometry of a grooved blade tip, viewed from a coordinate system fixed relative to the blade, is shown in Fig. 1. The outer shroud can be considered moving in the general direction from the suction side to the pressure side, with relative velocity equal to U_w. The leakage flow, as denoted by U in the figure, is driven by the pressure difference between two sides of the blade and flows in the direction opposite to the shroud motion. With this general configuration in mind, the grooved tip problem can be categorized as

* Work done under NASA grant NAG 3-623
† Present Address: Department of Mechanical Engineering,
Carnegie Mellon University, Pittsburgh, PA 15213

C-5

fluid flow and heat transfer over a shrouded rectangular cavity. The flow field over a cavity is characterized by flow separation and shear layer reattachment resulting in complex flow patterns with substantial effects on the friction drag and heat transfer [5-7]. Most of the previous studies on cavity problems have been considered as a flow system in which the cavity is open to a usually well-specified approaching flow over an otherwise smooth and stationary surface. The approaching flow may be a wall boundary layer for external flow or a well developed channel flow.

The grooved tip differs from the aforementioned unshrouded situation by virtue of the confined nature of the geometry as well as by the proximity of moving shroud. The degree of similarity between the heat transfer characteristics of the grooved tip and those of previous cavity studies has been unclear until recently [7-9]. The results reported in several relating studies, including the one presented earlier in the HOST program [8], have generally indicated that the characteristic of flow pattern and heat transfer in a tip region is virtually unaffected by the relative shroud movement. The nature of the shear layer separated from the sharp edge of a cavity upstream wall has predominated the transport mechanisms in a cavity so that the effect from the shroud motion becomes secondary. Consequently, the cavity shape and the gap size are the two most influential parameters. This implies that the entire tip leakage problem can be modeled in a stationary system without the shroud-moving effect.

In Ref. [8], detailed local heat transfer characteristics on all surfaces of shrouded, rectangular cavities are reported. The varying parameters include the cavity depth-to-width ratio, D/W, gap clearance-to-cavity width ratio, C/W, relative shroud moving speed, U_w/U, and Reynolds number, $Re = UC/\nu$. The naphthalene ($C_{10}H_8$) sublimation mass transfer technique in association with a computer-controlled, automated surface contouring measurement system is employed. This experimental system provides better control and high data accuracy for a local study. The mass transfer results can be transformed into their counterparts in heat transfer by invoking an analogy between these two transfer processes [10,11].

This paper, an extension to Ref. [8], describes the updated development of the project currently being conducted at Arizona State University. It consists of two major parts. First is the continuing measurement effort of the mass transfer from cavities, with an emphasis on the effect of cavity orientations relative to the main flow direction. The second part is a finite-difference computation for turbulent air flow and heat transfer over a two-dimensional, shrouded, rectangular cavity. This is intended to numerically model the experimental system studied in Ref. [8], and the fundamental aspects of the cavity problem, as reflected in the measured data, can thus be understood.

EXPERIMENTAL STUDY

Objectives and Despcription of Model

To gain a detailed understanding of the heat transfer fundamentals

in a complex separated-flow system and to provide turbine manufacturers with design information, it is desirable to model the grooved tip by using a cavity with an actual blade airfoil shape. Fig. 2 shows a typical blade shape and grooved configuration for a low-aspect-ratio, small/medium size engine in which tip leakage is a critical problem. In this case, the pressure differential across the tip leakage-passage is non-uniform along the chordwise direction. Thus the leakage flow may have an angle-of-attack to the tip groove different from that of a normally positioned cavity. This also implies that the flow separates from a sharp edge which is not perpendicular to the flow mainstream direction. The flow is more complex than that of a normally positioned cavity and involves heat transfer with three-dimensional, separated shear flow. It is speculated that vortices with different orientations and strength may exist in the cavity, and that the vortices rotate in a helical fashion creating wavy characteristics in both the flow field and the heat transfer.

As a preliminary study to the tip cavity with an actual blade shape, the present work emphasizes on determining the effect of the flow angle-of-attack on the cavity heat transfer. This is facilitated by placing a rectangular cavity with its two parallel side walls inclined to the flow mainstream direction, as shown in Fig. 3. For a fixed flow direction, the term "skewed cavity" can thus be used to describe this geometry. The degree of cavity skewness is represented by the magnitude of θ as defined in Fig. 3. In the present study, θ varies between 90° and 75° ($\theta = 90^\circ$, 85°, 80° and 75°), where $\theta = 90^\circ$ represents the case without skewness generally referred to be the rectangular cavity in the literature and used in Ref. [8]. Along the cavity spanwise direction (Z-axis in Fig. 3), the skewness can produce pressure gradients and flow components which in general are either nonexistent or insignificant in a normally positioned, two-dimensional cavity. Although a thorough understanding of the transport mechanism associated with this phenomena is lacking, experimental data from previous studies of heat transfer enhancement have indicated that a skewed flow-separation can result in a higher heat transfer than its unskewed counterpart [12], provided that the skewed flow-separation is sufficiently strong. In the present application, the degree of skewness is moderate. It is intended to investigate the effect of θ variation on the heat transfer in a skewed cavity as compared to its unskewed counterpart. The comparison will help to assess the utility of results from the rectangular cavity experiments, e.g. Ref. [8], in predicting heat transfer in the more complex cavities existing on actual turbine blades. In addition to θ variation, four different cavity depth-to-width ratios, $D/W = 0.9$, 0.45, 0.23, and 0.15, are tested for each θ .

To isolate the primary effect of interest, no attempt is made to model the detailed, complex leakage flow field as it exists with the actual blade shape. Since the shroud effect, especially the movement relative to the cavity, is considered to be unimportant in most of the turbine applications, it is excluded in the present test. However, a comparison between the present results and those from studies with shroud or confined cavities [7,8] will be made, so that the influence of shroud presence on the heat transfer in a cavity can be understood.

Experimental System

The naphthalene ($C_{10}H_8$) sublimation mass transfer technique is employed herein. The subliming mass transfer process takes place when the solidified naphthalene is exposed to the air stream in a tunnel. The local mass transfer coefficient at a certain location can be inferred from the depth change of naphthalene at this location before and after a test run. A computer-controlled, automated surface profile measurement system had been developed earlier for this project, which provides high data accuracy and operational convenience. The mass transfer results can be transformed into their counterparts in heat transfer by invoking an analogy between these two transfer processes. Details on the measurement system and analogy has already been discussed in Ref. [8,11].

A specially designed open-circuit wind tunnel, approximately 4.5 meters in total length, is used for the present study. Air is drawn from a 100 HP compressor into the tunnel, passing a series of screen pads before reaching the test section. The test section, located approximately 0.9 meter upstream of the tunnel exit, has a uniform cross-section of 101 mm high by 152 mm wide. The side walls are made of acrylic plastic (Plexiglas) with a thickness of 19 mm. The framework of cavities being tested is made of aluminum tooling plate. Details of the cavity geometry are shown in Fig. 3. The shaded region shown in the figure represents the mass transfer active area where the surface is coated with naphthalene. The naphthalene covered cavity is inserted into the test section of the wind tunnel and tightened by screws against the tunnel floor.

Depths of the cavity walls are physically identical for all the cases, D = 5.72 mm (0.225"). The effective cavity span across the tunnel is maintained at 152 mm (6.0") which is equivalent to approximately 26 times the cavity depth. For cavities with $\theta = 90^\circ$, this high span/depth ratio tends to result in a generally two-dimensional separated flow and mass transfer. The mass transfer measurements in this study are made covering the entire cavity, with the number of measured data points increasing with the size of mass transfer active area. Approximately 200 data points are measured for D/W = 0.9 and 800 points for D/W = 0.15. For a given value of a cavity aspect ratio, the naphthalene coated area increases with an increase in cavity skewness, as shown in Figure 3.

The measured velocity profile at the location of the naphthalene leading edge reveals characteristics of a fully turbulent boundary layer, and the boundary layer thickness (0.99 U) thickness at that location is 11 mm ($\approx$1.9D). The Reynolds number based on the cavity depth and U is about 1.76×10^3.

Results and Discussion

Most of the mass transfer results are presented in terms of the Stanton number, $St = h_m/U$, where h_m is the mass transfer coefficient. For a comparison purpose, the mass transfer measurements have been made on a flat naphthalene plate without a cavity in the same tunnel operating with the same flow conditions and $\theta = 90^\circ$. The local Stanton

number shows a power law dependency on the streamwise coordinate (X_n/D) of the type 4.19×10^{-3} $(X_n/D)^{-0.23}$, where X_n is the streamwise distance from the mean starting point of mass transfer (see Fig. 1). Based on this equation, the area-averaged Stanton numbers are 3.24, 3.03, 2.76 and 2.58×10^{-3} for the same streamwise distance as that for an unskewed cavity with D/W = 0.9, 0.45, 0.23 and 0.15, respectively. The equation compares favorably with correlations [13] for heat transfer from a flat plate to a turbulent boundary layer with a zero freestream pressure gradient, although the absolute values of Stanton numbers are somewhat different. This is believed to be due partially to the inactive mass transfer starting length. The agreement provides confidence in the present mass transfer technique as well as in the measurement system. The uncertainty in the local Stanton number, based on the methods of Ref. [14], is estimated to be approximately 10%. The repeatability of all the present tests is within 5%.

Local mass transfer results are shown in Figs. 4 to 6. The open symbols represent the measured data for different values of θ along the center-line of test section (Z/D = 0). It is expected that the asymmetric mass transfer behavior exists across the cavity span (Z direction), at least for $\theta \neq 90^{\circ}$. However, the data measured within the domain $|Z/D| \leq 9.0$ is quite scattering and no clear trend or correlation between St and Z/D can be found. Thus, in addition to the center-line data, the range of the corresponding data over the entire measurement domain is given as a shaded region on each figure. The aforementioned effect is likely due to the relatively moderate degree of skewness coupling with the complex separated flow field and transfer mechanism and different cavity geometries. This is also supported by an auxiliary study using the graphite-oil technique to visualize the flow streak line on a cavity floor. An inclined, distorted flow separation-reattachment line on a cavity floor can only be seen when $D/W \leq 0.1$ and $\theta \leq 60^{\circ}$. For all the cases tested in the present mass transfer study, a wavy flow motion has been observed across the cavity span. The motion, having an amplitude in the order of cavity width, appears to be stronger near the central region (Z/D = 0) and with a higher degree of cavity skewness. This phenomena is also observed in the previous studies dealing with rectangular cavities with normal flow angle-of-attack [15]. The wavy motion, at least in part, may be responsible for the data variation along the Z direction.

Figure 4 shows the distribution of local St on the cavity floor and surfaces upstream and downstream of the cavity. The streamwise coordinate in these figures is normalized by the cavity height, D. The mass transfer variation with X/D is similar for the different values of D/W. The mass transfer coefficient is generally low near the front corner of the cavity and increases with X/D to reach a maximum. This is followed by a decrease toward the downstream wall. The magnitude of this maximum has the lowest value for D/W = 0.9 and the highest for D/W = 0.23, and its location moves downstream as the width of the cavity increases. The increase of mass transfer with X/D in the front portion of the cavity is characteristic of a separated boundary layer from a sharp-edged, downstream-facing step. For a normally positioned cavity, a recirculating region is formed immediately downstream of the step, and it is followed by a reattachment zone if no downstream wall (the upstream-facing wall) is present or if the cavity aspect ratio, D/W, is

low. For cavities with a medium/small value of the aspect ratio, e.g. $0.2 \leq D/W \leq 1$, an elliptic vortex is formed as a result of a part of the separated shear layer impinging on the cavity downstream wall and then flowing toward the cavity floor [5]. The resulting vortex fills the entire cavity. In addition, a very unsteady, small, but high-strength vortex is found near the lower corner immediately ahead of the downstream wall. High turbulence may be induced by this vortex, increasing the heat or mass transfer in the region. To a certain extent, the vortex structure is expected to be affected by the cavity-skew. The wide scattering of data near the cavity downstream corner, in particular for $D/W = 0.23$, could be caused by these reasons. The overall trend of the mass transfer distributions on the cavity floor shown in Fig. 4 agrees very favorably with previous studies for normally positioned cavities [6-8].

A distinct mass transfer characteristic on the floor is observed for $D/W = 0.45$. An additional, but rather moderate, local maximum of St occurs at $X/D = 0.5$, which is followed by a local minimum near the mid-point of the cavity floor. Similar behavior is also observed in Ref. [6,8]. According to a flow visualization study [5], for D/W approximately equal to 0.5, a stagnant region of a weak recirculation behind the cavity upstream wall is observed in addition to the primary vortex. This may account for the peculiar mass transfer distribution on the cavity floor for $D/W = 0.45$. To be noted is that, for cavities confined by a shroud as studied in Ref. [8], this peculiar mass transfer distribution occurs at $D/W = 1.0$, not $D/W \approx 0.5$. This may be attributed to the fact that the presence of shroud causes the shear-layer reattachment effect to persist in deeper cavities as compared to the cases without shroud present. In general, the characteristics of flow and heat transfer in an unshrouded cavity are corresponding to those in a shrouded cavity with a higher value of D/W.

Mass transfer measurements have also been made on the naphthalene surfaces extending one cavity depth (1D) upstream and downstream of a cavity. For a normally positioned cavity, mass transfer from the surface upstream of the cavity behaves similar to that of a flat surface with a developing boundary layer, and it is virtually unaffected by the presence of the cavity [6]. Nevertheless, this is different if the actual inlet condition of leakage flow is of concern. The sharp-edge inlet effect produces a recirculating bubble, or the vena-contracta, at the entrance region of the leakage passage. The resulting heat or mass transfer distribution in the region is characterized with a local maximum in the mid-portion of the surface, as shown in Ref. [8]. In this study, the mass transfer coefficient is very high at the leading edge of the surface and decreases with a downstream position. The effect of the θ variation on the St appears to be stronger for a larger value of D/W, as is also the range of data across the cavity span.

As a contrast to the surface upstream of a cavity, the mass transfer from the surface downstream of a cavity is dependent on the cavity width. A cavity with a small value of D/W permits the shear layer originating from the cavity upstream wall to grow thicker and to generate more turbulence in the layer before it impinges the cavity downstream wall. At least part of this highly turbulent layer may be

deflected toward the cavity top gaining a velocity component normal to the mainstream direction after the impingement. This is due mainly to the pressure difference between the region of impingement and the mainstream. For D/W = 0.15, the local maximum of St near the mid-point of the surface downstream of the cavity is believed to be due to the effect of the deflected shear-layer reattachment. This is often observed in a flow system with a sharp-edge boundary layer development. For D/W $\geq$ 0.23, this reattachment effect becomes insignificant or even non-existent and a thin separated shear layer bridges the entire cavity. The external flow would skim past the cavity without a strong interaction with the flow inside. As a consequence, the behavior of mass transfer downstream of a large D/W cavity can primarily be determined by the characteristics of the mainstream flow. The mass transfer characteristic is similar to that of a new developing boundary layer.

Figure 5 shows the local mass transfer distributions along the upstream side-wall of the cavity, i.e. the downstream-facing wall. The mass transfer from the upstream wall seems to be dominated by the vortex attached behind the wall, and it is generally lower than that of other portions of the cavity. For D/W = 0.9, the stagnant flow motion in the vortex induces a local minimum of the mass transfer coefficient at Y/D $\cong$ 0.7. For D/W $\leq$ 0.45, the mass transfer distributions are very similar; the lowest mass transfer coefficient occurs near the lower corner while the highest occurs near the top of the wall. This implies the mass transfer behavior on a cavity upstream wall may be unaffected by the aspect ratio of the cavity. The variation of St with θ is about the same along the center line for all the values of D/W tested. However, the range of St across the cavity span appears to be stronger for D/W = 0.45. This is expected to be caused by the secondary vortex existing near the front corner of the cavity, as previously discussed.

Local mass transfer distribution on the cavity downstream wall (the upstream-facing wall) is shown in Fig. 6. The fundamental mode of mass transfer mechanism for the upstream-facing wall is the impingement of the shear layer on the wall, and it generally results in a higher mass transfer coefficient as compared to a downstream-facing wall. The local St increases almost linearly with Y/D. D/W = 0.45 has the highest variation range of St across the cavity span, as it does with the mass transfer of the upstream side wall. A comparison with the results in Ref. [8] reveals that the shroud effect is insignificant on the mass transfer from the cavity side walls.

The value of the mass transfer averaged over an area is obtained by numerical integration. Fig 7 shows the area-averaged Stanton number ($\overline{St}$, left-ordinate) and the normalized overall mass transfer rate (right-ordinate) for the entire cavity. Since the variation of $\overline{St}$ vs θ is near the range of estimated experimental uncertainty, a data bar is used to represent the $\overline{St}$ for all the values of θ at a certain aspect ratio of the cavity. As shown in Fig. 7, D/W = 0.23 has the highest value of $\overline{St}$ and D/W = 0.9 has the lowest. For D/W $\geq$ 0.23, $\overline{St}$ decreases with an increase in the value of D/W. This implies that, in general, a deeper groove results in a lower heat transfer coefficient.

In the literature, the average heat transfer coefficient on the cavity floor has commonly correlated between the average Nusselt number, the Reynolds number and the cavity aspect ratio. A power correlation reported in Ref. [5] has suggested that, for $D/W \leq 0.12$, $\overline{St}$ increases as the aspect ratio (D/W) increases. However, the present results show that the opposite trend exist when $D/W \geq 0.23$; $\overline{St}$ decreases with an increase of D/W. Similar results have been reported in Ref. [6]. As a result, the cavity heat transfer within the present range of D/W is unable to be presented by a single correlation. In addition, the overall trend of average Stanton number is unaffected by the variation of cavity-skew at least within the present studying range, as shown in Fig. 7.

If the overall heat transfer rate is the major concern, the additional heat transfer area due to an increase in cavity depth becomes an important factor. The results shown in Fig. 7 indicates that, despite the lower mass transfer coefficient, the deeper cavities experience higher overall mass transfer rate than the shallower ones. This result agrees favorably with those from Ref. [7,8]. It is suggested in Ref. [7] that to groove a blade tip having a cavity with $D/W \geq 0.5$ may be undesirable.

NUMERICAL COMPUTATION

As previously mentioned, numerical computation is attempted to simulate the flow field and heat transfer near a grooved tip. The problem is modeled as the turbulent air flow over a two-dimensional, rectangular, shrouded cavity. A control-volume based finite-difference method is employed for solving a system of partial differential equations describing the conservation of mass, momentum, energy and turbulent flowfields. The formulation entails an elliptic system of equations for properly describing the separated, recirculating flow. The computer program uses the SIMPLER algorithm [16] to explicitly solve for the velocity and pressure fields. The turbulent parameters are determined by a low-Reynolds-number, $k-\varepsilon$ model developed by Jones and Lauder [17]. The model is capable of describing the boundary layer laminarization and the boundary conditions explicitly, which is considered to be important for the present application. The momentum, continuity, and turbulence equations, together with their coupling characteristics, constitute five equations to be solved simultaneously for the converged velocity field. This is followed by the separate solution for the energy equation. For a computational domain similar to Fig. 1, the computation uses a 40 x 26 grid for all cases studied and a non-uniform spacing with dense placement near solid walls. A typical run on an IBM 3081 mainframe computer takes approximately 400 iterative steps for a converged velocity field, and an additional 30 steps are required for the temperature computation.

Fig. 8 shows a sample result of computed mean-flow pattern in a cavity with $C/W = 0.1$, $D/W = 1.0$ and $Re_c = 2 \times 10^4$. For a cavity having aspect ratio near unity, it is typical for a recirculating bubble to fill the entire cavity, and the separated shear layer to partially impinge the downstream side wall. The results compare favorably with a similar study using a high-Reynolds-number, $k-\varepsilon$ turbulence model [9]. In Ref. [9], the inlet condition is specified at the leading edge of

the surface upstream of a cavity, and a uniform velocity profile at this location is assumed. As a result, the effect of recirculation, or vena contracta, near the gap sharp-entrance region disappears. It is argued that the transport mechanism in a cavity is largely determined by the characteristics of the shear layer separated at the sharp-edge of the upstream side wall. A perfect modeling of the inlet velocity profile may not be critical, particularly if the heat transfer inside the cavity is the major concern. This inlet condition problem is remedied in the present computation by extending the flow inlet condition further upstream from the actual gap entrance. The lower left corner in Fig. 8, denoted by i-i', is where the flow inlet condition is specified, and a uniform mean flow profile with a 10% turbulence intensity is assumed. The sharp-edge entrance effect is thus revealed and, as a result, a recirculation exists near the front portion of the gap.

Heat transfer results from the present computation are compared with the data measured in Ref. [8]. Fig. 9 shows two samples of comparison, D/W = 0.1 and 0.5 (with C/W = 0.14, $Re_c = 2.0 \times 10^4$ being the same for both), for heat transfer on the cavity floor and the surfaces upstream and downstream of the cavity. The agreement in general is very favorable, in particular for the cavity with a small value of D/W. The effect of recirculation and reattachment near the gap entrance results in a local maximum of heat transfer in the mid-portion of the surface upstream of the cavity.

CONCLUDING REMARKS

The ongoing study of heat transfer in the blade tip region emphasizes on the acquisition of detailed local information in cavities with an actual blade shape. One of the distinct characteristics involved is that the flow separates skewedly from a sharp edge which is not normal to the main flow direction. As a preliminary study to the measurement with an actual blade, this effect is investigated experimentally by performing mass transfer measurements on rectangular cavities with different flow angles-of-attack. For a moderate range of angle variation, which is typical to most turbine applications, the average heat transfer in a skewed cavity is agreeable to that in a normally positioned cavity to approximately 10%. The characteristic local heat transfer distribution is found to be mainly dependent on the cavity aspect ratio rather than the flow angle-of-attack. This implies, to a certain extent, that the utility of results from the normally positioned, rectangular cavity for predicting heat transfer in the more complex cavities used on actual turbine blades is appropriate. Additional work reported is a numerical computation of the heat transfer and fluid flow in shrouded cavities. A computer code with a finite-difference method and a low-Reynolds-number, k-ϵ turbulence model is developed for this modeling. The results compare favorably with the measurements obtained previously for this project.

REFERENCES

1. Hennecke, D.K., "Heat Transfer Problems in Aero-Engines," Heat and Mass Transfer in Rotating Machinery, D.E. Metzger and N.H. Afgan, eds. Hemisphere, Washington, D.C., 1984, pp. 353-379.

2. Metzger, D.E. and Mayle, R.E., "Heat Transfer Gas Turbine Engines," Mech. Eng., 105, No. 6, June 1983, pp. 44-52.

3. Mayle, R.E. and Metzger, D.E., "Heat Transfer at the Tip of an Unshrouded Turbine Blade," 7th International Heat Transfer Conference, Munich, 3, 192, pp. 87-92.

4. Aung, W., "Separated Force Convection," Keynote Paper, ASME/JSME Thermal Eng. Conf., Honolulu, March 20-24, 1983.

5. Yamamoto, H., Seki, N. and Fukusako, S., "Forced Convection Heat Transfer on Heated Bottom Surface of a Cavity," J. Heat Transfer, 101, 1979, pp. 475-479.

6. Chyu, M.K. and Goldstein, R.J., "Local Mass Transfer in Rectangular Cavities with Separated Turbulent Flow," Heat Transfer 1986, 3, pp. 1065-1070, Hemisphere Publication, 1986.

7. Metzger, D.E. and Bunker, R.S., "Cavity Heat Transfer on a Grooved Wall in a Narrow Flow Channel," ASME Paper 85-HT-57, 1985.

8. Chyu, M.K., Moon, H.K. and Metzger, D.E., "Heat Transfer in the Tip Region of a Rotor Blade Simulator," NASA-Lewis 5th Host Workshop, Cleveland, Oct. 21-22, 1986.

9. Chyu, M.K., Metzger, D.E. and Hwan, C.L., "Heat Transfer in Shrouded Rectangular Cavities," J. Thermophysical and Heat Transfer, 1, 1987, pp. 247-252.

10. Eckert, E.R.G., "Analogies to Heat Transfer Processes," Measurements in Heat Transfer, ed. by Eckert, E.R.G. and Goldstein, R.J., Hemisphere Publication, Washington D.C., 1976.

11. Goldstein, R.J., Chyu, M.K. and Hain, R.C., "Measurement of Local Mass Transfer on a Surface in the Region of the Base of a Protruding Cylinder with a Computer-Controlled Data Acquisition System," Int. J. Heat and Mass Transfer, 28, 1985, pp. 977-985.

12. Han J.C., Glicksman, L.R. and Rohsenow, W.M., "An Investigation of Heat Transfer and Friction for Rib-Roughened Surfaces," Int. J. Heat and Mass Transfer, 21, 1978, pp. 1143-1156.

13. Reynolds, W.C., Kays, W.M. and Kline, S.J., "Heat Transfer in the Turbulent Incompressible Boundary Layer I - Constant Wall Temperature," NASA Memo. 12-1-58W, 1958.

14. Kline, S.J. and McClintock, F.A., "Describing Uncertainties in Single Sample Experiments," Mechanical Engineering, 75, January, 1953.

15. Maull, D.J. and East, L.F., "Three-Dimensional Flow in Cavities," J. Fluid Mechanics, 16, 1963, pp. 620-632.

16. Patankar, S.V., Numerical Heat Transfer and Fluid Flow, Hemisphere Publication, 1980.

17. Jones, W.P. and Launder, B.E., "The Prediction of Laminarization with a Two-Equation Model of Turbulence," Int. J. Heat and Mass Transfer, 15, 1972, pp. 301-303.

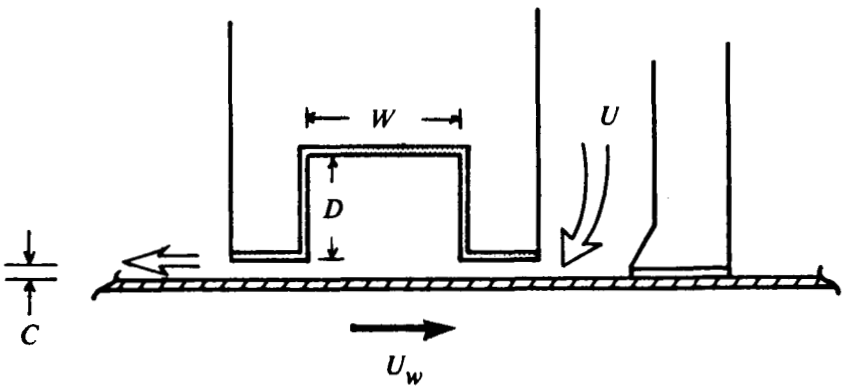

FIGURE 1. Schematic View of Shrouded Cavity

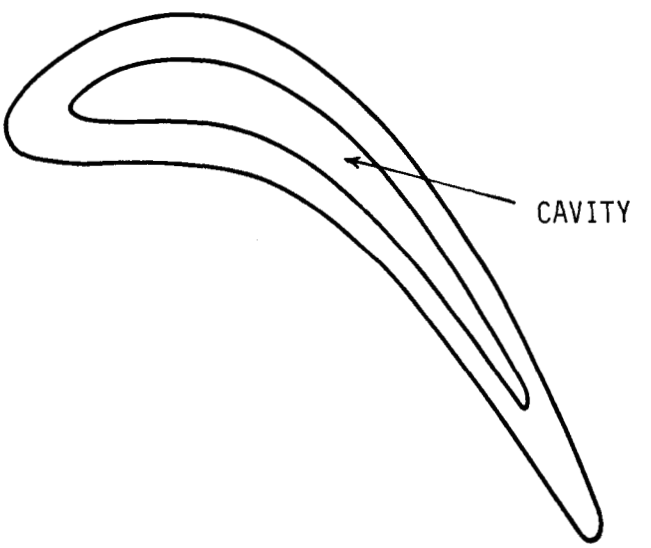

FIGURE 2. Cavity with Actual Blade Shape

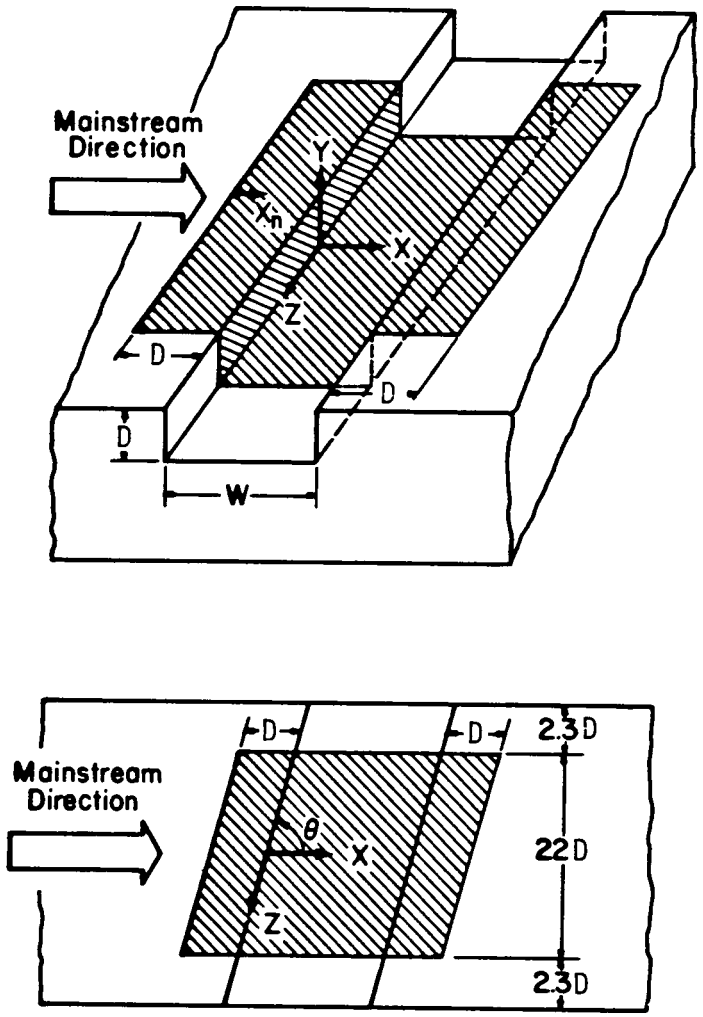

(Top View)

FIGURE 3. Skewed Rectangular Cavity

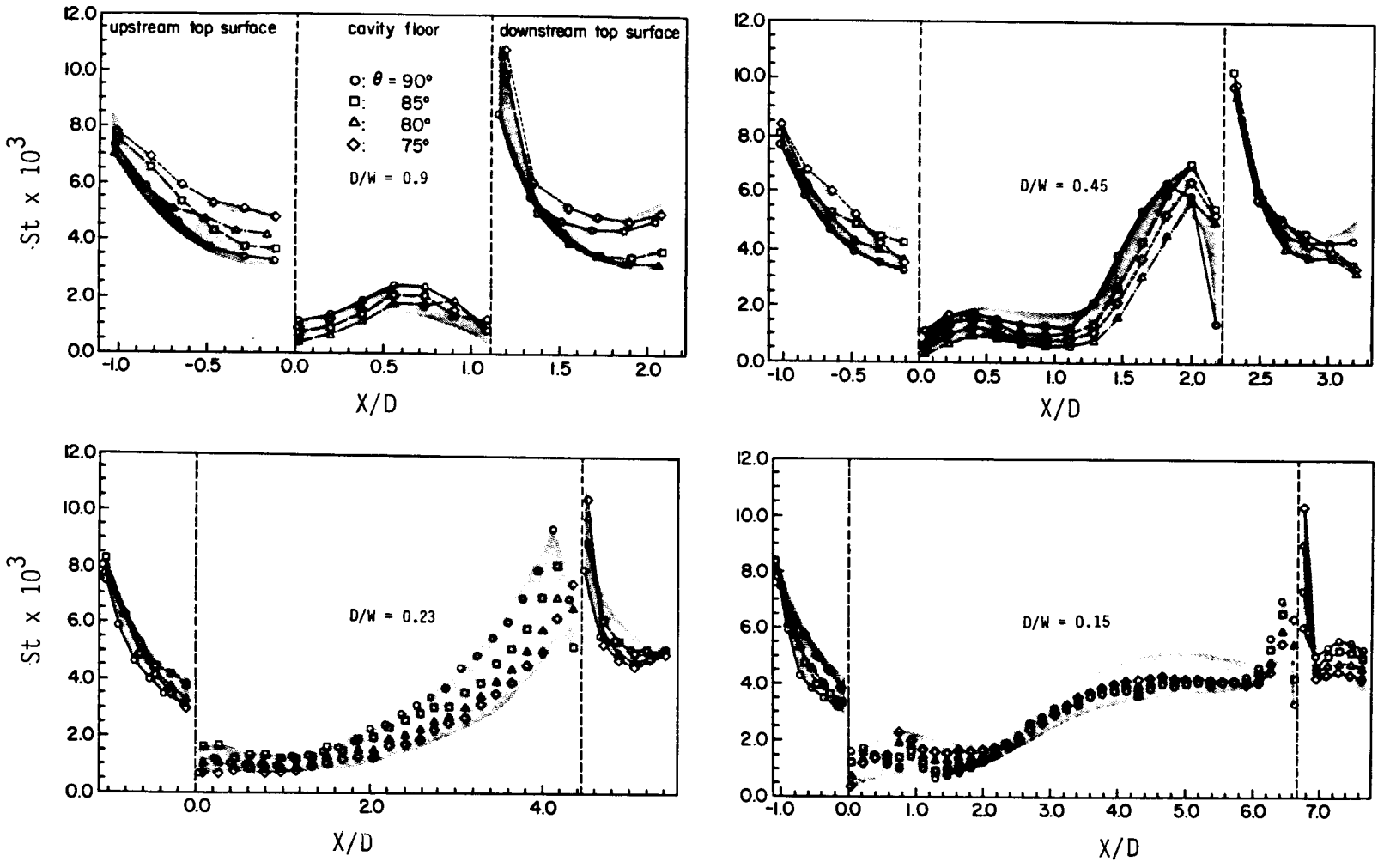

FIGURE 4. Local Mass Transfer Distribution on Cavity Floor and Surfaces Upstream and Downstream of Cavity, (Z/D = 0)

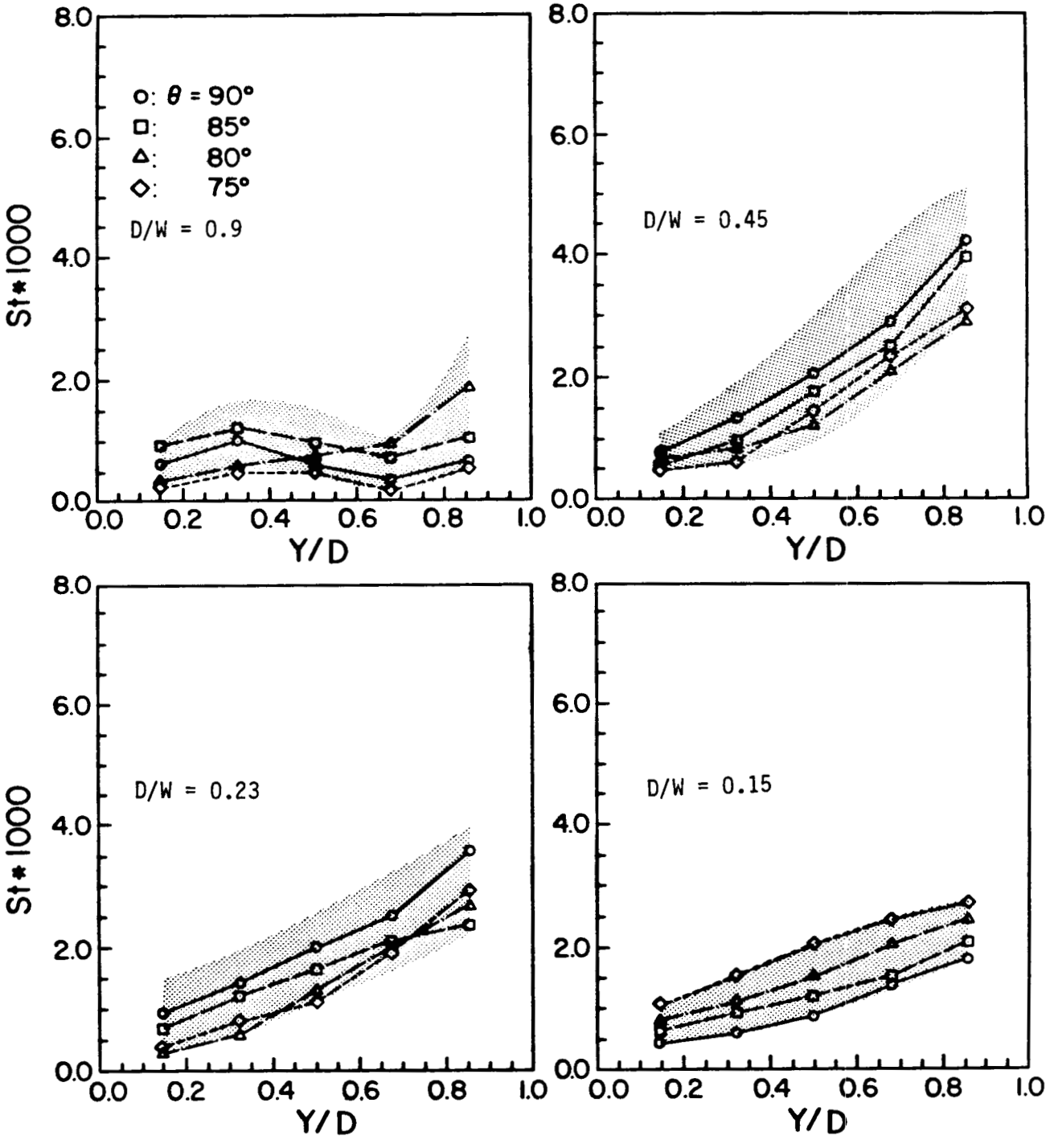

FIGURE 5. Local Mass Transfer Distribution on Cavity Upstream Side-Wall, (Z/D = 0)

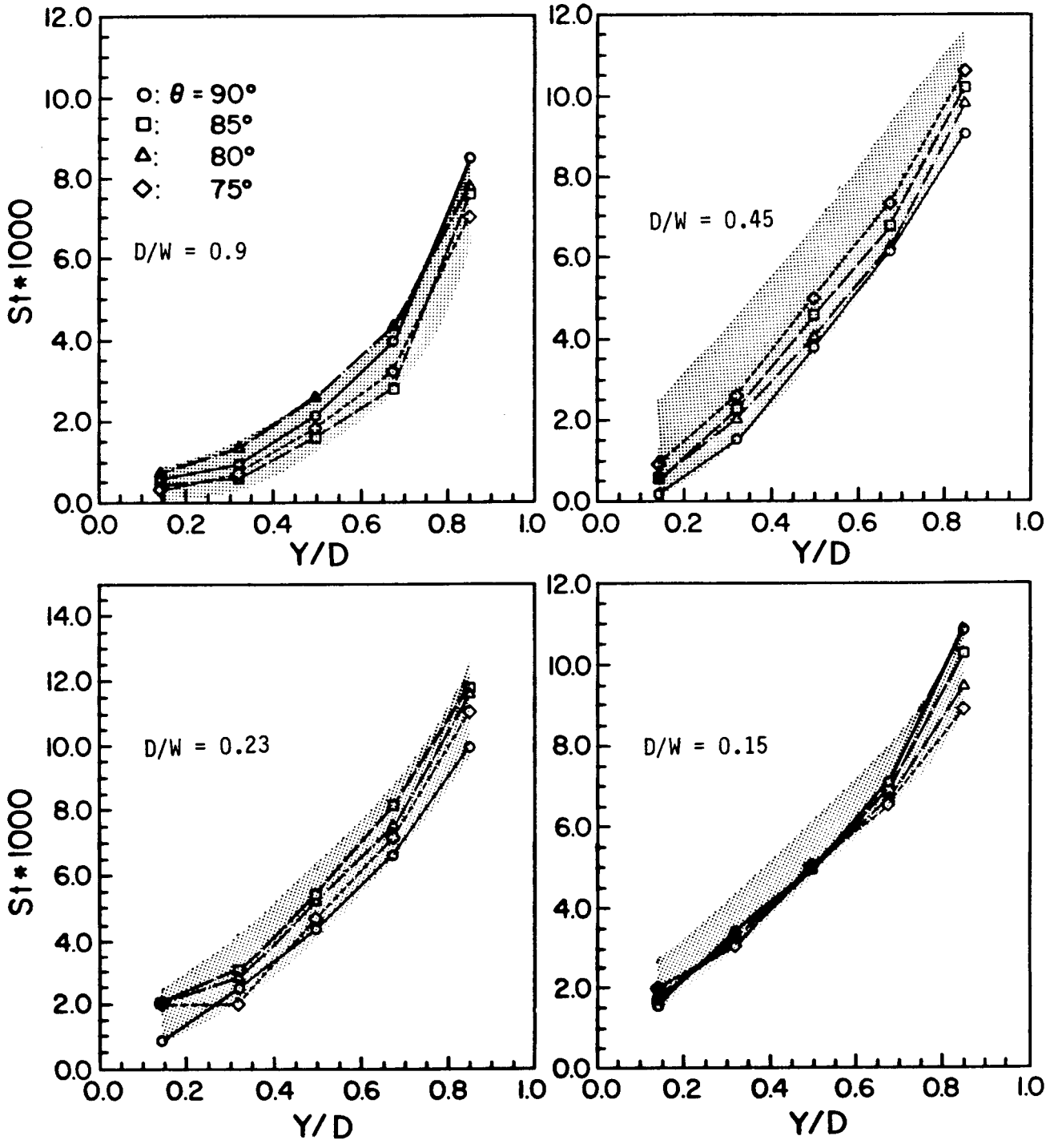

FIGURE 6. Local Mass Transfer Distribution on Cavity Downstream Side-Wall, (Z/D = 0)

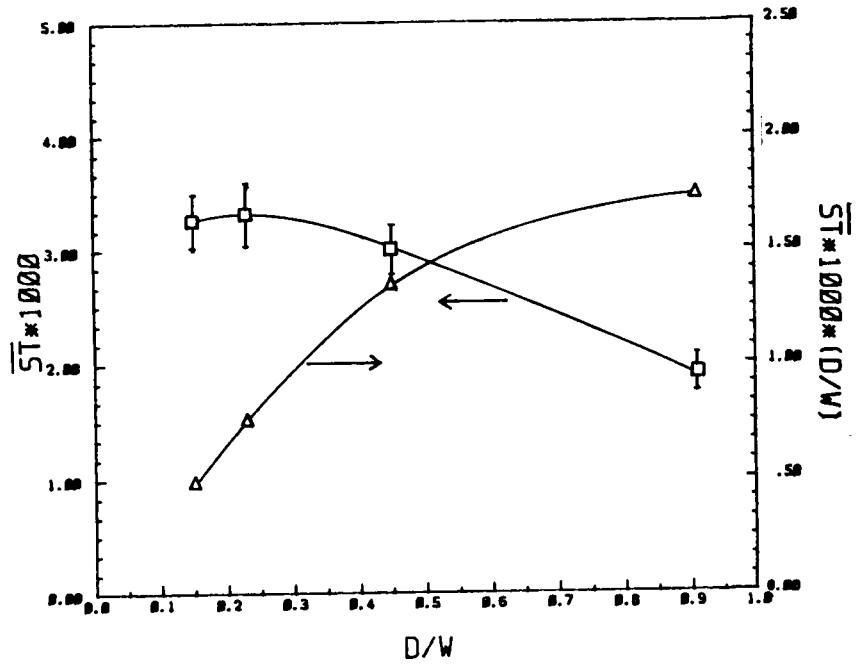

FIGURE 7. Area-Averaged Mass Transfer

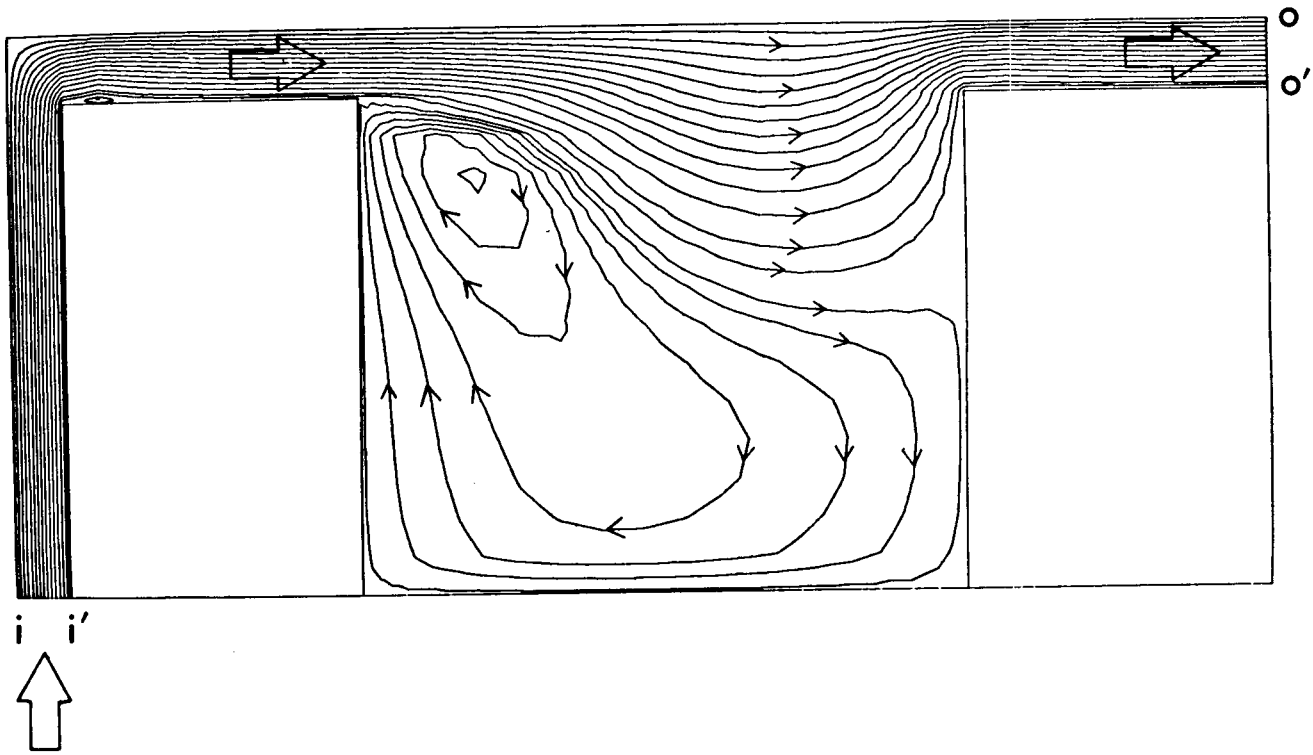

FIGURE 8. Computed Streamline Pattern;
C/W = 0.1, D/W = 1.0, Re_c = 2.0 x 10^4.

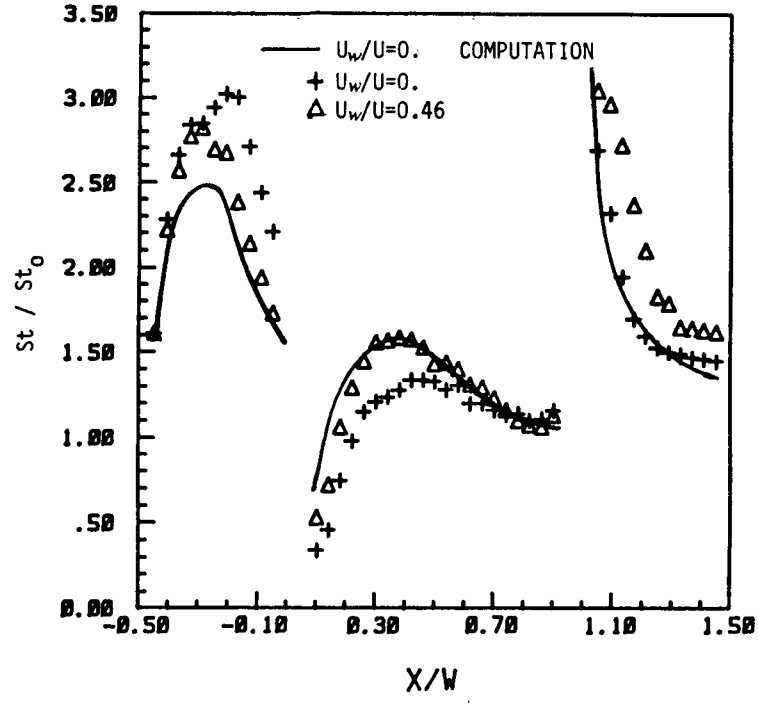

(a). D/W = 0.1

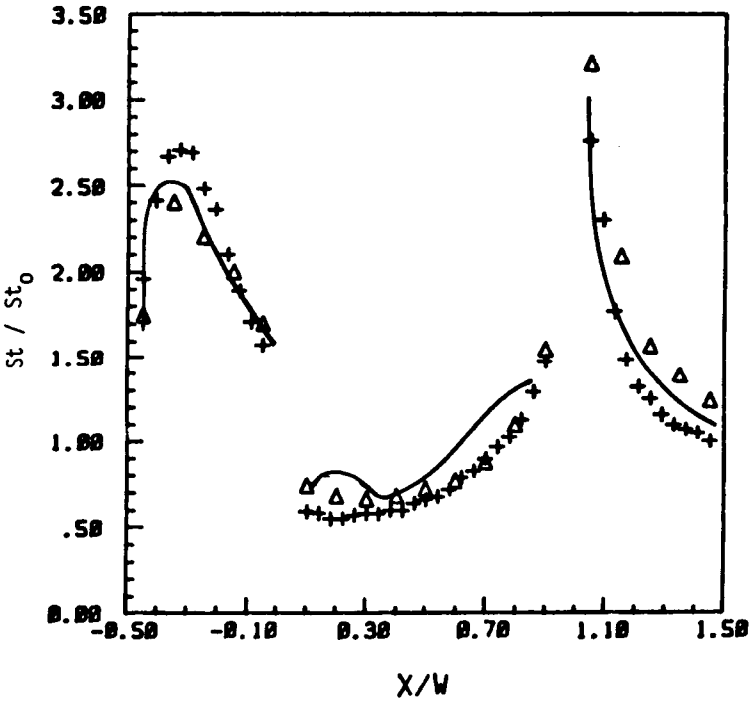

(b). D/W = 0.5

FIGURE 9 Local Mass Transfer; C/W = 0.14, Re_c = 2.0 x 10^4

TWO- AND THREE-DIMENSIONAL TURBINE BLADE ROW FLOW FIELD SIMULATIONS*

R.C. Buggeln, W.R. Briley, H. McDonald
S.J. Shamroth, and B.C. Weinberg
Scientific Research Associates, Inc.
Glastonbury, Connecticut

A major problem area associated with the successful design and operation of modern gas turbine engines is the turbine. This section represents a considerable challenge to both the design and research engineer as it contains significant regions of complex three-dimensional flows which include both aerodynamic and heat transfer phenomena. As a result, the turbine section has been the object of extensive investigation via both analysis and experiment. The present paper discusses work performed to date by Scientific Research Associates under the NASA HOST program in the numerical simulation of turbine passage flows via a Navier-Stokes appproach. The paper is a summation of the work performed between 1984 and 1987. This work includes both laminar and turbulent simulations in both two and three dimensions. An outline of the approach and background as well as an overview of the results follow.

APPROACH AND BACKGROUND

The present approach solves the ensemble-averaged Navier-Stokes equations via the Linearized Block Implicit (LBI) technique of Briley and McDonald (Ref. 1). Boundary conditions for subsonic inflow and outflow (the usual case) set upstream stagnation pressure, upstream stagnation temperature, upstream flow angle and downstream static pressure. Additional conditions used are density derivative on the inflow (upstream boundary), and velocity and temperature second derivatives on the downstream boundary. On the cascade blade, no-slip conditions and a zero normal pressure gradient condition are applied along with either a specified temperature or a specified heat transfer rate. In general, the first grid point off the wall is taken so as to place a point in the viscous sublayer. The governing equations are written in general tensor form and solved in a body-fitted coordinate system. The procedure can be used either for laminar or turbulent flow. When used for turbulent flow either a mixing length model or a two-equation, $k-\varepsilon$, model is available. Transition can be modeled either through the $k-\varepsilon$ equation or via a specified transition location. Details of the governing equations, numerical techniques, grid construction, turbulence model, etc. are given in References 2-4.

*The work presented here has been performed under NASA Contract NAS3-24358 and NAS3-23695. Work under the latter contract was performed under subcontract to Allison Gas Turbine Operations.

INITIAL C3X - "O"-GRID RESULTS STUDIES

The computational efforts pursued under this program all considered the Allison C3X turbine cascade configuration. A computer generated plot of this configuration with an O-type computational grid is shown in Figure 1. This coordinate system consists of 30 points in the pseudo-radial direction and 120 points in the pseudo-azimuthal direction. The upstream boundary is placed at 2.25 axial chords upstream of the leading edge and the downstream boundary is placed at 2.65 axial chords downstream of the trailing edge. High radial resolution is obtained near the surface of the blade, with the first coordinate line located at a distance of 1.0×10^{-6} axial chords from the surface which is within the turbulent boundary layer viscous sublayer. In addition, high pseudo-azimuthal resolution is obtained at both leading and trailing edges.

Calculations made with the SRA procedure using this grid are shown in Figure 2. The case was run with flow parameters corresponding to test case 144 of Reference 5. The parameters were a ratio of upstream total to downstream static pressure of 1.66, an exit Mach number of 0.90, an exit Reynolds number of 2.43×10^{6}, a ratio of average blade surface temperature to inlet gas total temperature of 0.75 and an average inlet turbulence intensity of .065. Figure 2 shows a comparison between data, the present Navier-Stokes approach and the inviscid approach of Delaney (Ref. 6). There is excellent agreement between the present calculations and the experimental data. Mixing length and k-ε two-equation turbulence models were employed, and (as expected) the result of calculations indicate very little difference in the prediction of the pressure coefficient. Due to the small viscous displacement effect, the inviscid calculations show close agreement with the present computed results. Also shown in this figure are the data from cases 148 and 158, which were run under nominally identical conditions (cf. Ref. 5) to indicate the relationship between the calculations and the experimental scatter.

In Figure 3 the distribution of the computed heat transfer coefficient is shown for case 144 with both film-cooling and non-film-cooling options. For the non-film cooling option, with the local surface temperature distribution given in Reference 5, a mixing length turbulence model in conjunction with a transition model was employed for which laminar flow was assumed in the region $x/c_x < 0.2$ followed by a transitional zone and thereafter by fully turbulent flow. The predictions obtained with the model compare very well with the experimental data taken with no film-cooling present. Following this initial calculation, the film-cooling option in the code was activated with air injected at 30° to the suction side over $0.8 < x/c_x < 0.9$ at a velocity of 7% of freestream. The local surface temperature was kept fixed at the same value as the non-film-cooling option. Although no data is available for comparison, the calculation does demonstrate the effect of film-cooling. From the onset of injection to the trailing edge the heat transfer rate drops to nearly zero. This behavior is a consequence of the buffer region of constant temperature cool gas which protects the blade surface from the hotter fluid in the cascade passage. The comparison of the pressure distribution for both film cooling and non-film-cooling options is shown in Figure 4. The effect of blowing on the pressure distribution is clear; i.e. the adverse pressure gradient that is generated, the resulting upstream influence, and the subsequent favorable pressure gradient that follows.

Following the two-dimensional calculations, a demonstration three-dimensional calculation was performed. A rectilinear cascade with the C3X geometry was assumed and a grid consisting of 100×25×15 points was used. For this demonstration case laminar conditions were assumed. The height of the blade above the endwall (to the symmetry plane, midspan) was set to be one axial chord, while the inlet boundary layer thickness was 20% of that value. In Figure 5, the velocity vector plots are presented for the forward portion of the C3X cascade at two different planes above the endwall. Very near the endwall (within 2.95% spanwise plane) a saddle point exists as indicated in the picture. This saddle point moves toward the leading edge and disappears beyond 2.95% spanwise plane. A stagnation point forms on the nose of the blade surface beyond 2.95% spanwise plane.

CONVERGENCE STUDIES

An important aspect of a practical Navier-Stokes calculation procedure for flows in which a steady solution is sought is that of rate of convergence to steady state. Rate of convergence to steady state and run time per time step or iteration determine run time to convergence. This run time determines the practicality of the procedure for use on a regular basis. Therefore, under the HOST effort a study of the existing convergence rate of the SRA procedure was undertaken.

The initial test case chosen for the convergence study was the Turner turbine cascade (Ref. 7). The convergence study calculation was run with a 'C' grid containing 113 pseudo-azimuthal grid points and 30 pseudo-radial grid points. High wall resolution was obtained with the first point off the wall being approximately 1.5×10^{-5} chords from the blade surface. In regard to convergence, several criteria can be considered. These include surface pressure distribution, maximum normalized residual and pressure coefficient at the stagnation point. In regard to these factors, it should be noted that in the present calculations it is the converged steady state flow field which is the item of interest. Therefore, although the current numerical procedure solves the unsteady flow equation, it is not necessary and, in fact, is uneconomical to obtain a time-accurate solution when seeking steady state solutions. Instead, matrix preconditioning techniques are used to obtain a converged solution as rapidly as possible. In these studies, the calculation was initiated from a very simple flow field in which the velocity magnitude and static pressure were set to constant throughout the flow with the velocity flow angle a function of axial location. Very simple profiles were used near the blade surface to bring the velocity to the no-slip condition.

A plot showing the maximum normalized flow residual is presented in Figure 6. The residual is defined as the imbalance of all steady terms and is normalized by the residual at the first time step. As can be seen, the maximum residual drops slightly over 4 orders of magnitude in 150 time step iterations and then levels. In general, based upon previous experience, three orders of magnitude drop in residual gives convergence suitable for many engineering applications. However, in addition to monitoring the residual behavior it is necessary to consider the flow field dependent variable behavior. Based upon experience, one sensitive item is the pressure coefficient at the stagnation point where C_p is taken as $(p-p_{ref})/\frac{1}{2}\rho_{ref}q^2_{ref}$.

The reference quantities are taken from the inflow boundary and consequently, since only total pressure, total temperature and flow angle are specified, these may vary with time. The results show the variation of stagnation point C_p with time-step iteration number. The calculation was run with an inflow Mach number of approximately 0.24; on an inviscid basis this should lead to a stagnation point C_p of 1.015. The present results converge to a value of approximately 1.005 for the Navier-Stokes simulation. As can be seen in Figures 7 and 8, the stagnation point C_p was obstensibly converged at 100 time steps although some slight oscillations occurred until 150 time steps.

The next set of convergence studies focused upon the C3X grid. Again a C-grid configuration was used. Convergence history results for a two-dimensional laminar calculation are given in Figure 9. As can be seen, the residual drops five orders of magnitude in 150 time steps. It is also of interest to note that doubling the number of grid points did not significantly effect the convergence rate. The convergence rate for the three-dimensional case is shown in Figure 10. Again, rapid convergence is obtained. A study of the two-dimensional turbulent C3X case is shown in Figure 11. The results shown in Figures 6-11 clearly indicate the rapid convergence attainable with the present procedure and its potential for use as an engineering tool.

FURTHER C3X CALCULATIONS

The last set of calculations performed to date consist of laminar and turbulent simulations for both two- and three-dimensional C3X configurations. Calculations were performed on a C-type computational grid. Both mixing length and two-equation turbulence models were utilized. Mach number contours are shown in Figure 12 for laminar and turbulent flow. The main difference in these cases is that the shear layers are very thin in the turbulence case and much thicker in the laminar case. Other typical results are shown in Figures 13 and 14 which show results for two-dimensional simulations using a two-equation $k-\varepsilon$ model. Calculations were also performed for three-dimensional simulations. Typical grids in a given plane parallel to the endwall are shown in Figure 15. Figure 16 presents velocity vectors in a plane adjacent to the endwall; the appearance of the saddle points is clearly evident. Velocity vector plots for surfaces normal to the endwall are shown in Figure 17.

SUMMARY AND CONCLUSIONS

Under the HOST effort, SRA has further developed and applied a cascade Navier-Stokes analysis to the turbine blade row problem. Calculations have been performed in two and three dimensions for both laminar and turbulent flow. Comparisons made with data for surface pressure and surface heat transfer distribution showed good agreement. The computed three-dimensional flows showed the physically expected flow features. Calculations required relatively short run times to convergence. Two-dimensional calculations for 3500 grid points required approximately 60 CPU secs of CRAY-XMP time whereas three-dimensional calculations for 170,000 grid points required approximately 2.5 hours of CRAY CPU time. Clearly, the two-dimensional analysis can be used on a regular engineering basis. Although run times for the three-dimensional calculation preclude daily use, they are still short enough to allow the three-dimensional analysis to be used as a design tool in conjunction with two-dimensional analyses, more approximate three-dimensional analyses and experiments.

REFERENCES

1. Briley, W.R. and McDonald, H.: Solution of the Multidimensional Compressible Navier-Stokes Equations by a Generalized Implicit Method. Journal of Computational Physics, Vol. 24, 1977, p. 372-397.

2. Shamroth, S.J., McDonald, H. and Briley, W.R.: Prediction of Cascade Flow Fields Using the Averaged Navier-Stokes Equations. ASME Journal of Engineering Gas Turbines and Power, Vol. 196, 1984, pp. 383-390.

3. Yang, R.-J., Weinberg, B.C., Shamroth, S.J. and McDonald, H.: Numerical Solutions of the Navier-Stokes Equations for Two- and Three-Dimensional Turbine Cascades with Heat Transfer. SRA Report R85-310004-F, 1985.

4. Weinberg, B.C., Yang, R.-J., McDonald, H. and Shamroth, S.J.: Calculations of Two- and Three-Dimensional Transonic Cascade Flow Fields Using the Navier-Stokes Equations. ASME Paper 85-GT-66, 1985.

5. Hylton, L.D., Mihelc, M.S., Turner, E.R., Nealy, D.A. and York, R.E.: Analytical and Experimental Evaluation of the Heat Transfer Distribution Over the Surface of Turbine Vanes. NASA-CR-168015, May 1983.

6. Delaney, R.A.: Time Marching Analysis of Steady Transonic Flow in Turbomachinery Cascades Using the Hopscotch Method. ASME Journal of Engineering for Power, Vol. 105, 1983, pp. 272-279.

7. Turner, A.B.: Local Heat Transfer Measurements on a Gas Turbine Blade. Journal of Mechanical Engineering Sciences, Vol. 13, 1971.

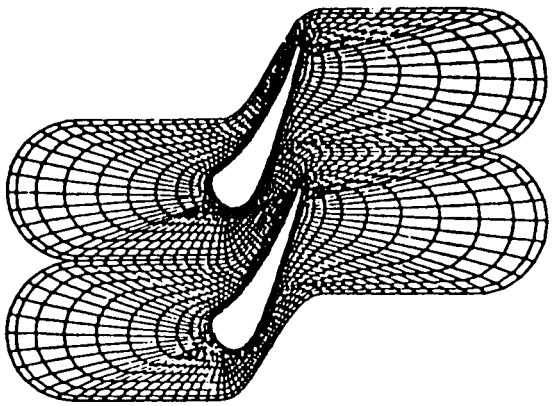

Fig. 1 C3X Turbine Blade "O"-Grid Mesh.

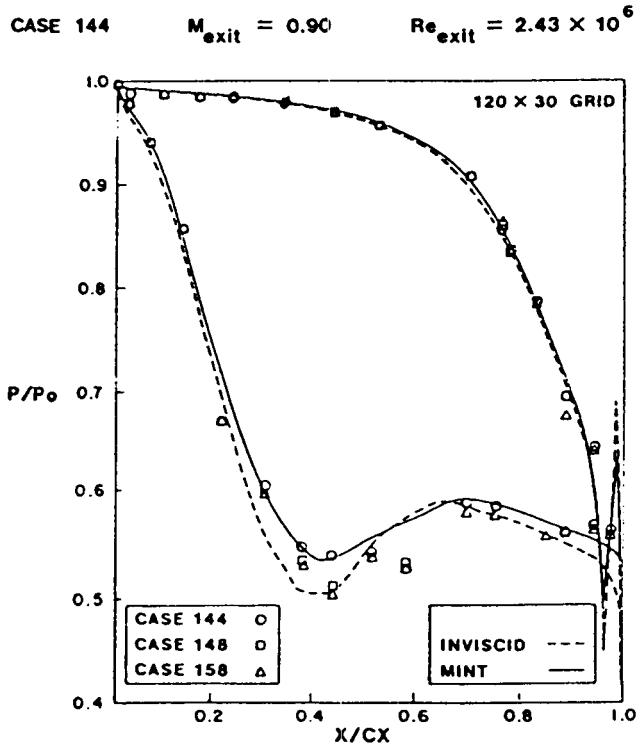

Fig. 2 Pressure Coefficient Distribution.

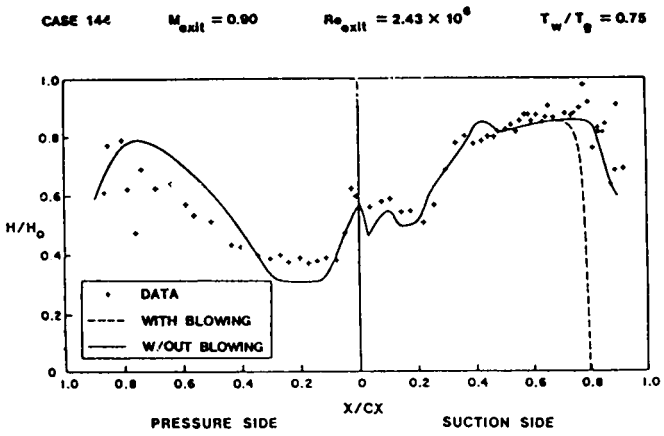

Fig. 3 Heat Transfer Coefficient.

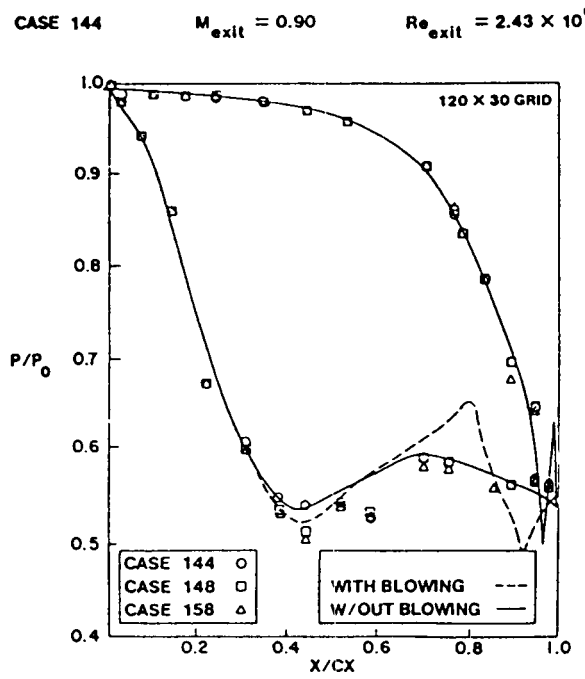

Fig. 4 Pressure Coefficient Distribution.

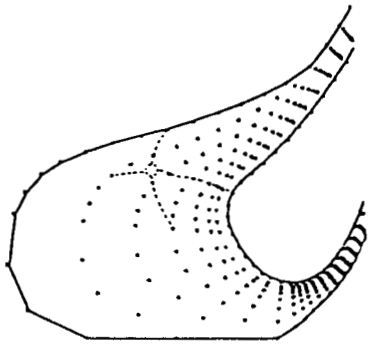

(a) VECTOR PLOT ON 0.135% SPANWISE PLANE

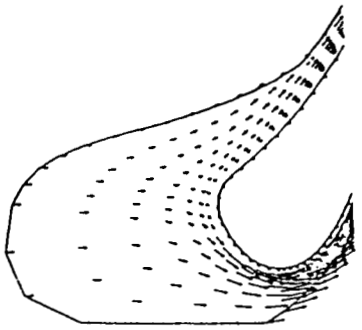

(b) VECTOR PLOT ON MIDSPAN PLANE

Fig. 5

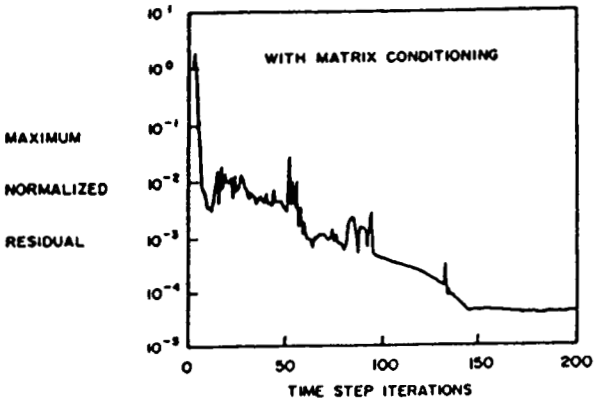

Fig. 6 Convergence Rate.

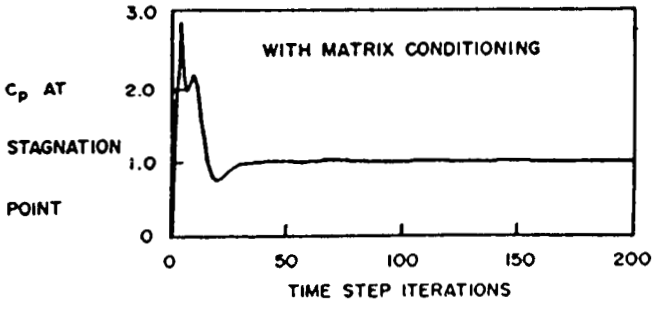

Fig. 7 Convergence of Pressure at Stagnation Point.

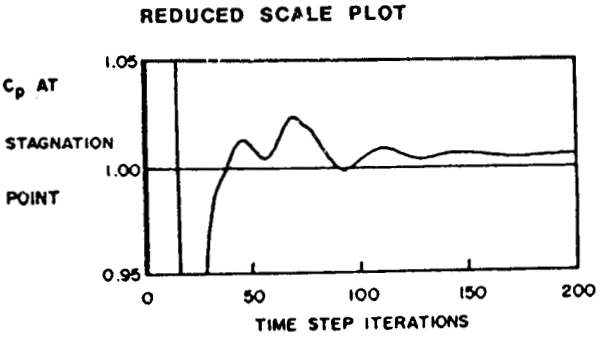

Fig. 8 Convergence of Pressure at Stagnation Point.

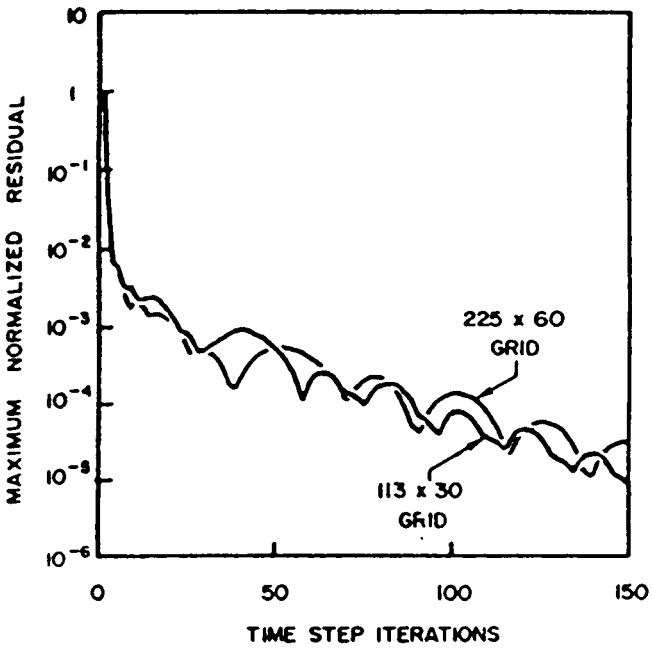

Fig. 9 Convergence Behavior, C3X Laminar 2-D Cascade.

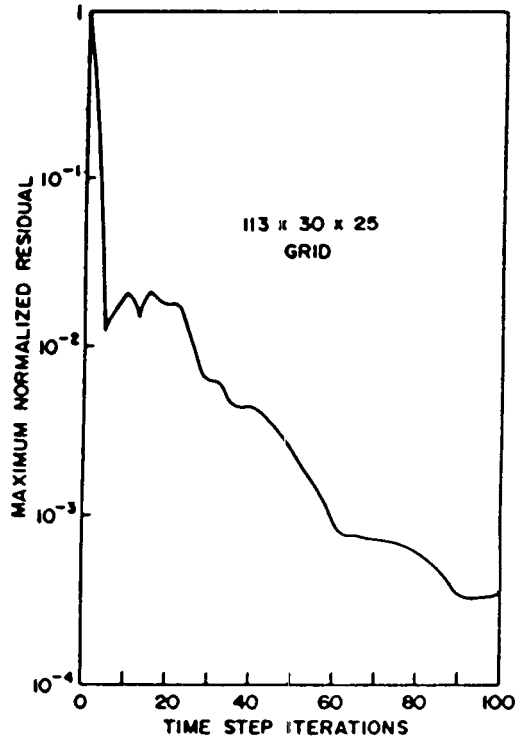

Fig. 10 Convergence Behavior, C3X Laminar 3-D Cascade.

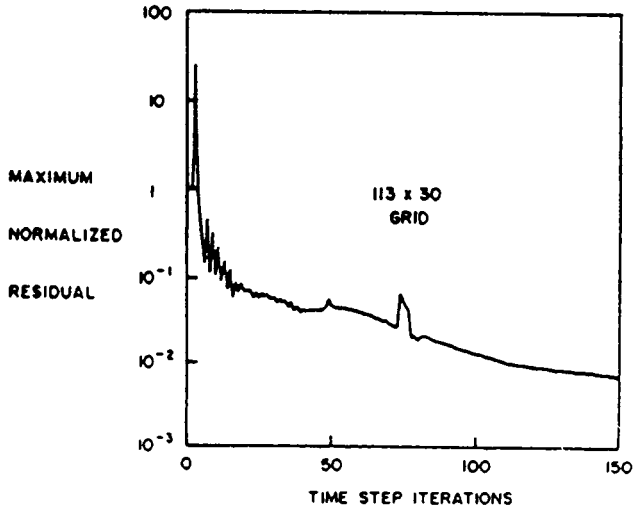

Fig. 11 Turbulent C3X Cascade.

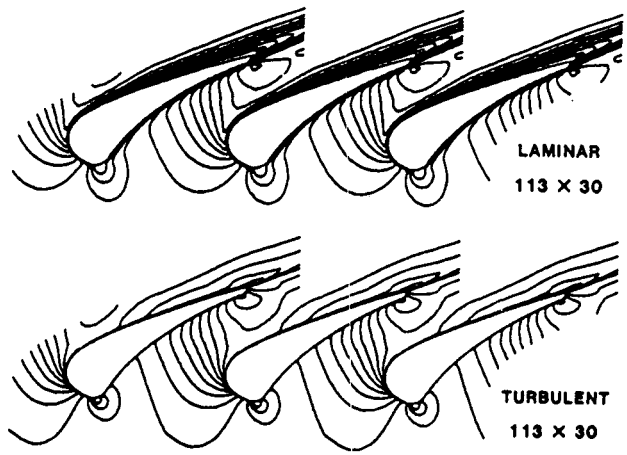

Fig. 12 C3X Cascade Mach Number Contours.

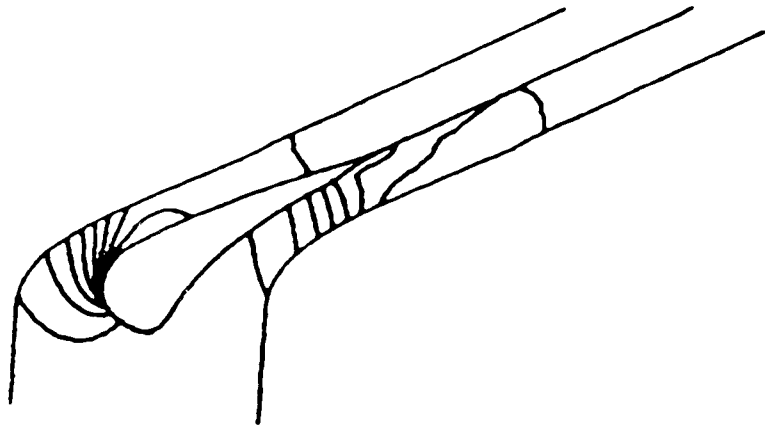

Fig. 13 Pressure Contours, C3X Cascade, Turbulent Flow, k-ε Model.

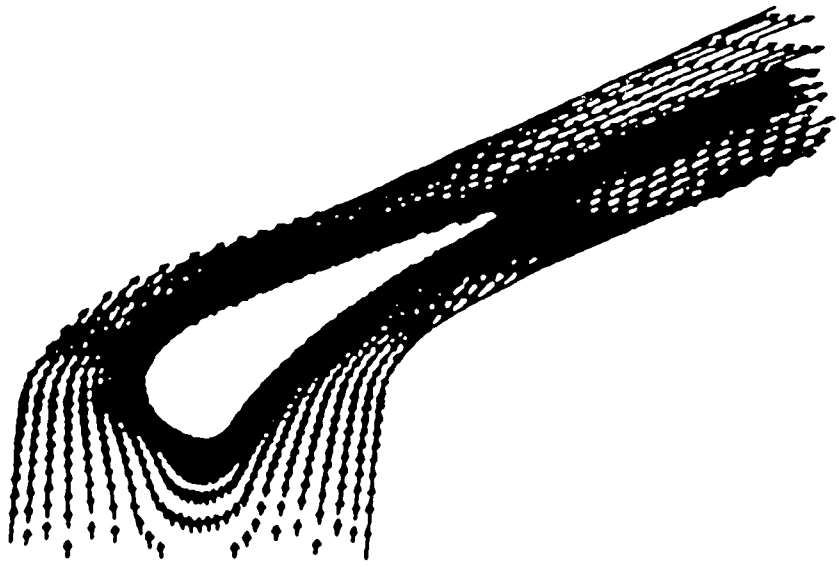

Fig. 14 Velocity Vectors, C3X Cascade, Turbulent Flow, k- ε Model.

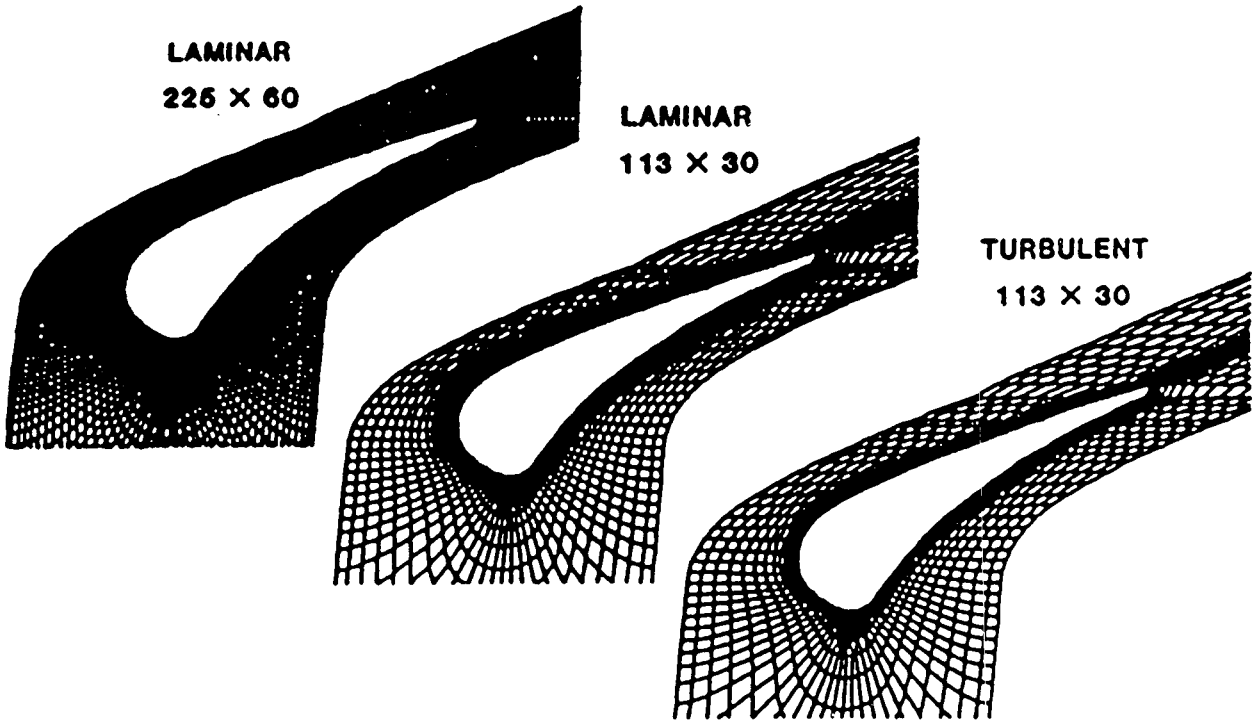

Fig. 15 C3X Grid for Three-Dimensional Calculation.

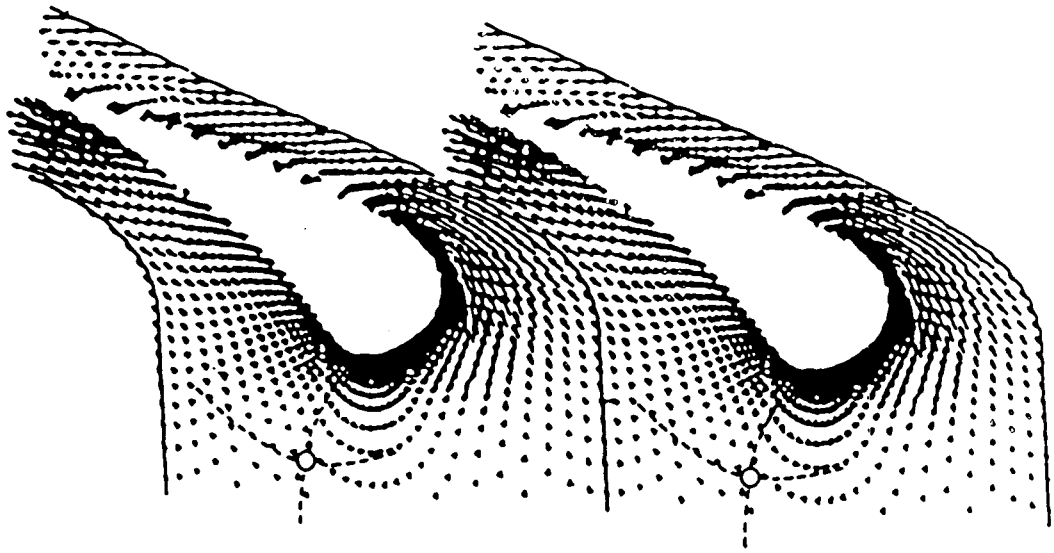

Fig. 16 C3X Three-Dimensional Calculation, Velocity Vectors in Plane Adjacent to Endwall.

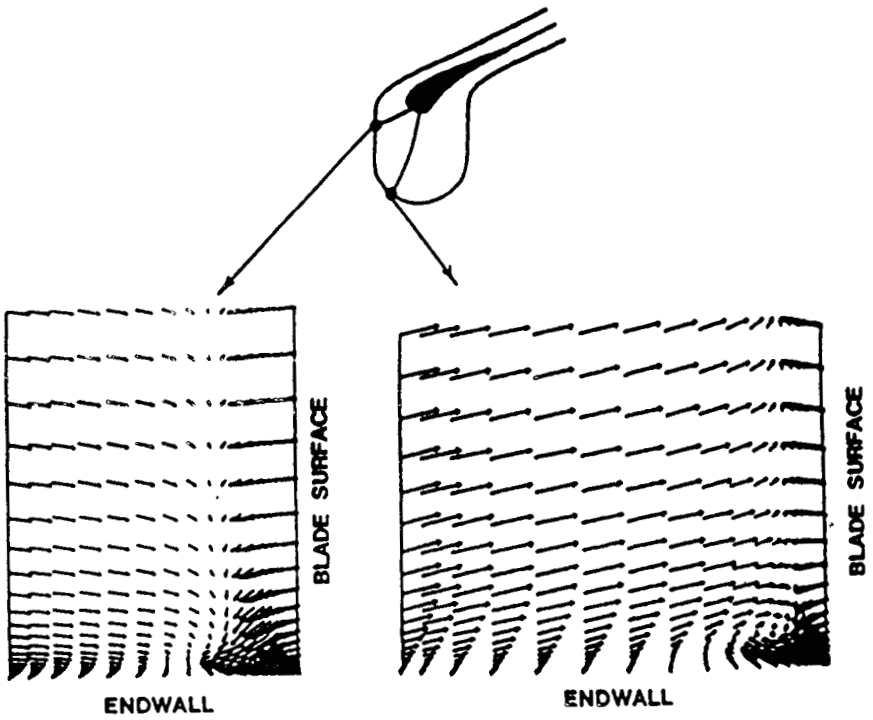

Fig. 17 C3x Three-Dimensional Calculation, Stagnation Region.

COOLANT PASSAGE HEAT TRANSFER WITH ROTATION*

T.J. Hajek
Pratt & Whitney Division
United Technologies Corporation
East Hartford, Connecticut

and

J.H. Wagner and B.V. Johnson
United Technologies Research Center
East Hartford, Connecticut

In current and advanced gas turbine engines, increased speeds, pressures and temperatures are used to reduce specific fuel consumption and increase thrust/weight ratios. Hence, the turbine airfoils are subjected to increased heat loads, escalating the cooling requirements to satisfy life goals. The efficient use of cooling air requires that the details of local geometry and flow conditions be adequately modeled to predict local heat loads and the corresponding heat transfer coefficients.

Improved turbine airfoil local temperature and hence, life predictions can be realized by accurately accounting for the effects of rotation on internal cooling. Although the effects of rotation, which give rise to Coriolis and buoyancy forces can be large, they are currently not adequately included in the heat transfer designs of blades. Experimental data is particularly needed for the higher Rayleigh and Reynolds number conditions that are characteristic of turbine airfoil cooling passages. This data is crucial for development of design correlations and for the verification of computer codes. Accurate prediction of local heat transfer coefficients will enable the designer to optimize cooling configurations and to minimize both metal temperature levels and thermal gradients. Consequently, blade life and engine efficiency can be significantly improved.

OBJECTIVE

The objective of this 36-month experimental and analytical program is to develop a heat transfer and pressure drop data base, computational fluid dynamic techniques and heat transfer correlations for rotating multipass coolant passages, with and without flow turbulators. The experimental effort is focused on the simulation of configurations and conditions expected in the blades of advanced aircraft high pressure turbines. With the use of this data base, the effects of Coriolis and buoyancy forces on the coolant side flow can be included in the design of turbine blades.

EXPERIMENTAL MODEL

The heat transfer model features a four pass serpentine arrangement, designed to reflect the coolant passages within a gas turbine blade. For the experiments, the model was fitted with smooth walls on all four walls or with skewed turbulators on two walls, as indicated in figure 1.

* NASA Contract NAS3-23691

Figure 2 shows a schematic diagram of the model with the instrumentation and wall sections indicated. Heat transfer coefficients are obtained for each wall section element. These wall elements, numbered 1 to 64, consists of a copper block backed with a thin film electrical resistance type heater and instrumented with two thermocouples. The copper wall sections are 10.7 mm. x 49.3 mm. (0.42 in. x 1.94 in.). Each section is thermally isolated from the adjoining section by a 1.5 mm. (0.060 in.) thick divider strip of low thermal conductivity G-11 composite material. The straight radial passages have a square cross section, 12.7 mm. x 12.7 mm. (0.5 in. x 0.5 in.).

DATA ACQUISITION AND REDUCTION

Sixty (60) experiments have been conducted to isolate the effects of rotation rate, flow rate, coolant-to-wall temperature variations, radial location and passage angle on heat transfer from the smooth and skewed trip models. These heat transfer experiments have been conducted with all the wall segments at a constant temperature. The data consists of measurements of thermocouple emf and heater power for each heated element. Engineering results are obtained with an analysis code and then printed in tabular form.

An energy balance is performed to determine the heat transfer characteristics for the model at each experimental condition. The energy convected to the coolant is determined by subtracting the energy lost through the power leads and the energy lost through the conduction from the backside of each element. The bulk-mean coolant temperature for a particular location in the passage is determined by summing the energy contributions from each element. The temperature increase from the inlet location is then calculated using simple thermodynamic relationships. The heat transfer coefficient is calculated with the local coolant and wall temperatures and the local net energy (or heat) flux.

A more complete description of the acquisition/analysis procedure is provided in the 1986 HOST report.

RESULTS

The heat transfer experiments with the smooth wall model and the 45-deg skewed trip rough wall model were completed prior to the previous HOST conference. Detailed analysis of results has continued throughout the past 12 months. The heat transfer characteristics of the flows in the first outward flow leg and the inward flowing leg are compared in this report. The effects of model orientation are also discussed.

The variations of heat transfer ratio, Nu/Nu_∞, from the leading and trailing surfaces with rotation parameter, $(\Omega d/V)$, are presented for the first and second leg in figure 3. The ΔT noted on the figure refers to the temperature difference between the coolant (at the inlet to the first leg) and the walls. The local ΔT's in the second leg of the rough wall model are 40 to 50 percent of the inlet ΔT due to the increase in fluid bulk temperature in the two legs and the first turn. Note that the heat transfer varies with both the rotation rate and the inlet-air-temperature to wall-temperature difference, ΔT. For all the data shown, the heat

transfer increases or remains constant with increasing ΔT. The magnitude of the increase, ΔNu, can be as large or larger for the rough wall model as it is for the smooth wall model (trailing surfaces for all segments shown). However, the percent changes are generally smaller for the rough wall model because the heat transfer level is higher. Note also that large increases and decreases in the heat transfer occurred due to variations in the rotation parameter. The most dramatic decrease with increasing rotation occurred for the rough walls on the leading surface of the first leg (with outward flow). The third principal feature of these results is that the effects of temperature difference generally increase at larger values of the rotation parameter, $\Omega d/V$. For both the smooth wall model and the rough wall model, the heat transfer was independent of ΔT at zero rotation. This result at zero rotation was consistent with previous studies. In view of the three previous observations, it was concluded that the rotation heat transfer results could not be correlated with only the rotation parameter.

The variation of the heat transfer ratio with the buoyancy parameter, $(\Delta\rho/\rho)(\Omega H/V)(\Omega d/V)$, is shown in figures 4a-f. The solid lines in the figure connect the heat transfer results from the experiments where the temperature difference between the inlet coolant and the wall were the largest. The dotted lines connect the results for experiments with similar rotation parameters but different inlet air to wall temperature differences, ΔT. In general, the heat transfer for any location on the high pressure side of the coolant passages is well correlated by the buoyancy parameter. The high pressure sides are the trailing side for flow outward and the leading side for flow inward. The secondary flow patterns generated by Coriolis forces are characterized by a redirection of the flow from the core of the passage toward the high pressure side of the passage. Note that the heat transfer ratio on the high pressure side of the outward flowing leg for both models does not change appreciably with streamwise location at higher values of the buoyancy parameter. The heat transfer from the high pressure side of the inward flowing leg decreases monotonically with increasing streamwise location.

In the second leg (figs. 4d-f), the flow direction and the buoyancy force are in the same direction. In this passage leg, the heat transfer is substantially decreased compared to that from the first leg. This decrease may be due to the change in the turbulent structure near the wall when the flow direction changes from the opposing-the-buoyance-force direction to the coinciding-with-the-buoyancy force direction.

The buoyancy parameter does not correlate the heat transfer results from the low pressure side of the passage as well as those from the high pressure side. For the first segment (fig. 4a), the heat transfer ratio on the low pressure side is a function of both rotation rate (different symbols) and the temperature difference (different flags). Note that the relative variation of heat transfer ratio with ΔT (at fixed rotation number) are greater for the smooth wall than the rough wall. The heat transfer ratios for the leading surface appear to have a maximum value for each rotation number. The locus of the maximum heat transfer ratios for each rotation number appears to be a function of the buoyancy parameter. The heat transfer ratio distributions from the skewed trip leading surface for fixed rotation numbers have shapes similar to the heat transfer ratio distributions for the smooth leading surface. At the downstream segment in

the first leg (fig. 4C), the heat transfer ratio for the smooth wall becomes well correlated by the buoyancy parameter. The correlation of the leading surface smooth wall results at the end of the first leg suggests that correlation of the results may be related to the hydrodynamic or thermal development of the flow. Heat transfer results from the inward flowing leg show similar variations of heat transfer ratio with temperature difference and rotation parameter. The decrease in the temperature dependence on the heat transfer ratios between the first and second legs is attributed in part to the decrease in the local ΔT as the flow.

Comparison of the heat transfer ratios from the smooth and skewed trip models show that, at zero rotation rate (zero buoyancy parameter), the heat transfer ratio from the smooth wall and skewed trip models is determined by the geometry of the coolant passages (i.e. smooth surfaces produce low heat transfer coefficients and surfaces with skewed trips produce high heat transfer coefficients). For large buoyancy parameters, the leading and trailing surface heat transfer distributions from the end of the first leg for both the smooth wall and skewed trip models asymptotically approach their respective levels. Half of the difference in the heat transfer ratio between the smooth wall and the skewed trip models for large buoyancy parameters on the trailing surface of the first leg can be attributed to the ratio of the actual surface area compared to the projected area used in the calculation of the heat transfer coefficients. In the outward flowing leg at a large value of L/d, the rotational buoyancy dominates the heat transfer more than the surface roughness at large (i.e. greater than 0.6) values of the buoyancy parameter.

Effect of Model Orientation

Heat transfer experiments with rotation were completed with both the smooth and skewed trip model oriented at α=45 degrees from the normal position. The model was rotated 45 degrees about the radial centerline such that the inlet of the model was trailing the centerline of the model. This orientation was selected to model the coolant passages in a turbine blade with a trailing edge root feed. The heat transfer ratios around the perimeter of the coolant passage for each streamwise location in the first passage are shown in figures 5 and 6. The model orientation and rotation direction are noted on each figure. Results from the smooth wall model have been connected with a continuous line because the model is symmetrical (fig. 5). However, the skewed trip results (fig. 6) are connected to show only the changes in heat transfer on each of the four walls from one orientation to the next. The heat transfer results for the smooth wall model show a symmetrical pattern around the perimeter of the passage. At α=45 deg, the two leading surfaces have approximately the same heat transfer ratio as the one leading surface for α=0. Likewise, at α=45 deg, the two trailing surfaces have approximately the same heat transfer ratios as the trailing surface for α=0 deg.

The heat transfer results for the skewed trip model (fig. 6) indicate an asymmetry in the heat transfer around the perimeter of the coolant passages due to the presence of the skewed trips. For this reason, the results are not connected around the perimeter as they were for the smooth wall results. Note that the heat transfer ratio is significantly larger for the sidewall surface on the bottom of each plot than that for the side wall surface on the top of each plot for segments B, C and D. These

"bottom" sidewall locations are located on the "downstream" end of the trips (see fig. 2, surfaces 2-4). The heat transfer is increased on the "downstream" surfaces due to the redirection of the main core flow along the skewed trip to these surfaces. The heat transfer ratio from the last "downstream" sidewall segment is the largest because of the development of trip generated secondary flow. In general, the heat transfer from the first leg of the skewed wall model was affected less by the change in orientation from $\alpha = 0$ to 45 deg than the heat transfer from the smooth wall model.

Streamwise location of test sections identified by A to R.
All four test section surfaces for streamwise locations A through R are heated.

- - - - - Leading test section surfaces

——— Trailing test section surfaces

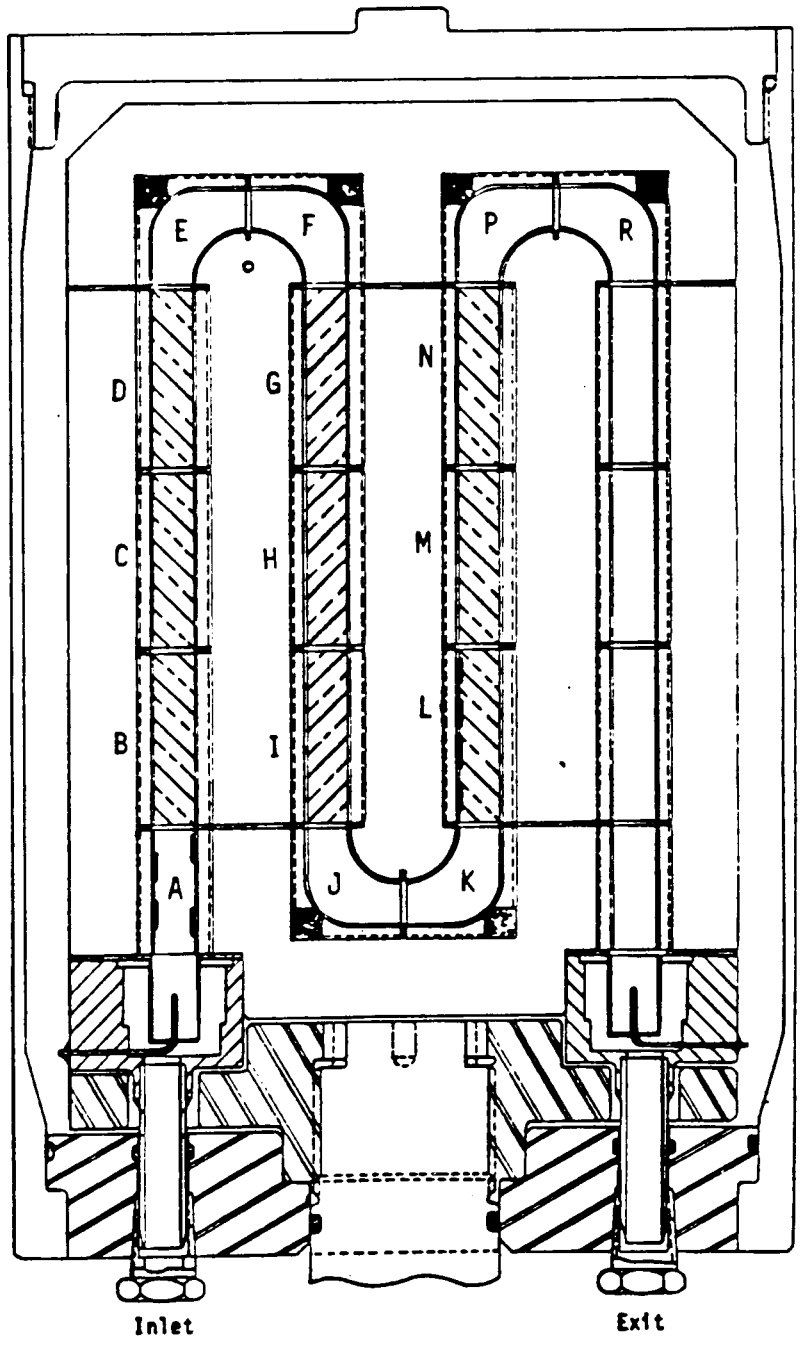

Figure 1 Cross Sectional View of Coolant Passage Heat Transfer Model Assembly With Skewed Trip Rough Walls

TEST SECTION ELEMENT IDENTIFICATION
SURFACES 1-32 ARE ON SIDE WALLS PERPENDICULAR TO VIEW SHOWN
SURFACES 33-48 ARE ON "+Ω" LEADING PLANE
SURFACES (49)-(64) ARE ON "+Ω" TRAILING PLANE
PRESSURE MEASUREMENT LOCATIONS [1] – [16]

NOTE EACH TEST SECTION SURFACE IS INSTRUMENTED WITH TWO THERMOCOUPLES

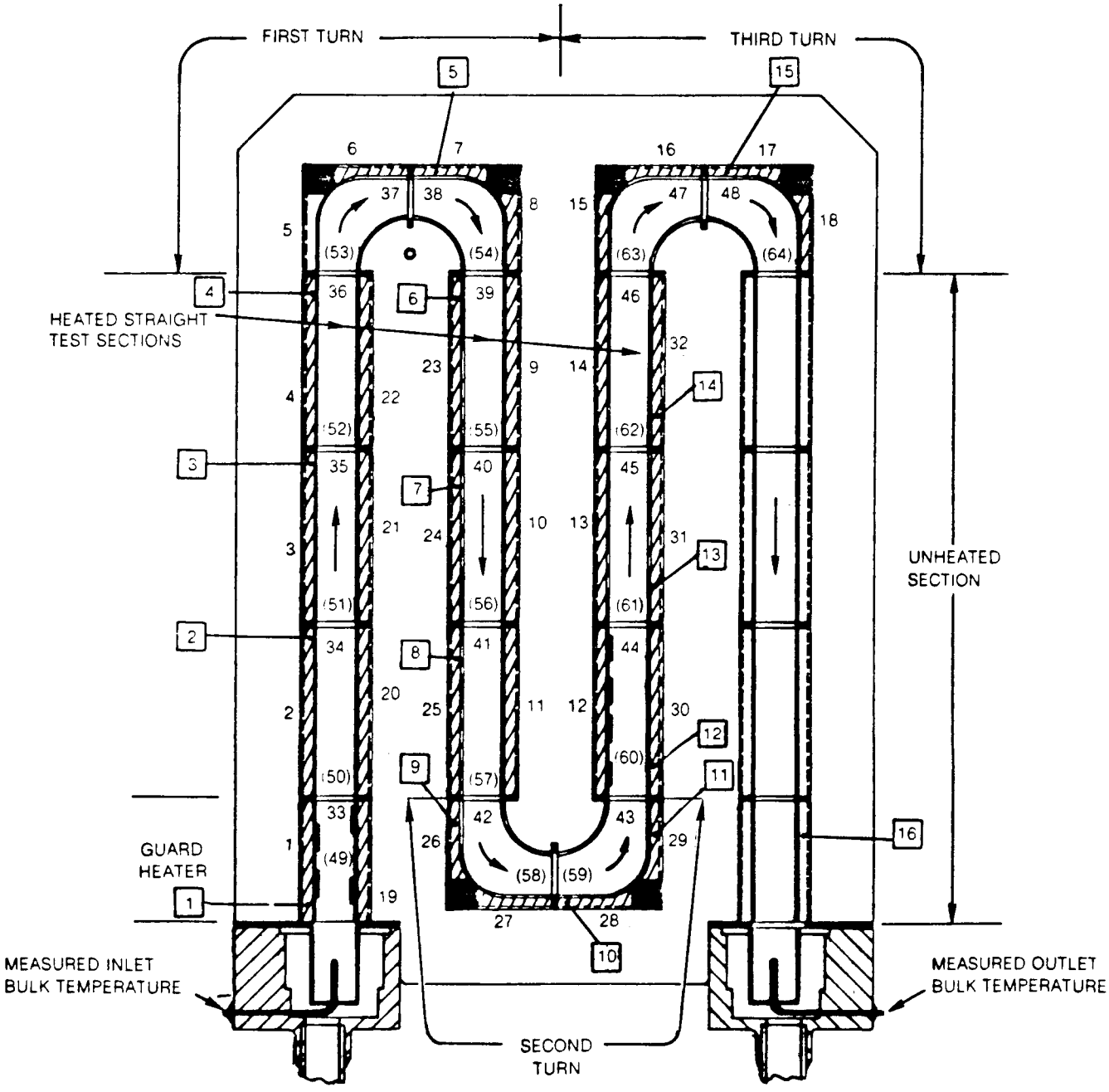

Figure 2 Instrumentation Plan for Coolant Passage Heat Transfer Model

Re = 25,000
Open Symbols - Smooth Wall
Solid Symbols - Rough Wall

	Symbol Flags
$\Delta T = 40^{\circ}F$	
$\Delta T = 80^{\circ}F$	
$\Delta T = 120^{\circ}F$	
$\Delta T = 160^{\circ}F$	

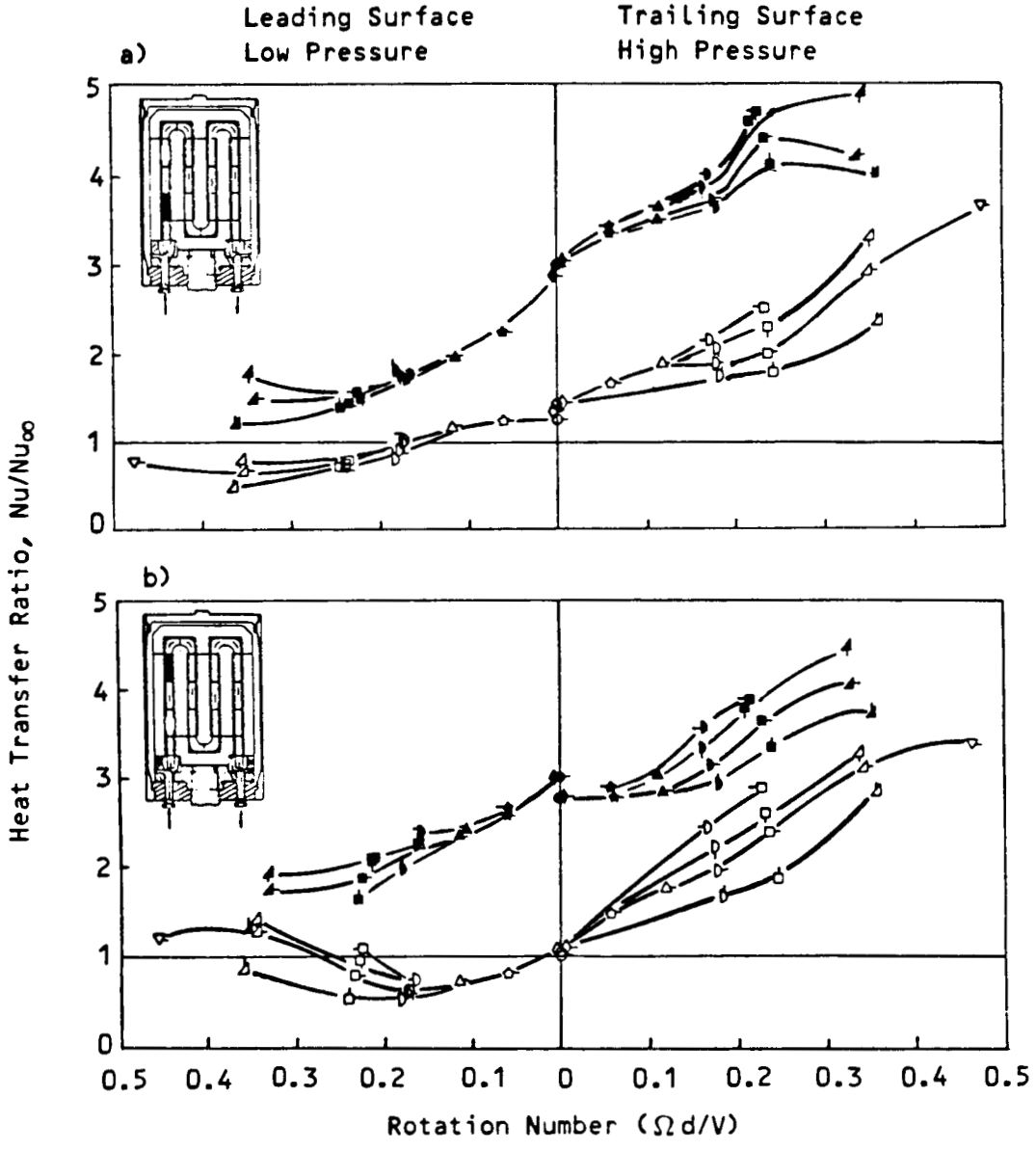

Figure 3 Effect of Rotation Number on Heat Transfer Ratio for Smooth Wall and Rough Wall Models

Re = 25,000
Open Symbols - Smooth Wall
Solid Symbols - Rough Wall

	Symbol Flags
ΔT = 40°F	○
ΔT = 80°F	○
ΔT = 120°F	○
ΔT = 160°F	○

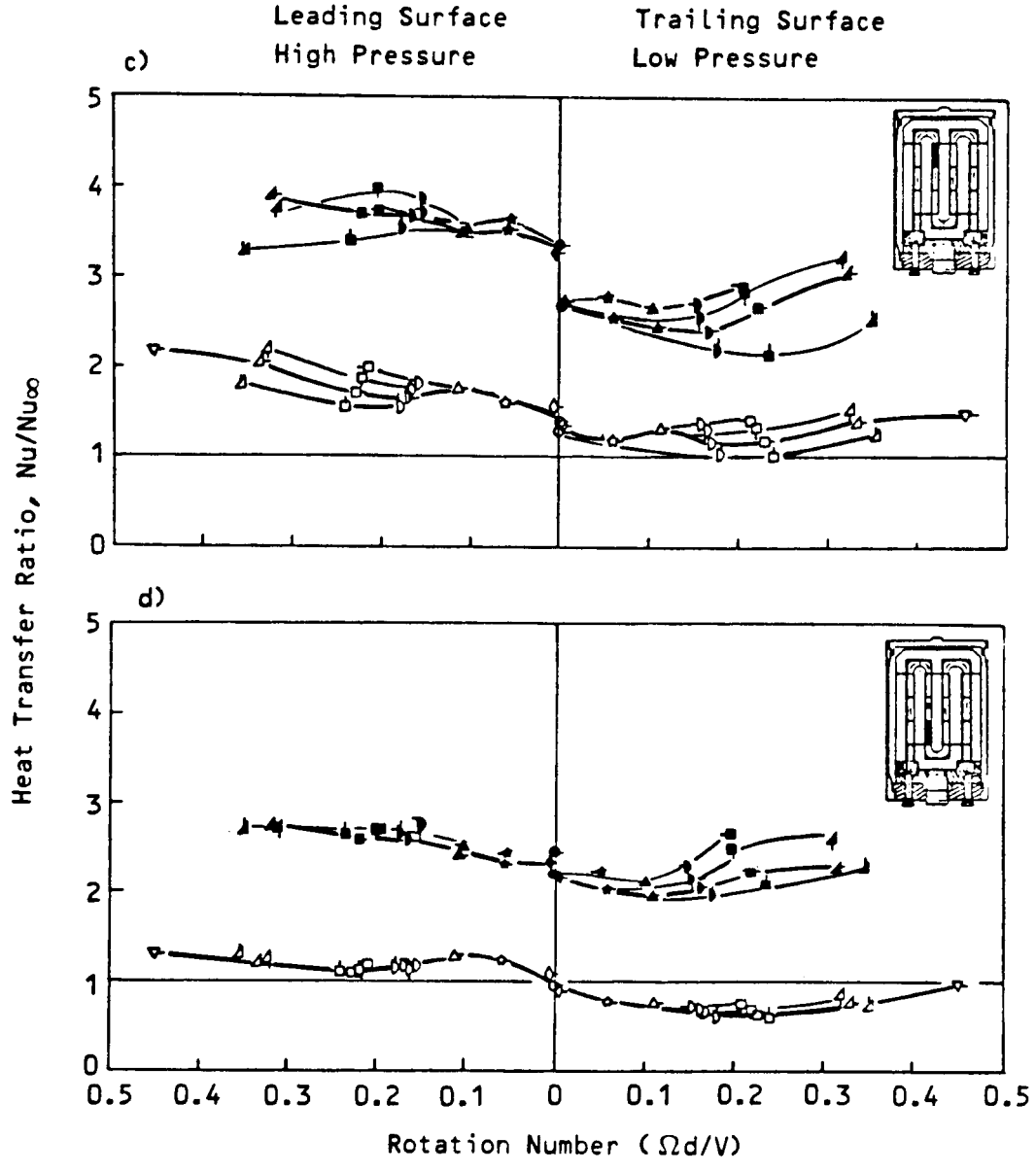

Figure 3 (Concluded) Effect of Rotation Number on Heat Transfer Ratio for Smooth Wall and Rough Wall Models

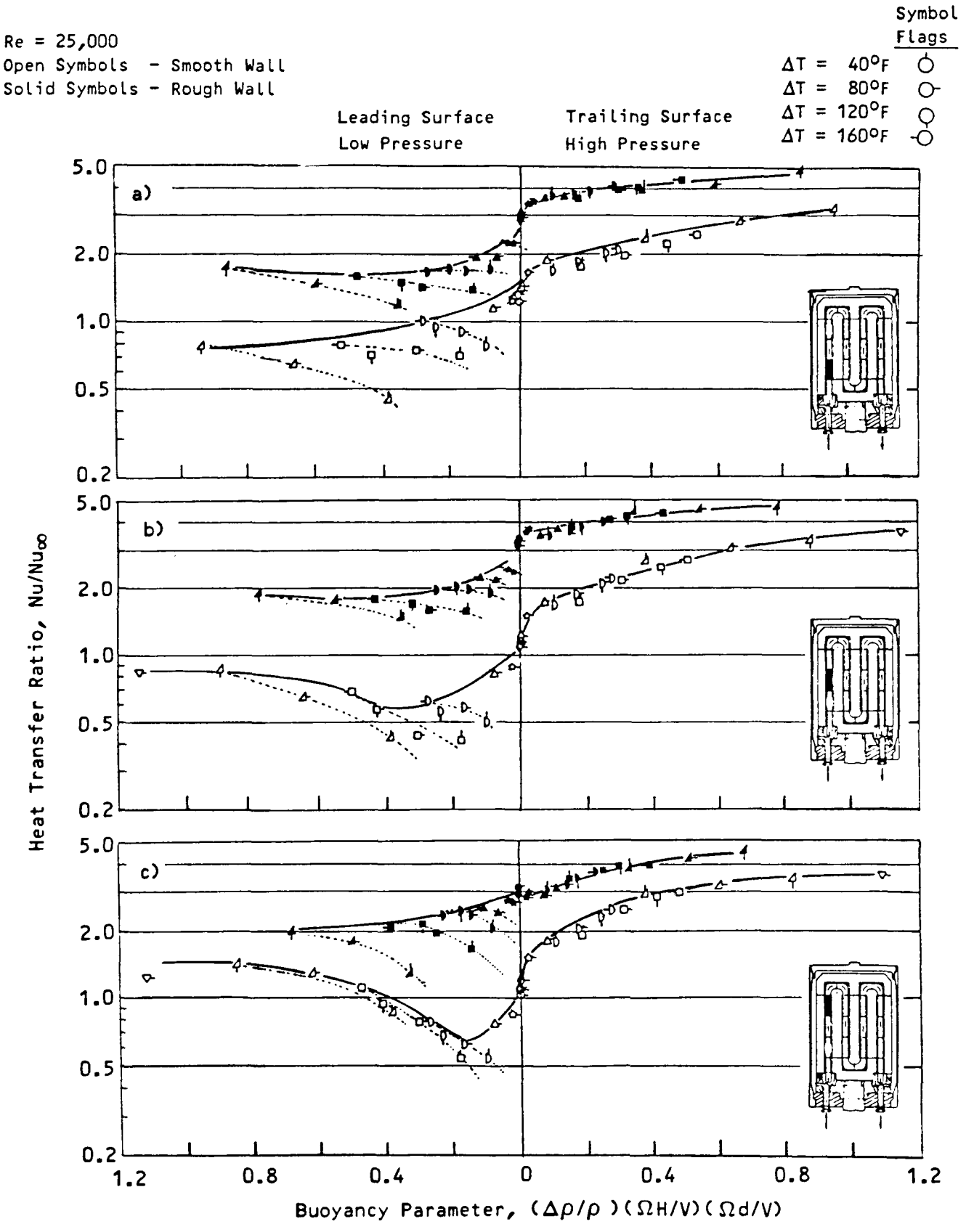

Figure 4 Effect of Buoyancy Parameter on Heat Transfer Ratio for Smooth Wall and Rough Wall Models

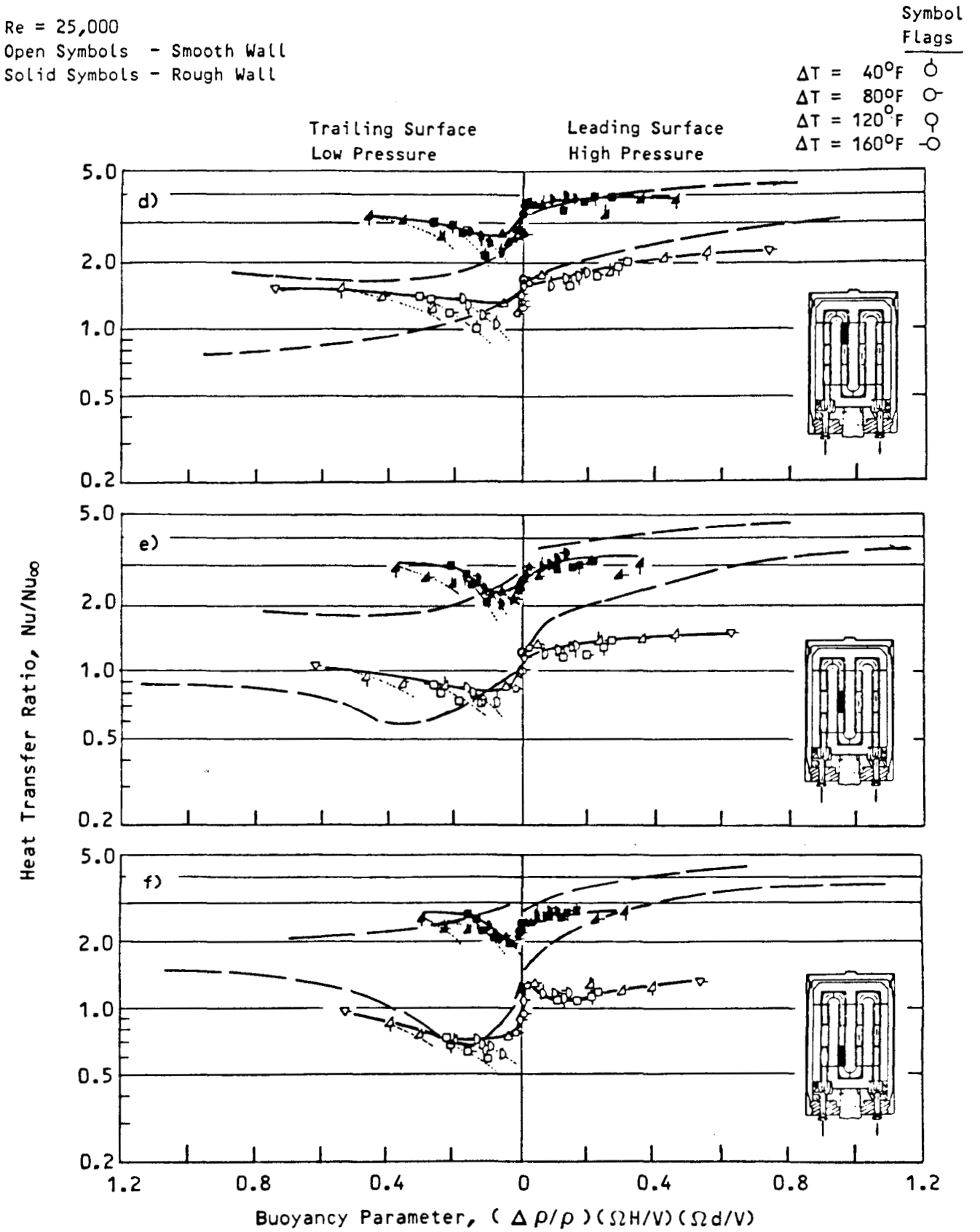

Figure 4 (Concluded) Effect of Buoyancy Parameter on Heat Transfer Ratio for Smooth Wall and Rough Wall Models

All test conditions standard except for α and $\Omega d/V$.

Symbol	○	●	□	■	△	▲
$\Omega D/V$	0		0.24 std		0.36	

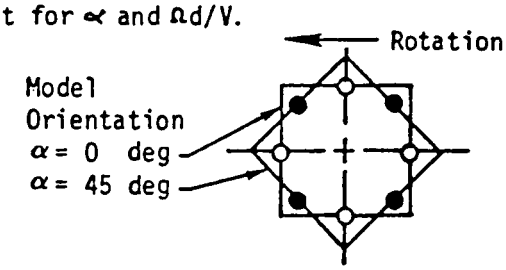

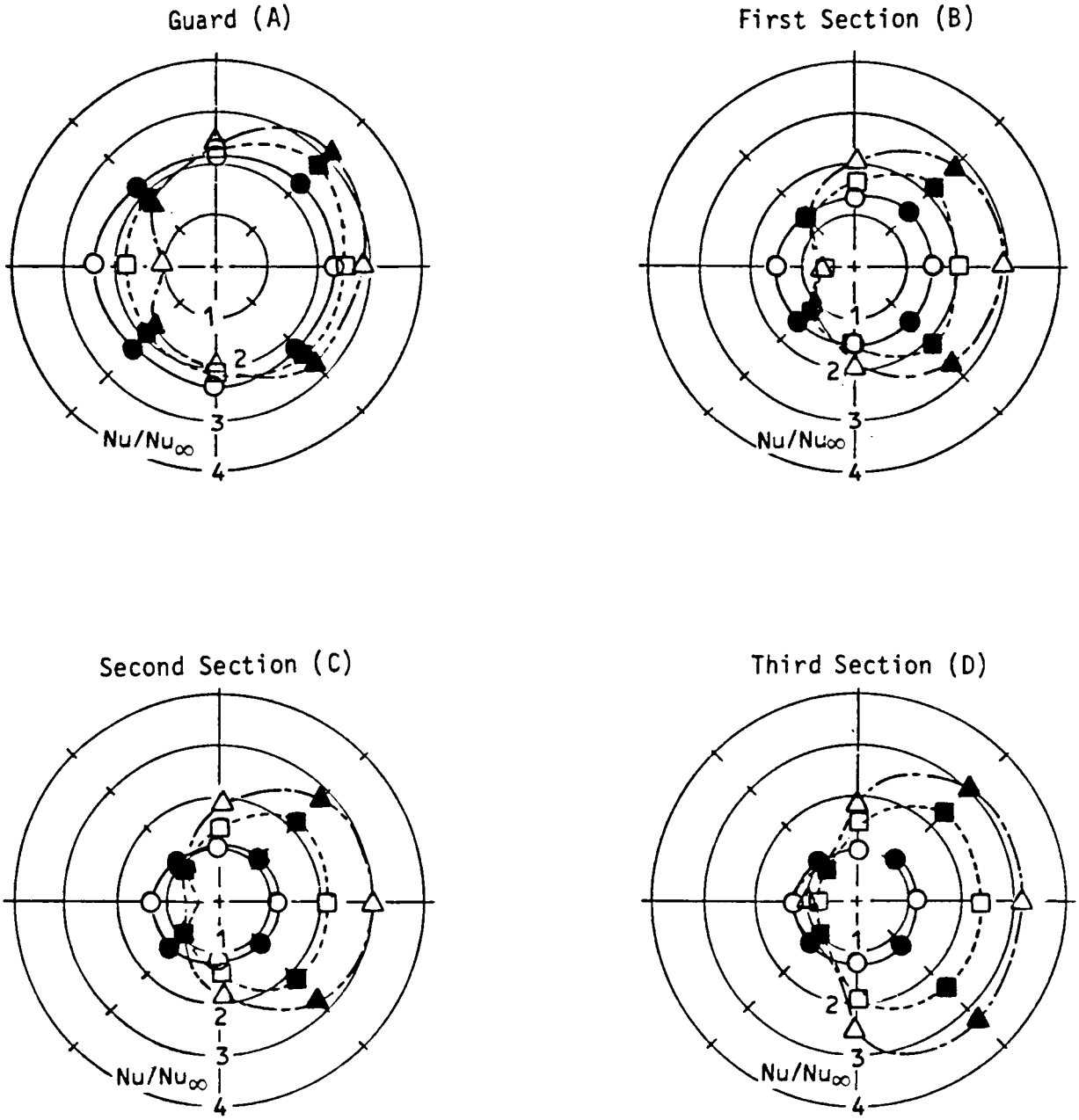

Figure 5 Variation of Heat Transfer Ratio Around Test Sections With Streamwise Locations, Rotation Number and Model Orientation for First Leg of Smooth Wall Model

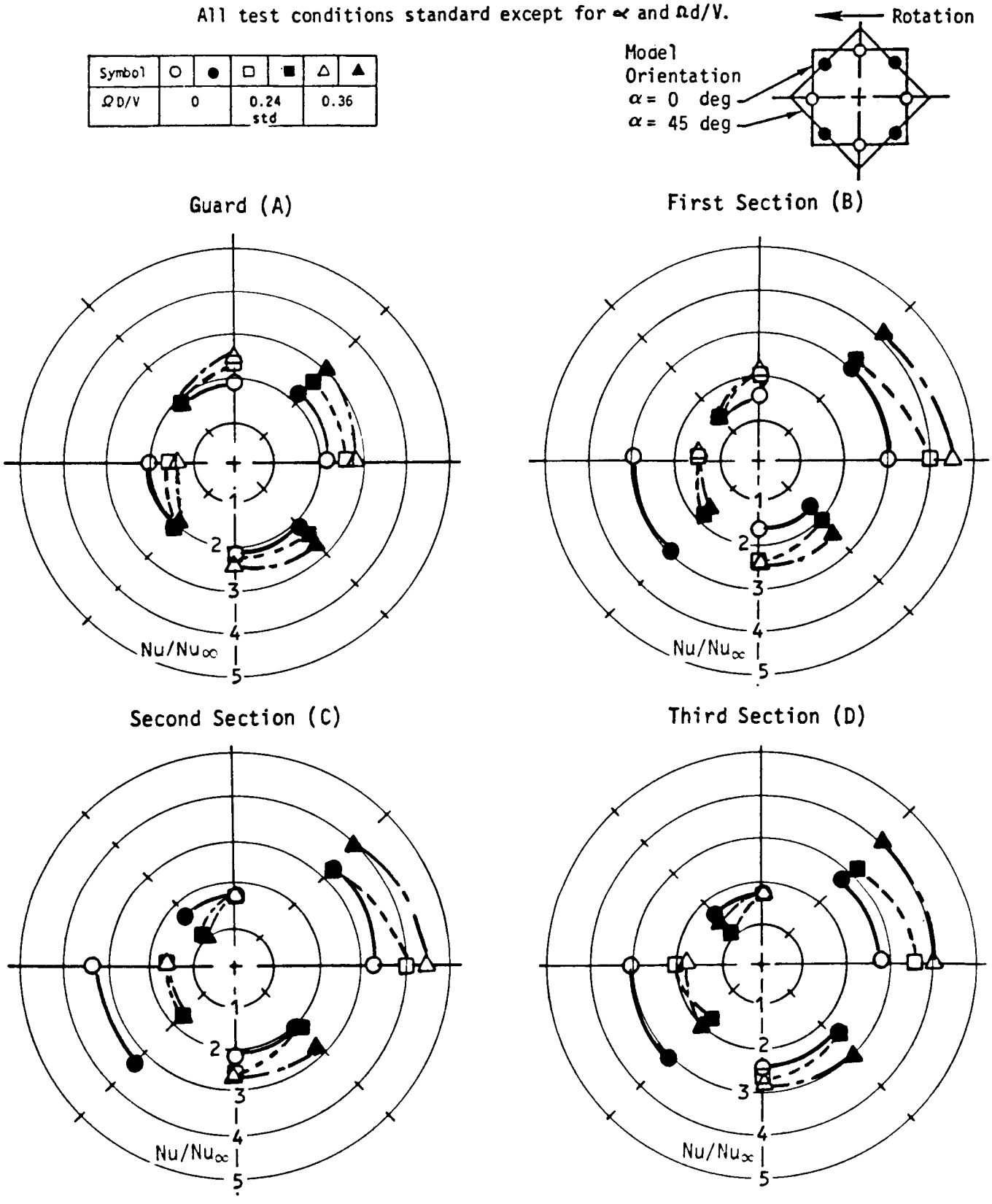

Figure 6 Variation of Heat Transfer Ratio Around Test Section With Streamwise locations, Rotation Number and Model Orientation for First Leg of Rough Wall Model

TURBINE AIRFOIL FILM COOLING*

L.D. Hylton, V. Nirmalan, B.K. Sultanian, and R.M. Kaufman
Allison Gas Turbine Division
General Motors Corporation
Indianapolis, Indiana

A combined analytical and experimental program is being conducted to develop an improved analytical approach, based on boundary layer theory, for predicting heat transfer to film cooled turbine airfoils. Extensive hot cascade tests have been performed at simulated engine conditions to provide film cooled airfoil heat transfer data to guide and verify development of new analytical tools. The results of the experimental phase of the program indicate that the film cooling process is a complex function of the thermal dilution and turbulence augmentation parameters with trends actually reversing as blowing strength and coolant-to-gas temperature ratio are varied. Some combinations of these parameters can actually result in increased heat transfer on portions of the airfoil. The pressure surface of the airfoil is shown to exhibit a considerably higher degree of sensitivity to changes in the film cooling parameters and, consequently, may prove to be more of a challenge than the suction surface in accurately predicting heat transfer levels with downstream film cooling.

INTRODUCTION

Emphasis is continuing to be placed on developing more accurate analytical models for predicting turbine airfoil external heat transfer rates. Performance goals of new engines require highly refined, accurate design tools to meet durability requirements. In order to obtain improvements in analytical capabilities, programs which focus on enhancing analytical techniques through verification of new models by comparison with relevant experimental data are required. The objectives of the current program are to develop an analytical approach, based on boundary layer theory, for predicting the effects of airfoil film cooling on downstream heat transfer rates and to verify the resulting analytical method by comparison of predictions with hot cascade data obtained under this program.

The overall approach to attaining the stated objective has involved a series of three programs. The initial program, performed under Contract NAS3-22761, assessed the capability of available modeling techniques to predict non-film cooled airfoil surface heat transfer distributions, acquired experimental data as needed for model verification, and provided verified improvements in the analytical models. This effort resulted in a baseline predictive capability and was reported in CR 168015 (ref. 1) published in May, 1983.

The problem of heat transfer predictions with film cooling was broken into sequential efforts with the effect of leading edge showerhead film cooling being investigated first, followed by a program to study the effects of the addition of discrete site suction and pressure surface injection. The effort on showerhead film cooling was performed under Contract NAS3-23695 and was reported in CR 174827 (ref. 2) published in July, 1985. As part of that program, a five-row, simulated common plenum

* This work is being performed under Contract NAS3-24619.

showerhead geometry was tested to determine differences between film and non-film cooled heat transfer coefficient distributions downstream of a leading edge, multiple hole film cooling array. Building on non-film cooling modeling improvements incorporated in a modified version of the STAN5 boundary layer code developed under Contract NAS3-22761, a program was developed to analytically model and predict differences resulting from leading edge mass injection.

The current program, being performed under Contract NAS3-24619, is intended to extend the analytical code development to include discrete site pressure and suction surface injection, with and without leading edge blowing, and to obtain relevant hot cascade data to guide and verify the model improvements.

PROGRAM DESCRIPTION AND STATUS

The current program contains separate, but interrelated, analytical and experimental tasks. The analytical task consists of three phases. The first phase, design mode analysis, has been completed. This effort consisted of demonstrating the use of the proposed boundary layer method in a design system environment. This demonstration resulted in predictions of heat transfer distributions for the film cooled airfoil used in the hot cascade tests performed during this program. The second analytical phase, method characterization, compares the predictions from the design mode analysis with the experimental data and establishes the deficiencies in the proposed method, and identifies modeling improvements that must be made. This effort is currently underway. The final analytical phase, method refinement/verification, will begin upon the completion of the method characterization phase. It will utilize the knowledge gained from the first two phases to develop an improved design tool for film cooled turbine airfoils.

The experimental task, which has just been completed, was an extension of the experimental work performed in the previous contract which was reported in reference 2. The hot cascade tests utilized the same facility, cascade and experimental techniques used in the previous contract, with the instrumented airfoil in the cascade replaced with one containing suction surface and pressure surface film cooling arrays in addition to a leading edge showerhead film cooling array. A photograph of the airfoil that was tested is shown in figure 1.

The airfoil cooling design incorporated three separate film cooling supply plenums. One plenum supplied an array of leading edge showerhead film cooling holes. The geometry of this film cooling hole array was identical to that utilized in Contract NAS3-23695. Two additional coolant supply plenums were incorporated into the vane; one to supply an array of holes on the suction surface and the other to supply an array of holes on the pressure surface of the airfoil. The three separate plenums allowed independent control of the flow to each region of the airfoil.

The suction surface array contained two staggered rows of holes centered at 25.2% of the suction surface length from the leading edge. Similarly, the pressure surface contained two staggered rows of holes centered at 22.5% of the pressure surface length from the leading edge.

All three hole arrays contained 1.0 mm (0.039 inch) diameter holes. The hole spacing-to-diameter ratio was 7.5 in the leading edge array and 3.0 for the other two arrays. The row spacing-to-diameter ratio was 4.0 in all three regions. The injection angle in the leading edge was the same as in the previous contract where the holes were aligned normal to the surface in the chordwise direction and at a

45° angle in the spanwise direction. The suction surface holes were inclined at 35° to the surface in the chordwise direction while the pressure surface holes were at 20° in the chordwise direction. Holes in both downstream arrays were normal to the surface in the spanwise direction. Also shown in figure 1 is the thermal barrier cutout region. This cut thermally isolated the film cooling supply plenums from the downstream regions of the airfoil where heat transfer measurements were made, similar to the technique used in the previous contract. Prior to testing, a thin, 0.254 mm (0.010 inch), shim was welded across the thermal barrier gap on both the pressure and suction surfaces. This provided a smooth, continuous surface on the airfoil. The retaining bar shown in figure 1 ensures that the airfoil profile was properly maintained after the thermal barrier cut was made.

The test matrix for which experimental data were obtained provided aerothermodynamic simulation of typical engine operating conditions. The test matrix is illustrated in figure 2. Data were obtained at cascade exit Mach numbers, M_2, of 0.75 and 0.90 and at exit Reynolds numbers, Re_2, of 1.5×10^6, 2.0×10^6, and 2.5×10^6. Coolant-to-gas absolute temperature ratios, TR or T_c/T_g, were varied from 0.65 to 0.85. The film cooling pressure ratio, PR or P_c/P_t, (film cooling supply plenum pressure-to-inlet stagnation pressure), was varied from 1.02 to 1.65 with most data taken in the range from 1.02 to 1.10.

RESULTS AND DISCUSSION

The testing associated with the experimental task has been completed, as has much of the data analysis. Efforts are just beginning on comparison of the data with the analytical model predictions. Consequently, the discussion that follows will focus primarily on a review of the experimental data and the trends that have been identified.

Prior to obtaining film cooled heat transfer data, baseline data (i.e. without film cooling) were obtained at the four base flow conditions (see fig. 2) corresponding to an exit Mach number, M_2 (or Ma_2), of 0.9 and exit Reynolds number, Re_2, of 1.5×10^6, 2.0×10^6, and 2.5×10^6 and at an exit Mach number of 0.75 with a Reynolds number of 2.0×10^6. In all cases, the inlet total temperature was maintained at a nominal value of 700K (1260 R). Figure 3 shows the vane surface-to-gas absolute temperature ratio, T_w/T_g, at an exit Mach number and Reynolds number of 0.9 and 2.0×10^6 respectively. In figure 3, and also in figures 4 through 14, the vertical dashed lines mark the locations of the film cooling hole rows and the vertical solid lines mark the locations of the thermal barrier on the suction and pressure surfaces. The cyclic vane surface temperature fluctuations seen near the trailing edge in figure 3 are due to coolant air flowing through the internal cooling holes. This temperature distribution, in addition to the internal boundary conditions at the 10 radial cooling holes, was used to obtain the local heat transfer coefficients by the method described in reference 2. The normalized local vane heat transfer coefficients, h/h_0, for this flow condition are presented in figure 4. The fluctuations in the local heat transfer coefficients are, again, caused by the presence of the radial coolant paths in the vane. Also in figure 4, the results predicted for the same conditions using the Allison - STANCOOL code developed under the previous NASA contracts (ref. 1 and 2), are given. Here, the solid curve is the predicted results with a constant wall temperature boundary condition. This prediction was made as part of the design mode analytical effort. The dashed curve is the prediction made using the actual measured surface temperature boundary condition. Since an appreciable temperature gradient existed, it seemed appropriate to use the variable temperature boundary condition for the prediction. Figure 4 shows a very reasonable comparison between the experimental data and the prediction using the

actual measured surface temperature for the boundary condition. This comparison illustrates the significance of the actual wall temperature boundary condition on heat transfer predictions.

The film cooled data that will be presented here include (a) data with only the suction side and pressure side film cooling arrays active, (b) data with all three film cooling arrays active, and (c) data with constant downstream injection and variable leading edge injection. The film cooling supply plenum pressure-to-inlet stagnation pressure ratio (P_c/P_t) was kept at nominal values of 1.02, 1.05 and 1.10 in the cases presented. In figures 5 through 14, the subscript le, on P_c/P_t, refers to the leading edge film cooling array, and the subscript ds refers to the downstream film cooling arrays on the pressure and suction surfaces. All tests were run with equal supply pressure for the two downstream arrays. Film coolant-to-gas absolute temperature ratios (T_c/T_g) were kept at nominal values of 0.65 (MIN), 0.75 (MED), and 0.85 (MAX).

To present the effects of film cooling on vane surface heat transfer, the ratio of Stanton number with film cooling to Stanton number without film cooling was calculated. However, instead of simply presenting the Stanton number ratio of film cooled to non-film cooled (St_{FC}/St_{NFC}), an alternate "no difference" parameter referred to as Stanton number reduction (SNR) and defined as

$$SNR = 1 - (St_{FC}/ST_{NFC}) \quad (1)$$

is used. Also, if the non-film cooled data and the film cooled data were obtained at equivalent exit Reynolds number and exit Mach number, SNR would approximately be equal to

$$SNR = 1 - (h_{FC}/h_{NFC}) \quad (2)$$

Figures 5 through 10 show some of the effects on Stanton number reduction of the different film cooling parameters for constant Mach number and Reynolds number conditions.

Figures 5 and 6 show the effects of varying the blowing strength at two constant thermal dilution (T_c/T_g) levels with only the downstream film cooling arrays active. The base flow conditions are at an exit Mach number of 0.9 and an exit Reynolds number of 2.5×10^6. Figure 5 shows the effect of varying the blowing strength (P_c/P_t) at the lowest coolant-to-gas temperature ratio ($T_c/T_g = 0.65$). A positive SNR is seen on both surfaces at all three blowing strengths indicating a comparatively large decrease in heat transfer due to downstream film cooling. A pronounced variation in SNR due to different blowing strengths is seen on the pressure surface. Also, on the pressure surface, as the blowing strength is increased, the effect of film cooling is felt further downstream. On the other hand, on the suction surface, there is hardly any effect due to varying blowing strengths. This is due to the lower freestream pressure on the suction surface causing the film coolant flow on that surface to be choked at this range of pressure ratios. Figure 6 shows similar behavior at a higher T_c/T_g ratio of 0.85 (MAX) though, as expected, with lower values of SNR due to a lower level of thermal dilution (warmer air being injected). Also, on the pressure surface near the film cooling holes, higher blowing strengths tend to increase heat transfer (i.e. a decrease in SNR values) by increasing the turbulence level in the region. This phenomena is more pronounced at the higher coolant-to-gas temperature ratios. It should also be noted that for the higher blowing strengths SNR increases over the last 60 percent of the airfoil; whereas, for the lower blowing strengths, the SNR decreases. This is the result of

the interaction of the thermal dilution and turbulence augmentation effects.

Figures 7 and 8 show some of the above data with additional data plotted to illustrate the effects of the thermal dilution at the lowest and highest blowing strengths of P_c/P_t = 1.02 (fig. 7) and 1.10 (fig. 8). On the suction surface, in both cases, there is a very noticeable effect due to different thermal dilution levels. Conversely, on the pressure surface, at the lowest blowing strength, as shown in figure 7, only a small effect is noticed. However, as seen in figure 8, there is a larger effect on the pressure surface due to varying thermal dilution at a higher blowing strength of P_c/P_t = 1.10. Also in figure 8, at T_c/T_g = 0.85, SNR is negative on the pressure surface at surface distance less than 50%. As mentioned before, this increase in heat transfer is due to the high blowing strength causing a higher turbulence level in the vicinity of the film cooling holes.

Figure 9 shows the effects of both the downstream and the leading edge film cooling arrays being active with varying blowing strengths at the MIN level of thermal dilution at the same flow conditions. In comparison to figure 5, the trends and levels of SNR are very similar to the case with only the downstream film cooling holes being active, indicating a very small effect due to the leading edge film cooling. However, on the pressure surface just downstream of the film cooling holes, higher values of SNR are seen due to the leading edge film cooling holes being active.

Figure 10 presents SNR data for the case where downstream film cooling hole arrays are at a constant blowing strength of 1.10 while the leading edge film cooling blowing strength is varied from 1.00 (no leading edge blowing) to 1.10. These data are at the flow conditions corresponding to an exit Mach number of 0.75 and an exit Reynolds number of 2.0×10^6. On the pressure surface, SNR is increased by low leading edge blowing values ($P_{c,le}/P_t$ = 1.02). However, at higher leading edge blowing strengths, SNR values drop off and at $P_{c,le}/P_t$ = 1.10 the SNR is lower than without any leading edge blowing. This indicates that high leading edge blowing rates can actually increase heat transfer over the entire pressure surface of the airfoil due to increased turbulence levels. On the other hand, very little effect of leading edge film cooling is seen on the suction surface.

Figures 5 through 10 represent the trends seen due to the various film cooling parameters and are very representative of other similar data at different cascade operating conditions.

Figures 11 and 12 illustrate the effect of varying the exit Mach number from 0.75 to 0.9 while keeping other flow and film cooling conditions constant. In these two instances, the downstream film cooling hole arrays are at blowing strengths, P_c/P_t, of 1.05 and the coolant-to-gas temperature ratios (T_c/T_g) are at 0.65 (MIN) (fig. 11) and 0.85 (MAX) (fig. 12). Also as before, SNR values indicate the effect of film cooling versus non-film cooling at identical flow conditions: therefore, in these cases, due to comparison of data at two different flow conditions, the two baseline conditions are also given in the legend. Figures 11 and 12 show that there is no major effect on SNR due to variations in Mach number on either the suction or pressure surfaces at the lower coolant-to-gas temperature ratio. However, on the pressure surface at the higher coolant-to-gas temperature ratio, figure 12 shows that at the lower Mach number, the effect of film cooling is more beneficial than at the higher Mach number.

Figures 13 and 14 show the effects of three different exit Reynolds numbers of 1.5×10^6, 2.0×10^6, and 2.5×10^6 on downstream film cooling. As in the previous

two figures, the baseline conditions for each set of data are also given in the legend. Figure 13 presents data at the lower coolant-to-gas temperature ratio of 0.65 and coolant pressure ratio of 1.10. On the pressure side, SNR increases with increasing Reynolds number indicating that a more favorable effect of film cooling is attainable at higher Reynolds numbers. A similar effect is seen on the suction surface, except that at two higher Reynolds numbers ($Re_2 = 2.0x10^6$ and $2.5x10^6$) the variations due to different exit Reynolds number is not as pronounced. In figure 14, where the coolant-to-gas temperature ratio is about 0.85, the effect of Reynolds number variation is not as marked as in the case of the lower coolant-to-gas temperature ratio.

In conclusion, the experimental data that have been obtained in this program at simulated engine conditions give insight into the physical phenomena that occur on a film cooled airfoil, and should provide a relevant data base for verification of new design tools. The results of the experimental phase of this program indicate that the downstream film cooling process is a complex function of the thermal dilution and turbulence augmentation parameters with trends actually reversing as blowing strength and coolant-to-gas temperature ratio are varied. The pressure surface of the airfoil is shown to exhibit a considerably higher degree of sensitivity to changes in the film cooling parameters and, consequently, should prove to be more of a challenge than the suction surface in accurately predicting heat transfer levels with downstream film cooling.

REFERENCES

1. L. D. Hylton, M. S. Mihelc, E. R. Turner, D. A. Nealy, and R. E. York, "Analytical and Experimental Evaluation of the Heat Transfer Distribution over the Surfaces of Turbine Vanes", NASA CR-168015, May 1983.

2. E. R. Turner, M. D. Wilson, L. D. Hylton, and R. M. Kaufman, "Turbine Vane External Heat Transfer", Vol I, NASA CR-174827, July 1985.

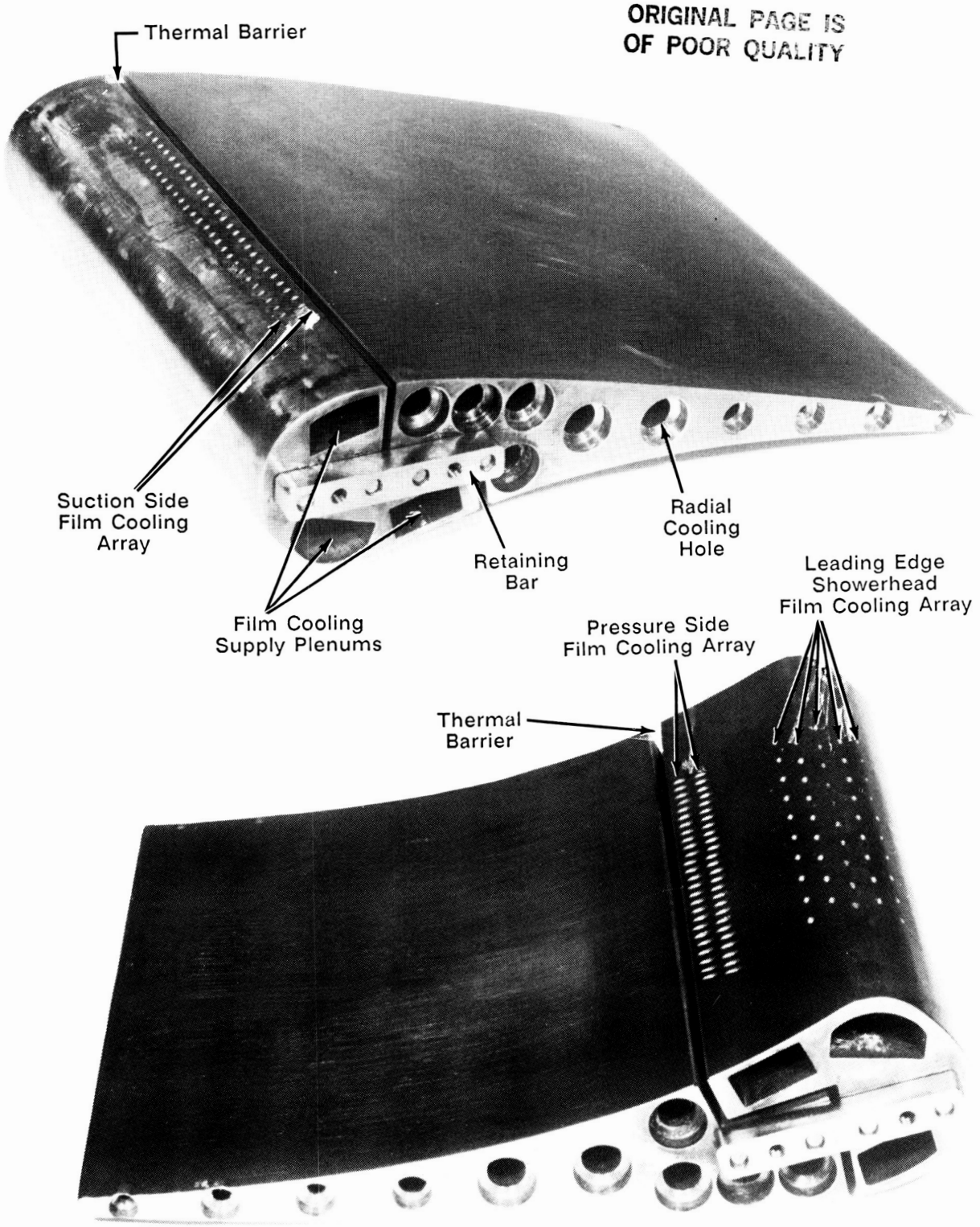

Figure 1. Film cooled airfoil for cascade tests

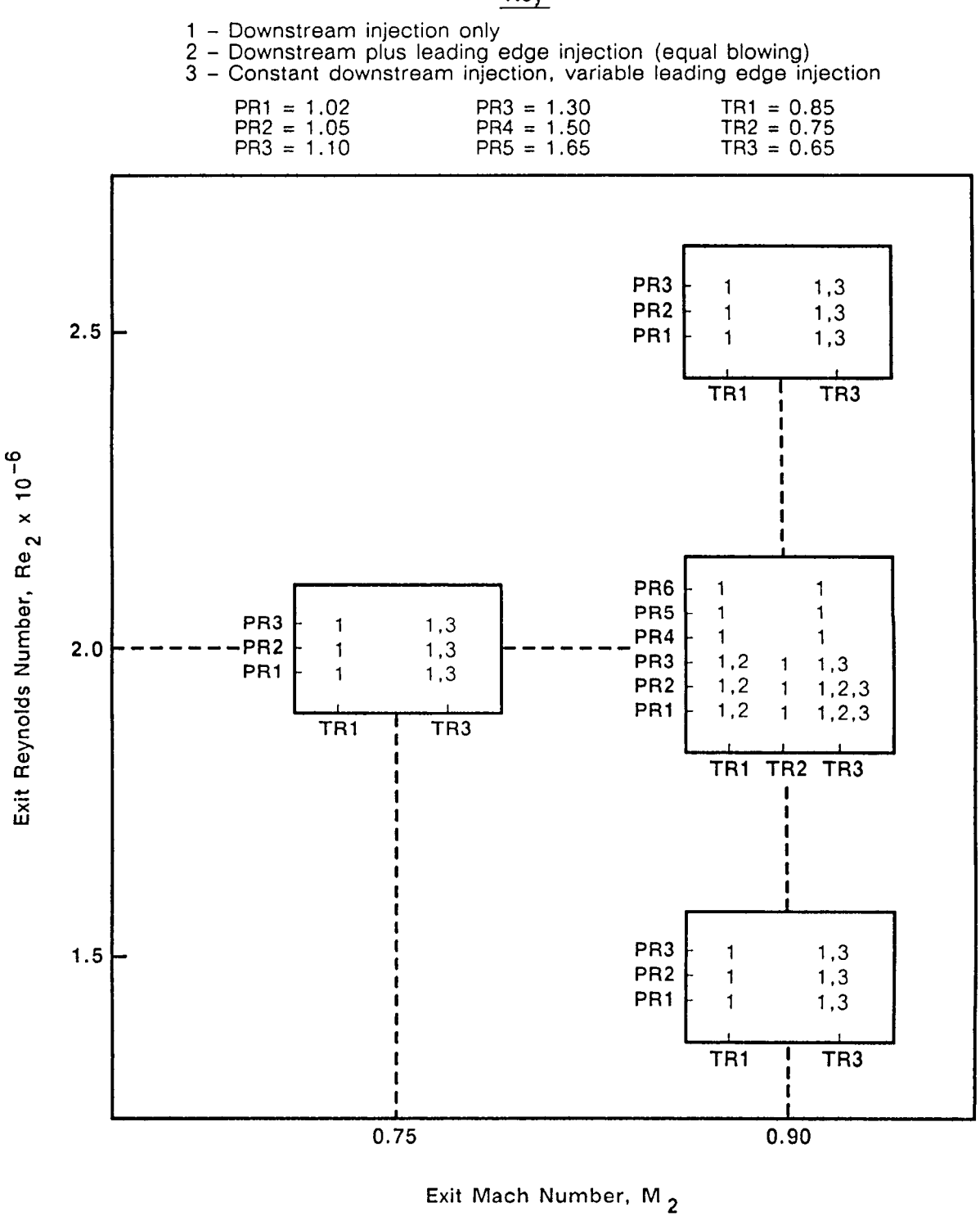

Figure 2. Test matrix

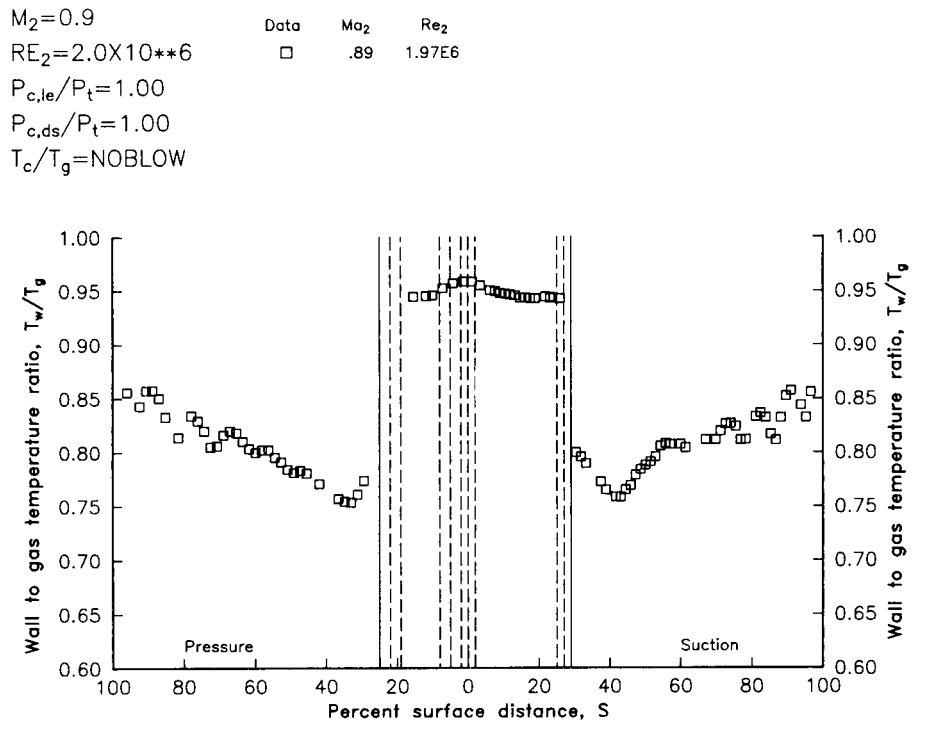

Figure 3. Vane surface-to-gas absolute temperature ratio distribution at baseline flow condition of Ma_2 = 0.9 and Re_2 = 2.0x10^6

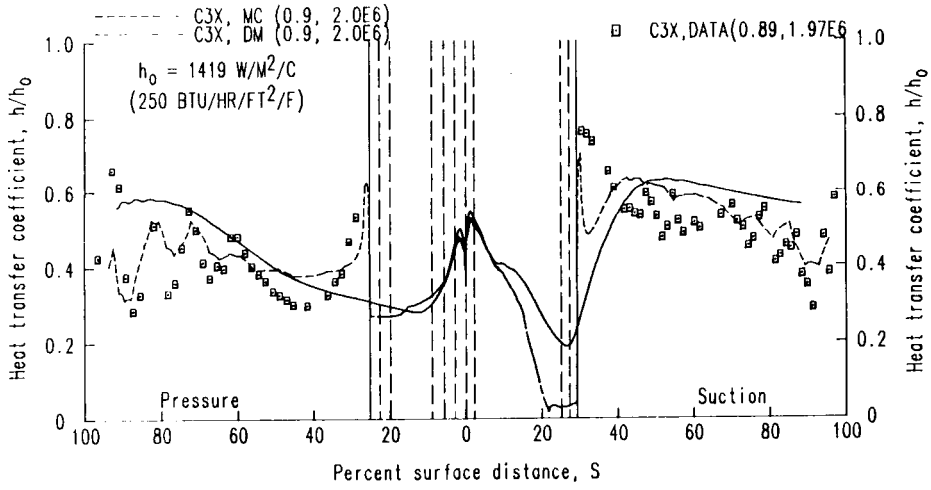

Figure 4. Vane surface local heat transfer coefficient distribution at baseline flow condition of Ma_2 = 0.9 and Re_2 = 2.0x10^6

M_2=0.9
RE_2=2.0X10**6
$P_{c,le}/P_t$=1.00
$P_{c,ds}/P_t$=VAR
T_c/T_g=MIN

Data	Ma_2	Re_2	$P_{c,ds}/P_t$	$P_{c,le}/P_t$	T_c/T_g
Base	.89	1.97E6			
△	.89	1.99E6	1.10	1.00	.68
◇	.90	2.00E6	1.05	1.00	.67
□	.90	1.99E6	1.02	1.00	.69

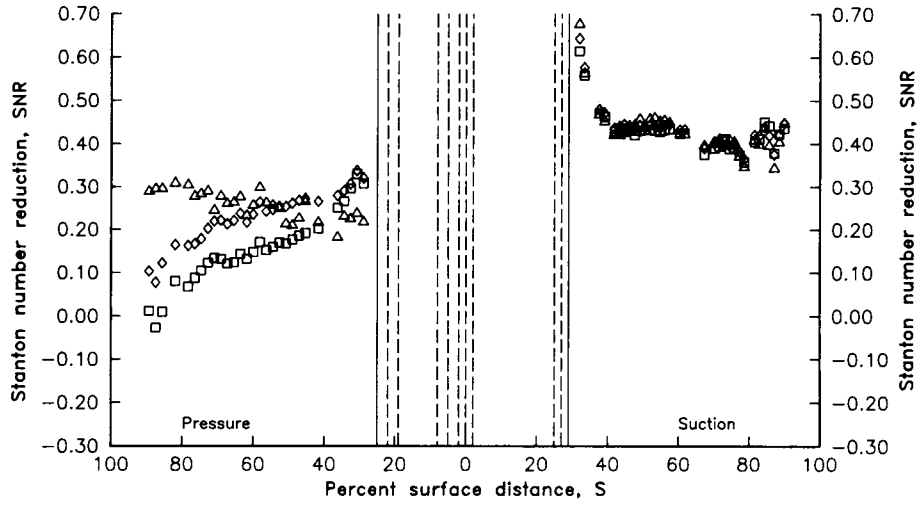

Figure 5. Effect of downstream blowing strength on heat transfer reduction (T_c/T_g = 0.65)

M_2=0.9
RE_2=2.0X10**6
$P_{c,le}/P_t$=1.00
$P_{c,ds}/P_t$=VAR
T_c/T_g=MAX

Data	Ma_2	Re_2	$P_{c,ds}/P_t$	$P_{c,le}/P_t$	T_c/T_g
Base	.89	1.97E6			
△	.90	2.03E6	1.11	1.00	.85
◇	.89	2.01E6	1.05	1.00	.86
□	.90	2.01E6	1.02	1.00	.84

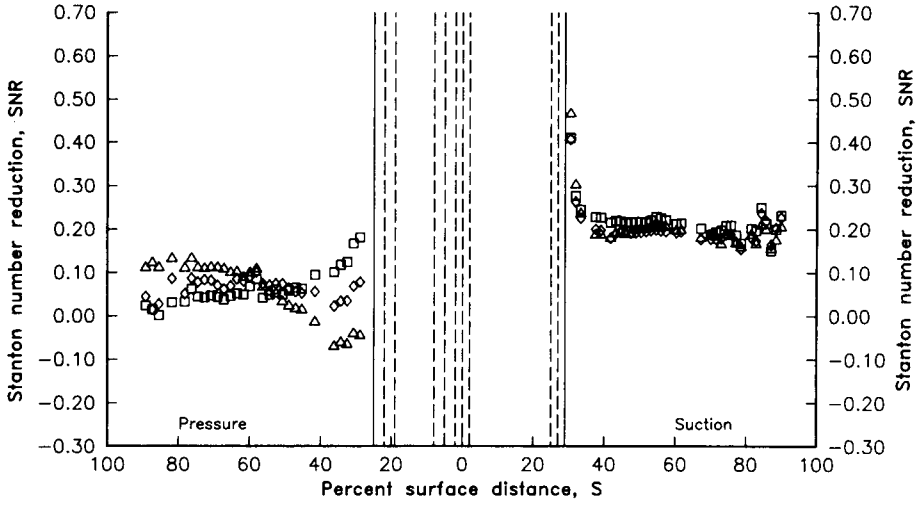

Figure 6. Effect of downstream blowing strength on heat transfer reduction (T_c/T_g = 0.85)

M_2=0.9
RE_2=2.0X10**6
$P_{c,le}/P_t$=1.00
$P_{c,ds}/P_t$=1.02
T_c/T_g=VAR

Data	Ma_2	Re_2	$P_{c,ds}/P_t$	$P_{c,le}/P_t$	T_c/T_g
Base	.89	1.97E6			
△	.90	2.01E6	1.02	1.00	.84
◇	.90	1.99E6	1.02	1.00	.75
□	.90	1.99E6	1.02	1.00	.69

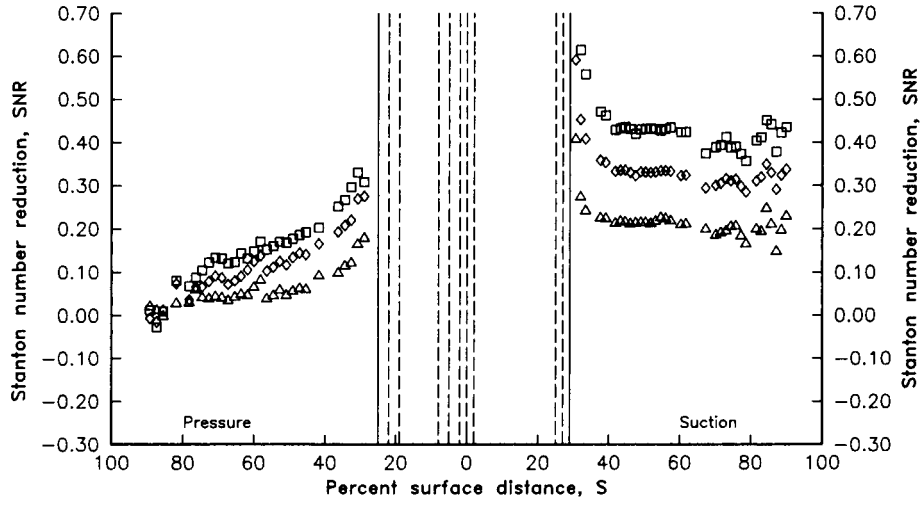

Figure 7. Effect of downstream film cooling thermal dilution on heat transfer reduction (P_c/P_t = 1.02)

M_2=0.9
RE_2=2.0X10**6
$P_{c,le}/P_t$=1.00
$P_{c,ds}/P_t$=1.10
T_c/T_g=VAR

Data	Ma_2	Re_2	$P_{c,ds}/P_t$	$P_{c,le}/P_t$	T_c/T_g
Base	.89	1.97E6			
△	.90	2.03E6	1.11	1.00	.85
◇	.90	2.01E6	1.11	1.00	.77
□	.89	1.99E6	1.10	1.00	.68

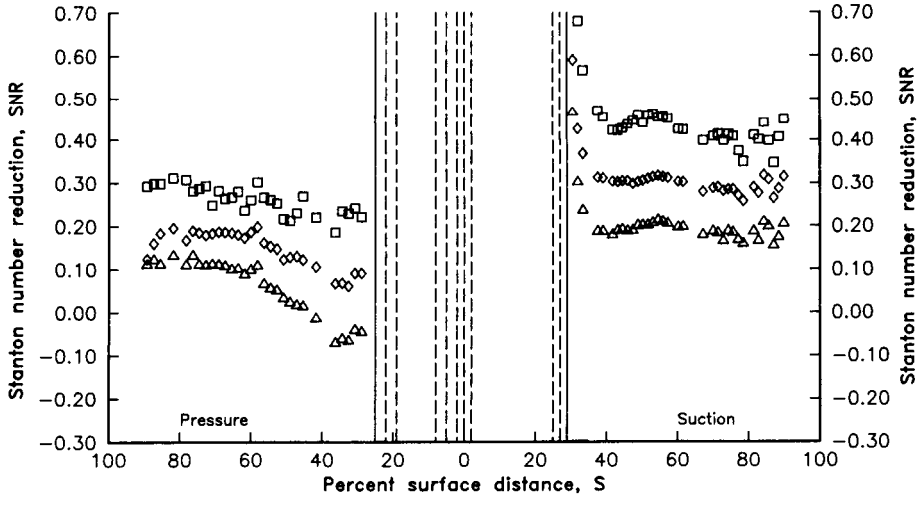

Figure 8. Effect of downstream film cooling thermal dilution on heat transfer reduction (P_c/P_t = 1.10)

M_2=0.9
RE_2=2.0X10**6
$P_{c,le}/P_t$=VAR
$P_{c,ds}/P_t$=VAR
T_c/T_g=MIN

Data	Ma_2	Re_2	$P_{c,ds}/P_t$	$P_{c,le}/P_t$	T_c/T_g
Base	.89	1.97E6			
△	.90	1.99E6	1.10	1.10	.66
◇	.90	2.03E6	1.05	1.05	.67
□	.92	2.04E6	1.02	1.02	.67

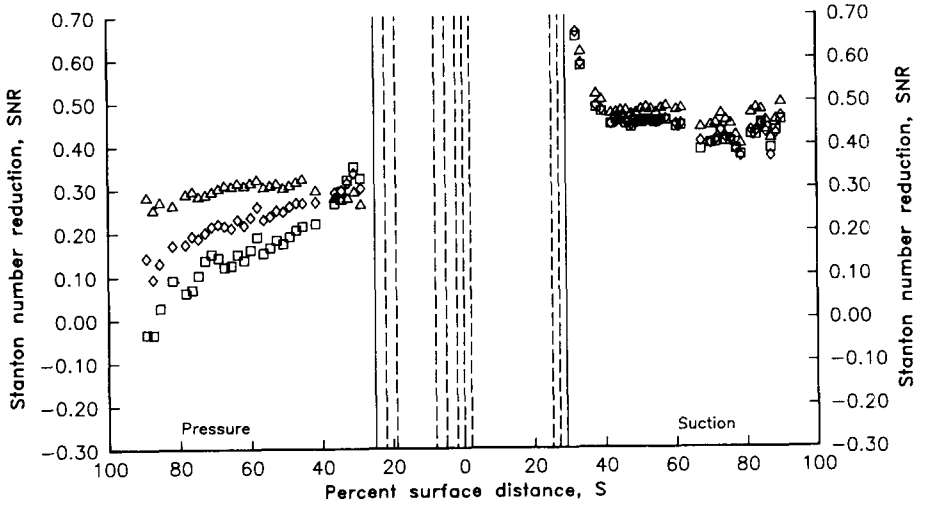

Figure 9. Effect of leading edge and downstream blowing strength on heat transfer reduction (T_c/T_g = 0.65)

M_2=0.75
RE_2=2.0X10**6
$P_{c,le}/P_t$=VAR
$P_{c,ds}/P_t$=1.10
T_c/T_g=MIN

Data	Ma_2	Re_2	$P_{c,ds}/P_t$	$P_{c,le}/P_t$	T_c/T_g
Base	.75	2.00E6			
○	.75	2.05E6	1.10	1.10	.67
△	.74	2.00E6	1.10	1.05	.65
◇	.75	2.01E6	1.10	1.02	.65
□	.75	2.00E6	1.10	1.00	.66

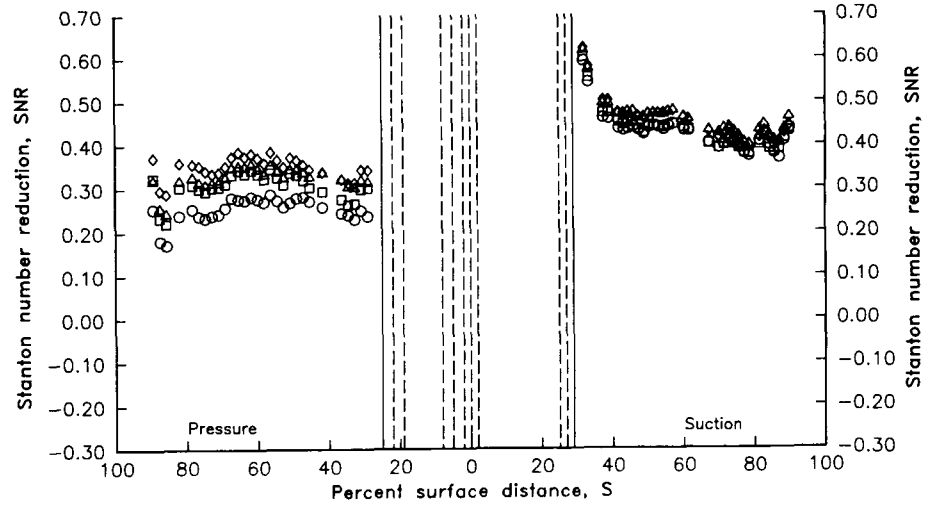

Figure 10. Effect of leading edge blowing strength with constant downstream blowing on heat transfer reduction (T_c/T_g = 0.65)

M_2=VAR
RE_2=2.0X10**6
$P_{c,le}/P_t$=1.00
$P_{c,ds}/P_t$=1.05
T_c/T_g=MIN

Data	Ma_2	Re_2	$P_{c,ds}/P_t$	$P_{c,le}/P_t$	T_c/T_g
Base	.75	2.00E6			
Base	.89	1.97E6			
◇	.75	2.00E6	1.05	1.00	.64
□	.90	2.00E6	1.05	1.00	.67

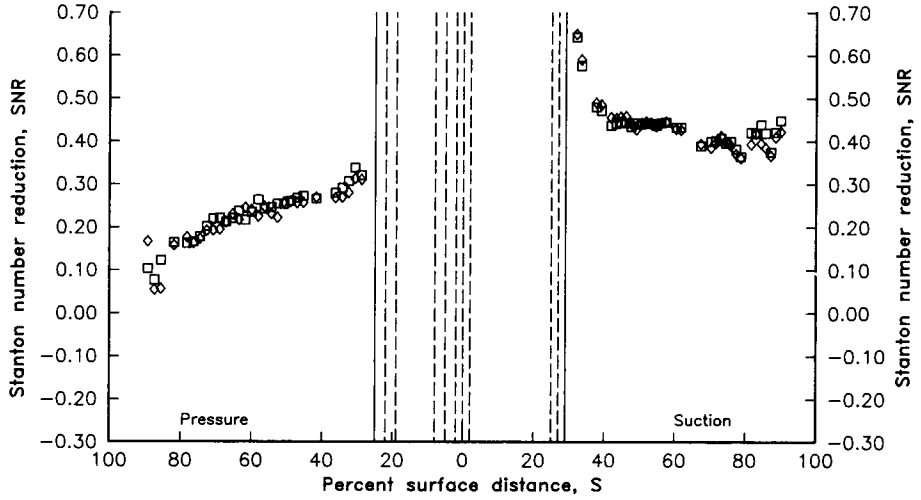

Figure 11. Effect of Mach number on heat transfer reduction (P_c/P_t = 1.05, T_c/T_g = 0.65)

M_2=VAR
RE_2=2.0X10**6
$P_{c,le}/P_t$=1.00
$P_{c,ds}/P_t$=1.05
T_c/T_g=MAX

Data	Ma_2	Re_2	$P_{c,ds}/P_t$	$P_{c,le}/P_t$	T_c/T_g
Base	.75	2.00E6			
Base	.89	1.97E6			
◇	.75	1.97E6	1.05	1.00	.86
□	.89	2.01E6	1.05	1.00	.86

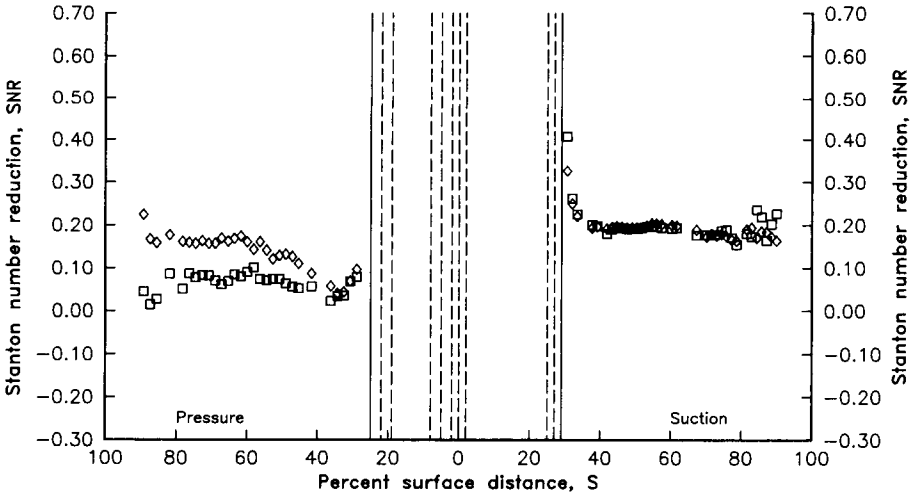

Figure 12. Effect of Mach number on heat transfer reduction (P_c/P_t = 1.05, T_c/T_g = 0.85)

M_2=0.9
RE_2=VAR
$P_{c,le}/P_t$=1.00
$P_{c,ds}/P_t$=1.10
T_c/T_g=MIN

Data	Ma_2	Re_2	$P_{c,ds}/P_t$	$P_{c,le}/P_t$	T_c/T_g
Base	.92	2.58E6			
Base	.89	1.97E6			
Base	.91	1.51E6			
△	.89	2.48E6	1.10	1.00	.66
◇	.89	1.99E6	1.10	1.00	.68
□	.89	1.55E6	1.10	1.00	.67

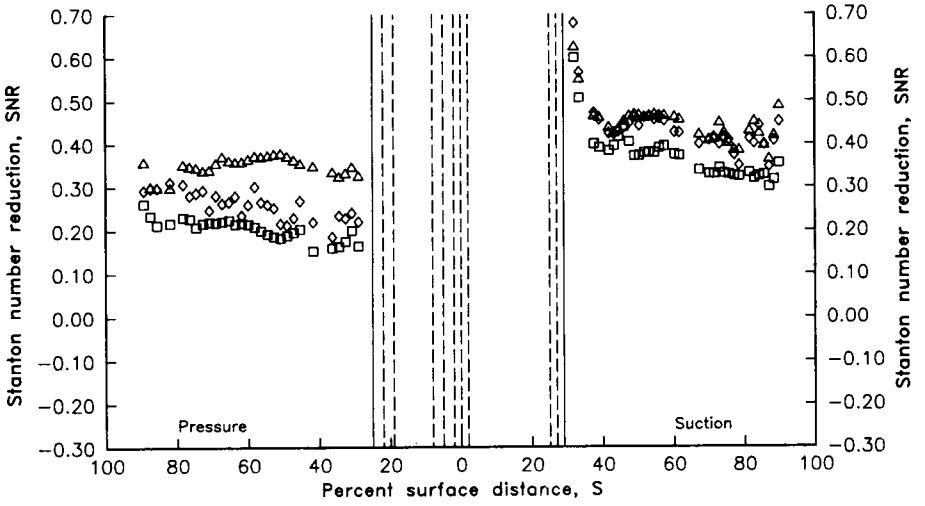

Figure 13. Effect of Reynolds number on heat transfer reduction (P_c/P_t = 1.10, T_c/T_g = 0.65)

M_2=0.9
RE_2=VAR
$P_{c,le}/P_t$=1.00
$P_{c,ds}/P_t$=1.10
T_c/T_g=MAX

Data	Ma_2	Re_2	$P_{c,ds}/P_t$	$P_{c,le}/P_t$	T_c/T_g
Base	.92	2.58E6			
Base	.89	1.97E6			
Base	.91	1.51E6			
△	.90	2.51E6	1.11	1.00	.86
◇	.90	2.03E6	1.11	1.00	.85
□	.90	1.52E6	1.11	1.00	.86

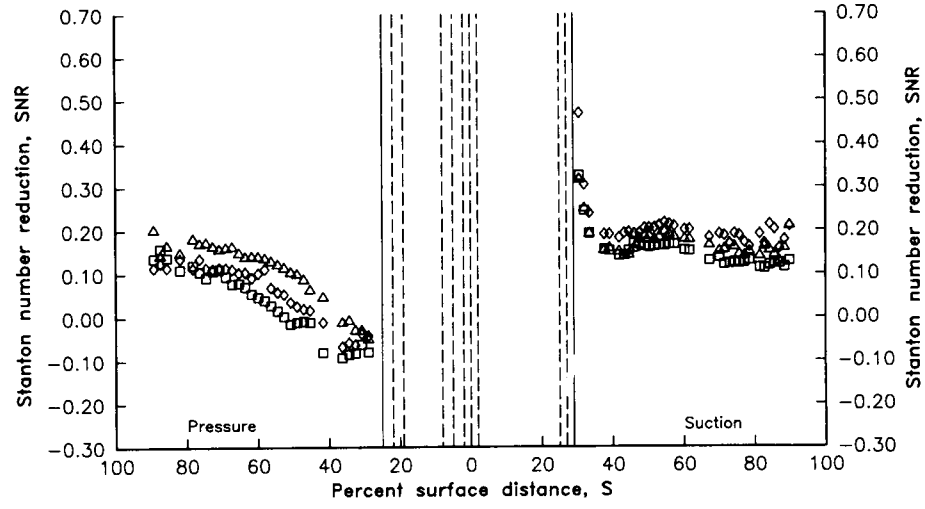

Figure 14. Effect of Reynolds number on heat transfer reduction (P_c/P_t = 1.10, T_c/T_g = 0.85)

3-D INELASTIC ANALYSIS METHODS FOR HOT SECTION COMPONENTS*

E.S. Todd
Pratt & Whitney Division
United Technologies Corporation
East Hartford, Connecticut

The objective of this program is to produce a series of new computer codes that permit more accurate and efficient three-dimensional inelastic structural analysis of combustor liners, turbine blades, and turbine vanes. Each code embodies a progression of mathematical models for increasingly comprehensive representation of the geometrical features, loading conditions, and forms of nonlinear material response that distinguish these three groups of hot section components.

Software in the form of stand-alone codes is being developed by Pratt & Whitney (P&W) with assistance from three uniquely qualified subcontractors: MARC Analysis Research Corporation (MARC), United Technologies Research Center (UTRC), and the State University of New York at Buffalo (SUNY-B). Special finite element models are being constructed by MARC, while mechanics of materials models and constitutive models are being assembled by UTRC. Development of advanced formulation (boundary element) models is being shared by P&W and SUNY-B. Verification of the various analysis packages is being done by P&W and at NASA Lewis Research Center.

The technical effort of the Inelastic Analysis Methods program is divided into two 24-month segments: a base program, and an optional program exercised at the discretion of the government. The first year (Task I) of the base program dealt with linear theory in the sense that stresses or strains and temperatures in generic modeling regions are linear functions of the spatial coordinates, and solution increments for load, temperature and/or time are extrapolated linearly from previous information. The second half of the base program (Task II), as well as the option program (Tasks IV and V), extend the models to include higher-order representations of deformations and loads in space and time and to deal more effectively with collections of discontinuities such as cooling holes and coating cracks. Work on Task V (general functions theory) has been mostly completed, and results are given in the Fourth Annual Status Reports. Base and option program computer codes, hereafter referred to as MOMM (Mechanics of Materials Model), MHOST (MARC-HOST), and BEST (Boundary Element Stress Technology), have been developed and delivered to NASA-Lewis Research Center.

Three increasingly sophisticated constitutive models are employed by MOMM, MHOST, and BEST to account for inelastic material behavior

*Work done under NASA Contract NAS3-23697.

(plasticity, creep) in the elevated temperature regime. The simplified model assumes a bilinear approximation of stress-strain response and glosses over the complications associated with strain rate effects, etc. The state-of-the-art model partitions time-independent (plasticity) and time-dependent (creep) in the conventional way, invoking the Von Mises yield criterion and standard (isotropic, kinematic, combined) hardening rules for the former, and a power law for the latter. Walker's viscoplasticity theory which accounts for the interaction between creep/relaxation and plasticity that occurs under cyclic loading conditions, has been adopted as the advanced constitutive model.

In brief, MOMM is a stiffness method finite element code that utilizes one-, two- and three-dimensional arrays of beam elements to simulate hot section component behavior. Despite limitations of such beam model representations, the code will be useful during early phases of component design as a fast, easy to use, computationally efficient tool. All of the structural analysis types (static, buckling, vibration, dynamics), as well as the three constitutive models mentioned above, are provided by MOMM. Capabilities of the code have been tested for a variety of simple problem discertizations.

The MHOST code employs both shell and solid (brick) elements in a mixed method framework to provide comprehensive capabilities for investigating local (stress/strain) and global (vibration, buckling) behavior of hot section components. Over the last decade, in order to support their commercially available software, the MARC Corporation has accumulated a great deal of technical expertise creating new, improved algorithms that will significantly reduce CPU (central processing unit) time requirements for three-dimensional analyses. The MHOST code development has taken advantage of this expertise. The third generation (Task V) MHOST code is operational and has been tested with a variety of academic as well as engine-related configurations.

Successful assembly of the all-new BEST code was possibly the most important accomplishment of the base program effort. The challenge of extending basic theory and algorithms to encompass inelastic dynamic effects in three-space was met by combining the special skills and efforts of the research and programming teams at SUNY-B and P&W. As with MHOST, the fourth version of BEST is executable and has been exercised with both small and large test cases. While MHOST and BEST are currently viewed as complementary, they are also competitors; and overall performance on large inelastic models will be watched with interest as the codes mature.

Work on Task V (general functions theory) and application of the codes to representative turbine blade and vane configurations is in process, and will be described at the Sixth Annual HOST Workshop.

3-D INELASTIC ANALYSIS METHODS FOR HOT SECTION COMPONENTS - BEST 3D CODE[1]

Raymond B. Wilson
Pratt & Whitney Division
United Technologies Corporation
East Hartford, Connecticut

and

Prasanta K. Banerjee
State University of New York at Buffalo
Buffalo, New York

The goal of the Advanced Formulation Development portion of the Inelastic Analysis Methods contract is the development of an alternative stress analysis tool, distinct from the finite element method, applicable to the engineering analysis of gas turbine engine structures. The boundary element method was selected for this development effort on the basis of its already demonstrated applicability to a variety of geometries and problem types characteristic of gas turbine engine components. This paper describes briefly major features of the BEST3D computer program and outlines some of the significant developments carried out as part the Inelastic Methods Contract.

BEST3D OVERVIEW

BEST3D (Boundary Element Stress Technology - Three Dimensional) is a general purpose three-dimensional structural analysis program utilizing the boundary element method. The method has been implemented for very general three-dimensional geometries, for elastic, inelastic and dynamic stress analysis. Although the feasibility of many of the capabilities provided had been demonstrated in a number of individual research efforts, the present code is the first in which they have been made available for large scale problems in a single code. In addition, important basic advances have been made in a number of areas, including the development and implementation of a variable stiffness plasticity algorithm, the incorporation of an embedded time algorithm for elastodymanics and the extensive application of particular solutions within the boundary element method. Major features presently available in the BEST3D code include:

- Very general geometry definition, including the use of doubly curved isoparametric surface elements and volume cells, with provision of full substructuring capability

[1]The work discussed in this paper was carried out as part of National Aeronautics and Space Administration contract NAS3-23697, "3-D Inelastic Analysis Methods for Hot Section Components". The program manager at NASA-Lewis Research Center is Mr. C. C. Chamis.

- General capability for the definition of complex, time-dependent boundary conditions
- Capability for nonlinear analysis using a variety of algorithms, solution proceedures and constitutive models
- A very complete elastodynamic capability including provision for free vibration, forced response and transient analysis

BEST3D has been successfully implemented on a variety of computers, including the IBM 3090, various CRAY models and the Hewlett-Packard HP9000.

The analytical basis and numerical implementation of the boundary element method for the major problem types considered are very briefly reviewed in the next two sections. Particular attention is devoted to the variable stiffness plasticity algorithm and the time-embedded elastodynamic algorithm. Full details of both the analysis and implementation may be found in references 1, 2 and 3.

QUASI-STATIC ANALYSIS

By making use of the reciprocal work theorem, the governing differential equations for a three-dimensional (homogeneous) structure under combined thermal, mechanical and body force loadings can be converted to an integral equation written on the surface of the structure. This integral equation is:

$$c_{ij}u_i = \int_S (G_{ij}t_i - F_{ij}u_i)\,dS + \int_V (G_{ij}f_i + \beta W_j T)\,dV \tag{1}$$

where T = temperature, $W_j = T_{ikj}\delta_{ik}$, β = coefficient of thermal expansion, T_{ikj} = the stress, σ_{ik}, due to a point force system, e_j, and G_{ij}, T_{ikj} and F_{ij} are defined reference 1. The equation

$$\sigma_{ij} = \int_S (D_{ijk}t_k - S_{ijk}u_k)\,dS + \int_V (T_{ijk}t_k + M_{ij}T)\,dV \tag{2}$$

allows calculation of stresses at any interior point where they are required. A similar equation for interior displacements can be obtained by setting $c_{ij} = \delta_{ij}$ in (1).

In a purely elastic problem BEM stress analysis can be carried out entirely on the boundary of the structure. Once a physically reasonable set of boundary conditions has been prescribed, (1) can, in principle, be solved for all of the remaining boundary displacements and tractions.

It is generally impossible to solve (1) exactly for real structures and loading conditions. Suitable approximations of the boundary geometry, displacements and tractions must be used in order to reduce (1) to a system of algebraic equations. The present version of BEST3D models boundary geometry and boundary values of field quantities using linear and/or quadratic isoparametric shape functions. The surface integrals in (1) are then evaluated numerically

using product Gaussian quadrature rules. The numerical implementation of the BEM is discussed in detail in textbooks (ref. 4), as well as in references 1 and 2.

In the case of inelastic analysis, the volume integrals in (1) cannot be calculated *a priori*, since they require knowledge of inelastic strain, which is itself a part of the solution. In this case equations (1), (2) and the inelastic material model can be regarded as a coupled system of nonlinear equations. In the numerical implementation of the BEM (2) is used to calculate the stresses at interior points, and the nonlinear material model is then used to evaluate inelastic strain. Since the volume integrals of inelastic strain vanish except in regions of nonlinear material response, approximations of geometry and field quantities are required only where nonlinearity is expected. In the original version of BEST3D, strain variation in the interior was represented using isoparametric volume cells, with the solution carried out using a relatively standard iteration proceedure. More recently, a new approach has been developed which exploits certain features of the constitutive relationships involved. The unknown nonlinear terms in the interior are now defined as scalar variables. A new direct numerical solution scheme comparable to the variable stiffness method used in finite element analysis has been developed and implemented, avoiding the requirement for an iterative solution.

For a standard elasto-plastic flow problem the evolution of plastic flow is governed by:

$$F(\sigma_{ij}, h) = 0 \tag{3}$$

$$\epsilon^p_{ij} = \dot{\lambda}\frac{\partial F}{\partial \sigma_{ij}} \tag{4}$$

These equations together with the consistency relations (i.e., the stress point must remain on a newly developing yield surface characterized by a change in the hardening parameter h) leads to an expression for the unknown plastic flow factor $\dot{\lambda}$ as:

$$\dot{\lambda} = L^{\sigma}_{ij}\,\dot{\sigma}_{ij} \tag{5}$$

where

$$L^{\sigma}_{ij} = \frac{1}{H}\frac{\partial F}{\partial \sigma_{ij}}$$

$$H = -\left(\frac{\partial F}{\partial \epsilon^p_{mn}} + \frac{\partial F}{\partial h}\frac{\partial h}{\partial \epsilon^p_{mn}}\right)\frac{\partial F}{\partial \sigma_{mn}}$$

It should be noted that L^{σ}_{ij} depends upon the current state variable, not on the incremental quantities.

However, the relationship given by (5) does not exist for ideal plasticity, as H vanishes for zero hardening. This can be avoided by reformulating the above expression in terms of strain increments:

$$\dot{\lambda} = L^{\epsilon}_{ij}\dot{\epsilon}_{ij} \tag{6}$$

where

$$L^{\epsilon}_{ij} = \frac{1}{H'}\frac{\partial F}{\partial \sigma_{ij}}$$

$$H' = \frac{\partial F}{\partial \sigma_{kl}} D_{klmn}\frac{\partial F}{\partial \sigma_{mn}} - \left(\frac{\partial F}{\partial \epsilon^p_{kl}} + \frac{\partial F}{\partial h}\frac{\partial F}{\partial \epsilon^p_{kl}}\right)\frac{\partial f}{\partial \sigma_{kl}}$$

where D_{ijkl} is the elastic constitutive tensor. It is evident that H' does not vanish for zero hardening (ideal plasticity).

The basic boundary element formulation for an inelastic body undergoing infinitesimal strain is given by:

$$c_{ij}\dot{u}_i(\xi) = \int_\Gamma [G_{ij}(x,\xi)\dot{t}_i(x) - F_{ij}(x,\xi)\dot{u}_i(x)]\, d\Gamma + \int_\Omega B_{ijk}(x,\xi)\, \dot{\sigma}^0_{ij}\, d\Omega \tag{7}$$

The stress rates at an interior point ξ are obtained from equation (7) via the strain-displacement relations and the constitutive relationships ($\dot{\sigma}_{ij} = D^e_{ijkl}\dot{\epsilon}_{kl} - \dot{\sigma}^0_{ij}$) as

$$\begin{aligned} \dot{\sigma}_{ij}(\xi) &= \int_\Gamma [G^\sigma_{ijk}(x,\xi)\dot{t}_i(x) - F^\sigma_{ijk}(x,\xi)\dot{u}_i(x)]\, d\Gamma \\ &\quad + \int_\Omega B^\sigma_{ipjk}(x,\xi)\, \dot{\sigma}^0_{ip}(x)\, d\Omega + J^\sigma_{ipjk}\, \dot{\sigma}^0_{ip}(\xi) \end{aligned} \tag{8}$$

where the kernel functions have been defined in the reference 2.

In equation (8) the volume integral must be evaluated in the sense of $(\Omega - D)$ with the limit taken as $D \to 0$, where D is a spherical exclusion of small arbitrary radians with ξ as its center. The term J^σ is the jump term derived from the analytical treatment of the integral over D. It is of considerable interest to note that the value of J^σ is independent of the size of the exclusion D, provided the initial stress distribution is locally homogeneous, i.e. uniform over its volume.

The evaluation of strains and stresses at boundary points can be accomplished by considering the equilibrium of the boundary segment and utilizing constitutive and kinematic equations. The stresses and global derivatives of the displacements which lead to strains at a point ξ can be obtained from the following set of coupled equations:

$$\begin{aligned} \dot{\sigma}_{ij}(\xi) - (\Delta\delta_{ij}\dot{u}_{k,k}(\xi) + \mu(\dot{u}_{i,j}(\xi) + \dot{u}_{j,i}(\xi))) &= -\dot{\sigma}^0_{ij}(\xi) \\ \dot{\sigma}_{ij}(\xi)n_j(\xi) &= \dot{t}_i(\xi) \\ \frac{\partial\xi_k}{\partial\eta_l}\frac{\partial\dot{u}_i(\xi)}{\partial\xi_k} &= \frac{\partial\dot{u}_i(\xi)}{\partial\eta_l} \end{aligned} \tag{9}$$

where η_i are a set of local axes at the field point ξ.

All the above nonlinear formulations include initial stresses in the governing equations which are not known *a priori* and, therefore, are solved by using iterative procedures. A non-iterative direct solution procedure is made feasible in this work by reducing the number of unknowns in the governing equations by utilizing certain features of the incremental theory of plasticity expressed by equations (3) to (6). The initial stresses σ^0_{ij} appearing in equations (7) to (9) can be expressed in the context of an elastoplastic deformation as:

$$\dot{\sigma}^0_{ij} = K_{ij}\dot{\lambda} \tag{10}$$

where $K_{ij} = D^e_{ijkl}\dfrac{\partial F}{\partial\sigma_{kl}}$.

Substituting (5) and (10) in equations (7) and (8) we can obtain:

$$c_{ij}\dot{u}_i(\xi) = \int_\Gamma [G_{ij}(x)\dot{t}_i(x) - F_{ij}(x,\xi)\dot{u}_i(x)]\, d\Gamma \tag{11}$$

and

$$\begin{aligned} \dot{\lambda}(\xi) \;=\; & L^\sigma_{jk}(\xi) \int_\Gamma [G^\sigma_{ijk}(x,\xi)\dot{t}_i(x) - F^\sigma_{ijk}(x,\xi)\dot{u}_i(x)]\, d\Gamma \\ & + L^\sigma_{jk}(\xi) \int_\Omega B^\sigma_{ipjk}(x,\xi)\; K_{ip}(x)\; \dot{\lambda}(x)\; d\Omega \\ & + L^\sigma_{jk}\; J^\sigma_{ipjk}\; K_{ip}(\xi)\; \dot{\lambda}(\xi) \end{aligned} \tag{12}$$

Equations (11) and (12) can be solved simultaneously to evaluate the unknown values of displacements, traction rates and the scalar variable $\dot{\lambda}$.

The equations for the boundary nodes (9) are similarly transformed to express them in terms of the scalar variable $\dot{\lambda}$ using equations (5) and (10).

TRANSIENT STRESS ANALYSIS

The direct boundary integral formulation for a general, transient, elastodynamic problem can be constructed by combining the fundamental point force solution of the governing equations (Stokes' solution) with Graffi's dynamic reciprocal theorem. Details of this construction can be found in Banerjee and Butterfield (ref. 4). For zero initial conditions and zero body forces, the boundary integral formulation for transient elastodynamics reduces to:

$$c_{ij}(\underline{\xi})u_i(\underline{\xi},T) = \int_S [G_{ij}(\underline{x},\underline{\xi},T) * t_i(\underline{x},T) - F_{ij}(\underline{x},\underline{\xi},T) * u_i(\underline{x},T)]\, dS(x) \tag{13}$$

where

$$G_{ij} * t_i = \int_0^T G_{ij}(\underline{x},T;\underline{\xi},\tau)\; t_i(x,\tau)\; d\tau \tag{14}$$

$$F_{ij} * u_i = \int_0^T F_{ij}(\underline{x},T;\underline{\xi},\tau)\; u_i(x,\tau)\; d\tau \tag{15}$$

are Reimann convolution integrals and $\underline{\xi}$ and $\underline{x}$ are the space positions of the receiver (field point) and the source (source point). The fundamental solutions G_{ij} and F_{ij} are the displacements and tractions at a point x and at a time T due to a unit force vector acting at a point $\underline{\xi}$ at a time τ. Equation (13) represents an exact formulation involving integration over the surface as well as the time history. It should also be noted that this is an implicit time-domain formulation because the response at time T is calculated by taking into account the history of surface tractions and displacements up to and including the time T. Furthermore, equation (13) is valid for both regular and unbounded domains.

Once the boundary solution is obtained, the stresses at the boundary nodes can be calculated without any integration by using the scheme described for the static case. For calculating displacements at interior points equation (13) can be used with $c_{ij} = \delta_{ij}$ and the interior stresses can be obtained from

$$\sigma_{ij}(\underline{\xi}, T) = \int_S [G^{\sigma}_{ijk}(\underline{x}, \underline{\xi}, T) * t_i(\underline{x}, T) - F^{\sigma}_{ijk}(\underline{x}, \underline{\xi}, T) * u_i(\underline{x}, T)]\, dS(x) \tag{16}$$

The functions G^{σ}_{ij} and F^{σ}_{ij} in the above equation are derived from the Stokes' solution by differentiation.

In the initial version of BEST3D, constant time stepping was used to obtain the transient dynamic response. It was found to be more effective to use a linear time variation of u and t on the boundaries. In this case:

$$u_i(\underline{x}, \tau) = \sum_{n=1}^{N} [\overline{M}_1\, u_i^{n-1}(\underline{x}) + \overline{M}_2\, u_i^{n}(\underline{x})] \tag{17}$$

$$t_i(\underline{x}, \tau) = \sum_{n=1}^{N} [\overline{M}_1\, t_i^{n-1}(\underline{x}, \tau) + \overline{M}_2\, t_i^{n}(\underline{x})] \tag{18}$$

where $\overline{M}_1$ and $\overline{M}_2$ are the time functions, and are of the form:

$$\overline{M}_1 = \frac{\tau_n - \tau}{\Delta T} \phi_n(\tau) \tag{19}$$

$$\overline{M}_2 = \frac{\tau - \tau_{n-1}}{\Delta T} \phi_n(\tau) \tag{20}$$

For illustration purposes, consider the boundary integral equation for the first time step, i.e.

$$c_{ij} u_i(\xi, T_1) - \int_{T_0}^{T_1} \int_S [G_{ij} t_i - F_{ij} u_i]\, dS\, d\tau = 0 \tag{21}$$

The time integration in equation (21) by utilizing (18) is done analytically. After the usual numerical integration and assembly process, the resulting system equation is of the form:

$$[A_2^1][X^1] - [B_2^1][Y_1] + [A_1^1][X^0] - [B_1^1][Y^0] = 0 \tag{22}$$

where:

- A and B are matrices related to the unknown and known field quantities, respectively:
- X and Y are the vectors of unknown and known field quantities, respectively:
- for X and Y the superscript denotes the time:
- for A and B the superscript denotes the time step at which they are calculated, and the subscript denotes the local time nodes (1 or 2) during that time-stepping interval.

Since all the unknowns at time $T = 0$ are assumed to be zero, equation (22) reduces to:

$$[A_2^1][X^1] = [B_2^1][Y^1] + [B_1^1][Y^0] \tag{23}$$

For second time step, the assembled system equation has the form

$$[A_2^1][X^2] - [B_2^1][Y^2] + [A_1^1][X^1] - [B_1^1][Y^1] = -[A_2^2][X^1] + [B_2^2][Y^1] - [A_1^2][X^0] + [B_1^2][Y^0] \tag{24}$$

As in the constant time variation scheme, only the matrices on the right hand side of equation (24) need be evaluated. However, one needs to integrate and assemble four matrices at each time step as compared to two in the case of constant time variation. This can be done with only a small increase in computing time by integrating all the kernels together and then assembling all the matrices together. Equation 24 can be rearranged such that:

$$[A_2^1][X^2] = [B_2^1][Y^2] - [A_1^1 + A_2^1][X^1] - [B_1^1 + B_2^2][Y^1] + [B_1^2][Y^1] \tag{25}$$

In the above equation, all the quantities on the right hand side are known. Therefore, the unknown vector X^2 at time T_2 can be obtained by solving the above equation.

Thus, for the present case, the boundary integral equation (25) can be written in discretized form as:

$$[A_2^1][X^N] - [B_2^1][Y^N] = -\sum_{n=2}^{N}[[A_2^n + A_1^{n-1}][X^{N-n+1}] - [B_2^n + B_1^{n-1}][Y^{N-n+1}] + [B_1^n][Y^0]] \tag{26}$$

or

$$[A_2^1][X^N] = [B_2^1][Y^N] + [R^N] \tag{27}$$

It is of interest to note that, if time interpolation functions $\overline{M}_1$ and $\overline{M}_2$ are replaced by $\overline{M}_1 = \overline{M}_2 = 0.5\phi_n(\tau)$, the time stepping scheme for linear variation can be used for the case of constant variation with averaging between the local time nodes.

SYMBOLS

δ_{ij}	Kronecker delta symbol
u_i, t_i	boundary displacements and tractions
G_{ij}	displacement point load solution
F_{ij}	traction kernel derived from G_{ij}
f_i	mechanical body forces
T	temperature
β	coefficient of thermal expansion
$B_{ijk}, T_{ijk}, D_{ijk}, S_{ijk}$	higher order kernels derived from G_{ij}
S	surface of three-dimensional structure
V	interior of a three-dimensional structure
σ_{ij}	stress tensor
ϵ_{ij}	strain tensor

c_{ij}	jump terms in boundary integral equation
$\dot{\lambda}$	plastic flow factor
$F(\sigma_{ij}, h)$	yield function
h	hardening parameter
$\cdot$, same as $\dot{\sigma}_{ij}$	time derivative
superscript ^{p}, as in ϵ^p_{ij}	plastic component
superscript ^{e}, as in ϵ^p_{ij}	elastic component
D^e_{ijkl}	elastic constitutive tensor
x, y, z	points in three-dimensional space
superscript $^\circ$, as in σ°_{ij}	initial stress (or strain)
B^σ_{ijkl}	higher order kernel derived from G_{ij}
λ, μ	Lamé constants
t, τ	denote time in dynamic analysis
$*$, as in $G_{ij} * t_i$	time convolution
M_1, M_2	shape functions for time variation
$[A^j_i], etc.$	coefficient matrices in time domain solution

REFERENCES

1. Todd, E. S., B. N. Cassenti, S. Nakazawa and P. K. Banerjee, *3-D Inelastic Analysis Methods for Hot Section Components - First Annual Status Report*, NASA CR-174700, United Technologies, Pratt & Whitney Engineering, East Hartford, CT.

2. Wilson, R. B., M. J. Bak, S. Nakazawa and P. K. Banerjee, *3-D Inelastic Analysis Methods for Hot Section Components - Second Annual Status Report*, NASA CR-175060, United Technologies, Pratt & Whitney Engineering, East Hartford, CT.

3. Wilson, R. B., and P. K. Banerjee, *3-D Inelastic Analysis Methods for Hot Section Components - Third Annual Status Report*, NASA CR-179517, United Technologies, Pratt & Whitney Engineering, East Hartford, CT.

4. Banerjee, P. K. and R. Butterfield, *Boundary Element Methods in Engineering Science*, McGraw-Hill (UK), 1981.

N89-17318

RESPONSE CHARACTERISTICS OF MHOST FOR 3-D INELASTIC ANALYSIS OF HOT-SECTION COMPONENTS

Lawrence K. Shen
Sverdrup Technology, Inc.
Lewis Research Center
Cleveland, Ohio

Hot-section durability problems appear in a variety of forms ranging from corrosion, erosion, and distortion to the occurrence of fatigue cracking. A modest change in the shape of an airfoil due to erosion or distortion can lead to the deterioration of the airfoil's performance. Such changes in the airfoil's shape or other critical components must be known as accurately as possible in order to design a propulsion system with long-term efficiency. A discussion of a code that has been developed under a contract with NASA Lewis Research Center to perform structural analysis of these types of components is presented in this paper.

General purpose finite-element computer codes containing a variety of three-dimensional elements and with capabilities to model inelastic materials have been available for more than a decade. Incorporation of such codes into one hot-section design process has been severely limited by high costs associated with the extensive labor and computer and/or time resources required to obtain reasonably detailed results. With today's computers and solution algorithms, models described by a few hundred displacement degrees of freedom commonly consume 1 to 3 hr of mainframe central processing unit (CPU) time during simulation of a single thermomechanical loading cycle. Since more accurate modeling of components with only a few geometrical discontinuities can easily contain several thousand degrees of freedom, performing a three-dimensional inelastic analysis of hot-section hardware with existing codes falls outside the realm of practicality.

The inelastic methods program addresses the need to develop more efficient and accurate three-dimensional inelastic structural analysis procedures for gas turbine hot-section components. A series of new stand-alone computer codes is being created for the comprehensive numerical analysis of combustor liners, turbine blades and vanes, and other hot-section components. Under NASA contracts, Pratt & Whitney Aircraft in partnership with MARC Analysis Corporation are participating in programs for development of modeling methods and are writing a new computer code to perform three-dimensional inelastic analysis. The code discussed in this paper is referred to as MHOST (MARC - Hot Section Technology). The models in the code address the effects of high-temperature and thermal and mechanical loading on the local (stress and strain) and global (dynamics and buckling) structural behavior of hot-section components. Attention is being given to the development of solution algorithms, integration algorithms for stiffness, strain recovery and residual terms, and modeling methods that permit accurate representations of thermal effects on structural loading and material properties, and geometrical discontinuities as well.

The finite elements for modeling three-dimensional inelastic analysis of hot-section components in MHOST are based on mixed finite-element methods derived from

the Hu-Washizu Principle (refs. 1 and 2). Three constitutive models are used in the code. These models are the secant elasticity model, von Mise's plasticity model, and Walker's creep plasticity model. Temperature dependency and anisotropy can be obtained through user subroutines. Nonlinear transient analysis and eigenvalue extraction for buckling and modal analyses are some of the important features in the program.

To test the validity of the MHOST finite-element code, considerable efforts have been made in applying the codes in different cases with results compared to theoretical predictions or numerical values generated by other codes. A cylindrical shell roof under dead weight loading was modeled using various types of elements from different codes in which the aspect ratio was varied by refining the element mesh size from 2 by 2 to 18 by 18.

Figure 1 shows the normalized vertical displacement of the center of the structure versus aspect ratio. Results in both solution schemes show convergence as the aspect ratio decreases. In order to study the effect of curvature on the solution, a test case of a clamped square plate subject to uniform pressure loading was investigated. The plate was divided into 4 by 4 meshes in the study, but the aspect ratio could be varied by changing the thickness of the plate.

The results given by the MHOST code in figure 2 show no effect due to the variation of the aspect ratio. A similar observation can also be found in the four- and eight-node element of the MSC/NASTRAN code. Transient analysis of a cantilever beam subject to two impulsive couples at the free end was then studied using the eight-node three-dimensional solid element to test the dynamic performance of the code.

Figure 3 shows the time history of displacement at a corner node located about two-thirds of the beam from the free end. Two solution algorithms, the mixed finite element and displacement methods, were adopted in the model with time step integrations of 2.0 and 0.5 sec, respectively. Since there is no damping involved in the vibration, no energy dissipation is expected in the response after the impulses.

The code was then applied to a real CF 6-50 engine blade and rotor model with data generated by a computational structural mechanics simulator system to predict the static and dynamic responses of the engine at any flight cycle condition. The simulator system provides data, such as pressure and temperature distribution, centrifugal force, and time duration, at various stages of flight. Figure 4 shows the variation of the radical displacement of the leading edge tip in the static condition during the entire flight without consideration of the centrifugal force effect.

The code was finally implemented in the sector model with different flight cycles, as mentioned in the static case, to perform the transient dynamic analysis of the blade-rotor system using the Newmark integration scheme with $\beta = 0.25$ and $\gamma = 0.5$. The curves with different time steps and/or material properties are designated by circles, squares, and triangles, respectively in figure 5. The curve with the triangles differs from the one with the squares since the thermal effects on material properties are taken into consideration.

Other results show similar trends but different magnitudes. The CPU time used in the shell roof test case, as an example, is given in table I. Results show that the MHOST code is more efficient than other codes if the standard displacement method

is used. The efficiency of using the mixed finite-element solution algorithms depends greatly on the convergence criteria provided by the user.

In summary, the advantages of the newly developed code are demonstrated by comparisons of the analyses with existing theoretical data as well as with other available finite-element programs. The new code shows a promise to significantly reduce the computer time and also permits accurate and efficient structural analyses of engine hot-section components. The methods and computer code described in this paper constitute the focused recent developments in advanced three-dimensional inelastic analysis for engine hot-section components.

REFERENCES

1. Hu, H.C.: "On Some Variational Principles in The Theory of Elasticity and Plasticity," Scintia Sinica, 4, pp. 33-54, 1955.

2. Washizu, K.: Variational Methods in Elasticity and Plasticity, Pergamon Press, Oxford, 1974.

TABLE I. - COMPARISON OF CPU TIME FOR CYLINDRICAL SHELL ROOF CASE

Mesh	MARC			MSC/NASTRAN			MHOST	
	4-node	8-node	20-node	4-node	8-node	20-node	4-node[a]	4-node[b]
	CPU time, sec							
2 by 2	9.61	9.73	8.12	1.42	1.91	2.61	2.48	0.90
4 by 4	10.06	-----	9.39	1.70	3.96	6.47	4.49	1.05
6 by 6	10.79	11.93	12.34	2.20	7.92	13.94	5.91	1.33
8 by 8	11.78	14.05	16.75	2.93	15.94	30.03	8.83	1.65
10 by 10	13.07	-----	25.94	4.0	29.36	65.8	12.67	2.11
12 by 12	14.66	22.13	35.26	5.03	56.58	144.15	17.37	2.66
14 by 14	16.59	27.65	48.96	6.47	106.45	328.89	22.90	3.33
16 by 16	19.20	36.73	69.95	8.33	202.45	745.73	30.59	4.43
18 by 18	21.90	43.90	103.48	10.17	471.36	1657.0	36.72	4.98

[a]Loubignac mixed finite element.
[b]Displacement method.

Figure 1 Displacement of Center for Cylindrical Shell Roof

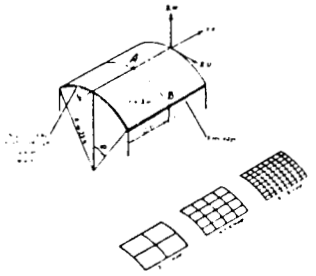

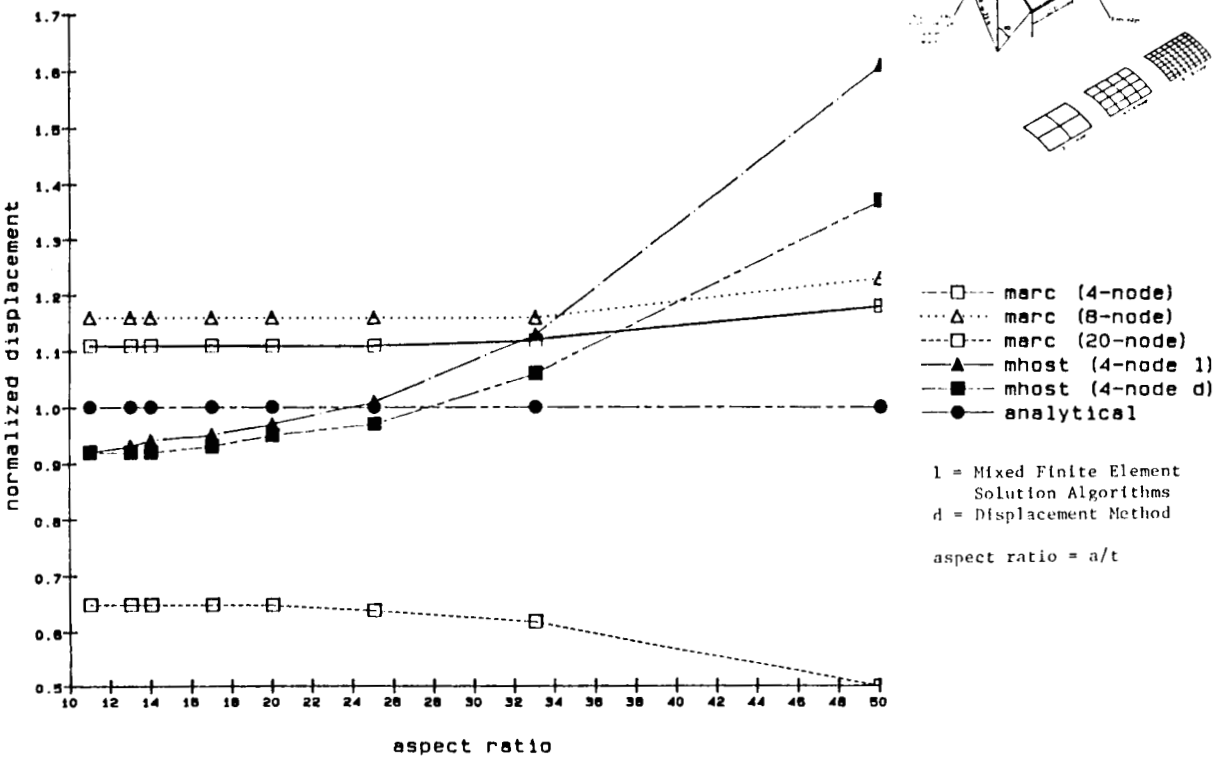

Figure 2 Displacement of Center for Clamped Flat Plate

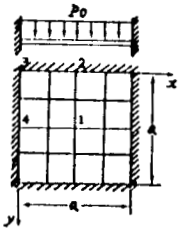

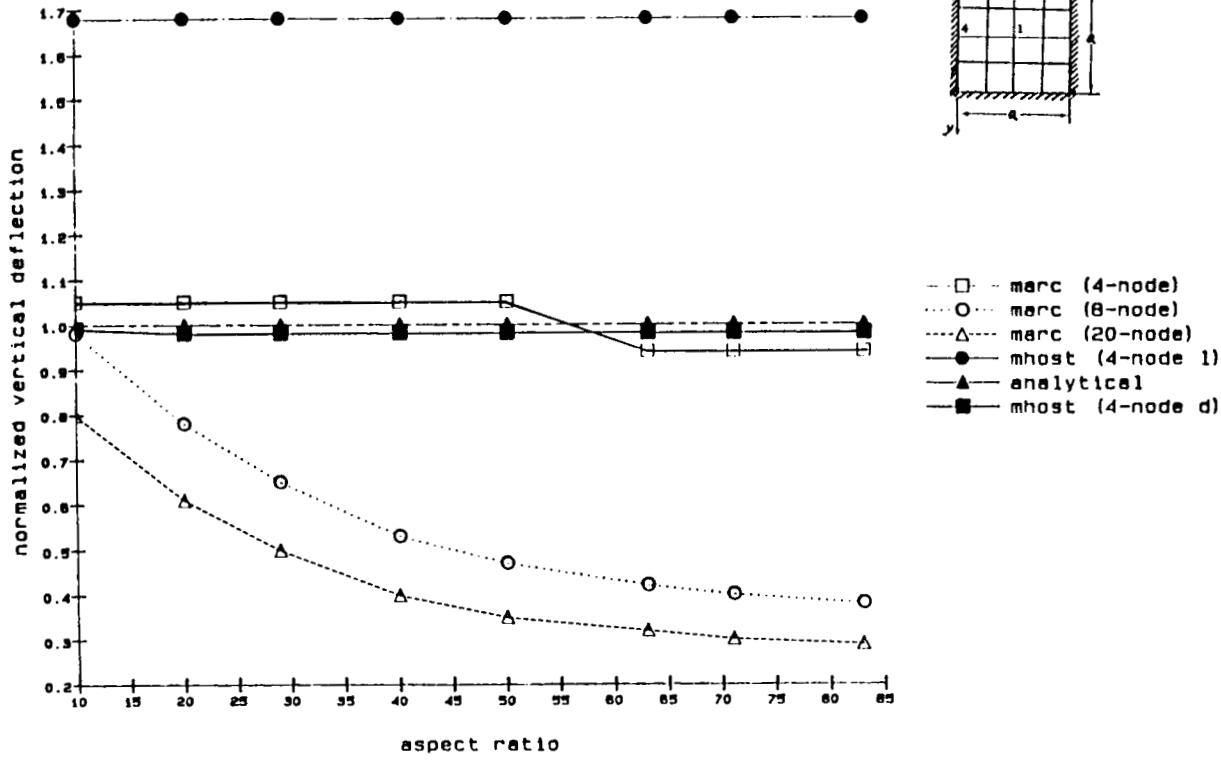

Figure 3 Transient Analysis of A 3-D Beam

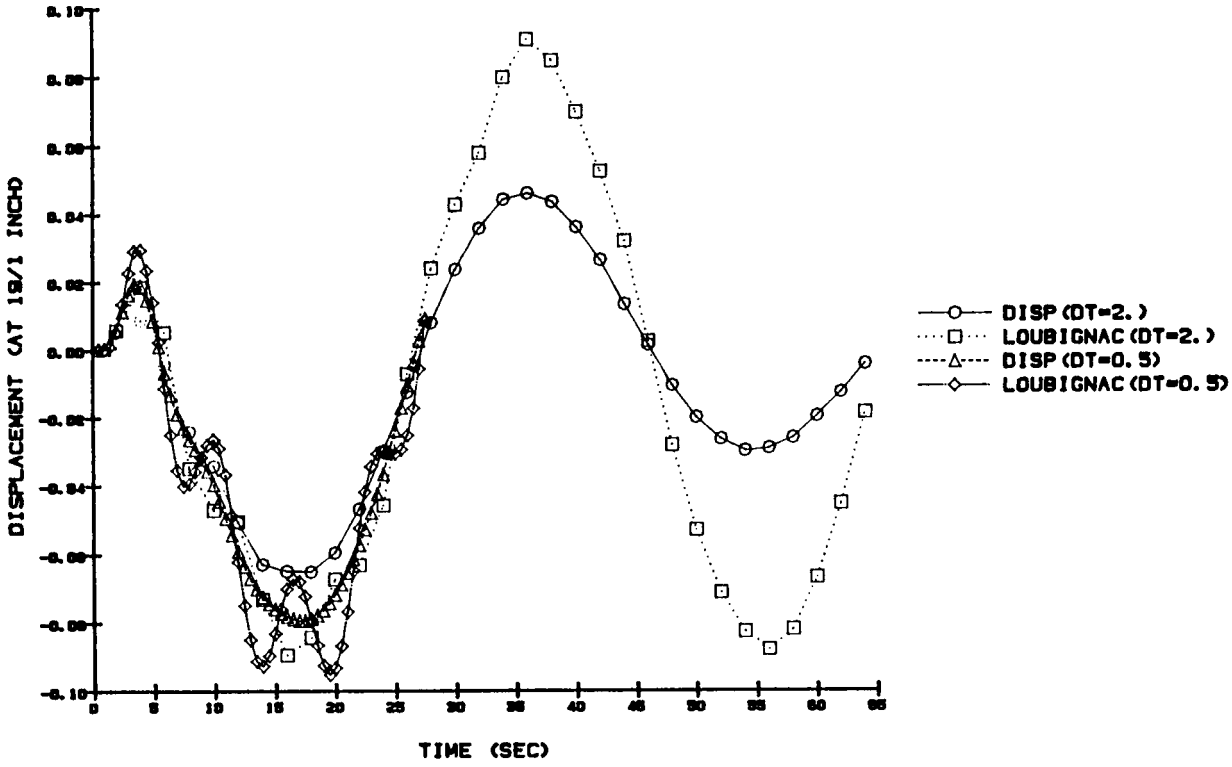

Figure 4 Radial Displacement of Leading Edge Tip (Static)

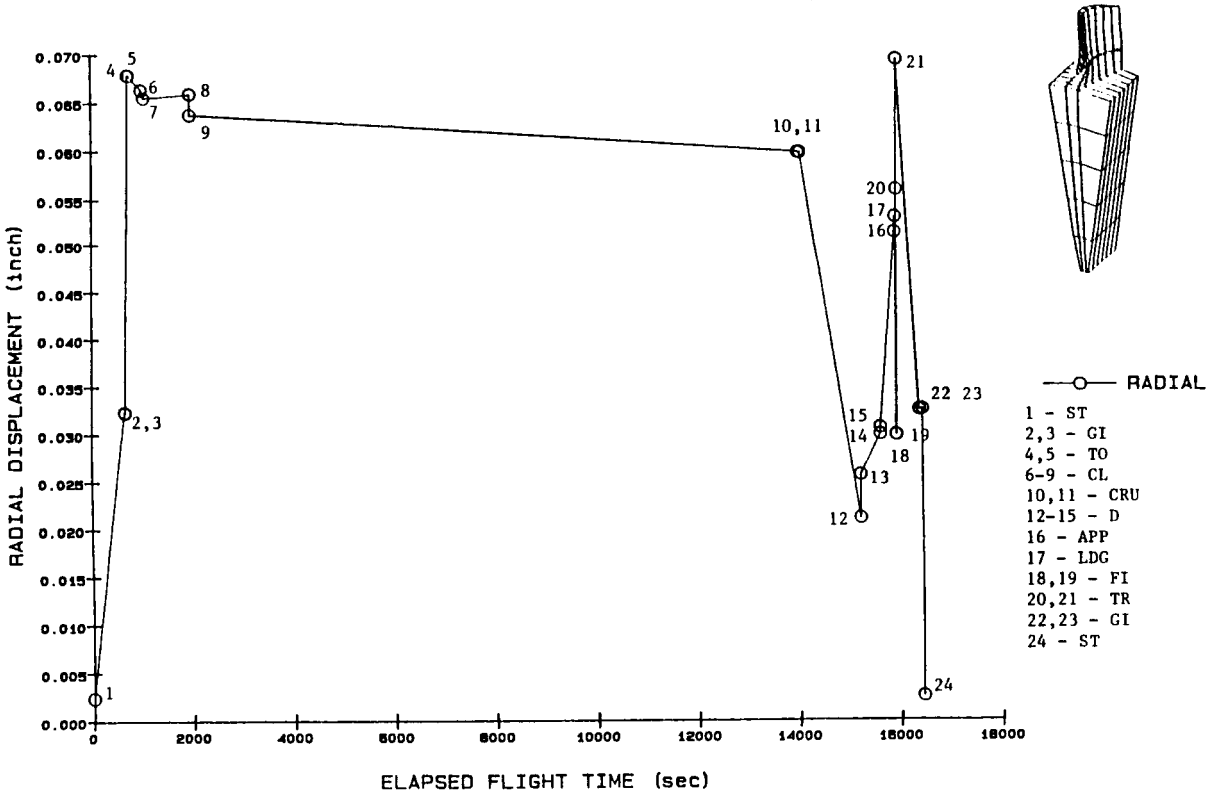

Figure 5 Radial Displacement of Leading Edge Tip (Tranient with Different Flight Conditions)

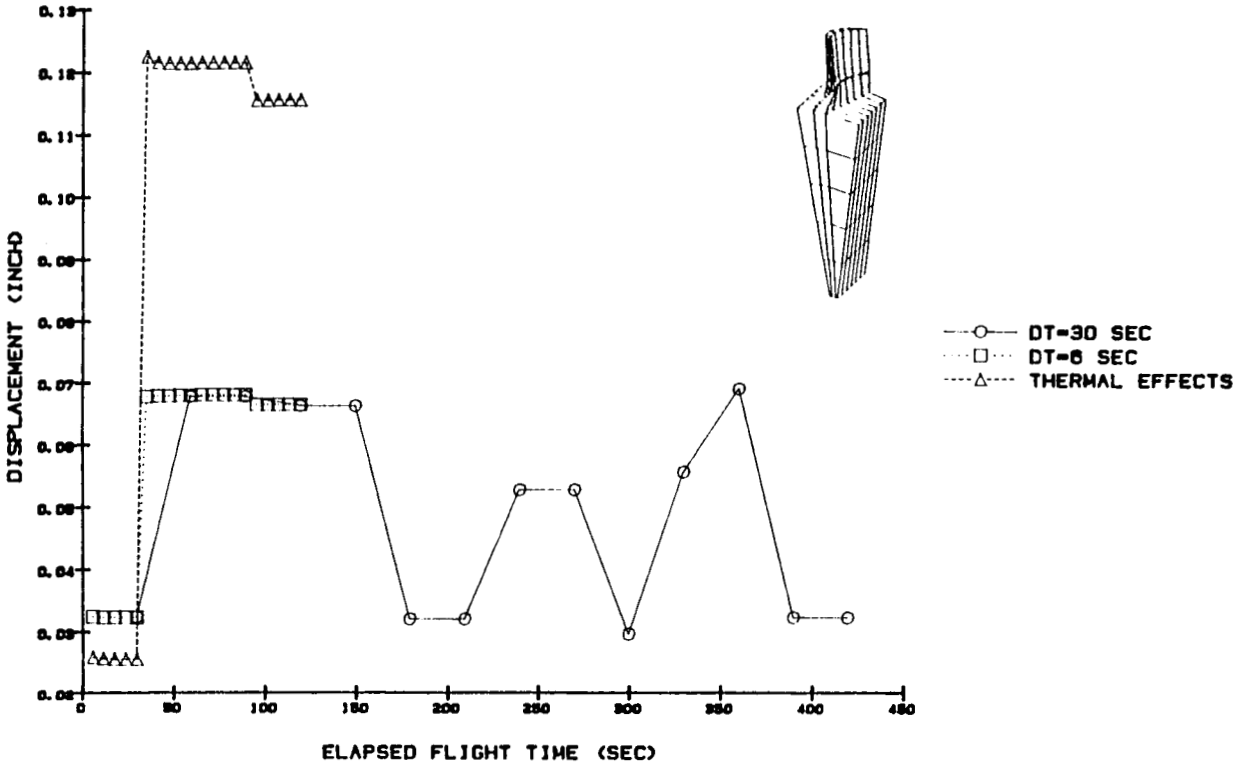

MECHANICS OF MATERIALS MODEL

Jeffrey P. Meister
Institute for Computational Mechanics in Propulsion
Lewis Research Center
Cleveland, Ohio

The Mechanics of Materials Model (MOMM) is a three-dimensional inelastic structural analysis code for use as an early design stage tool for hot-section components. MOMM is a stiffness method finite-element code that uses a network of beams to characterize component behavior.

The Mechanics of Materials Model contains three material models to account for inelastic material behavior. These include the simplified material model, which assumes a bilinear stress-strain response; the state-of-the-art model, which utilizes the classical elastic-plastic-creep strain decomposition; and Walker's viscoplastic model, which accounts for the interaction between creep and plasticity that occurs under cyclic-loading conditions.

Static and transient analyses can be performed utilizing the MOMM code for applied loads, thermal loads, and enforced displacements. The transient analysis is performed using Newmark's integration scheme. Frequency and buckling problems are solved for by using conventional eigenvalue extraction techniques. Frequency and buckling analyses may be performed by using the initial or tangent stiffness.

Input parameters for the computer code consist of information defining the analysis model (geometry, material, boundary conditions, and loads) and information describing the method of solution to be selected. The model is defined by four-node rectangular elements called framework cells. The framework cells are transformed internally into a network of six beams (four edge beams and two diagonal beams). The initial material properties to be input include the modulus of elasticity, Poisson's ratio, mass density, coefficient of thermal expansion, and yield stress. A hardening slope must also be input for use with the simplified material model. The initial temperature is input and the time at initial conditions is set to zero. Boundary conditions are specified at each node by indicating a constrained or non-constrained condition for the six degrees of freedom. The number and type of load increments must also be specified. The user may specify various types of loads including concentrated loads, line loads, surface pressures, centrifugal loads, enforced displacements, and thermal loads.

Input associated with the method of solution includes (1) choice of constitutive model, (2) choice of static or transient analyses, (3) choice of buckling and/or frequency analyses, and (4) choice of initial or tangent stiffness for buckling or frequency analyses. A convergence value, defining the allowable relative difference in energy between two consecutive iterations to satisfy convergence, must also be input by the user. Figures 1 to 3 illustrate results obtained using the MOMM code for three sample problems.

CANTILEVERED PLATE RESULTS

LENGTH, 4 IN.; WIDTH, 1.0 IN.; THICKNESS, 0.05 IN.; ELASTIC MODULUS, 1.0×10^7 PSI; POISSON'S RATIO, 0.25

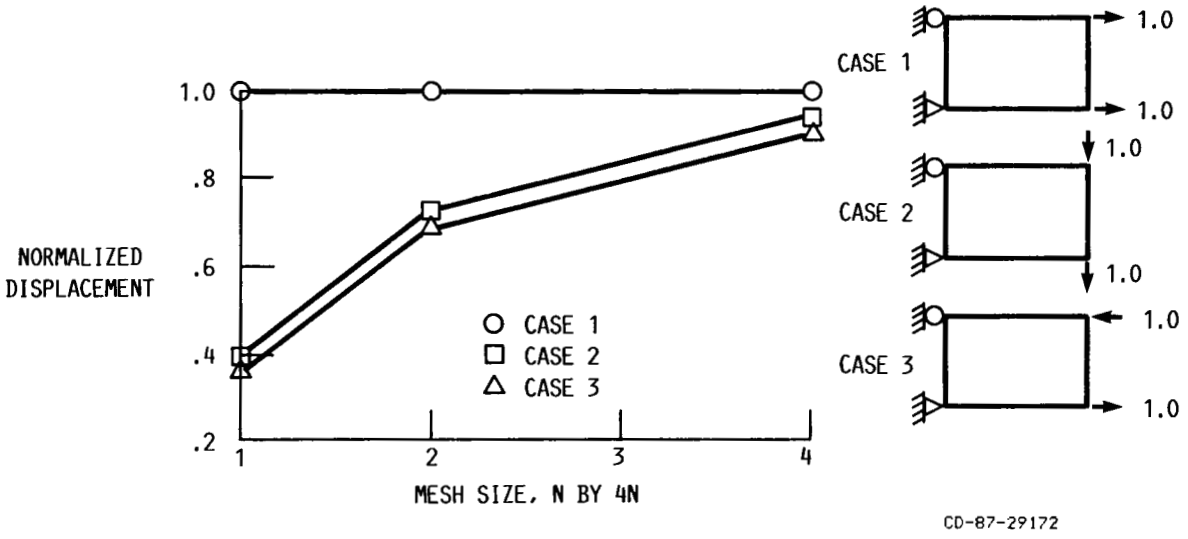

Figure 1

CLAMPED PLATE RESULTS

LENGTH, 20 IN.; WIDTH, 20 IN.; THICKNESS, 0.5 IN.; ELASTIC MODULUS, 3.0×10^7 PSI; POISSON'S RATIO, 0.316; LOAD, 1.0 LB

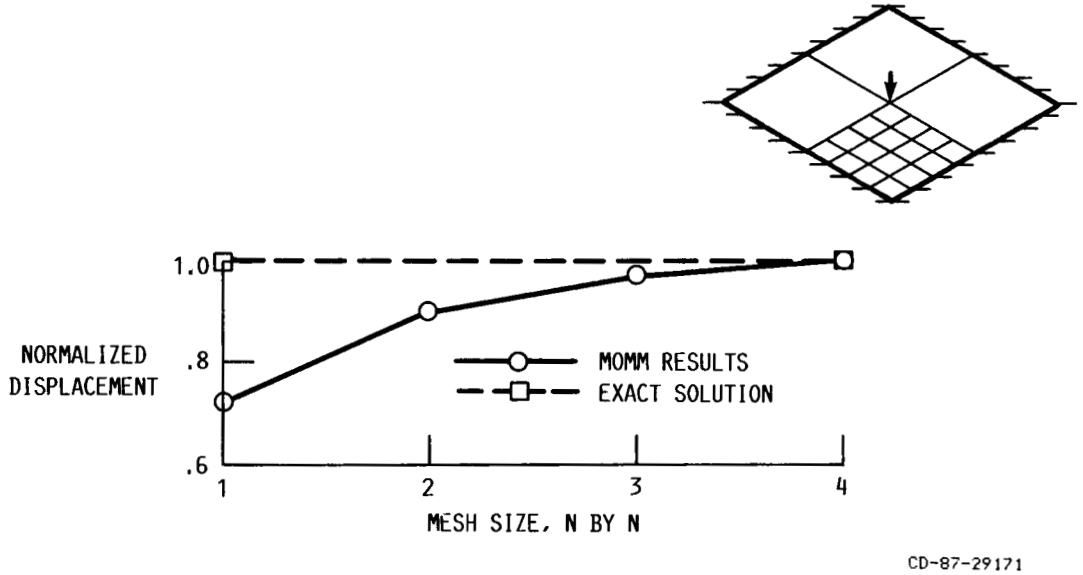

Figure 2

SHELL ROOF RESULTS

LENGTH, L, 50 FT; RADIUS, R, 25 FT; THICKNESS, 3 IN.; ELASTIC MODULUS, 3.0×10^6 PSI; POISSON'S RATIO, 0.0; SHELL WEIGHT, 360 PCF (LB-FT^3); $\Phi = 40^0$

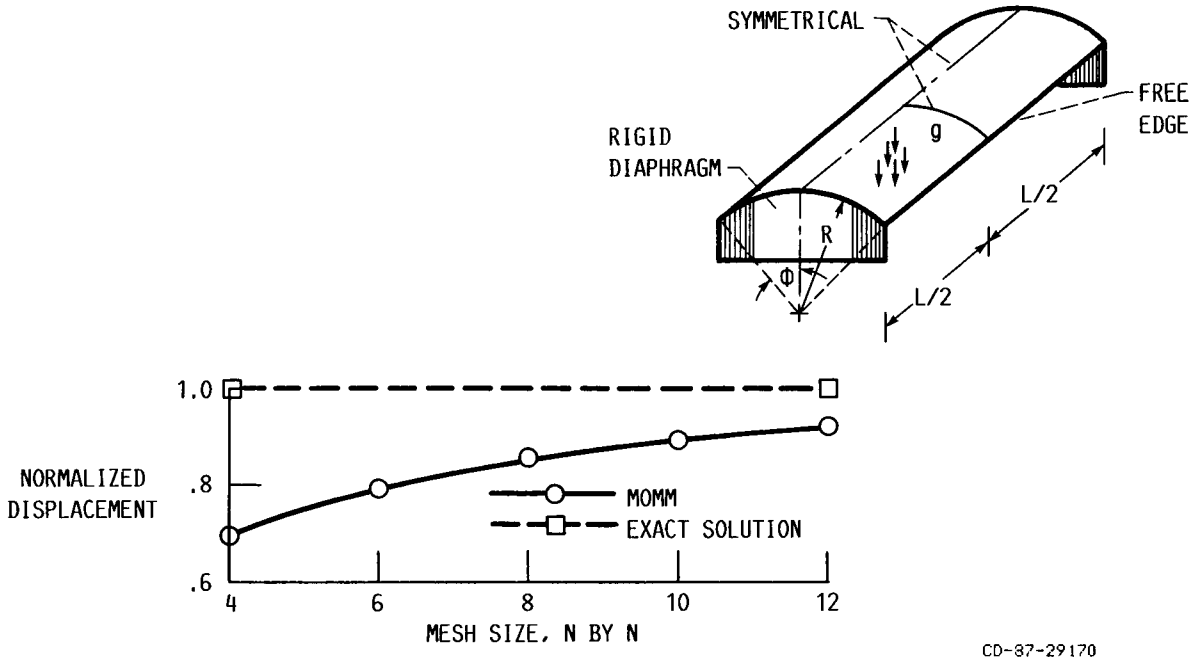

Figure 3

COMPONENT SPECIFIC MODELING

R.L. McKnight and M.T. Tipton
General Electric Aircraft Engines
Cincinnati, Ohio

The overall objective of this program was to develop and verify a series of interdisciplinary modeling and analysis techniques specialized to address hot section components. These techniques incorporate data as well as theoretical methods from many diverse areas including cycle and performance analysis, heat transfer analysis, linear and nonlinear stress analysis, and mission analysis. Building on the proven techniques already available in these fields, the new methods developed through this contract were integrated into a system which provides an accurate, efficient, and unified approach to analyzing hot section structures. The methods developed under this contract predict temperatures, deformation, stress and strain histories throughout a complete flight mission.

The Component Specific Modeling program is shown in Figure 1. Nine separate tasks were performed in two parallel activities. The component specific thermomechanical load mission modeling activities are shown in Figure 2. The products of these activities were the develoOment of computer simulation models for the engine mission cycle, the engine thermodynamic performance, and the component thermal prediction. The Component Specific Structural Modeling activities are shown in Figure 3. The product of these activities were the development of a computer system controlled through an executing module which directs the work of the component specific thermomechanical load mission modeling software, the component geometric modeling software, and the component structural analysis software to perform a component specific nonlinear analysis.

The results of this program have exceeded original expectations. As a productivity enhancer, this system has demonstrated the ability to compress the time span of a hot section component mission analysis from months to less than a day. Along with this time compression comes increased accuracy from the advanced modeling and analysis techniques. As a result of this, more analytical design studies can be performed, reducing the chances for field surprises and the amount of component testing required.

THERMODYNAMIC AND THERMOMECHANICAL MODELS

The Thermodynamic Engine Model (TDEM) is the subsystem of computer software which translates a list of mission flight points and delta times into time profiles of major engine performance parameters. Its present data base contains CF6-50C2 engine performance data. In order to adapt this system to a different engine requires only the restocking of this data base with the appropriate engine performance data.

The Thermodynamic Loads Model (TDLM) is the subsystem of computer software which works with the output of the TDEM to produce the mission cycle loading on the individual hot section components. There are separate segments for the combustor, the turbine blade, and the turbine vane. These segments translate the major engine performance parameter profiles from the TDEM into profiles of the local thermodynamic loads (pressures, temperatures, RPM) for each component. The formulas which perform this mapping in the TDLM models were developed for the specific engine components. To adapt these models to a different engine would require evaluating these formulas for their simulation capability and making any necessary changes.

COMPONENT SPECIFIC STRUCTURAL MODELING

The heart of the Component Specific Structural Modeling is geometric modeling and mesh generation using the recipe concept. This idea has proved its worth as a productivity enhancer. A generic geometry pattern is determined for each component. A recipe is developed for this basic geometry in terms of point coordinates, lengths, thicknesses, angles, and radii. These recipe parameters are encoded in computer software as variable input parameters. A set of default numerical values are stored for these parameters. The user need only input values for those parameters which are to have different values. These recipe parameters then uniquely define a generic component with the defined dimensions. The software logic then works with these parameters to develop a finite element model of this geometry consisting of 20-noded isoparametric elements. The user specifies the number and distribution of these elements through input control parameters. Figure 4 shows the generic geometry and recipe for a combustor liner panel.

The subsystem which performs the three-dimensional nonlinear finite element analysis of the hot section component model was that developed in the NASA HOST program, "3D Inelastic Analysis Methods for Hot Section Structures." This software performs incremental nonlinear finite element

analysis of complex 3D structures under cyclic thermomechanical loading with temperature dependent material properties and material response behavior. The nonlinear analysis considers both time independent and time dependent material behavior. Among the constitutive models available is the Haisler-Allen classical model which performs plasticity analysis with isotropic material response, kinematic material response, or a combination of isotropic and kinematic material response. This is combined with a classical creep analysis formulation. A major advance in the ability to perform time-dependent analyses is a dynamic time incrementing strategy incorporated in this software.

COSMO SYSTEM

The COSMO system consists of an executive module which controls the TDEM, TDLM, the geometric modeler, the structural analysis code, the file structure/data base, and certain ancillary modules. These ancillary modules consist of a bandwidth optimizer module, a deck generation module, a remeshing/mesh refinement module and a postprocessing module. The executive directs the running of each module, controls the flow of data among modules and contains the self-adaptive control logic. Figure 5 is a flow chart of the COSMO system showing the data flow and the action positions of the adaptive controls. The modular design of the system allows each subsystem to be viewed as a plug-in module. They can be abstracted and run alone or replaces with alternate systems.

CONCLUSIONS

The ideas, techniques, and computer software developed in the Component Specific Modeling Program have proven to be extremely valuable in advancing the productivity and design-analysis capability for hot section structures. This software in conjunction with modern supercomputers is able to reduce a design task which previously required man-months of effort over a time period of months to a one man, less than a day effort. The ideas are amenable to further generalization/specialization and extension to all areas of the engine structure. These techniques will have their major payoff in the next generation of aerospace propulsion systems with their increasingly larger number of parametric variations.

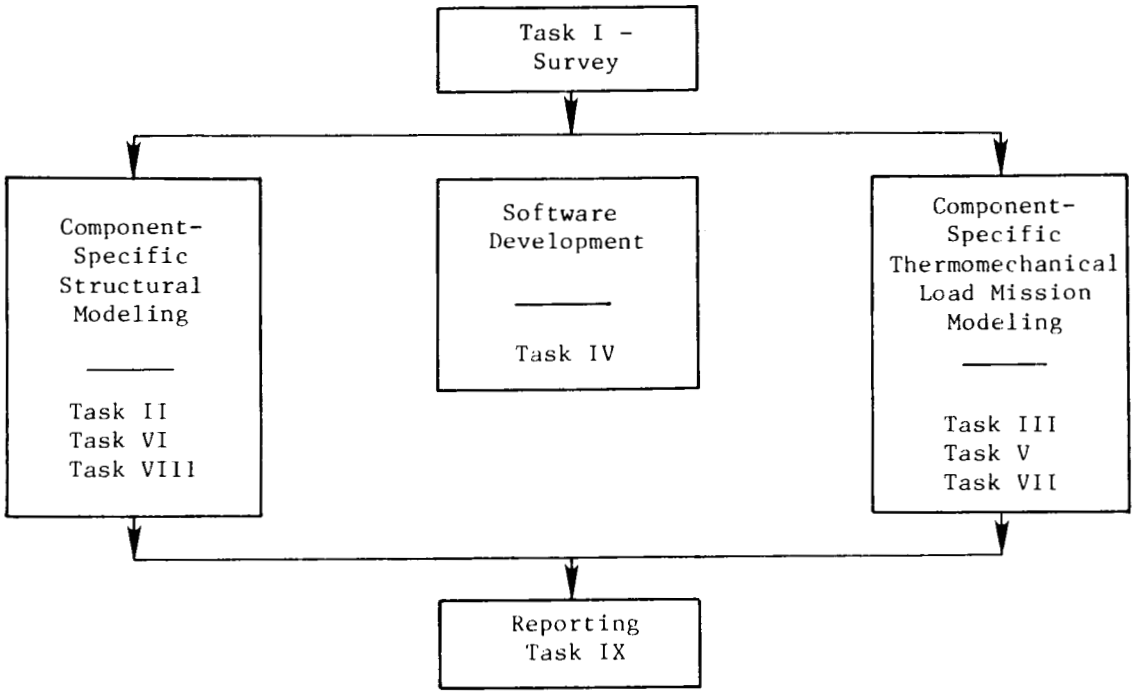

Figure 1. Component Specific Modeling Base Program.

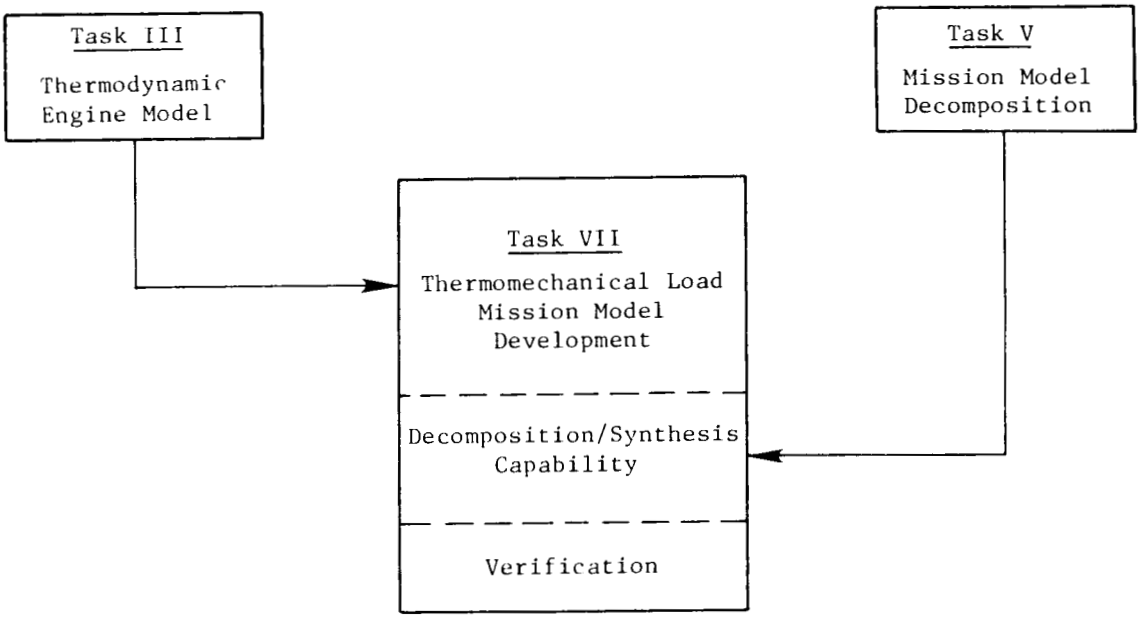

Figure 2. Component Specific Thermomechanical Load Mission Modeling.

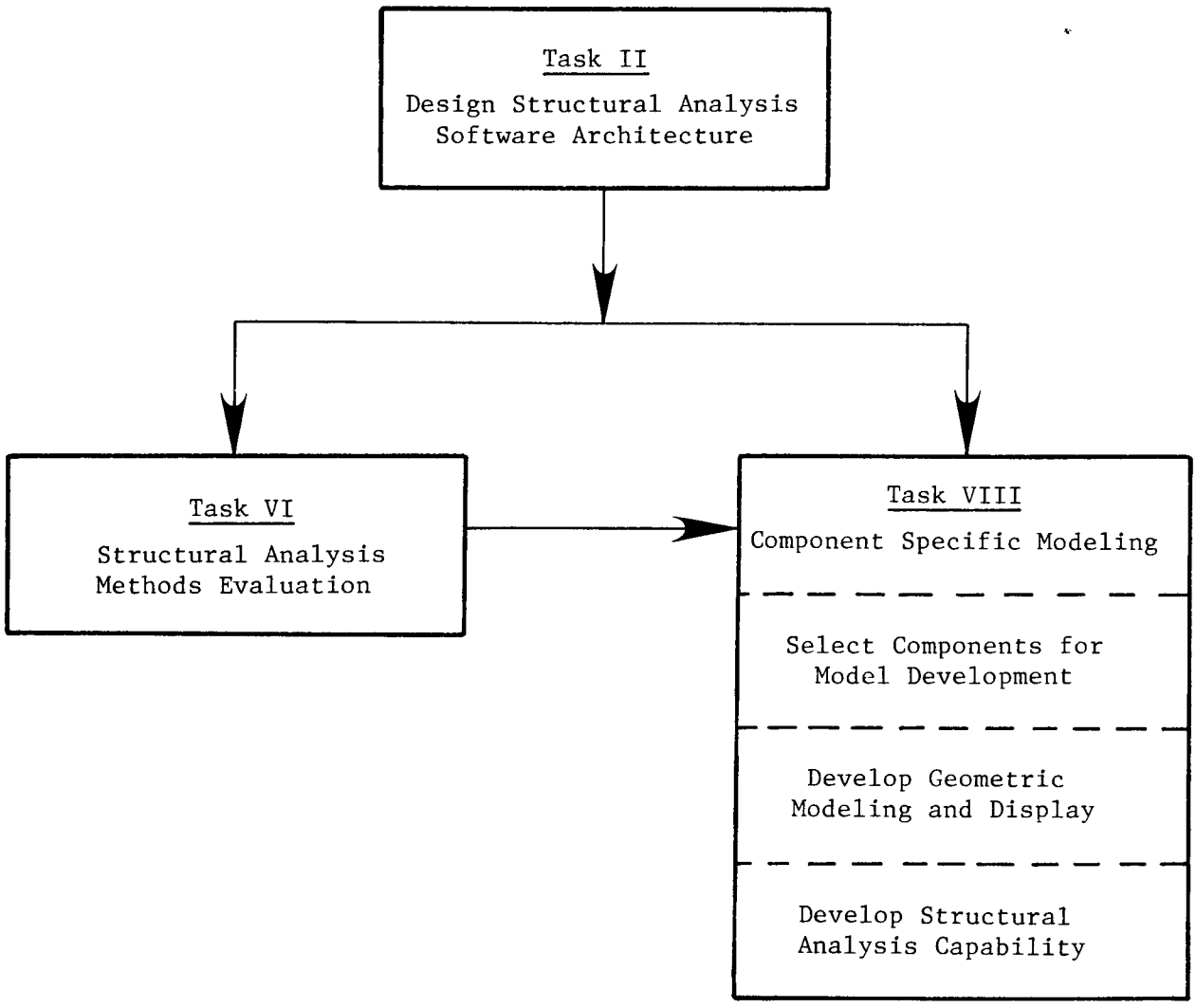

Figure 3. Component Specific Structural Modeling.

Combustor Liner Parameter List

Code	Name	Default	Code	Name	Default
1	X_1	0.0	2	Y_1	0.0
3	α_1	0.0	4	L_1	10.5
5	L_2	2.0	6	L_3	0.5
7	L_4	6.0	8	L_5	0.8
9	L_6	1.0	10	L_7	2.0
11	T_1	0.5	12	T_2	0.7
13	T_3	0.5	14	T_4	0.65
15	T_5	0.5	16	θ_1	90.0
17	θ_2	90.0	18	R_1	1.0
19	R_2	1.0	20	R_3	0.75
21	R_4	1.5	22	R_5	1.5
23	R_6	1.5			

X = Coordinate

Y = Coordinate

α = Angle wrt, x - Axis

L = Length

T = Thickness

θ = Angle of Rotation

R = Radius of Curvature

(n)= Parameter Code Number

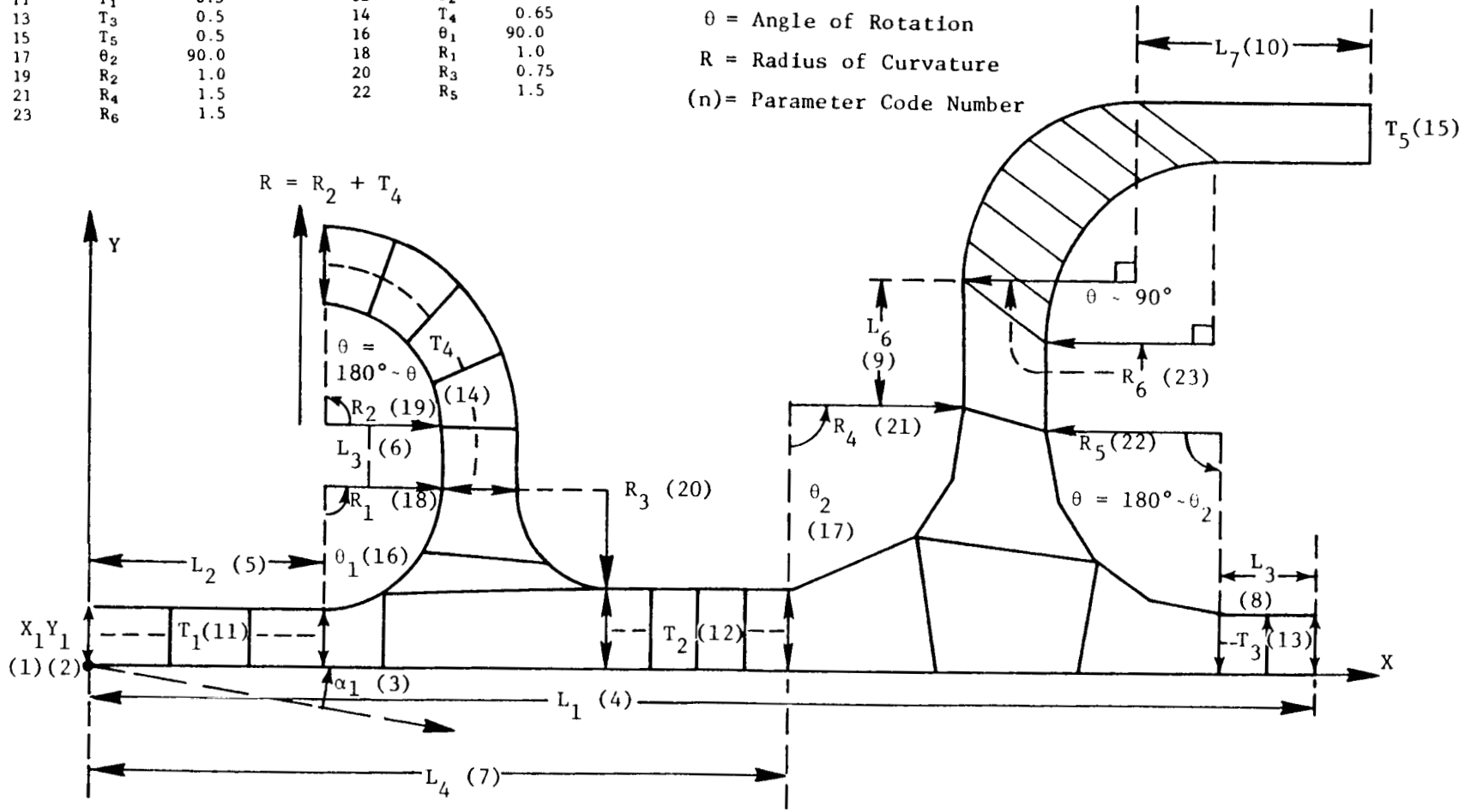

Figure 4. Combustor Liner Parameters.

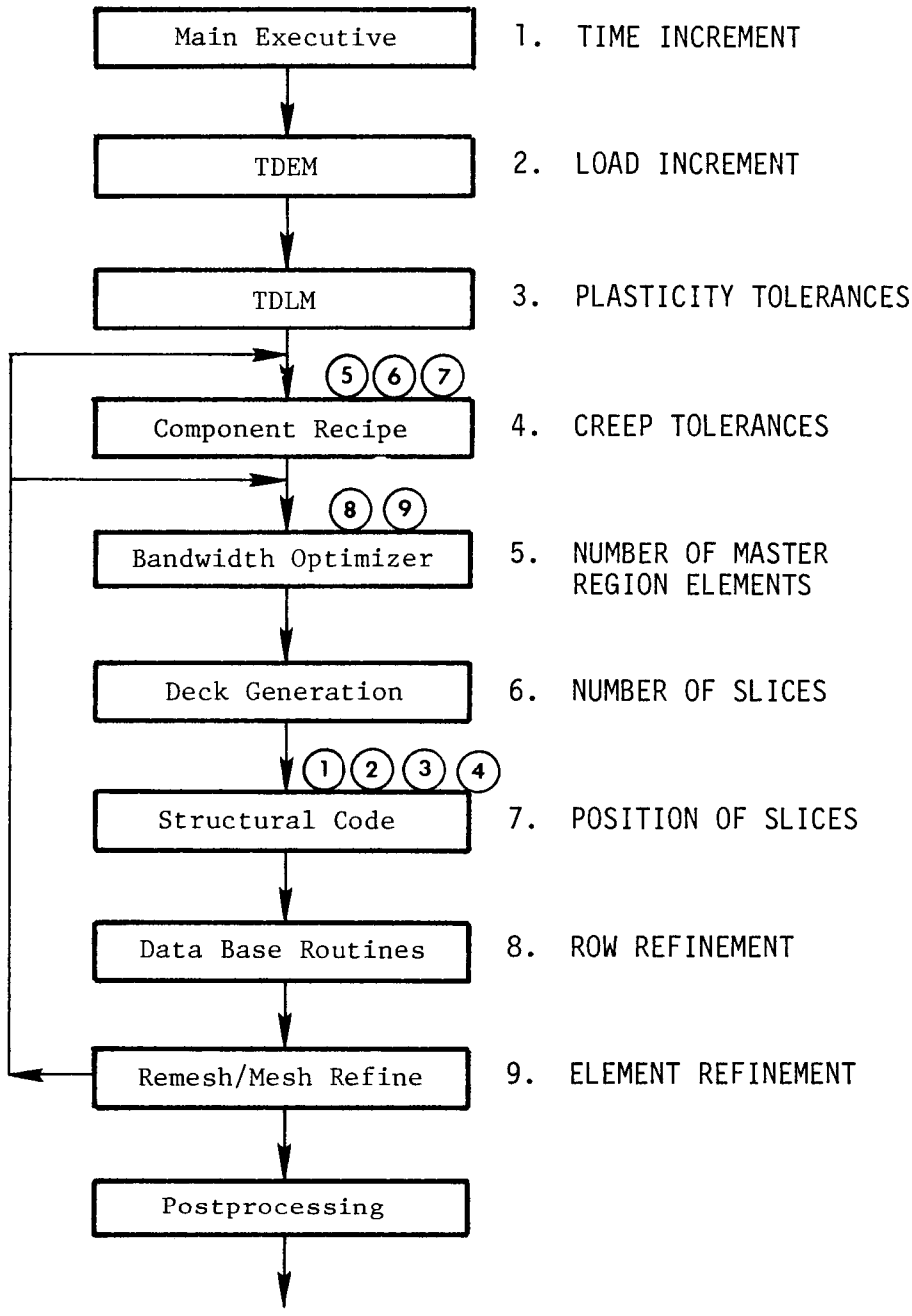

Figure 5. System Flow Chart Showing Adaptive Control Positions.

THREE-DIMENSIONAL INELASTIC ANALYSIS METHODS FOR HOT SECTION COMPONENTS

Joseph Lackney
Sverdrup Technology, Inc.
Lewis Research Center
Cleveland, Ohio

and

C.C. Chamis
NASA Lewis Research Center
Cleveland, Ohio

Under a two-year program at the General Electric Company, a series of three-dimensional inelastic structural analysis computer codes were developed and delivered to NASA.[1] A summary of the present state of the capabilities of these computer codes is presented here.

The objective of this program was to develop analytical methods capable of evaluating the cyclic time-dependent inelasticity which occurs in hot section engine components. Because of the large excursions in temperature associated with hot section engine components, the techniques developed must be able to accommodate large variations in material behavior including plasticity and creep (ref. 1). To meet this objective, General Electric developed a matrix consisting of three constitutive models and three element formulations. A separate program for each combination of constitutive mode - element model was written, making a total of nine programs. The source codes of the nine programs range in size from 7300 lines for the Bodner/twenty node to 19 000 lines for the Haisler and Allen/nine node. Table I shows the length of each source code. All of the codes were given a stand-alone capability of performing cyclic nonlinear analysis.

The three constitutive models consist of a simple model, a classical model, and a unified model. In an inelastic analysis, the simple model uses a bilinear stress-strain curve to determine the plastic strain and a power law equation to obtain the creep strain. The second model is the classical model of Haisler and Allen (ref. 2). The third model is the unified model of Bodner, Partom, and Partom (ref. 3). The attributes of the three constitutive models are listed in Table II. All of the models were programmed for a linear variation of loads and temperatures with the material properties being temperature dependent.

The three element formulations used are an eight-node isoparametric shell element, a nine-node shell element, and a twenty-node isoparametric solid element. The eight-node element uses serendipity shape functions for interpolation and Gaussian quadrature for numerical integration. Lagrange shape functions are used in the nine-node element. For numerical integration, the nine-node element uses

---

[1]Work done under NASA contract NAS3-23698.

Simpson's rule. The twenty-node solid element uses Gaussian quadrature for integration. The other attributes of these elements are listed in Table III.

For the linear analysis of structures, the nine codes use a blocked-column skyline, out-of-core equation solver. To analyze structures with nonlinear material behavior, the codes use an initial stress iterative scheme. Aitken's acceleration scheme was incorporated into the codes to increase the convergence rate of the iteration scheme.

The ability to model piecewise linear load histories was written into the codes. Since the inelastic strain rate can change dramatically during a linear load history, a dynamic time-incrementing procedure was included. The maximum inelastic strain increment, maximum stress increment, and the maximum rate of change of the inelastic strain rate are the criteria that control the size of the time step. The minimum time step calculated from the three criteria is the value that is used.

In dynamic analysis, the eigenvectors and eigenvalues can be extracted using either the determinant search technique or the subspace iteration method. These methods are only included with those finite-element codes containing the eight-node shell element.

The nine codes have been compiled on the CRAY-1 machine at NASA Lewis Research Center. Table IV shows those features contained in the codes that have been checked. Additional work has to be done in examining the other features contained in these codes. Also, test problems need to be analyzed so that the performance of these codes can be examined.

REFERENCES

1. McKnight, R.L.; Chen, P.C.; Dame, L.T.; Holt, R.V.; Huang, Ho; Hortle, M.; Gellin, S.; Allen, D.H.; and Haisler, W.E.: 3-D Inelastic Analysis Methods for Hot Section Components, Turbine Engine Hot Section Technology - 1986, NASA CP-2444, pp. 257-268.

2. Allen, D.H.; and Haisler, W.E.: A Theory of Thermoplastic Materials, Computers and Structures, Vol. 13, pp. 129-135, 1981.

3. Bodner, S.A.; Partom, I.; and Partom, Y.: Uniaxial Cyclic Loading of Elastic-Viscoplastic Material, ASME J. Appl. Mech., Vol. 46, p. 805, 1979.

TABLE I. - APPROXIMATE LENGTH OF THE NINE SOURCE CODES

Constitutive models	Element formations		
	20-Node	8-Node	9-Node
	Length of code, number of lines		
Simple	8300	13 800	17 900
Classical	9200	16 300	19 000
Unified	7300	13 800	17 600

TABLE II. - CONSTITUTIVE MODELS

Simple model	Classical model	Unified model
Uncoupled plasticity and creep	Uncoupled plasticity and creep	----------
Plasticity	Plasticity	No yield surface
Isotropic hardening	Combined isotropic and kinematic hardening	Isotropic hardening
Piecewise linear stress-strain curves	Piecewise linear stress-strain curves	----------
Prandtl-Reuss flow rule	Modified Prandtl-Reuss flow rule	----------
Nonisothermal	Nonisothermal	Nonisothermal
Creep Steady state Isotropic hardening Prandtl-Reuss flow rule Nonisothermal	Creep Steady state Isotropic hardening Prandtl-Reuss flow rule Nonisothermal	Second-order Adams-Moulton rule used to carry out integration

TABLE III. - ELEMENT FORMULATION

8-Node shell	9-Node shell	20-Node solid
Five degrees of freedom 3 Displacements 2 Rotations	Five degrees of freedom 3 Displacements 2 Rotations	Three degrees of freedom 3 Displacements
Serendipity shape functions	LaGrange shape functions	----------
No rotational stiffness about the normal to the mid-surface; deleted prior to assembly	Rotation about the normal to the mid-surface is treated as a prescribed displacement	----------
Isotropic or orthotropic elastic properties	Isotropic or orthotropic elastic properties	Isotropic or orthotropic elastic properties
Surface, line, nodal, RPM, thermal, and gravity loads	Surface, line, nodal, RPM, thermal, and gravity loads	Surface, nodal, RPM, thermal, and acceleration loads
Prescribed displacements	Prescribed displacements	Prescribed displacements
Gaussian quadrature used for numerical integration	Simpson's rule used for numerical integration	Gaussian quadrature used for numerical integration

TABLE IV. - CODE FEATURES[a]

Feature	Simple model			Classical model			Unified model		
	8-Node	9-Node	20-Node	8-Node	9-Node	20-Node	8-Node	9-Node	20-Node
Free format data input	X[a]	X	X	X	X	X	X	X	X
Global coordinate system									
Cartesian	X	X	X	X	X	X	X	X	X
Spherical[b]	—	—	—	—	—	—	—	—	—
Cylindrical[b]	—	—	—	—	—	—	—	—	—
Local coordinate system									
Cartesian	X	X	X	X	X	X	X	X	—
Spherical[b]	—	—	—	—	—	—	—	—	—
Cylindrical[b]	—	—	—	—	—	—	—	—	—
Automatic generation of nodal coordinates	—	—	N/A[c]	—	—	N/A	—	—	N/A
Automatic generation of element connectivities	X	X	N/A	X	X	N/A	X	X	N/A
Restart capability	—	—	—	—	—	—	—	—	—
Dynamic allocation	X	X	X	X	X	X	X	X	X
Blocked column skyline equation solver	X	X	X	X	X	X	X	X	X
Initial stress iterative scheme	—	—	—	—	—	—	—	—	—
Aitken's acceleration scheme	—	—	X	—	—	X	—	—	X
Dynamic time incrementing	—	—	X	—	—	X	—	—	X
Convergence criteria									
Effective plastic strain	—	—	X	—	—	X	—	—	X
Effective stress	—	—	X	—	—	X	—	—	X
Dynamic analysis									
Eigenvalue	X	N/A	N/A	X	N/A	N/A	X	N/A	N/A
Eigenvector	X	N/A	N/A	X	N/A	N/A	X	N/A	N/A
Material change option	—	—	—	—	—	—	—	—	—
Element removal option	—	—	—	—	—	—	—	—	—
Loads	X	X	X	X	X	X	X	X	X
Midsize node generation	—	—	—	—	—	—	—	—	—
Skewed coordinate system	X	X	X	X	X	X	X	X	X
Orthotropic orientation definition	X	X	X	X	X	X	X	X	X

[a]X = Feature has been checked.
[b]*Cylindrical and spherical coordinate systems have not been checked.*
[c]N/A = Not a feature of this particular code.

CONSTITUTIVE MODELING FOR ISOTROPIC MATERIALS

Ulric S. Lindholm and Kwai S. Chan
Southwest Research Institute
San Antonio, Texas

This report covers the fourth and final year of a HOST project with the initial objective "to develop a unified constitutive model for finite element structural analysis of turbine engine hot section components." During the first three years of this project, two existing models of the unified type were further developed for application to isotropic, cast, nickel-base alloys used for air-cooled turbine blades and vanes. The two models are those of Walker (ref. 1) and of Bodner and Partom (ref. 2). Both models were demonstrated to yield good correlation with experimental results for two alloys: PWA alloy B1900+Hf and MAR-M247. The experimental correlations were made with testing under uniaxial and biaxial tensile, creep, relaxation, cyclic, and TMF loading conditions over a range in strain rates and temperatures to 1100°C. Also, both models were entered into the MARC finite element computer code with test cases run for a notched round tensile specimen and an airfoil portion of a typical cooled turbine blade. The airfoil was exercised through three full flight spectra of taxi, take off, climb, cruise, descent, taxi, and shutdown. Computational efficiency with the unified models was as good or better than with a more classical elastic-plastic approach. Significant difference in stress range and accumulated strain after three flight cycles was shown for the unified models when compared with the classical creep-plasticity models. Previous work has been reported in references 3-5.

The final year's work to be reported on herein has been primarily involved with the study of nonisothermal problems and the potential for thermal history effects to occur explicitly in the constitutive equations. The following discussion will present the results from this work.

THERMO-MECHANICAL CONSTITUTIVE TESTS

Experimental Setup

The thermo-mechanical test specimens were of tubular geometry, heated externally by induction heating, and cooled by forced air over both the external and internal surfaces. Mechanical loading in tension or compression was provided by an MTS closed-loop hydraulic machine. Total strain was measured with a ceramic reach-rod extensometer with 25.4 mm gage length. A dynamic temperature monitoring (thermocouple) and control system was developed to compensate in real time for thermal strains based on measured nonlinear thermal expansion coefficients. In the thermo-mechanical test, the thermal strain signal is summed with the prescribed mechanical strain signal for total strain

feedback control. Test results are presented in terms of mechanical strain only. Controlled temperature response curves are shown in figure 1 indicating typical heating and cooling rates. Most experiments were performed in the range from 538°C to 982°C.

Nonisothermal Tensile Tests

Experiments and analysis were performed with B1900+Hf in monotonic tensile loading with a ramp change in temperature ($\dot{T}$ = 4.4°C/sec) at approximately 1% strain. A uniform strain rate of 10^{-4}/sec was maintained throughout the loading. Figures 2 and 3 show the experimental and computed (Bodner-Partom model) results. The experiments indicate negligible thermal history effect in that for either increasing or decreasing temperature change the isothermal hardening curve is achieved rapidly after the temperature change is completed. The B-P model calculation is similar, however a preliminary yield type behavior is observed with an asymptotic approach to the isothermal hardening curve. However, this predicted behavior is not the result of thermal history but of the plastic work history, since cumulative plastic work is used as the measure of the hardening state variables in this model.

Nonisothermal Creep

Creep testing was performed with step changes in both stress and temperature during a given test. An example strain-time curve is shown in Figure 4. After each change, conditions were held until a steady state creep rate was achieved. The steady-state creep rates are plotted in figure 5 for both isothermal and nonisothermal histories along with the B-P model prediction. The isothermal and nonisothermal tests are seen to fall within the same scatter and both agree rather well with the model. In the model, thermal recovery of hardening is insignificant at 760°C but becomes a major factor at 982°C. The nonisothermal testing was designed to include this transition in hardening mechanism.

Thermo-mechanical Strain Cycling

In figure 6, we show a single specimen cycled to saturation initially at 538°C, a temperature increase to 982°C with saturated loops achieved at that temperature, and a return to 538°C, all under constant strain range control. Two observations again evidence absence of thermal history effect. The high-temperature excursion resulted in no change in the hysteresis loop at 538°C, and the cyclic stress range associated with a given cyclic strain was the same under this type of nonisothermal history as under strictly isothermal cycling, as shown in Figure 7. Both types of cycling agree with the B-P model prediction which is based on isothermal data only.

Additional in-phase and out-of-phase TMF cycling experiments were also performed with the cyclic loop shape compared with B-P model predictions. The results were similar to those previously reported in reference 5, indicating that reasonably good predictions of complex nonisothermal histories can be

made for this class of alloy based upon material constants derived from isothermal testing only. For other alloys, where strong strain aging effects are present, more complex thermo-mechanical history dependence may be required in the constitutive model as reported by Robinson and Bartolotta in reference 6.

Dislocation Structures

The dislocation structures observed in the nonisothermal specimens were compared to those observed in isothermal specimens previously reported by Moreno et al in reference 7. The comparison revealed that in both cases the dislocation arrangements in B1900+Hf consisted of cellular networks around the γ' precipitates. Such dislocation cell structures appear to form at low strain levels (a few percent) and appear to be the stable configuration for specimens tested under different loading paths. The theoretical implication is that the saturation stress concept postulated in many unified constitutive models can be considered to be the flow stress associated with the saturated dislocation configuration, i.e., the stress required to move dislocations to and from the walls of the dislocation cellular network. Since the saturated dislocation structure is independent of the thermo-mechanical loading path, the saturation stress and the limiting values of the internal hardening variables should therefore be independent of the thermo-mechanical loading path. The values of the saturation stress should, however, depend on temperature and strain rate through the dependence of the critical resolved shear stress on these quantities.

CONCLUSIONS

The last year's efforts have demonstrated that for the cast nickel-base alloys studied, B1900+Hf and MAR-M247, both isothermal and nonisothermal, complex loading histories can be well predicted using the unified constitutive model approach with all necessary material constants derived solely from isothermal test data. Additional work is needed to determine if this conclusion can be extended to other alloy systems which may exhibit more complex hardening or recovery mechanisms.

We believe the complete four-year program has demonstrated rather conclusively that the unified constitutive model concept is a very powerful tool for predicting material response in hot section components under complex, time-varying, thermo-mechanical loadings. This confidence is gained from extensive correlations between two existing models and a large base of experimental data covering the range in stress, strain rate, and temperature of interest. The unified constitutive models have also been demonstrated to be computationally efficient when incorporated into a large finite element computer code (MARC). While there is still much room for improvement or extension of the existing constitutive models and for efficiency in their computational implementation, it is expected their use will grow rapidly in engineering applications.

REFERENCES

1. Walker, K. P.: NASA CR-165533, 1981.

2. Bodner, S. R.; and Partom, Y: ASME J. of Applied Mechanics, Vol. 42, 1975, p. 385.

3. Lindholm, U. S.; Chan, K. S.; Bodner, S. R.; Weber, R. M.; Walker, K. P.; and Cassenti, B. N.: NASA CR-174718, May 1984.

4. Lindholm, U. S.; Chan, K. S.; Bodner, S. R.; Weber, R. M.; Walker, K. P.; and Cassenti, B. N.: NASA CR-174980, July 1985.

5. Chan, K. S.; Lindholm, U. S.; Bodner, S. R.; Hill, J. T.; Weber, R. M.; and Meyer, T. G.: NASA CR-179522, August 1986.

6. Robinson, D. N.; and Bartolotta, P. A.: NASA CR-174836, 1985.

7. Moreno, V.; Nissley, D. M.; and Lin, L. S.: NASA CR-174844, 1985.

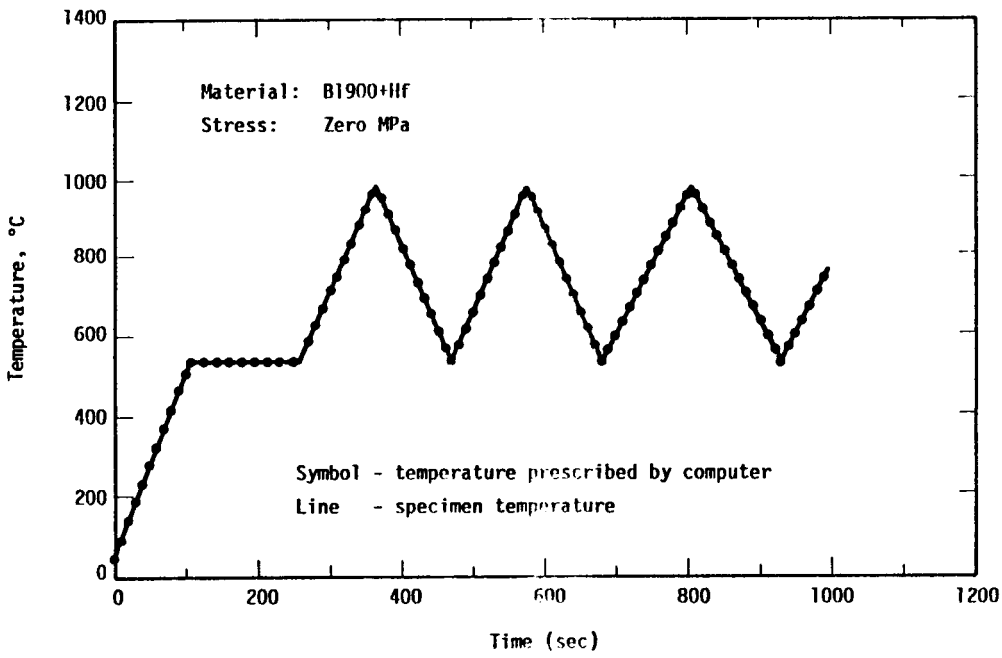

FIGURE 1. COMPARISON OF PRESCRIBED TEMPERATURE WITH MEASURED SPECIMEN TEMPERATURE

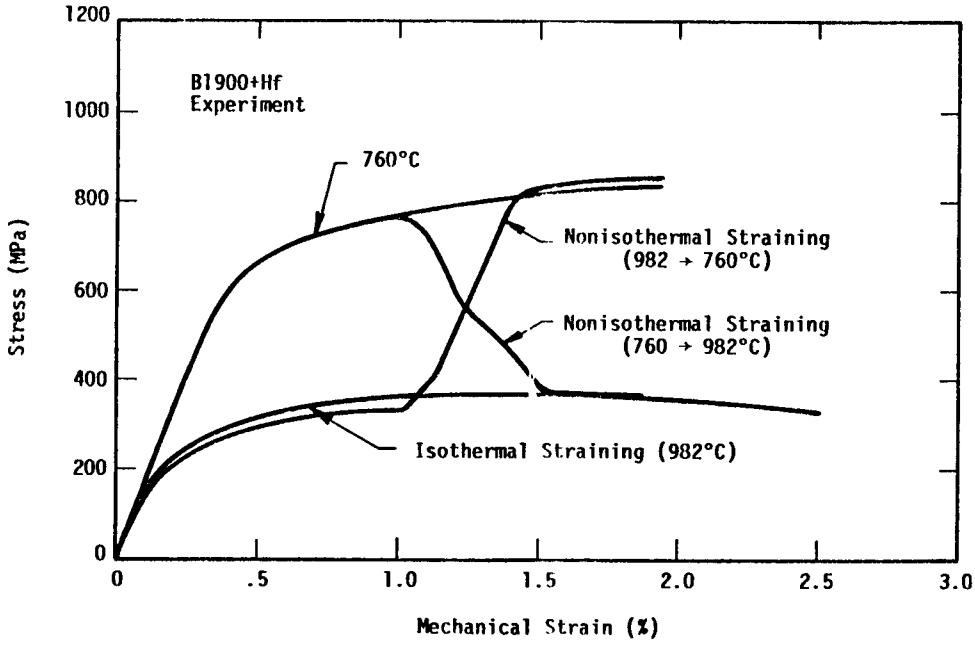

FIGURE 2. EXPERIMENTAL ISOTHERMAL AND NONISOTHERMAL TENSILE STRESS-STRAIN CURVES

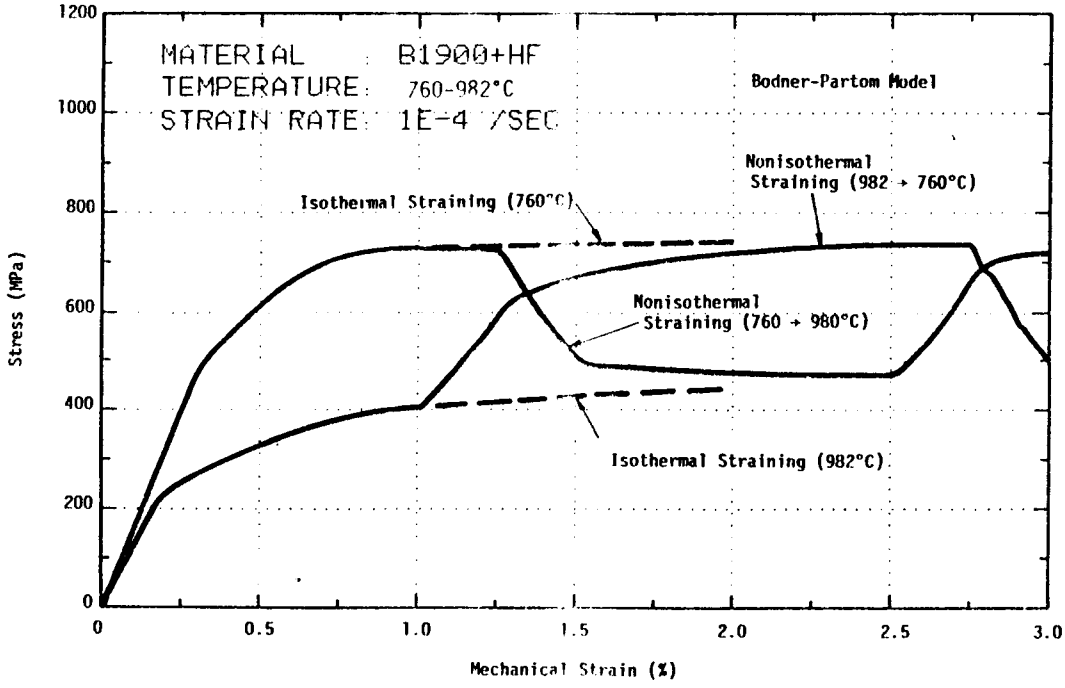

FIGURE 3. BODNER-PARTOM MODEL PREDICTIONS OF NONISOTHERMAL TENSILE CURVES COMPARED TO ISOTHERMAL TENSILE CURVES

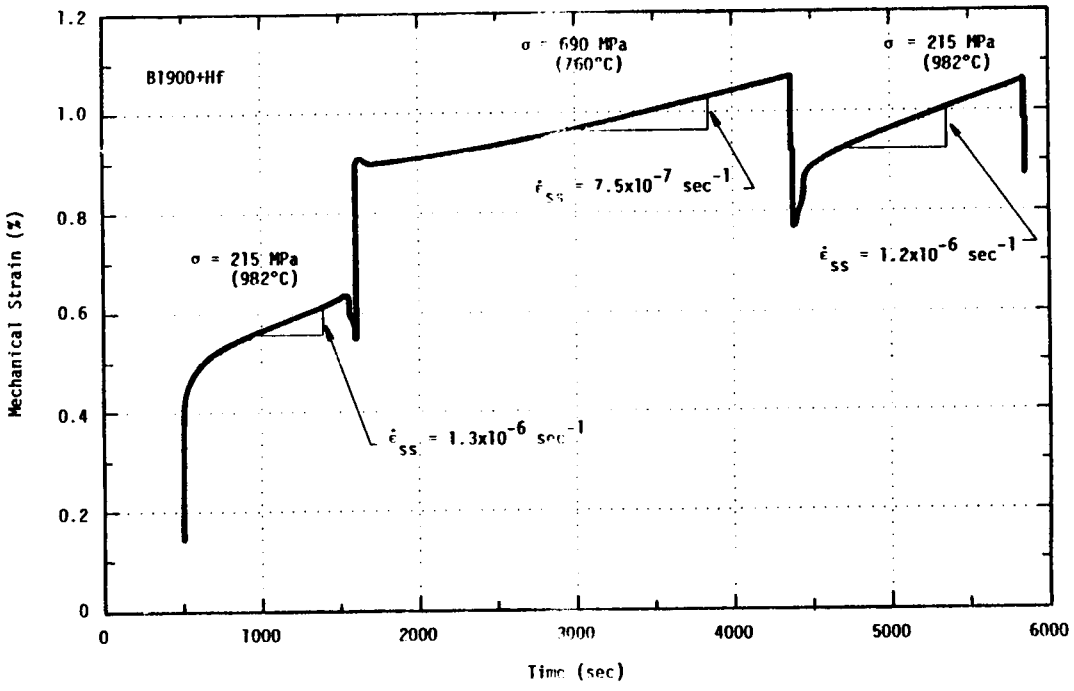

FIGURE 4. CREEP TEST WITH STEP CHANGES IN LOAD AND TEMPERATURE

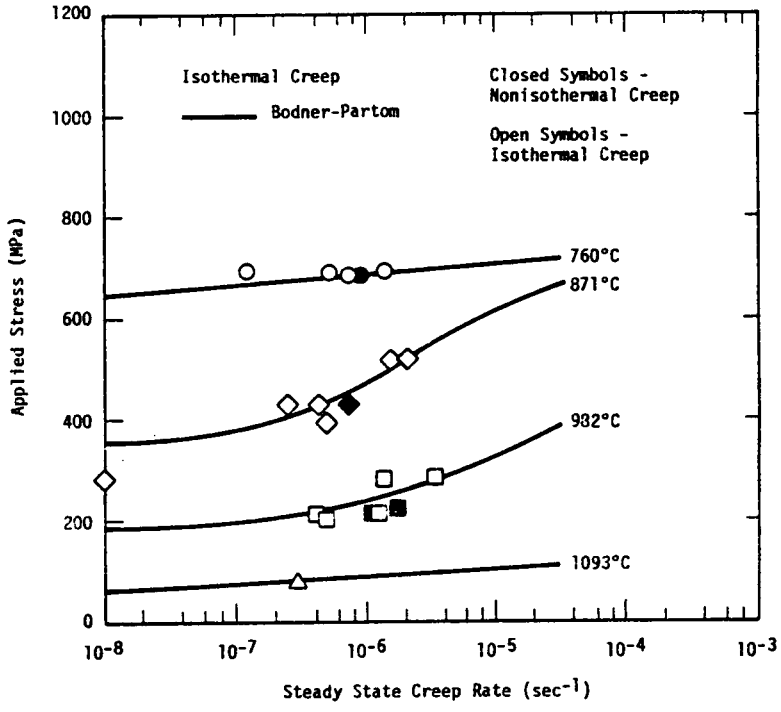

FIGURE 5. COMPARISON OF NONISOTHERMAL CREEP DATA WITH ISOTHERMAL CREEP DATA AND MODEL PREDICTIONS

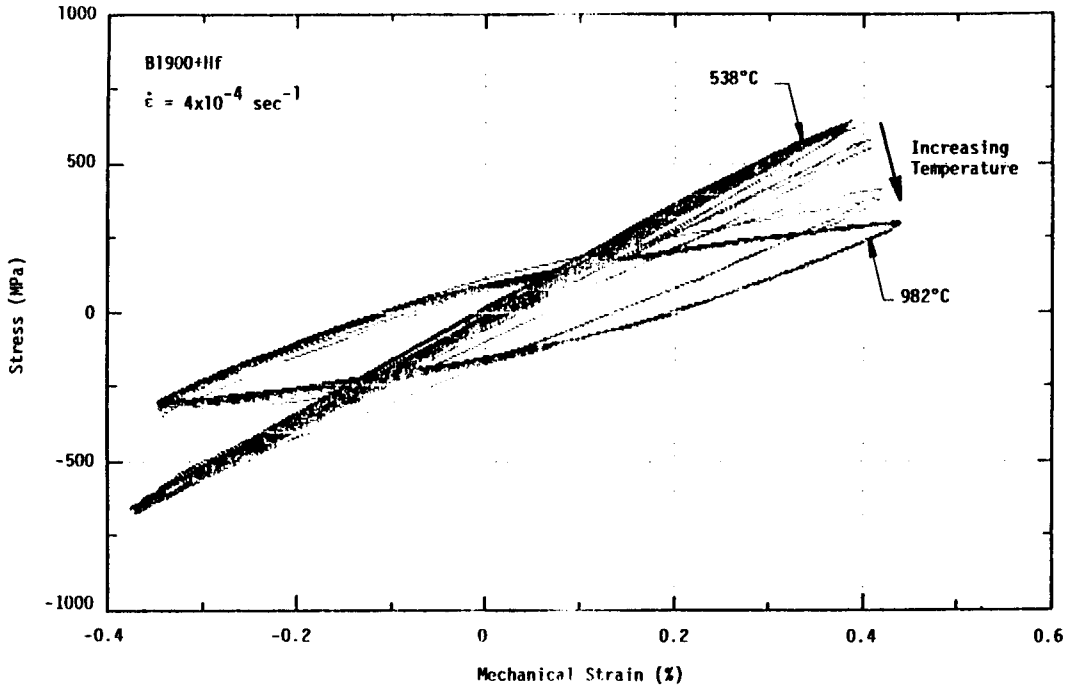

FIGURE 6. CONTROLLED STRAIN CYCLING WITH TEMPERATURE CHANGE FROM 538°C TO 982°C TO 538°C

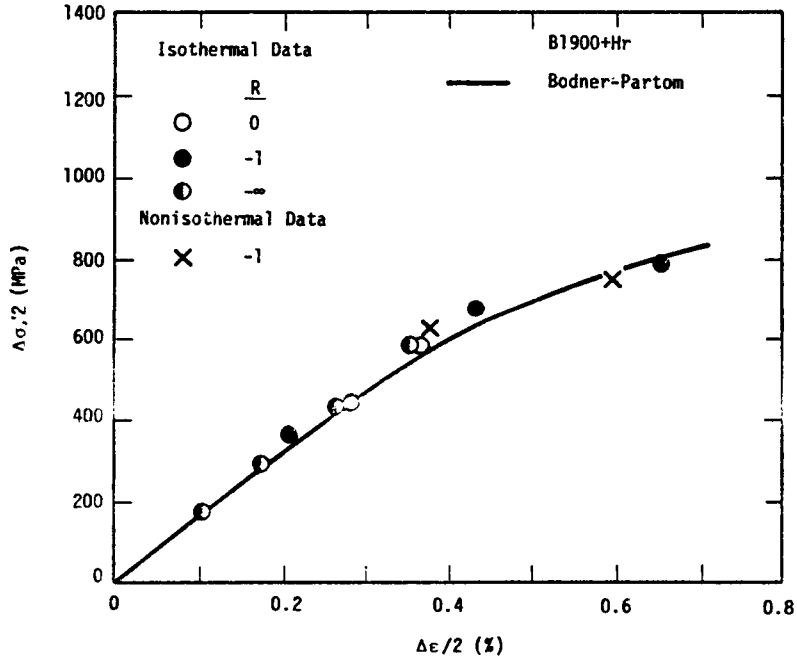

FIGURE 7. COMPARISON OF ISOTHERMAL AND NONISOTHERMAL CYCLIC DATA OF B1900+Hf AT 760°C

A CONTINUUM DEFORMATION THEORY FOR METAL-MATRIX COMPOSITES AT HIGH TEMPERATURE

D.N. Robinson*
Akron University
Akron, Ohio

Structural alloys used in high-temperature applications exhibit complex thermomechanical behavior that is time-dependent and hereditary. Recent attention is being focused on metal-matrix composite materials for aerospace applications that, at high temperature, exhibit all the complexities of conventional alloys (e.g., creep, relaxation, recovery, rate sensitivity) and, in addition, exhibit further complexities because of their strong anisotropy.

Here, a continuum theory is presented for representing the high-temperature, time-dependent, hereditary deformation behavior of metallic composites that can be idealized as pseudohomogeneous continua with locally definable directional characteristics. Homogenization of textured materials (molecular, granular, fibrous) and applicability of continuum mechanics in structural applications depends on characteristic body dimensions, the severity of gradients (stress, temperature, etc.) in the structure and on the relative size of the internal structure (cell size) of the material. Examination reveals that the appropriate conditions are met in a significantly large class of anticipated aerospace applications of metallic composites to justify research into the formulation of continuum-based theories.

The point of view taken here is that the composite is a material in its own right, with its own properties that can be measured and specified for the composite as a whole. Experiments for this purpose are outlined in detail in reference 1. This viewpoint is aimed at satisfying the structural analyst or design engineer who needs reasonably simple methods of structural analysis to predict deformation behavior in complex multiaxial situations, particularly at high temperature where material response is enormously complex. Indeed, the prediction of component lifetime depends critically on the accurate prediction of deformation behavior.

THEORETICAL DEVELOPMENT

As in references 1 and 2, the starting point here is the assumed existence of a dissipation potential function Ω for the composite material; that is,

$$\Omega = \Omega(\sigma_{ij}, \alpha_{ij}, d_i d_j, T) \tag{1}$$

in which σ_{ij} denotes the components of (Cauchy) stress, α_{ij} the components of a tensorial internal state variable (internal stress), $d_i d_j$ the components of a directional tensor, and T the temperature. The symmetric tensor $d_i d_j$ is formed by a self product of the unit vector d_i denoting the local fiber direction. As pointed out in reference 3, account can be taken of more than a single family of

*Resident Research Associate at Lewis Research Center.

fibers inherent to the continuum element. An extension of the present work to two families of fibers has been considered by the author but is not presented here. The function Ω is taken to depend on temperature, however the present emphasis is on isothermal deformation at high homologous temperature so that the temperature dependence will not be shown explicitly hereafter. The presumption of constant high homologous temperature justifies ignoring extensive cyclic hardening. Extension to a full nonisothermal theory is in progress.

A simple thermodynamic formalism based on reasonable assumptions is shown in reference 4 to support the existence of a dissipation potential for a homogeneous (one-constituent) solid. Here, this formalism is assumed to be extendable to a two-constituent (fiber/matrix), psuedohomogeneous composite material. The thermodynamic structure leads to the generalized normality conditions,

$$\dot{\varepsilon}_{ij} = \frac{\partial \Omega}{\partial \sigma_{ij}} \tag{2}$$

and

$$\frac{\dot{-\alpha}_{ij}}{h} = \frac{\partial \Omega}{\partial \alpha_{ij}} \tag{3}$$

in which $\dot{\varepsilon}_{ij}$ denotes the components of the rate of (small) strain and h is a scalar function of the internal stress α_{ij}. The orientation tensor $d_i d_j$ is taken to be constant under small deformations, otherwise an evolutionary equation would need to be specified for it as well.

As in references 1, 2, and 5, Ω is taken to depend on the state variables through the scalar functions F and G; that is,

$$\Omega = \Omega(F,G) \tag{4}$$

where

$$F(\Sigma_{ij},\ d_i d_j) \tag{5}$$

$$\Sigma_{ij} = s_{ij} - a_{ij} \tag{6}$$

and

$$G(a_{ij},\ d_i d_j) \tag{7}$$

The term Σ_{ij} is the effective stress and s_{ij} and a_{ij} are the deviatoric parts of σ_{ij} and α_{ij}, respectively.

The functions F and G each depend on two symmetric second-order tensors. Form invariance (objectivity) of F and G, and hence of Ω, requires that they depend only on certain invariants and invariant products of their respective tensorial arguments (integrity basis - ref. 6). A subset of these invariants for F (i.e., $F(I_1,I_2,I_3)$) is taken as follows:

$$I_1 = J_2 - I + \frac{1}{4} I_3 \tag{8}$$

$$I_2 = I - I_3 \tag{9}$$

$$I_3 = (I_0)^2 \tag{10}$$

where

$$J_2 = \frac{1}{2}\,\Sigma_{ij}\Sigma_{ji} \tag{11}$$

$$I = d_i d_j \Sigma_{jk}\Sigma_{ki} \tag{12}$$

$$I_0 = d_i d_j \Sigma_{ji} \tag{13}$$

The invariant I_1 corresponds to the square of the maximum effective shear stress on planes containing the fibers and in a direction normal to them (transverse shear), I_2 corresponds to the square of the maximum effective shear stress on planes containing the fibers but directed along the fibers (longitudinal shear) and I_3 is the square of the effective normal stress in the local fiber direction. A similar set of invariants is chosen for G, denoted by I_1', I_2', and I_3', and is obtained by replacing Σ_{ij} by a_{ij} in equations (11) to (13).

The function $F(I_1,I_2,I_3)$ is chosen to be linear in I_1, I_2, I_3 (quadratic in stress) as

$$F = \left(\frac{I_1}{K_T^2} + \frac{I_2}{K_L^2} + \frac{9}{4Y_L^2}\,I_3\right) - 1 \tag{14}$$

where K_T, K_L, and Y_L correspond physically to the (threshold) strengths of the composite element in transverse shear, longitudinal shear, and longitudinal tension (compression), respectively. Defining

$$\eta = \frac{K_L}{K_T} \tag{15}$$

and

$$\omega = \frac{Y_L}{Y_T} \tag{16}$$

where Y_T relates to the strength in transverse tension (compression), F becomes

$$F = \frac{1}{K_T^2}\left[I_1 + \frac{1}{\eta^2}\,I_2 + \frac{9}{4(4\omega^2 - 1)}\,I_3\right] - 1 \tag{17}$$

Experiments for determining K_T, η, and ω using thin-walled tubular specimens with varying fiber orientations are outlined in reference 1. Here, F plays the role of a Bingham-Prager threshold function with K_T (as indicated earlier) a threshold shear stress in transverse shear. If no threshold exists - that is, if inelastic

deformation occurs for applied stress however small - the function F can be taken homogeneous in stress with K_T playing the role of a "drag" stress as identified in other theoretical developments.

It is noted that with $\eta = \omega = 1$ (and with $K_T = K_L = K$) F reduces to

$$F = \frac{J_2}{K^2} - 1 \tag{18}$$

as taken in reference 5 for an isotropic solid.

Similarly, the function G is taken as

$$G = \frac{1}{K_T^2}\left[I_1' + \frac{1}{\eta^2} I_2' + \frac{9}{4(4\omega^2 - 1)} I_3'\right] \tag{19}$$

Using equations (4) to (19) in equations (1) to (3), taking h in equation (3) as $h(G)$ and

$$f(F) = \frac{\partial \Omega}{\partial F} \tag{20}$$

and

$$\gamma(G) = h(G) \frac{\partial \Omega}{\partial G} \tag{21}$$

results in a flow law

$$\dot{\varepsilon}_{ij} = f(F)\Gamma_{ij} \tag{22}$$

and an evolutionary law

$$\dot{a}_{ij} = h(G)\dot{\varepsilon}_{ij} - \gamma(G)\pi_{ij} \tag{23}$$

where

$$\Gamma_{ij} = \Sigma_{ij} - \xi[d_k d_i \Sigma_{jk} + d_j d_k \Sigma_{ki} - 2I_0 d_i d_j] - \frac{1}{2}\zeta I_0(3d_i d_j - \delta_{ij}) \tag{24}$$

and

$$\pi_{ij} = a_{ij} - \xi[d_k d_i a_{jk} + d_j d_k a_{ki} - 2I_0' d_i d_j] - \frac{1}{2}\zeta I_0'(3d_i d_j - \delta_{ij}) \tag{25}$$

where

$$\xi = \frac{\eta^2 - 1}{\eta^2} \qquad 0 \leq \xi \leq 1 \tag{26}$$

$$\zeta = \frac{4(\omega^2 - 1)}{4\omega^2 - 1} \qquad 0 \leq \zeta \leq 1 \tag{27}$$

Once again, with $\eta = \omega = 1$ ($\xi = \zeta = 0$) equations (22) and (23) reduce to the flow and evolutionary laws of reference 5 for an isotropic solid.

Equations (17), (19), (22), and (23), with the accompanying definitions, provide an anisotropic representation that accounts for observed monotonic behavioral features such as strain-rate dependent plasticity, primary creep, and secondary creep. Application to a particular composite requires specification of the parameters η and ω, characterizing the anisotropy; K_T, the strength in transverse shear; and the functions $f(F)$, $h(G)$, and $\gamma(G)$ (ref. 1).

CONSIDERATIONS FOR STRESS REVERSALS AND REDUCTIONS

Reversals and reductions of stress following inelastic deformation of metallic alloys are known to initiate micromechanistic processes that are not present, or at least not controlling, under monotonic conditions. For example, forward stressing may result in hardening through pile-ups of gliding dislocations against obstacles (for example, "forest" dislocations threading slip planes that accumulate in front of moving dislocations - ref. 7). Upon abrupt reversal of stress the immobilized dislocations become remobilized, finding fewer obstacles in their paths as they begin to move backward along their slip planes. This constitutes a relatively rapid microstructural rearrangement; that is, an abrupt change in mobile dislocation density, precipitated by a reversal of stress (dynamic recovery). Interpreted on a somewhat more macroscopic scale, this may correspond closely to the very rapid changes in the "stored energy of cold work" observed upon stress reversal by Halford (ref. 8).

Reductions in stress at elevated temperature are also known to cause microstructural rearrangements in time (thermal recovery) through diffusion-controlled mechanisms such as climb and annihilation of dislocations, even in the absence of significant inelastic strain recovery. Although, at high temperature, these mechanisms always may be present and contribute as competing mechanisms under steady-state conditions, they may become the controlling mechanisms, at least for some time, following stress reductions.

Phenomenological representations in which internal state variables (e.g., α_{ij}) serve as macroscopic measures of the current microstructure must reflect these sometimes abrupt internal changes that occur upon stress reversals and the more gradual changes that occur under reductions of stress. The theory for isotropic metals presented in reference 5 accounts for these behaviors by allowing analytically different regions of the state space: that is, regions of the space (σ_{ij}, α_{ij}) governed by different analytical forms for the evolution of the internal state (α_{ij}). Such idealizations have strong precedent in classical continuum plasticity. Details of the representation are given in reference 5. Here, it is assumed that the idealization can be extended to the anisotropic behavior of metallic composites.

Guided by reference 5, the crucial regions of the state space are bounded by

$$F \lesseqgtr 0 \quad , \quad s_{ij}\Gamma_{ji} \lesseqgtr 0 \quad \text{and} \quad s_{ij}\pi_{ji} \lesseqgtr 0 \tag{28}$$

Accordingly, the flow and evolutionary equations (22) and (23) are modified, respectively, as

$$\dot{\varepsilon}_{ij} = P(s_{ij}\,\Gamma_{ji})\, f\langle F\rangle\, \Gamma_{ij} \tag{29}$$

$$\dot{a}_{ij} = h(\hat{G})\,\dot{\varepsilon}_{ij} - \gamma(\hat{G})\pi_{ij} \tag{30}$$

where

$$\hat{G} = (G - G_0)P(s_{ij}\pi_{ji}) + G_0 \tag{31}$$

$$P(x) = 1 \qquad x > 0$$

$$P(x) = 0 \qquad x \leq 0 \tag{32}$$

and

$$f\langle F\rangle = \begin{cases} f(F) & F > 0 \\ 0 & F \leq 0 \end{cases} \tag{33}$$

A complete statement of the isothermal theory is thus given by equations (17), (19), (29), and (30), with the accompanying definitions. It is again noted that for $\eta = \omega = 1$ these equations reduce to those of reference 5 that have been applied successfully in representing the cyclic thermomechanical response of isotropic solids and structures (refs. 5 and 9 to 11).

IMPLEMENTATION IN STRUCTURAL ANALYSIS CODES

The present theory has been implemented into the commercial finite element code MARC by Dr. A.K. Arya (ref. 11). Several trial calculations have been made under uniaxial conditions using material functions and parameters that approximate a tungsten/copper composite material (ref. 3). A transversely isotropic continuum elasticity theory (ref. 12) has been used in conjunction with the present viscoplastic theory. The results of the calculations (ref. 11) show the expected responses of rate-dependent plasticity, creep, and relaxation as well as appropriate anisotropic features.

The theory has also been implemented into a research-oriented code NFAP developed by Prof. T.Y. Chang together with his colleagues and students at the University of Akron. Several of the uniaxial predictions of MARC have been successfully duplicated using NFAP and predictions of structural response - for example, composite beams, plates, and shells - are in progress.

REFERENCES

1. Robinson, D.N.; Duffy, S.F.; and Ellis, J.R.: A Viscoplastic Constitutive Theory for Metal-Matrix Composites at High Temperature. Thermal Stress, Material Deformation, and Thermo-Mechanical Fatigue, H. Sehitoglu and S.Y. Zamrik, eds., ASME Special Publication, PVP Vol. 123, ASME, 1987. (NASA CR-179530).

2. Robinson, D.N.: Constitutive Relationships for Anisotropic High-Temperature Alloys, Nucl. Eng. Des., vol. 83, no. 3, Dec (II), 1984, pp. 389-396.

3. Spencer, A.J.M.: Deformations of Fibre-Reinforced Materials. Clarendon Press, Oxford, 1972.

4. Ponter, A.R.S.: General Theorems for the Dynamic Loading of Structures for a State Variable Description of Material Behavior. Mechanical Properties at High Rates of Strain - 1979, Institute of Physics, Bristol, England, 1980, pp. 130-141.

5. Robinson, D.N.: A Unified Creep-Plasticity Model for Structural Metals at High-Temperature. ORNL/TM-5969, 1978.

6. Spencer, A.J.M.: Theory of Invariants. Continuum Physics, Vol. 1, A.C. Eringen, ed., Academic Press, 1971, pp. 355-487.

7. Orowan, E.: Causes and Effects of Internal Stresses. Internal Stresses and Fatigue in Metals, G.M. Rassweiler and W.L. Grube, eds., Elsevier, 1959, pp. 59-80.

8 Halford, G.R.: Stored Energy of Cold Work Changes Induced by Cyclic Deformation. Ph.D. Thesis, University of Illinois, 1966.

9. Hornberger, K.; and Stamm, H.: Anwendung Viskoplasticher Stoffgesetze in Finite Element Programmen. Kernforschungszentrum Karlsruhe 4254, 1987.

10. Arya, V.K.; and Kaufman, A.: Finite Element Implementation of Robinson's Unified Viscoplastic Model and Its Application to Some Uniaxial and Multiaxial Problems. NASA TM-89891, 1987.

11. Arya, V.K.: Finite Element Implementation of Viscoplastic Models. Turbine Engine Hot Section Technology Workshop, NASA CP-2493, 1987, pp. 335-348.

12. Lekhnitskii, S.G.: Theory of Elasticity of an Anisotropic Body. Mir Publishers, Moscow, 1981.

ACKNOWLEDGMENT

This research was conducted under NASA Grant NAG3-379 and funded through the HOST project. The author is grateful to NASA Lewis Research Center and to the HOST project for their support.

ANISOTROPIC CONSTITUTIVE MODELING FOR NICKEL BASE SINGLE CRYSTAL SUPERALLOY RENE N4 AT 982 °C

D.C. Stouffer, N. Jayaraman, M.Y. Sheh, and D. Alden
University of Cincinnati
Cincinnati, Ohio

Nickel base single crystal superalloys attracted considerable interest for use in gas turbine jet engine because their superior high temperature properties. In polycrystalline turbine parts, rupture is usually due to crack propagation originating at the grain boundaries. Since single crystal alloys have no grain boundaries, use of the alloy has significant advantages for increased strength and longer life.

The purpose of this paper is to report an anisotropic constitutive model developed based on crystallographic approach for Ni-base single crystal superalloy. The current equations modified a previous model proposed by Dame and Stouffer[1] where a Bodner-Partom equation with only the drag stress was used to model the local inelastic response in each slip system. Their model was considered successful for predicting both the orientation dependence and tension/compression asymmetry for tensile and creep histories for single crystal alloy Rene N4 at 1400°F. However, certain properties including fatigue were not satisfactorily modeled. In this work, a back stress state variable has been incorporated into the local slip flow equation based on the observed experimental observations. Model predictability is improved especially for mechanical properties such as anelasticity and fatigue loops. Comparison of the model predictions and the experimental data for single crystal superalloy Rene N4 at 1800°F are presented.

MODEL DEVELOPMENT

The application of the crystallographic approach to single crystal nickel base superalloys began with the work of Paslay et al[2], and lately by Shah[3] to the γ' phase of these alloys. The principal advantage of this approach is that a significant portion of the model is based on the physics of the deformation mechanisms. Presumably, this will enhance the predictive capability of the model. Furthermore, as additional information is obtained about deformation mechanisms at different loading conditions, the local constitutive models can be modified to accommodate the new knowledge.

The model developed by Dame and Stouffer[1] was based on unified theory by separating the total global strain into elastic and inelastic components. The elastic strains were calculated using cubic symmetry. The inelastic strain rate was calculated, using crystallographic approach, by summing the contributions of each slip system. The inelastic slip rate on each slip system was computed from a local inelastic constitutive equation that depends

on local resolved shear stress components in each slip direction and local state variables. Due to different mechanical responses exhibited by octahedral and cube slip systems[4,5], two separate flow equations were used to compute the inelastic strain rate on each of the two slip systems. A non-Schmid's law formulation was used to model the tension compression asymmetry and orientation dependence in the octahedral slip system. This was achieved by incorporating the "core width effect" proposed by Lall, Chin and Pope[6] where stress-aided Shockly partials and thermally-aided cross-slip mechanisms were used to explain the tension/compression asymmetry. A Schmid's law concept was used to model the inelastic response in the cube system since tension/compression asymmetry was insignificant. In both slip systems, a Bodner-Partom type of flow equation was used to model the response at higher strain rates(i.e. tensile response). At lower strain rates(i.e. creep response), where diffusion is the controlling mechanism, a diffusion model similar to the Bodner-Partom equation was used. This constitutive model for local slip was also based on a system of state variables to model the drag stress. Back stress was not included, since this is typically associated with dislocation pile-ups at obstacles like grain boundaries which are absent in single crystals. This model was considered successful for predicting both the orientation dependence and tension/compression asymmetry for tensile and creep histories for single crystal alloy Rene N4 at 1400^{o}F; however, properties including fatigue and anelastic recovery were not satisfactorily modeled.

The motivation to incorporate a back stress state variable in the current model was due to the fact that back stress/drag stress representation has several advantages over a drag stress model including the ability to accurately predict fatigue loops for polycrystalline materials[7,8]. However, use of these state variables has its physical background. Drag stress and back stress state variable models are used to reflect the evolution of the microstructure during deformation. Drag stress is used to approximate the resistance to inelastic flow, i.e dislocation motions, due to obstacles such as precipitates. Generally, dislocations pass through or around the precipitates by shearing or looping mechanism. Thus the local obstacles impede the dislocation motion. Whereas, back stress is usually used to characterize the increase in resistance due to dislocation pile-ups against permanent barriers such as grain boundary, which create a repelsive stress between adjacent dislocations. It was assumed by Dame and Stouffer that back stress should not be present in single crystal alloys due to lack of grain boundaries. Thus only the drag stress was included in their model. However, it is too restrictive to assume that back stress can only be created by dislocation pile-up mechanism. For example, Milligan and Antolovich[9] showed in their study of deformation behavior of single crystal superalloy PWA 1480 that when dislocations emerged from precipitates those portions of the dislocations within the precipitate are constricted due to high anti-phase boundary energy(APBE), while those portions of the same dislocations which had exited the precipitates are split due to elastic repulsion. Therefore, it is likely that elastic repulsion, i.e. back stress, should be included in the force equilibrium equation. More generally, it is suspected that dislocation interaction and/or rearrangement will also result in creation of back stress in the single crystals[10], except the effect may be insignificant compared to

the pile-up mechanism. Thus, it was decided to evaluate the macroscopic effect of the back stress in the mechanical test.

In order to better understand how back stress affect the inelastic strain rate, the following mathematics are required. A typical drag stress/back stress model[5,6] for polycrystalline metals has the functional form as

$$\dot{\varepsilon}^{I}_{ij} = F\left(\frac{Z}{|\sigma_{ij}-\Omega_{ij}|}\right) \text{sign}(\sigma_{ij}-\Omega_{ij}) \qquad (1)$$

where Z is the drag stress and Ω_{ij} the back stress. Based on this formulation, inelastic flow can be present even when the applied stress, σ_{ij} is zero, i.e. as long as the back stress is non-zero and is large enough to produce meaningful strain rates. This is normally seen in the relaxation test at zero stress. Therefore two special single crystal tests were designed and performed in the beginning of this research. The results of these tests are shown in Figure 1 and Figure 2. The predicted results in these figures will be discussed in a later section. Figure 1a and 1b shows double tensile tests on specimens in [100] and [111] orientation, respectively, with a 120 second hold time. In both tests, samples were first loaded to 1.5% strain at strain rate of $1x10^{-4}$/sec, unloaded immediatedly to zero stress within 10 seconds, and following the 120 seconds hold period and then reloaded at higher strain rate of $6x10^{-4}$/sec. Significant anelastic recovery has occurred during the hold period for the [100] sample, whereas the recovery is minimum for the [111] specimen. These results clearly demonstrate that the recovery mechanism is orientation dependent. Second, without the presence of back stress term similar to equation (1), a single drag stress formulation cannot predict this anelastic behavior. Thus, modification of Dame and Stouffer's model to include a back stress variable is necessary.

EXPERIMENTAL PROGRAM

All the mechanical tests were performed on a MTS mechanical test unit with a 20,000 kip load frame. The tests were run under total strain control at $1800^{\circ}F$. The control of the MTS unit and data collection were done by computer, with software generated at the University of Cincinnati. To date, five different types of tests have been performed and five nominal crystal orientations were used. The five tests were: 1)monotonic tensile; 2)double tensile with wait period at zero stress; 3)fully reversed fatigue; 4)fatigue with a tensile hold time in each cycle; and 5)fatigue with a compressive hold time in each cycle. The five orientations were: [123], [011], [012], [001] and [111].

RESULTS

Shown in Figure 3 are comparisons of experimental data and predicted responses of tensile tests ran at $1x10^{-4}$(in/in)/sec for different specimen

orientations. The responses in [100] and [111] were used to determine material constants and the response in [110] orientation was the predicted result. The model predicted well in elastic moduli, harding characteristics (the knee part) and the saturated values for these orientations. Predictions of double tensile tests with hold time in [100] and [111] orientations are shown in Figure 1 and 2, respectively. The model predicted very well in both cases not only for the recovery part but also the hardening characteristics of the subsequent loading and rate sensitivity effect.

Experimental results showed that fatigue tests in [100], [111] and [123] orientations at 1800^{o}F stablized within 5 loops and exhibited no work hardening or softening throughout the lives, therefore drag stress remained constant and the evolution equation was not used. The only information used from the experimental data in determining constants was the ratio of yield stress in tension and in compression. The predictions of the loops are purely based on constants determined from the tensile tests. These predictions are shown in Figure 4 and Figure 5 for [100] and [111] orientations, respectively. In Figure 4, the model predicted very well in tension/compression asymmetry, hardening characteristic and rate effect for the [100] orientation. However, tension/compression asymmetry disappeared in Figure 5 for the [111] orientation, which the model also predicted well.

CONCLUSION

An back stress/drag stress constitutive model based on crystallographic approach to model single crystal anisotropy is presented in this paper. Experimental results has demonstrated the need for back stress variable in the inelastic flow equations. Experimental findings also suggested that back stress is orientation dependent and controlling both the strain hardening and recovery characteristics. Due to the observed stable fatigue loops at 1800^{o}F, drag stress is considered constant for this temperature. The constitutive model operated with constants determined only from tensile data was extensively tested from simple tensile, fatigue to complicated stress and strain hold tests. The model predict very well in those conditions. Future works on test at other temperatures will be conducted. It is expected some strain hardening or softening of the single crystals in cyclic tests should occur.

REFERENCE

1. Dame, L.T. (1986) and Stouffer, D.C., "Anisotropic Constitutive Model for Nickel Base Single Crystal Alloys: Development and Finite Element Implementation. NASA CR-175015, Lewis Research Center.

2. Paslay, P. (1970), Wells, C., and Leverant, G., "An Analysis of Primary Creep of Nickel-Base Superalloy Single Crystals", Journal of Applied Mechanics, ASME, p. 759.

3. Shah, D. (1983), "Orientation Dependence of Creep Behavior of Single Crystal γ' (Ni_3Al)", Scripta Metallurgica, Vol. 17, p. 997.

4. Miner, R. (1986a), Voigt, R., Gayda, J., and Gabb, T., "Orientation and Temperature Dependence of Some Mechanical Properties of the Single-Crystal Nickel-Base Superalloy Rene N4: Part I. Tensile Behavior", Metall. Trans., Vol. 17A, P. 491.

5. Miner, R. (1986b), Gabb, T., Gayda, J., and Hemker, K. J., "Orientation and Temperature Dependence of Some Mechanical Properties of the Single-Crystal Nickel-Base Superalloy Rene N4: Part III. Tensile-Compression Anisotropy," Metall. Trans., Vol. 17A, P. 507.

6. Lall, C. (1979), Chin, S., and Pope, D., "The Orientation and Temperature Dependence of the Yield Stress of Ni_3 (Al, Nb) Single Crystals", Metall. Trans. A, Vol. 10A, p. 1323.

7. Ramaswamy, V.G. (1986), "A Constitutive Model for the Inelastic Multiaxial Cyclic Response of a Nickel Base Superalloy Rene'80. NASA CR-3998.

8. Walker, K.P. (1981), "Research and Development Program for Nonlinear Structural Modeling and Advanced Time-Temperature Dependent Constitutive Relationships," NASA CR165533.

9. Milligan W.W. (1987) and Antolovich, S.D., "Yielding and Deformation Behavior of the Single Crystal Superalloy PWA 1480," Metall. Trans. Vol. 18A, p. 85.

10. Jackson, P.J. (1986), "The Mechanisms of Plastic Relaxation in Single-crystal Deformation," Mat. Sci. Engr., 81:169-174.

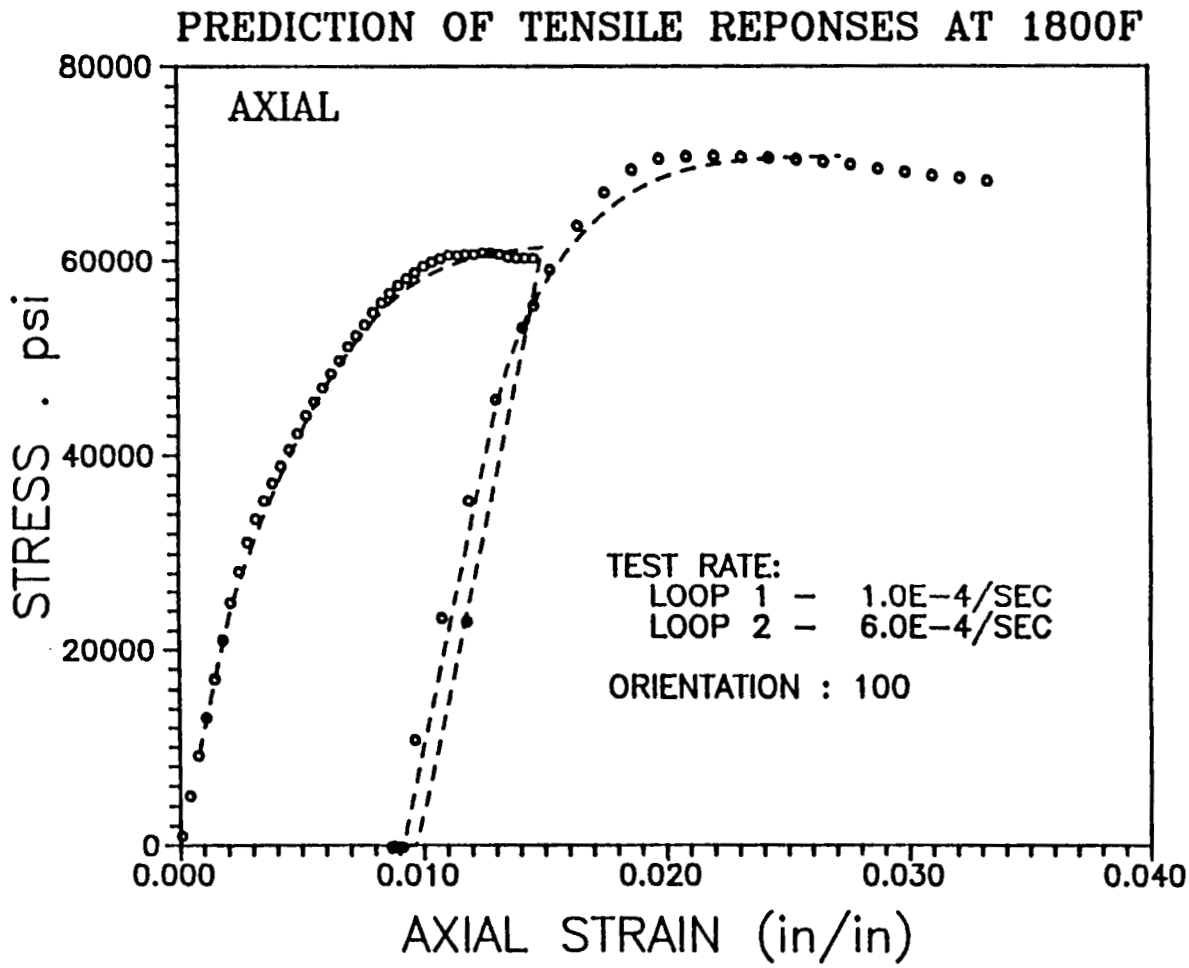

Figure 1. Predicted Response and Experimental Data for a Multiple Tensile Test in (100) Orientation with 120 seconds Hold Period. Notice significant recovery (anelasticity) during Hold Period. (RENE' N4 at 1800°F)

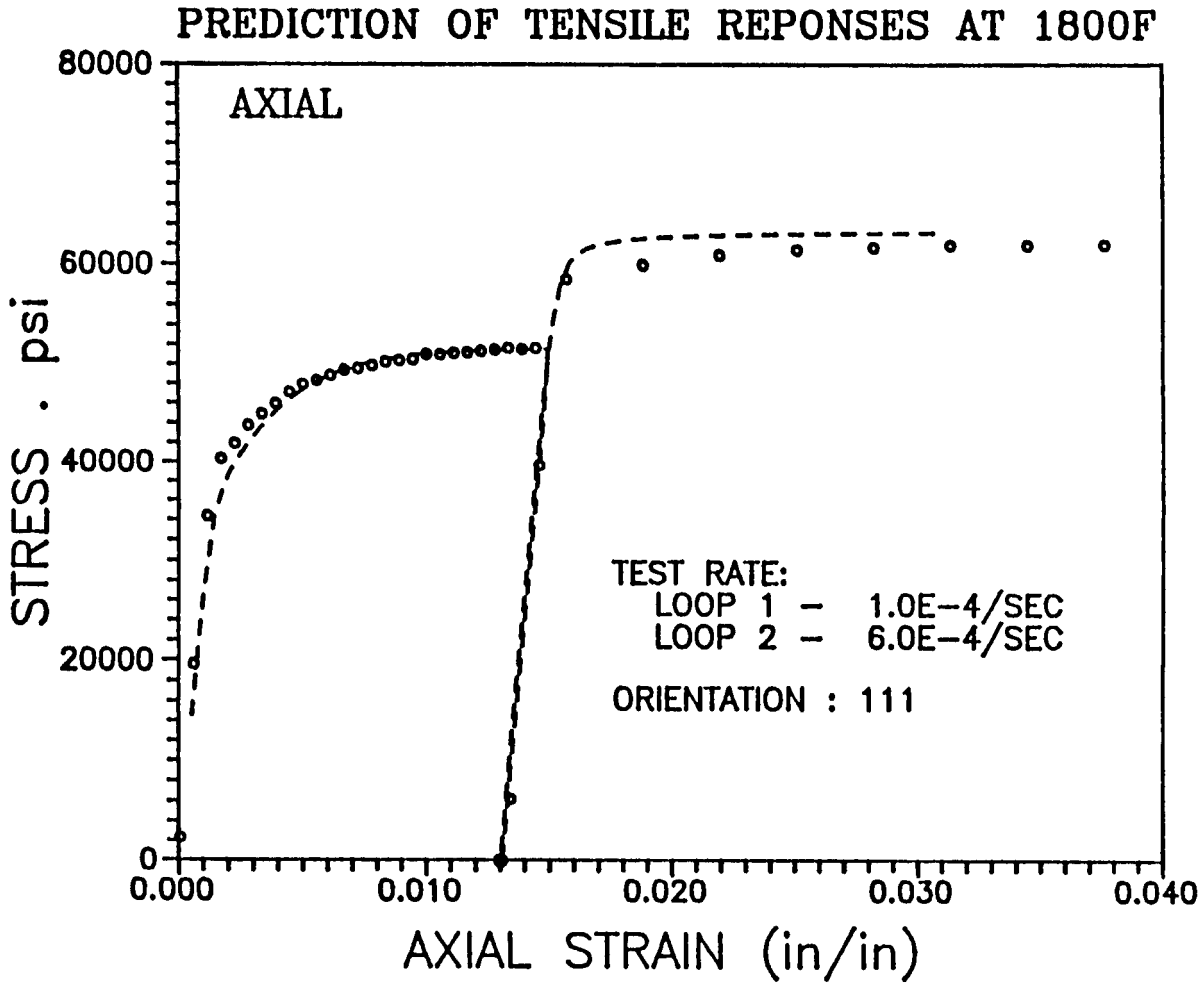

Figure 2. Predicted Response and Experimental Data for a Multiple Tensile Test in (111) Orientation with 120seconds Hold Period. Notice no recovery(anelasticity) during Hold Time.

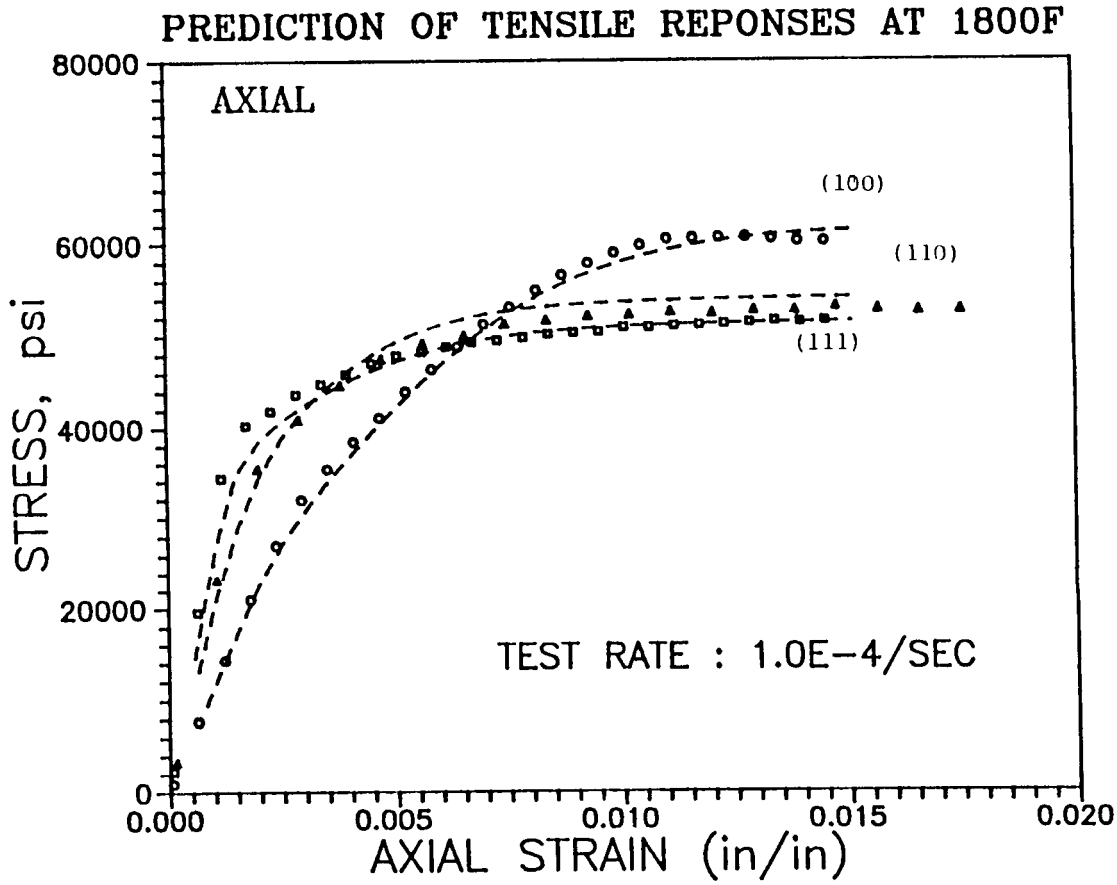

Figure 3. Predicted Tensile Responses and Experimental Data for Specimens in (100), (110) and (111) Orientation, RENE' N4, 1800°F.

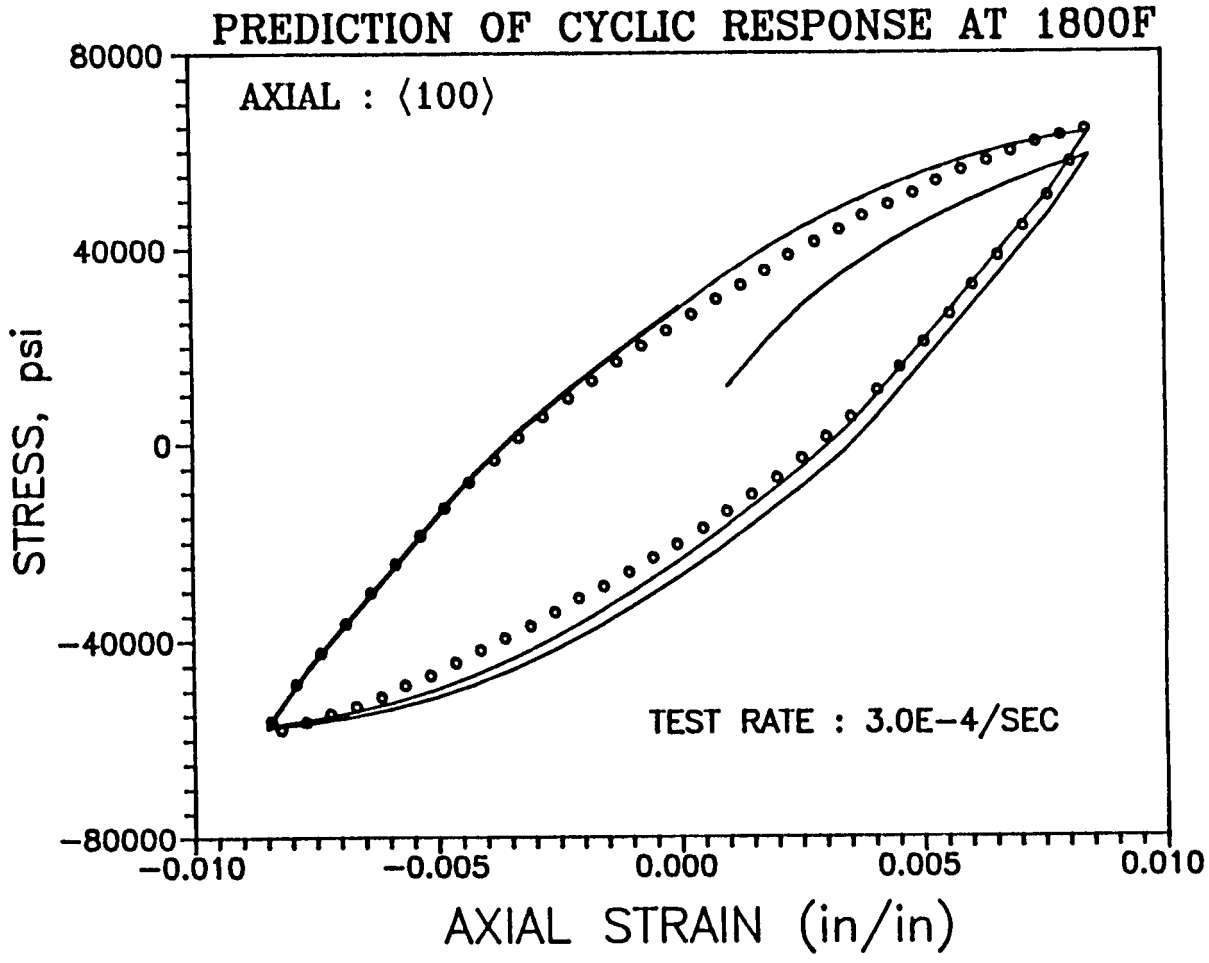

Figure 4. Predicted Response and Experimental Data for Cyclic Test in (100) Orientation, RENE' N4, 1800°F.

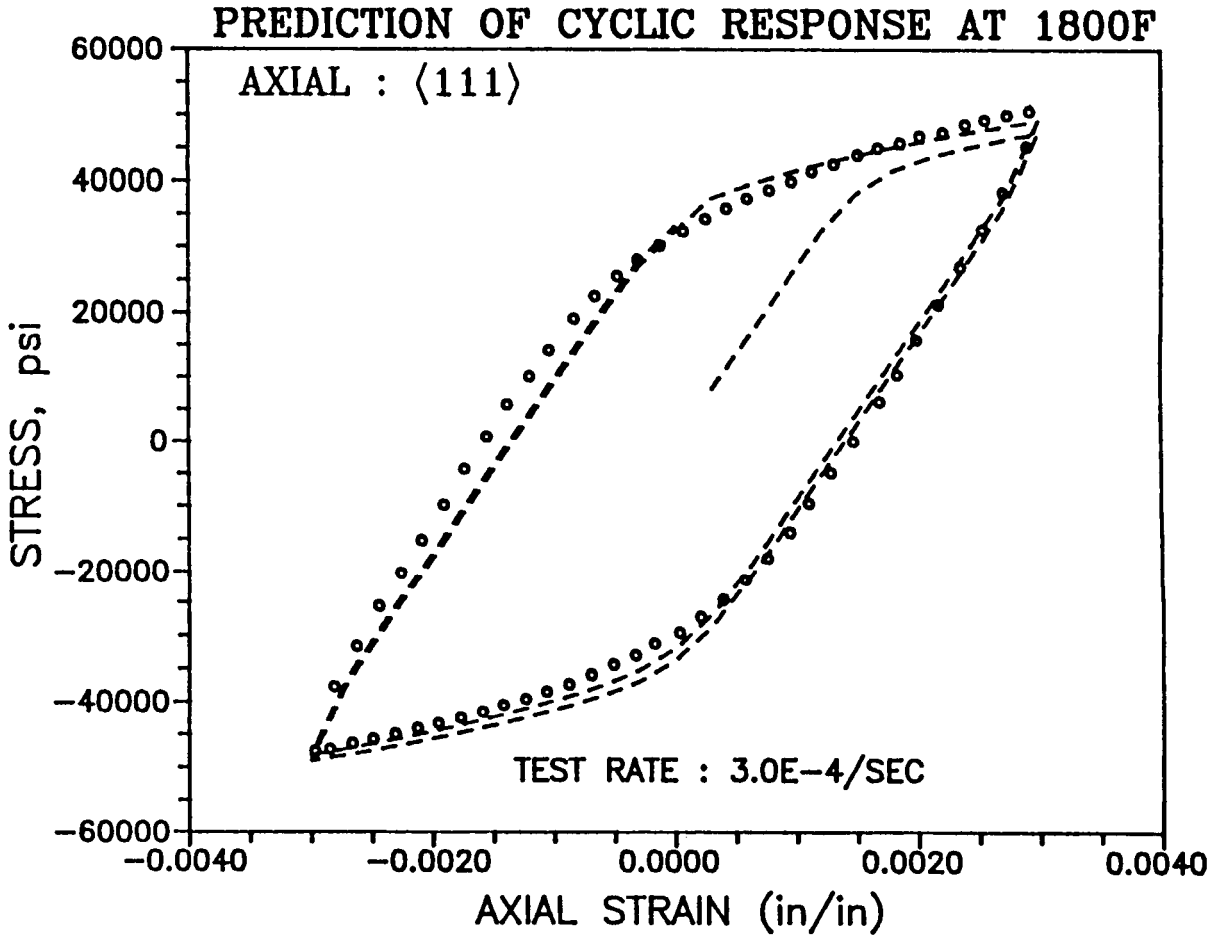

Figure 5. Predicted Response and Experimental Data for Cyclic Test in (111) Orientation, RENE' N4, 1800°F.

CONSTITUTIVE MODELLING OF SINGLE CRYSTAL AND DIRECTIONALLY SOLIDIFIED SUPERALLOYS*

Kevin P. Walker**
Engineering Science Software, Inc.
Smithfield, Rhode Island

and

Eric H. Jordan***
University of Connecticut
Storrs, Connecticut

Nickel-base monocrystal superalloys have been under development by turbine manufacturers for a number of years. Successful attempts have now been made under grant NAG3-512 to the University of Connecticut to model the deformation behavior of these materials based on both a macroscopic constitutive model and a micromechanical formulation based on crystallographic slip theory. These models have been programmed as FORTRAN subroutines under contract NAS3-23939 to Pratt & Whitney and included in the MARC nonlinear finite element program. They are currently being used to simulate thermalmechanical loading conditions expected at the "fatigue critical" locations on a single crystal (PWA 1480) turbine blade. Such analyses form a natural precursor to the application of life prediction methods to gas turbine airfoils.

SINGLE CRYSTAL FORMULATIONS

The difficulty in analyzing the deformation behavior of single crystal materials lies in their anisotropic behavior. Two separate unified viscoplastic constitutive models for monocrystal PWA 1480 have been completely formulated. In one model the directional properties of the inelastic deformation behavior are achieved by resolving the summed crystallographic slip system stresses and strains onto the global coordinate system. In the other model the required directional properties are achieved by operating on the global stresses and strains directly with fourth rank anisotropy tensors. The crystallographic slip based model is more accurate and has more physical significance than the macroscopic model, but is more computationally intensive than its macroscopic counterpart.

The material constants in both models can be obtained from uniaxial tests on <001> and <111> orientated uniaxial specimens, or from uniaxial and torsion tests on <001> orientated tubular specimens. Both models achieve good correlation with

---

* Work performed under NASA grant NAG3-512
** Engineering Science Software, Inc., Smithfield, R.I. 02917.
*** University of Connecticut, Storrs, CT. 06268.

the experimental data in the <001> and <111> corners of the stereographic triangle, and both models correctly predict the deformation behavior of specimens orientated in the <011> direction. In grant NAG3–512 the tension–torsion tests on tubular specimens orientated in the <001> direction were carried out at a temperature of 1600F at the University of Connecticut. Further tests at temperatures ranging from room temperature to 2100F have been carried out at Pratt & Whitney under contract NAS3–23939. Good correlations and predictions are uniformly achieved at temperatures above 1200F, but further work appears to be necessary to correctly model the deformation behavior of PWA 1480 monocrystal material below 1200F.

MATERIAL CONSTANT DETERMINATION

The determination of the material constants in anisotropic monocrystal materials poses many difficulties and is greatly facilitated by using an iterative nonlinear least squares program. If x_m denotes the vector which contains the material constants, the computed stress will depend on the material vector x_m and can be written as $\sigma(x_m)$, where m ranges from 1 to N, with N being the number of material constants in the vector x_m. The test result corresponding to the computed value of $\sigma(x_m)$ is denoted by σ^T.

The material constant vector x_m can be determined by minimizing the square of the difference between the test results and the computed results at the user selected points 1, 2, ... , M in the experimental data files. The total number of experimental points in the experimental data files is usually much larger than M.

In the minimization procedure the function to be minimzed is then

$$U=\sum_{r=1}^{M}\left(\sigma_r(x_m)-\sigma_r^T\right)^2.$$

If x_m^G denotes an estimated or guessed value for the material constant vector, this vector will not result, in general, in a minimum value for the objective function U. Let the vector which results in a minimum value be denoted by x_m. Then we can write

$$x_m = x_m^G + c_m,$$

where c_m is the amount, or correction, which must be added to the guessed value to produce the value which minimizes U. If the guessed vector, x_m^G, is close to the true vector, x_m, then the correction vector, c_m, will be small in comparison with x_m^G. By expanding the objective function into a Taylor series the correction vector can be determined by solving the system of equations

$$\sum_{q=1}^{N} A_{pq} c_q = b_p \text{ for } p = 1, 2, 3, \ldots, N,$$

where

$$A_{pq} = \sum_{r=1}^{M} \left(\partial \sigma_r(x_m^G)/\partial x_p\right)\left(\partial \sigma_r(x_m^G)/\partial x_q\right) \text{ and } b_p = -\sum_{r=1}^{M} \left(\sigma_r(x_m^G) - \sigma_r^T\right)\left(\partial \sigma_r(x_m^G)/\partial x_p\right),$$

by means of a Gaussian elimination method. Since only the first term in the Taylor series is kept in the preceding expansion, the solution vector c_m is not exact. However, it may be added to the guessed material constant vector x_m^G to obtain the improved vector

$$x_m^{\text{Improved}} = x_m^G + \beta c_m.$$

This process is repeated in an iterative manner until convergence is achieved. The parameter β is used to stabilize the method and assumes small values when the initial guess for the material constant vector is far from the true solution, and approaches unity as convergence is achieved.

The preceding iterative technique has proved to be of great value in estimating the material constants required for use in unified viscoplastic formulations. This is especially the case in anisotropic formulations where simplified means of estimating the material constants are not available.

USE OF INELASTIC STRAIN AS A BASIS FOR ANALYZING THERMOMECHANICAL TEST DATA

P.A. Bartolotta and J.R. Ellis
NASA Lewis Research Center
Cleveland, Ohio

Experimental investigations of isothermal and thermomechanical material behavior have been conducted for many years (refs. 1 to 5). In these investigations, comparisons of general material behavior trends have been made utilizing data collected by strip chart recordings and x-y plots. Typically, these comparisons were usually drawn from data in the form of stress range versus cycles. This method was useful to identify general material hardening characteristics, but totally ignored the wealth of information about inelastic material response throughout a cycle. Inelastic material response can be used to give insight to isothermal and thermomechanical behavior in a form that is more consistent with constitutive equation development. Likewise, other traditional approaches for data representation (i.e., tensile or compressive stress amplitude versus cycle, number of cycles to failure versus inelastic strain range, etc.) are useful and necessary to identify general material trends, but fail to illustrate the material's inelastic response. To obtain any other information such as inelastic strain-time response or inelastic strain rate - stress plots were time consuming and cumbersome. The task of obtaining this information usually entailed either hand calculations or, if a computer was going to be used, the data from the strip charts (or x-y plots) needed to be digitized. One possible solution to this problem is to use a computer system to acquire and manipulate experimental data. Therefore, recent efforts at NASA Lewis Research Center under the HOST program have been focused on the development of improved acquisition and representation of experimental data. In this paper a new approach for data representation will be introduced. A brief discussion about new thermomechanical testing systems recently installed at Lewis will also be presented. Finally, preliminary comparisons of thermomechanical and isothermal data using inelastic strain response will be presented.

EXPERIMENTAL DETAIL

The equipment and procedures used in the isothermal experiments have been previously described in detail (ref. 4). These experiments were conducted under uniaxial loading on closed-loop, electrohydraulic test systems. The specimens tested had a 3.175-cm parallel working section with a 0.795-cm outside diameter. Strains were measured over a 2.54-cm gage length using an axial extensometer. The specimens were heated using an RF induction heater and considerable effort was extended in achieving uniform temperature profiles over the gage length. Usually, temperatures fell within ±5 °C of the nominal test temperature throughout the experiments.

The isothermal experiments were performed in strain control over a longitudinal strain range ($\Delta\varepsilon_t$) of ±0.3 percent at a constant strain rate ($\dot{\varepsilon}_t$) of 10^{-4} sec^{-1}. Stress and strain responses as a function of time were recorded using both a strip chart recorder and a Bascom-Turner recorder. The Bascom-Turner system was programmed to acquire data at predetermined intervals.

Thermomechanical tests were conducted utilizing new digitally controlled electro-hydraulic test systems. These test systems are described in detail in reference 6. Special features of these systems include

(1) Hydraulic actuator bearings for maintaining alignment throughout the length of the stroke

(2) Hydraulic water-cooled grips for assured specimen alignment and ease of specimen installation

(3) Dual servo-valves for high system fidelity

Specimens were again heated using an RF induction heater. Specimen cooling was by means of the test system's water-cooled grips. This was the preferred approach as it allowed temperature profiles to be maintained within acceptable limits during the cooling process. Also to assist in this regard, the gage length over which strain measurements were made was reduced to 1.27 cm in these experiments. The net result was that temperatures in the specimen's gage length were within ±10 °C of programmed values during temperature cycling.

A Data General S/20 microcomputer was used for control purposes and data acquisition. Total strains ε_t and strain rate $\dot{\varepsilon}_t$ were programmed such that the mechanical strain range $\Delta\varepsilon_m$ was maintained at ±0.3 percent with a constant mechanical strain rate $\dot{\varepsilon}_m$ of 10^{-4} sec^{-1}. Both mechanical strains and temperature were programmed to follow triangular waveforms which were 180° out-of-phase. Temperature rates were held constant at 200 °C min^{-1}. Due to time limitations, tests were conducted for 5000 cycles unlike the isothermal tests which were conducted until fatigue failure occurred.

The following test procedures were adopted for the thermomechanical experiments:

(1) Static thermal profiles were achieved for the median temperature.

(2) In load control with zero load, the temperature was then cycled and the thermal strain-temperature response was recorded.

(3) For the maximum, mean, and minimum temperatures, the elastic modulus was found by carefully cycling the load such that the material response remained elastic.

(4) Finally, the thermomechanical test was started. Mechanical strain range and rates were controlled using information obtained in step (2).

(5) After 5000 cycles the test was stopped and the specimen was brought back to a zero-stress, zero-strain state.

(6) Procedures (2) and (3) were again conducted.

The material under investigation was Hastelloy-X in the solution annealed condition. Hastelloy-X is an austenitic nickel-based superalloy used in gas turbine components that require oxidation resistance up to 1200 °C. The material was obtained in 0.19 mm o.d. bar form, meeting the requirements of Aerospace Material Specification (AMS) 5754H. Overall specimen geometry for the thermomechanical experiments was the same as the specimens used for the isothermal tests except that

the gripping ends were smooth shanks instead of threaded. Smooth shank ends exhibit better alignment characteristics along with efficient heat transfer characteristics. Surface finish for these specimens was 16 rms.

DATA MANIPULATION

The key components of the data manipulation scheme adopted for both isothermal and thermomechanical data are the computer test system and its network. Figure 1 illustrates schematically the computer test system used for this study. This system consists of a 32-bit superminicomputer which serves as the host for 14 other 16-bit satellite minicomputers. The satellite minicomputer is presently used as an expert waveform generator to control both mechanical loading and specimen temperature. The satellites are also used for data acquisition. Data including strain, stress, and specimen temperature are collected at a constant sampling rate that is set for 500 observations per predetermined cycle, and are stored on the satellite's hard disk. Once the test is over, the test data is transferred over to the host computer where it is stored on both hard disk and magnetic tape. The data can be manipulated either by the host computer or by a personal computer (PC). For this study, the PC was chosen for the following reasons:

(1) The PC is equipped with graphics terminal and plotters for ease of data analysis.
(2) The PC has a "user friendly" statistical graphics software package.

The experimental data are transferred to the PC via a laboratory network line. This same link can be utilized in such a way that the PC can become a terminal for either the host or one of the satellite computers, thus making it easy to check on an experiment's progress from the researcher's desk.

The approach adopted for analyzing the isothermal data was as follows:

(1) Stress-strain hysteresis loops were partitioned into upper and lower halves at the reversal peaks.

   (a) Upper half - started at the compressive peak and ended at the tensile peak
   (b) Lower half - started at the tensile peak and ended at the compressive peak

(2) Time references were created at the reversal peaks.

   (a) Upper half - time origin located at compressive peak
   (b) Lower half - time origin located at tensile peak

(3) Inelastic strains were calculated for each half by

$$\varepsilon_{in} = \varepsilon_t - \sigma/E$$

where ε_{in} is the inelastic strain, ε_t is the total strain, σ is the associated stress, and E is the elastic modulus calculated from the first quarter cycle of the test.
(4) Inelastic strain-time response was plotted (fig. 2) for each half of the cycle.

(5) From these plots inelastic strain maxima (or minima) were located along with their corresponding time ($t = time_{max/min}$).

(6) From $0 \leq t \leq time_{max/min}$ a second order polynomial fit was used on the inelastic strain-time curve. And from $time_{max/min} \leq t \leq time_{end}$ a third order polynomial was used.

(Note: Two constraints were imposed for both fits. First at $t = time_{max/min}$, $\varepsilon_{in} = \varepsilon_{in,max/min}$ and secondly at $t = time_{max/min}$, $\dot{\varepsilon}_{in} = 0.$)

(7) Fitting constants for both halves of the cycle were tabulated in the form shown in tables I and II.

To analyze the thermomechanical data, the approach adopted was similar to that adopted for the isothermal data except that the apparent strains (thermal strains) had to be accounted for and the elastic modulus is now a function of temperature. The procedures for this approach were as follows:

(1) An apparent strain-temperature function was formulated and used to find mechanical strains ε_m:

$$\varepsilon_m = \varepsilon_t - \varepsilon_a(T)$$

where $\varepsilon_a(T)$ is the apparent strain as a function of temperature.

(2) Two linear functions for the elastic modulus-temperature relationships were formulated. This was accomplished by calculating the elastic moduli for the upper, middle, and lower temperatures for each specimen by test procedures (3) and (6). The two lines were then fitted between the elastic modulus-temperature pairs.

(3) Inelastic strains were calculated by

$$\varepsilon_{in} = \varepsilon_m - \sigma/E(T)$$

Because of the unique shape of the inelastic strain-time response the same approach used for the isothermal fitting could not be adopted for the thermomechanical data fitting. Therefore, procedures need to be developed. Unfortunately, at this time the routine is still being formulated and is not ready for this publication.

RESULTS AND DISCUSSION

Results obtained from a 425 °C isothermal experiment and its fitted relationships are shown in figures 3 to 8. Figures 3 to 5 compare the fitted and experimental data in two forms. The stress - total strain form was chosen to compare how well the fit reproduced a typical experimental hysteresis loop, while the stress - inelastic strain form was chosen to build confidence in calculating inelastic strain rates using the fit equations. The fitted data curves were obtained utilizing equations and constants from tables I and II as follows:

(1) The time length of a half cycle was found by taking the strain range and dividing it by the strain rate of the experiment.

(2) The time length was divided into equal time intervals of 0.24 sec.

(3) Total strain-time response was found for each time interval.

In general:	ε_t	$= \dot{\varepsilon}_t(t) + \varepsilon'_t$
upper half:	ε_t	$= 100\ \mu\varepsilon(t) - 3000\ \mu\varepsilon$
lower half:	ε_t	$= -100\ \mu\varepsilon(t) + 3000\ \mu\varepsilon$

where ε'_t is the total strain value located at the starting reversal peak.

(4) Likewise for each time interval, inelastic strain-time response was calculated from the equations and appropriate constants from tables I and II.

(5) Stresses were finally calculated for each interval.

$$\sigma = E\ (\varepsilon_t - \varepsilon_{in}) \times 10^{-6}$$

Maximum differences between the experimental and fitted data are 50 με for inelastic strains and 15 MPa for stresses. These error values are relatively low. In fact the fit appears to improve with increasing number of cycles. The applicability of this approach has been demonstrated on other isothermal experiments. However, in a few experiments slight variations in the orders of the polynomial equations are necessary.

One can differentiate the general fit equations (table I and II) and calculate inelastic strain rates with a reasonable level of confidence in the results. Figures 6 to 8 present curves of the stress-inelastic strain rate response of the same 425 °C isothermal data of figures 3 to 5. Expressing data in this form provides insight regarding the variation of inelastic strain rate during cycling. It should be noted that the stresses used in these plots are experimental values and the inelastic strain rates are the only calculated values.

The material hardening behavior and its relationship with inelastic strain rates are illustrated in figures 6 to 8. In these figures, the stress - inelastic strain response seems to be asymmetric about a skewed axis. Another trend illustrated by these figures is the way the two curve halves move closer together, finally meeting, as the material hardens. Also note that as the curves move closer together, the skewed axis of asymmetry seems to rotate counter-clockwise until parts of the curves at cycle 5000 become the skewed axis. At the present time, physical and theoretical interpretations of the information are being investigated by constitutive modelers at NASA Lewis Research Center.

Results obtained from two isothermal (205 and 425 °C) and one out-of-phase thermomechanical (200 to 400 °C) experiments are presented in figures 9 to 11. The thermomechanical test was conducted in such a way that the mechanical strain range and mechanical strain rate were similar to what was used for the isothermal experiments. Because of the temperature response limitations of the experiment itself, it should be noted that at the tensile peaks of each thermomechanical cycle, the temperature overshot its lower bound by -5 °C (195 instead of 200 °C).

From figure 9 it can be observed that at the tenth cycle of the isothermal tests the stress - inelastic strain responses are similar. As for the thermomechanical test, the stress - inelastic strain response is slightly different compared to the isothermal data. This is probably due to the difference in mechanical strain range caused by the temperature overshoot. As can be seen from figures 9 and 10, the stress - inelastic strain response for the thermomechanical experiments seems to follow more closely that of the lower temperature isothermal test. As cycling continues, the thermomechanical material response seems to start following that of

the higher temperature isothermal experiment. This observation was also observed in another thermomechanical experiment (400 - 600 °C), which suggests that this trend is a general material hardening characteristic, but further investigation will have to be conducted before this can be confirmed.

CONCLUSIONS

It has been shown from this study that the proposed data analysis method, based on inelastic strain-time response, can be used effectively to represent cyclic response at elevated temperatures for Hastelloy-X. A high level of confidence in this method was built by making comparisons of the experimental and fitted data in two forms (figs. 3 to 5). Because of this level in confidence, the analysis was taken one step further and inelastic strain rates were calculated from the derivatives of the fit equations. With the data in this form, constitutive modelers should gain insight towards understanding hardening characteristics of materials under cyclic loading at elevated temperatures.

Preliminary inelastic strain comparisons between isothermal and thermomechanical experimental data have proven useful in developing a better understanding of thermomechanical material response for Hastelloy-X. From these types of comparisons it appears that general thermomechanical material behavior can be extracted from isothermal experimental data, but information concerning changes in material strain hardening behavior must come from thermomechanical test data. Further work is continuing to formulate a scheme to calculate the inelastic strain rate response.

FUTURE WORK

The emphasis of future work will be directed at simplifying the constant tables. For example, this can be accomplished by formulating relationships that are functions of cycle numbers. Once this idea has been investigated and worked out, the rest of the isothermal data base that has been collected for Hastelloy-X at NASA Lewis Research Center will be condensed into tabular form, and published in a report.

Future emphasis for thermomechanical deformation tests will entail completing a data base for thermal cycles involving a 200 °C temperature range and repeating some of the earlier experiments. As was stated in previous sections, the fitting routine for inelastic strains of thermomechanical tests will be formulated. It is anticipated that careful analysis of this data will provide insight towards differences in strain hardening behavior that exists between isothermal and thermomechanical loading.

REFERENCES

1. Sheffler, K.D. and Doble, G.S.: Influence of Creep Damage on the Low Cycle Thermal-Mechanical Fatigue Behavior of Two Tantalum Base Alloys. (TRW ER-7592, TRW, Inc.; NASA Contract NAS3-13228) NASA CR-121001, 1972.

2. Halford, G.R. and Manson, S.S.: Life Prediction of Thermal-Mechanical Fatigue Using Strainrange Partitioning. Thermal Fatigue of Materials and Components, ASTM STP-612, D.A. Spera and D.F. Mowbray, eds., ASTM, 1976, pp. 239-254. (NASA TM X-71829.)

3. Kuwabara, K.; Nitta, A.; and Kitamura, T.: Thermal-Mechanical Fatigue Life Prediction in High-Temperature Component Materials for Power-Plant. Advances in Life Prediction Methods, D.A. Woodford and J.R. Whitehead, eds., ASME, 1983, pp. 131-141.

4. Bartolotta, P.A.: Thermomechanical Cyclic Hardening Behavior of Hastelloy-X. NASA CR-174999 (University of Akron), November 1985.

5. Ellis, J.R.; Bartolotta, P.A.; Allen, G.P.; and Robinson, D.N.: Turbine Engine Hot Section Technology 1986, NASA CP-2444, October 1986, p. 293.

6. Bartolotta, P.A. and McGaw, M.A.: A High Temperature Fatigue and Structures Testing Facility. NASA TM-100151, August 1987.

TABLE I

TABLE OF CURVE-FITTING CONSTANTS FOR THE UPPER HALF OF THE HYSTERESIS LOOP OF A 425 °C ISOTHERMAL TEST; E = 175.149 GPa

CYCLE	C1	B1	A1	D2	C2	B2	A2	TIME, SEC
5	0.651	-12.113	-1496.782	-0.003560	1.357	-24.342	-1441.291	9.310
10	.576	-10.729	-1449.155	-.002911	1.268	-22.875	-1393.738	9.319
20	.579	-12.123	-1382.321	-.003571	1.324	-26.542	-1308.885	10.470
100	.435	-10.250	-1253.793	-.002087	1.154	-26.345	-1160.644	11.787
200	.470	-10.804	-1188.877	.000275	.898	-20.762	-1131.388	11.504
500	.373	-10.178	-1079.978	.000230	.900	-24.708	-980.446	13.659
1000	.303	-8.846	-974.562	.002743	.628	-20.052	-888.642	14.576
2000	.305	-9.442	-827.634	.007796	.075	-7.920	-824.936	15.487
5000	.229	-11.505	-579.182	.006213	.278	-25.693	-351.876	25.109

CD-87-29304

TABLE II

TABLE OF CURVE-FITTING CONSTANTS FOR THE LOWER HALF OF THE HYSTERESIS LOOP OF A 425 °C ISOTHERMAL TEST; E = 175.149 GPa

CYCLE	C1	B1	A1	D2	C2	B2	A2	TIME, SEC
5	-0.583	7.940	1206.806	0.000548	-1.015	13.748	1187.124	6.808
10	-.625	9.901	1145.612	.001955	-1.132	17.552	1115.806	7.918
20	-.504	8.509	1093.498	.000678	-1.004	16.801	1058.730	8.435
100	-.512	10.756	957.700	.000437	-.967	20.176	908.463	10.508
200	-.453	10.288	900.838	-.000190	-.895	20.381	843.457	11.343
500	-.305	8.310	818.786	.000165	-.928	25.195	704.034	13.616
1000	-.276	8.474	735.091	-.001950	-.721	23.515	616.127	15.350
2000	-.243	7.972	623.451	-.006956	-.169	11.144	582.133	16.391
5000	-.206	9.400	443.576	-.011082	.345	1.541	467.496	22.798

CD-87-29305

SCHEMATIC OF COMPUTER TEST SYSTEM SHOWING KEY ELEMENTS FOR TEST CONTROL, DATA ACQUISITION, AND DATA MANIPULATION

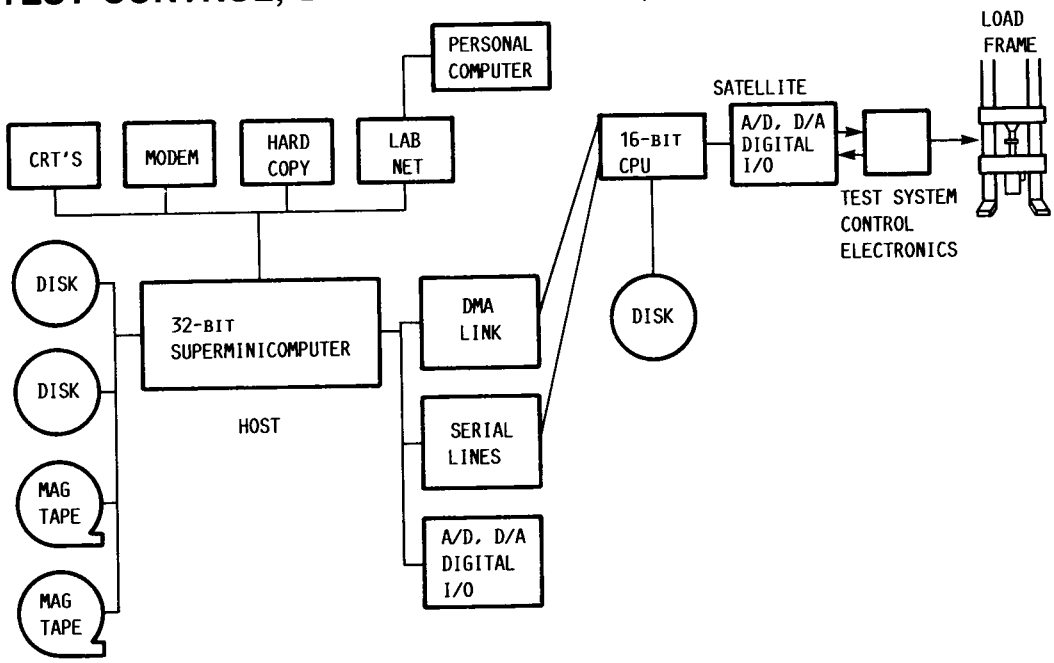

Figure 1

CURVE-FITTING APPROACH ILLUSTRATED BY TYPICAL INELASTIC STRAIN-TIME RESPONSES OF A CYCLE

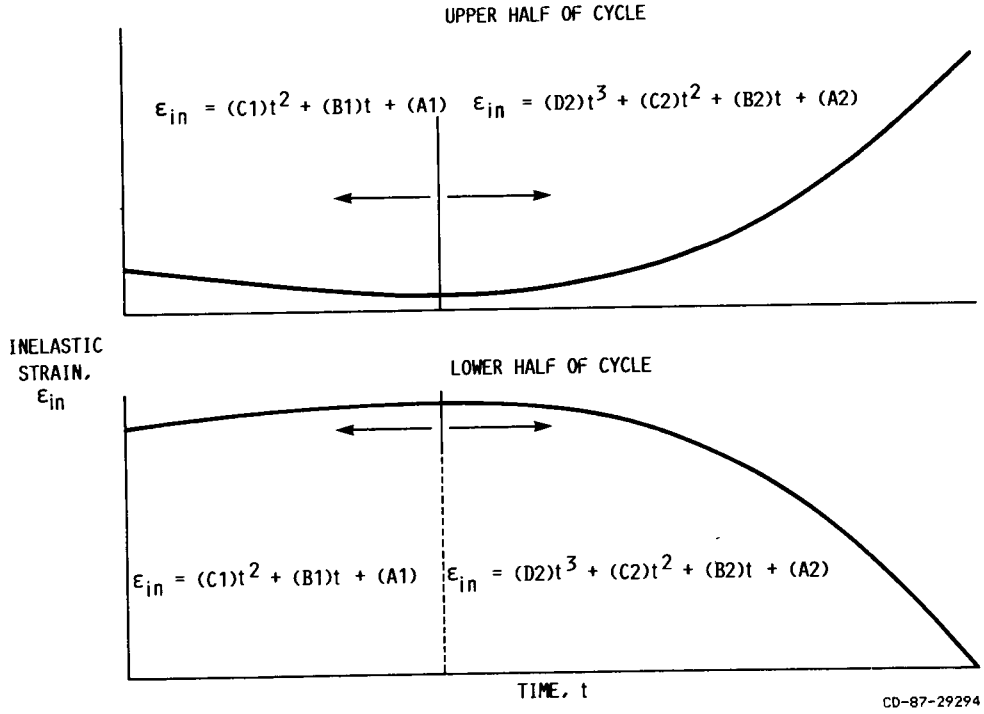

Figure 2

COMPARISON OF EXPERIMENTAL AND FITTED DATA DETERMINED UNDER ISOTHERMAL CYCLIC LOADING FOR CYCLE 10 (425 °C)

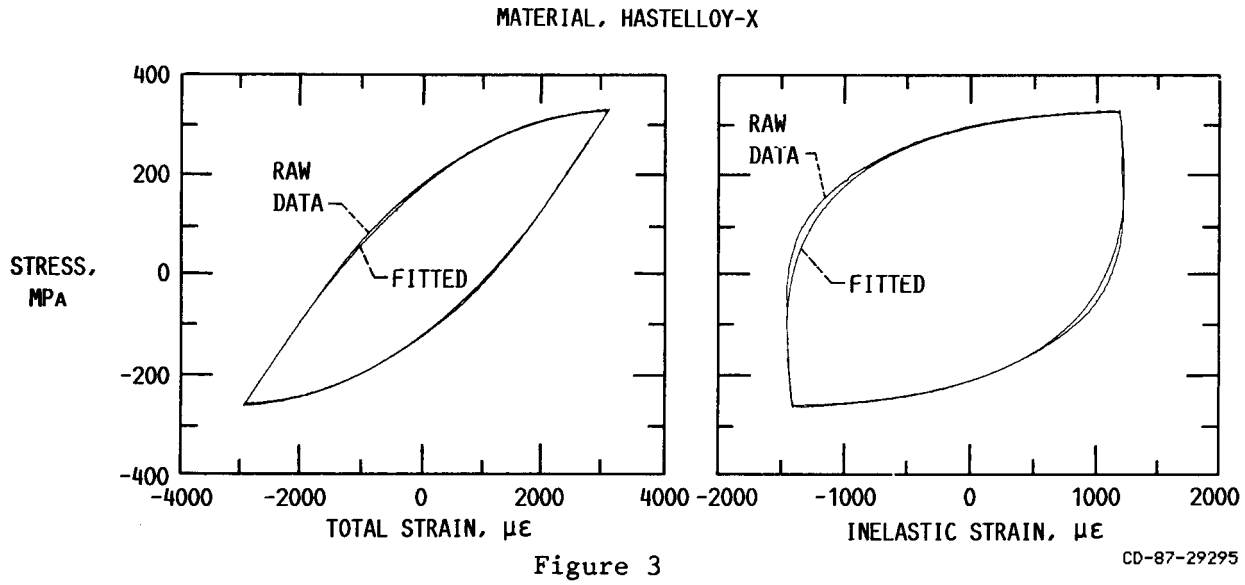

Figure 3

COMPARISON OF EXPERIMENTAL AND FITTED DATA DETERMINED UNDER ISOTHERMAL CYCLIC LOADING FOR CYCLE 100 (425 °C)

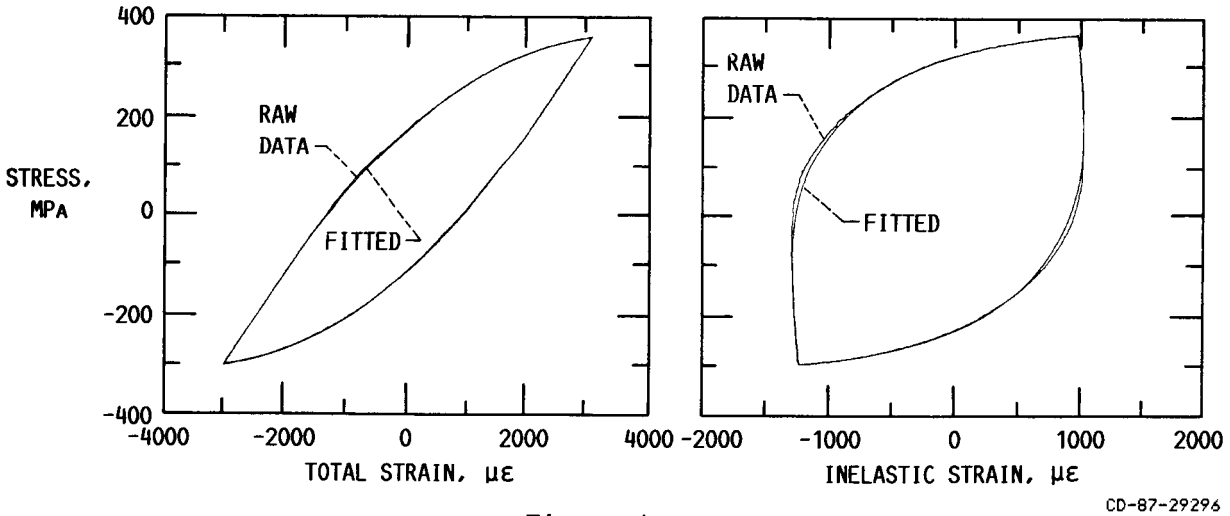

Figure 4

COMPARISON OF EXPERIMENTAL AND FITTED DATA DETERMINED UNDER ISOTHERMAL CYCLIC LOADING FOR CYCLE 5000 (425 °C)

MATERIAL, HASTELLOY-X

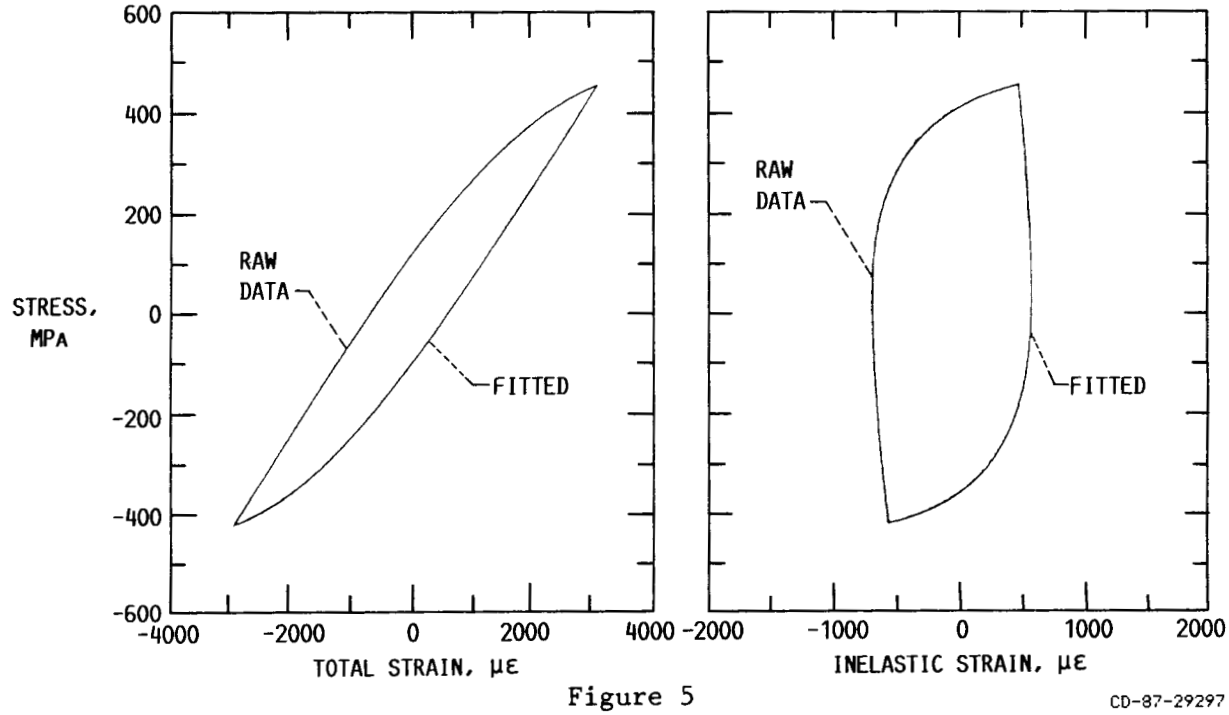

Figure 5

CD-87-29297

INELASTIC STRAIN RATES DEVELOPED DURING CYCLIC LOADING FOR CYCLE 10 (425 °C)

MATERIAL, HASTELLOY-X

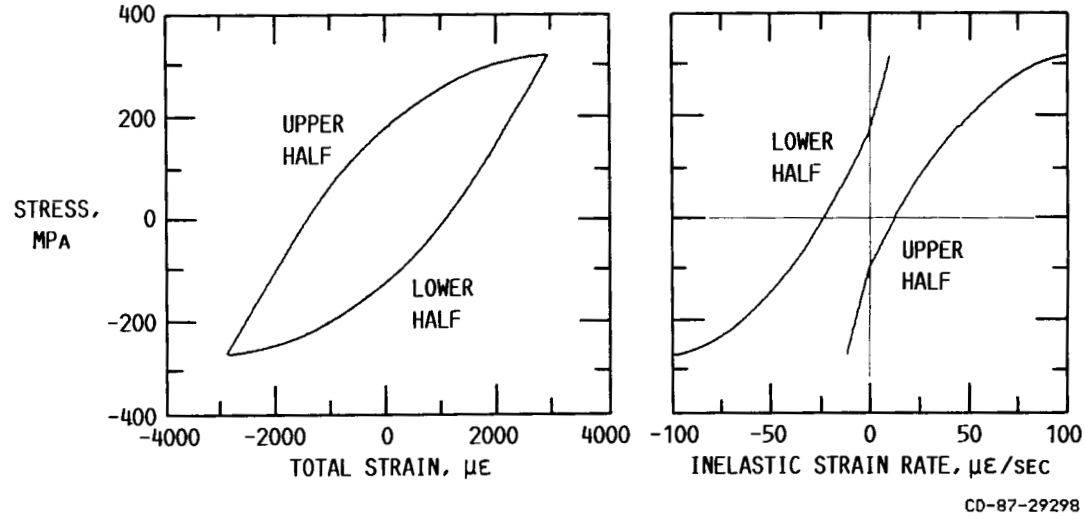

CD-87-29298

Figure 6

INELASTIC STRAIN RATES DEVELOPED DURING CYCLE LOADING FOR CYCLE 100 (425 °C)

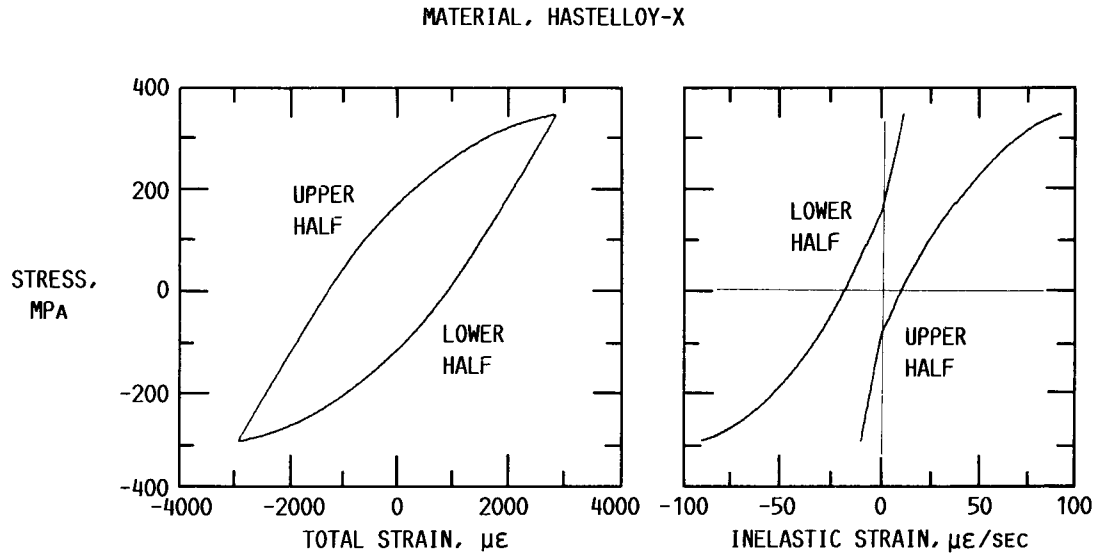

Figure 7

INELASTIC STRAIN RATES DEVELOPED DURING CYCLIC LOADING FOR CYCLE 5000 (425 °C)

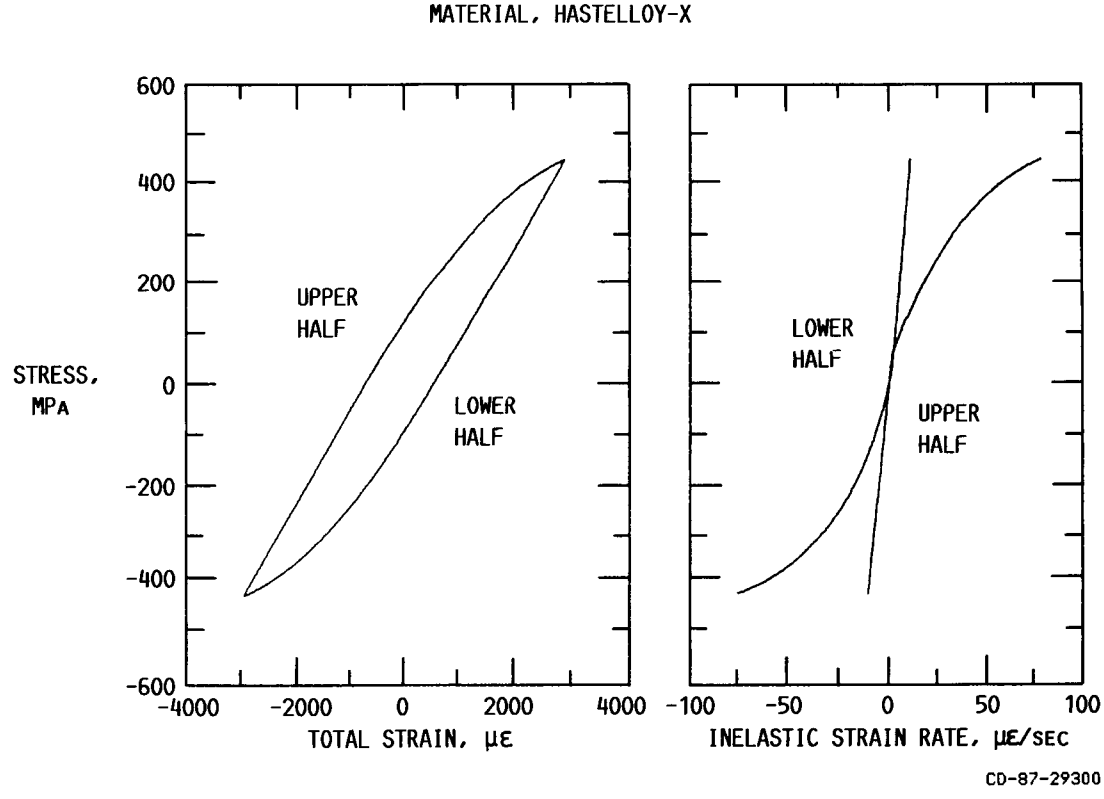

Figure 8

COMPARISON OF MATERIAL RESPONSE DETERMINED UNDER ISOTHERMAL AND THERMOMECHANICAL CYCLIC LOADING FOR CYCLE 10

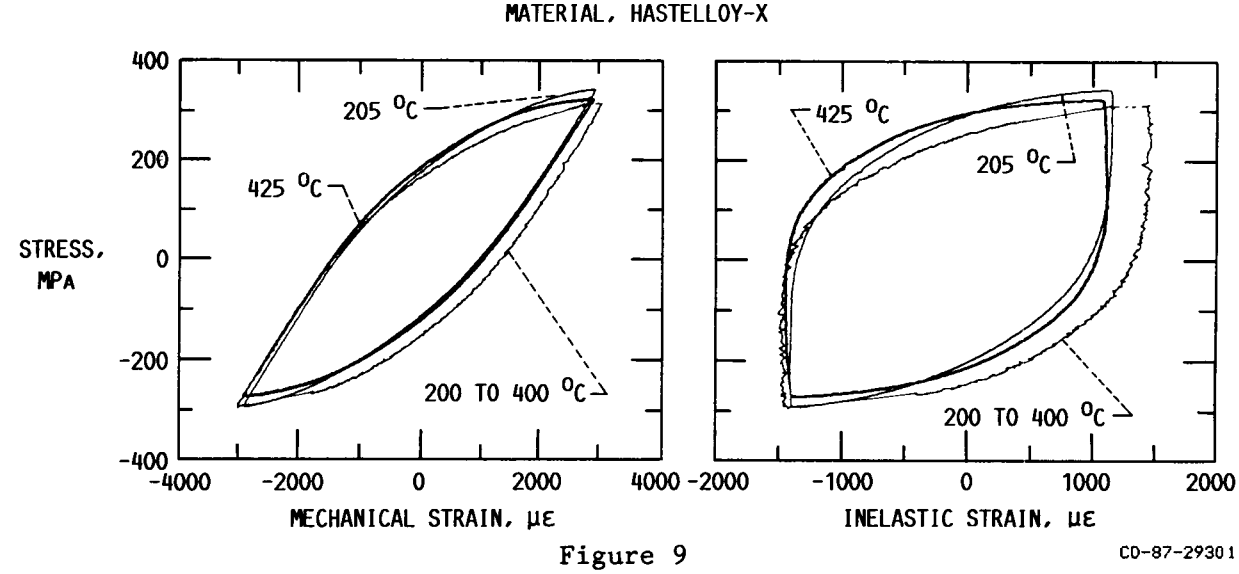

Figure 9

COMPARISON OF MATERIAL RESPONSE DETERMINED UNDER ISOTHERMAL AND THERMOMECHANICAL CYCLIC LOADING FOR CYCLE 100

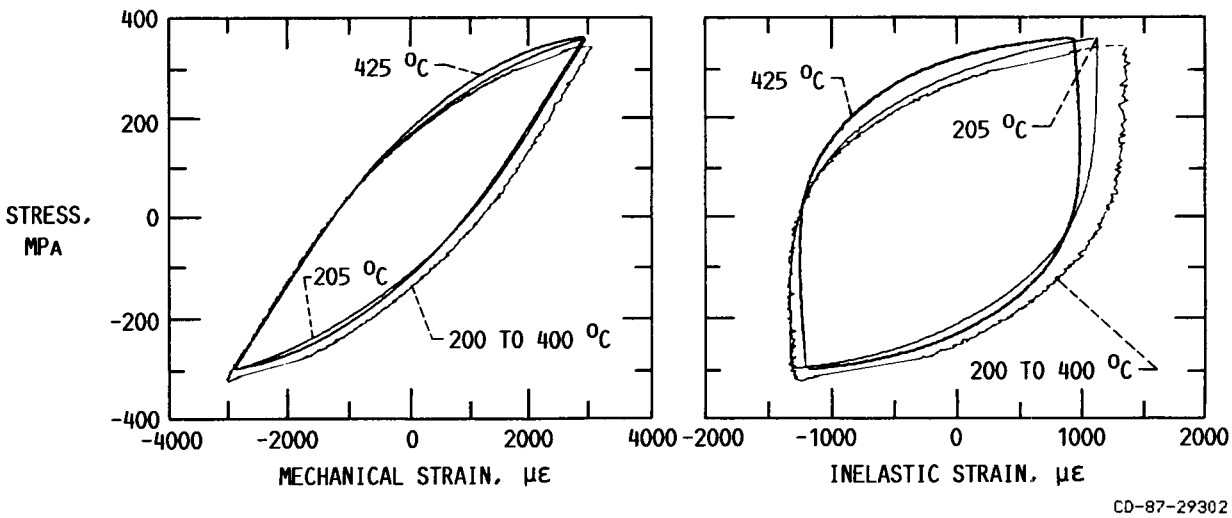

Figure 10

COMPARISON OF MATERIAL RESPONSE DETERMINED UNDER ISOTHERMAL AND THERMOMECHANICAL CYCLIC LOADING FOR CYCLE 5000

MATERIAL, HASTELLOY-X

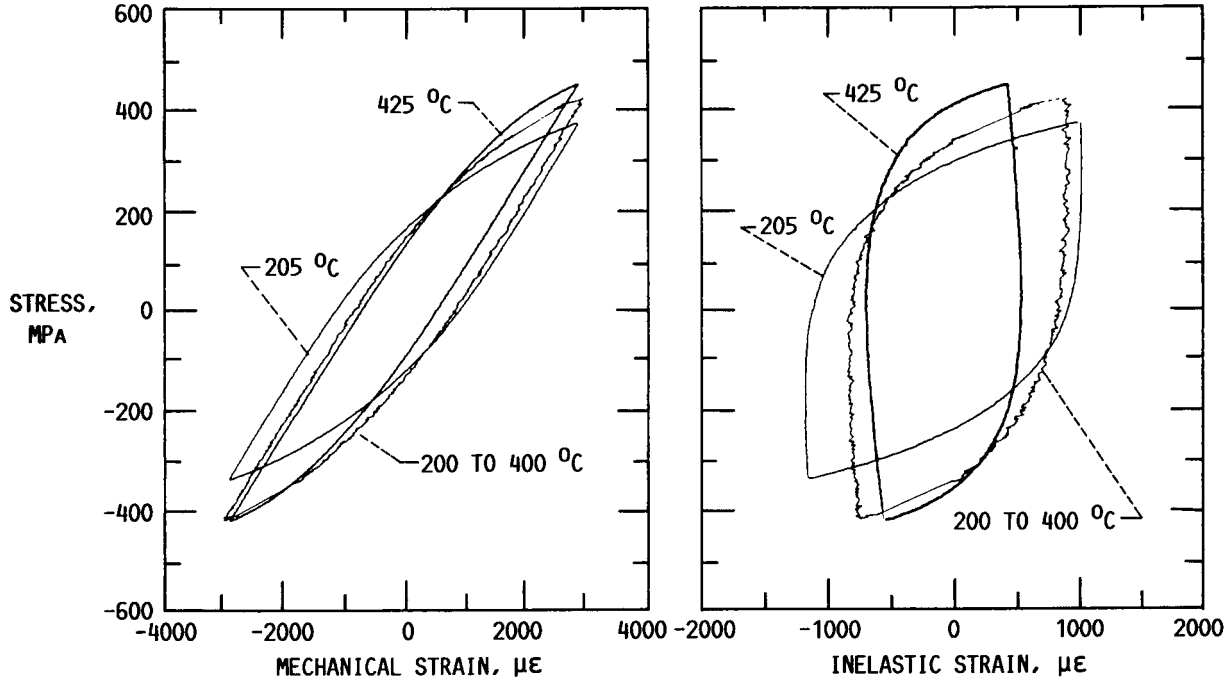

Figure 11

PRELIMINARY STUDY OF CREEP THRESHOLDS AND THERMOMECHANICAL RESPONSE IN HAYNES 188 AT TEMPERATURES IN THE RANGE 649 TO 871 °C

J.R. Ellis, P.A. Bartolotta, and S.W. Mladsi*
NASA Lewis Research Center
Cleveland, Ohio

One effort within the HOST Program has been the development of an improved thermomechanical testing capability at the NASA Lewis Research Center. This work is part of a long-term research program aimed at developing advanced viscoplastic constitutive models for materials subjected to thermomechanical loadings (refs. 1, 2, and 3). As a result of this effort, two additional electrohydraulic test systems were recently installed in the Fatigue and Structures Laboratory. These systems incorporated a number of features intended to meet the special needs of high-precision deformation testing. Experience had shown that such experiments require optimum performance in the areas of servohydraulic response, specimen alignment, and specimen heating. The measures taken to assure such performance with the latest equipment are outlined in the first part of the paper.

The first series of experiments conducted on these test systems was in support of the Space Station Solar Receiver Program. By way of background, solar receivers, used in conjunction with compressors, turbines and generators, are intended to provide a continuous source of electrical power up to 25 kW per unit (fig. 1). One unique feature of the design shown is that it uses a phase change material (PCM) to store solar energy. Simply stated, the aim is to use the latent heat of solidification of the PCM as a source of thermal energy during periods of eclipse. The phase change material used is a LiF - CaF_2 eutectic which is stored in small canisters (1.78 in. o.d. x 1.0 in. long) manufactured from Haynes 188 (fig. 2). A total of 96 canisters are individually attached to each working fluid tube and the receiver is lined with 82 such tubes.

During review of the subject design, questions were raised regarding the validity of basing the design of the PCM containment canisters on purely elastic stress analysis. Two factors giving rise to this concern are the high operating temperatures, 694°C to 834°C, and the 30-year service life. The approach adopted in resolving these concerning was to determine the stress levels or "thresholds" at which creep deformations first become significant in Haynes 188 over the temperature range of interest. This was to be accomplished in a series of short-term creep tests conducted under constant stress and constant temperature. In service, however, solar receiver components experience thermal cycles at 1.5 hour intervals. A second series of experiments was conducted, therefore, to establish whether the thresholds determined under monotonic conditions also apply in the case of thermomechanical loading. The results obtained in the two series of experiments are described in the second part of the paper.

*Summer intern in the Case-NASA Cooperative Aerospace R&D Fellowship Program. Presently at Virginia Polytechnic Institute, Blacksburg, Virginia.

EXPERIMENTAL DETAILS

An overall view of one of the closed-loop, electrohydraulic test systems is shown in Figure 3. The system features a two-post load frame with ±50 kip capacity. One point of interest is that the load cell is an integral part of the loadframe crosshead. This helps in keeping the length of the load train to a minimum which in turn helps in maintaining specimen stability under compressive loading. Another feature of the load frame is that it incorporates hydraulic bearings designed to impart high lateral stiffness to the linear actuator. Stiffness of this type is viewed as being a first requirement in achieving precise specimen alignment. With regards to servohydraulic response, the system incorporates dual 10 gpm servovalves. This particular combination was shown by trial to be capable of following rapid changes in programmed loading with high fidelity.

Further details of specimen gripping and specimen heating arrangements are shown in Figure 4. Specimens are installed in water-cooled hydraulic grips which incorporate collets for specimen gripping purposes. A variety of collets is available for testing flat plates, smooth shank cylindrical specimens, and threaded-end cylindrical specimens. Checkout experiments conducted using a number of strain gaged specimens clearly demonstrated the superiority of the smooth shank design in achieving minimum specimen bending. The results of checkout experiments obtained using such a specimen are shown for illustration purposes in Table 1. Here, it can be seen that careful grip alignment and use of smooth shank specimens resulted in specimen bending strains as low as $+10\mu\varepsilon$. note that in obtaining these results, the strain gages were zeroed before specimen installation and no further adjustments were made during the experiments. One interesting feature of these results is that the installation bending strains are not changed significantly by loading in either the tensile or the compressive senses. Further, the loading system can be seen to exhibit minimum hysteresis when the direction of loading is reversed.

Specimen heating is accomplished using 5 kW radio frequency (RF) induction heaters. One advantage of this approach is that it allows ready access to the specimen's surface. As indicated in Figure 4, this allows commercially available extensometers to be used for strain measurement with minimum complication. Further, RF heating can be used to advantage in thermomechanical tests because of the localized nature of specimen heating. This means that fairly rapid thermal cycling can be achieved, again with minimum complication. A major disadvantage of this heating method is that specimen temperature profiles are extremely sensitive to heater load coil design. Thus, considerable time can be spent with conventional coil designs in obtaining temperature profiles meeting ASTM requirements. This problem has been eliminated to a large extend by developing fixturing which allows load coils to be split into sections (fig. 4). Further, the fixturing allows individual sections to be adjusted in a straightforward and systematic manner in both the vertical and the radial senses. Recent experience has shown that this approach results in considerable time saving in obtaining optimum load coil configurations. Typical temperature profiles are shown in Table (2) for the experiments described in detail later in the paper. Inspection of these data shows that the ASTM requirement of being within ±1 percent of the mean temperature was met in all cases. It is re-emphasized that these results were obtained with minimum effort once the basic coil configuration had been decided.

Details of the thin-walled tubular specimen used in the investigation are given in Figure (5). The length of the parallel gage section is 1.375 inches, the o.d. is 0.450 inch, and the wall thickness is 0.060 inch. One less than desirable feature of the design is that it utilizes threaded ends. As indicated earlier, this compromises the excellent alignment possible with smooth shank designs. To illustrate, checkout experiments had shown that the use of threads can introduce installation bending strains as high as $\pm 300 \mu\varepsilon$ into a precisely aligned loading system. Unfortunately, the limited time available for this program meant that existing specimens had to be used and this in turn led to the use of the specimen design shown in Figure 5.

The material under investigation, Haynes 188, is a cobalt-based structural alloy. Two characteristics of the alloy important in the present application are good corrosion resistance and good high-temperature strength. The former property is obtained by including lanthanum in the alloy system which forms a protective oxide scale. High temperature strength is obtained by including tungsten which provides solid solution strengthening. Additional strengthening is provided by carbon which precipitates in the form of M_6C and $M_{23}C_6$ carbides. The chemical composition specified for the alloy is compared in Table (3) to the results of analysis performed at NASA Lewis on the test material. The two most obvious deviations are that the percentage by weight of both tungsten and phosphorous fall above the specified range. Although these deviations might prove important in long-term service, they are not judged to be limiting in the present study.

EXPERIMENTAL APPROACH

As noted earlier, the first objective of this work was to determine the stress levels or "thresholds" at which creep deformation becomes significant during the 1.5 hour hold periods typical of solar received service. As indicated in Figure 6, the approach adopted was to subject specimens to a series of short-term creep tests conducted under constant stress and constant temperature. The three temperatures selected for this stage of the program were 649, 760, and 871°C. The intent was to start at a low value of stress and to increase stress in a stepwise manner until some target value of creep strain was exceeded. Selection of this target value was not straightforward and involved a degree of judgment. Ideally, the value should be as small as possible to avoid changing the state of the material significantly during the course of the experiment. In practice, a combination of high and low frequency noise on the strain signals meant that a relatively large value of creep strain, ~ 50 $\mu\varepsilon$, was needed to avoid misinterpretation of the data. The high frequency noise, caused for the most part by the RF heating system, had a peak-to-peak value of about ±5 mV (± 10 $\mu\varepsilon$). The low frequency noise, resulting from cyclic variation of the laboratory environment, had a peak-to-peak value of about ±10 mV (±20 $\mu\varepsilon$). With these values in mind, a target value of ~ 50 $\mu\varepsilon$ appeared to be a reasonable compromise.

Because of the uncertainties noted above, two experiments were judged to be necessary to establish thresholds at a particular temperature. The first was viewed as being exploratory and the second as being an attempt to determine a more precise value. It should be noted that a fresh specimen was used in each experiment. Adopting this approach, the specimen used in the second experiment had not experienced prior inelastic straining. Stated differently, the final threshold determination was made on material in the original solution annealed condition. The initial stress values and stress increments used in these

experiments are summarized in Table (4). As indicated, relatively large stress increments were used in the first experiment to establish the approximate location of the threshold with a minimum of loading steps. These experiments showed that the thresholds fall within the following stress ranges: 30 to 35 ksi at 649°C, 5 to 11 ksi at 760°C, and 2 to 4 ksi at 871°C. In light of this information, more realistic initial stresses could be selected for the second experiment. This in turn meant that that stress increments could be kept as small as possible. As indicated in Table (4), a value of 1 ksi was used in final threshold determinations at all three temperatures.

Selection of the test values for the thermomechanical experiments was more straightforward. This was because the results of thermal analysis and elastic stress analysis were available to help guide this process. With regard to temperature values, analysis had shown that the peak solar flux occurs at an axial location about 3 feet from the aperture plate (fig. 1). A thermal history for a canister at this location is shown in idealized form in Figure 7. On coming out of eclipse, time zero in the figure, the PCM is in solid form and the canister temperature is 649°C at the location selected for detailed analysis. During the first 10 minutes, temperature increases to a value of 778°C at which point the PCM starts to liquify. The peak temperature of the cycle, 834°C, is reached after about 52 minutes, at which time the space station goes into eclipse. Subsequently, the canister temperature drops quite rapidly to a value of about 778°C when the PCM starts to solidify. Temperature then remains constant until the solidification process is completed at about 80 minutes into the cycle. During the balance of the cycle, heat is rejected from the receiver with the PCM in solid form. After about 90 minutes, the space station comes out of eclipse and the cycle is repeated. The combinations of temperature and time used in simulating this cycle under computer control are summarized in Table (5). As indicated in the table, a single temperature history was used throughout.

As noted earlier, an elastic stress analysis had been performed using the MARC finite element code. The aim of this analysis had been to determine the maximum values of stress and strain introduced into canisters by the thermal cycle described above. The stresses determined in this analysis are listed in Table (5) under the heading, Test 1. As implied by this designation, the first test was an attempt to simulate service conditions as predicted by preliminary analysis. It can be seen that the maximum and minimum stresses predicted for service are 7.21 ksi and 3.22 ksi and that the mean stress is about 5.16 ksi. Because of concerns regarding electrical noise, it was decided to conduct two additional experiments at somewhat higher stresses. This was accomplished by simply conducting the additional tests at higher values of mean stress. As indicated in Table (5), the mean stresses for Tests 2 and 3 were 6.17 ksi and 10.16 ksi. In summary, the approach adopted in conducting thermomechanical tests was to use computer control to subject specimens to predetermined temperature cycles and stress cycles. It was anticipated at any inelastic deformation occurring in the material would be detected by the mechanical extensometer used to monitor strain. This particular mode of control was adopted for reason of experimental convenience.

EXPERIMENTAL RESULTS

The data obtained in the threshold experiments conducted at 871°C are shown for illustration purposes in Figures 8 and 9. Data was acquired in these experiments using strip chart recorders. This was the preferred method since

recordings made in this manner provided a clear indication of both the high frequency and the low frequency noise. Average curves were fitted by hand to establish the amount of creep strain, ε_c, accumulated during the 1.5 hour hold periods. An assessment was then made regarding the stress level giving the target value of creep strain. Creep thresholds determined in this manner are summarized in Table (6) for the three temperatures investigated.

Strip chart records were also used in the thermomechanical experiments because of noise considerations. In these experiments, recordings were made of temperature versus time, stress versus time, and total strain versus time. Temperature and stress were monitored to check how closely the programmed waveforms were being followed. As no control problems were encountered in these experiments, the recordings were near-identical to those programmed.

The data of primary interest in these experiments were the recordings of total strain versus time. To aid the reduction process, these recordings were digitized and all subsequent reduction performed using a personal computer. A plot of total strain versus time regenerated using the computer is shown in Figure 10. As indicated, the digitized data represents average behavior for the major part of the cycle. An attempt was made, however, to represent the raw data as closely as possible for times ranging from 10.5 minutes to 51.5 minutes. This was because almost all the inelastic straining had been found to occur during this portion of the cycle.

Raw data were also recorded during the thermomechanical tests on x-y plotters. Following normal practice, stress was recorded as ordinate and total strain as abscissa. Stress-strain hysteresis loops determined in this manner are shown in Figures 11 and 12 for cycles 1 and 5 of the thermomechanical test with a mean stress of 10.16 ksi. Originally, data in this form were intended to fulfill a backup role. In the event, hysteresis loops of this type were found to be useful in establishing average slopes relating stress and total strain for portions of the cycle involving purely elastic response. These values were used to check the accuracy of computer generated data.

One feature of the data described thus far is that the total strain includes a component resulting from thermal expansion of the specimen. An experimental approach was used to establish this apparent strain. Prior to thermomechanical testing, specimens were subjected to thermal cycles with the stress held at zero. The output of the extensometer in these experiments provided a direct measure of the apparent strain. It was then assumed that this apparent strain versus time history also applied under thermomechanical loading conditions. Adopting this approach, it was possible to subtract the apparent strain from the total strain during a cycle and to determine the corresponding values of mechanical strain. Plots of stress versus mechanical strain could then be determine, as illustrated in Figures 13 and 14. It should be noted that determination of data in this form was not straightforward because the mechanical component of strain frequently was small compared to the apparent component. This meant that any errors in the experimental determination of apparent strain caused large errors in the computed values of mechanical strain.

The data reduction process was carried one stage further by calculating the time dependent strains. As noted earlier, essentially all inelastic straining occurred during the portion of cycles corresponding to time ranging from 10.5 minutes to 51.5 minutes. The time dependent component of strain was

obtained for this portion of loading by subtracting the elastic components from the mechanical component. The values of Young modulus used in these calculations were obtained from the initial loading stage of the threshold experiments. Creep curves determined in this manner are shown in Figure 15 and 16. Note that time zero in these plots corresponds to 10.5 minutes into the thermomechanical cycle.

DISCUSSION

Consideration is given first to the performance of the electrohydraulic test system used in this investigation. As noted earlier, the three areas of particular interest are servohydraulic response, specimen alignment, and specimen heating. The results shown in Tables (1) and (2) clearly indicated that very precise specimen alignment and temperature profiles are attainable with the subject test system. Whether or not improved servohydraulic response is possible with these systems remains to be demonstrated. However, the electrical noise problems arising in the threshold experiments indicated that further improvements are necessary in the area of specimen heating. The possibility of using solid state RF generators which generate minimum noise presently is being investigated.

The results shown in Figures 8 and 9 were taken to indicate that creep thresholds can be determined using the latest electrohydraulic test equipment, provided test durations are relatively short and relatively large accumulations of creep strain are used in defining the threshold. Significant improvements in specimen heating and in the control of laboratory environment are necessary if these conditions are to be relaxed. Another concern in these threshold determinations is that the practice of conducting a series of loadings on a single specimen is open to question. The concern here is that these loadings can alter the state of the material. Evidence of this can be seen in Figure 9 where the test conducted at 5.13 ksi resulted in 74 $\mu\varepsilon$ of creep strain being accumulated during the 1.5 hour hold period. It appears likely that this relatively low value resulted from the material being "hardened" as a result of the two prior loadings. The obvious solution to the problem is to use a number of fresh specimens in identifying the threshold condition. However, such an approach might prove time consuming, particularly if the data exhibit significant scatter.

As shown in Table (6), the threshold experiments showed the expected result that early creep response is highly temperature dependent. It can be seen that at 649°C, stress levels must exceed 30 ksi before creep strains become significant during the 1.5 hour hold periods. At temperatures of 760°C and 871°C, the corresponding values of stress are 11 ksi and 4 ksi, respectively. One important point to be noted about this result is that it would not have been predicted by inspection of handbook data. This is because material handbooks provide little or no information regarding the early stages of creep. It follows that problems can arise if decisions regarding the need for inelastic analysis are based on casual inspection of handbook data. The present study clearly indicated that some form of inelastic analysis is necessary for components operating at temperatures as high as 871°C if stress levels are expected to exceed 4 ksi.

Turning to the results of the thermomechanical experiments, no difficulties were experienced in simulating the anticipated service history of the solar receiver canisters. Problems did arise, however, in interpreting the data

generated at the lower stress levels because of the electrical noise problems discussed earlier. For this reason, attention will be directed first at the results obtained for the cycle involving a 10.16 mean stress. The most obvious feature of the data shown in Figure 13 is that it exhibits creep ratchetting. That is creep strains are accumulated on a cycle-by-cycle basis resulting in large overall accumulations of strain in relatively few cycles. For the data shown in Figure 13, almost 0.1 percent strain was accumulated in five cycles. Clearly, ratchetting of this type should be given serious consideration in design applications involving service lives of the order of 30 years.

Another feature of the data shown in Figure 13 is that the amount of creep strain accumulated per cycle decreases as the number of cycles is increased. On Cycle (1), for example, the accumulated creep strain is ~ 100 $\mu\varepsilon$. One interpretation of this result is that the material is hardening and might shake down to purely elastic response given a sufficient number of cycles. It should be noted, however, that shutdown and subsequent startup of the solar received could reinitiate the ratchetting process.

Similar ratchetting behavior can be observed in the data shown in Figure 14 for a mean stress 6.17 ksi. In this case, the creep strain accumulated during cycle (1) was about 100 $\mu\varepsilon$. On subsequent cycles, the creep occurring per cycle was ~ 50 $\mu\varepsilon$ or less and the data exhibited considerable scatter. The reason for the scatter is the electrical noise which complicated interpretation of the 6.17 ksi mean stress data. As might be expected, the situation was even worse for the 5.16 ksi mean stress data, the noise preventing meaningful analysis of the data.

Finally, attention is directed at the creep curves shown in figures 15 and 16. The somewhat unusual form of these curves is due, of course, to the fact that both temperature and stress are varying during the test. It was found that the curves could be fitted quite closely using second order polynomials. No physical significance is attached to this result, the expressions being reported to aid regeneration of the data. The results shown in Figure 16 can be seen to exhibit considerable scatter. It can also be seen that the results obtained for cycles (2) and (5) are not shown. This was because these creep curves exhibited excessive scatter and were not thought to be meaningful. Unfortunately, this was also the case for the creep curves determined for a mean stress of 5.16 ksi. Regardless of these data reduction difficulties, the observation was that considerable inelastic straining occurred in all three thermomechanical experiments.

CONCLUSIONS

The following conclusions were drawn from this preliminary study of creep thresholds and thermomechanical response in Haynes 188:

1. Creep threshold can be determined using the latest electrohydraulic test equipment, provided test durations are short and relatively large accumulations of creep strain are used in defining the threshold.

2. Significant creep strains were measured under monotonic loading as stress levels as low as 4 ksi at temperatures predicted for solar receiver service.

3. The material exhibited creep ratchetting during simulated service cycles. This result was not predicted by analysis using current constitutive models for Haynes 188.

FUTURE WORK

An experimental program will be initiated to develop an advanced viscoplastic constitutive model for Haynes 188. The model will be implemented in a general purpose finite element code and the analysis of critical components repeated. Further, steps will be taken to include Haynes 188 in existing research programs aimed at developing improved damaging modeling techniques for applications involving extended service at elevated temperatures.

REFERENCES

1. Robinson, D. N. and Bartolotta, P. A.: Viscoplastic Constitutive Relationships with Dependence on Thermomechanical History. NASA CR-174836 (University of Akron), March 1985.

2. Bartolotta, P. A.: Thermomechanical Cyclic Hardening Behavior of Hastelloy-X. NASA CR-174999 (University of Akron), November 1985.

3. Ellis, J. R., Bartolotta, P. A., Allen, G. P., and Robinson, D. N.: Thermomechanical Characterization of Hastelloy-X under Uniaxial Cyclic Loading. NASA CP 2444, October 1986.

LOAD (lb)	STRAIN AT LOCATION INDICATED (με)				AVERAGE STRAIN (με)	BENDING STRAIN AT LOCATION INDICATED (με)			
	1	2	3	4		1	2	3	4
0	-9	5	8	-5	-1	-8	6	9	-4
1000	162	175	177	166	170	-8	5	7	-4
2000	330	345	346	335	339	-9	6	7	-4
3000	449	514	515	504	508	-9	6	7	-4
2000	330	345	346	334	339	-9	6	7	-5
1000	161	176	178	165	170	-9	6	8	-5
0	-9	7	8	-6	0	-9	7	8	-6
-1000	-179	-164	-162	-177	-171	-8	7	9	-6
-2000	-347	-332	-331	-346	-339	-8	7	8	-7
-3000	-515	-500	-499	-514	-507	-8	7	8	-7
-2000	-347	-331	-330	-345	-338	-9	7	8	-7
-1000	-179	-163	-162	-178	-171	-8	8	9	-7
0	-8	7	8	-7	0	-8	7	8	-7

NOTE: THE STRAIN GAGES WERE LOCATED AT 90° INTERVALS AT THE SPECIMEN'S MIDSECTION. NUMBERING WAS IN THE COUNTERCLOCKWISE SENSE, VIEWED FROM ABOVE, AND LOCATION 1 CORRESPONDS TO THE FRONT OF THE TEST SYSTEM.

TABLE (1) SPECIMEN BENDING AFTER LOAD TRAIN ALIGNMENT

THERMO-COUPLE NUMBER	THERMOCOUPLE LOCATION	NOMINAL TEST TEMPERATURE (°C)							
		647		760		871		778	
		TEST 1	TEST 2	TEST 3	TEST 4	TEST 5	TEST 6	TEST 7	TEST 8
1	0.25 in. ABOVE MIDSECTION	644	640	758	757	874	870	774	773
2	0.25 in. ABOVE MIDSECTION	643	645	757	756	867	868	773	770
3	AT MIDSECTION	646	649	757	759	--	866	781	--
4	AT MIDSECTION	645	648	761	760	877	870	777	773
5	0.25 in. BELOW MIDSECTION	649	643	757	--	879	877	780	773
6	0.25 in. BELOW MIDSECTION	645	650	757	759	879	877	778	773

NOTE: THERMOCOUPLES AT PARTICULAR SPECIMEN LOCATIONS ARE DIAMETRICALLY OPPOSED. FURTHER, THERMOCOUPLES 1, 3, AND 5 ARE ALIGNED WITH THE SPECIMEN AXIS, AS ARE THERMOCOUPLES 2, 4, AND 6.

TABLE (2) - TEMPERATURE PROFILES OVER 0.5 in. SPECIMEN GAGE LENGTHS

ELEMENT (Wt %)											
Co	Cr	Ni	W	Fe	Mn	Si	C	La	B	P	S
SPECIFIED CHEMICAL COMPOSITION											
BAL.	21 to 23	20 to 24	13 to 15	3 max.	1.25 max.	0.2 to 0.5	0.05 to 0.15	0.03 to 0.12	0.05 max.	0.02 max.	0.015 max.
MEASURED CHEMICAL COMPOSITION											
34.2	21.0	23.6	17.5	1.5	0.8	0.4	0.14	600 (ppm)	400 (ppm)	0.6	0.001

TABLE (3)-COMPARISON OF SPECIFIED AND MEASURED CHEMICAL COMPOSITIONS FOR HAYNES 188

TEMPERATURE (°C)	TEST 1		TEST 2	
	INITIAL STRESS (ksi)	STRESS INCREMENT (ksi)	INITIAL STRESS* (ksi)	STRESS INCREMENT (ksi)
649	5	5	30	1
760	5	5	6	1
871	2	2	2	1

*VALUES BASED ON THE RESULTS OF THE FIRST EXPERIMENT

TABLE (4) -- SUMMARY OF STRESS LEVELS USED IN ESTABLISHING CREEP THRESHOLDS

TIME (MIN.)	TEMPERATURE AND STRESS VALUES			
	TEMPERATURE (°C)	STRESS (ksi) TEST (1)	TEST (2)	(TEST 3)
0	694	3.22	4.22	8.23
10.5	778	5.16	6.17	10.16
51.5	834	7.21	8.25	12.23
57.0	778	5.32	6.33	10.33
79.7	778	4.93	5.91	9.91
91.0	694	3.22	4.22	8.23

TABLE (5) -- COMBINATIONS OF TEMPERATURE AND STRESS USED IN DEVELOPING IDEALIZED THERMOMECHANICAL CYCLES

TEMPERATURE (°C)	CREEP THRESHOLD* (ksi)
649	30
760	11
871	4

*STRESS LEVELS AT WHICH CREEP STRAINS ~ 50$\mu\epsilon$ WERE ACCUMULATED DURING 90 MINUTE PERIODS

TABLE (6) -- CREEP THRESHOLDS DETERMINED FOR HAYNES 188 AT TEMPERATURES IN THE RANGE 649°C TO 871°C

DESIGN CONCEPT FOR SPACE STATION SOLAR RECEIVER

DIAMETER, 6.1 FT; LENGTH, 9.8 FT

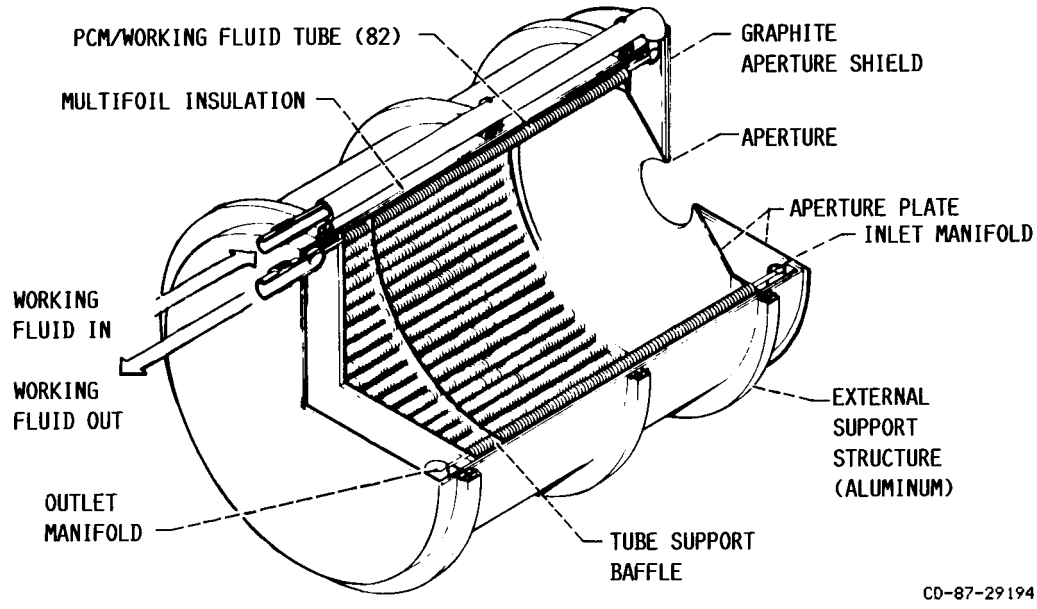

Figure 1

POSSIBLE SOLAR RECEIVER TUBE CONFIGURATION

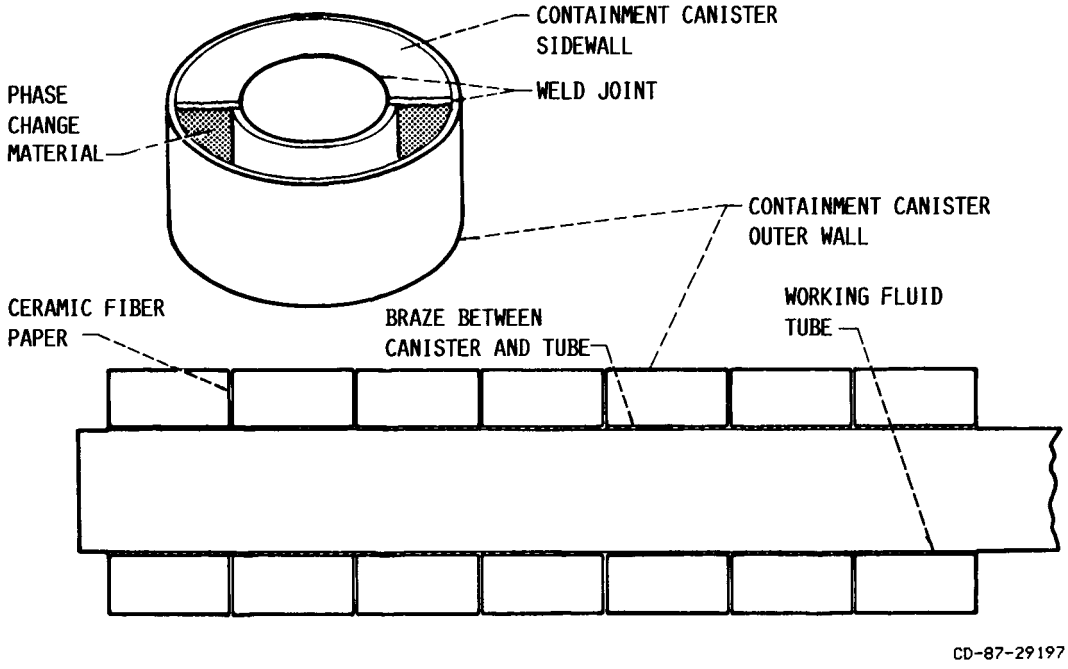

Figure 2

OVERALL VIEW OF THE CLOSED LOOP, ELECTROHYDRAULIC TEST SYSTEM

CD-87-29200

Figure 3

METHOD OF SPECIMEN HEATING AND STRAIN MEASUREMENT

CD-87-29199

Figure 4

DETAILS OF THE THIN-WALLED TUBULAR SPECIMEN

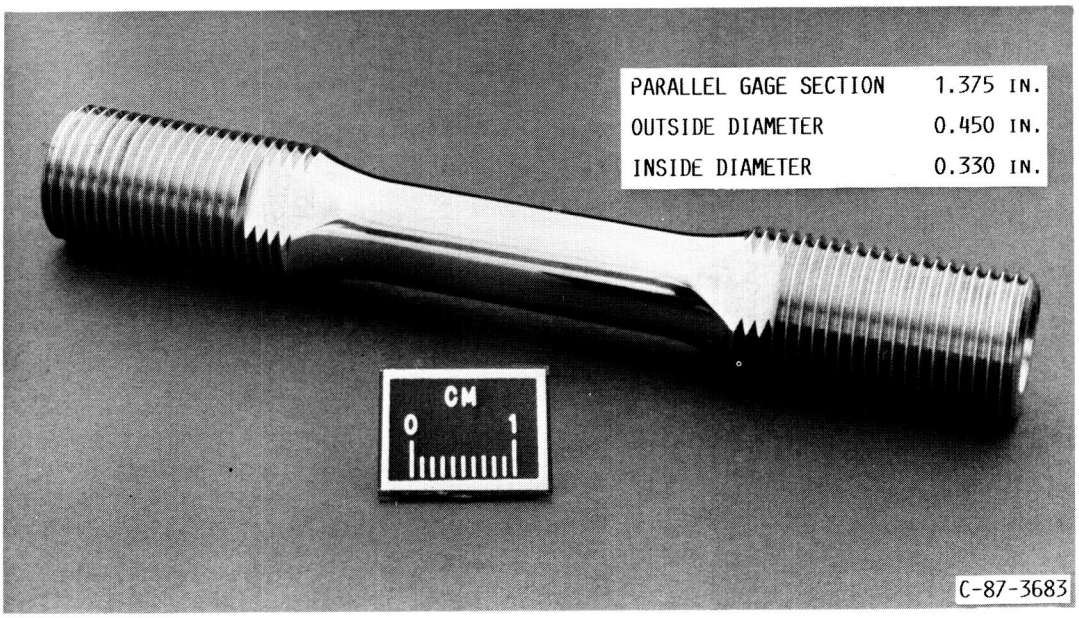

CD-87-29198

Figure 5

APPROACH ADOPTED IN DETERMINING CREEP THRESHOLDS UNDER ISOTHERMAL CONDITIONS

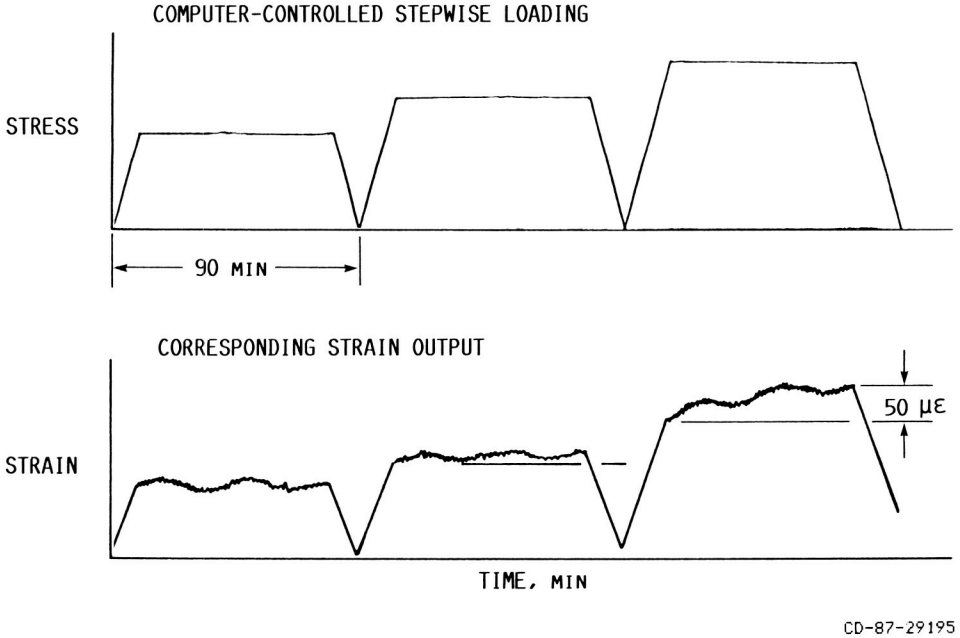

CD-87-29195

Figure 6

THERMOMECHANICAL CYCLE FOR MEAN STRESS LEVEL OF 10.16 ksi

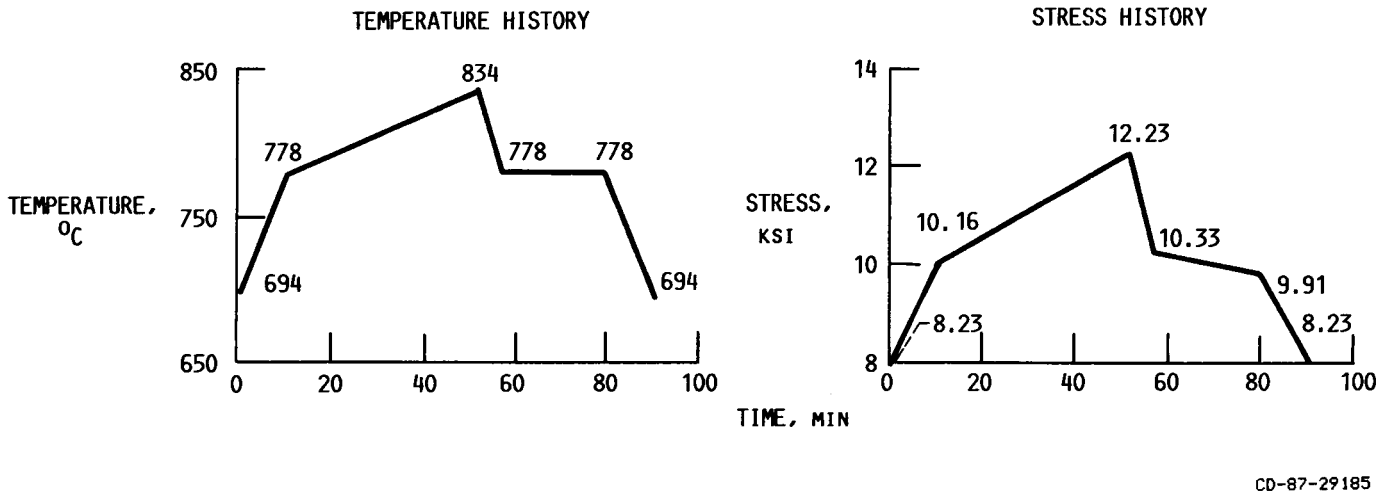

Figure 7

SHORT-TERM CREEP RESPONSE OF HAYNES-188 DETERMINED UNDER THREE LEVELS OF LOADING AT 871 °C

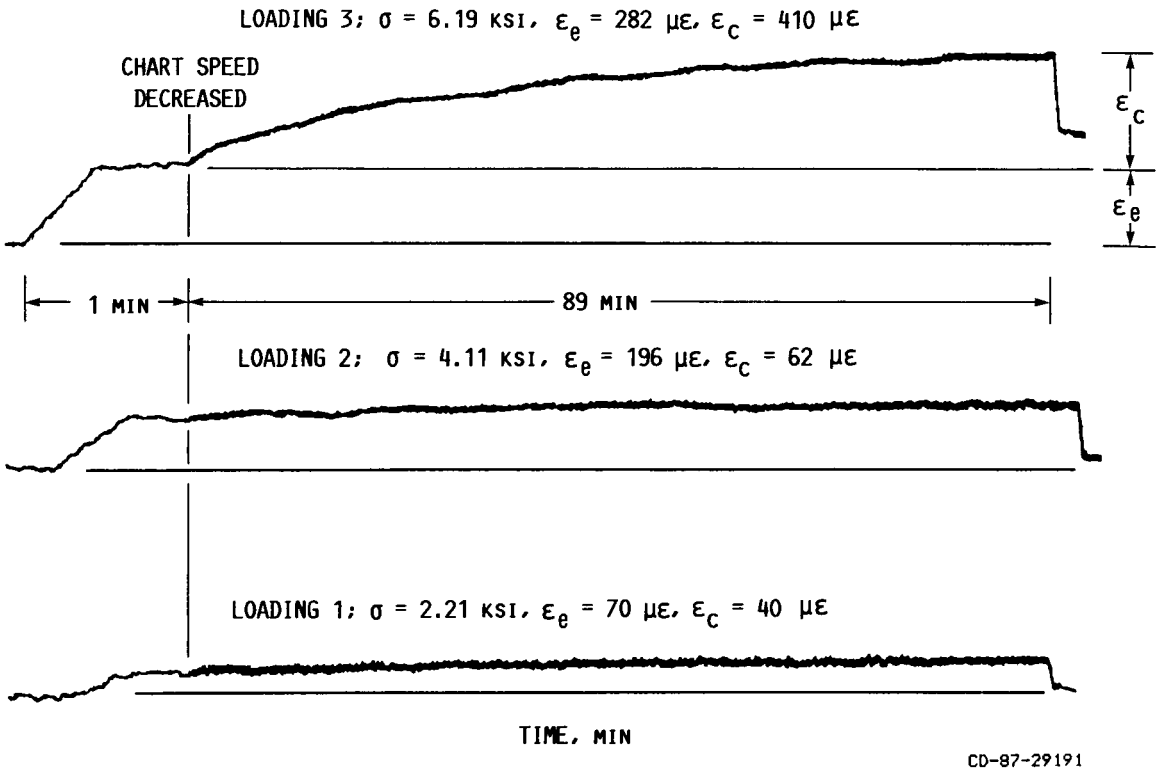

Figure 8

SHORT-TERM CREEP RESPONSE OF HAYNES-188 DETERMINED UNDER FOUR LEVELS OF LOADING AT 871 °C

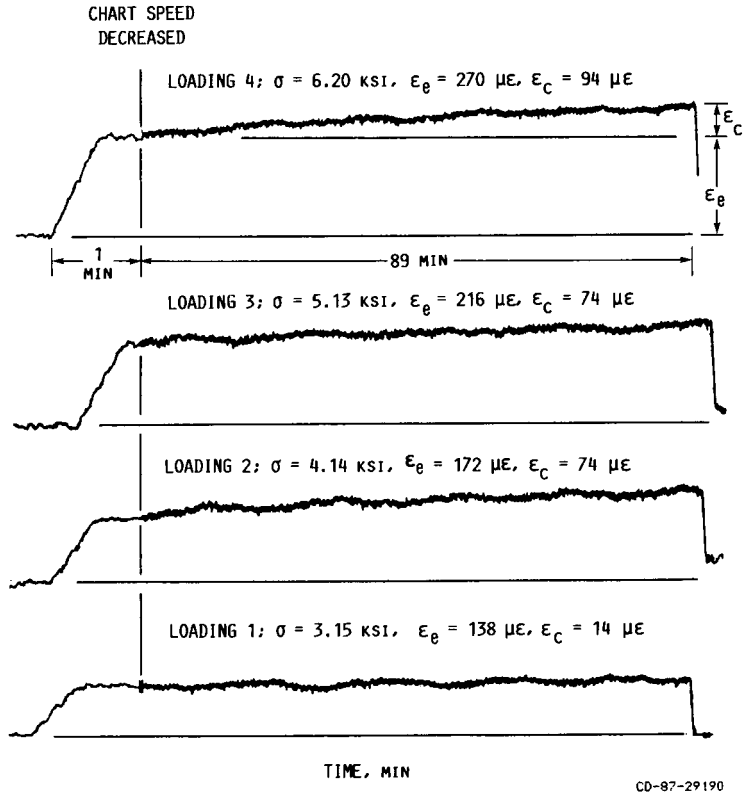

Figure 9

TOTAL STRAIN VERSUS TIME HISTORY OBTAINED UNDER THERMOMECHANICAL LOADING FOR CYCLE 1

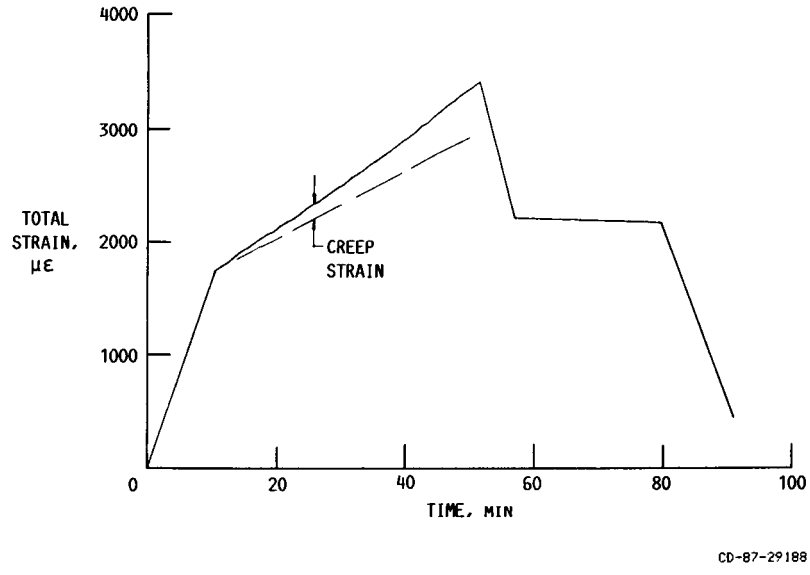

Figure 10

STRESS-STRAIN RESPONSE OBTAINED UNDER THERMOMECHANICAL LOADING FOR CYCLE 1

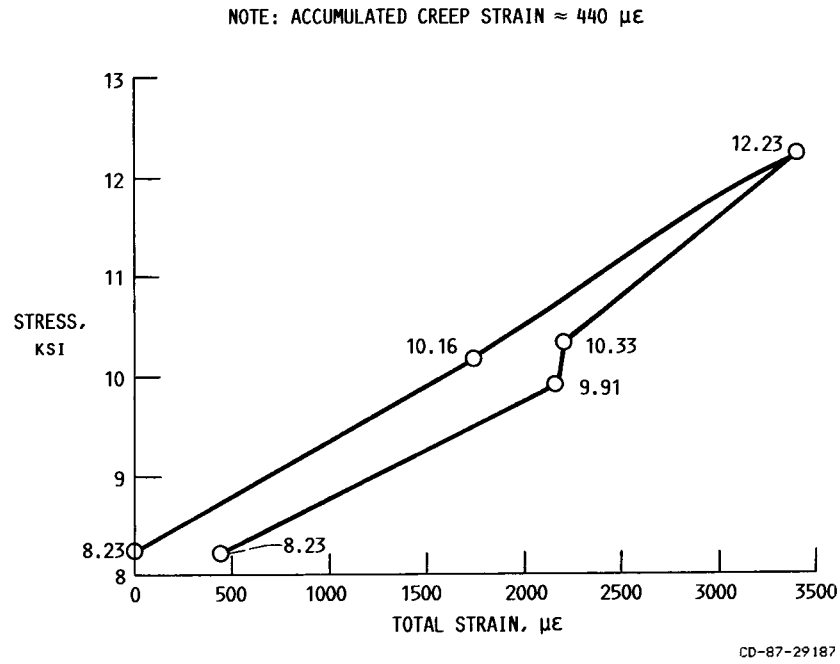

Figure 11

STRESS-STRAIN RESPONSE OBTAINED UNDER THERMOMECHANICAL LOADING FOR CYCLE 5

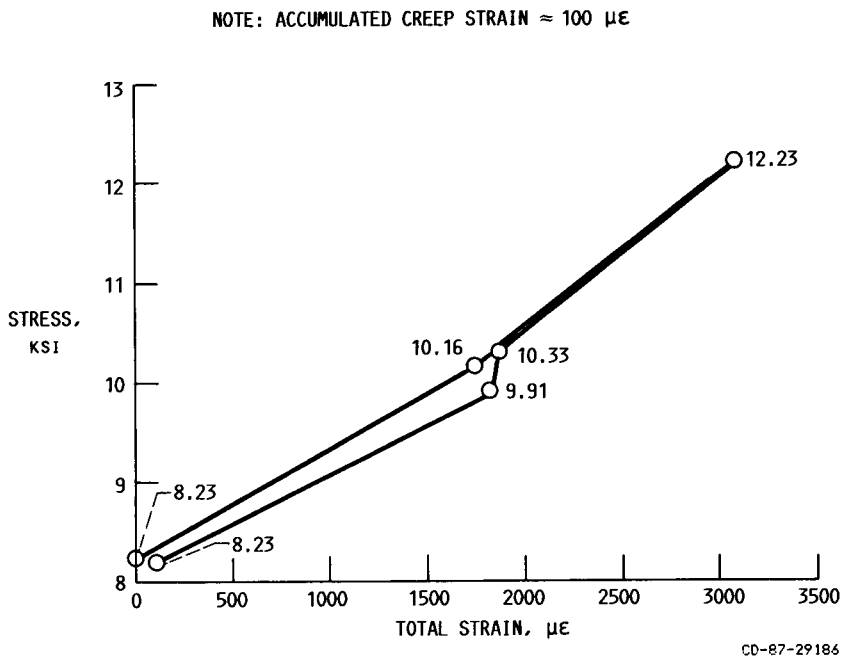

Figure 12

CREEP RATCHETTING RESULTING FROM THERMOMECHANICAL CYCLES FOR 10.16-ksi MEAN STRESS

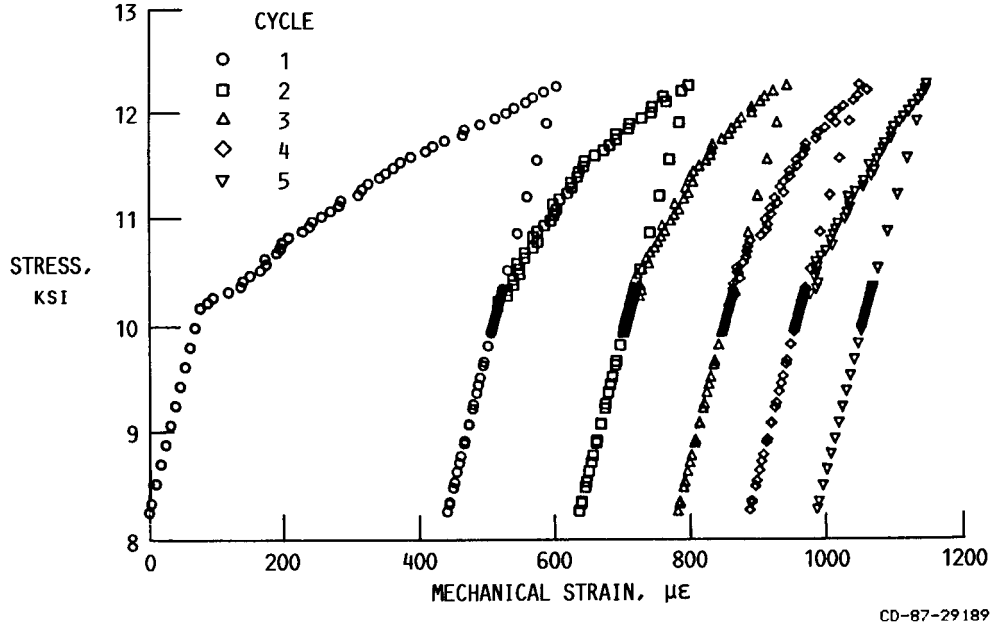

Figure 13

CREEP RATCHETTING RESULTING FROM THERMOMECHANICAL CYCLING FOR 6.17-ksi MEAN STRESS

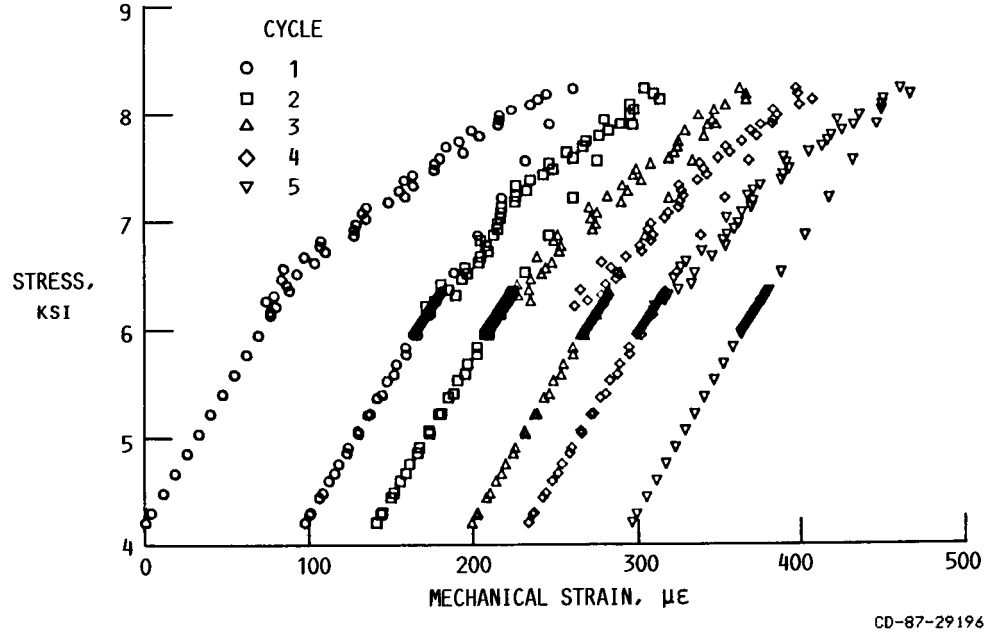

Figure 14

CREEP RESPONSE UNDER THERMOMECHANICAL LOADING FOR 10.16-ksi MEAN STRESS

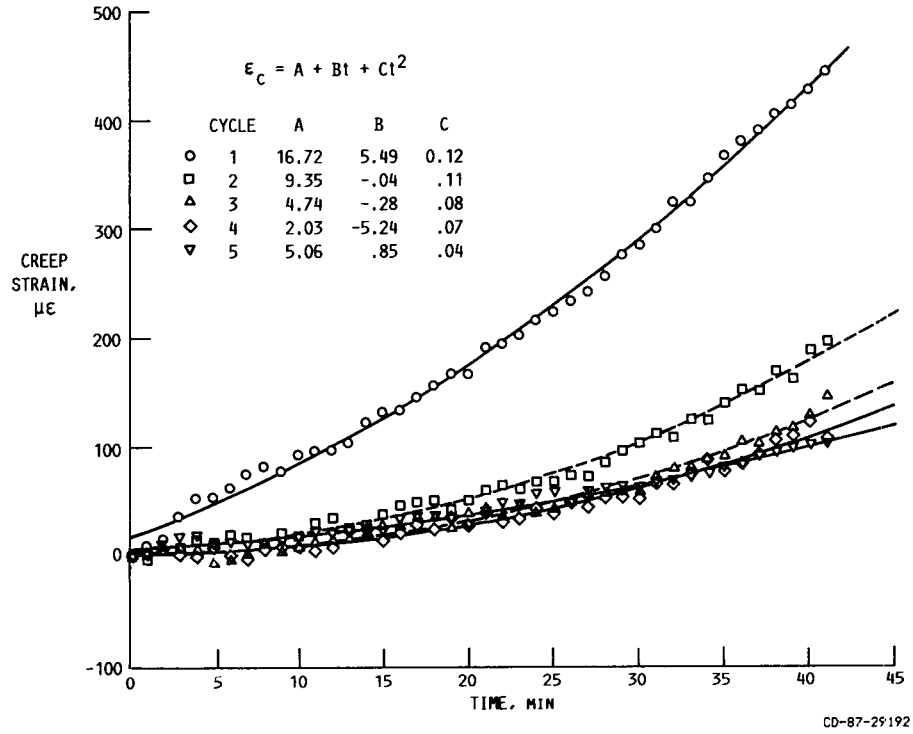

Figure 15

CREEP RESPONSE UNDER THERMOMECHANICAL LOADING FOR 6.17-ksi MEAN STRESS

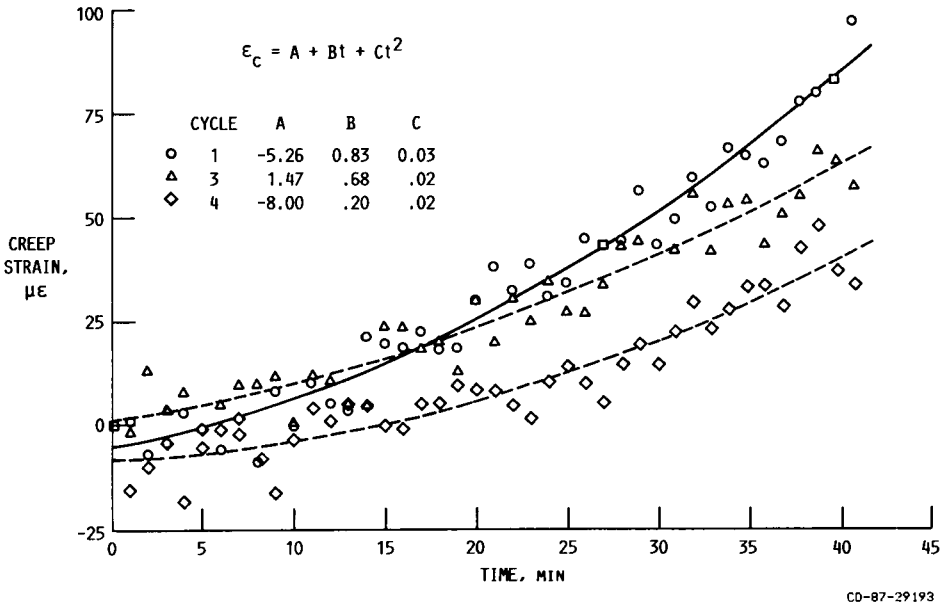

Figure 16

FINITE ELEMENT IMPLEMENTATION OF VISCOPLASTIC MODELS

V.K. Arya*
NASA Lewis Research Center
Cleveland, Ohio

The need for an accurate and realistic description of inelastic, high-temperature behavior of materials has attracted the attention of numerous investigators in recent years. As a result of their concerted efforts, a number of constitutive models called viscoplastic models has emerged. These models consider all the inelastic strain (including creep, relaxation, etc.) as a unified quantity and, in general, provide a better description of high-temperature inelastic behavior of materials. Since these models incorporate as much material science as possible, their mathematical structure is very complex. To use these models effectively and reliably for the analysis and design of turbine engine hot section components, we must demonstrate their feasibility by incorporating the models in nonlinear finite element structural analysis codes and perform nonlinear stress/life analyses for these components.

With this objective in mind, the NASA Lewis Research Center has mounted an in-house effort to implement some of the more commonly used viscoplastic models into the general purpose finite element structural analysis code - MARC. The intent is to provide the designer and structural analyst with a tool for realistic and rational analysis and designs of hot section components.

This paper gives a brief description of the implementation in MARC of two viscoplastic models developed by Robinson (refs. 1 and 2). One model is for isotropic materials and the other for metal matrix composites. Also presented are analytical results obtained for hot section components using these models. Future work is also discussed.

VISCOPLASTIC MODELS

Robinson's models for isotropic materials and metal matrix composites are based on the concept of a flow potential. The flow and growth laws for the internal variables are derived from this flow potential. The material behavior is elastic for all the stress states within the potential, and it is viscoplastic for all the stress states outside the flow potential. The displacements (strains) are assumed to be small, and the total strain is assumed to be the sum of elastic and inelastic components. The models include two internal state variables to account for the kinematic and isotropic hardenings.

A brief description of the constitutive equations of these two models and the values of constants utilized in the numerical computations are given below.

---

*NASA-NRC Resident Research Associate.

Isotropic Model

The constitutive equations for the isotropic model developed by Robinson (ref. 1) are

Flow law. -

$$2\bar{\mu}\dot{\varepsilon}_{ij} = \begin{cases} \dfrac{F^n}{\sqrt{J_2}}\,\Sigma_{ij} ; & F > 0 \quad \text{and} \quad S_{ij}\Sigma_{ij} > 0 \\ 0 ; & F \leq 0 \quad \text{or} \quad F > 0 \quad \text{and} \quad S_{ij}\Sigma_{ij} \leq 0. \end{cases}$$

Evolution law. -

$$\dot{\alpha}_{ij} = \begin{cases} 2\mu h\dot{\varepsilon}_{ij} - r\dfrac{\alpha_{ij}}{\sqrt{I_2}} ; & G > G_0 \quad \text{and} \quad S_{ij}\alpha_{ij} > 0 \\ 2\mu h_0\dot{\varepsilon}_{ij} - r_0\dfrac{\alpha_{ij}}{\sqrt{I_2}} ; & G > G_0 \quad \text{and} \quad S_{ij}\alpha_{ij} \leq 0. \end{cases}$$

where

$$S_{ij} = \sigma_{ij} - \frac{1}{3} S_{kk}\,\delta_{ij} \qquad h_0 = \frac{H}{G_0^{\beta}}$$

$$\Sigma ij = S_{ij} - \alpha_{ij} \qquad F = \left(\frac{J_2}{\kappa^2}\right) - 1$$

$$J_2 = \frac{1}{2}\,\Sigma_{ij}\Sigma_{ji} \qquad G = \sqrt{I_2}/\kappa^2$$

$$I_2 = \frac{1}{2}\,\alpha_{ij}\alpha_{ij} \qquad r = RG^{m-\beta}$$

$$h = \frac{H}{G^{\beta}} \qquad r_0 = RG_0^{\,m-\beta}$$

In the above equations, σ_{ij} denotes the stress, $\dot{\varepsilon}_{ij}$ the inelastic strain rate, δ_{ij} the Kronecker delta, and Σij the effective stress. Repeated subscripts imply summation. κ is the drag stress and α_{ij} is the back stress.

Numerical values of constants. - The values of constants are for 2-1/4Cr-1Mo steel.

$\mu = 3.61\text{x}10^7$ $\qquad \bar{\mu} = \mu \exp(\Theta_1)$

$n = 4$ $\qquad m = 7.73$

$\beta = 1.5$ $\quad R = 9.0\text{x}10^{-8} \exp(\theta_2)$

$H = 1.37\text{x}10^{-4}$ $\quad G_0 = 0.14$

and

$$\theta_1 = (23.8\theta - 2635)\left(\frac{1}{811} - \frac{1}{\theta}\right)$$

$$\theta_2 = 40\ 000\left(\frac{1}{811} - \frac{1}{\theta}\right)$$

Here, θ is the absolute temperature in degrees Kelvin.

Metal Matrix Composite Model

The constitutive equations for this model, taken from reference 2, are summarized as follows:

Flow law. -

$$\dot{\varepsilon}_{ij} = \frac{F^n}{2\mu}\,\Gamma_{ij} ,$$

Evolution law. -

$$\dot{\alpha}_{ij} = \frac{H}{G^\beta}\,\dot{\varepsilon}_{ij} - RG^{m-\beta}\Pi_{ij} ;$$

where

$$\Gamma_{ij} = \Sigma_{ij} - \xi[d_k d_i \Sigma_{jk} + d_j d_k \Sigma_{ki} - 4I_3 d_i d_j] - 4\zeta I_3(3d_i d_j - \delta_{ij})$$

$$\Pi_{ij} = \alpha_{ij} - \xi[d_k d_i \alpha_{jk} + d_j d_k \alpha_{ki} - 4I_3' d_i d_j] - 4\zeta I_3'(3d_i d_j - \delta_{ij})$$

$$F = \frac{1}{K_t^2}\left[I_1 - \xi I_2 - 12\zeta I_3^2\right] - 1 \qquad G = \frac{1}{K_t^2}\left[I_1' - \xi I_2' - 12\zeta I_3'^2\right]$$

$$I_1 = \frac{1}{2}\,\Sigma_{ij}\Sigma_{ij} \qquad I_1' = \frac{1}{2}\,\alpha_{ij}\alpha_{ij}$$

$$I_2 = d_i d_j \Sigma_{jk}\Sigma_{ki} - 4I_3^2 \qquad I_2' = d_i d_j \alpha_{jk}\alpha_{ki} - 4I_3'^2$$

$$I_3 = \frac{1}{2}\,d_i d_j \Sigma_{ji} \qquad I_3' = \frac{1}{2}\,d_i d_j \alpha_{ji}$$

$$\xi = \frac{\eta^2 - 1}{\eta^2} \qquad \zeta = \frac{4(\omega^2 - 1)}{4\omega^2 - 1}$$

Here, d_i denotes a unit vector along the preferred direction at a point of the material, and ω and η denote the anisotropic parameters.

Numerical values of constants. - In the absence of experimental data, the following values of the constants are assumed to carry out the numerical computations:

$\mu = 3.60 \times 10^7$ $\quad$ $n = 4$

$m = 7.73$ $\quad$ $\beta = 0.75$

$G_0 = 0.005$ $\quad$ $K_t = 0.82$

$R = 8.87 \times 10^{-8}$ $\quad$ $\omega = 7$

$\eta = 3$

IMPLEMENTATION IN MARC

The user subroutine HYPELA in the MARC code provides the user with an efficient way of implementing and integrating the general nonlinear constitutive relationships of Robinson's model. The details of this implementation may be found in reference 3.

To avoid the numerical instabilities encountered due to the "stiff" and "discontinuous" nature of constitutive equations, the use of "smoothing functions" (or "spline functions") is made. The spline functions used in the computations are defined in references 1 and 3.

RESULTS

Numerical results using the Robinson's models are depicted in figures 1 to 18. Figures 1 to 9 exhibit the results for the isotropic model, whereas figures 10 to 18 show the results for the metal matrix composite model.

Isotropic Model

The cyclic thermal and mechanical loads used to generate the uniaxial hysteresis loops are shown in figure 1. Three different strain rates for isothermal, non-isothermal in-phase, and nonisothermal out-of-phase loadings are shown in figures 2 to 4, respectively. Figure 5 shows excellent agreement between experiment and predictions, and verifies the correct finite element implementation of the model.

The results for the multiaxial problem of a thick internally pressurized cylinder are exhibited in figures 6 to 9. The analytical results shown in these figures were obtained using the expressions given in reference 3. The MARC and analytical results agree very well and establish the feasibility of performing a nonlinear structural analysis using the viscoplastic model.

Metal Matrix Composite Model

The results of uniaxial calculations using Robinson's metal matrix composite model are depicted in figures 10 to 18. These figures show the hysteresis loops, creep curves, and relaxation curves generated with the finite element implementation of the model. The implementation clearly shows all the expected characteristics (e.g., strain-rate sensitivity, creep, relaxation, etc.) and the effect of preferred orientations (anisotropy) of the composites. The experimental work to determine the values of constants in the model for a metal matrix composite material is in progress at Lewis.

CONCLUSIONS AND FUTURE WORK

The viscoplastic models for the isotropic material and metal matrix composites developed by Robinson have successfully been implemented in MARC. The results obtained (in particular using the isotropic model) support the feasibility of performing nonlinear structural analyses using these models. These models will provide for more realistic and rational designs of gas turbine engine hot section components.

The implementation of other viscoplastic models in MARC - such as (1) viscoplastic models for nickel-base superalloys, (2) viscoplastic models for single crystal alloys, and (3) viscoplastic models for metal matrix composites including damage - is in progress. The implementation of these models and their results, uniaxial and multiaxial predictions, will be reported subsequently.

REFERENCES

1. Robinson, D.N.; and Swindeman, R.W.: Unified Creep-Plasticity Constitutive Equations for 2-1/4Cr-1Mo Steel at Elevated Temperature. ORNL TM-8444, Oct. 1982.

2. Robinson, D.N.; Duffy, S.F.; and Ellis, J.R.: A Viscoplastic Constitutive Theory for Metal Matrix Composites at High Temperature. NASA CR-179530, 1986.

3. Arya, V.K.; and Kaufman, A.: Finite Element Implementation of Robinson's Unified Viscoplastic Model and Its Application to Some Uniaxial and Multiaxial Problems. NASA TM-89891, 1987.

CYCLIC THERMAL AND MECHANICAL LOADINGS USED TO GENERATE HYSTERESIS LOOPS BY FINITE ELEMENT CODE—MARC

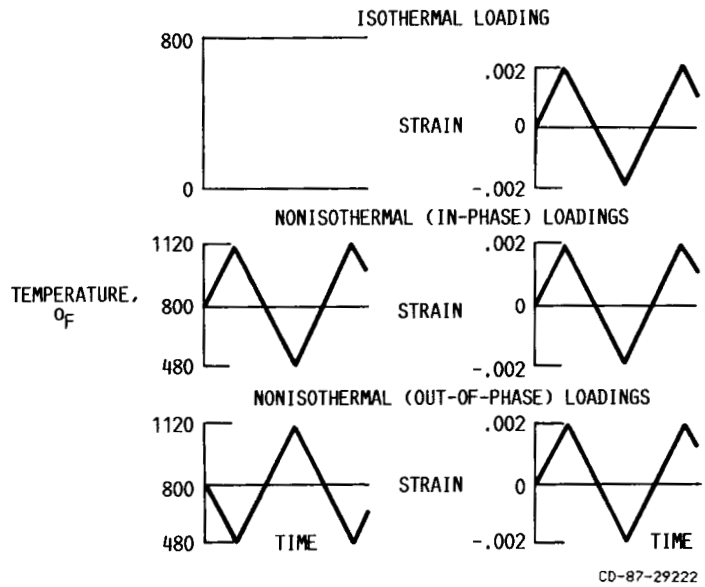

Figure 1

HYSTERESIS LOOPS AT DIFFERENT STRAIN RATES USING ROBINSON'S MODEL—ISOTHERMAL CASE, 800 °F

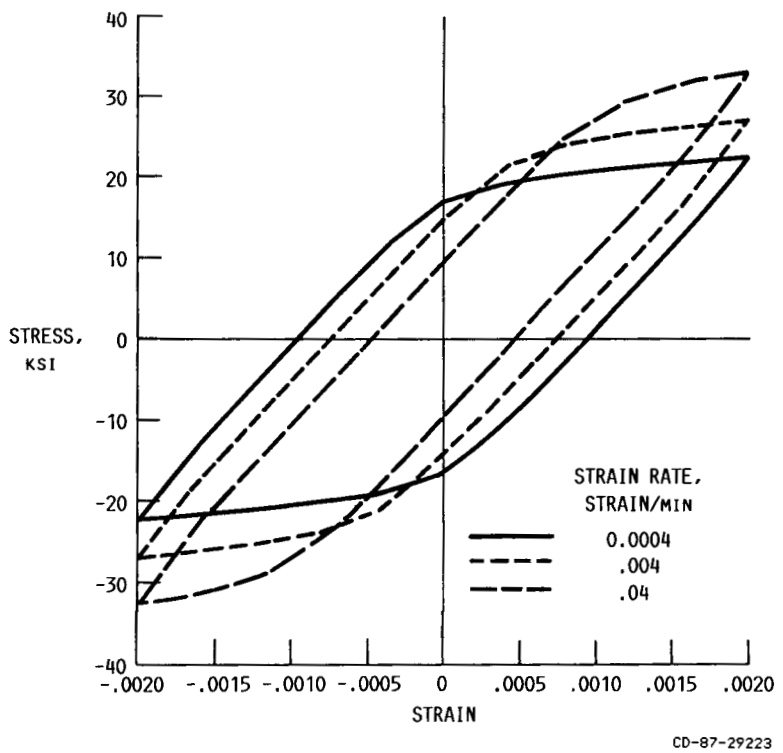

Figure 2

HYSTERESIS LOOPS AT DIFFERENT STRAIN RATES USING ROBINSON'S MODEL—NONISOTHERMAL CASE

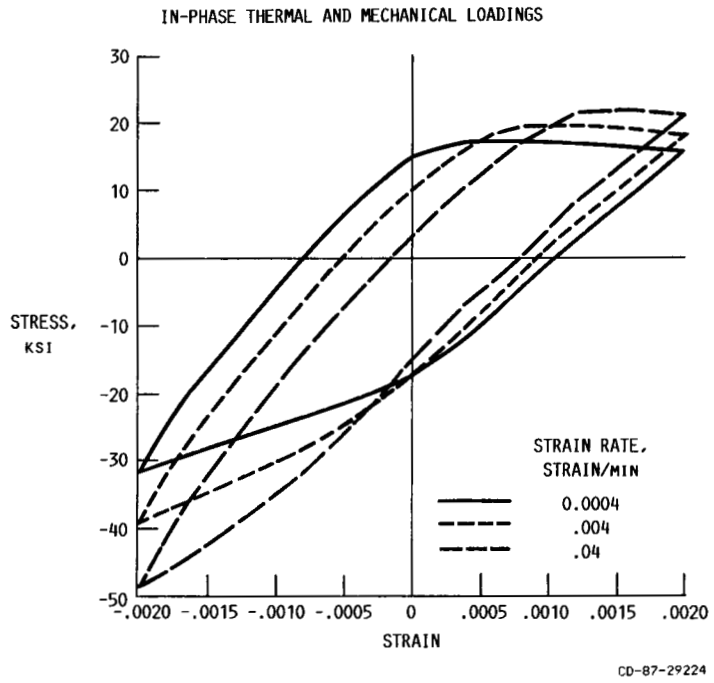

Figure 3

HYSTERESIS LOOPS AT DIFFERENT STRAIN RATES USING ROBINSON'S MODEL—NONISOTHERMAL CASE

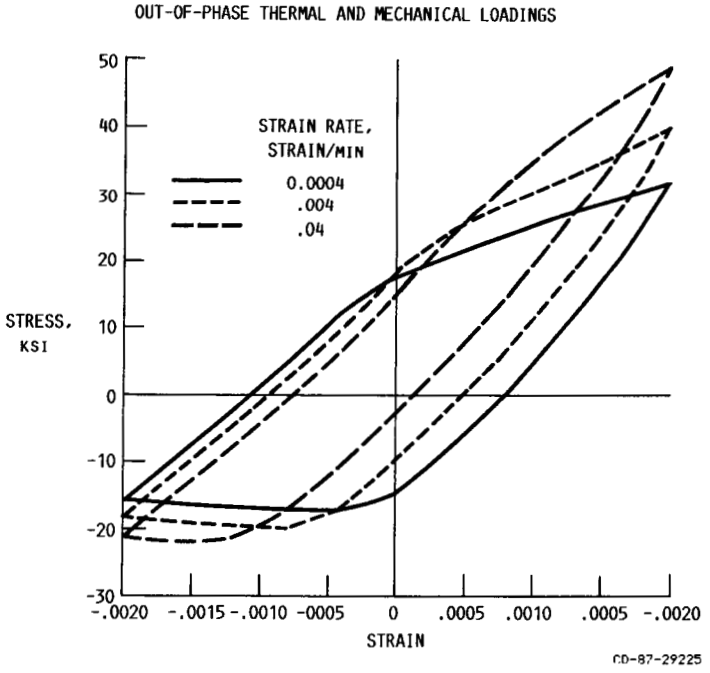

Figure 4

COMPARISON OF MARC AND EXPERIMENTAL HYSTERESIS LOOPS AT 1000 °F

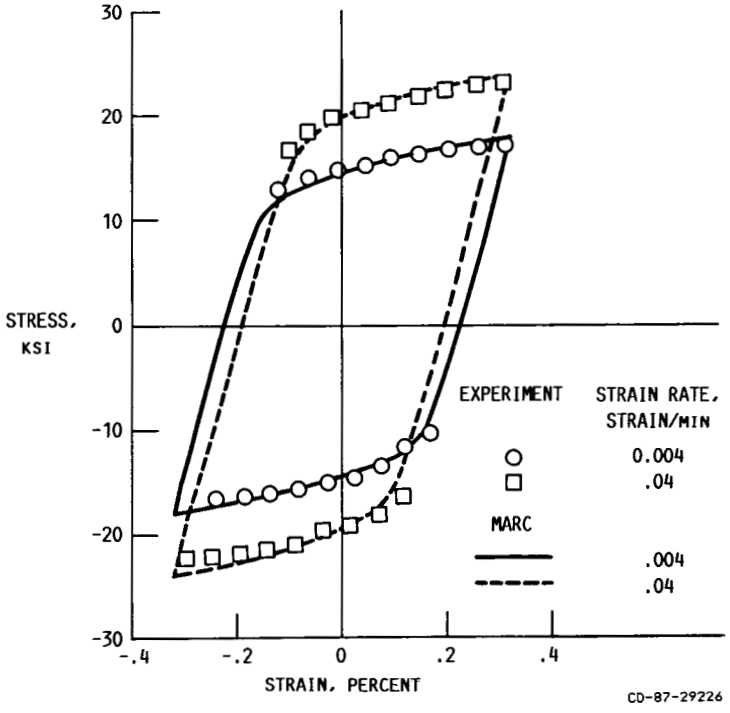

Figure 5

STRESS DISTRIBUTION IN AN INTERNALLY PRESSURIZED THICK CYLINDER USING ROBINSON'S MODEL (FEM-MARC SOLUTION)

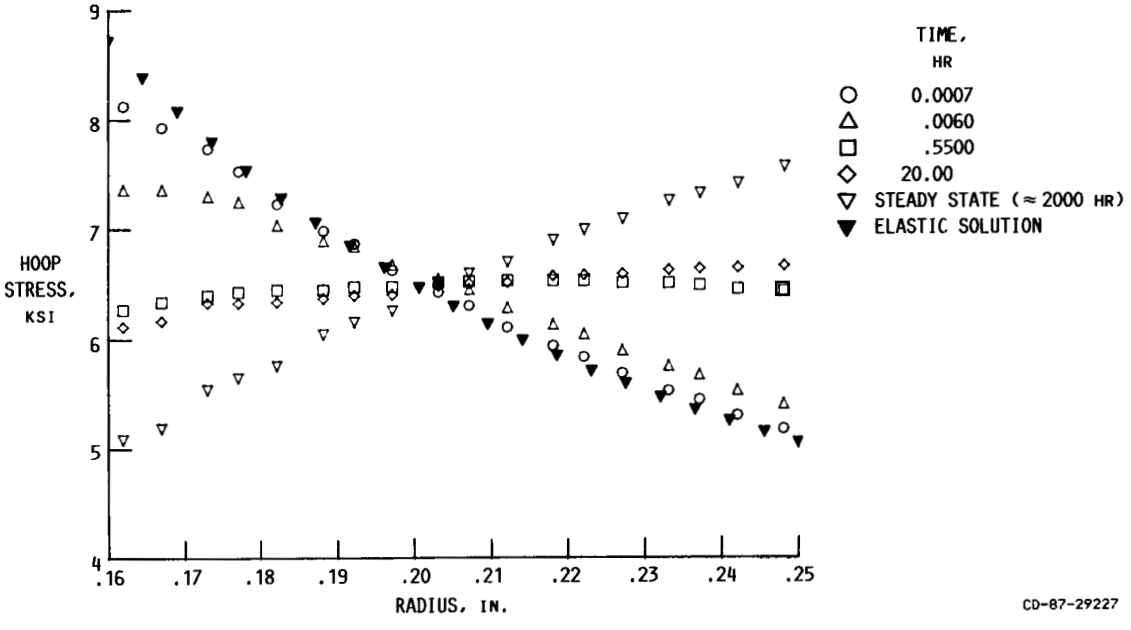

Figure 6

COMPARISON OF MARC AND ANALYTICAL RESULTS FOR STRAIN DISTRIBUTION IN AN INTERNALLY PRESSURIZED THICK CYLINDER USING ROBINSON'S MODEL

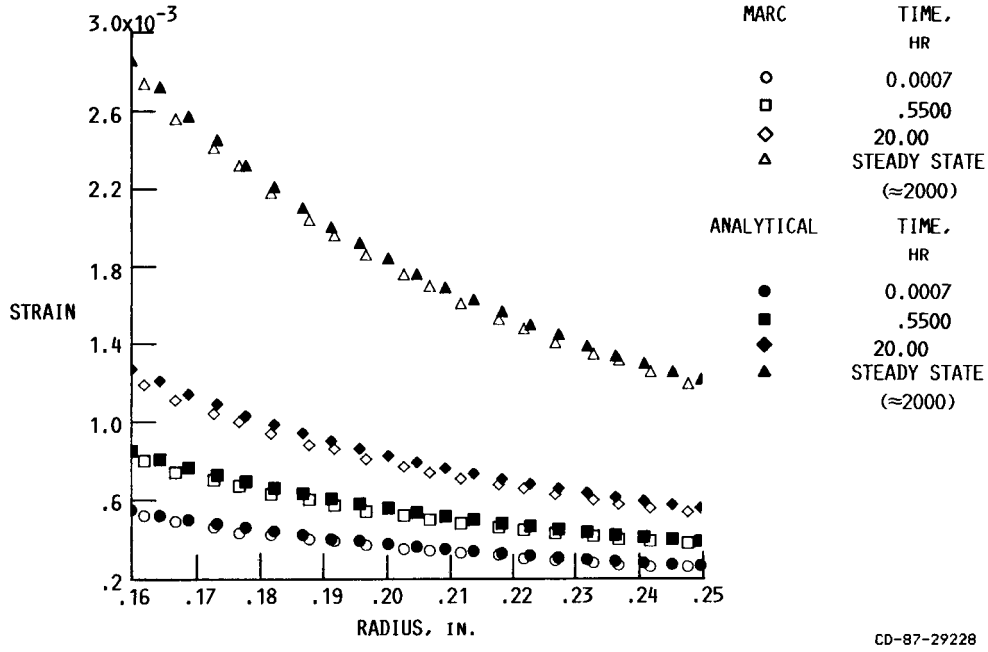

Figure 7

COMPARISON OF MARC AND ANALYTICAL RESULTS FOR STRESS DISTRIBUTION IN AN INTERNALLY PRESSURIZED THICK CYLINDER USING ROBINSON'S MODEL

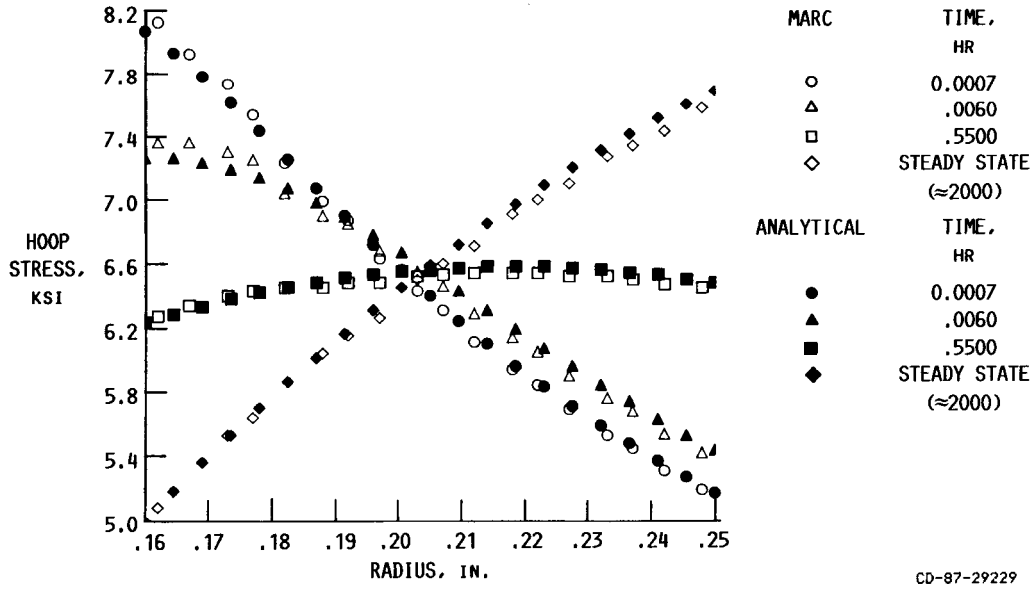

Figure 8

STRAIN DISTRIBUTION IN AN INTERNALLY PRESSURIZED THICK CYLINDER (FEM-MARC SOLUTION) USING ROBINSON'S MODEL

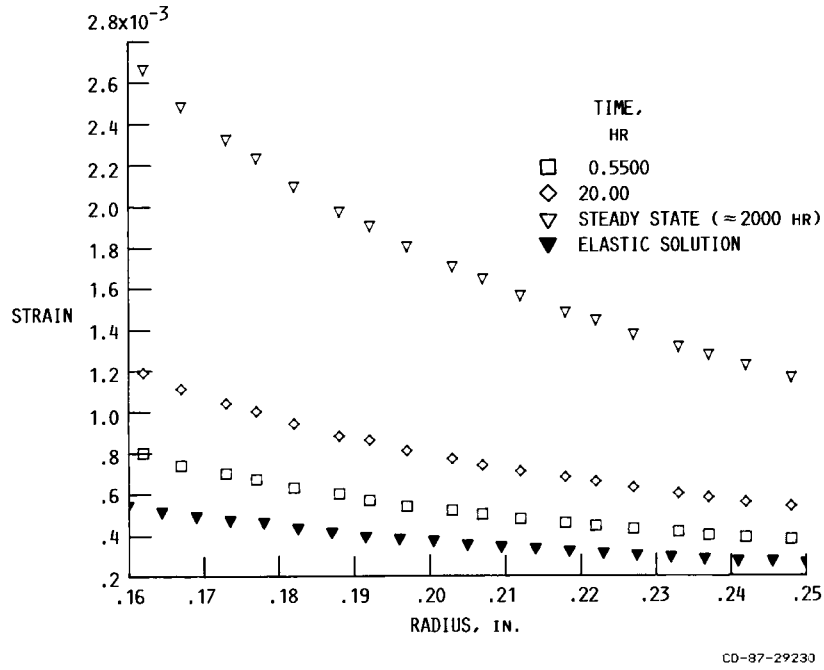

Figure 9

HYSTERESIS LOOPS AT DIFFERENT STRAIN RATES; ORIENTATION ANGLE = 0°

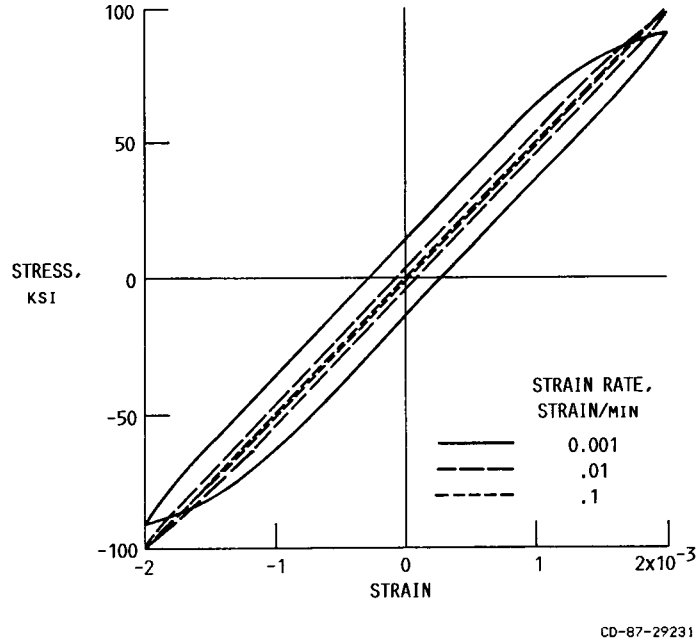

Figure 10

HYSTERESIS LOOPS AT DIFFERENT STRAIN RATES; ORIENTATION ANGLE = 30°

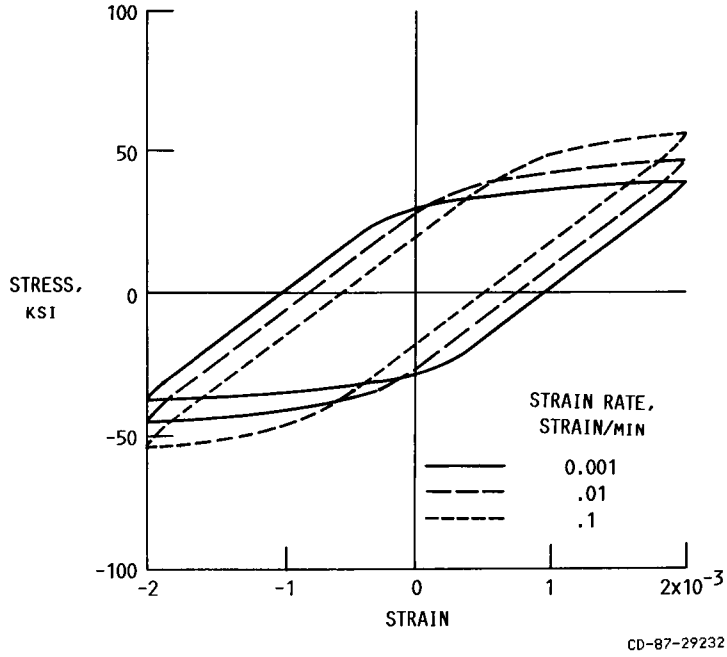

Figure 11

HYSTERESIS LOOPS AT DIFFERENT STRAIN RATES; ORIENTATION ANGLE = 60°

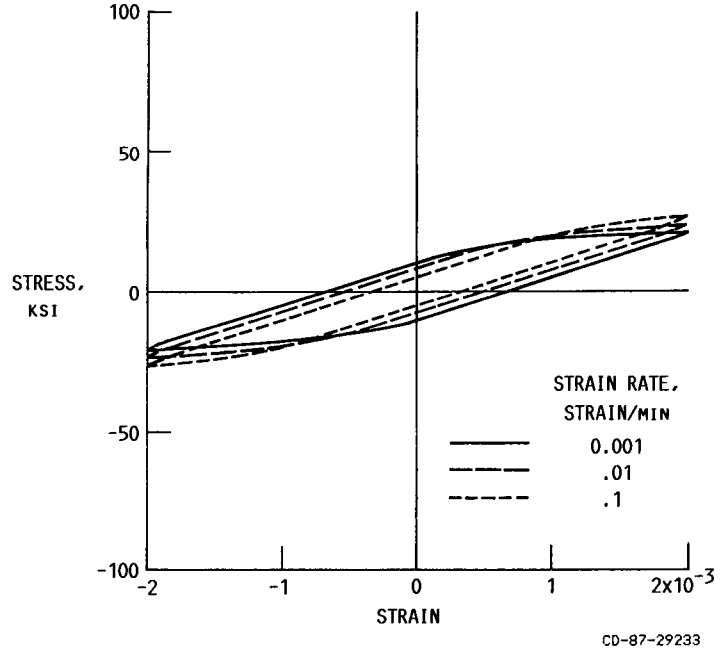

Figure 12

HYSTERESIS LOOPS AT DIFFERENT STRAIN RATES; ORIENTATION ANGLE = 90°

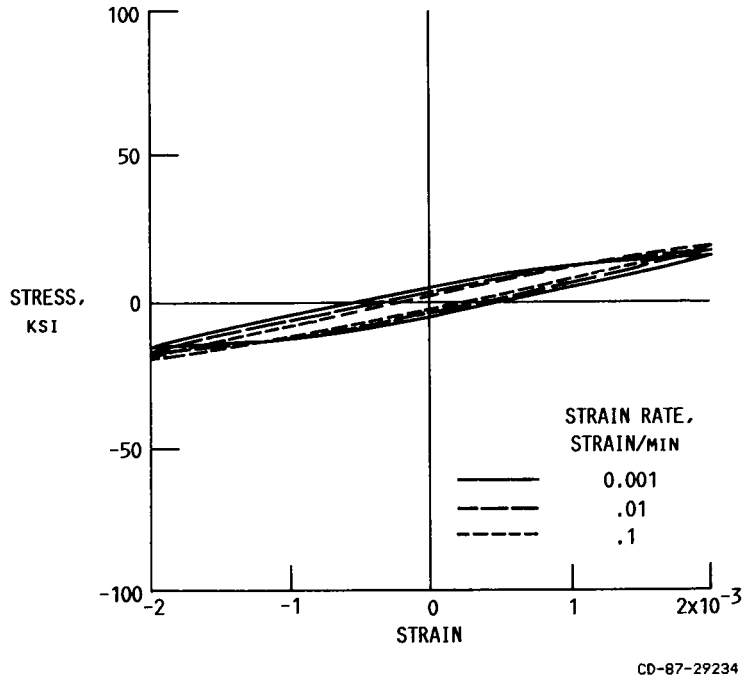

Figure 13

CREEP CURVES FOR DIFFERENT FIBER ORIENTATION ANGLES

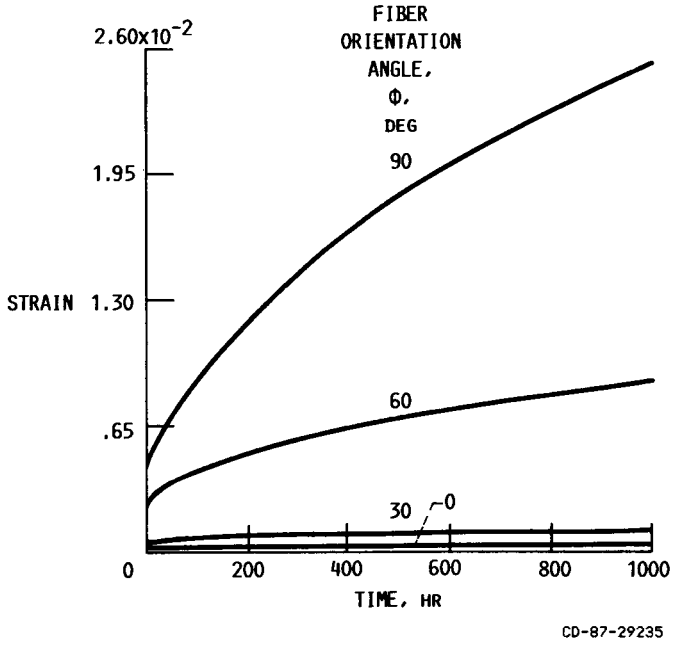

Figure 14

RELAXATION CURVES FOR DIFFERENT FIBER ORIENTATION ANGLES

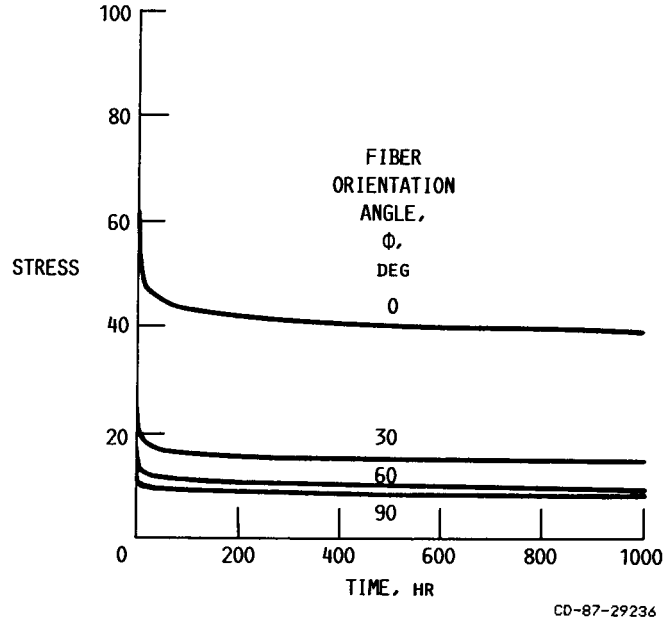

Figure 15

HYSTERESIS LOOPS FOR DIFFERENT FIBER ORIENTATION ANGLES; STRAIN RATE = 0.001/MIN

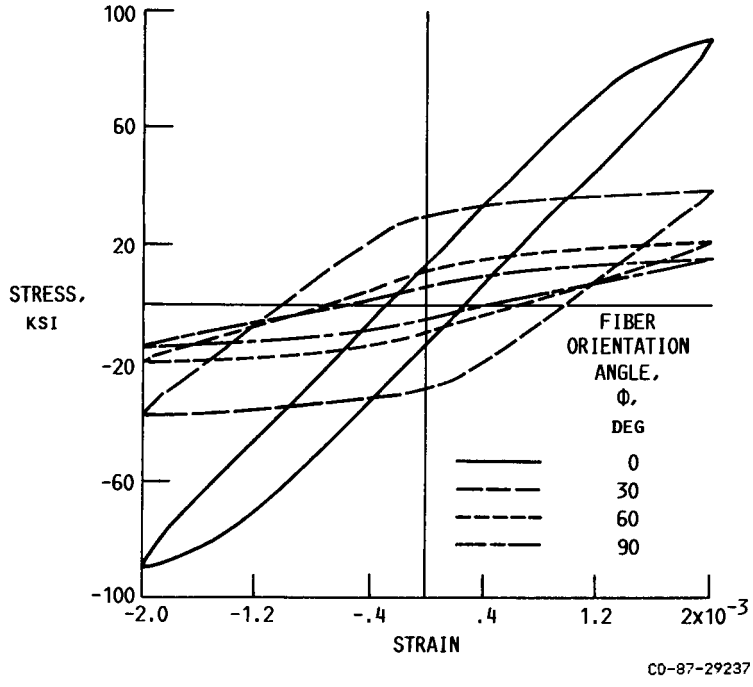

Figure 16

HYSTERESIS LOOPS FOR DIFFERENT FIBER ORIENTATION ANGLES; STRAIN RATE = 0.01/MIN

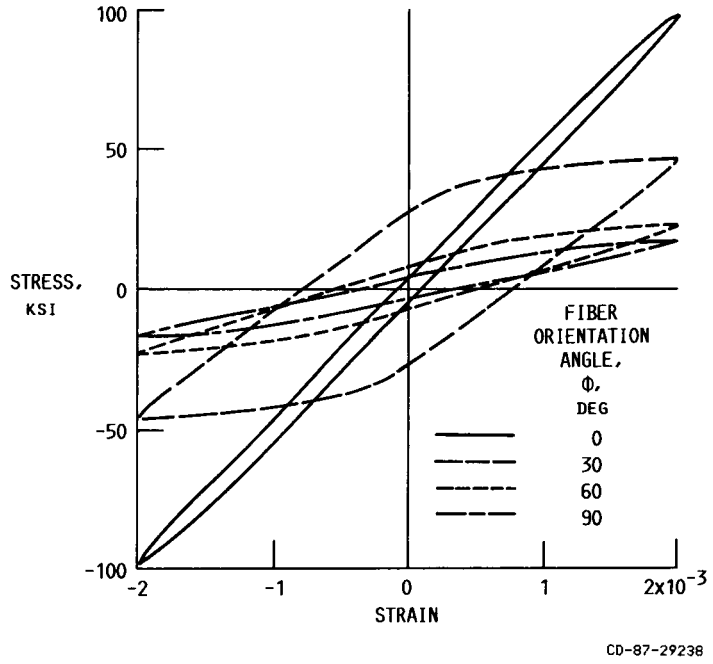

Figure 17

HYSTERESIS LOOPS FOR DIFFERENT FIBER ORIENTATION ANGLES; STRAIN RATE = 0.1/MIN

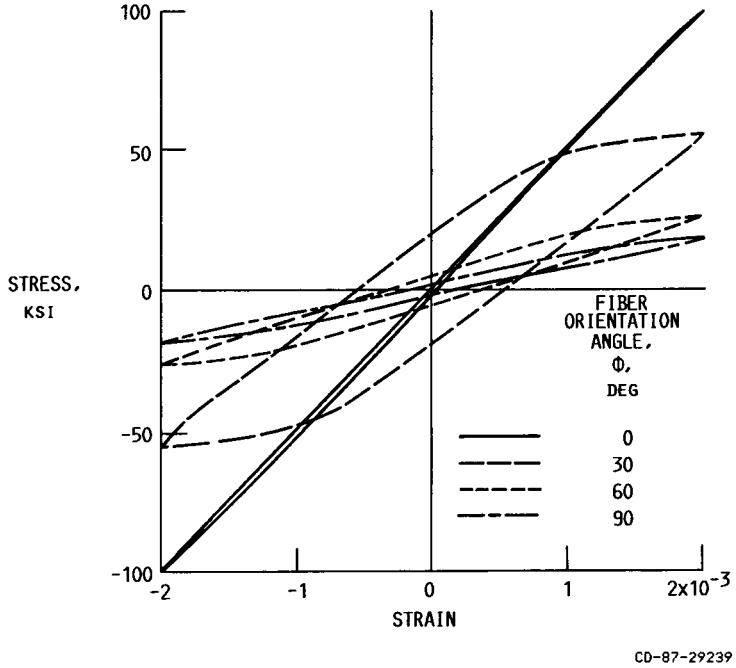

Figure 18

STRUCTURAL RESPONSE OF AN ADVANCED COMBUSTOR LINER: TEST AND ANALYSIS

Paul E. Moorhead and Robert L. Thompson
NASA Lewis Research Center
Cleveland, Ohio

and

M. Tong and M. Higgins
Sverdrup Technology, Inc.
Lewis Research Center
Cleveland, Ohio

An advanced (segmented) combustor liner supplied by Pratt & Whitney Aircraft is being tested in the Structural Component Response Rig at Lewis. To evaluate the segmented liner's effectiveness and performance, we will compare the test results and analyses with those obtained from the conventional sheet metal louver liner, which was tested last year and reported at last year's HOST Workshop. The data obtained will also be used for verification of models and computational methods. The two liners compared had about the same heat flux. Obtaining the same heat flux required modest changes in the operating conditions for the segmented liner because of its larger diameter. About 500 thermal test cycles have been completed on the segmented liner. Each cycle is 2.2 min and simulates a take-off cruise and landing mission profile.

TEST LINER

The test liner, consisting of segments and an outer support shell to which the segments are attached, was instrumented with 125 thermocouples (TC's) - 73 TC's on the hot side of the segments and 52 TC's on the support shell. The instrumented liner is shown in figures 1 and 2. A grid system of lines of temperature-sensitive points was applied to over half of the segments in the liner to increase the area in which we could observe temperature changes. An infrared camera system is being used to obtain temperature maps of a portion of the outer shell of the liner through a quartz viewing window. Over the same field of view, high-resolution photographs of the outer shell are also being taken to determine the total strain during cycling.

RESULTS

Figure 3 is an isometric plot of the thermocouple temperature measurements of the hot side of the liner segments (which shows the cylindrical liner as if it were cut open and flattened out and shows a maximum temperature of 1400 °F at the maximum quartz lamp power (cruise) condition). Figure 4 is a similar plot of the outer shell which shows the maximum temperature to be about 600 °F. Transient data are also being obtained. The thermal point did not indicate a maximum temperature of more than about 1200 °F. The infrared data and the high-resolution photographs are being reduced and analyzed.

THERMAL/STRUCTURAL/LIFE ANALYSES

Three-dimensional thermal and nonlinear structural analyses of the conventional test liner and the segmented test liner were performed using the MARC finite element program. Eight-node three-dimensional solid elements were used to construct the liner models. The conventional liner model has 546 elements and 1274 nodes, and the segmented liner model has 536 elements and 1117 nodes.

Thermal analyses were first performed to obtain the transient temperature distribution in the liners. The same heat fluxes were applied to both liners. These temperatures were then used for the subsequent structural analyses of the liners. Both Walker and Bodner viscoplastic theories were used in the structural analyses. These theories account for the interaction between creep and plasticity. Results for the conventional liner were presented at the last HOST Workshop. Temperature, stress, and strain distributions for a symmetrical panel of the segmented liner at the maximum power level are shown in figures 5 to 7. The results showed that the critical stress-strain location in the segmented liner is at the retention loop. For the conventional liner, the critical location is at the seam weld. Based on the stress-strain and temperature at the critical location, the lives of both liners were assessed. The results are summarized and compared in table I. The estimated life of the conventional liner (400 to 1000 cycles) is based on limited published data, while tests showed liner cracking at the seam weld after 1500 cycles. Based on the limited number of tests and the preliminary analyses, the segmented liner will have a much longer life than a conventional liner because it has a lower operating temperature (about 400 °F lower) and no structural constraint in the circumferential direction.

CONCLUSIONS

The segmented liner is operating at much lower temperatures than the conventional liner (about 400 °F lower) for the same heat flux. At the lower temperatures and low thermal gradients, little distortion to the segments has been observed. Based on the test results and analyses, the operating conditions are not severe enough to distort or damage the segmented liner. In view of this, the next series of tests on the segmented liner will have more severe operating conditions such that they will result in increasing the liner hot-side surface temperatures to temperature levels consistent with those measured on the hot side of the conventional liner.

TABLE I. - SUMMARY OF STRUCTURAL-LIFE ANALYSES OF COMBUSTOR LINERS AT A CRITICAL LOCATION

(a) Conventional liner

Analytical method	Temperature range, °F	Strain range, με		Mean stress, psi	Predicted life, cycles
		Mechanical	Inelastic		
Unified (Walker)	950 to 1630	5870	3150	-35 000	400 to 1000
Unified (Bodner)	950 to 1630	5800	2700	-28 000	400 to 1000

(b) Segmented liner

Analytical method	Temperature range, °F	Strain range, με		Mean stress, psi	Predicted life, cycles
		Mechanical	Inelastic		
Unified (Walker)	755 to 1180	810	10^{-1}	10 000	$>10^6$
Unified (Bodner)	755 to 1180	820	10^{-1}	15 000	$>10^6$

SEGMENTED COMBUSTOR LINER INSTRUMENTED FOR TESTING

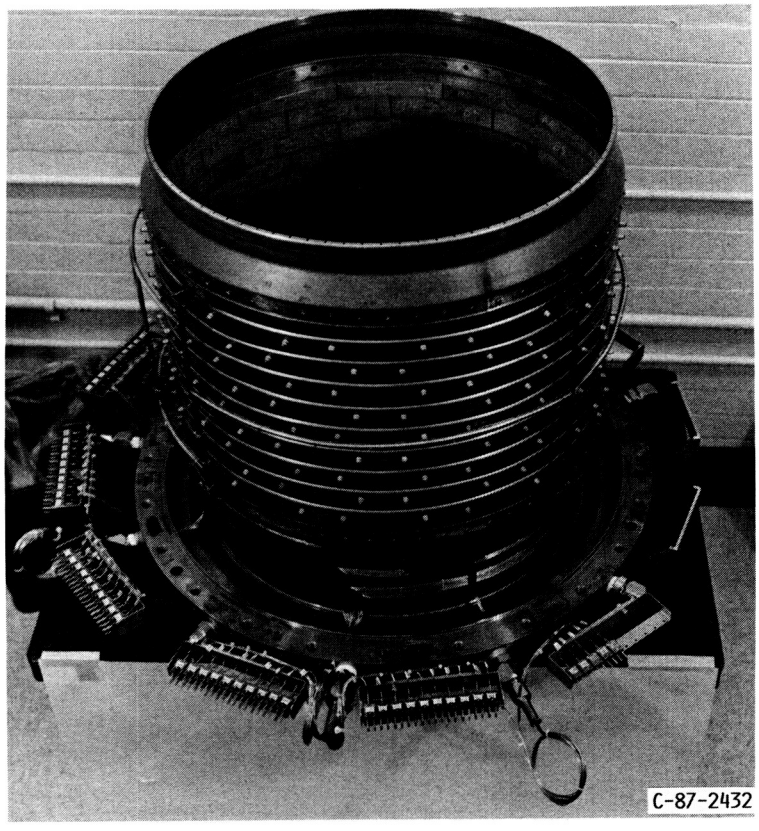

CD-87-29346

Figure 1

SEGMENTED LINER SHOWING THERMOCOUPLES AND THERMAL PAINT GRID

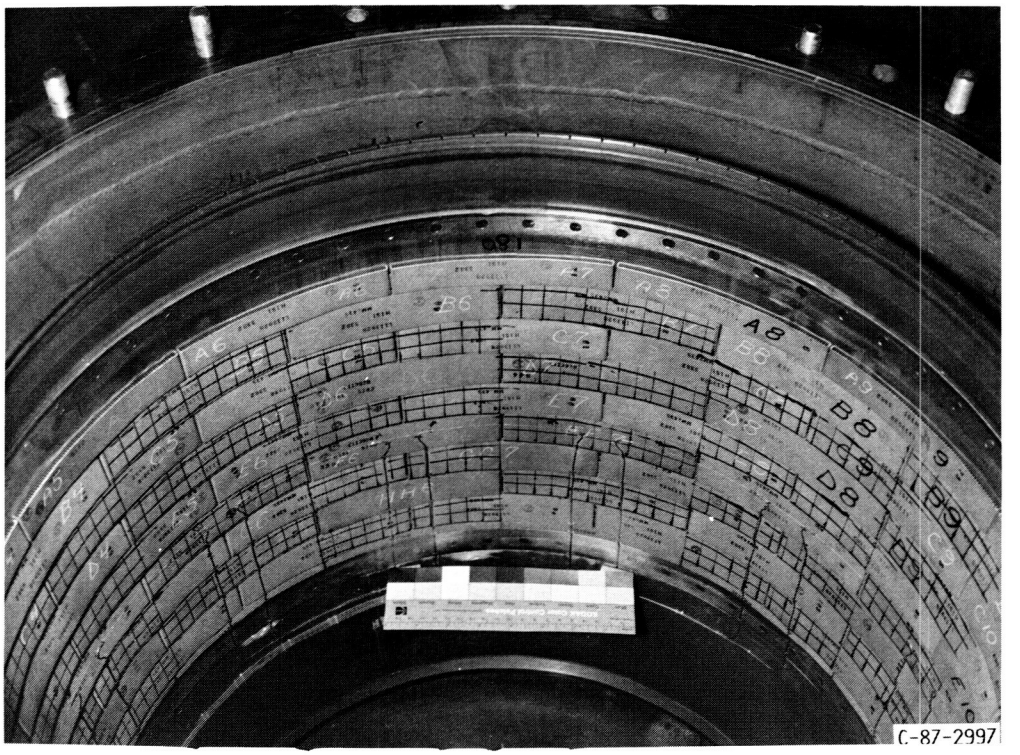

Figure 2

ISOMETRIC PLOT OF TEMPERATURE ON INSIDE OF SEGMENTED COMBUSTOR LINER

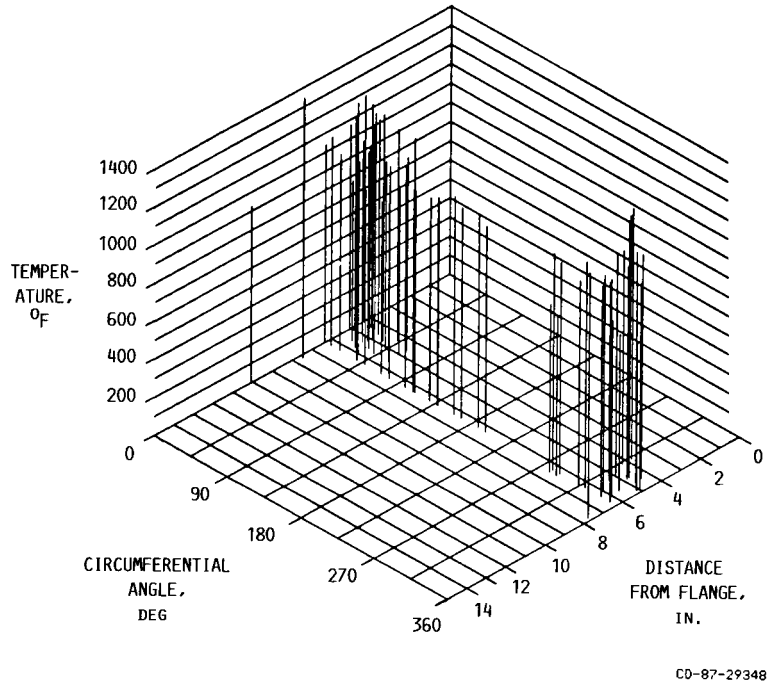

Figure 3

ISOMETRIC PLOT OF TEMPERATURE ON OUTER SHELL OF SEGMENTED COMBUSTOR LINER

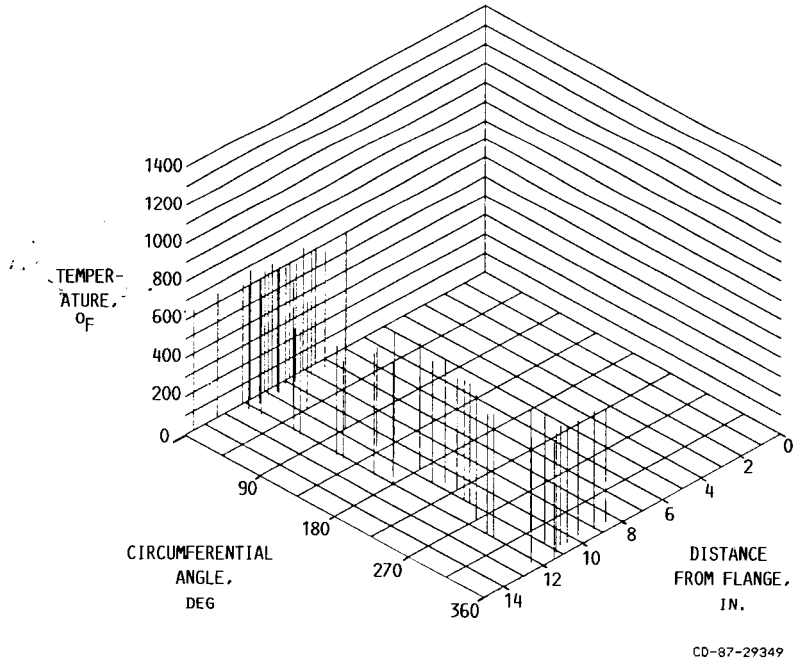

Figure 4

ADVANCED COMBUSTOR LINER TEMPERATURE DISTRIBUTION ON A SYMMETRICAL PANEL AT AN 83-PERCENT POWER LEVEL

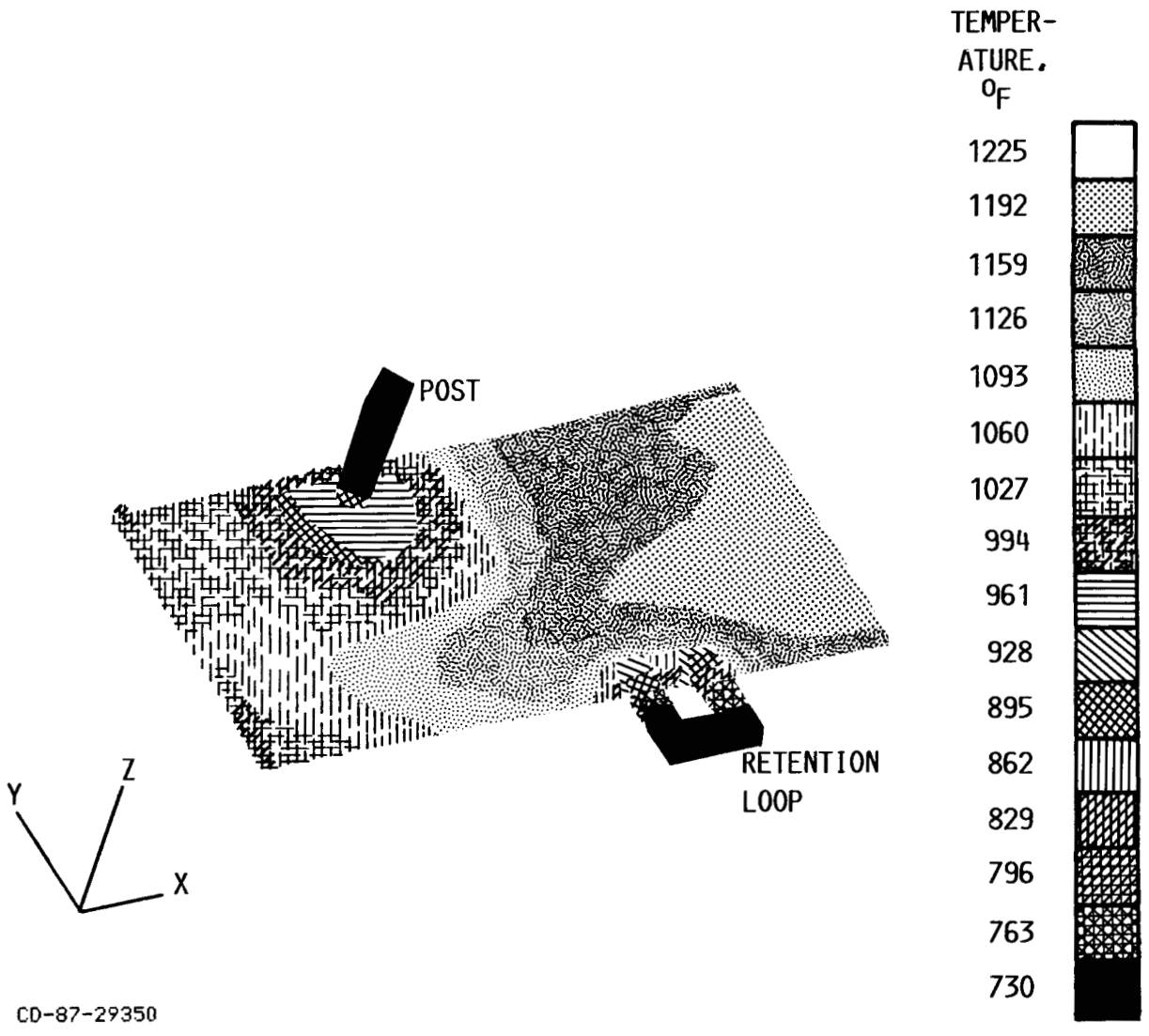

Figure 5

ADVANCED COMBUSTOR LINER STRESS DISTRIBUTION ON SYMMETRICAL PANEL AT AN 83-PERCENT POWER LEVEL (X-DIRECTION)

VISCOPLASTIC CONSTITUTIVE MODEL: WALKER THEORY (3RD CYCLE)

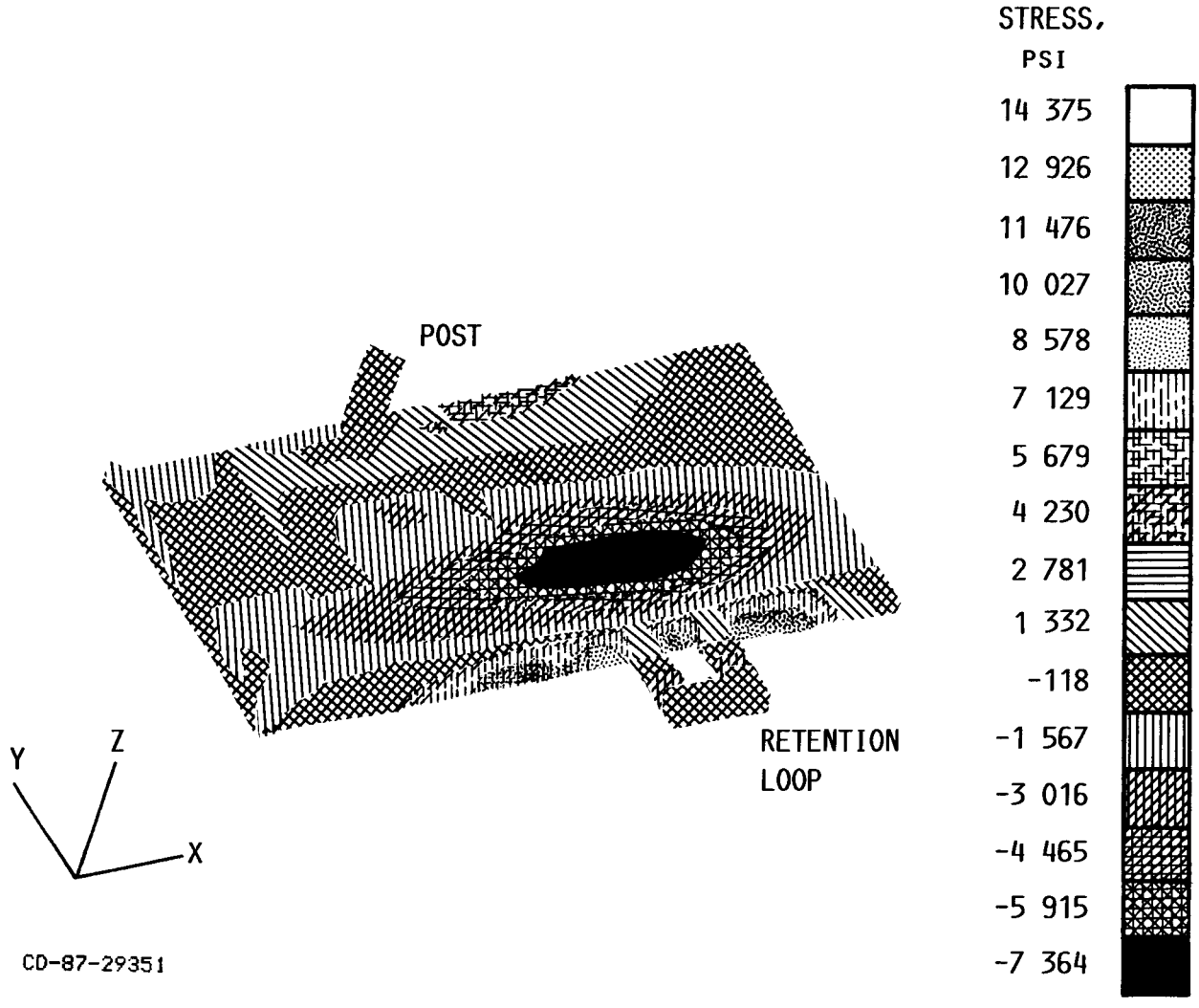

Figure 6

ADVANCED COMBUSTOR LINER TOTAL STRAIN DISTRIBUTION ON A SYMMETRICAL PANEL AT AN 83-PERCENT POWER LEVEL (X-DIRECTION)

WALKER THEORY (3RD CYCLE)

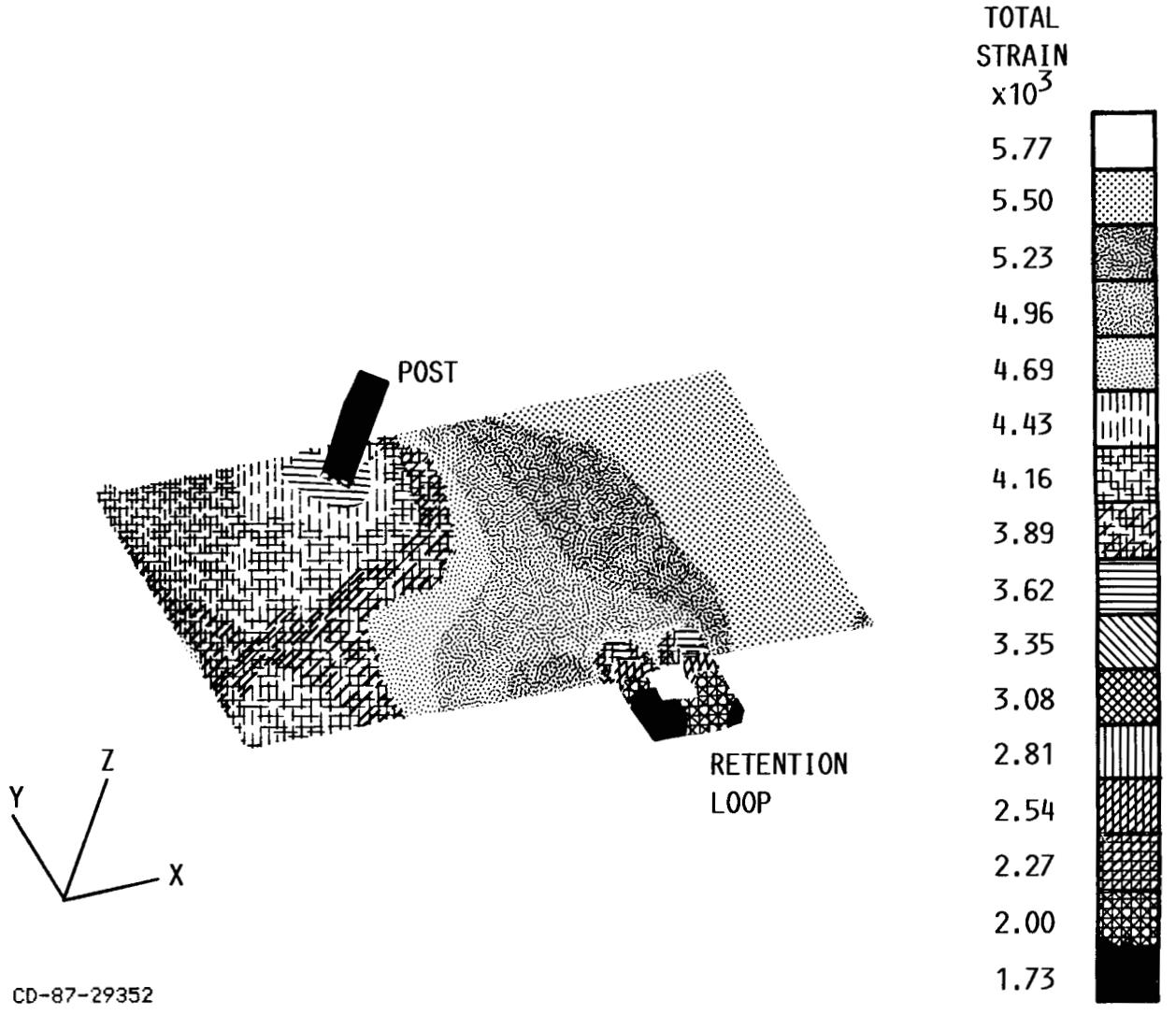

Figure 7

THERMAL EXPANSION MISMATCH AND PLASTICITY IN THERMAL BARRIER COATING

George C. Chang and Woraphat Phucharoen
Cleveland State University
Cleveland, Ohio

and

Robert A. Miller
NASA Lewis Research Center
Cleveland, Ohio

1. INTRODUCTION

The basic objective of this investigation is the quantitative determination of stress states in a model thermal barrier coating (TBC) as it cools in the air to 600°C from an assumed stress-free state at 700°C. This model is intended to represent a thin plasma-sprayed zirconia-yttria ceramic layer with a nickel-chromium-aluminum-yttrium bond coat on a cylindrical substrate made of nickel-based superalloys typically found in gas turbines.

The problem under study is a complex one due to layering, uneven interface between the ceramic and the bond, oxidation, and thermal expansion mismatch, as reported in references 1, 2, and 3. Thus, a concerted effort has been made to use the versatile finite element method to represent a cylindrical model TBC which resembles those that had been tested in a laboratory (refs. 1 and 3). The modeling concept is illustrated in figure 1.

To implement this finite element scheme, a generic code called MARC (ref. 4) has been utilized with the aid of a supercomputer (known as CRAY-XMP) at NASA Lewis Research Center. The latest finite element model which is known as TBCGEP, contains 1316 nodal points and 2140 generalized plane strain elements. This finite element model is now capable of representing both the ceramic layer and the bond coat with classical elastic-perfectly plastic materials.

Numerical results from previous studies have been reported in references 2, 3, 5, and 6. Parameters studied include: (1) variation of material properties involved, (2) oxidation of the bond coat, (3) cracking at the ceramic-bond interface, (4) coefficient of thermal expansion and Poisson's ratio of bond coat, and (5) plasticity in the bond coat.

The newly revised code TBCGEP has been used to study the influence of plasticity in ceramic layer on stress states, particularly on stresses in the "critical zone" shown in figure 2. Detailed results from three lengthly computer runs are presented in section 3 of this paper.

2. FINITE ELEMENT MODELING OF A CYLINDRICAL TBC

The uncoated superalloy cylindrical test specimens used in reference 1 had a radius (R_s) of 0.65 cm and a length of 7.60 cm. The specimens were plasma-sprayed in air with a thin zirconia-yttria (ZrO_2 - 8 wt. % Y_2O_3) layer on a thin nickel-chromium-aluminum-zirconium bond coat. The test specimen is sufficiently long, as compared to its radius, that the problem can be approximated by a two-dimensional generalized plane-strain case in the context of classical elasticity. The resulting finite element model is illustrated in figure 2. Details for an early model (known as TBC) was given in reference 2. That model features a rather sharp sinusoidal interface with an amplitude and a period of 50 micrometers (μm).

The next finite element model known as TBCGEP has a more smooth interface (15μm) than TBC. Detailed finite element discretization has been presented in reference 5.

3. INFLUENCE OF PLASTICITY IN CERAMIC LAYER ON STRESS STATES

With the aid of the latest computer code named TBCGEP, the influence of plasticity in ceramic layer on stress states throughout the TBC has been studied on a preliminary basis. Three cases, i.e. T-17, T-18, and T-19, have been investigated. As shown in Table 1, these three cases are identically the same as that of Case B-2 with the sole exception of varying degree of plasticity. The plastic behavior, as known in the classical theory of plasticity, is controlled by the parameter called YP1 which is the measure in von Mises yeild criterion in an elastic-perfectly-plastic solid.

The stress states have been calculated by using ten increments of -10°C each, starting at an assumed stress-free temperature of 700°C. The results for Case T-18 are presented in figures 6-8. Also presented in figures 9-11 are results for Case T-19. For comparison purposes, corresponding stresses for the perfectly elastic case known as B-2 are also shown in figures 3-5.

From figures 3, 6, and 9, it can be seen that the x-stress in the ceramic layer experiences very significant reduction with increasing plasticity. Furthermore, a rather localized redistribution in stresses is seen to have taken place in the vicinity of the critical zone. These results are expected within the realm of classical plasticity. The same can also be said about the x-stress in the bond coat adjacent to the ceramic-bond interface. Indeed, the experience with y-stress and shearing stress is substantially similar to the x-stress. In short, these results have shown the widespread influence of ceramic plasticity as well as the forgiven nature of plasticity in a solid material.

Now, figure 12 presents data on stresses in the critical zone in a model TBC as a function of temperature and plasticity. Stresses in x-direction increased linearly with decreasing temperature in Case B-2. These stresses, however, tend to increase with decreasing temperature at a rate much slower than that of Case B-2 as more plasticity is involved. At 600°C, the x-stress in Case T-19 is only about 40 percent of the corresponding stress in the elastic case, B-2.

Similar reductions in y-stresses can be seen as a function of plasticity as well. The magnitudes of reduction, however, are even more pronounced than that of Case B-2. Much of the same can be said of shearing stresses as shown in figure 12.

In short, data shown in figure 12 clearly illustrates the very significant influence ceramic plasticity has on stresses in the critical zone. Given the nature of plasticity in a medium, the results are entirely expected.

4. CONCLUDING REMARKS

In the present work, the computer code TBCGEP has been used to generate numerical solutions to the model thermal barrier coating, as shown in figures 3 to 12.

In section 3, nine stress-field contours and figure 12 illustrate the very important influence ceramic plasticity has on the stresses in the critical zone as a coating system is cooled from an assumed stress free temperature. The importance is in marked contrast with the slight impact bond coat plasticity had on stresses in the critical zone or elsewhere in the model TBC (ref. 6). Nonetheless, additional data will have to be generated and analyzed before a firm conclusion can be drawn.

The question of combined influence of plasticity in both ceramic layer and the bond coat, is of significant interest at present. Of equal importance is the determination of the effect of bond coat oxidation on stress states, in the presence of plasticity. Such are some of the major directions for future TBC investigations.

REFERENCES

1. Miller, R. A.; and Lowell, C. E.: Failure Mechanism of Thermal Barrier Coatings Exposed to Elevated Temperatures. Thin Solid Films, 95, 1983, pp. 265-273.

2. Chang, G. C.; Phucharoen, W.; and Miller, R. A.: Thermal Expansion Mismatch and Oxidation in Thermal Barrier Coatings. NASA CP-2405, 1985, pp. 405-425.

3. Chang, George C.; Phucharoen, Woraphat; and Miller, Robert A.: Behavior of Thermal Barrier Coatings for Advanced Gas Turbine Blades. Surface and Coatings Technology, 30, 1, 1987, pp. 13-28.

4. Anonymous, MARC Finite Element Program User Manual, Version K-2, MARC Analysis Research Corporation, 1986.

5. Chang, George C.; Phucharoen, Woraphat; and Miller, Robert A.: A Study on Thermal Barrier Coatings including Thermal Expansion Mismatch and Bond Coat Oxidation. NASA-CP-2444, 1986, pp. 415-434.

6. Chang, G. C.; Phucharoen, W.; and Miller, R. A.: Finite Element Thermal Stress Solutions for Thermal Barrier Coatings. Paper presented at the 14th International Conference on Metallurgical Coatings, San Diego, CA., March 23-27, 1987.

TABLE 1 MATERIAL AND OTHER PARAMETERS

Parameters	Case A-2	Cases B-2, T-17, T-18, T-19
Young's Modulus (MPa)		
Substrate	0.1758×10^6	0.1758×10^6
Bond	0.1379×10^6	0.1379×10^6
Ceramic	0.0276×10^6	0.0276×10^6
Poisson's Ratio		
Substrate	0.25	0.25
Bond	0.27	0.27
Ceramic	0.25	0.25
Coefficient of Thermal Expansion (/°C)		
Substrate	13.91×10^{-6}	13.91×10^{-6}
Bond	15.16×10^{-6}	15.16×10^{-6}
Ceramic	10.01×10^{-6}	10.01×10^{-6}
YP1 - value (MPa)		
Substrate	0.069×10^6	0.069×10^6
Bond	0.069×10^6	0.069×10^6
Ceramic	0.069×10^6	(B-2) 0.069×10^6 (T-17) 34.48* (T-18) 17.24 (T-19) 8.62
Oxidation	NO	NO
Interface Roughness Amplitude (μm)	50	15

*5,000 psi.

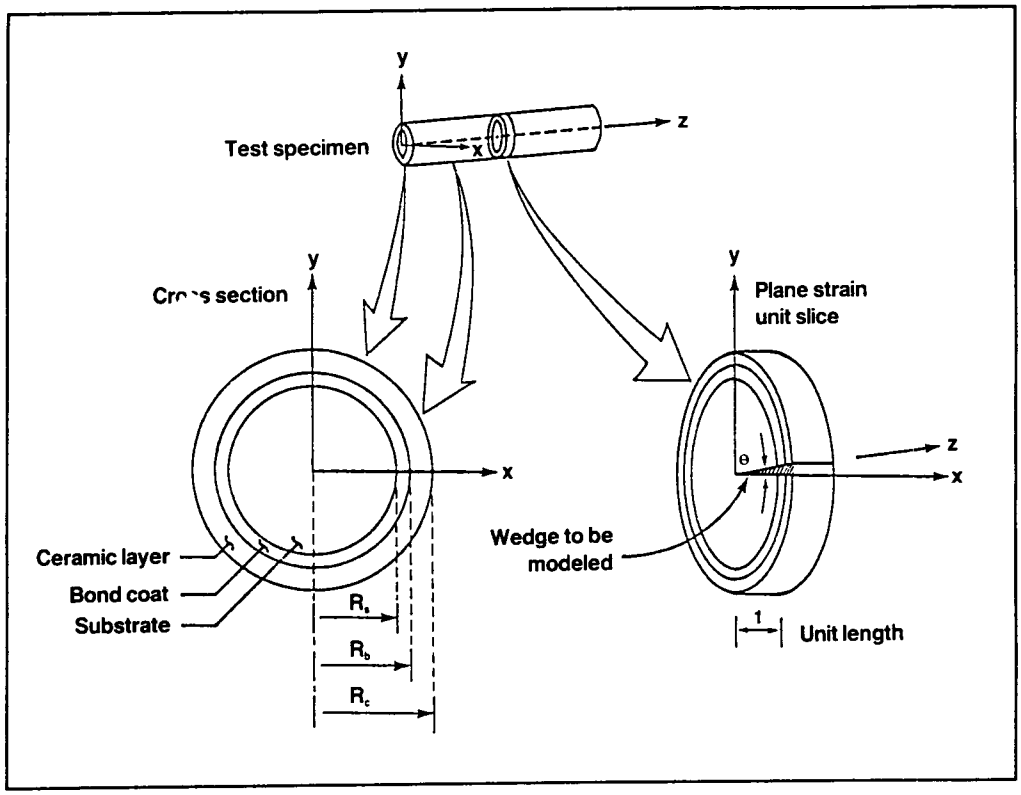

Figure 1. CYLINDRICAL TBC TEST SPECIMEN

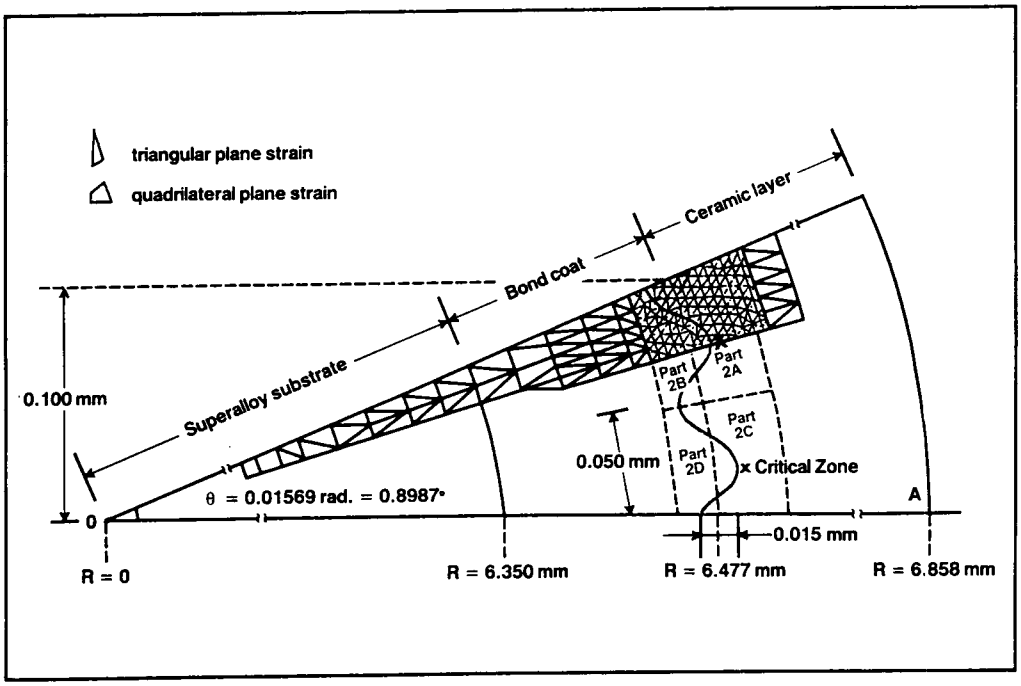

Figure 2. THE TBCGEP FINITE ELEMENT MODEL

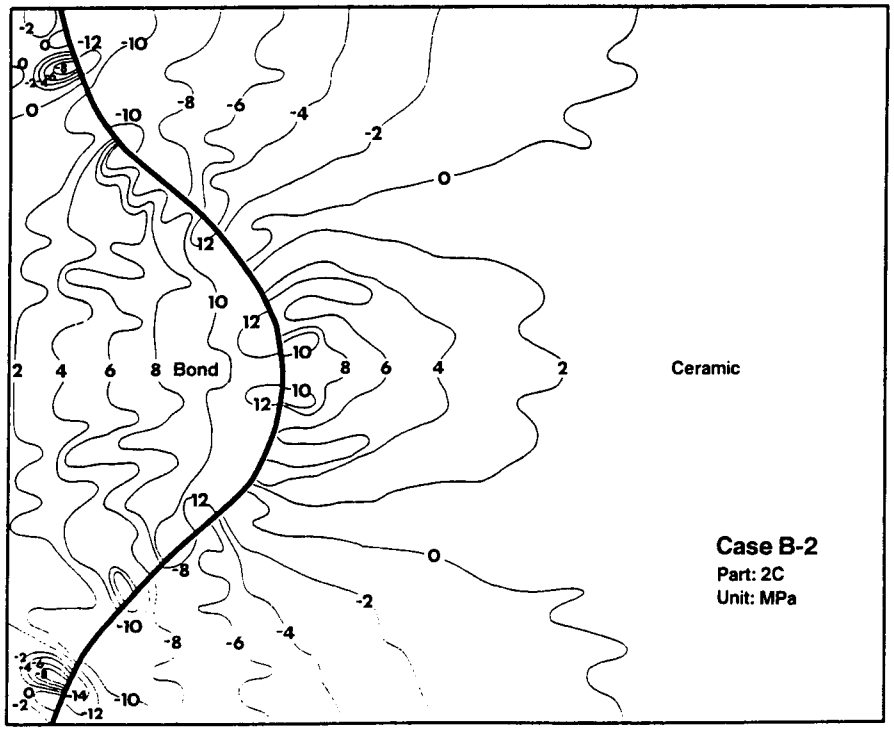

Figure 3. STRESS IN X-DIRECTION DUE TO THERMAL EXPANSION MISMATCH

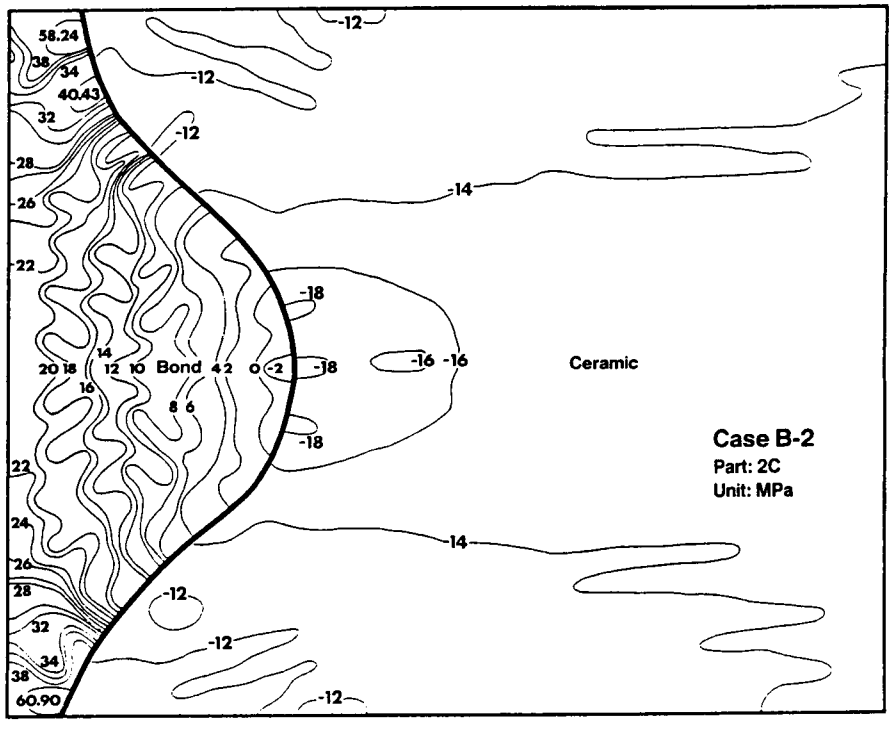

Figure 4. STRESS IN Y-DIRECTION DUE TO THERMAL EXPANSION MISMATCH

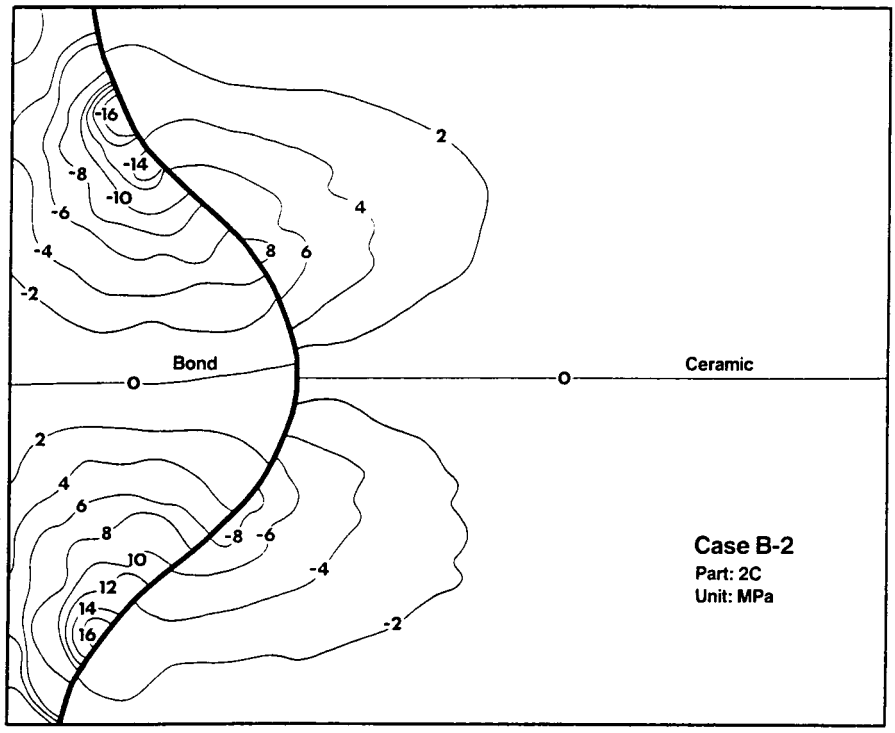

Figure 5. SHEARING STRESS DUE TO THERMAL EXPANSION MISMATCH

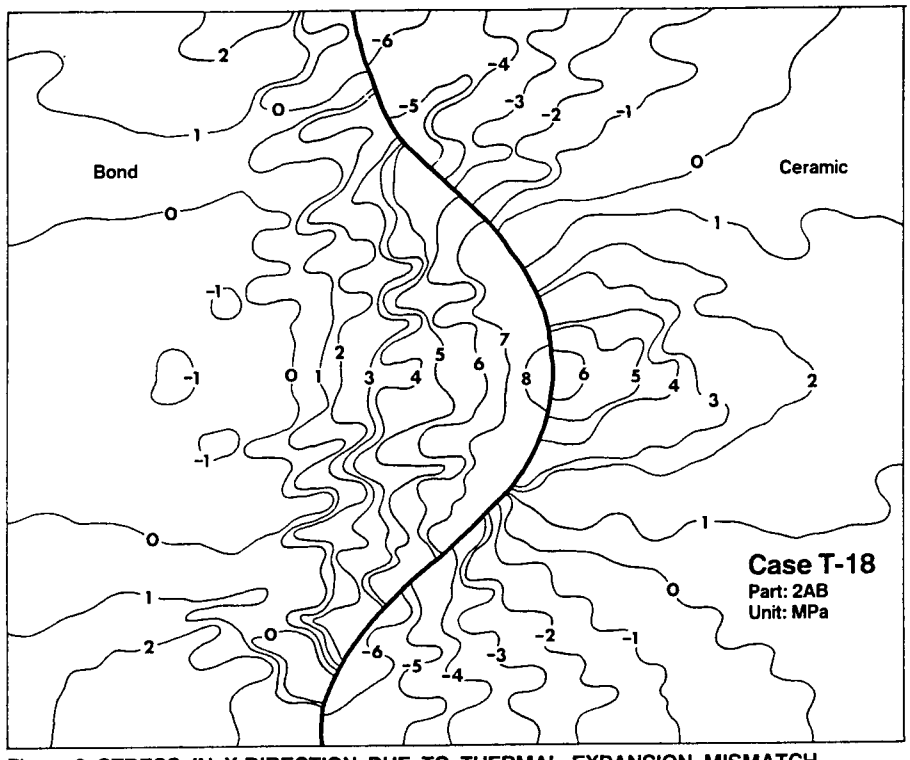

Figure 6. STRESS IN X-DIRECTION DUE TO THERMAL EXPANSION MISMATCH AND PLASTICITY

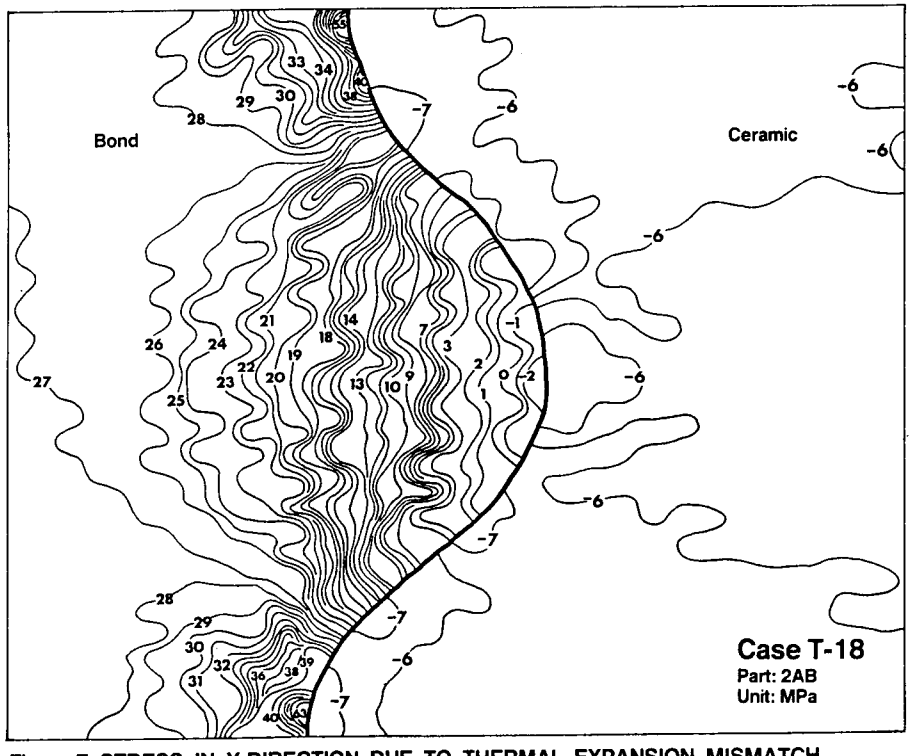

Figure 7. STRESS IN Y-DIRECTION DUE TO THERMAL EXPANSION MISMATCH AND PLASTICITY

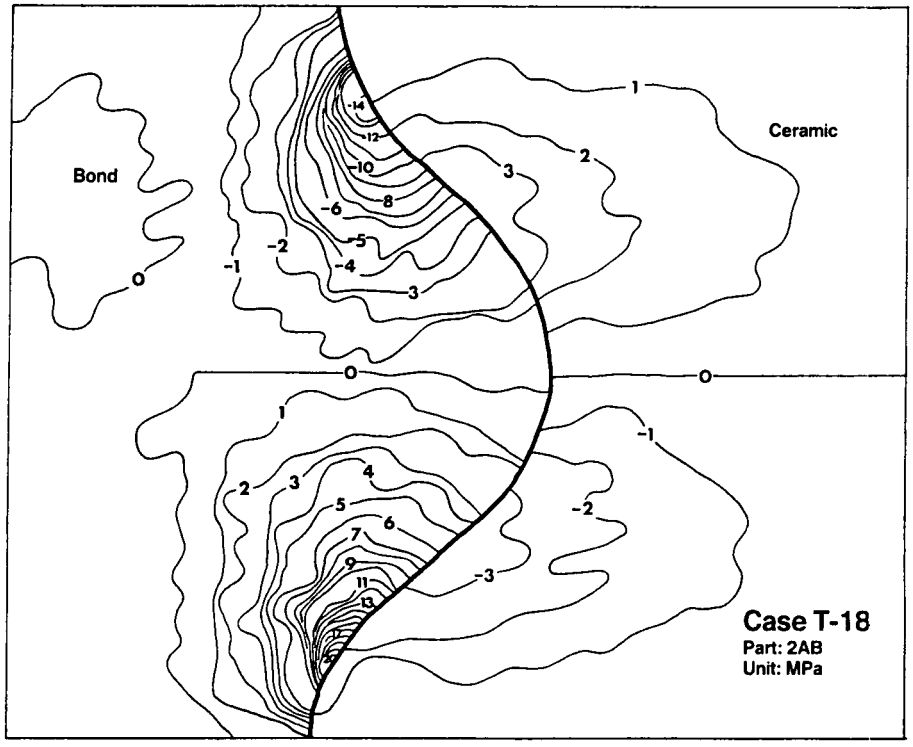

Figure 8. SHEARING STRESS DUE TO THERMAL EXPANSION MISMATCH AND PLASTICITY

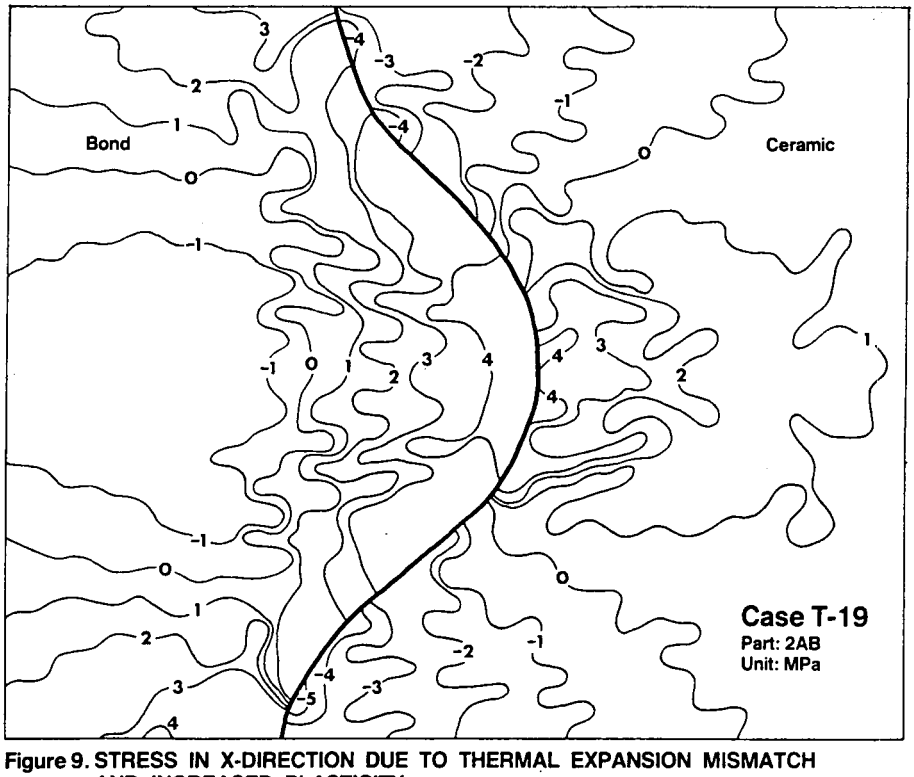

Figure 9. STRESS IN X-DIRECTION DUE TO THERMAL EXPANSION MISMATCH AND INCREASED PLASTICITY

C-5

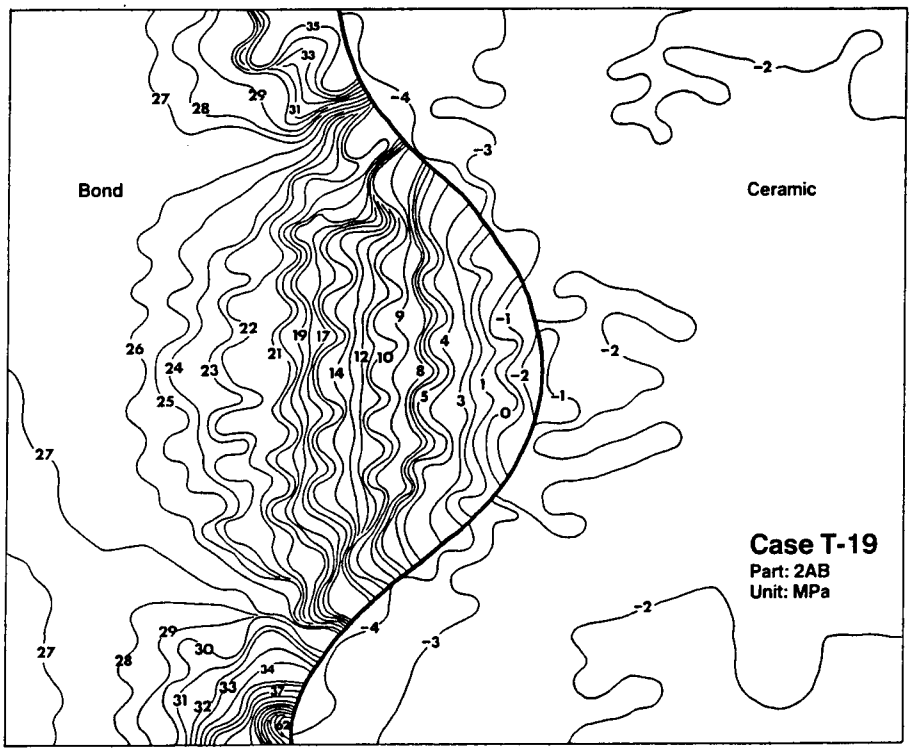

Figure 10. STRESS IN Y-DIRECTION DUE TO THERMAL EXPANSION MISMATCH AND INCREASED PLASTICITY

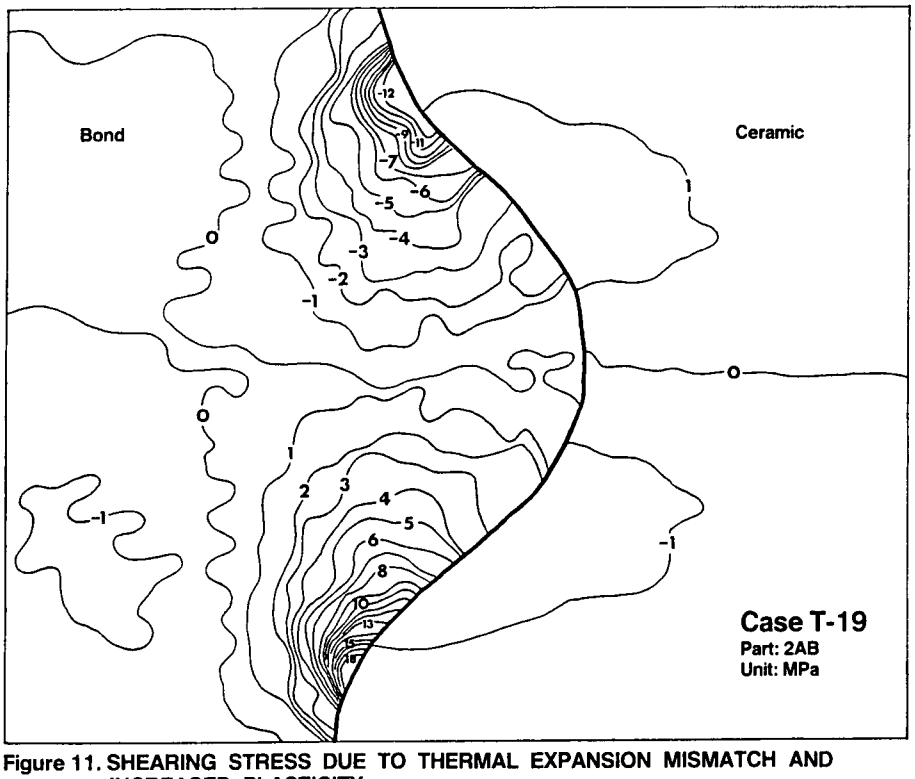

Figure 11. SHEARING STRESS DUE TO THERMAL EXPANSION MISMATCH AND INCREASED PLASTICITY

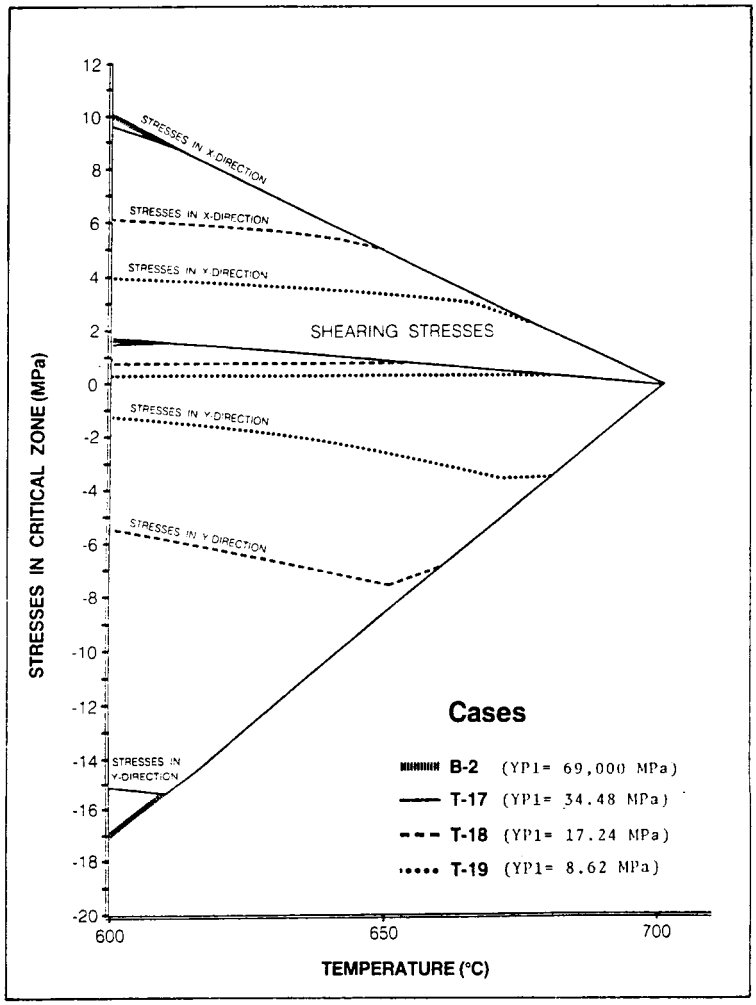

Figure 12. VARIATION OF STRESSES WITH TEMPERATURE

THERMAL BARRIER COATING LIFE-PREDICTION MODEL DEVELOPMENT

T.E. Strangman, J.F. Neumann, and A. Liu
Garrett Turbine Engine Company (GTEC)*
Phoenix, Arizona

Thermal barrier coatings (TBCs) for high-performance engine turbine airfoils represent advanced materials technology with both performance and durability benefits. The greatest TBC benefit is the reduction of heat transferred into air-cooled components, allowing higher turbine operating temperatures and/or reduced component cooling for improved engine performance. Recognizing the benefits of TBCs, the Garrett Turbine Engine Company (GTEC) has developed mechanistic thermochemical and thermomechanical life models in this program to facilitate reliable exploitation of TBC benefits.

This program focuses on predicting the lives of two types of strain-tolerant and oxidation-resistant TBC systems that are produced by commercial coating suppliers to the gas turbine industry. The plasma-sprayed TBC system, composed of a low-pressure plasma spray (LPPS), or an argon-shrouded plasma spray (ASPS) applied oxidation-resistant NiCrAlY (or CoNiCrAlY) bond coating, and an air-plasma-sprayed (APS) yttria (8 percent) partially stabilized zirconia insulative layer (Figure 1), is applied by Chromalloy (Orangeburg, New York), Klock (Manchester, Connecticut), and Union Carbide (Indianapolis, Indiana). The second type of TBC is applied by the electron beam evaporation-physical vapor deposition (EB-PVD) process by Edwards-Temescal (Berkeley, California).

The primary objective of this program was to develop an operative TBC design model for life prediction. This objective was successfully accomplished with the development, calibration, and demonstration of a mechanistic thermochemical model, which rapidly predicts TBC life as a function of engine, mission, and materials system parameters (Figure 2). This thermochemical design model accounts for the three operative TBC damage modes (bond coating oxidation, zirconia toughness reduction, and molten salt film damage), which all contribute to spalling of the insulating zirconia layer. The model has been calibrated for three plasma-sprayed systems and one EB-PVD TBC system, which are applied by commercial sources. The GTEC preliminary design TBC life-prediction system has been demonstrated for three TFE731 turbofan engine cycles (business aircraft, maritime surveillance, and factory endurance test).

It should be noted that the preliminary TBC life model is primarily driven by the thermal analysis for the component and the anticipated mission usage of the aircraft. This feature permits the designer to economically consider the TBC early in the component design process, which facilitates full incorporation and exploitation of its benefits for turbine airfoil applications.

---

*Work performed under NASA Contract NAS3-23945.

In addition to achieving the primary objective, significant progress was achieved in the development of a thermomechanical stress-based, finite-element micromodel, which has the potential to more accurately model TBC spalling mechanisms for improved final design life predictions (Figure 3). As presently developed, the micromodel is capable of calculating localized stresses within the TBC system, which arise from ceramic-metal thermal expansion mismatch, thermal, and centrifugal strains. The micromodel is further designed to have sufficient flexibility for future incorporation of refinements, such as analysis of:

- Time- and temperature-dependent changes in local stresses arising from bond-coating oxidation
- Stress redistribution associated with bond-coating creep (stress relaxation)
- Zirconia sintering shrinkage
- Cyclic crack propagation in the zirconia

Substantial burner rig and mechanical properties data (Figures 2 and 4) have been obtained to facilitate development and calibration of these thermochemical and thermomechanical life prediction models. Interestingly, it was observed that the toughness of plasma-sprayed zirconia coatings remained stable during short exposures at high temperatures, but transitioned to lower values after longer exposures. Furthermore, the approximate transition time to the lower toughness value was similar to average spalling lives for the TBC system that were observed in burner rig tests in the 1100 to 1150 °C temperature range, where comparable data were obtained. Zirconia sintering densification ("mud-flat" cracking) and interfacial oxide scale growth (Union Carbide TBC specimens only) appeared to be associated with the reduced level of zirconia toughness.

Thermal conductivity is the critical design property of TBCs, which govern heat transfer into air-cooled turbine components. Component metal temperatures and thermal strains are dependent on the thermal conductivity of the zirconia layer. Consequently, thermal conductivity data were obtained for both plasma-sprayed and EB-PVD zirconia coatings. These data are presented in Figure 5 and are in excellent agreement with published data from other NASA-sponsored programs. They indicate that yttria-stabilized zirconia coatings have thermal conductivities that are lower by about a factor of 30 than typical superalloys.

Finally, effective exploitation of TBCs requires that critical materials properties be verified. The insulative TBC system capability is dependent on thickness. Mechanical integrity of TBCs is dependent on the size of critical flaws. Therefore, feasibility of using nondestructive evaluation (NDE) to verify critical TBC properties (thickness and flaw size) was demonstrated. Eddy current analysis was verified to be a viable method for measuring zirconia thickness. High-frequency ultrasonics showed promise in detecting flaws at the ceramic-metal interface.

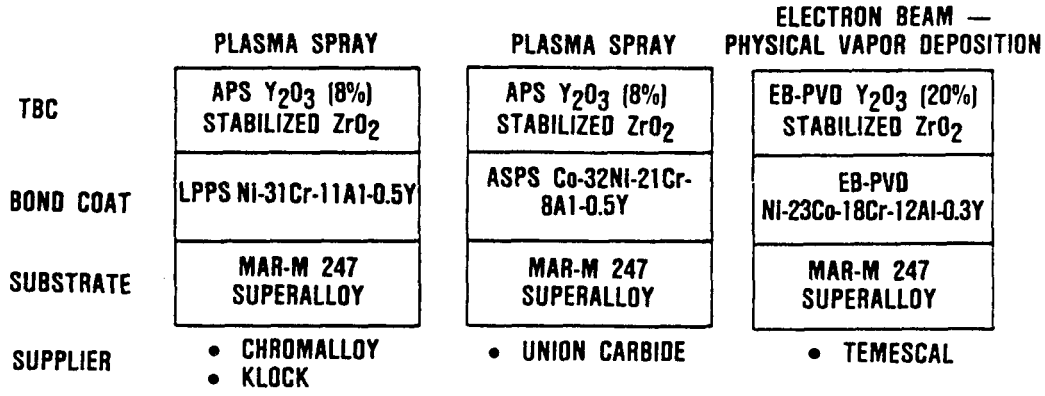

66-239-20

Figure 1. Life Prediction Models are Calibrated for Plasma-Sprayed and EB-PVD TBC Systems.

PRELIMINARY TBC LIFE ANALYSIS METHOD

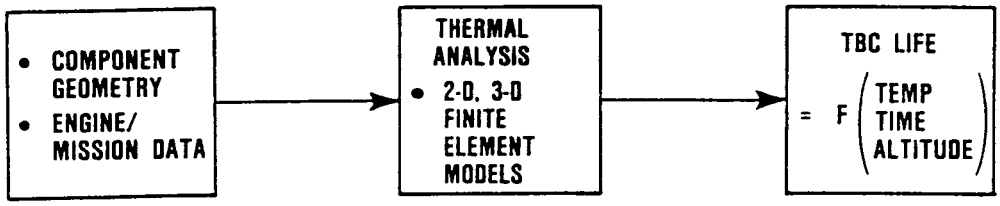

THERMOCHEMICAL MODEL CALIBRATION

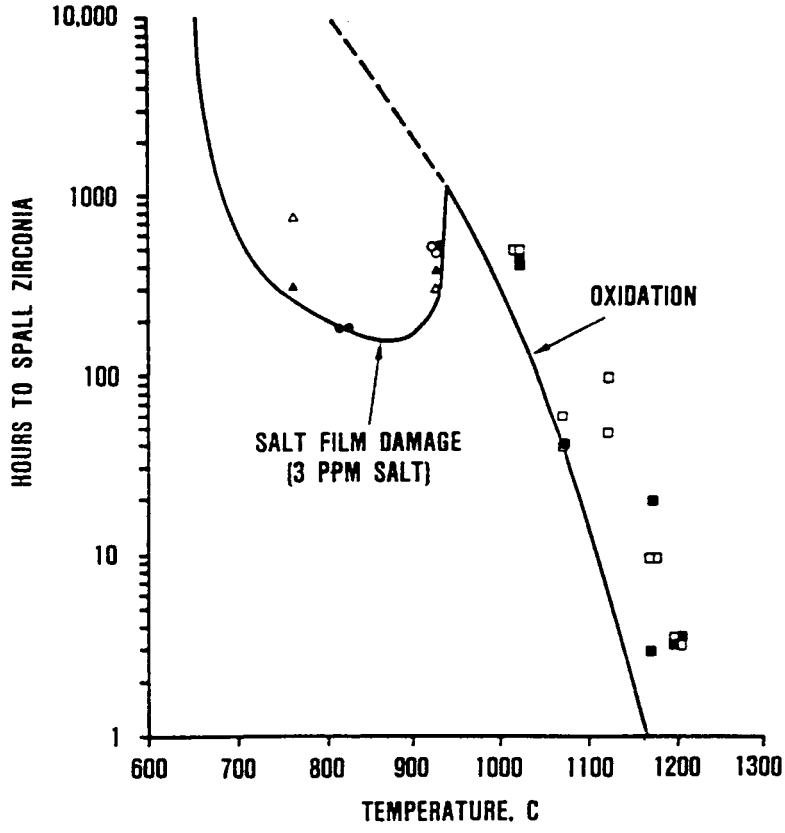

MISSION ANALYSIS PREDICTIVE CAPABILITY HAS BEEN DEMONSTRATED

TBC SYSTEM	BUSINESS JET	MARITIME SURVEILLANCE
PLASMA SPRAY		
CHROMALLOY	16,517 HOURS	9843 HOURS
UNION CARBIDE	6656 HOURS	5207 HOURS
KLOCK	49,644 HOURS	29,973 HOURS
EB-PVD		
TEMESCAL	55,607 HOURS	2106 HOURS

G7012-21

Figure 2. Inexpensive Design Analysis Iterations are Facilitated by Thermomechanical TBC Life Model.

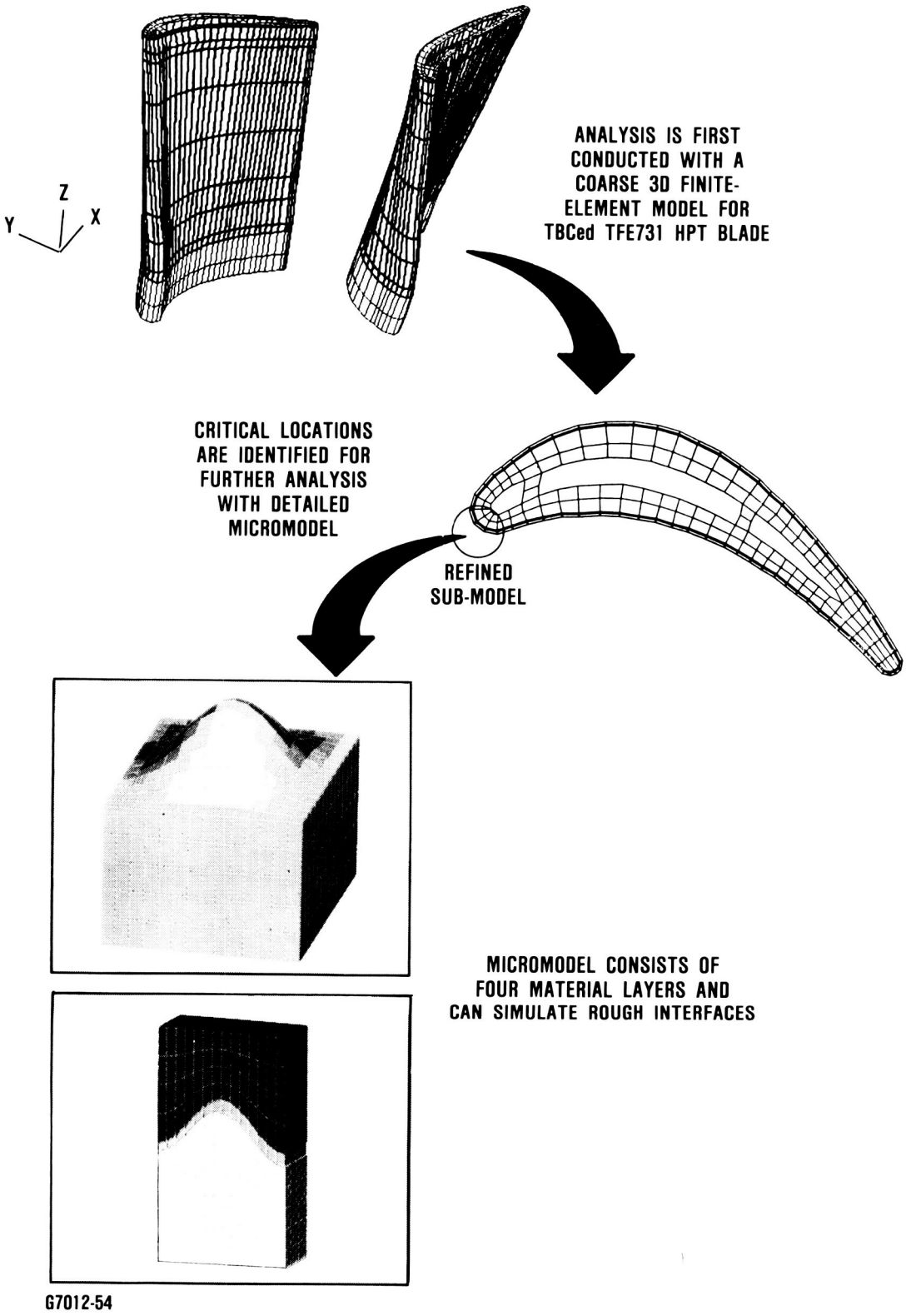

Figure 3. 3-D Finite-Element Thermomechanical Micromodel was Developed and Interfaced with a Design Grade Coarse Model.

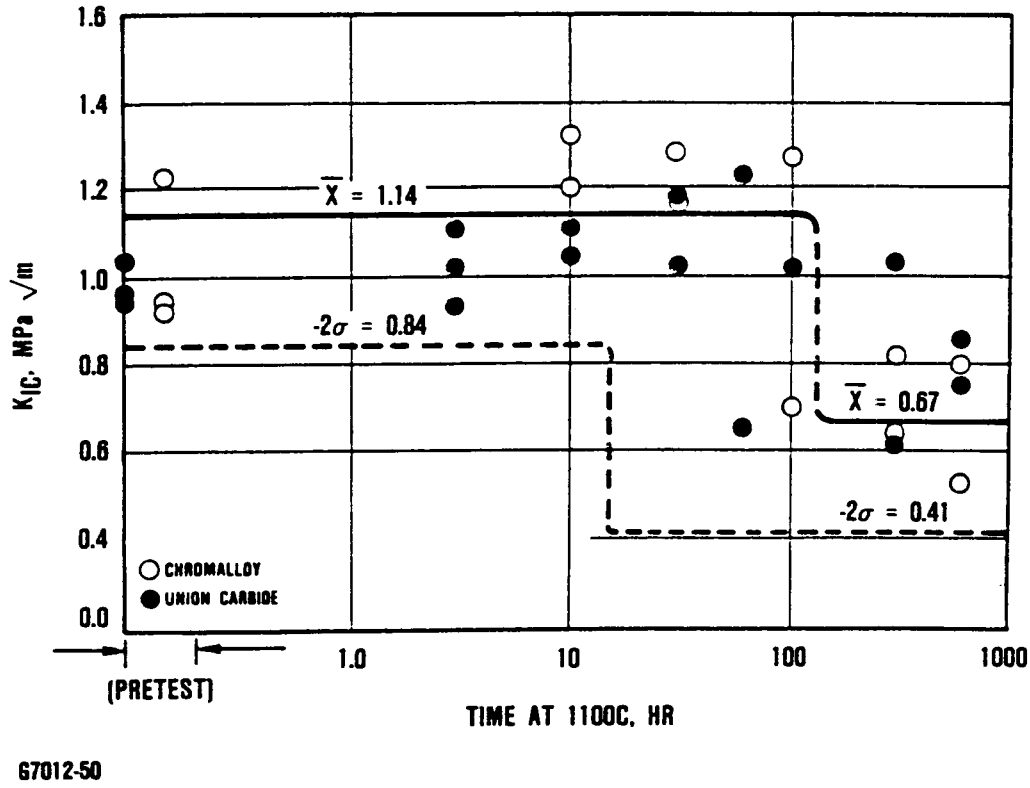

Figure 4. Fracture Toughness of Plasma-Sprayed, Yttria-Stabiliized Zirconia Coating is Reduced After Long Exposures at High Temperatures.

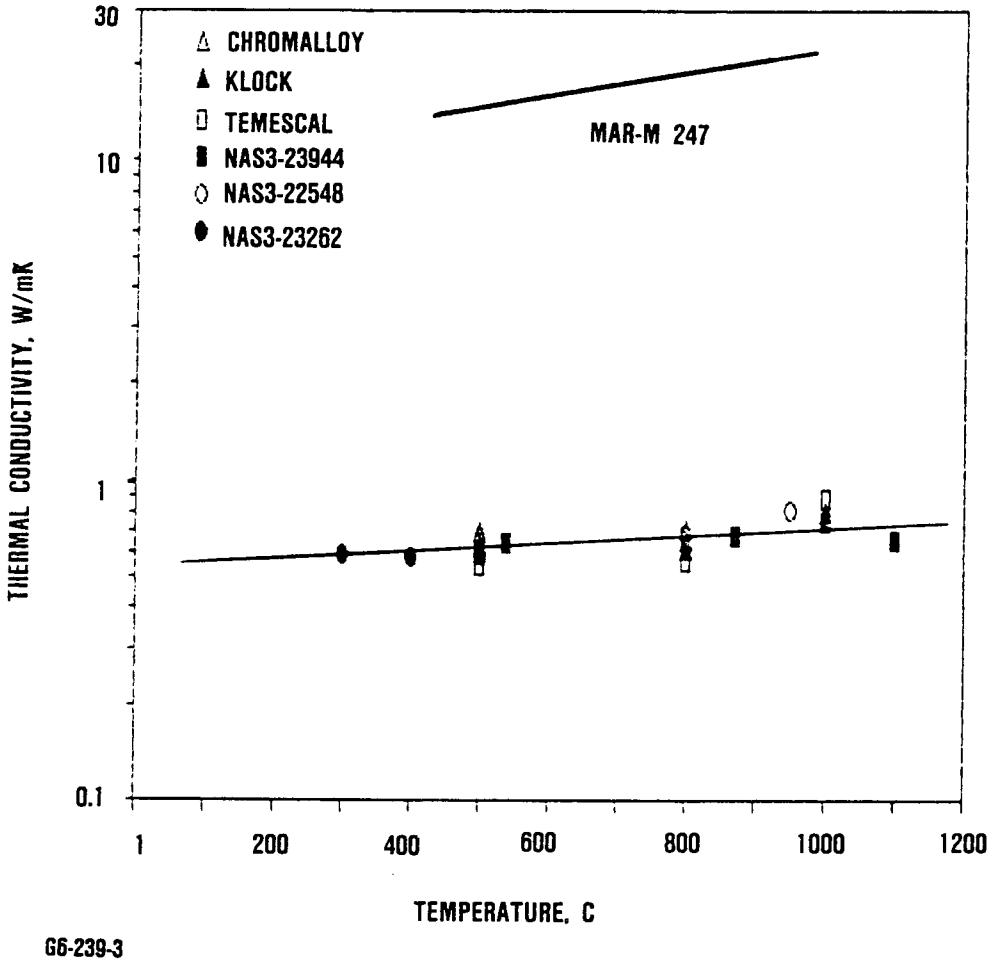

Figure 5. Plasma-Sprayed and EB-PVD TBCs Have Equivalent Thermal Conductivity

THERMAL BARRIER COATING LIFE PREDICTION MODEL

B. Pilsner, R. Hillery, R. McKnight, T. Cook, and M. Hartle
General Electric Aircraft Engines
Cincinnati, Ohio

The objectives of this research were to determine the predominant modes of degradation of a plasma sprayed thermal barrier (TBC) system, and then develop and verify life prediction models accounting for these degradation modes. The TBC system consists of a low pressure plasma sprayed (LPPS) bond coat layer of Ni-22Cr-10Al-0.3Y, an air plasma sprayed (APS) yttria partially stabilized zirconia (ZrO_2-$8Y_2O_3$) top coat on a conventionally cast Rene'80 (Ni-base) substrate.

Thermal cycle testing of TBCs was employed to evaluate the effect of coating edges, bond coat oxidation, bond coat creep, top coat thickness, and bond coat thickness. Two different thermal cycle tests were employed (one utilized an isothermal exposure, while the other imposed a temperature gradient through the ceramic). Increases in life were associated with increases in bond coat creep strength and minimizing the effect of coating edges, while decreases in life were associated with increases in top coat thickness and isothermal pre-exposure damage.

In addition to the thermal cycling, some tests were conducted using coated cylindrical low cycle fatigue specimens in servohydraulic fatigue frames. These specimens were inductively heated and used high temperature extensometers to measure the elongation in the gage section. The first test simply duplicated the thermal cycle of the isothermal exposure test. Subsequent tests then imposed a mechanical strain on the thermal strain and producing the desired thermal-mechanical cycle. The majority of the cycles were in compression (a tensile stress was achieved for only a part of one cycle). Remarkably, in all cases, failure occurred in the substrate prior to detectable coating failure, demonstrating the significant stress tolerance of TBCs.

A time dependent, non-linear finite element model was developed to predict the stresses/strains present in the TBC system. The model was used to evaluate the effects of coating edges, bond coat oxidation, bond coat creep, changes in geometry, and temperature gradient across the TBC system as identified in the thermal cycle tests. The model predicts that TBC life can be extended by minimizing the effect of edges. It also predicts that, although the growth of oxide scale produces strains due to the material addition, it also reduces the strains produced by the thermal expansion mismatch between the bond coat and the top coat.

Property determinations of the bond coat and the top coat have been made. These included tensile strength, Poisson's ratio, dynamic modulus, and coefficient of thermal expansion (1). The properties were required for the modeling work and allow evaluation of material changes in the TBC system.

A TBC Life Prediction Model was developed based on the above tests and finite element analysis. The model relates the ranges of normal and shear strains produced during a thermal cycle (isothermal exposure test) to TBC cycle life as shown by:

$$\Delta\varepsilon_{RZ} + 0.4\,\Delta\varepsilon_{R} = 0.084\,N_f^{-1.445}$$

where $\Delta\varepsilon_{RZ}$ is the shear strain range
$\Delta\varepsilon_{R}$ is the normal strain range
N_f is the cycles to failure

As indicated, the model predicts failure in the TBC due to imposed strains based on the foregoing considerations; hence, changes in substrate and bond coat material, in geometry, in thickness, and the effect of oxidation can be accommodated by this model.

Present work is aimed at evaluating the model's predictive capabilities. Future work will be aimed at incorporating fracture mechanics into the model.

Reference:

1. R.V. Hillery, B.H. Pilsner, T.S. Cook, and K.S. Kim, "Thermal Barrier Coating Life Prediction Model - Second Annual Report," NASA CR-179504, 1986.

Baseline Thermal Barrier Coating System
(Weight Percent)

- **Substrate (Rene'80):** Ni-14Cr-9. 5Co-5Ti-4W-4Mo-3Al-0.17C-0.3Zr-0.015B
- **Bond Coating:** Ni-22Cr-10Al-0.3Y (Low Pressure Plasma Spray)
- **Top Coating:** ZrO_2 - $8Y_2O_3$ (Air Plasma Spray)

Figure 1

Specimen Configurations

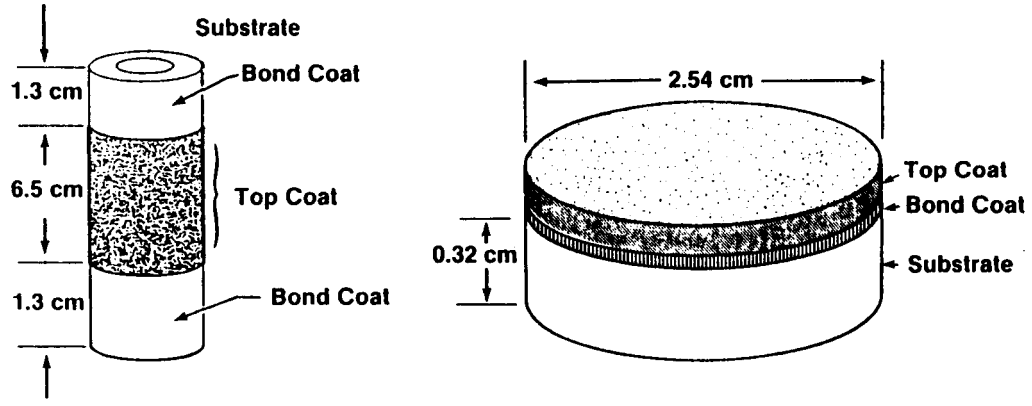

Figure 2

TBC Thermal Cycle Tests

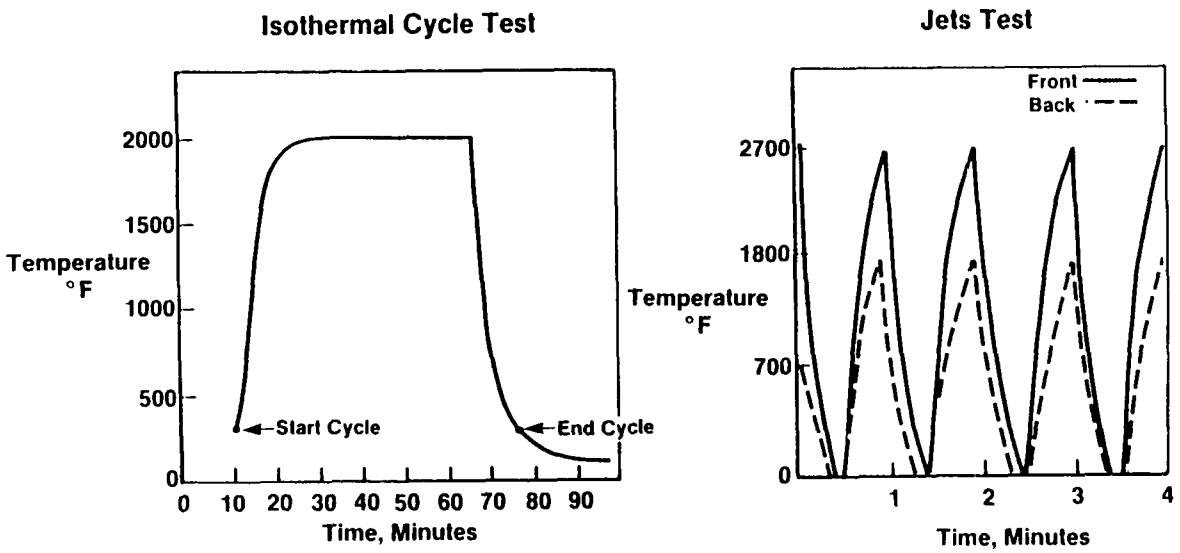

Figure 3

Rapid Temperature Thermal Cycle Test at 2000° F
45 Minute Exposure — 15 Minute Cool Down

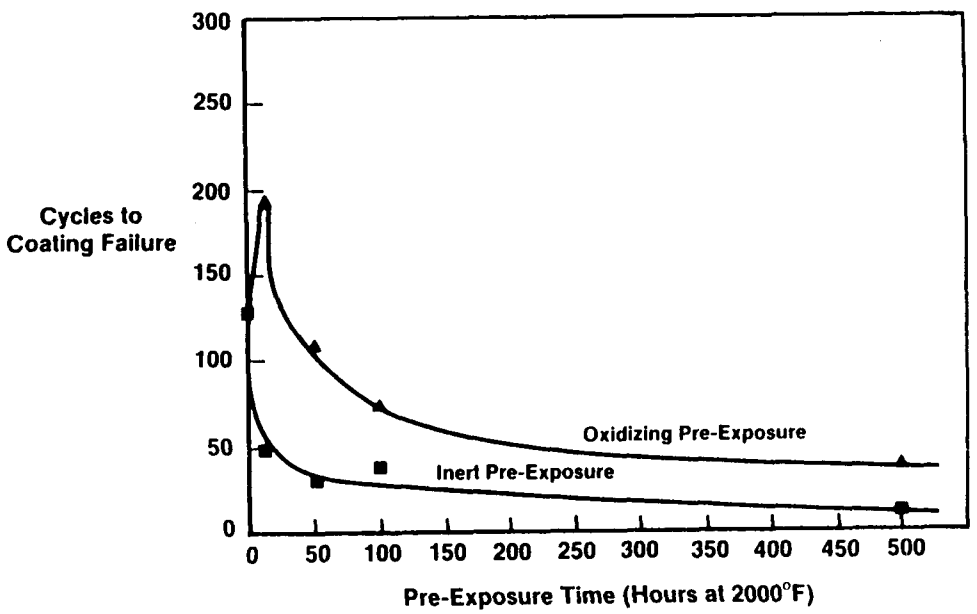

Figure 4

Effect of Bond Coat Creep Strength on TBC System Failure

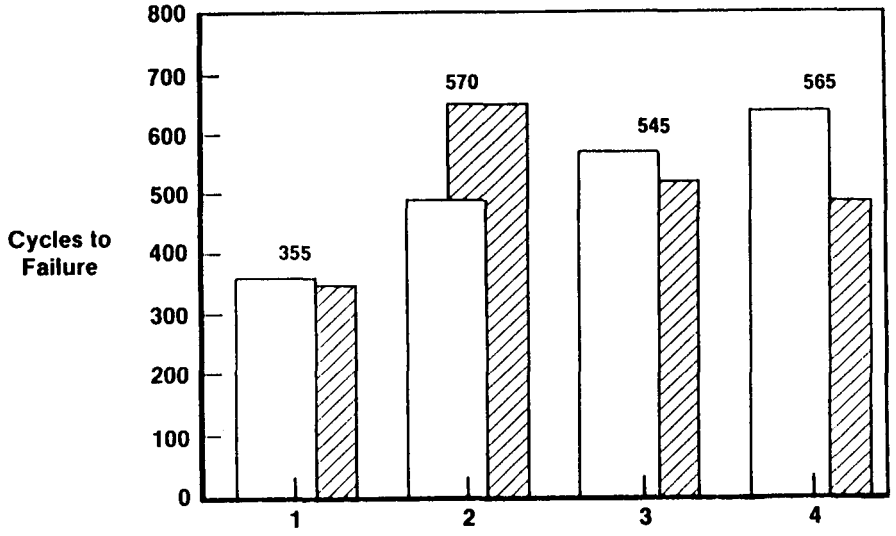

1 Ni-22Cr-10Al-0.3Y
2,3,4 Modified NiCrAlY Bond Coats

Figure 5

Jets Test Thermal Cycle Results (10% Failure Criterion)

	Bond Coat Thickness (Mils)	Top Coat Thickness (Mils)	Specimen Diameter	Cycles
• Baseline	5	10	1"	21,000
	5	20	1"	4,000
	5	30	1"	2,000
	5	10	1.25"	— *
	5	10	1.50"	— **

* 4% Spallation Through 27,000 Cycles
** No Spallation Through 27,000 Cycles

Figure 6

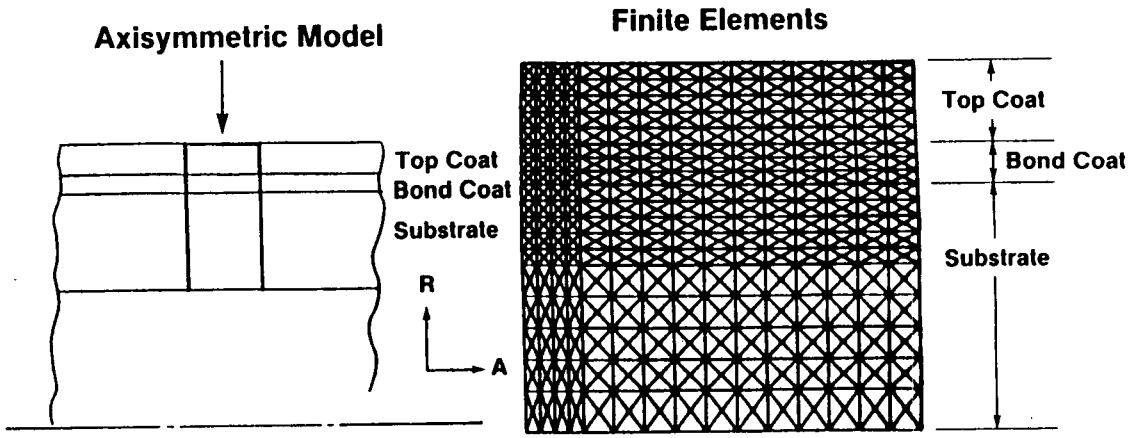

Figure 7

Variation of Effective Stress in Temperature Gradient Cyanide Analysis

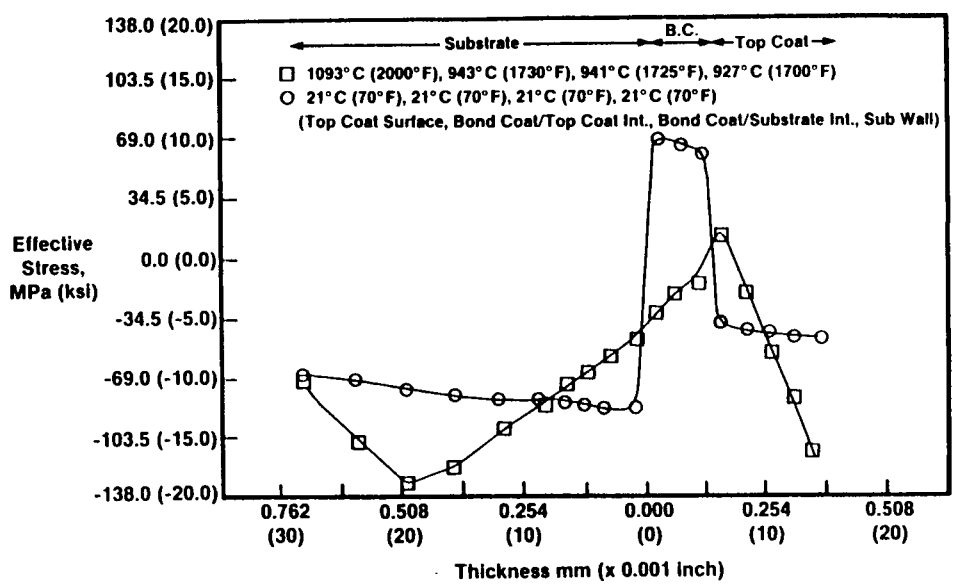

Figure 8

TBC Cylinder
Variation of RZ Total Strain

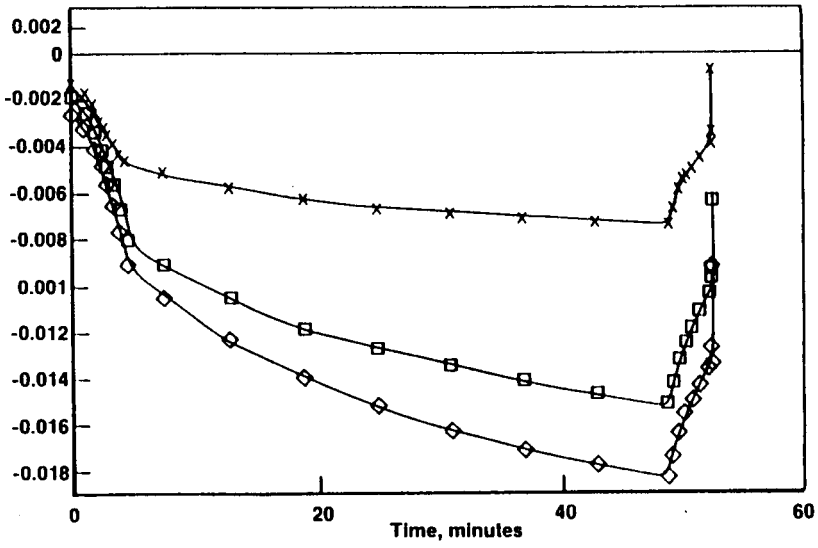

Figure 9

TBC Life Prediction Model

- $\Delta\varepsilon_{RZ} + 0.4\,\Delta\varepsilon_{R} = 0.084\,N_f^{-1.445}$

  Where:

  - $\Delta\varepsilon_{RZ}$ is the Shear Strain Range
  - $\Delta\varepsilon_{R}$ is the Normal Strain Range
  - N_f is the Cycles to Failure

Figure 10

THERMAL BARRIER COATING LIFE PREDICTION MODEL DEVELOPMENT[1]

J.T. DeMasi, S.L. Manning, M. Ortiz, and K.D. Sheffler
Pratt & Whitney Division
United Technologies Corporation
East Hartford, Connecticut

The objectives of this program are to increase understanding of Thermal Barrier Coating (TBC) degredation and failure modes, to generate quantitative ceramic failure life data under cyclic thermal conditions which simulate those encountered in gas turbine engine service, and to develop an analytical methodology for prediction of coating life in the engine.

This program is being conducted in two phases. The first phase, which is complete, was conducted with a plasma deposited thermal barrier coating system, designated PWA 264, which currently is bill-of-material on various stationary turbine components in several commercial engines. The second phase, which was initiated in July 1987, will adapt the plasma deposited life model to a more recently developed electron beam-physical vapor deposited ceramic coating, designated PWA 266, which has shown the potential to provide up to ten times the cyclic thermal coating durability of the plasma deposited coating. These two coatings are compared in Figure 1.

Phase I - Plasma Deposited Ceramic

Phase I observations of degredation and failure modes in plasma deposited ceramic indicate that spallation failure results from progressive cracking of the ceramic parallel to and adjacent to, but not coincident with the metal-ceramic interface. Typical ceramic failures are shown in Figure 2. Figure 3 shows the progressive accumulation of ceramic cracking damage in laboratory specimens suspended from test at various fractions of their spallation life.

Phenomenological evidence obtained by burner rig testing of specimens pre-exposed in oxidizing and non-oxidizing environments indicates that oxidation is involved in the degredation process. Test results plotted in Figure 4 clearly show a substantial reduction of life for air pre-exposed specimens, with no such reduction seen for specimens pre-exposed in Argon.

Based on the observation of mechanical failure within the ceramic layer, effort was devoted to exploration of ceramic mechanical behavior. A significant conclusion from this work was the observation of substantial inelastic deformation at all temperatures from ambient to 1204°C (2200°F).

[1] NASA Contract NAS3-23944

Uniaxial tensile stress-strain curves obtained on the plasma deposited ceramic at room temperature and 1204°C (2200°F) (Figure 5) clearly show this non-linear deformation. A typical uniaxial compression stress-strain curve (Figure 6) exhibits a combination of linear and non-linear behavior with substantially higher strength than in tension. A hysteresis loop obtained by reversing the orientation of a strain gauged room temperature four point bend specimen at zero load (Figure 7) exhibits significant reversed inelastic strain. ("Kinks" in this curve at the zero load crossing are thought to result from slight material recovery during the time required to reverse the orientation of the specimen.) Evidence of significant creep at 982°C (1800°F) and of exceptionally stress sensitive fatigue failure ($b \approx 50$) are shown in Figure 8.

Following the approach of Miller (1), an existing fatigue model was selected as the basis for the TBC life prediction model (Figure 9). The mechanical damage driver in this model is inelastic strain range ($\Delta\varepsilon_i$). Environmental degradation is accounted for by incorporating the proportionality constant in the exponential term and causing it to be dependent on progressive oxidation damage (Figure 10).

To calculate inelastic strain range for incorporation in the life model, ceramic constituitive behavior was fitted to a time dependent inelastic model developed by Walker (2). An example of the application of this model is shown in Figure 11, where calculated tensile and compressive strains are compared with measured data. A. Walker model calculation of ceramic stress-strain behavior for a typical TBC thermal cycle (Figure 12), clearly shows the large amount of reversed inelastic strain produced by thermal cycling of the TBC system.

Prediction of oxide thickness as a function of time and temperature for incorporation in the life model was based on an oxidation model developed at NASA (3). Constants for this model were established by correlation of oxide thickness measured on laboratory exposed specimens of the thermal barrier coating system (Figure 13).

Experimental TBC spallation life data for calibration of the life model constants was obtained from cyclic burner rig tests of a rotating, externally heated and internally cooled hollow cylindrical specimen illustrated in Figure 14. Burner rig test conditions (maximum and minimum cycle temperature and time at maximum temperature) were varied in each test to vary the relative emphasis on each of the two primary life drivers (inelastic strain range and oxide thickness) as illustrated in Figure 15. Results of twenty such tests were correlated with the life model to produce best fit values of the model constants shown in Figure 16. Results of this correlation show calculated life to be within a factor of ±3 of observed life for nineteen of the twenty experimental results (Figure 17). The twentieth data point could not be correctly predicted with any reasonable variation of the model constants, and is assumed to be in error.

To substantiate the life prediction model, six additional tests were conducted, four using the previously described burner rig test method and two using a radiant source to heat a flat panel coated with plasma TBC. The primary differences in the two test methods are the specimen geometry and the substantially higher heat flux obtained from the radiant source, which more closely simulates that experienced in the gas turbine engine. Results of these tests are included in Figure 17, and are seen to be within the ±3X deviation band, thus substantiating the prediction capability of the model.

To summarize results of the first phase of this program, plasma deposited TBC ceramic spallation has been observed to result from progressive near interfacial cracking of the ceramic. Phenomenological evidence indicates that interfacial oxidation accelerates this process. Mechanical behavior of the ceramic has been found to be unusual, exhibiting highly inelastic stress strain behavior at ambient temperature, creep, fatigue, and cyclically reversible inelastic deformation. A life prediction model has been developed which incorporates cyclic inelastic strain and interfacial oxidation as the primary degredation modes. This model has been shown to correlate cyclic thermal spallation life results within a factor of ±3 over a broad range of relative mechanical and oxidative exposure severities.

PHASE II - Electron Beam-Physical Vapor Deposited Ceramic

The goals of the second phase of this program are similar to those of the first phase; that is, to understand the degredation and failure modes of the Electron Beam-Physical Vapor Deposited ceramic shown on the right in Figure 1, to generate quantitative failure data, and to develop a life prediction model for this ceramic.

Preliminary results show the EB-PVD ceramic to be at least four to ten times as spallation resistant as the plasma deposited ceramic, depending on the relative severities of the oxidative vs. mechanical damage induced by exposure (Figure 18). (In some of these tests, failure of the specimen was initiated by thermal fatigue cracking of the B-1900 + Hf substrate, suggesting that the life increase of the EB-PVD ceramic may be greater than that shown in Figure 18). This relative durability improvement has been substantiated in side-by-side field service testing of plasma and EB-PVD ceramic, as shown in Figure 19. Examination of spalled EB-PVD ceramic shows the failure mode to be different from plasma TBC. Whereas the plasma system fails as a result of cracking in the ceramic layer, EB-PVD ceramic failure occurs predominantly at the metal-ceramic interface, as shown in Figure 20.

The approach which will be taken to model the spallation life of the EB-PVD ceramic coating is outlined in Figure 21. The program objectives

will be accomplished in four tasks, numbered V through VIII. Task V will involve evaluation and modeling of EB-PVD ceramic mechanic behavior, while in Task VI, oxidation at the metal-ceramic interface will be measured and modeled. Quantitative life data will be generated and modeled over a broad range of relative oxidizing and mechanical severities in Phase VII, and in Phase VIII substantiation tests will be conducted to verify the model. It is anticipated that this effort will take fifteen months starting from July 1987.

REFERENCES

1. Miller, R.A., "Oxidation-Based Model for Thermal Barrier Coating Life", J. Am. Cer. Soc., V.67, No: 8, pp 517-521, 1984.

2. Walker, K.P., "Research and Development Program for Non-Linear Structural Modeling with Advanced Time-Temperature Dependent Constituitive Relationships", NASA CR 165533.

3. Miller, R.A., Private Communication

Phase I
Plasma deposited ceramic
(PWA 264)

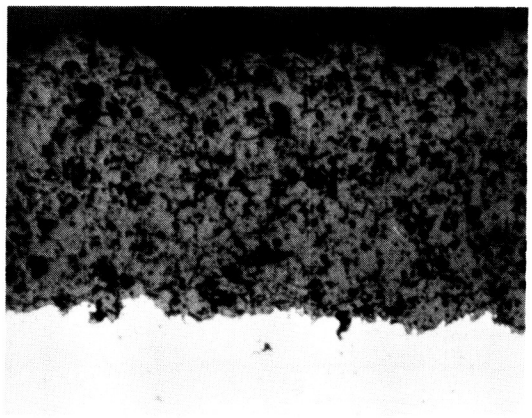

Bill-of-material
JT9D
PW2037
PW4000
V2500

Phase II
Electron beam — physical
vapor deposited ceramic
(PWA 266)

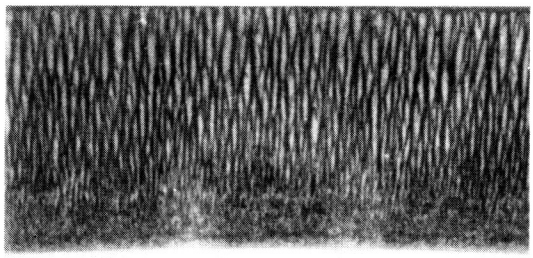

Advanced coating
offers substantially improved
coating durability

Figure 1 Program Conducted in Two Phases

Engine

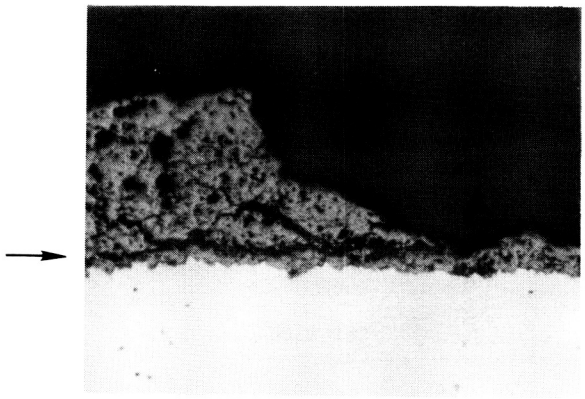

125X

Lab test

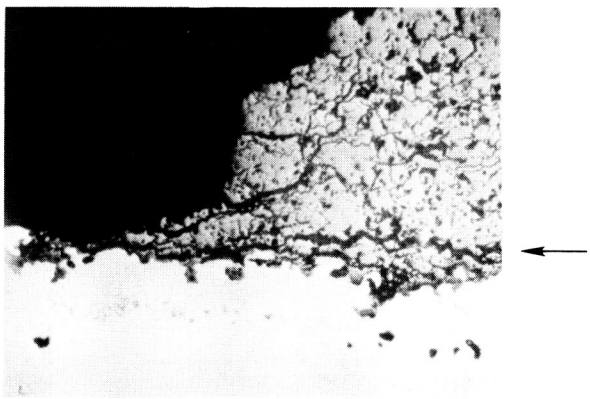

200X

Arrows indicate primary failure sites

Figure 2 Typical Ceramic Failures

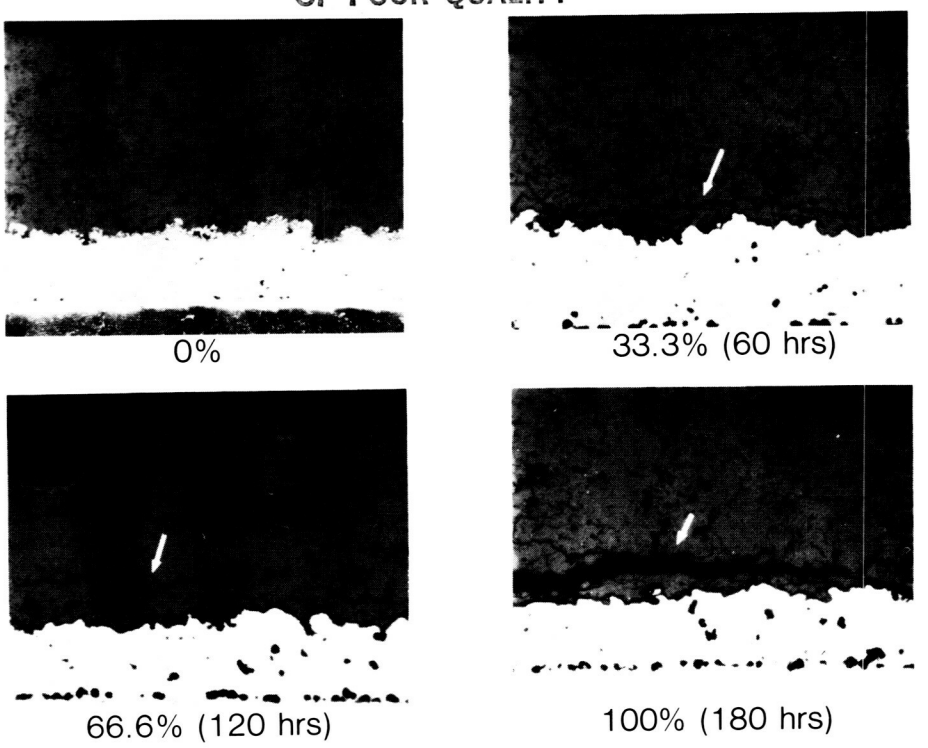

Figure 3 Ceramic Cracking Damage Accumulates Progressively

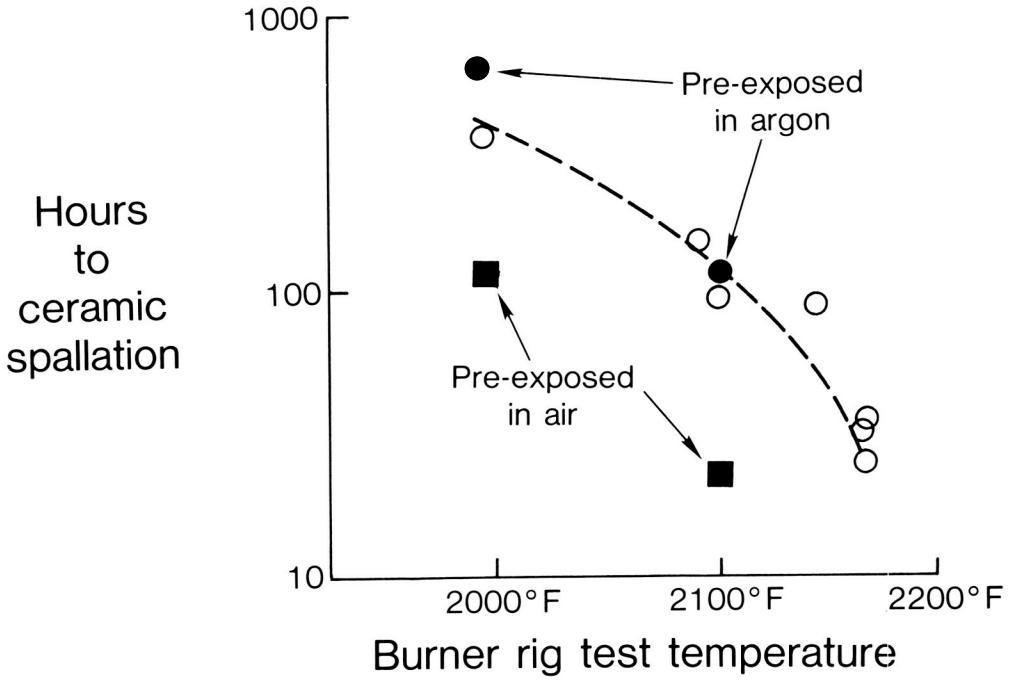

Figure 4 Phenomenological Evidence Suggests Environmental Interaction

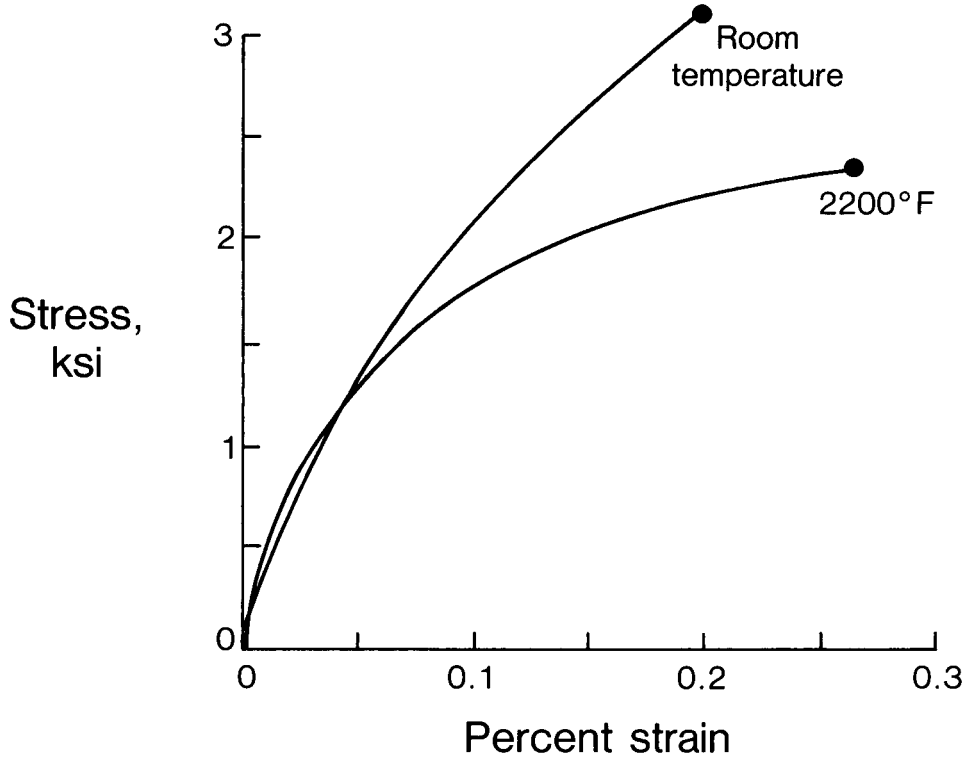

Figure 5 Ceramic Tensile Deformation Completely Inelastic

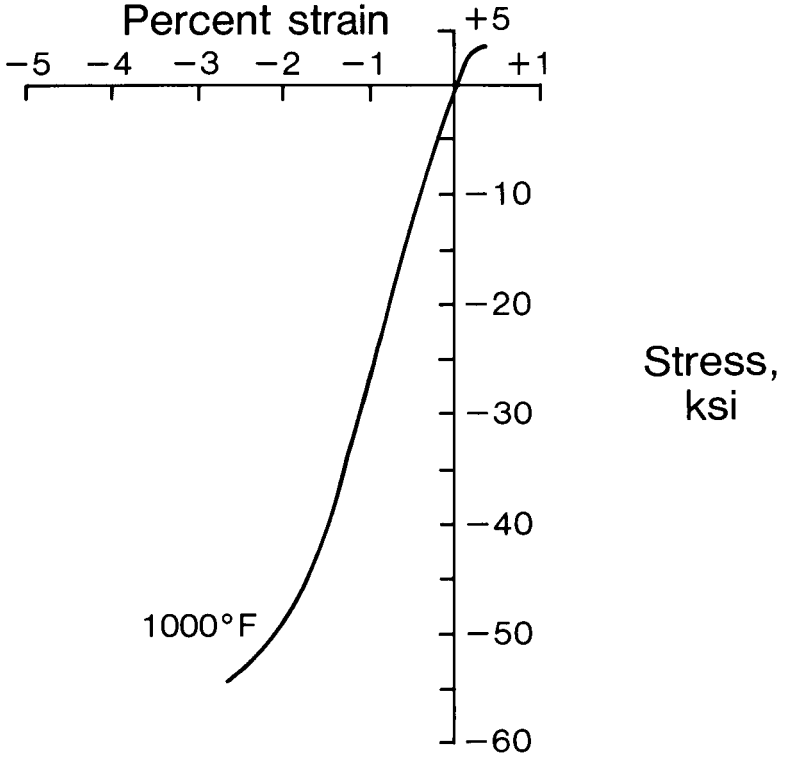

Figure 6 Ceramic Compressive Deformation is Elastic/Inelastic

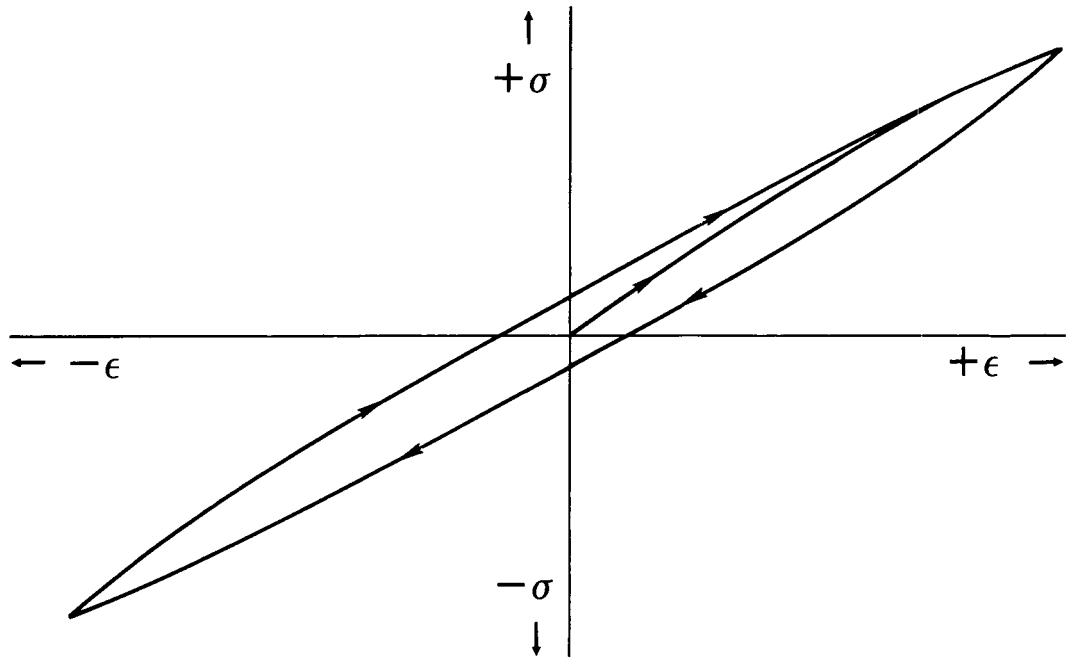

Figure 7 Reversed Deformation Exhibits Significant Hysteresis

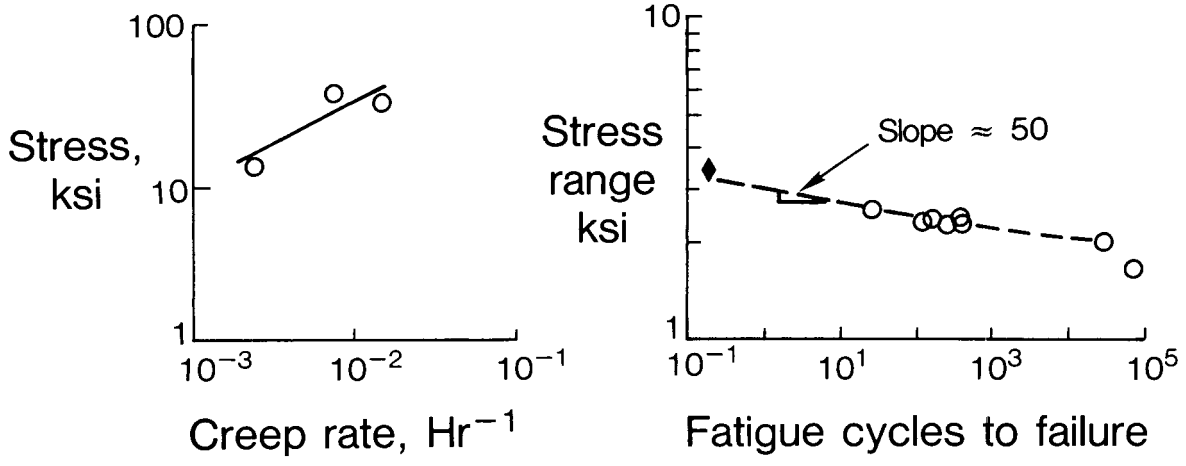

Figure 8 Ceramic Exhibits Significant Creep and Fatigue

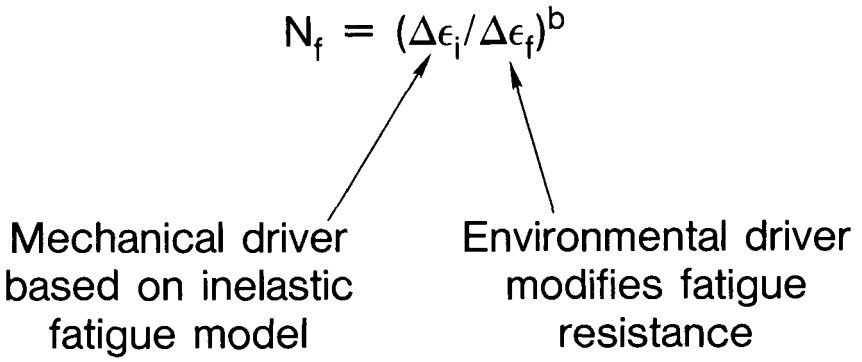

Figure 9 Life Prediction Model Incorporates Mechanical and Environmental Drivers

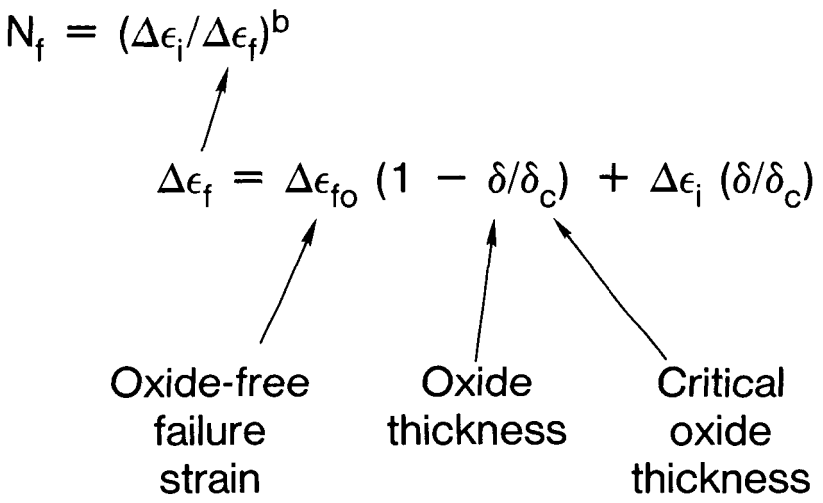

Figure 10 Environmental Driver Modifies Fatigue Resistance

(NAS 3-22055)

$$\dot{\epsilon}_{\text{inelastic}} = \left(\frac{\sigma - \Omega}{K}\right)^n$$

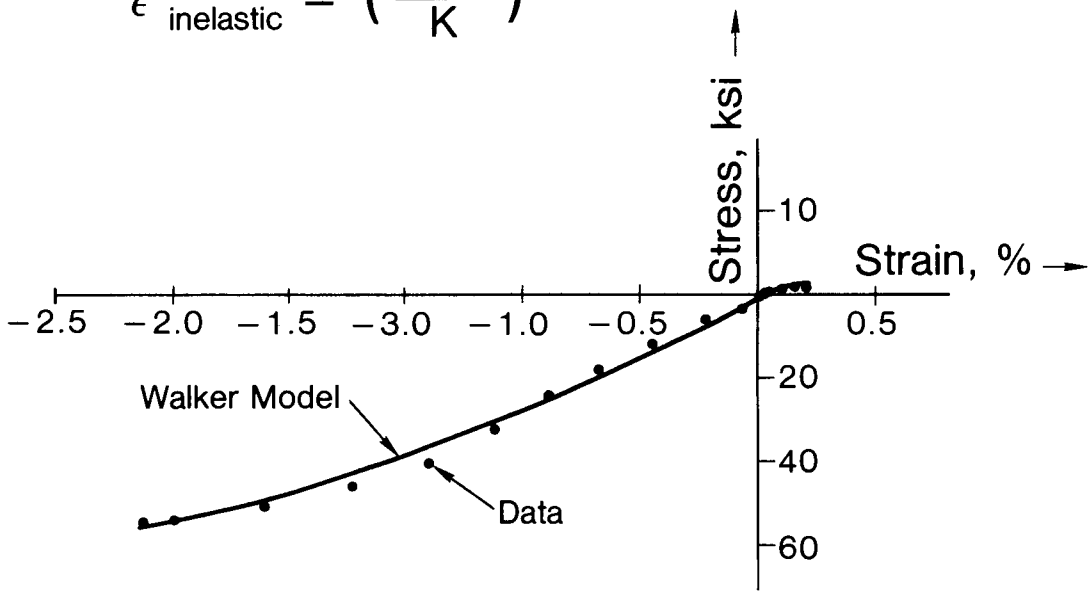

Figure 11 Ceramic Behavior Modeled With Walker Equation

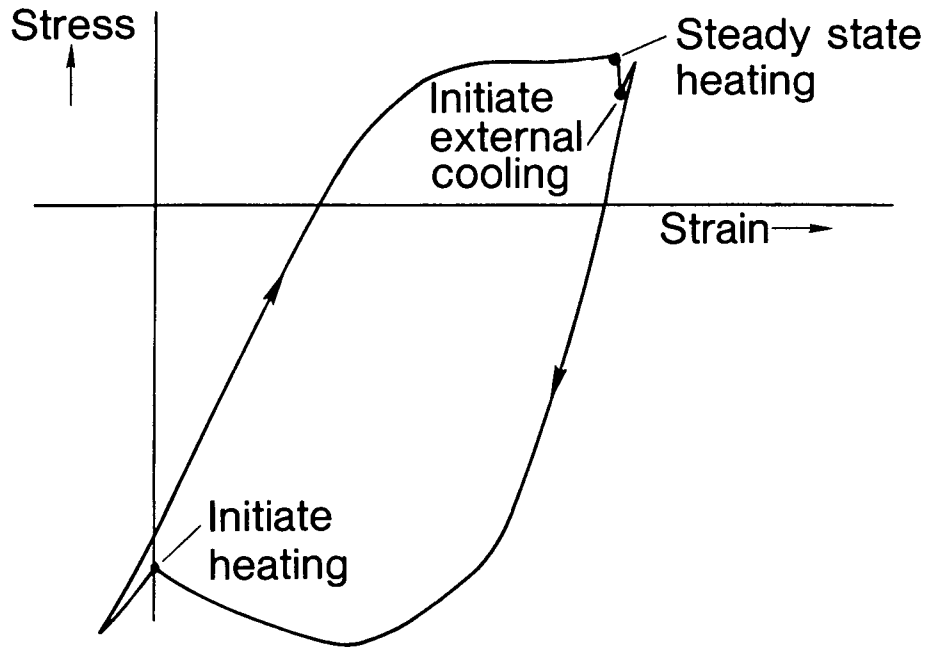

Figure 12 Walker Model Predicts Large Reversed Inelastic Strain Range

△ Oxide emphasis
▲ Strain emphasis
◭ Mixed made

$\delta = 1.20 \times 10^{-4} (5.714 \times 10^{11} e^{-104856/RT} t)^{0.5}$

R = 1.987, δ = (CM)
T = (°K)
t = (SEC)

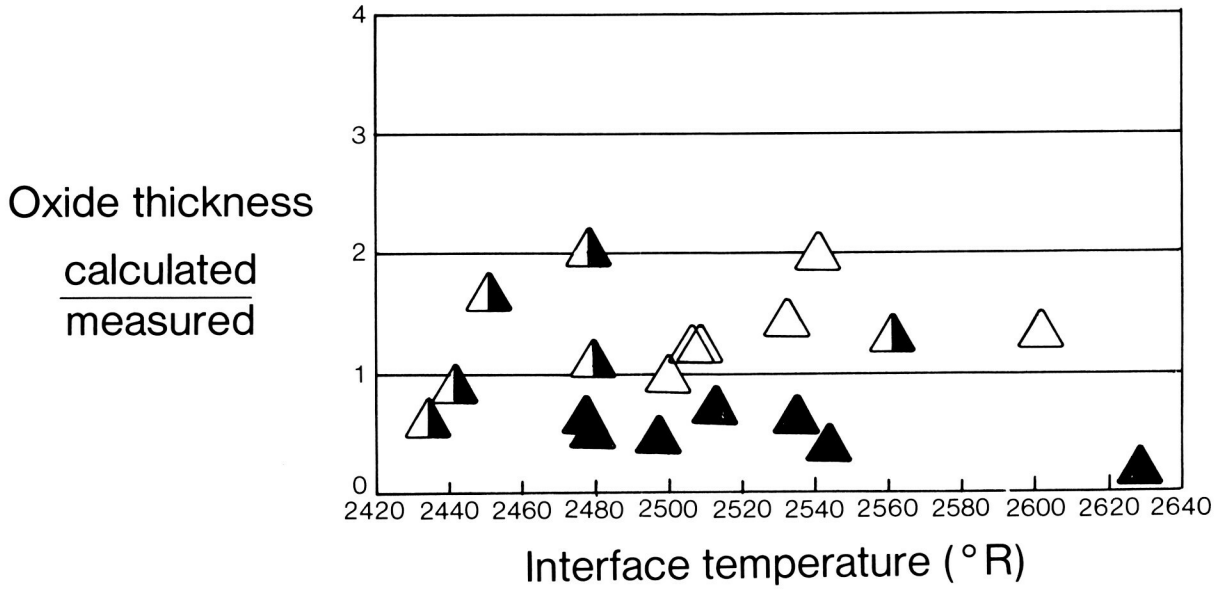

Figure 13 Oxidation Driver Based on Modified NASA Model

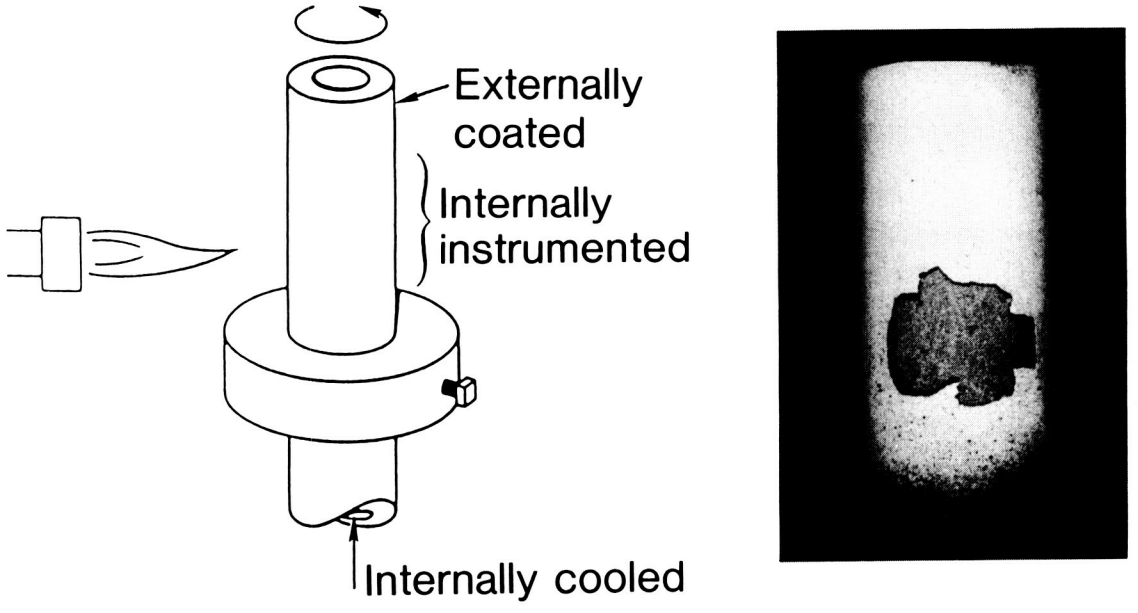

Figure 14 Design Data Generated With Internally Cooled Specimen

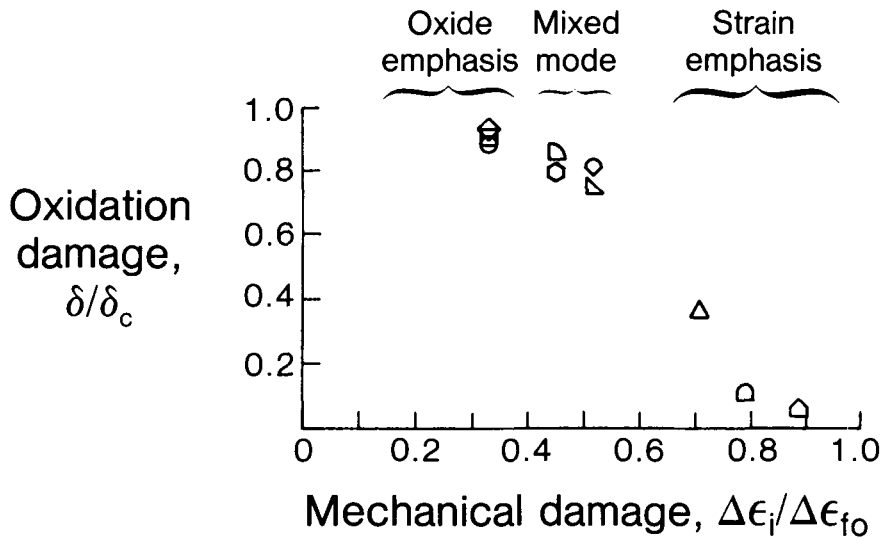

Figure 15 Design Data Tests Cover Wide Range of Mechanical and Oxide Induced Damage

$$N_f = (\Delta\epsilon_i/[\Delta\epsilon_{fo}\ (1 - \delta/\delta_c) + \Delta\epsilon_i\ (\delta/\delta_c)])^b$$

$\Delta\epsilon_{fo} = 0.0040$; static failure strain

$\delta_c = 0.000370$ in.; critical oxide thickness

$b = -10.87$

Figure 16 Correlation of Design Data Provides "Best Fit" Constants

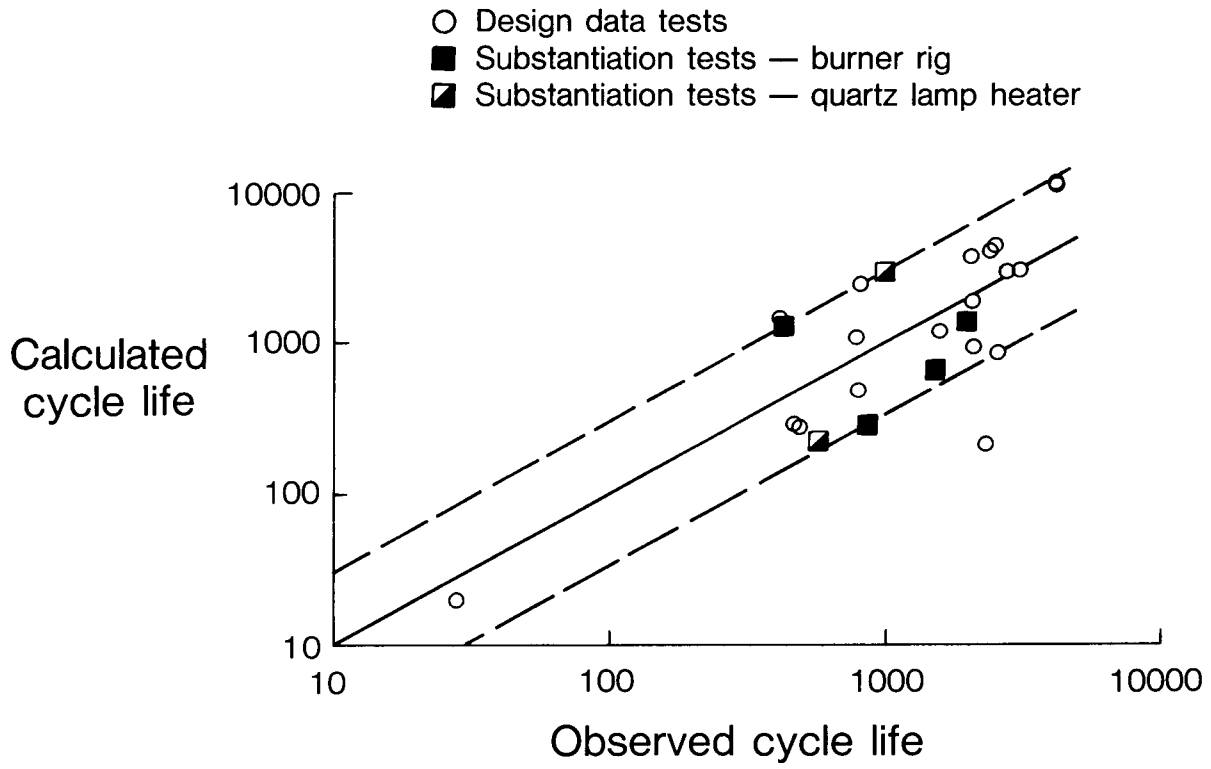

Figure 17 Optimized Correlation ±3X on Life

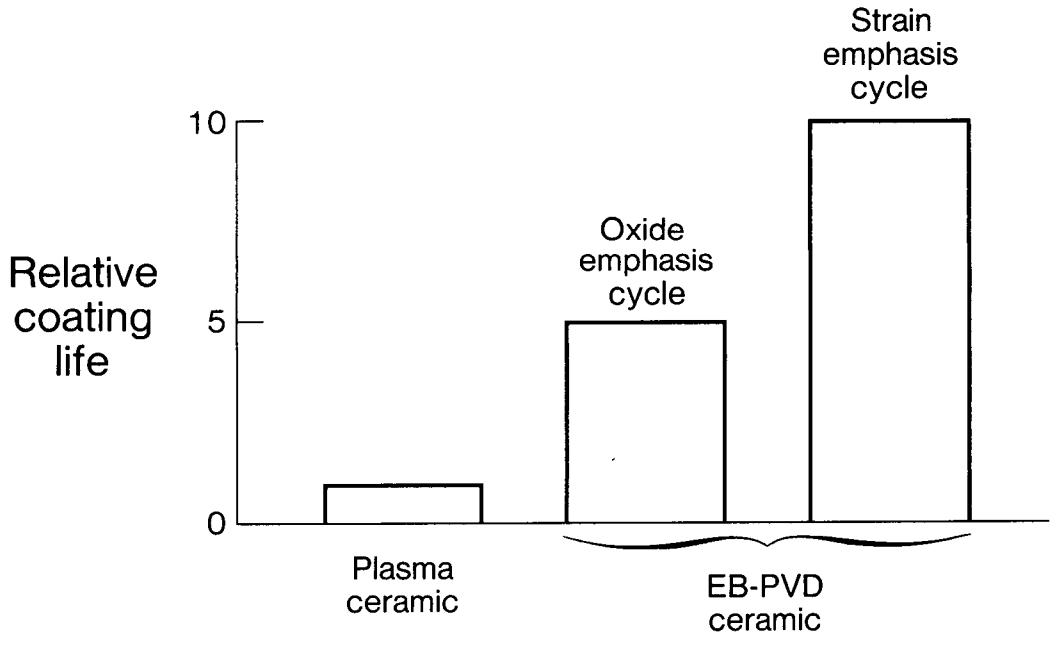

Figure 18 EB-PVD Ceramic Benefits Are Cycle Dependent

Figure 19 EB-PVD Ceramic Engine Evaluation

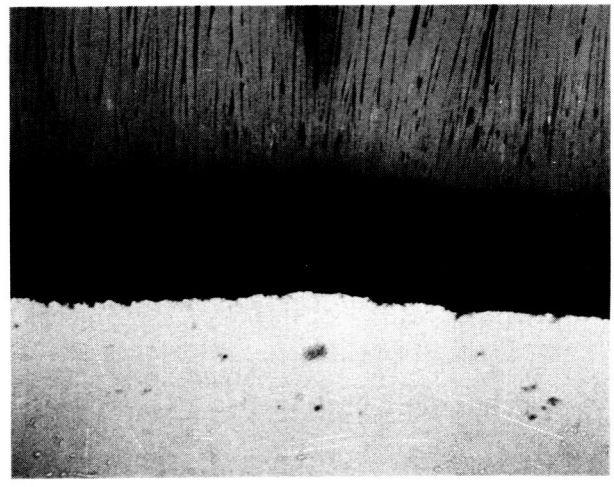

Figure 20 EB-PVD Ceramic Fails at Interface

Task V Evaluate mechanical driver
- Property evaluation
- Modeling

Task VI Evaluate environmental driver
- Measure oxidation kinetics
- Modeling

Task VII Life correlation
- Generate life data
- Correlate model

Task VIII Verification testing

Figure 21 Phase II Program Approach

HIGH TEMPERATURE CONSTITUTIVE AND CRACK INITIATION MODELING OF COATED SINGLE CRYSTAL SUPERALLOYS*

Thomas G. Meyer, David M. Nissley, and Gustav A. Swanson
Pratt & Whitney Division
United Technologies Corporation
East Hartford, Connecticut

The purpose of this program is to develop life prediction models for anisotropic materials used in gas turbine airfoils. In the base portion of the program, two coated single crystal alloys are being tested. They are PWA 286 overlay coated and PWA 273 aluminide coated PWA 1480 and PWA 286 overlay coated Alloy 185. Viscoplastic constitutive models for these materials are also being developed to predict the cyclic stress-strain histories required for life prediction of the lab specimens and actual airfoil designs. This report highlights some of the accomplishments of the program this year. Refer to Reference 1 for more information.

SINGLE CRYSTAL CONSTITUTIVE MODEL

Two candidate constitutive models have been developed for single crystal materials. A "microscopic" model computes inelastic quantities on the crystallographic slip systems and achieves the required directional properties as a consequence of resolving the slip system stresses and strains onto the global coordinate system. The second model, the "macroscopic" model, uses anisotropic sensors operating on the global quantities directly to achieve the required directional properties. Material constants from 427C (800F) to 1038C (1900F) have been obtained for both models based on cyclic tests. Additional tests are being conducted to obtain model constants up to 1149C (2100F).

Each model has been encoded in a format consistent with that required in the MARC (Ref. 2) finite element program (via user subroutine HYPELA). Significant reduction in computing time is achieved by formulating and inverting the structural stiffness matrix only once in an analysis using elastic constants at a "reference temperature" (Ref. 3). During the incremental structural analysis, any elastic stress change due to change in temperature from the reference temperature is added to the incremental inelastic stress vector.

Simple finite element analyses are being conducted to verify proper operation of the models in the MARC program.

* Work performed under NASA contract NAS3-23939.

COATING CONSTITUTIVE MODEL

PWA 1480 turbine airfoil TMF cracks originate from a coating crack. Thus, for airfoil life prediction, it is important to model the coating mechanical behavior as well as that of the PWA 1480. In this program, viscoplastic constitutive models are being developed for two fundamentally different coating types which are commonly used in gas turbines to provide oxidation protection: 1) PWA 286 plasma sprayed NiCoCrAlY overlay and 2) PWA 273 NiAl diffusion.

Walker's isotropic formulation (Ref. 4) was chosen as the overlay coating constitutive model based on its ability to reproduce isothermal and thermal mechanical hysteresis loop data.

MARC (Ref. 2) finite element computer program user subroutine HYPELA has been developed for the overlay coating to permit analysis of coated specimens and components.

Aluminide diffusion coating constitutive model development is continuing. Because diffusion coating properties depend on the substrate material, tests are conducted on two thicknesses of coated PWA 1480 material. Subsequently, the "effective" aluminide coating material constants will be determined by applying the overlay coating Walker model formulation to both specimen thicknesses and extrapolating to zero substrate thickness. Isothermal stress relaxation testing of the 0.25mm (0.010") thick specimens was completed. The observed specimen response at 871C (1600F) is presented in Figure 1. Testing of the 0.13mm (0.005") thick specimens and model constant determination is pending.

LIFE PREDICTION TESTS

Over 45 TMF tests of coated PWA 1480 specimens have been completed. Although many different strain-temperature cycle conditions were investigated, the bulk of TMF tests were out-of-phase. All four orientations (<001>, <011>, <111>, and <123>) initiated cracks at sites where coating cracking had occurred. This initiation mode is consistent with previously conducted experiments and turbine airfoil experience.

Isothermal specimen tests are also being conducted. Contrary to the TMF test experience; however, many non-<001> oriented substrate specimens initiated cracks underneath the specimen outer surface in either the PWA 1480 or coating/PWA 1480 interfacial region, especially in the higher temperature tests. In <001> oriented PWA 1480 specimens, crack initiation was limited to the coating. This initiation mode shift between <001> and non-<001> specimen orientations occurred because <001> specimens were tested at higher strain ranges than the other orientations to obtain roughly equivalent specimen lives. The higher strains reduce the coating fatigue life below that of the PWA 1480. However, there was one exception. PWA 286 coated <001> specimen tests conducted at temperatures greater than 927C (1700F) generated coating cracks, but those cracks did not grow into the PWA 1480. In such cases, specimen failure was caused by crack initiation at the uncoated I.D. specimen surface.

LIFE PREDICTION MODELS

The original life prediction approach which limited the crack initiation mode to just coating cracking must be extended to include the other observed specimen cracking modes:

$$Nf = Nc + Nsc + Nsp$$

or

$$Nf = Nsi + Nsp$$

whichever is the smallest.

where: Nc = Cycles to initiate a crack through the coating.

Nsc = Cycles for coating initiated crack to penetrate a small distance into the substrate. Currently defined as .25 mm (.010").

Nsi = Cycles to initiate a substrate crack due to macroscopic slip, oxidation effects, or defects.

Nsp = Cycles to propagate substrate crack to failure.

Nf = Total cycles to fail specimen or component.

Nc for Overlay Coating

The following modified tensile hysteretic energy model was developed for the overlay coating:

$$Nc = C\, W_t^{-b}\, \nu^{m}$$

where:

$$\nu = \frac{1}{\sum_{cycle} \frac{r(T_i)}{r(T_o)}\, t_i \cdot D_o} \quad ; \quad \nu \leq 1.0$$

$r(T) = r_o \exp(-Q/T)$ = temp. and time dependent damage rate.

W_t = Tensile hysteretic energy, N-m/m^3 (in-lbf/in^3).

Ti = Individual temperature levels in the cycle, K (R).

ti = Time at Ti (min), including 100% of tensile hold and 30% of compressive hold times in the cycle, if any.

To = Threshold temperature for temperature dependent damage, assumed to be 1088K (1960R).

Do = "incubation damage" = 9.985

Q = Normalized activation energy for temperature and time dependent damage.

Q = activation energy/gas constant, $\Delta H/R$
Q = 28366°K(51100°R)

The term, ν, is an extension of Ostergren's time dependent damage term (Ref. 5) that includes both temperature and time dependent damage functions to model thermally activated processes.

Model constants were determined from isothermal tests conducted at 427, 760, 927, and 1038C (800, 1400, 1700, and 1900F). Coating hysteresis loops were predicted using the PWA 286 constitutive model incorporated into a one-dimensional model. This model determines the stress-strain of the substrate and coating by imposing an equivalent displacement history. Differences in coefficient of thermal expansion are included in the model.

The life model collapses isothermal and thermal mechanical fatigue lives within a factor of about 2.5 (Fig. 2). Generally, the worst predicted test lives were limited to 1149C (2100F) max. temperature TMF tests. Prediction of these tests should improve when 1149C (2100F) isothermal tests are included in the data set used to determine model constants.

Ultimately, coated TMF life prediction must consider biaxial coating loads introduced by the thermal growth mismatch between the coating and substrate. For example, MARC finite element analysis of a simple two element structure was performed to obtain the coating hysteretic response to a uniaxial, out-of-phase TMF test conducted at 427-1038C (800-1900F), +-.15%, and 1 cpm. Predicted hysteresis loops from the finite element and one-dimensional analyses are presented in Figure 3. The coating tensile hysteretic energy was obtained from the finite element analysis by the method proposed by Garud (Ref. 6). For this test condition, biaxial coating loads increased the tensile energy 70% which reduced the predicted life by a factor of about 1.5.

Nc for Aluminide Coating

Total strain range correlation of aluminide coating life at 927C (1700F) indicated that the life of this coating type depended upon the PWA 1480 substrate orientation. Fractographic analysis of the specimen crack initiation regions indicated that most of the non-<001> oriented PWA 1480 specimens initiated cracks under the specimen surface as discussed previously. The correlation was markedly improved by removing the substrate crack initiated specimens from consideration (Fig. 4). The square symbol points in Figure 4 were tests which exhibited PWA 1480 initiation (Nsi).

Nsc or Nsi for Single Crystal Substrate

Initial PWA 1480 life correlations evaluated the following models: Coffin-Manson, Ostergren, crack tip opening displacement (CTOD) from linear elastic fracture mechanics (LEFM), elastic modulus modified strain range model, and the modified hysteretic energy approach developed by DeLuca and Cowles (Ref. 7) which considers crystallographic effects. Each of these models was applied to the data set presented in Table 1. All the models, except CTOD, correlated the lives within a factor of about 2.5.

The elastic modulus modified strain range, Ostergren, and modified hysteretic energy models were chosen for further development based on regression analysis. Subsequently, the Ostergren model was judged to be a subset of the modified hysteretic energy model and, as such, will not be developed further. The modified strain range and modified hysteretic energy model correlations are presented in Figures 5 and 6.

The modified hysteretic energy approach was also applied to an expanded 971C (1700F) data set which included PWA 286 and PWA 273 coated PWA 1480 lives associated with both Nsc and Nsi type initiation modes (Fig. 7). This correlation indicates that the different initiation modes produce separate life trends, but that, within a given mode, lives from both coating types (i.e. overlay and aluminide) are reasonably correlated by a single expression. Also, at this temperature, the PWA 1480 cracking life from the Nsc initiation mode is less than for the Nsi mode. Lastly, for the Nsi initiation mode, greater life data scatter was observed in the overlay coated PWA 1480 lives than the aluminide coated lives. This was attributed to the fact that the PWA 1480 crack initiation in the overlay coated specimens generally occurred deeper in the specimen (i.e. farther from the O.D. surface) than that in the aluminide coated specimens. Since replication cannot monitor subsurface cracks, larger data scatter was expected from the overlay coated specimens.

FUTURE

Isothermal fatigue and TMF tests will continue. These will include preexposed (100 hr. at 1093C (2000F)) fatigue tests designed to understand long term exposure effects, biaxial fatigue tests, and coated Alloy 185 tests. Life model development will focus on prediction of PWA 1480 observed life, especially the PWA 1480 life associated with cracks originating from a coating crack (Nsc).

REFERENCES

1. Swanson, G. A.; Linask, I.; Nissley, D. M.; Norris, P. P.; Meyer, T. G.; and Walker, K. P.: Life Prediction and Constitutive Models for Engine Hot Section Anisotropic Materials Program. NASA CR-179594, April 1987.

2. MARC General Purpose Finite Element Program, MARC Corporation, Palo Alto, Ca.

3. Cassenti, B. N.: Research and Development Program for Nonlinear Structural Modeling with Advanced Time-Temperature Dependent Constitutive Relationships, Vol. I - Theoretical Discussion. NASA CR-168191, July 1983.

4. Walker, Kevin P.: Research and Development Program for Nonlinear Structural Modeling with Advanced Time-Temperature Dependent Constitutive Relationships. NASA CR-165533, Nov. 1981.

5. Ostergren, W. J.: A Damage Function and Associated Failure Equations for Predicting Hold Time and Frequency Effects in Elevated-Temperature Low-Cycle Fatigue. Jl. of Testing and Evaluation, Vol. 4, No. 5, Sept. 1976, pp. 327-339.

6. Garud, Y. S.: A New Approach to the Evaluation of Fatigue Under Multiaxial Loadings. ASME Jl. of Eng. Mat. and Tech., Vol. 103, April 1981, pp. 118-125.

7. DeLuca, D. P. and Cowles, B. A.: Fatigue and Fracture of Advanced Blade Materials. AFWAL-TR-84-4167, Feb. 1985.

TABLE I

Summary of 927°C (1700°F) Crack Initiation Information Used to Evaluate PWA 1480 Life Models

Spec. ID	Condition		E GPa (ksi)	σ_t MPa (ksi)	$\Delta\varepsilon_{in}$ Percent	$\Delta\sigma$ MPa (ksi)	$\Delta\sigma$[111] MPa (ksi)	$\Delta\varepsilon E/2$ MPa (ksi)	$\sigma_t \Delta\varepsilon_{in} \frac{\Delta\sigma[111]}{E}$ Pa (psi)	<hkl>	$N_{.030} - N_{ac}$ [1] (cycles)
JB-23	+/-.3 percent	8 cpm	87.8 (12735)	280. (40.6)	.0307	556. (80.6)	185. (26.9)	263. (38.2)	181. (.0263)	<001>	8100
JB-28	+/-.34 percent	7 cpm	87.8 (12735	319. (46.1)	.0337	607. (88.1)	203. (29.4)	299. (43.3)	247. (.0358)	<001>	3080
JB-31	+/-.4 percent	6 cpm	87.8 (12735)	384. (55.7)	.0514	720. (104.4)	240. (34.8)	351. (50.9)	539. (.0782)	<001>	2875
LB-180	+/-.25 percent	10 cpm	245.1 (35550)	526. (76.3)	.1065	1035. (150.1)	1035. (150.1)	613. (88.9)	2366. (.3431)	<111>	<<3941
LB-195	+/-.2 percent	12.5 cpm	245.1 (35550)	472. (68.4)	.0285	892. (129.4)	892. (129.4)	490. (71.1)	490. (.0710)	<111>	1780
LB-236	+/-.17 percent	14 cpm	245.1 (35550)	380. (55.1)	.0172	761. (110.4)	761. (110.4)	416. (60.4)	203. (.0294)	<111>	2.2-6.1k
KB-23	+/-.25 percent	10 cpm	169.3 (24550)	418. (60.6)	.0167	816. (118.4)	544. (78.9)	423. (61.4)	224. (.0325)	<011>	2440
KB-31	+/-.2 percent	12.5 cpm	169.3 (24550)	330. (47.9)	.0137	665. (96.5)	443. (64.3)	338. (49.1)	119. (.0172)	<011>	5-20k
KB-28	+/-.3 percent	8 cpm +60 sec at +.3 percent	169.3 (24550)	299. (43.3)	.0919	903. (130.9)	602. (87.3)	508. (73.7)	975. (.1414)	<011>	1150
MB-21	+/-.25 percent	10 cpm	169.3 (24550)	416. (60.4)	.0315	808. (117.2)	692. (100.4)	423. (61.4)	536. (.0778)	<123>	2910
MB-18	+/-.3 percent	8 cpm	169.3 (24550)	505. (73.2)	.0528	973. (141.1)	834. (120.9)	508. (73.7)	1313. (.1904)	<123>	920
MB-4	+/-.3 percent	8 cpm +60 sec at +.3 percent	169.3 (24550)	343. (49.8)	.1348	926. (134.3)	794. (115.1)	508. (73.7)	2170. (.3147)	<123>	770

NOTE: All σ_t, $\Delta\varepsilon_{in}$, $\Delta\sigma$ were determined from specimen data at approximately $(N_{.030} - N_{ac})/2$ cycles.

1) $N_{.030} - N_{ac}$ = Cycles to .762mm (.030") surface crack length minus cycles to surface crack length equal to 2X coating thickness. This definition does not discriminate between N_{sc} and N_{si} failure modes.

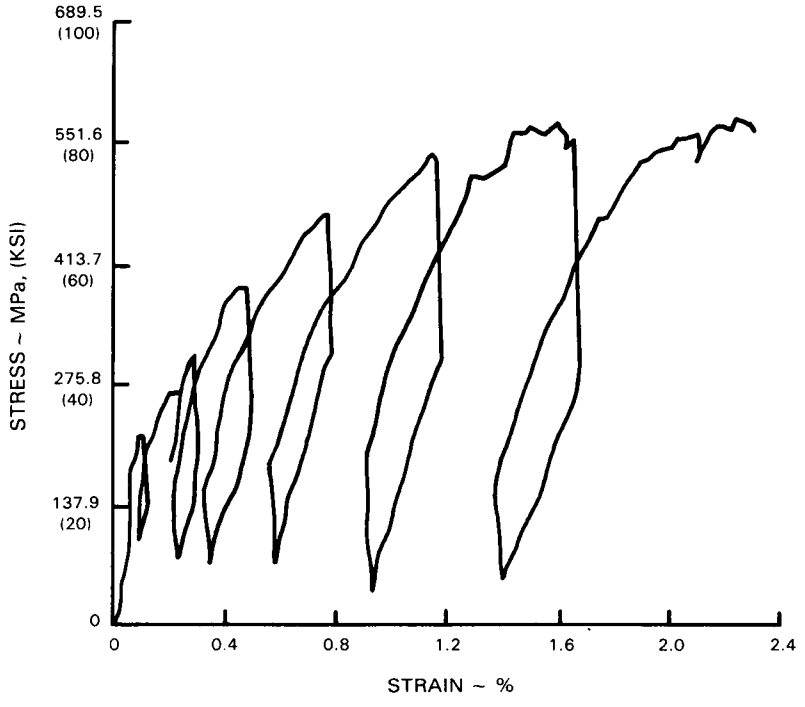

Figure 1 Stress Relaxation Test of PWA 273 Aluminide Coated 0.25 mm (0.010") <001> PWA 1480 Strip Conducted at 871°C (1600°F).

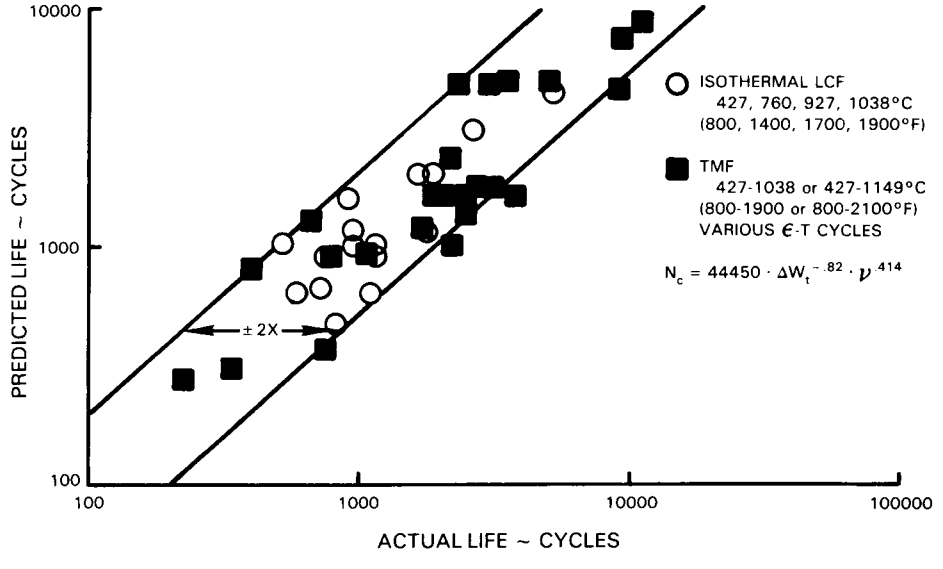

Figure 2 PWA 286 Coating Model Prediction of Isothermal LCF and TMF Life.

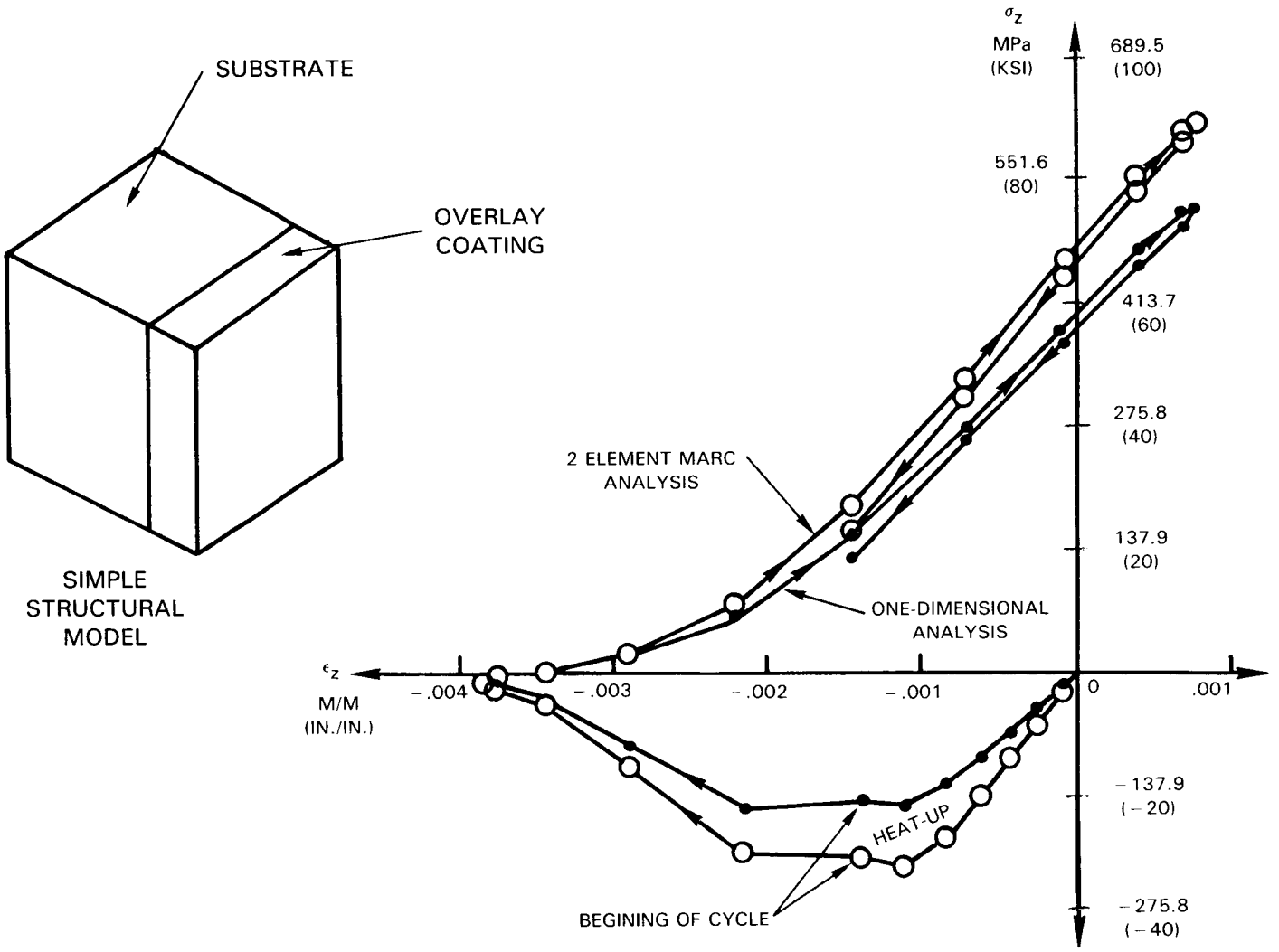

Figure 3 Predicted PWA 286 Coating Response to 427-1038C (800-1900F), ± .15%, 1 CPM, Out-of-Phase Uniaxial TMF Test.

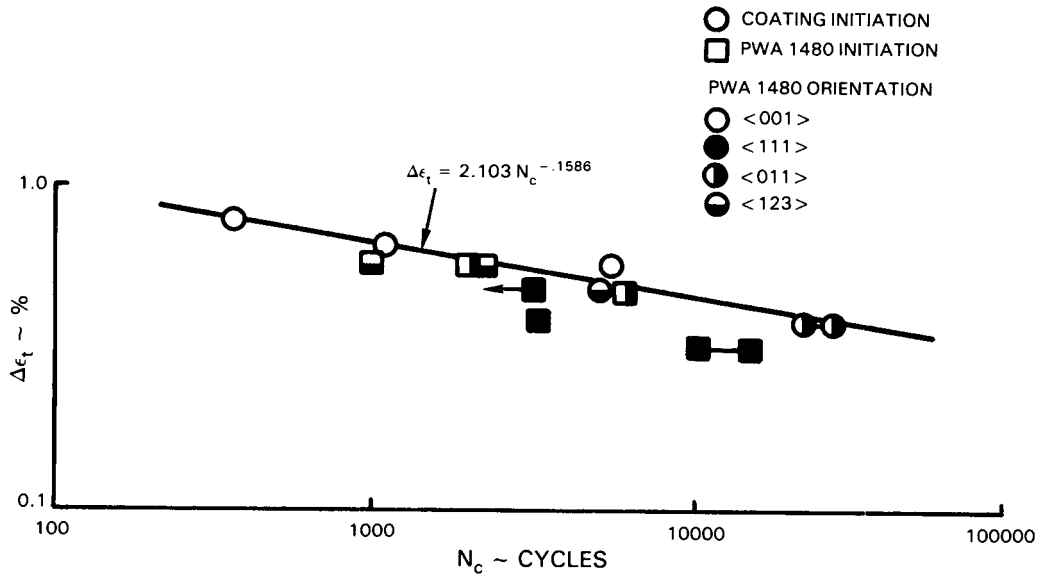

Figure 4 Total Strain Correlation of PWA 273 Aluminide Coating Cracking Life at 927C (1700F).

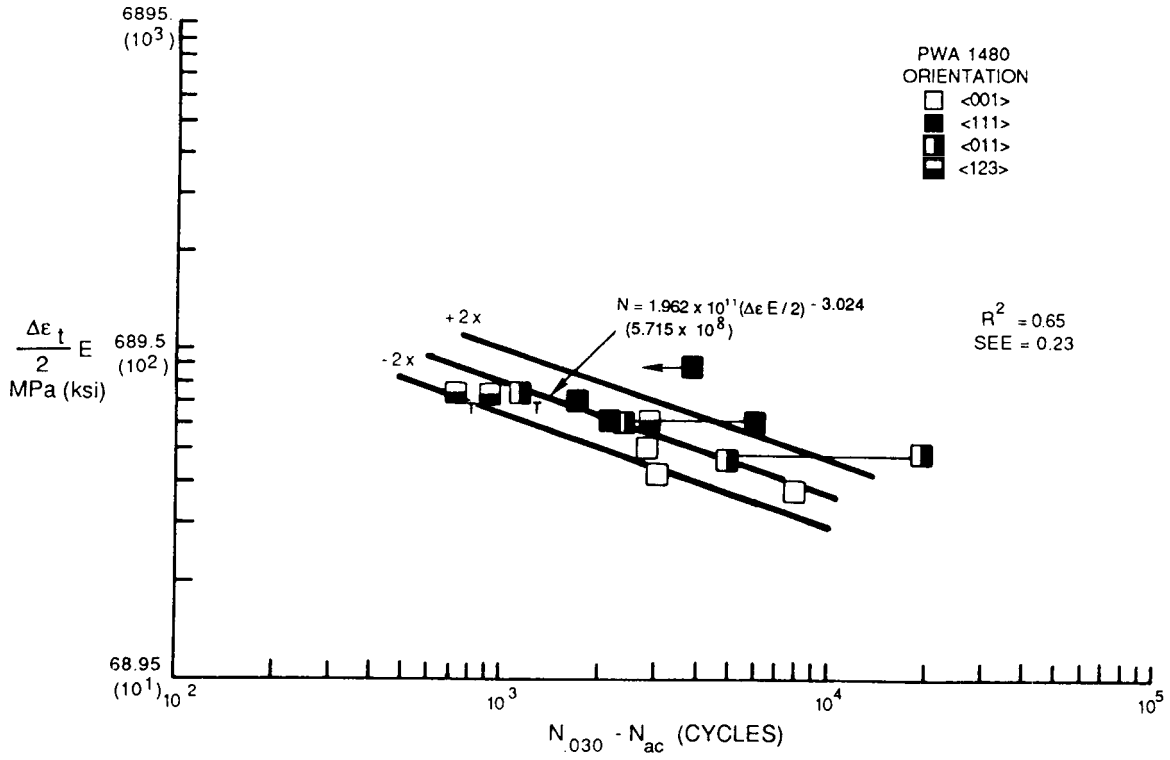

Figure 5 Modified Strain Range Model Correlation of PWA 273 Coated PWA 1480 Cracking Lives at 971C (1700F).

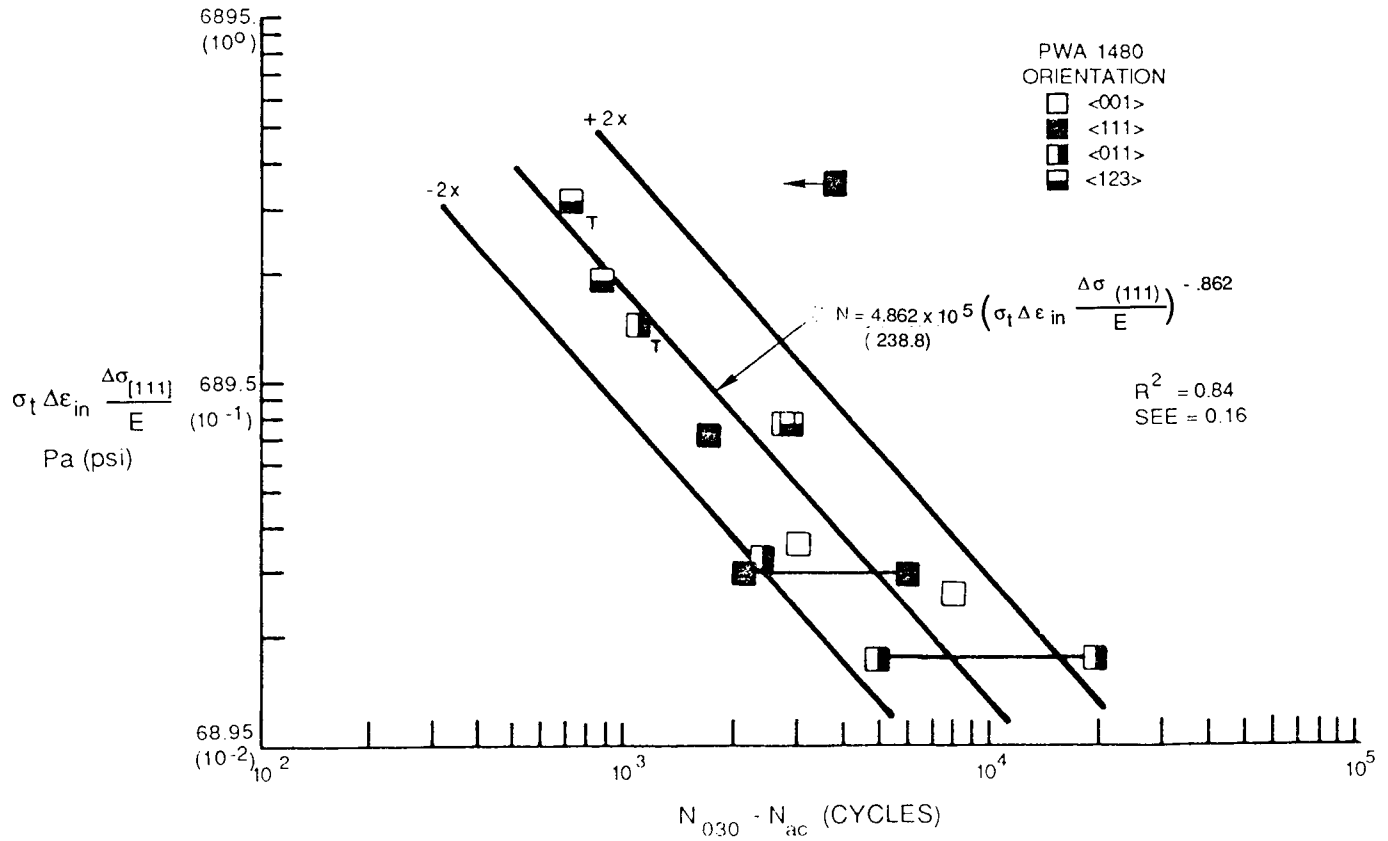

Figure 6 Modified Hysteretic Energy Model Correlation of PWA 273 Coated PWA 1480 Cracking Lives at 971C (1700F).

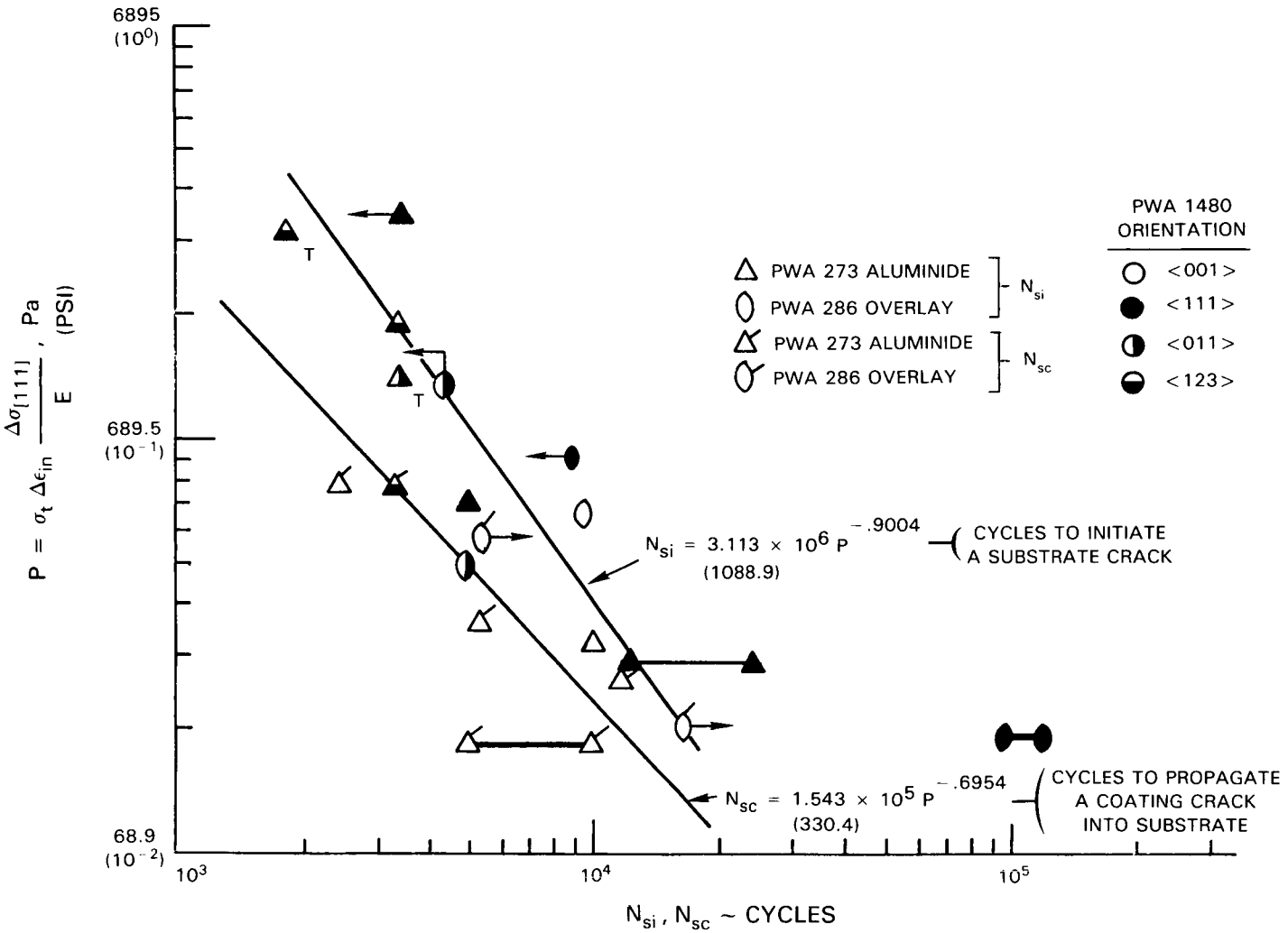

Figure 7 Modified Hysteretic Energy Approach Correlation of PWA 1480 Lives at 972C (1700F). Both N_{SC} and N_{Si} Crack Initiation Modes are Shown.

ELEVATED TEMPERATURE CRACK GROWTH*

K.S. Kim, R.H. Van Stone, S.N. Malik, and J.H. Laflen
General Electric Aircraft Engines
Cincinnati, Ohio

Critical gas turbine engine hot section components such as blades, vanes, and combustor liners tend to develop minute cracks during the early stages of operation. These cracks may then grow under conditions of fatigue and creep to critical size. Current methods of predicting growth rates or critical crack sizes are inadequate, which leaves only two extreme courses of action. The first is to take an optimistic view with the attendant risk of an excessive number of service failures. The second is to take a pessimistic view and accept an excessive number of "rejections for cause" at considerable expense in parts and down time. Clearly it is very desirable to develop reliable methods of predicting crack growth rates and critical crack sizes.

To develop such methods, it is desirable to relate the processes that control crack growth in the immediate vicinity of the crack tip to parameters that can be calculated from remote quantities, such as forces, stresses, or displacements. The most likely parameters appear to be certain path-independent (P-I) integrals, several of which have already been proposed for application to high temperature inelastic problems. A thorough analytical and experimental evaluation of these parameters needs to be made which would include elevated temperature isothermal and thermomechanical fatigue, both with and without thermal gradients.

In any investigation of fatigue crack growth, the role of crack closure should be addressed in order to develop the appropriate crack growth model. Analytically, this requires the use of gap elements in a nonlinear finite element code to predict closure loads. Such predictions must be verified experimentally through detailed measurements; the best method for measuring crack closure has not been established in previous studies.

It is the purpose of this contract (NAS3-23940) to determine the ability of currently available P-I integrals to correlate fatigue crack propagation under conditions that simulate the turbojet engine combustor liner environment. The utility of advanced fracture mechanics measurements will

*Work done under NASA Contract NAS3-23940.

also be evaluated and determined during the contract. To date, the bulk of the experimental data has been collected, and the final analytical effort is in progress. It has shown that the experimentally measured displacements and loads can be accurately predicted by finite element analyses that consider the growth of the fatigue crack. These results are being used to evaluate nonlinear fracture mechanics parameters for correlating the observed fatigue crack growth rates for different strain ranges. In previous years, the selection of Alloy 718, the specimen design and analysis, the review of the P-I integrals, and the analysis of a temperature gradient specimen test have been presented. This report will summarize only the work performed during the previous year. A final report will be released next year.

DATA ANALYSIS

During the past year, extensive analysis has been made of the isothermal and thermal mechanical fatigue (TMF) crack growth test data. The primary effort of this activity was to use the experimental results to set the boundary conditions for the finite element analyses. Also, this effort is providing a linear elastic fracture mechanics description of the data. The way in which the boundary conditions are derived will be illustrated using results for specimen N4-3, a buttonhead, single edge notch (SEN) specimen tested at 538C with a strain range of 1.15% and a strain R-ratio of -1.

BOUNDARY CONDITIONS FOR FINITE ELEMENT ANALYSIS

Figure 1 shows a schematic of the gage section of the buttonhead SEN specimen and the location of the three extensometers. It was found that the crack mouth opening displacement (CMOD) data clearly showed the cusping in the hysteresis loop, indicating the presence of crack closure. This test program was one of the first to simultaneously use different displacement measurements to detect closure. These data illustrated that the ability to detect closure was highly dependent on the location of the displacement measurement. Of the greatest significance was the apparent absence of cusping in the back face displacements. This may suggest that back face deflection is not a very sensitive technique to detect crack closure in a SEN specimen.

The points of crack closure (decreasing load) and crack opening (increasing load) were determined by numerically differentiating the data points of each CMOD hysteresis loop. When a cusp occurs, there should be a change in the slope of the load-CMOD curve and a discontinuity in the second

derivative of load and CMOD. Using a seven point sliding polynomial technique, the second derivative of load with respect to CMOD was calculated for both increasing and decreasing load situations. The point of the discontinuity was determined for both situations. Comparison of the loads at crack closure with the hysteresis loops showed that this corresponded to the cusps in the loops.

Figure 2 shows the variation of maximum load (X), minimum load (+), closure load (square), and opening load (triangle) with cycle number for Specimen N4-3. At the beginning of the test, the CMOD loop does not show much cusping and it is difficult to reliably detect the presence of closure. As the crack grows, it becomes easier to detect closure. This results in a large amount of scatter in the opening and closure loads early in the test.

The finite element analyses were performed in two stages. The first was to use the maximum and minimum deflection boundary conditions as two load cases per cycle. A node releasing technique was used to permit the crack to propagate across the entire specimen, releasing two nodes per cycle. The purpose of this analysis was to build up the history-dependent crack surface wake. The results of this analysis were stored off and used as the starting point of more detailed finite element analysis. The second stage analysis was done at two fixed crack lengths. Ten loading steps were introduced to predict the occurrence of crack closure and opening. The P-I integrals were computed for these loading steps.

It was previously determined that the boundary conditions for this specimen geometry are linear displacements along the positions of the control and back face extensometer contact (6.4 mm above and below the plane of the crack). The displacements are determined by extrapolation of the control and back face extensometer readings. During a given cycle, the degree of bending increases with increasing load and deflection, resulting in a variation in the slope of the specimen deflections within a cycle. Thus, the experimental data were used to select the boundary conditions for these more extensive cyclic analyses.

The boundary conditions for the coarser finite element analysis were determined by iterating between the available data points. The solid line in Figure 3 shows the variation in crack length (a) with cycle number. The crack length positions corresponding to the finite element node locations are shown as triangles. The cycle count at these positions was calculated by linear interpolation between the actual data points. In a similar fashion, the maximum and minimum deflections corresponding to the interpolated cycle number were also calculated. The interpolated values were used as the boundary conditions for the coarser finite element analysis. A similar interplolation was also performed for loads and CMOD. These values were compared to those calculated from the finite element analysis.

Two crack lengths were selected from each test specimen to perform the more extensive cyclic analysis. Based on the crack growth rate data, the crack lengths of 0.95 and 2.54 mm were selected to provide a significant difference in crack length, bending strain, and crack growth rates. A total of 40 boundary conditions were obtained to describe the strain cycle for both crack lengths. These conditions were determined by placing a load case at maximum and minimum deflection, crack closure deflection, and crack opening deflection. Nine other load cases were placed between each of the following:

1. minimum and crack opening deflection
2. crack opening and maximum deflection
3. maximum and crack closure deflection
4. crack closure and minimum deflection

The load case positions were separated by a constant amount of CMOD within each of the four segments listed above. This is shown schematically in Figure 4 where the closed points indicate the four end points mentioned above. In the finite element analysis, 10 load cases were selected from the total set of 40.

This procedure was performed for the cycles on each side of the desired crack lengths. As in the case of the coarser boundary conditions, a linear interpolation was performed between the two experimental hysteresis loops. The remote displacements were reported at the same positions in the hysteresis loops.

FINITE ELEMENT RESULTS

Finite element simulations of crack growth at 538C were done for three ranges of strain: 0.5%, 1.15%, and 1.7%. These analyses used the GE-AE finite element code called CYANIDE. The crack was propagated from the initial length 0.32 mm to 2.54 mm with increments of 0.32 mm at each tensile peak. The computed and experimental loads were compared at the tensile and compressive peaks at different crack lengths. The correlations were very good for all three cases. The CMOD was also examined at different crack lengths, and a good agreement was again found between the analysis and test. The load versus crack length and the CMOD versus crack length plots are given in Figure 5 and Figure 6, respectively, for the medium strain range. The crack closure and opening analysis was made at two crack lengths (0.95 mm and 2.54 mm). The nominal stress (load/cross-sectional area) versus CMOD loops were plotted for all the cases, and they were compared with test results. In general, the computed load-displacement loop agreed

well with the test loop except for a shift in the CMOD measure. The reason for this is currently under investigation, but it is believed to be related to the cracks growing in a stable shear mode. The analysis predicted the closure and opening points within acceptable accuracies. The predicted loops for the medium strain range are compared with the experimental data in Figures 7 and 8 for the two different crack lengths of 0.95 mm and 2.54 mm. In constructing these figures, the experimental data were shifted by a constant amount to agree with the analytical predictions at the minimum load point.

CONCLUSIONS

As in previous reports, the prior year efforts are showing excellent progress toward the contract objectives. The finite element and test correlations demonstrate that an excellent, well understood set of consistent data has been generated. These data should lead to understanding the growth of cracks under cyclic conditions in the inelastic range. Currently, efforts are being directed toward utilizing the finite element results to evaluate the correlative ability of current nonlinear fracture mechanics parameters.

Additionally, analysis will be completed of the TMF data, and a final report will be written during the coming year.

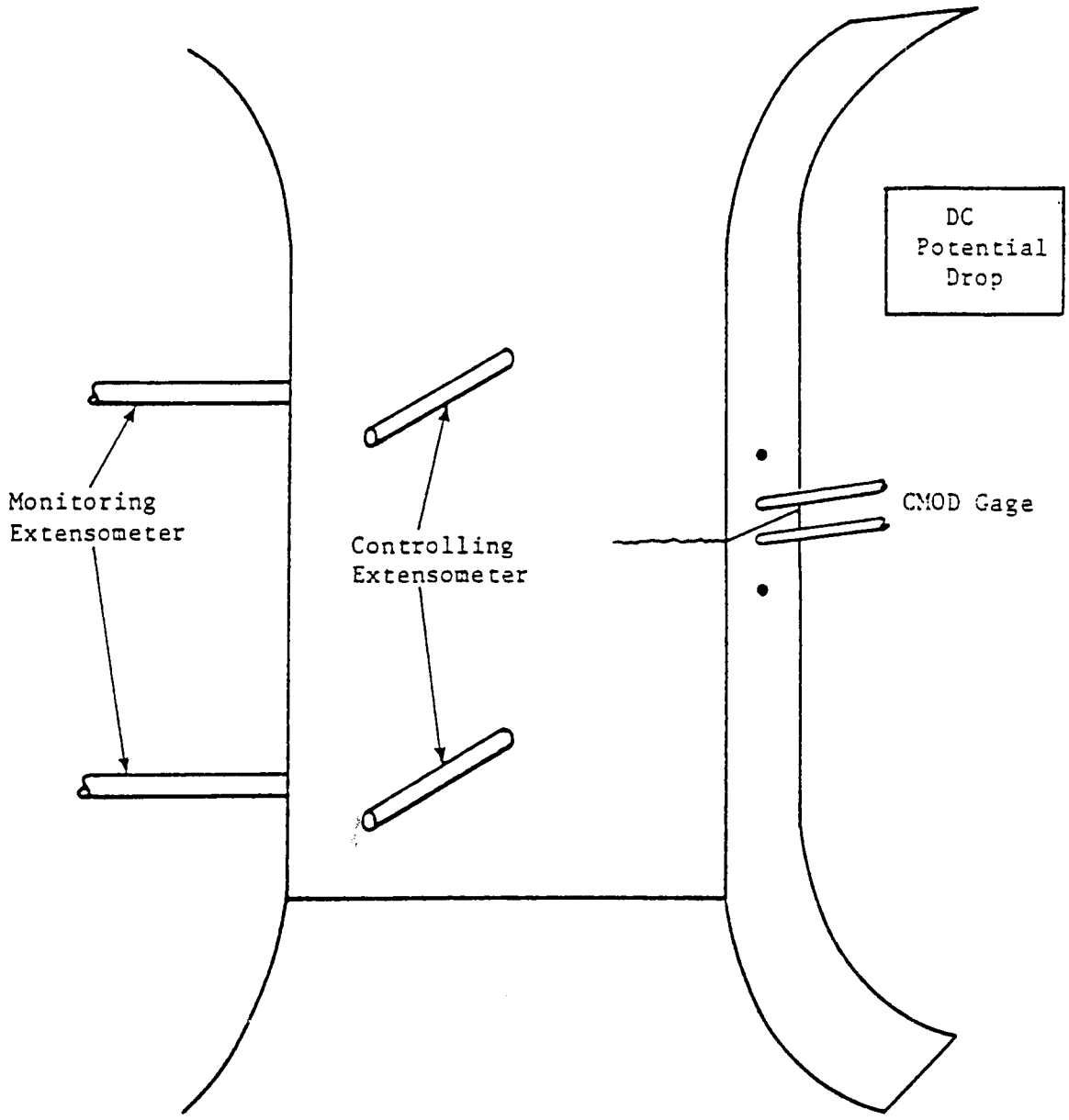

Figure 1. Schematic Drawing of SEN Test Method.

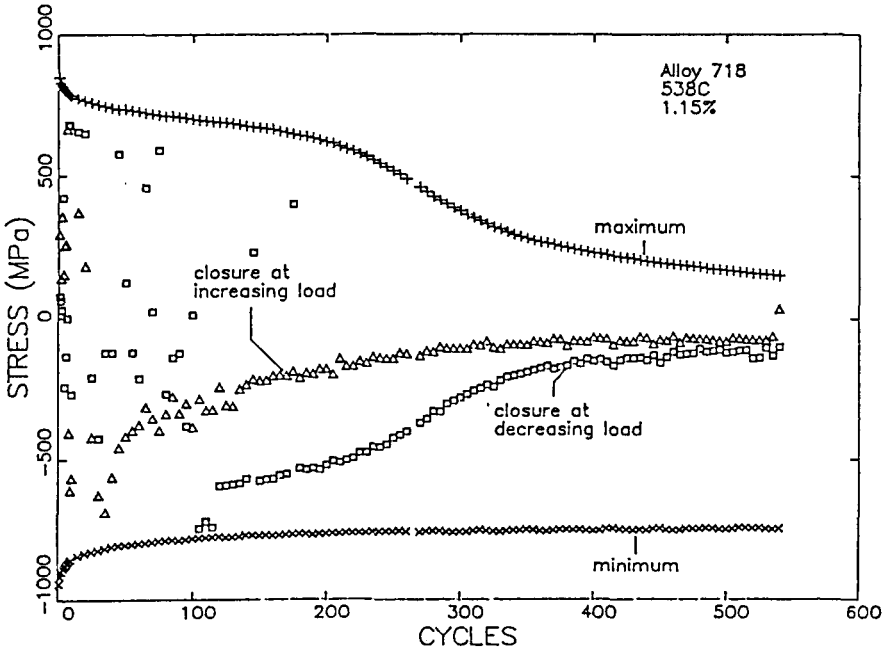

Figure 2. Derived Closure Stress Points Compared to Maximum and Minimum Loads from Specimen N4-3

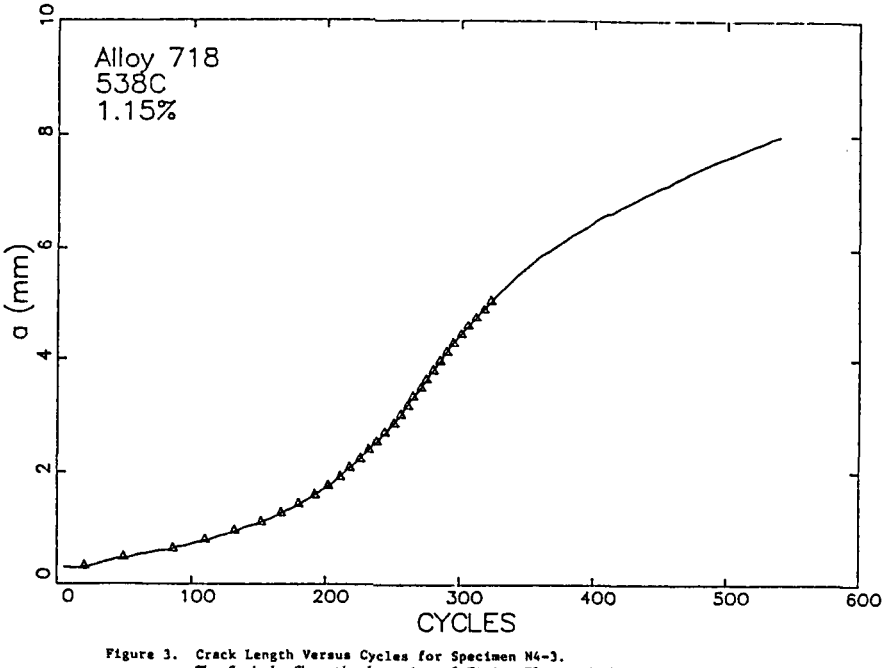

Figure 3. Crack Length Versus Cycles for Specimen N4-3. The Symbols Show the Location of Finite Element Node Points.

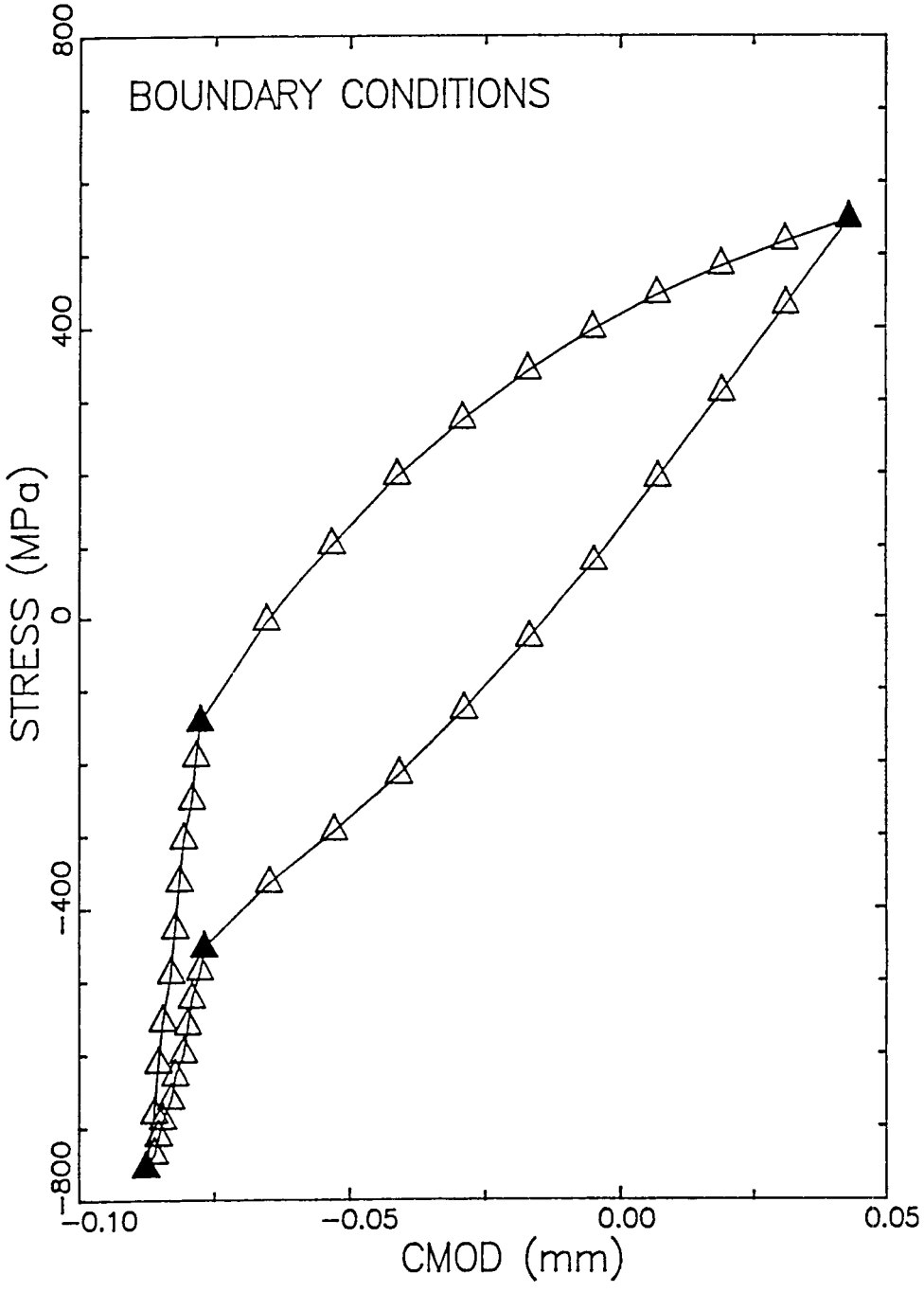

Figure 4. Selection of Boundary Conditions.

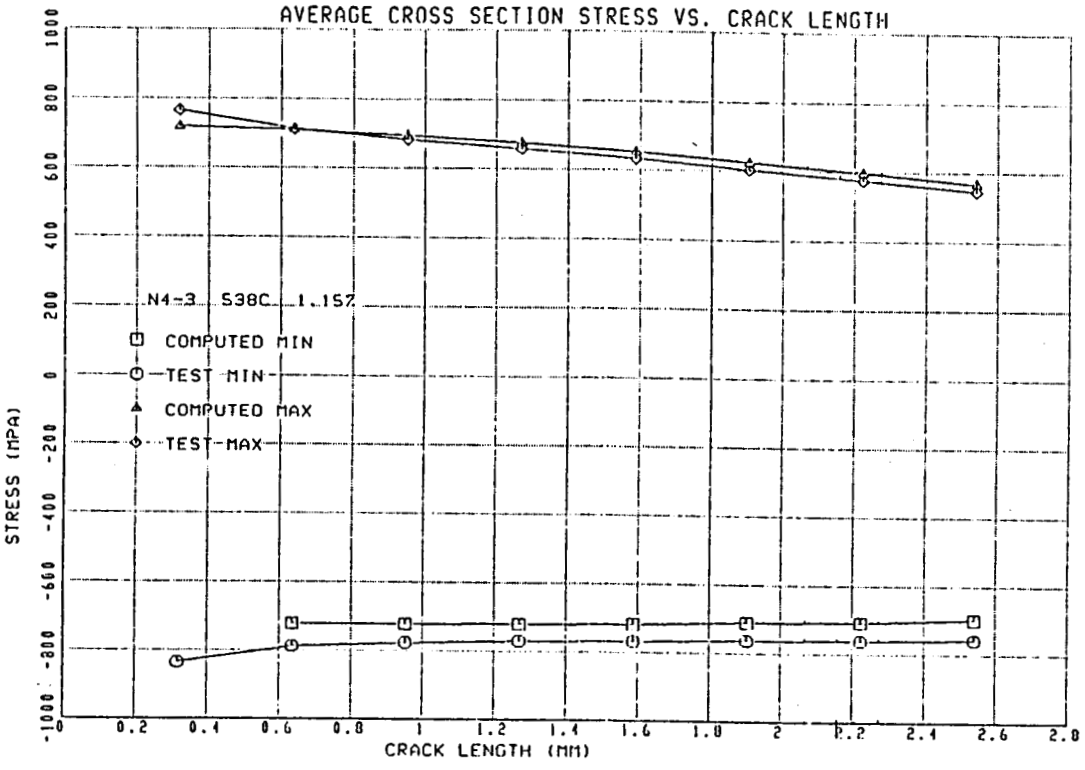

Figure 5. Predicted Stress As A Function of Crack Length - Coarse FEM

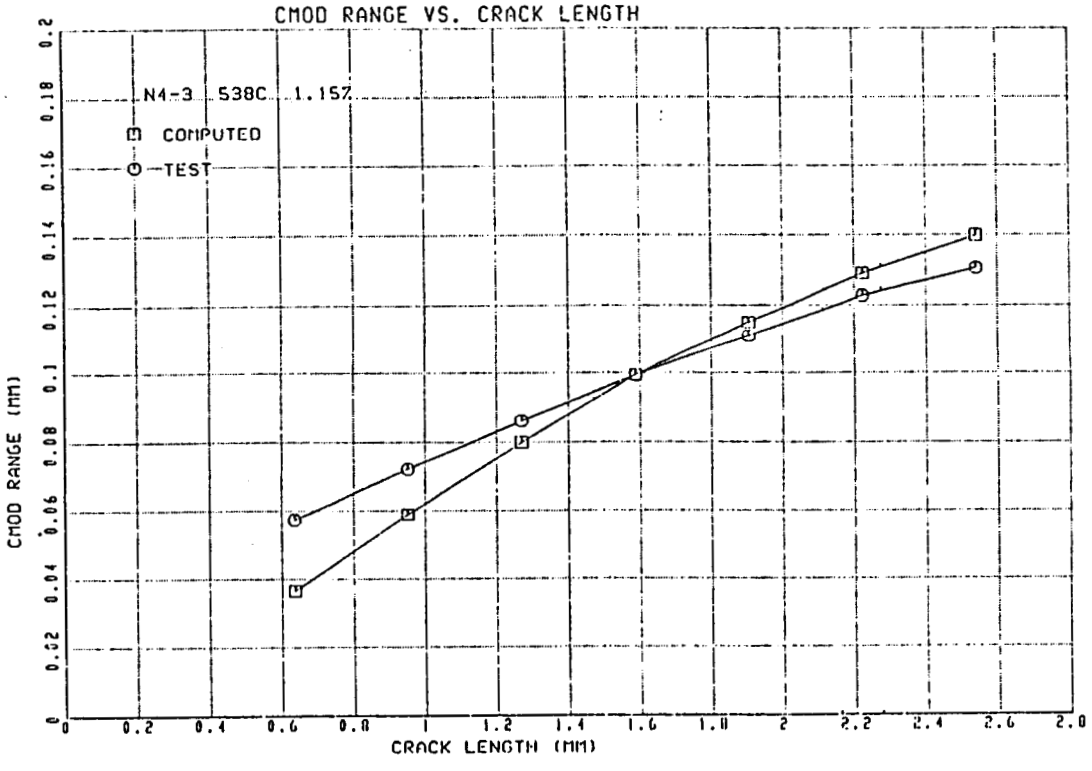

Figure 6. Predicted CMOD Range Versus Crack Length - Coarse FEM

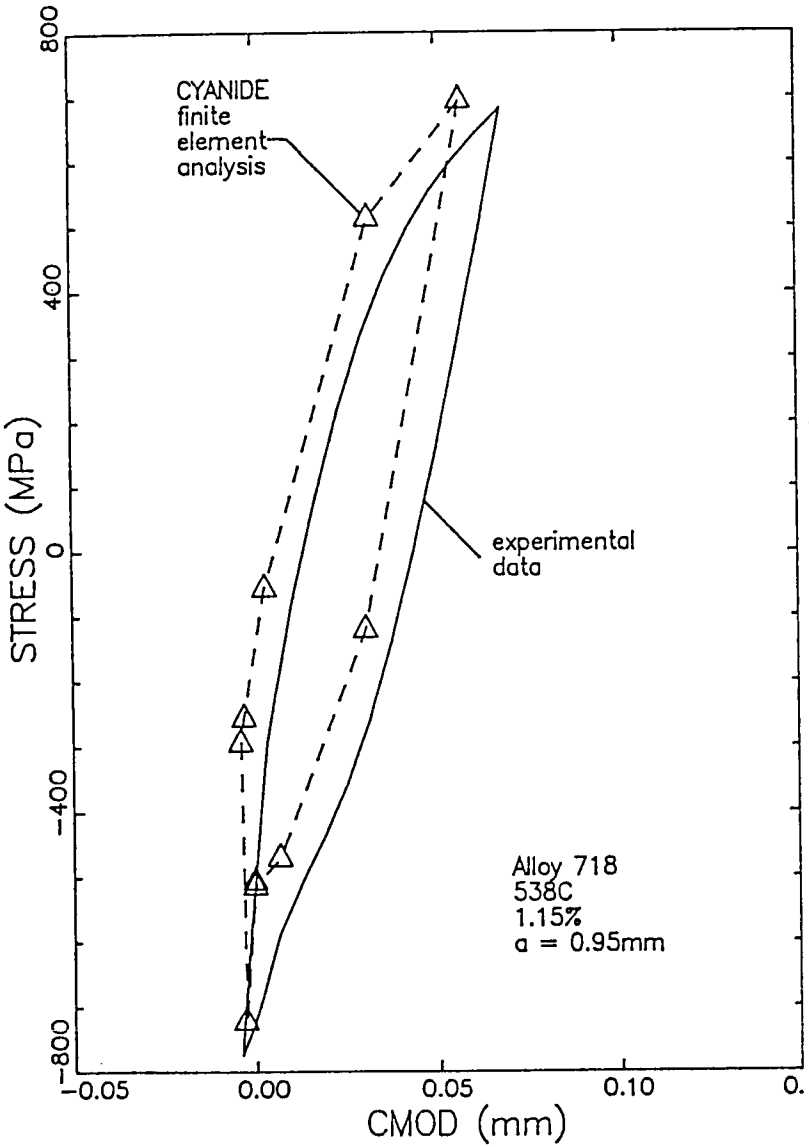

Figure 7. Comparison of Predicted and Experimentally Observed Stress-CMOD Hysteresis Loops for a Crack Length of 0.95 mm.

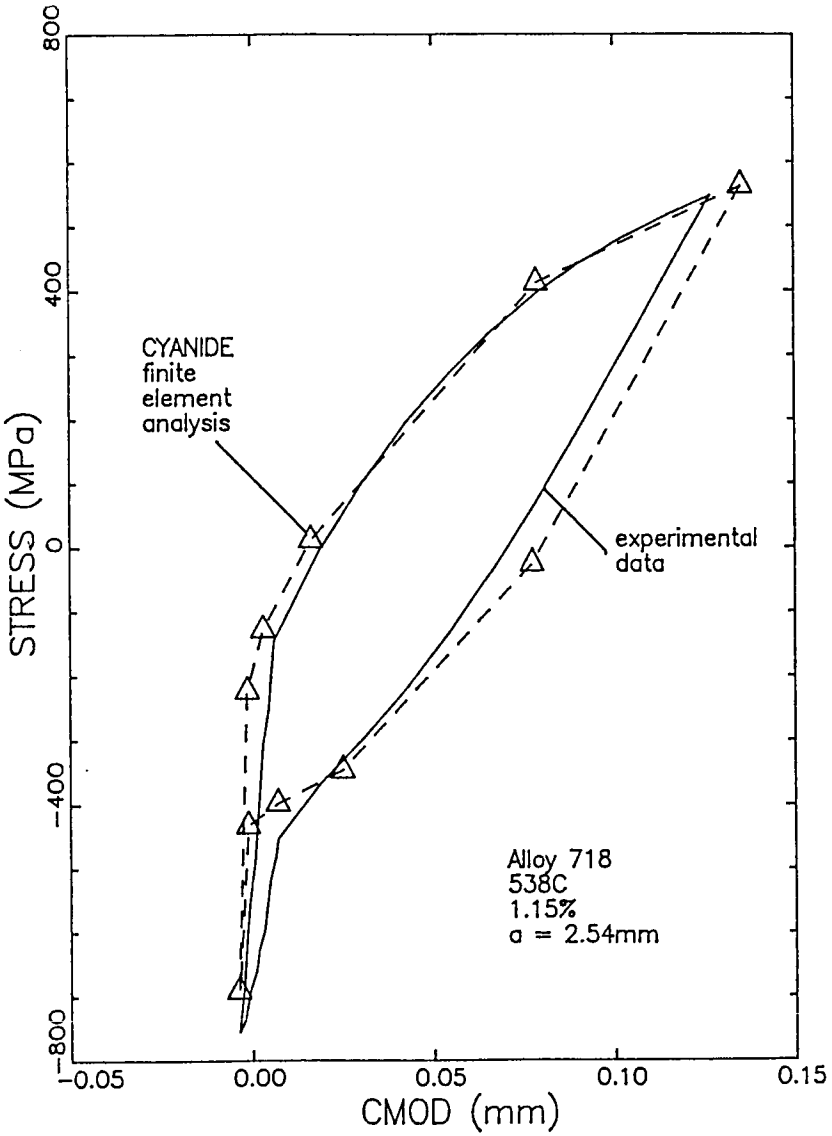

Figure 8. Comparison of Predicted and Experimentally Observed Stress-CMOD Hysteresis Loops for a Crack Length of 2.54 mm.

CREEP FATIGUE LIFE PREDICTION FOR ENGINE HOT SECTION MATERIALS (ISOTROPIC) FIFTH YEAR PROGRESS REVIEW*

Richard S. Nelson and Peter R. Harvey
Pratt & Whitney Division
United Technologies Corporation
East Hartford, Connecticut

As gas turbine technology continues to advance, the need for advanced life prediction methods for hot section components is becoming more and more evident. The complex local strain and temperature histories at critical locations must be accurately interpreted to account for the effects of various damage mechanisms (such as fatigue, creep, and oxidation) and their possible interactions. As part of the overall NASA HOST effort, this program is designed to investigate these fundamental damage processes, identify modeling strategies, and develop practical models which can be used to guide the early design and development of new engines and to increase the durability of existing engines.

This contract has recently been modified to be a 6-year effort, consisting of a 2-year base program and a 4-year option program. Two different isotropic materials (B1900+Hf and INCO 718) will be used, along with two protective coating systems (overlay and diffusion aluminide). The base program, which was completed during 1984, included comparison and evaluation of several popular high-temperature life prediction approaches as applied to continuously cycled isothermal specimen tests. The optional program, of which three years have been completed, is designed to develop models that can account for complex cycles and loadings, such as thermomechanical cycling, cumulative damage, multiaxial stress/strain states, and environmental effects. The base program has already been discussed in reference 1 and therefore no additional review of that work will be presented in this paper.

THERMOMECHANICAL MODEL DEVELOPMENT

A significant task under the option program is the development of a life prediction model which is valid under conditions of thermomechanical fatigue (TMF). The specimen testing under this task was completed in December, 1986, with a total of 55 B1900+Hf TMF specimen tests. Of these, 32 specimens were tested in the uncoated condition, 12 had NiCoCrAlY overlay coating, and 11 had

*Work done under NASA Contract NAS3-23288

diffusion aluminide coating. The test variables included strain range, temperature range, mean strain, cycle type, and hold times. The conditions were chosen to complement both the uncoated TMF tests and the baseline isothermal fatigue tests. Particular attention was focused on the low strain, high life regime, since modern turbomachinery is typically designed for good durability. Some of the non-standard cycle types used (such as elliptical and dogleg cycles) have demonstrated that TMF damage cannot always be predicted in the same manner as isothermal tests. The model chosen must be sensitive to accumulation of damage from any arbitrary strain-stress-temperature cycle and yet be practical for use in design applications.

Ten baseline coated TMF specimen tests were completed at two nominal strain ranges, using both in-phase and out-of-phase cycling. The temperature range was 538-871°C (1000-1600°F), and the cyclic rate was 1 CPM. Both fully reversed and one-way compression strain cycles were used, but there was no obvious effect of mean strain on specimen life. A plot of initiation life vs. total mechanical strain range is shown in Figure 1, along with median life lines from uncoated TMF tests at the same conditions. Note that the coated data lie approximately 2X higher in life than the uncoated data, indicating that for these conditions, the coatings reduced the damage done by mechanisms such as oxidation. It is known, however, that the reverse is often true: coatings can themselves reduce the life under certain TMF strain cycles. For example, a "dogleg" cycle overlay coated specimen test was also run, using a non-isothermal strain hold at the minimum cycle strain combined with a rapid (6 second) fully reversed isothermal strain excursion at the minimum temperature. This test produced an initiation life which was lower than what had been observed for an uncoated specimen. This once again serves to emphasize the need to understand and model the actual damage mechanisms active under these conditions. Simple data correlations based on one or the other cycle type may not always give conservative predictions.

Perhaps the most interesting results obtained during this task are those from the elliptical cycle tests (strain and temperature are sinusoidal with time and shifted in phase by $\pm 135°$). Five coated specimen tests were completed under this series, including two clockwise (CW) and three counterclockwise (CCW) cycles. The CCW cycle is a good simulation of the strain-temperature history experienced by many actual hot section components. Although there are some components which have a CW movement around their strain-temperature history, the CW cycle results are most valuable when compared to the CCW results; the only apparent difference is the direction of motion around the loop. Figure 2 shows a plot of the elliptical test results for the coated specimens relative to the median lives from the out-of-phase coated tests. It is clear that there is approximately a 5X initiation life difference between the two types of cycles. Note that life prediction methods based solely on the extremes of the cycle will not be able to predict this behavior, since they cannot distinguish between these two cycles. To account for such cycle dependent effects, an advanced incremental form of the CDA life prediction model is under development which can be integrated around any arbitrary strain-temperature history curve. Four other coated specimens were also run using various types of TMF cycles involving both isothermal and non-isothermal hold times. These also showed strong effects of cycle path on initiation life.

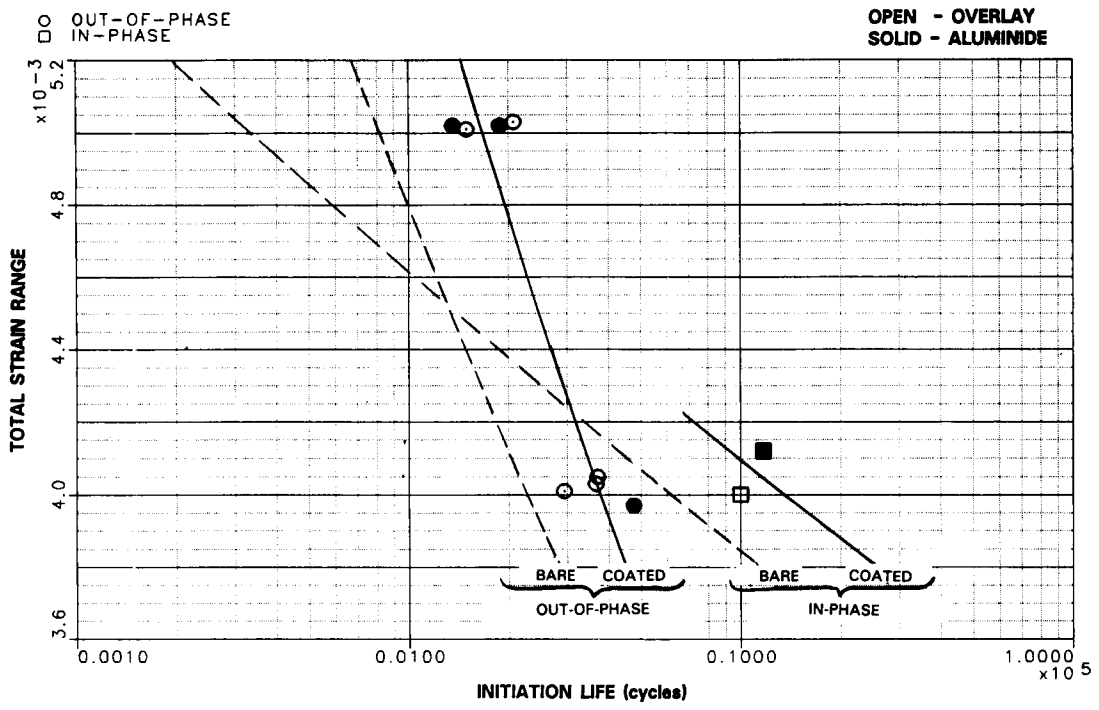

IN-PHASE AND OUT-OF-PHASE TMF TESTS
(PWA 1455, 1000-1600°F, 1 CPM)

FIGURE 1

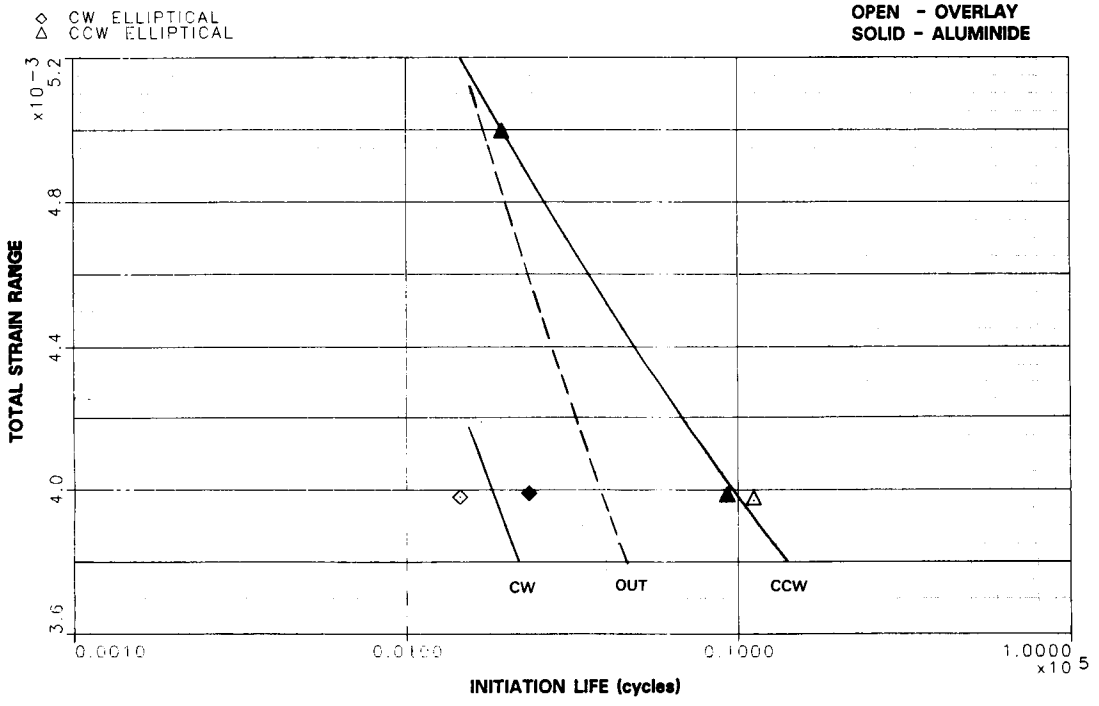

ELLIPTICAL CYCLE TMF TESTS
(PWA 1455, 1000-1600°F, 1 CPM)

FIGURE 2

Four other coated specimens were run at a higher temperature range (1000-1800°F) to determine if trends seen at the baseline temperature range would still hold true. Figure 3 shows these results, and all the data are seen to be shifted lower in life than the median data at the baseline temperatures. However, note that the life increase for an elliptical cycle relative to an out-of-phase cycle is still present.

Figures 4 and 5 show optical micrographs of fracture surfaces typical of those observed during the coated TMF testing. In general, the fracture surfaces were heavily oxidized, making exact determination of the location of the crack origin difficult. However, the typical crack initiation site was in the coating surface, often accompanied by either localized porosity or small allowable defects in the coating. The lives from specimens which failed from ID-initiated cracks were adjusted to reflect the growth of cracks on the coated OD surface only.

Several modifications to the basic Cyclic Damage Accumulation life prediction model developed during the base program are being considered, including conventional cyclic variable methods and incremental techniques. Figure 6(a) shows a correlation of initiation life data from the uncoated TMF testing using total strain range alone, and Figure 6(b) shows the same data correlated using the stress range and the maximum stress as additional parameters as used by the CDA model. Figure 7 shows the same correlations for the coated TMF data. In both cases, the correlation is improved using the additional parameters, but obviously more work is needed to ensure good predictions in cases where no data is available for reference. Work is continuing on the incremental model, which is expected to be able to meet this goal.

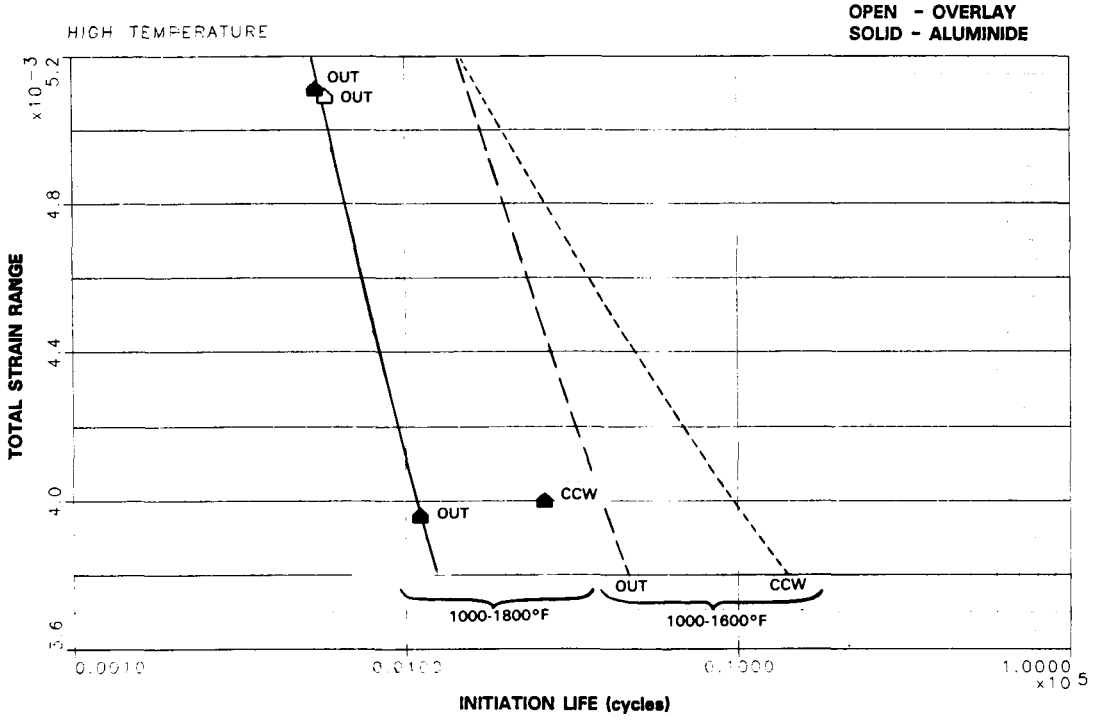

HIGH TEMPERATURE RANGE TMF TESTS
(PWA 1455, 1000-1800°F, 1 CPM)

FIGURE 3

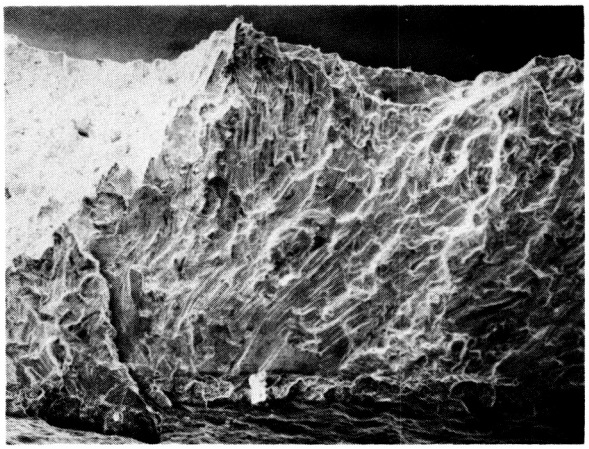

(a) 0.5 mm / 50X

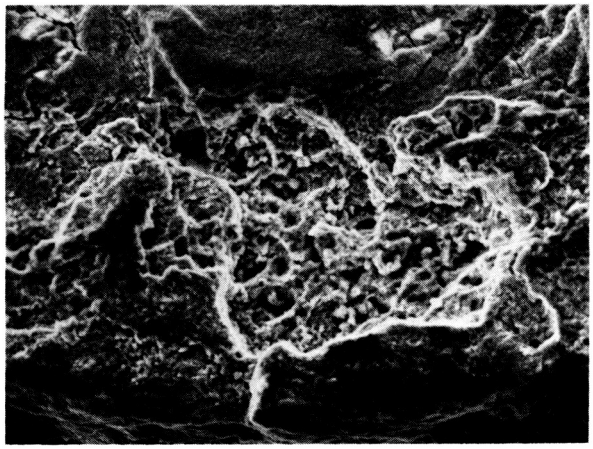

(b) 40 μm / 500X

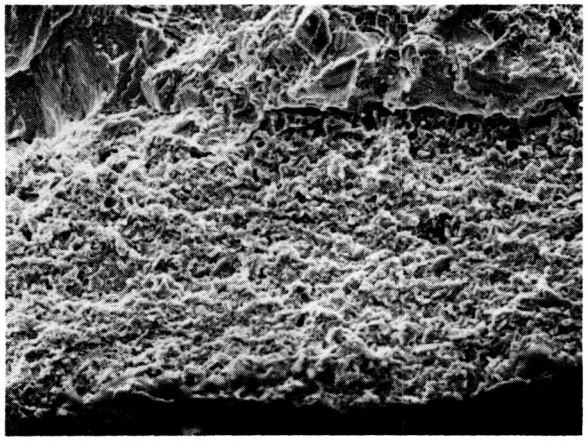

(c) 40 μm / 500X

PWA 286 COATED TMF SPECIMEN 120B. Cycle I, $\Delta\varepsilon$ = 0.4%, 1000-1600°F, R=-1, INITIATION LIFE = 2938 CYCLES.

(a) SEM Micrograph of O.D. Initiation Site.
(b) Higher Magnification of (a) Showing Porous Appearance of Coating in Initiation Area
(c) SEM Micrograph of Coating in Area Fractured at Room Temperature

FIGURE 4

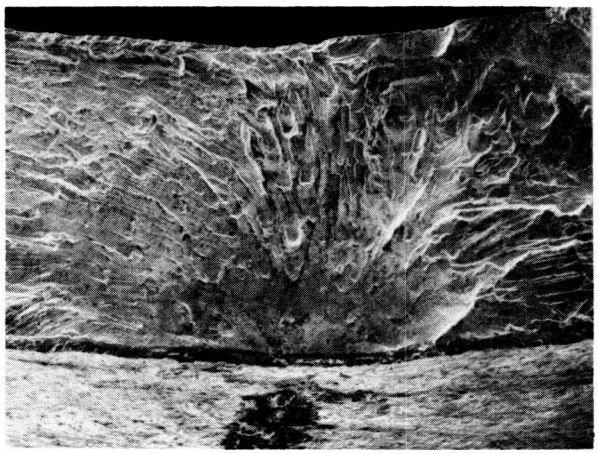

0.5 mm / 50X

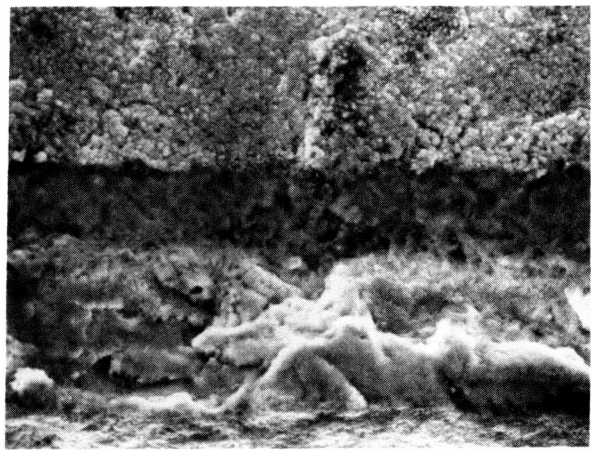

20 μm / 1000X

PWA 273 COATED TMF SPECIMEN 114A. Cycle I, $\Delta\varepsilon$ = 0.4%, 1000-1600°F, R=1, Initiation Life = 4753 Cycles. SEM Micrographs of Primary O.D. Initiation Site. Dark Band Between Coating and Base Metal is the Diffusion Zone.

FIGURE 5

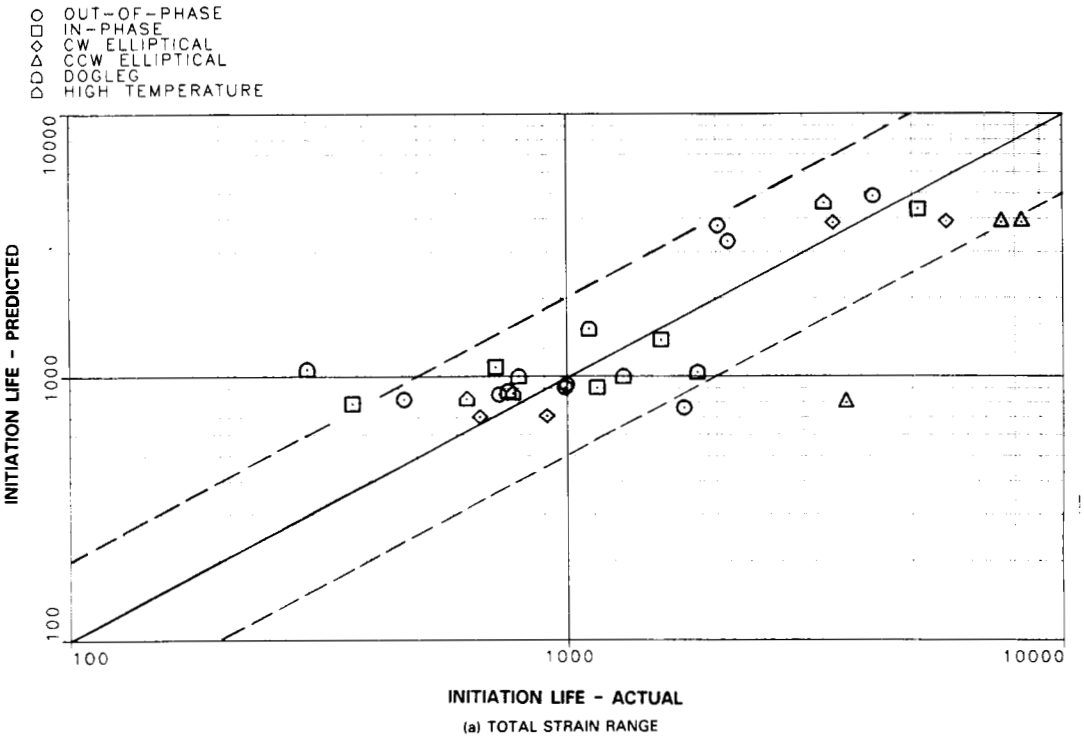

(a) TOTAL STRAIN RANGE

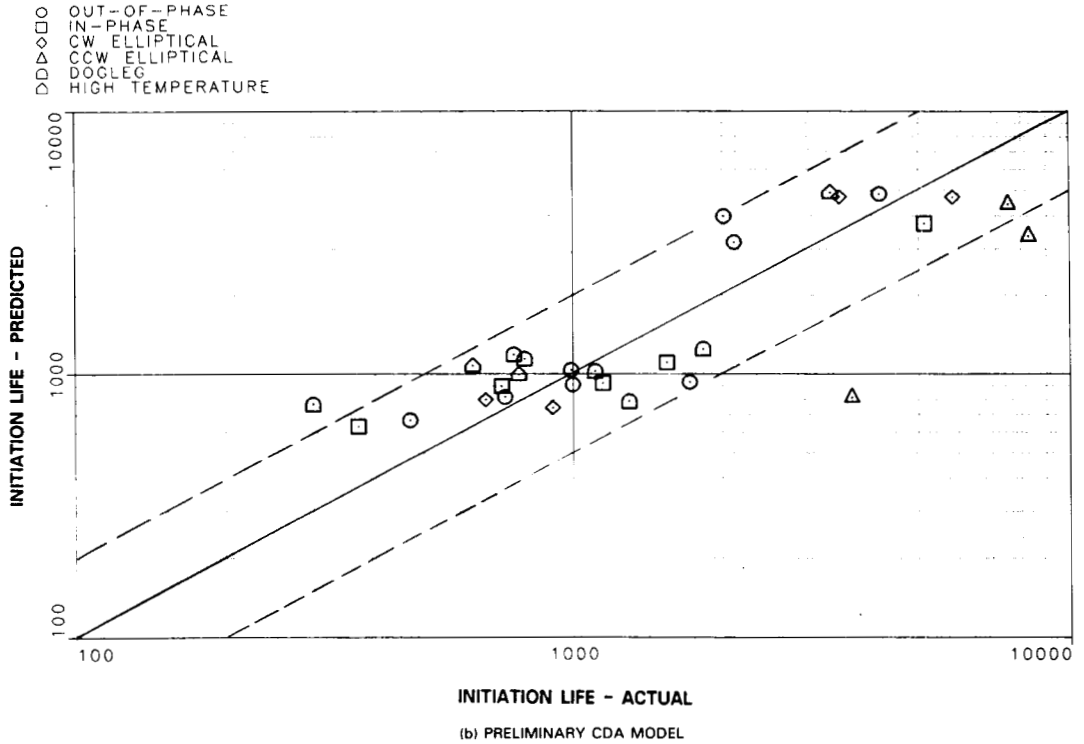

(b) PRELIMINARY CDA MODEL

TMF LIFE MODEL COMPARISONS FOR UNCOATED PWA 1455

FIGURE 6

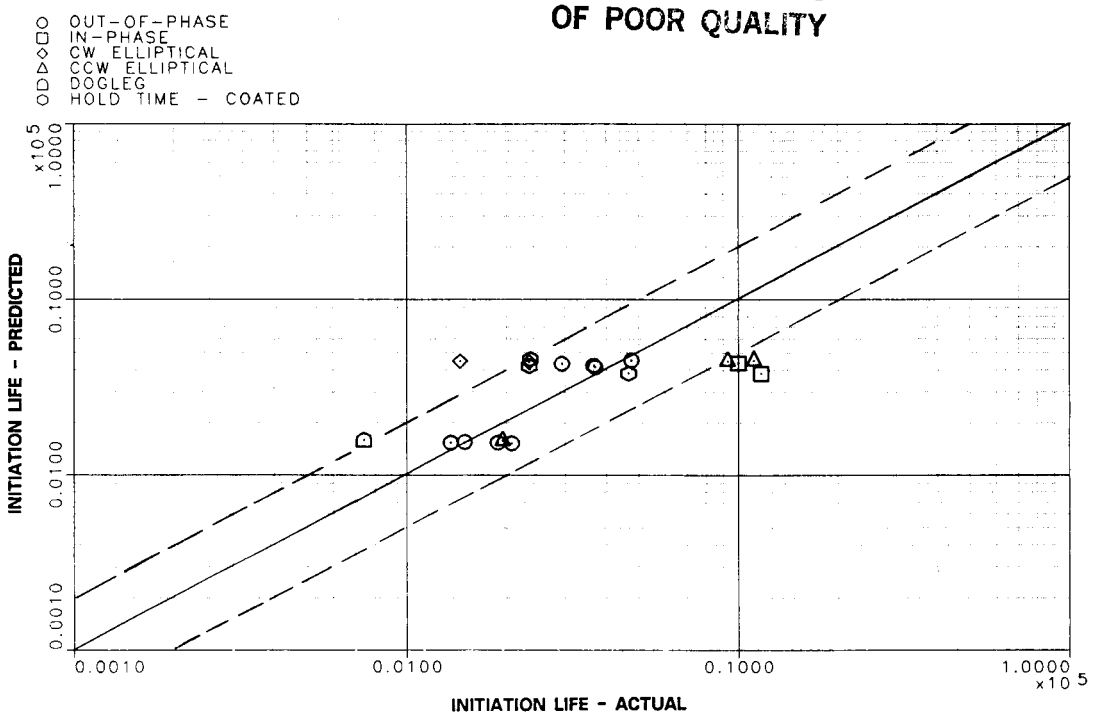

(a) TOTAL STRAIN RANGE

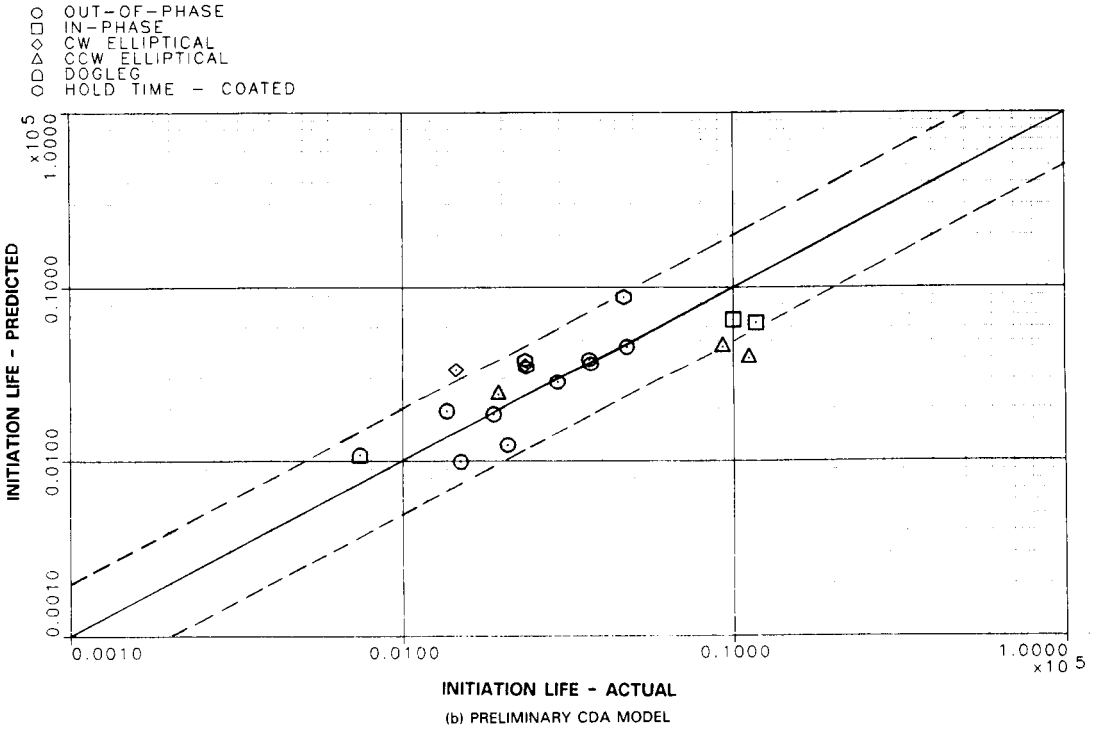

(b) PRELIMINARY CDA MODEL

TMF LIFE MODEL COMPARISONS FOR COATED PWA 1455

FIGURE 7

The specimen testing portion of this task has now been completed, comprising a total of 26 tests using thin-walled (0.050 in.) tubular specimens. Four types of strain cycles were employed in these tests: simple tension, simple torsion, combined in-phase tension-torsion (proportional loading), and combined 90° out-of-phase tension-torsion (non-proportional loading). The torsion-to-tension ratio was 1.5 for all the combined strain tests. The additional variables investigated were temperature, strain range, and strain rate. Figure 8 shows a typical dislocation structure for an out-of-phase, non-proportional test, showing wavy dislocation segments that are roughly parallel to one another and surrounding the gamma prime particles. This structure is similar to what was observed following both pure torsion and in-phase proportional tests.

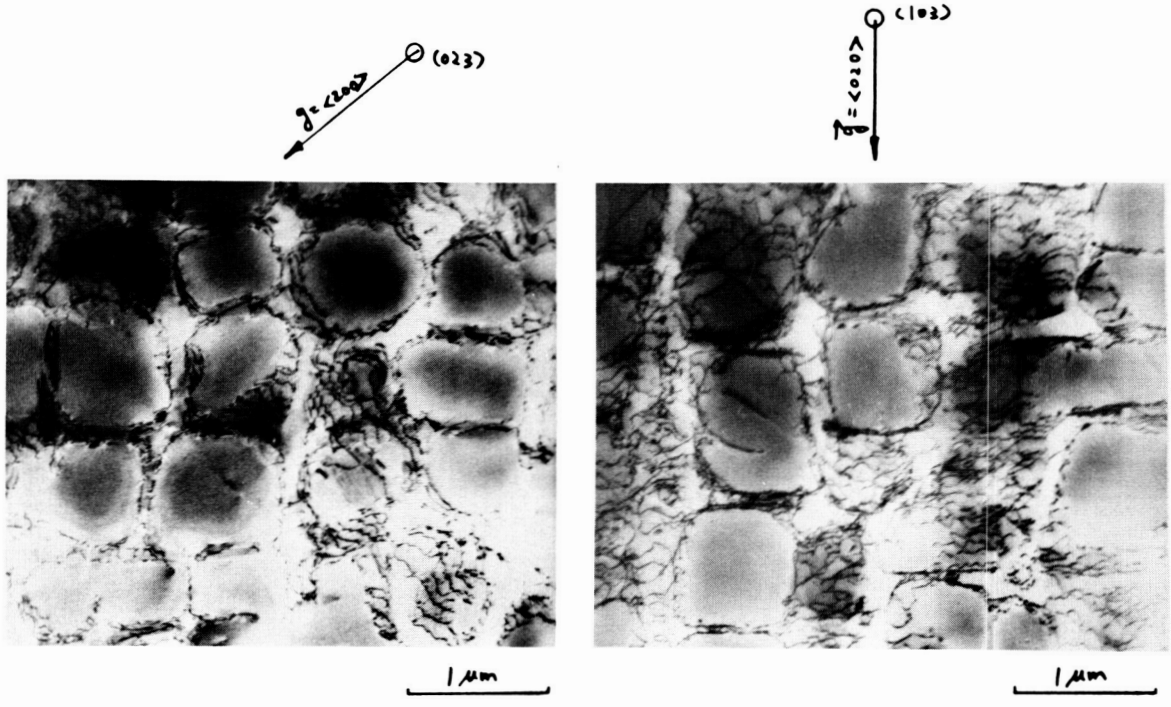

MULTIAXIAL SPECIMEN 216 DISLOCATION STRUCTURE AFTER 90° OUT-OF-PHASE TENSION-TORSION TESTING (1600°F, $\Delta\varepsilon = \pm 0.250\%$, $\Delta\gamma = \pm 0.375\%$, 90° Out-of-Phase, 10CPM, Initiation Life = 1250 Cycles, Total Test Life = 1973 Cycles).

FIGURE 8

Several data correlation methods have been investigated for the multiaxial loading tests, including equivalent strain, maximum shear strain, plastic work, and maximum normal strain range. The first three parameters had only limited success, due in part to their inability to predict correctly the somewhat higher lives resulting from the pure torsion tests. Also, the data showed very little cyclic inelasticity, which made any theory based on inelastic quantities

very difficult to apply. Figure 9 shows the results of the testing at both 1000°F and 1600°F correlated using maximum normal strain range. The data is fairly well grouped, with the out-of-phase tests and the axial data being the lowest. The in-phase tension-torsion and the simple torsion tests still tend to be somewhat higher than the other conditions, but the sample size is too small to draw statistically significant conclusions. Note that the effect of cyclic rate is evident at both temperatures; no effect of cyclic rate was observed during the baseline uniaxial testing at 1000°F.

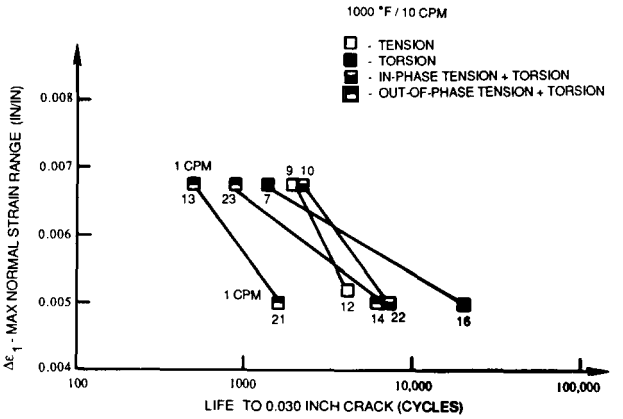

Maximum Normal Strain Range vs Cyclic Life
(a) 1000°F Tests

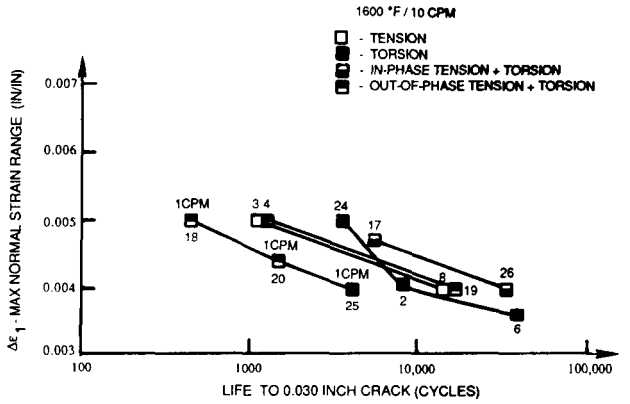

Maximum Normal Strain Range vs Cyclic Life
(a) 1600°F Tests

PWA 1455 MULTIAXIAL TESTS

FIGURE 9

ENVIRONMENTAL ATTACK MODEL

A controlled atmosphere creep-fatigue test matrix with 27 specimen tests has been determined for this task. The initial 9 screening tests are being conducted in three different environments: lab air, high pressure oxygen (same partial pressure as encountered in high pressure turbines), and high purity argon. The remaining 18 tests will use the environment which produces the largest effect and will examine sequence effects to support development of an advanced life model which can account for the observed life trends.

The stainless steel, low pressure chamber for this task has been completed and overpressure tested. Figure 10 shows the water-cooled MTS extensometer in place in front of the specimen. A total of 8 initial screening tests in lab air and 75 psia oxygen have been completed at baseline conditions at both 1600 and 1800°F. The lives in the high pressure oxygen are less than half of the baseline values for the slow rate tests, indicating a strong environmental effect on fatigue life under these conditions. The chamber has now been fitted with a Centorr argon purifier to assure very low oxygen levels, and initial trials show that the environment is satisfactory.

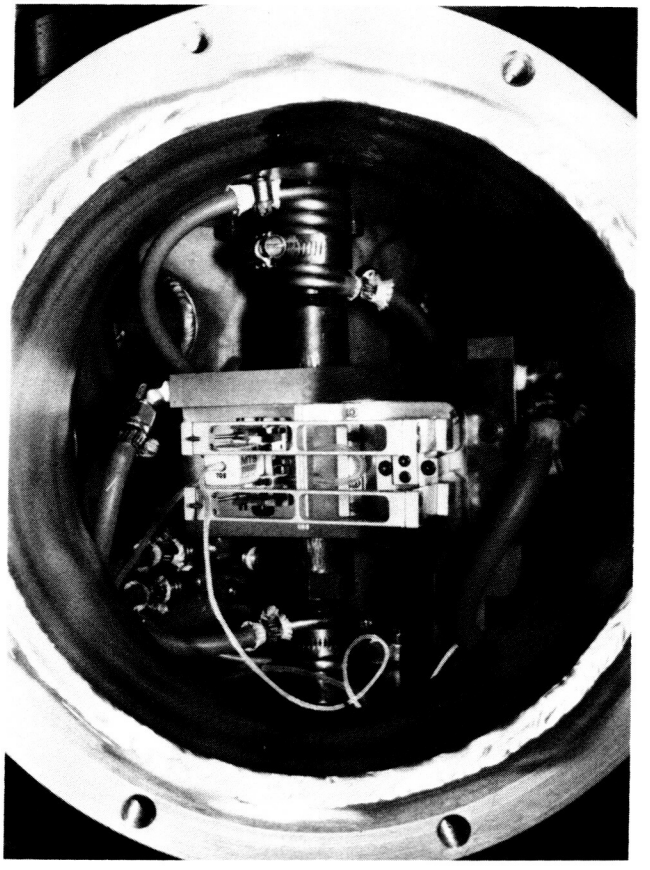

WATER COOLED EXTENSOMETER IN ENVIRONMENTAL TEST CHAMBER

FIGURE 10

A total of 8 overlay coated specimen tests have been completed. The coated specimens showed initiation lives which were 2X-7X higher than the lives of uncoated specimens run at similar conditions. Apparently the effect of oxidation was significantly reduced by the coating, so long as the ductility of the coating was not exceeded. For example, Figure 11 shows a specimen which experienced initiation from typical porosity in the B1900+Hf substrate. The crack clearly propagated outward from the substrate toward the specimen surface. This requires a two-mode model to capture correctly both coating and substrate initiation lives. The coating life model being developed under a companion HOST contract (reference 2) is being considered for integration with the CDA model to accomplish this capability.

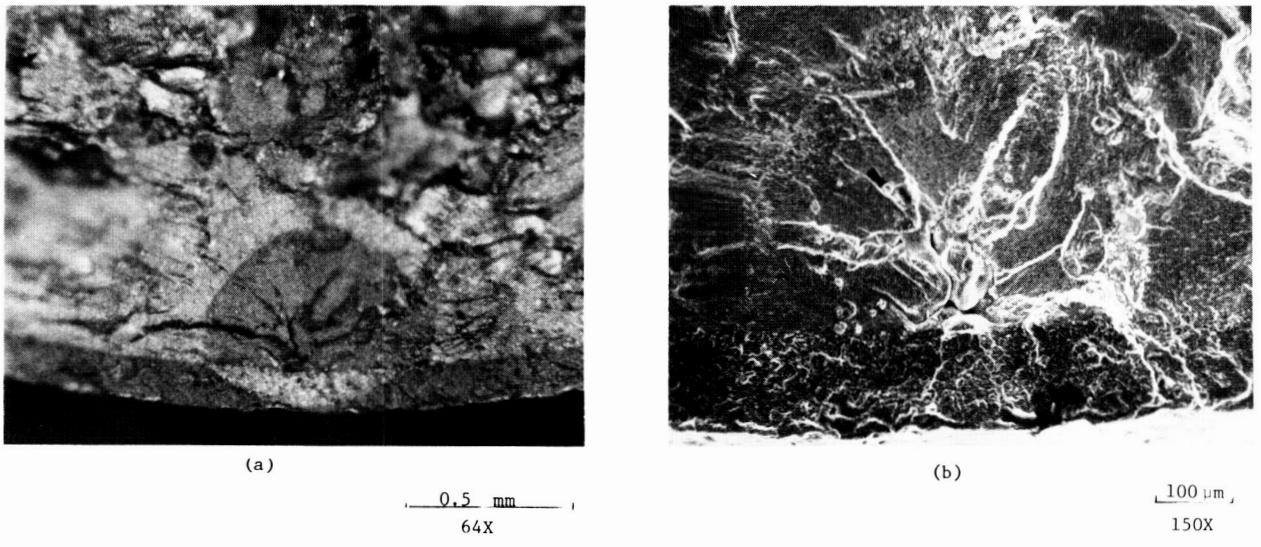

SPECIMEN 117A (1600°F, $\Delta\varepsilon$ = 0.5%, R=0, 10 CPM, Initiation Life = 3799 Cycles, Separation Life = 4041 Cycles).

(a) Optical and (b) SEM Micrographs Showing Crack Origin at Porosity in the Base Material.

FIGURE 11

CYCLIC MEAN STRESS MODEL

A total of 25 controlled mean stress tests are planned for this task, including five under TMF conditions. All five TMF tests have been completed, using load control to achieve the desired mean stress. The results show that the lives under such conditions can be much lower than what might be expected from a linear combination of creep and TMF damage. The isothermal portion of this testing will be conducted by Prof. Ghonem at the University of Rhode Island. Initial specimen trials have been completed at the URI lab and have demonstrated their capability to reproduce P&W results under baseline conditions.

ALTERNATE MATERIAL TESTING

A total of 10 isothermal fatigue tests using INCO 718 material have now been completed. The results so far suggest that the particular ring-rolled AMS 5663 forging used to produce these specimens has excellent creep resistance as well as good fatigue capability. Tests at 1200°F show little difference between 30 CPM and 1 CPM cyclic rates. Creep, tensile, and multiaxial tests are also underway, with a view to developing the constants needed for the CDA life model. Of particular interest will be the influence of the pronounced cyclic softening noted during all the fatigue testing. It is expected that some modification to the form of the CDA model will be necessary to account for this.

FUTURE TASKS

Further work is continuing on all the above tasks, with the goal of producing a creep-fatigue model, which is both practical and accurate. During the last year of the contract effort, the focus will continue to shift from generation of test data to analytical model development activities. The generation of CDA model constants for INCO 718 will be completed, followed by additional refinement of the CDA life prediction model.

REFERENCES

1. Moreno, V., Nissley, D. M., and Lin, L. S., " Creep Fatigue Life Prediction for Engine Hot Section Materials (Isotropic) - Second Annual Report," NASA CR-174844, March 1985.

2. Swanson, G. A., Linask, I., Nissley, D. M., Norris, P. P., Meyer, T. G., and Walker, K. P., " Life Prediction and Constitutive Models for Engine Hot Section Anisotropic Materials Program - Second Annual Status Report," NASA CR-179594, April 1987.

TOTAL STRAIN VERSION OF STRAINRANGE PARTITIONING FOR THERMOMECHANICAL FATIGUE AT LOW STRAINS

G.R. Halford and J.F. Saltsman
NASA Lewis Research Center
Cleveland, Ohio

A new method is proposed for characterizing and predicting the thermal fatigue behavior of materials. The method is based on three recent innovations in characterizing high-temperature material behavior: (a) the bithermal concept of thermal fatigue testing, (b) advanced, nonlinear, cyclic constitutive models, and (c) the total strain version of traditional Strainrange Partitioning.

INTRODUCTION

Thermal fatigue cracking continues to present a significant economic maintenance and safety problem in the hot section of aeronautical gas turbine engines. Efforts to formulate accurate and reliable life-prediction methods at reasonable costs have also been continuing as evidenced by the proliferation of thermal fatigue life-prediction approaches over the past two decades (ref. 1). The HOST project has contributed its share of approaches, including the three approaches discussed earlier in this session by representatives of two major engine manufacturers (refs. 2 to 4). A fourth approach, which has culminated very recently from ongoing developments at the Lewis Research Center over several years, is being presented formally for the first time. Our approach capitalizes on several recent innovations in the area of high-temperature material behavior. These include (1) advanced, nonlinear, cyclic constitutive equations for thermal cycling (ref. 5), (2) the concept of bithermal fatigue (refs. 6 and 7) for characterizing failure behavior of materials subjected to thermal cycling, and (3) the total strain version (refs. 8 and 9) of the method of Strainrange Partitioning (SRP). The total strain version permits the use of more tractable total strains rather than inelastic strains, which may be incalculable in practical applications.

BACKGROUND

Strainrange Partitioning (SRP) (ref. 10) was originally formulated on an inelastic strainrange versus cyclic life basis for isothermal conditions. The approach has worked well in the high-strain, low-life regime where the inelastic strains are large enough to be determined accurately by analytical and experimental methods.

To extend the method into the low-strain, long-life regime where the inelastic strains are small and difficult to determine, it was necessary to consider the total rather than just the inelastic strainrange. Formulating SRP on a total strain basis (TS-SRP) (refs. 8 and 9) required the determination of both the inelastic and the elastic strainrange versus cyclic life relations for cycles involving creep strain. The elastic strainrange versus life relations for cycles involving creep are

influenced significantly by temperature, hold time, wave shape (PP, CC, CP, and PC), and how creep is introduced into the cycle (stress hold, strain hold, slow strain rate, etc.). To make the analysis tractable, we have assumed that the elastic life lines are displaced parallel to themselves and are parallel to the elastic life line for PP cycling. This means that for a given imposed cycle type at a specific temperature, the elastic line intercept (elastic strainrange at N_f = 1 cycle) is a function only of the time of the cycle. In the first version of TS-SRP (ref. 8), the elastic line intercept was determined by the use of an empirical equation with constants determined using data obtained from failure tests. Efforts to reduce testing requirements led to the development of an updated version of TS-SRP (ref. 9). This development was based on a derived relation between failure behavior (inelastic strainrange versus cyclic life) and flow behavior (cyclic stress-strain response) and greatly reduced the time and cost of characterizing the TS-SRP behavior of an alloy. Failure behavior is characterized readily in the high-strain, low-life regime where testing times are reasonable, and the critical flow behavior is characterized in the desired low-strain, long-life regime by cycling a specimen just long enough for the stress-strain hysteresis loop to approach stability. With this approach, the elastic line intercept can be established with a minimum of long-time testing.

Traditionally, thermomechanical fatigue[1] (TMF) resistance of materials has been estimated by conducting isothermal fatigue tests at the expected maximum temperature in the TMF cycle, with effects of creep being determined by imposing hold periods at peak tensile or compressive strain. Computer-controlled testing equipment and techniques have recently been developed to the point where thermomechanical fatigue tests can be conducted routinely, so isothermal testing is no longer as justifiable. However, true TMF cycles become difficult to control, analyze, and interpret at low strainranges, and bithermal fatigue testing has been proposed (ref. 6) to avoid this difficulty.

Existing methods for predicting TMF life of components in the low-strain regime are lacking in accuracy or generality. Thus, we have actively pursued development of a TMF life-prediction method that would overcome these deficiencies. As a starting point, we have selected the SRP method because of past successes. For example, the inelastic strain version of SRP has been successfully applied to a thermomechanical fatigue problem (ref. 11) at a strain level where the inelastic strainrange could be determined accurately and for which the life relations are temperature independent. Also, the TS-SRP version has been applied successfully to isothermal problems (refs. 8 and 9) where the inelastic strainrange cannot be determined accurately. These successes suggest that the total strain version has the potential to be extended to predict the lives of TMF cycles at low strainranges.

This report examines the extension of TS-SRP into the TMF regime by the use of a hypothetical example for the pressure vessel and piping steel alloy 2-1/4Cr-1Mo. The cyclic stress-strain-time, that is, flow response, has been determined for both thermomechanical and bithermal cycles using the Robinson flow model (ref. 5). Unfortunately, adequate TMF failure data for this alloy, especially in the low strain regime, are not available so we cannot verify the TS-SRP life predictions at this time. The characterization of an alloy by TS-SRP requires the determination of both failure and flow responses.

---

[1]The term "thermomechanical fatigue" is used to indicate variable temperature fatigue in which the mechanical strain is imposed only by externally applied loads. Temperature gradients within the test volume are not permitted.

SYMBOLS

A	general constant in empirical flow equations
A'	general constant in empirical flow equations
B	intercept of elastic strainrange versus life relation
C	intercept of inelastic strainrange versus life relation
C'	intercept of equivalent inelastic line for combined creep-fatigue cycles with parallel inelastic failure lines
CC	creep strain in tension, creep strain in compression
CP	creep strain in tension, plastic strain in compression
f	frequency
F	strain fraction
K	cyclic strain-hardening coefficient
N	number of cycles to failure
PC	plastic strain in tension, creep strain in compression
PP	plastic strain in tension, plastic strain in compression
R	mean stress correction term for nonisothermal fatigue
r	correlation coefficient
t	hold time per cycle
V	fatigue mean stress correction term; isothermal and nonisothermal
y	general dependent variable
Δ	range of variable
ϵ	strain
σ	stress
τ	period of one cycle

Subscripts:

amp	amplitude
bi	bithermal

c compression

cc creep strain in tension, creep strain in compression

cp creep strain in tension, plastic strain in compression

el elastic

eff effective

fm failure; mean stress condition

f0 failure; zero mean stress condition

in inelastic

ij pp, cc, pc, cp

m mean

max maximum value

min minimum value

pc plastic strain in tension, creep strain in compression

pp plastic strain in tension, plastic strain in compression

pre predicted

t tension or total strain

tm thermomechanical

σ stress

Superscripts:

b time-independent power of cyclic life for elastic strainrange versus life relation

c power of cyclic life for inelastic strainrange versus life relations

m general power of time in empirical flow equations

n time-independent, cyclic strain-hardening exponent

α power on total strainrange in empirical flow equations

Cycle type (nonisothermal):

HRIP high-rate inphase cycle producing 100-percent PP strainrange

HROP high-rate out-of-phase cycle producing 100-percent PP strainrange

THIP tensile hold inphase cycle with hold period at maximum tensile strain producing CP and PP strainranges

CHOP compressive hold out-of-phase cycle with hold period at minimum compressive strain producing PC and PP strainranges

ANALYSIS

In formulating TS-SRP for isothermal fatigue (refs. 8 and 9), we assumed that the inelastic and elastic strainrange versus life lines for creep-fatigue cycles are parallel to the corresponding lines for pure fatigue or PP cycles, as shown in figure 1. This is not an arbitrary assumption since our experience with several alloys suggests that this is reasonable behavior for isothermal conditions. Note that the frequency modified approach of Coffin (ref. 12) also uses parallel inelastic and elastic lines. We assume, in the absence of data for guidance, that this will also be the case for nonisothermal conditions.

Based on the above assumptions, a relationship between failure behavior and flow behavior can be established. Failure behavior is expressed by the equations for elastic and inelastic strainrange versus cyclic life:

$$\Delta\epsilon_{el} = B(N_{f0})^b \tag{1}$$

$$\Delta\epsilon_{in} = C'(N_{f0})^c \tag{2}$$

where

$$C' = [\Sigma F_{ij}(C_{ij})^{1/c}]^c \tag{3}$$

and

$$ij = pp,\ cc,\ pc,\ \text{or}\ \ cp$$

Equation (3) is derived from the interaction damage rule (IDR) of reference 13 and the four generic SRP inelastic strainrange - cyclic life relations for a theoretical zero mean stress condition. In the past the inelastic line intercepts for creep cycles (C_{pc}, C_{cp}, and C_{cc}) were taken to be independent of time. But recent developments (ref. 14) indicate that they may be time dependent at elevated temperatures, and procedures have been proposed for expressing the time dependencies analytically. The following development of the TMF life-prediction method based on TS-SRP will not explicitly consider the time dependency of the inelastic lines, although it could be added if needed.

The four generic SRP relations are

$$\Delta\epsilon_{in} = C_{ij}(N_{ij})^c \tag{4}$$

The IDR is written as follows:

$$\sum\left[\frac{F_{ij}}{N_{ij}}\right] = \frac{1}{N_{f0}} \tag{5}$$

where $\Sigma F_{ij} = 1.0$. Using equation (4) to solve for N_{ij} and substituting into equation (5), we obtain equation (3). Flow behavior is expressed by an equation relating elastic and inelastic strainranges:

$$\Delta\epsilon_{el} = K_{ij}(\Delta\epsilon_{in})^n \tag{6}$$

where $n = b/c$.

Based on the assumption that the inelastic and elastic failure lines for creep-fatigue cycles are parallel to the corresponding failure lines for PP cycles, it follows that the strain-hardening exponent n in equation (6) is a constant as shown in figure 2.

For isothermal conditions the strain-hardening coefficient K_{ij} is a function of temperature, hold time, how creep is introduced into the cycle (stress hold, strain hold, etc.), and the strainrate-hardening characteristics of the alloy. For nonisothermal conditions it is also a function of the maximum and minimum temperatures and the phase relation between strain and temperature.

The time-dependent behavior of the elastic strainrange-life relation for creep cycles is shown schematically in figure 3. Setting equation (1) equal to equation (6) and eliminating N_{f0} using equation (2), we obtain the following equation relating flow and failure behavior:

$$B = K_{ij}(C')^n \tag{7}$$

In this equation the inelastic line intercepts C_{ij} and the exponent c used to determine C' are considered to be failure terms. The strain fractions F_{ij}, the strength coefficient K_{ij}, and the strain-hardening exponent n are considered to be flow terms. Thus, the elastic line intercept B can be determined for a creep cycle from a combination of flow and failure data. Note that K_{ij} and F_{ij} will, in general, depend on waveform.

We are now in a position to establish a total strainrange versus life relation and thus predict life on a total strainrange basis. Note that the SRP inelastic strainrange versus life relations and the flow relations are determined for a specified minimum and maximum temperature and phase relationship between strain and temperature. The total strainrange is

$$\Delta\epsilon_t = \Delta\epsilon_{el} + \Delta\epsilon_{in} \tag{8}$$

From equations (1) and (2) we obtain

$$\Delta\epsilon_t = B(N_{f0})^b + C'(N_{f0})^c \tag{9}$$

A schematic plot of equation (9) is shown in figure 1. Note that the solution of this equation gives the cyclic life N_{f0} for a theoretical zero mean stress condition. The final step in a life prediction is to adjust the computed life to account for any mean stress effects that may be present.

A method for accounting for mean stress effects on life for isothermal conditions has been proposed in reference 15;

$$(N_{fm})^b = (N_{f0})^b - V_{eff} \tag{10}$$

where N_{fm} and N_{f0} are the lives with and without mean stress, respectively, and V_{eff} is the effective mean stress correction term. For isothermal fatigue, V_{eff} has been determined by the following equation:

$$V_{eff} = V_{\sigma} \exp\left[-70\left(\frac{\Delta\epsilon_{in}}{\Delta\epsilon_{el}}\right)^2\right] \tag{11}$$

where $V_{\sigma} = \sigma_m/\sigma_{amp}$. Note that this method of correcting for the mean stress effect on cyclic life was developed for a specific nickel-base alloy and may not apply to other alloys or even to other nickel-base alloys. The analyst must determine that the mean stress correction equation used is applicable to the alloy of interest.

For TMF an alternate definition of V_{eff} is in order since a mean stress can naturally develop because of the temperature dependency of the yield strength in tension and compression. Hence, V_{eff} in equation (10) should be determined (ref. 1) by the following:

$$V_{eff} = \frac{1 + \frac{R_{\sigma}}{R_y}}{1 - \frac{R_{\sigma}}{R_y}} \tag{12}$$

where R_{σ} is equal to $\sigma_{min}/\sigma_{max}$ and R_y is the absolute value of the ratio of the compressive yield strength to the tensile yield strength at their respective maximum and minimum temperatures and strain rates in the TMF cycle. To date there is no direct experimental verification of this method for accounting for mean stress effects for nonisothermal fatigue.

To predict life on a total strainrange basis, it is necessary first to determine the PP inelastic and elastic lines and the desired SRP inelastic strainrange versus life relations experimentally. Note that these relations are to be established for a theoretical zero mean stress condition. Empirical estimation methods developed for isothermal fatigue, such as the ductility-normalized SRP relations (ref. 16) are not recommended at this time as they have not been verified for application to TMF. Ideally, failure and flow behavior would be determined from TMF tests duplicating the cycles for which lives are to be predicted. However, this approach is impractical as it lacks generality of use. For example, if the cycle were to change, the entire data base would have to be regenerated at a doubling of cost and lead time. Further changes would in turn require further repetition of experiments. A more basic approach is thus required. While an isothermal approach would offer advantages in terms of costs because of the vast background of isothermal data bases, we do not, at this time, recommend doing so. This recommendation comes as a result of an indepth survey (ref. 1) comparing the TMF and isothermal fatigue resistances of many alloys. Only under special circumstances of temperature invariant deformation and cracking mechanisms could isothermal fatigue resistance be used to accurately predict TMF results.

At this stage of development of the TS-SRP approach, we recommend resorting to bithermal fatigue tests (ref. 6) to generate the experimental inelastic strainrange-life relations required by TS-SRP. Bithermal fatigue offers the simplicity of isothermal testing, yet it captures the first-order effects of inphase and out-of-phase

TMF cycling. The bithermal tests should cover a sufficient temperature range to encompass the deformation and cracking mechanisms pertinent to the TMF cycles of interest. Determination of the critical temperature ranges for testing will require a rudimentary understanding of the metallurgical factors governing the deformation and cracking mechanisms. Thermomechanical flow tests would normally be conducted to properly characterize the stress-strain response, but bithermal flow tests could be conducted at the lower strain ranges where the inelastic strains are small and it is difficult to analyze the thermomechanical hysteresis loops. The stress-strain response of the two types of cycles should be similar in this strain regime, and the bithermal cycle would be a good approximation to the thermomechanical cycle. The thermomechanical and bithermal cycles used in this report are shown in figure 4.

Techniques are described in reference 6 for determining PP life relations for inphase and out-of-phase bithermal cycles, CP inphase, and PC out-of-phase inelastic strainrange-life relations. Proposals for the determination of a CC bithermal life relation have not been discussed because of the exclusion of such a strainrange component in TMF cycles at small inelastic strainranges.

The strain-hardening coefficient K_{ij} and the strain fraction F_{ij} can be determined using an appropriate constitutive flow model for which the material constants are available. As an alternative, they could be determined by conducting flow tests for the creep-fatigue cycles of interest. Using these data, one can determine the necessary empirical correlations describing flow behavior. The latter approach is the most viable option at this time because reliable constitutive flow models in the low strain regime and the required material constants are not yet generally available. The procedures for determining the flow correlations are described in the following section.

The strainrange analysis presented above is based on the assumption that the inelastic and elastic versus life lines for creep-fatigue cycles are parallel to the corresponding lines for PP cycles. This may not always be a satisfactory assumption. (The case of nonparallel lines is addressed in ref. 17.)

ANALYSIS USING ROBINSON CONSTITUTIVE MODEL

The choice of a constitutive model for use with TS-SRP was somewhat arbitrary. We have selected the Robinson model (refs. 5 and 18) because it has been validated for TMF application (using the alloy 2-1/4Cr-1Mo steel in the post-weld, heat-treated condition). Using Robinson's model, we have obtained the simple power law correlation shown below. This same power law form was also used successfully to correlate isothermal flow data (ref. 9):

$$y = A(t)^m \tag{13}$$

where y is the dependent variable representing several different flow variables, as will be discussed shortly, and t is the hold time per cycle.

Generally, the intercept A (value of y at $t = 1$) is a function of total strainrange. The results obtained from the Robinson model for thermomechanical cycles and earlier results for isothermal cycles using the Walker model (refs. 9 and 18) show that the family of lines shown in figure 5 can be taken as parallel. Thus, the exponent on time m is assumed to be independent of total strainrange. By a process of trial and error, we determined that the intercept A can be correlated with total strainrange by another power law as shown in figure 6;

$$A = A'(\Delta\epsilon_t)^{\alpha} \tag{14}$$

thus

$$y = A'(\Delta\epsilon)^{\alpha}(t)^{m} \tag{15}$$

The dependent variable y is now a function of two independent variables, $\Delta\epsilon_t$ and t. If both sides of equation (15) are divided by $(\Delta\epsilon_t)^{\alpha}$ the family of lines shown schematically in figure 5 collapse to the single line of figure 7. The values of A', α, and m vary with the dependent variable y and the mechanical properties of the alloy. Note that TS-SRP is not dependent on the form of the equation used to correlate the flow data and that equation (15) could be of many different forms. The only requirement is that it represent the flow data in a tractable form with sufficient accuracy.

Five flow correlations based on equation (15) are used herein to determine the required flow variables: K_{ij}, F_{ij}, $\Delta\sigma$, σ_t, and σ_c. The first two are used to determine the coefficients B and C' in equation (9). The remaining three are used to determine the term R_σ in the mean stress correction using equation (12).

Note that, in principle, each of these correlations could be obtained directly from a suitable constitutive model. Although the exact form of the relations would no doubt differ somewhat from the one used here, the trends would be quite similar. The empirical correlations are used only because of their extreme simplicity and comparatively good accuracy.

For a specific alloy, these correlations depend on the maximum and minimum temperature of the cycle, the wave shape, how creep is introduced into the cycle (stress hold, strain hold, etc.), the straining rate during loading and unloading, and the phase relation between strain and temperature. Only inphase and out-of-phase continuous cycles and strain-hold cycles with zero mean strain are considered at the moment. These are shown in figure 4. When computing the stresses and strains for the postulated bithermal hysteresis loops, the temperature is changed at zero stress on the tension-going and compression-going sides of the loops. And when calculating the TMF loops, the temperature ramp rate is determined by the maximum and minimum temperatures in the cycle and the mechanical straining rate. The relation between strainrate and temperature rate for a sawtooth waveform is derived in the following manner for inphase and out-of-phase cycles. For a constant strainrate,

$$\dot{\epsilon} = 2f(\Delta\epsilon_t) \tag{16}$$

The period of one cycle is the reciprocal of the frequency f ($\tau = 1/f$), and the temperature range is traversed in one-half the cycle period.

Let τ' equal $\tau/2$, thus the time required to go from one strain limit to the other is

$$\tau' = \frac{\Delta\epsilon_t}{\dot{\epsilon}} \tag{17}$$

Let ΔT equal the temperature range of the cycle of interest (inphase or out-of-phase). The temperature ramp rate $\dot{T}$ is given by the temperature range divided by the time required to traverse the cycle. Note that $\dot{T}$ is positive if the temperature is increasing and negative if the temperature is decreasing;

$$\dot{T} = \frac{\Delta T(\Delta \epsilon_t)}{\dot{\epsilon}} \tag{18}$$

Inphase and out-of-phase thermomechanical and bithermal hysteresis loop results were obtained from the Robinson model for the following conditions:

Total strainrange values:

Continuous cycling: 0.002 to 0.010 in increments of 0.001
Strain-hold cycling: 0.002, 0.003, 0.004, 0.006, 0.008, 0.010
Hold time, sec: 60, 300, 600, 1800, 3600
Minimum temperature, °C: 250
Maximum temperature, °C: 600
Strainrate, in./in./min: 0.04

A review of the results of these computations for the cycles considered herein reveals the following differences in the stress-strain response of the thermomechanical and bithermal cycles for a given total strainrange and hold time.

Inphase cycles	Out-of-phase cycles
$\lvert\sigma_{t,tm}\rvert > \lvert\sigma_{t,bi}\rvert$	$\lvert\sigma_{t,tm}\rvert < \lvert\sigma_{t,bi}\rvert$
$\lvert\sigma_{c,tm}\rvert < \lvert\sigma_{c,bi}\rvert$	$\lvert\sigma_{c,tm}\rvert > \lvert\sigma_{c,bi}\rvert$
$\lvert\Delta\sigma_{tm}\rvert < \lvert\Delta\sigma_{bi}\rvert$	$\lvert\Delta\sigma_{tm}\rvert < \lvert\Delta\sigma_{bi}\rvert$
$\lvert\Delta\epsilon_{el,tm}\rvert < \lvert\Delta\epsilon_{el,bi}\rvert$	$\lvert\Delta\epsilon_{el,tm}\rvert < \lvert\Delta\epsilon_{el,bi}\rvert$

The above results are as expected. For example, in an inphase bithermal cycle, the stress is acting at the maximum temperature for the entire duration of the tensile half, but in a thermomechanical cycle the stress is acting at the maximum temperature only briefly at the maximum strain limit. Thus σ_t will be greater in a thermomechanical cycle than in a bithermal cycle because of the greater thermal recovery in the bithermal cycle. A similarly based argument also applies to σ_c.

We are now able to determine the flow correlations listed above using equation (15), but first the strain-hardening exponent n in equation (6) must be determined using time-independent PP flow data. The strainrate of 0.04/min may not be fast enough to obtain time-independent (PP) deformation during loading and unloading but was the fastest rate used when the material constants for the model were determined. We have assumed that this rate produces no time-dependent inelastic strains. Note also that it is highly unlikely that the high-temperature ramp rate T implied by equation (18) could be achieved during the cooling leg of a thermomechanical cycle. Nevertheless, the following results were obtained:

$$\Delta\epsilon_{el} = 0.0045(\Delta\epsilon_{in})^{0.107} \tag{19}$$

for thermomechanical cycles and

$$\Delta\epsilon_{el} = 0.0044(\Delta\epsilon_{in})^{0.105} \tag{20}$$

for bithermal cycles. The relations for inphase and out-of-phase PP cycles are identical.

The differences between the thermomechanical and bithermal results are virtually nill under the current circumstances. These correlations are shown in figure 8 wherein the symbols represent values calculated using the Robinson model and the line represents the empirical correlation. Correlation coefficients of 0.990 and 0.995 for the thermomechanical and bithermal cycles, respectively, indicate an exceptionally good representation of the Robinson model. In the following, we present only results for TMF cycling.

Correlation Between Cyclic Strain-Hardening Coefficient and Hold Time

Equation (15) expressed for K_{ij} is as follows:

$$K_{ij} = A'(\Delta\epsilon_t)^{\alpha}(t)^{m} \tag{21}$$

The strain-hardening coefficient K_{ij} for each loading condition considered using the Robinson model (hold time, total strainrange, phase relation, etc.) is calculated using equation (6) and the proper value of the strain-hardening exponent from equations (19) and (20). Previously (ref. 9), K_{ij} was taken to be independent of total strainrange, but additional analysis indicates that it is a weak function of total strainrange. A multiple regression analysis of the appropriate values gives the following correlations for out-of-phase and inphase TMF cycling with $n = 0.107$:

$$\frac{K_{pc}}{(\Delta\epsilon_t)^{0.020}} = 4.689\times10^{-3}(t)^{-0.0167} \tag{22}$$

for out-of-phase cycling and

$$\frac{K_{cp}}{(\Delta\epsilon_t)^{0.037}} = 5.052\times10^{-3}(t)^{-0.0158} \tag{23}$$

for inphase cycling. These equations are represented in figure 9, and their excellent ability to correlate the calculated results is shown in figure 10.

Correlation Between Strain Fraction and Hold Time

Equation (15) expressed for F_{ij} is as follows:

$$F_{ij} = A'(\Delta\epsilon_t)^{\alpha}(t)^{m} \qquad F_{ij} \leq 1.0 \tag{24}$$

Analysis of the strain fraction - hold time data showed that equation (24) is not applicable over the entire range of the data. However, good correlations were obtained by dividing the data into two regimes as indicated below.

For $0.002 \leq \Delta\epsilon_t \leq 0.004$,

$$\frac{F_{pc}}{(\Delta\epsilon_t)^{-2.073}} = 1.416\times10^{-6}(t)^{0.0506} \tag{25}$$

for out-of-phase cycles and

$$\frac{F_{cp}}{(\Delta\epsilon_t)^{-2.110}} = 1.204\times10^{-6}(t)^{0.0448} \tag{26}$$

for inphase cycles. These equations are expressed in figure 11, and their ability to correlate the calculated results is represented by correlation coefficients of 0.993 and 0.994, respectively.

For $0.004 \leq \Delta\epsilon_t \leq 0.010$,

$$\frac{F_{pc}}{(\Delta\epsilon_t)^{-1.367}} = 6.062\times10^{-5}(t)^{0.0744} \tag{27}$$

for out-of-phase cycles and

$$\frac{F_{cp}}{(\Delta\epsilon_t)^{-1.364}} = 6.166\times10^{-5}(t)^{0.0733} \tag{28}$$

for inphase cycles. These equations are expressed in figure 12, and the correlation coefficients are 0.999 and 0.997, respectively. The constants for the correlations for K_{ij} and F_{ij} for TMF cycling (eqs. (21) to (28)) are summarized in table I.

Correlations Between Stress and Hold Time

Our experience suggests that better correlations for σ_t and σ_c are usually obtained when σ_t is used for cycles where creep occurs in the tensile half of the hysteresis loop (CP cycle) and when σ_c is used where creep occurs on the compressive side of the loop (PC cycle). The results obtained here show that stress is a very weak function of hold time and could be omitted with little loss of accuracy. But this may not be true generally, and we have chosen to include it for illustrative purposes. The resulting stress correlations are summarized in table IV.

LIFE PREDICTION OF TMF

In this section we outline the steps required to predict the life of a TMF cycle. For purposes of illustration, an inphase tensile strain-hold cycle (THIP) is selected. The mechanical strainrate and temperature limits are given in the previous section.

TMF cycles invariably contain both time-dependent and time-independent components of inelastic strain. Thus a THIP cycle will contain both PP and CP strain components, and the appropriate generic SRP inelastic strainrange versus life relations, equation (4), are required. Both relations must be for inphase cycling. Unfortunately, the numerical values of the material constants C_{ij} and c are not available at present. As discussed earlier, bithermal testing is recommended for determination of these material constants. For now, we proceed as if C_{ij} and c values are known;

$$\Delta\epsilon_{in} = C_{pp}(N_{pp})^c \tag{29}$$

$$\Delta\epsilon_{in} = C_{cp}(N_{cp})^c \tag{30}$$

The intercept C' of the equivalent inelastic line in equation (9) can now be determined. From equation (3),

$$C' = \left[F_{pp}(C_{pp})^{1/c} + F_{cp}(C_{cp})^{1/c}\right]^c \tag{31}$$

Since $F_{pp} = 1.0 - F_{cp}$, equation (3) can be rewritten as follows:

$$C' = \left[(C_{pp})^{1/c} - F_{cp}\left[(C_{pp})^{1/c} - (C_{cp})^{1/c}\right]\right]^c \tag{32}$$

The strain fraction F_{cp} is determined using the appropriate correlation given in the previous section.

If F_{cp} is very small ($\simeq 0$), $C' \simeq C_{pp}$; and if F_{cp} approaches unity, $C' \simeq C_{cp}$. The equivalent elastic line intercept B in equation (9) can now be determined using equation (7). The value of K_{cp} is determined using the correlation given in the previous section, and the value of C' is determined using equation (31);

$$B = K_{cp}(C')^n \tag{33}$$

The ingredients required to make a life prediction are now available. With a knowledge of $\Delta\epsilon_t$ and the proper constants for equation (9), we can now solve for N_{f0}. The value of N_{f0} can be determined by trial-and-error or by direct use of the inversion method given in reference 19. Note that N_{f0} is the cyclic life for a theoretical zero mean stress condition (ref. 15).

The final step in a life prediction is to account for the effects of mean stress on cyclic life. Rewriting equation (10) yields

$$N_{fm} = \left[(N_{f0})^b - V_{eff}\right]^{1/b} \tag{34}$$

The value of V_{eff} can be determined using equation (12) or some other method. If equation (12) is used, the values of σ_{min} and σ_{max} are obtained using the appropriate stress versus hold time correlations given by the constants in table II.

CONCLUDING REMARKS

The total strainrange version of Strainrange Partitioning (TS-SRP) was developed originally for isothermal fatigue. This development makes it easier to characterize an alloy and predict cyclic life in the low-strain regime without having to conduct failure tests in this regime. This development is based on a derived relation between failure behavior and the cyclic stress-strain or flow response of an alloy. Failure testing is done only in the high-strain regime where test times and costs are more reasonable, and flow testing is done in both the high- and low-strain regime. The flow tests need be run only until the stress-strain hysteresis loop approaches cyclic stability. Failure tests should also be done to determine the

effects of mean stress on cyclic life. If mean stress effects are not accounted for, inaccurate life predictions will result from using this or any other life-prediction method in the low-strain, long-life regime.

A method for extending TS-SRP to characterize an alloy and predict the lives of thermomechanical cycles in the low-strain regime is presented. This method is based on nonisothermal rather than isothermal data. Bithermal fatigue testing is recommended at this time to generate the nonisothermal data required to determine the inelastic strainrange-life relations required by TS-SRP. Bithermal fatigue testing offers the simplicity of isothermal testing but captures the first-order effects of inphase and out-of-phase TMF cycling. Thermomechanical flow tests would normally be conducted to properly characterize the stress-strain response, but bithermal flow tests could be conducted at the lower strainranges where the inelastic strains are small, and it is difficult to analyze the thermomechanical hysteresis loops.

The data from flow testing are used to determine flow response of an alloy. This response is approximated using a simple power law with two independent variables with constants determined by a multiple repression analysis. These same power law relations were used in the isothermal version of TS-SRP. It is not a requirement that this particular power law be used, since any relation could be used provided it accurately represents the data. Currently, there are no TMF data to validate the proposed life-prediction method.

REFERENCES

1. Halford, G.R.: Low-Cycle Thermal Fatigue. Thermal Stresses II, R.B. Hetnarski, ed., Elsevier, 1987, pp. 329-428.

2. Nelson, R.; and Schoendorf, J.: Cyclic Damage Accumulation Model for High Temperature Fatigue of Isotropic Hot Section Alloys. Turbine Engine Hot Section Technology 1987, NASA CP-2493, 1987, pp. 423-434.

3. Meyer, T.; Nissley, D.; and Swanson, G.: High Temperature Constitutive and Crack Initiation Modeling of Single Crystal Super alloys. Turbine Engine Hot Section Technology 1987, NASA CP-2493, 1987, pp. 401-412.

4. Kim, K.S., et al.: Elevated Temperature Crack Growth. Turbine Engine Hot Section Technology 1987, NASA CP-2493, 1987, pp. 413-422.

5. Robinson, D.N.; and Swinderman, R.W.: Unified Creep-Plasticity Constitutive Equations for 2-1/4 Cr-1Mo Steel at Elevated Temperature. ORNL/TM-8444, 1982.

6. Halford, G.R., et al.: Bithermal Fatigue, a Link Between Isothermal and Thermomechanical Fatigue. Symposium on Low Cycle Fatigue - Directions for the Future, ASTM STP-942, ASTM, 1987, pp. 625-637.

7. Gayda, J., et al.: Bithermal Low-Cycle Fatigue Behavior of a NiCoCrAlY-Coated Single Crystal Superalloy. NASA TM-89831, 1987.

8. Halford, G.R.; and Saltsman, J.F.: Strainrange Partitioning - A Total Strain Range Version. ASME International Conference on Advances in Life Prediction Methods, D.A. Woodford and J.R. Whitehead, eds., ASME, 1983, pp. 17-26.

9. Saltsman, J.F.; and Halford, G.R.: An Update of the Total Strain Version of SRP. Symposium on Low Cycle Fatigue - Directions for the Future, ASTM, STP-942, ASTM, 1987.

10. Manson, S.S.; Halford, G.R.; and Hirschberg, M.H.: Creep-Fatigue Analysis by Strain-Range Partitioning. Design for Elevated Temperature Environment, S.Y. Zamrik, ed., ASME, 1971, pp. 12-28. (NASA TM X-67838.)

11. Halford, G.R.; and Manson, S.S.: Life Prediction of Thermal-Mechanical Fatigue Using Strainrange Partitioning. Thermal Fatigue of Materials and Components, ASTM STP-612, D.A. Spera and D.F. Mowbray, eds., ASTM, 1976, pp.239-254. (NASA TM X-71829.)

12. Coffin, L.F., Jr.,: The Effect of Frequency on High Temperature Low Cycle Fatigue. Proceedings of the Air Force Conference on Fatigue and Fracture of Aircraft Structures and Materials, AFFDL-TR-70-144, 1970, pp. 301-312.

13. Manson, S.S.: The Challenge to Unify Treatment of High Temperature Fatigue - A Partisan Proposal Based on Strainrange Partitioning. Fatigue at Elevated Temperatures, ASTM STP-520, A.E. Carden, A.J. McEvily, and C.H. Wells, eds., ASTM, 1973, pp. 744-775. (NASA TM X-68171.)

14. Kalluri, S.; Manson, S.S.; and Halford, G.R.: Environmental Degradation of 316 Stainless Steel in High Temperature Fatigue, Proceedings, Third International Conference on Environmental Degradation of Engineering Materials, Penn State Univ., 1987, pp. 503-519. (NASA TM-89931.)

15. Halford, G.R.; and Nachtigall, A.J.: Strainrange Partitioning Behavior of an Advanced Gas Turbine Alloy, AFE-1DA. J. Aircr., vol. 17, no. 8, Aug. 1980, pp. 598-604.

16. Halford, G.R.; Saltsman, J.F.; and Hirschberg, M.H.: Ductility-Normalized Strainrange Partitioning Life Relations for Creep-Fatigue Life Prediction. Environmental Degradation of Engineering Materials, M.R. Louthan and R.P. McNitt, eds., Virginia Polytechnic Institute and State Univ., Blacksburg, VA, 1977, pp. 599-612.

17. Saltsman, J.F.; and Halford, G.R.: Life Prediction of Thermomechanical Fatigue Using Total Strain Version of SRP - A Proposal. NASA TP-2779, 1987.

18. Chang, T.Y.; and Thompson, R.L.: A Computer Program for Predicting Nonlinear Uniaxial Material Responses Using Viscoplastic Models. NASA TM-83675, 1984.

19. Manson, S.S.; and Muralidharan, U.: A Single Expression Formula for Inverting Strain-Life and Stress-Strain Relationships. NASA CR-165347, 1981.

TABLE I. - CONSTANTS FOR K_{ij} AND F_{ij} CORRELATIONS FOR THERMOMECHANICAL STRAIN-HOLD CYCLING FOR $y = A'(\Delta\epsilon_t)^{\alpha}(t)^{m}$

[Material, 2-1/4CR-1Mo steel; post-weld, heat-treated condition.]

Cycle type	Total strain-range, $\Delta\epsilon_t$	Flow variable, y	Constant, A'	Power on total strain-range, α	Power of time, m	Correlation coefficient, r
PC (out-of-phase)	--------	K_{pc}	4.689×10^{-3}	0.020	-0.0167	0.857
	0.002 to 0.004	F_{pc}	1.416×10^{-6}	-2.073	.0506	.993
	0.004 to 0.010	F_{pc}	6.062×10^{-5}	-1.367	.0744	.999
CP (inphase)	--------	K_{cp}	5.052×10^{-3}	0.037	-.0158	.929
	0.002 to 0.004	F_{cp}	1.204×10^{-6}	-2.110	.0448	.994
	0.004 to 0.010	F_{cp}	6.166×10^{-5}	-1.364	.0733	.997

TABLE II. - CONSTANTS[a] FOR STRESS CORRELATIONS FOR THERMOMECHANICAL STRAIN-HOLD CYCLING FOR $y = A'(\Delta\epsilon_t)^{\alpha}(t)^{m}$

[Material, 2-1/4Cr-1Mo steel; post-weld, heat-treated condition.]

Cycle type	Flow variable, y	Constant, A'	Power on total strain-range, α	Power of time, m	Correlation coefficient, r
PC	$\Delta\sigma$	1394.7	0.230	0.0008	0.990
	σ_c	722.3	.183	.0019	.989
CP	$\Delta\sigma$	1379.8	0.227	0.0008	0.987
	σ_t	781.4	.329	.0007	.986

[a]Stresses in units of MPa (1 ksi = 6.895 MPa).

BASIS OF TOTAL STRAIN VERSION OF SRP

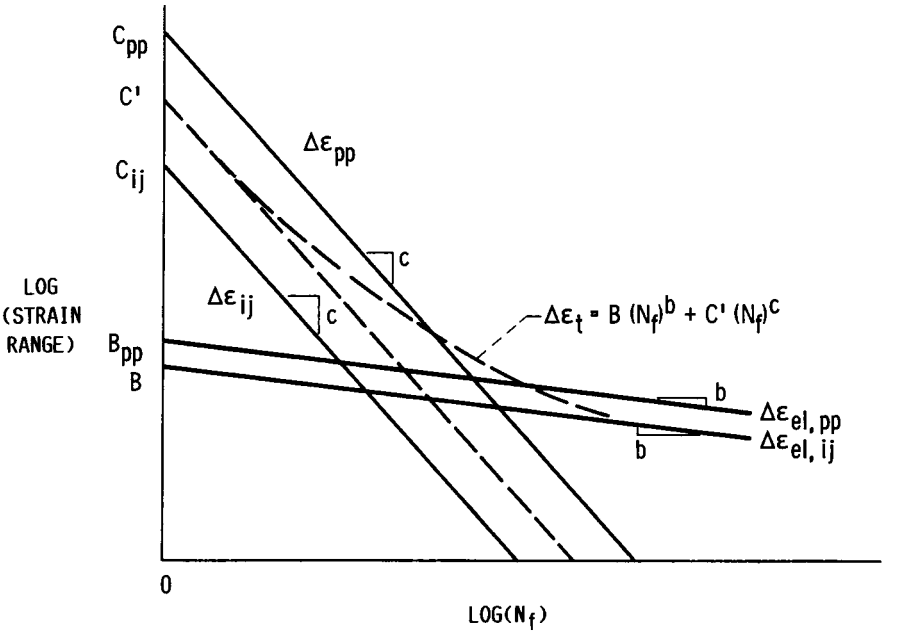

Figure 1

CYCLIC ELASTIC-INELASTIC STRAINRANGE RELATION DEFINING K_{ij}

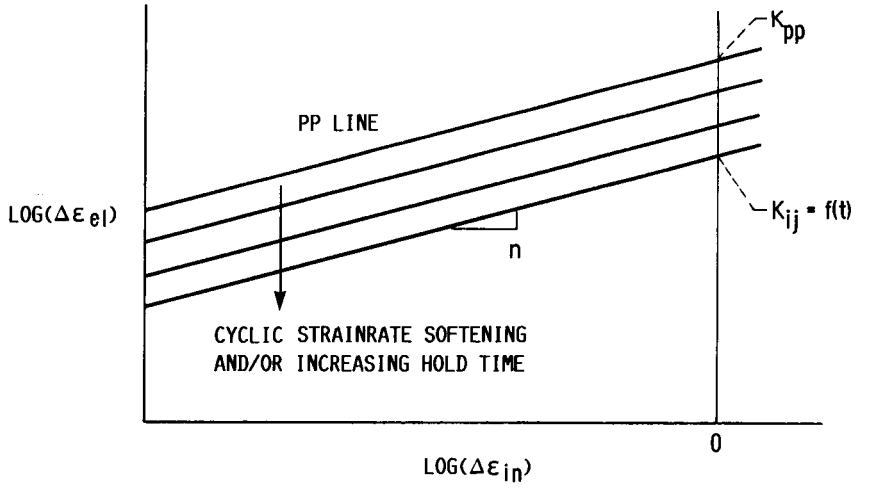

Figure 2

ELASTIC STRAINRANGE VERSUS LIFE RELATION DEFINING B

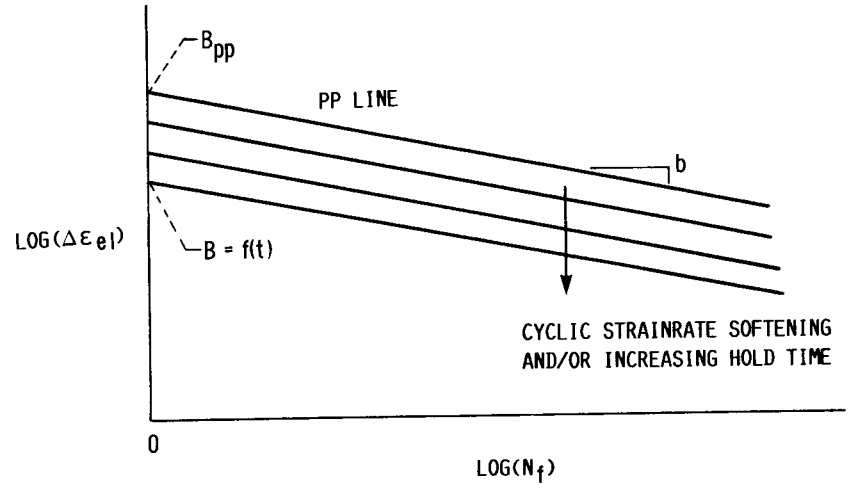

Figure 3

BITHERMAL AND TMF WAVE SHAPES

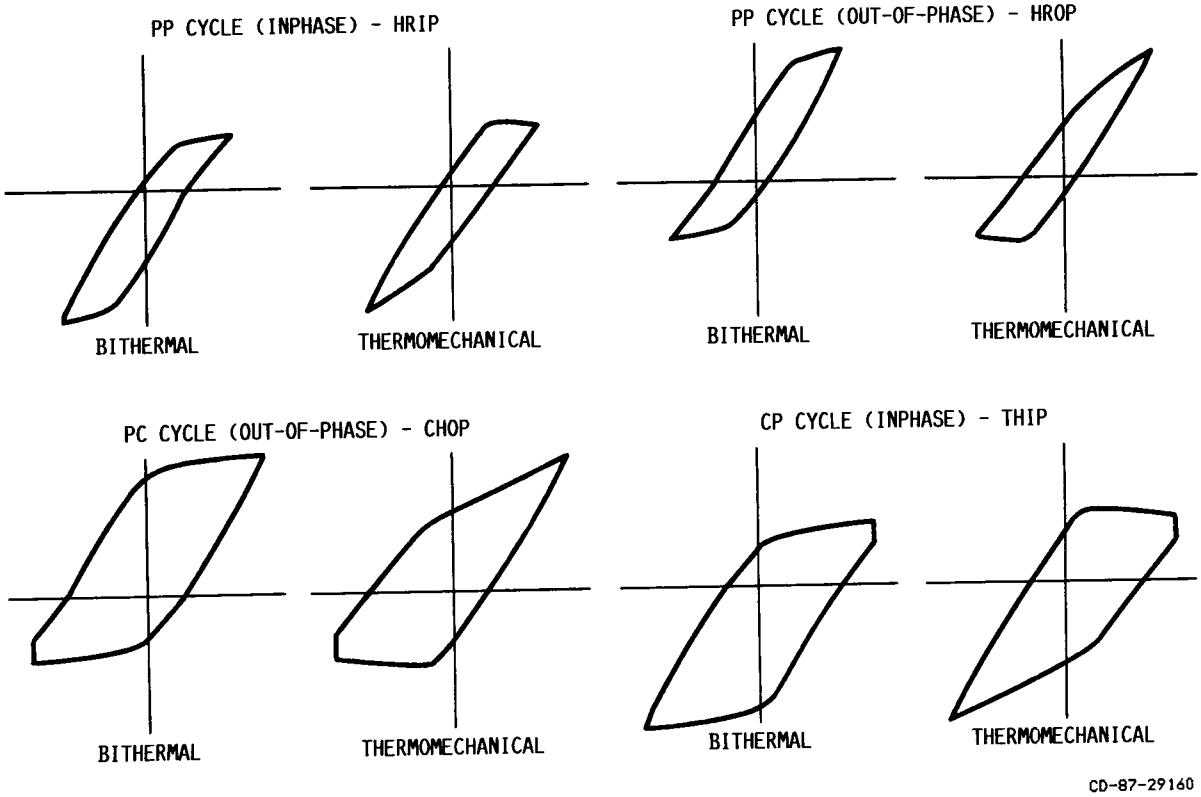

Figure 4

SCHEME FOR REPRESENTING FLOW BEHAVIOR

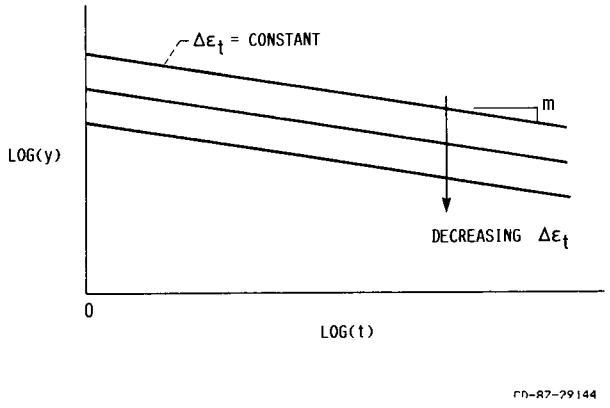

Figure 5

BASIS FOR NORMALIZING FLOW BEHAVIOR TO TOTAL STRAINRANGE

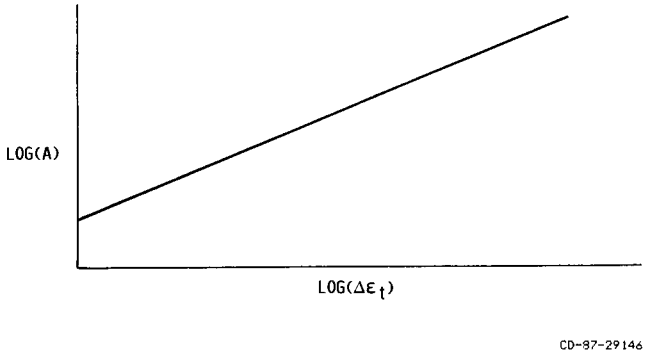

Figure 6

NORMALIZED FLOW BEHAVIOR

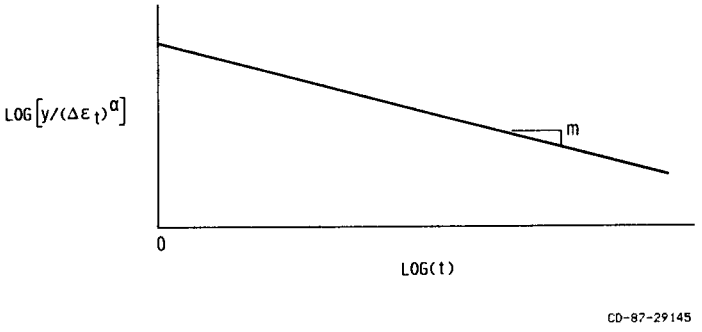

Figure 7

POWER LAW SIMPLIFICATION OF ROBINSON'S TMF CONSTITUTIVE MODEL FOR CYCLIC STRESS-STRAIN

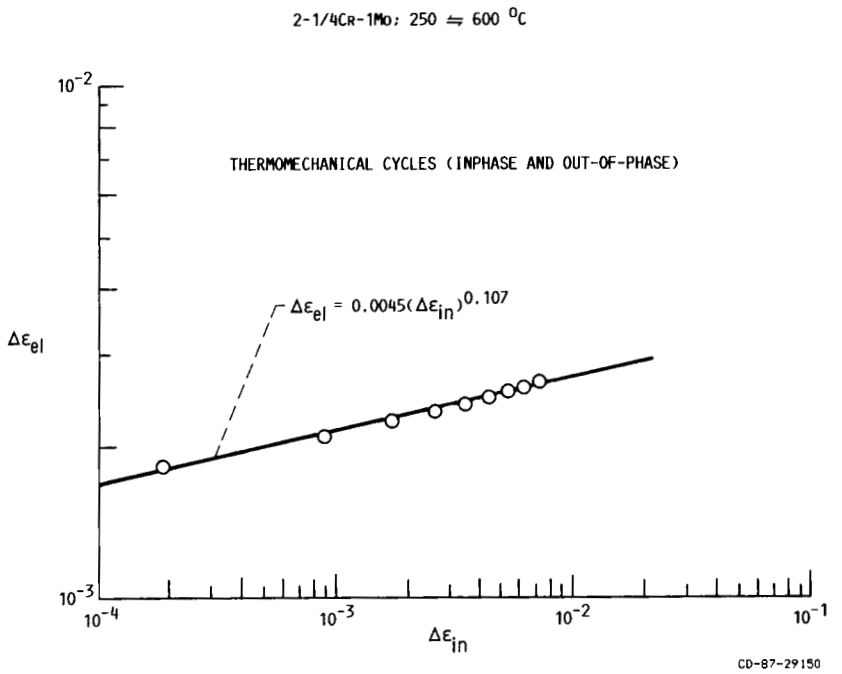

Figure 8(a)

POWER LAW SIMPLIFICATION OF ROBINSON'S TMF CONSTITUTIVE MODEL FOR CYCLIC STRESS-STRAIN

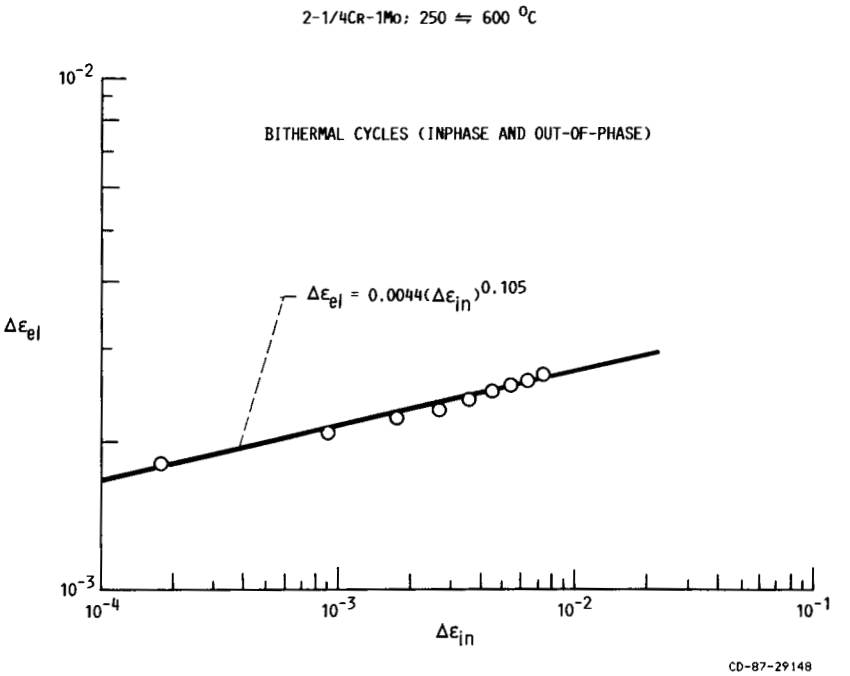

Figure 8(b)

POWER LAW SIMPLIFICATION OF ROBINSON'S CONSTITUTIVE MODEL FOR K_{ij}

2-1/4Cr-1Mo; 250 ⇋ 600 °C

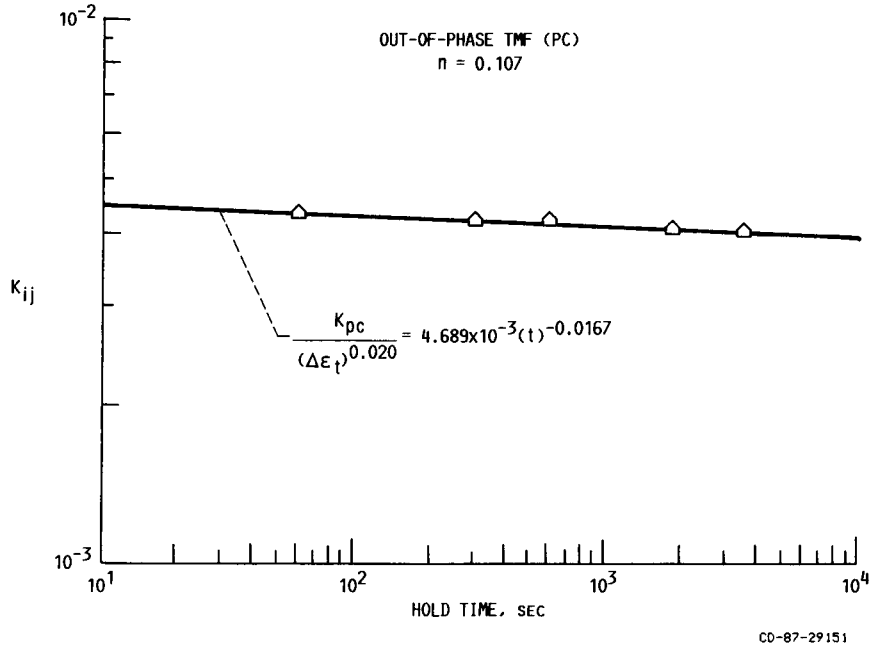

Figure 9(a)

POWER LAW SIMPLIFICATION OF ROBINSON'S TMF CONSTITUTIVE MODEL FOR K_{ij}

2-1/4Cr-1Mo; 250 ⇋ 600 °C

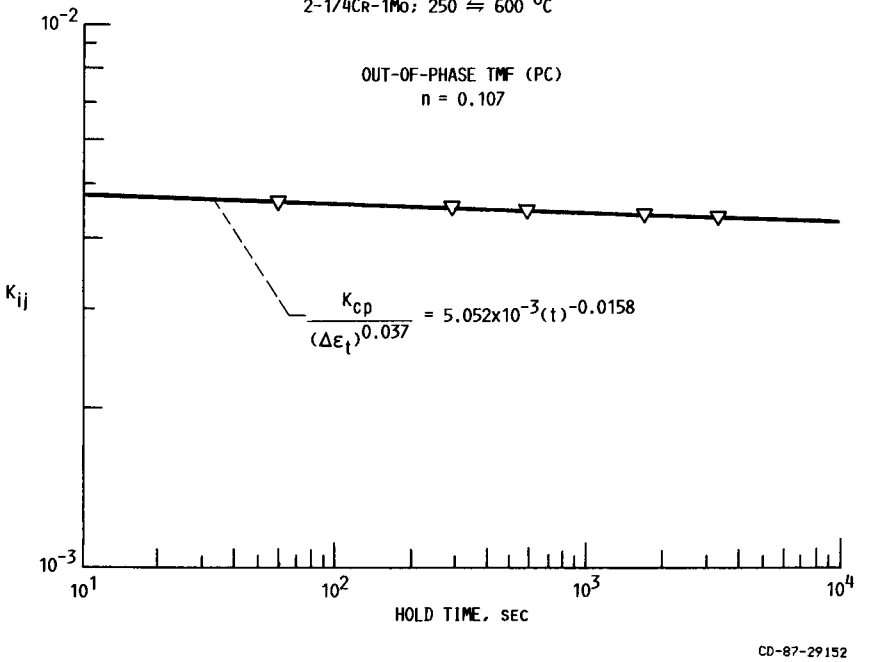

Figure 9(b)

CORRELATION OF K_{ij} FOR TMF CYCLING TMF (PC)

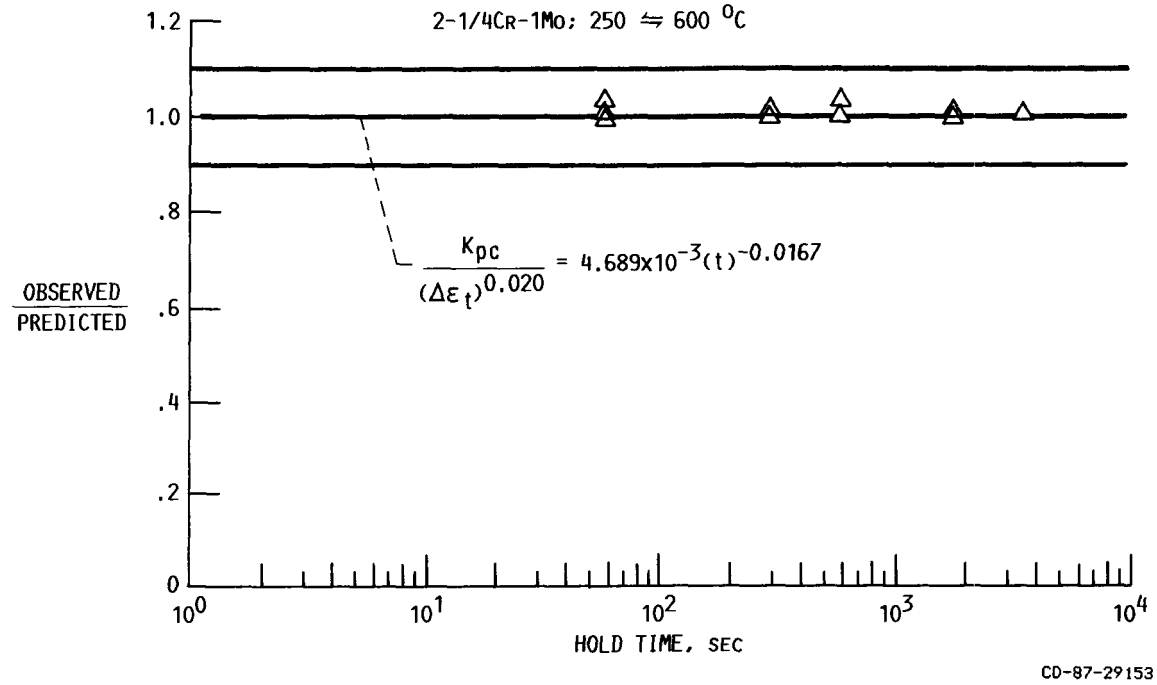

Figure 10(a)

CORRELATION OF K_{ij} FOR TMF CYCLING

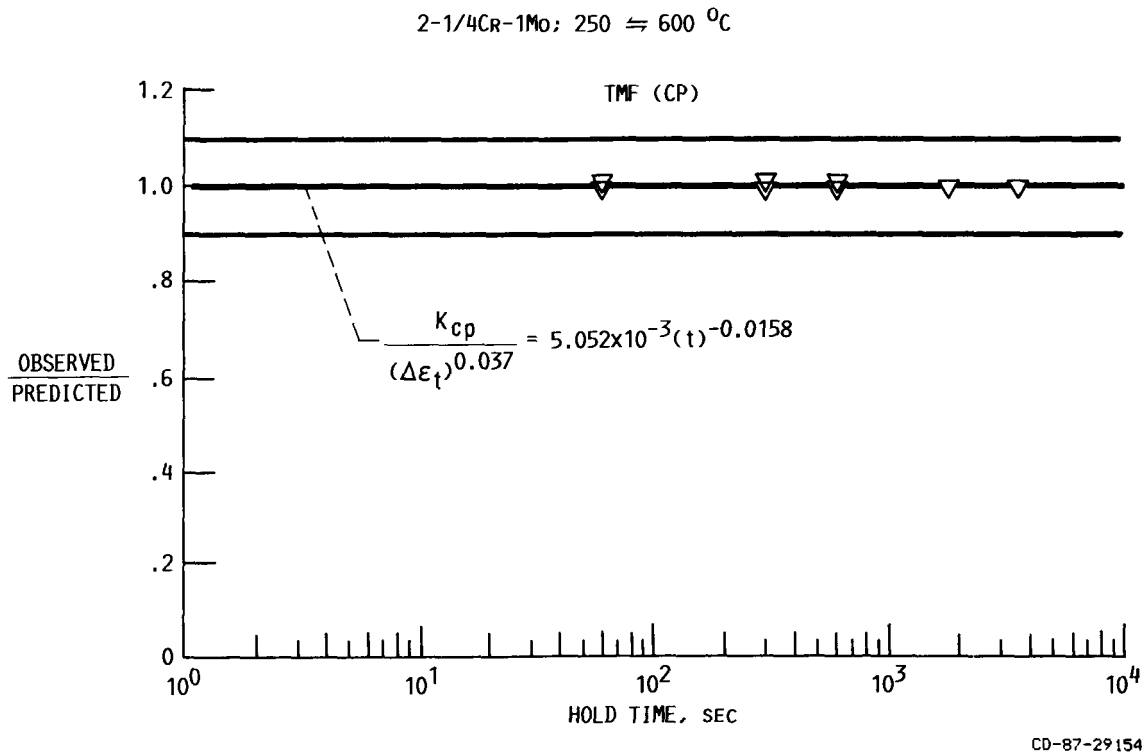

Figure 10(b)

POWER LAW SIMPLIFICATION OF ROBINSON'S TMF CONSTITUTIVE MODEL FOR F_{ij}

2-1/4Cr-1Mo; 250 ⇋ 600 °C

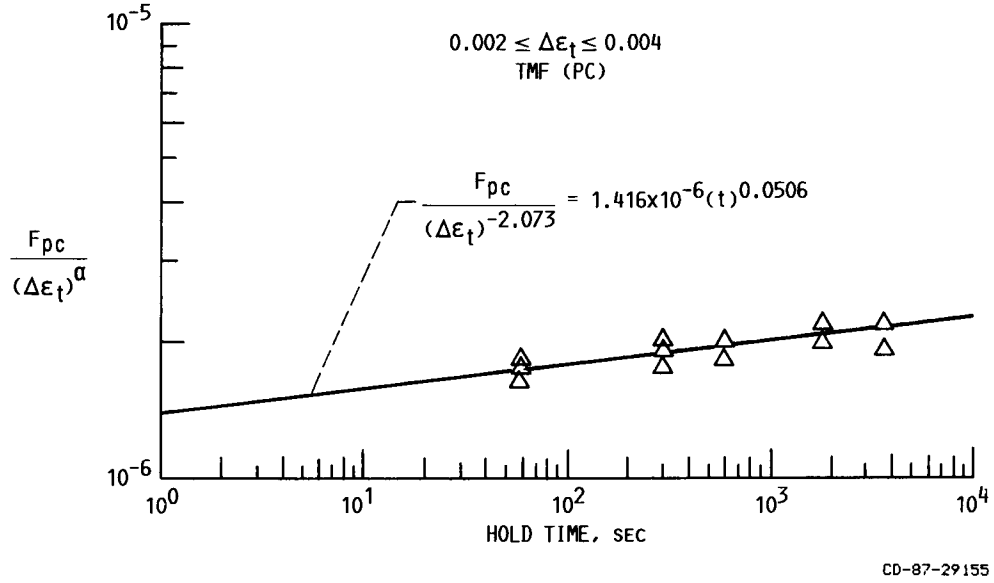

Figure 11(a)

POWER LAW SIMPLIFICATION OF ROBINSON'S TMF CONSTITUTIVE MODEL FOR F_{ij}

2-1/4Cr-1Mo; 250 ⇋ 600 °C

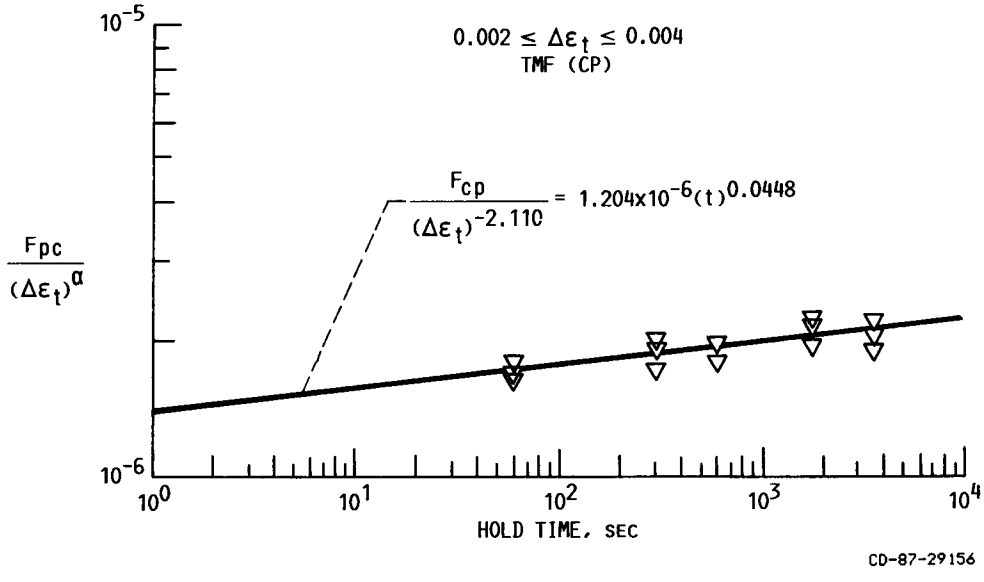

Figure 11(b)

POWER LAW SIMPLIFICATION OF ROBINSON'S TMF CONSTITUTIVE MODEL FOR F_{ij}

2-1/4CR-1MO; 250 ⇋ 600 °C

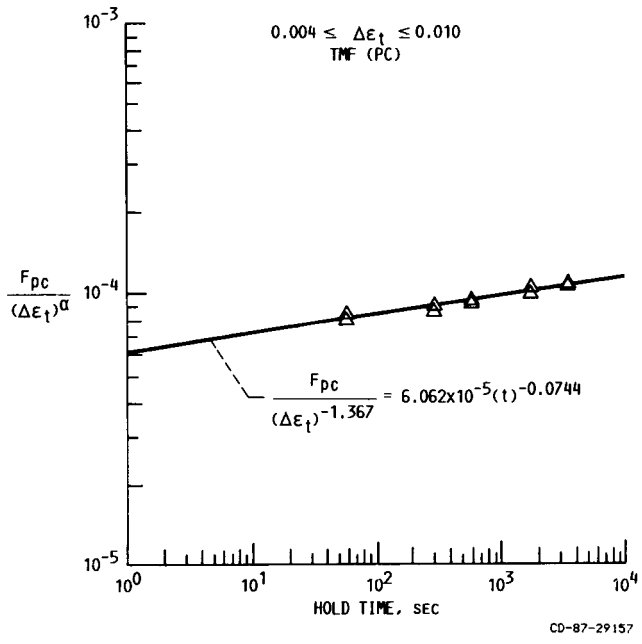

Figure 12(a)

POWER LAW SIMPLIFICATION OF ROBINSON'S TMF CONSTITUTIVE MODEL FOR F_{ij}

2-1/4CR-1MO; 250 ⇋ 600 °C

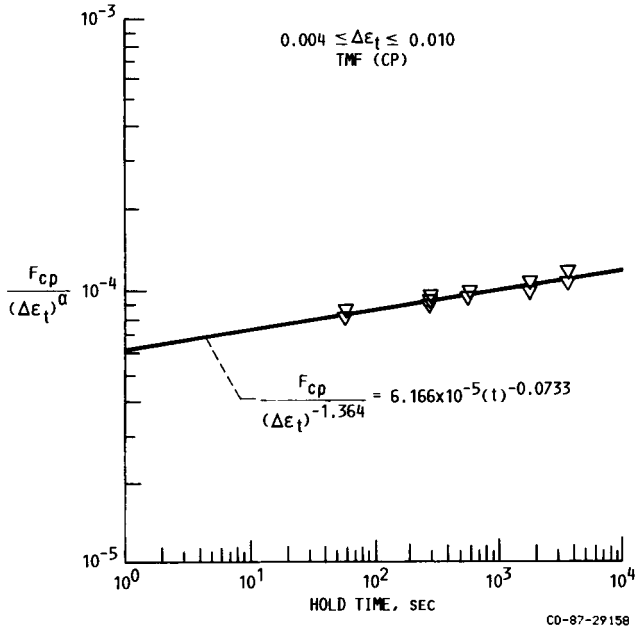

Figure 12(b)

CONCLUDING REMARKS: SIXTH ANNUAL WORKSHOP FOR THE HOST PROJECT

Daniel E. Sokolowski
NASA Lewis Research Center
Cleveland, Ohio

As reported at this workshop, the HOST Project's technical activities have produced substantial results. Many contractor reports are available and are listed in a bibliography of HOST papers included at the end of this publication.

The nature of the problem of durability requires not only that numerous disciplines be involved, as discussed in the opening remarks, but also that the research itself be interdisciplinary. The success of the HOST Project has been due in large part to unprecedented teamwork at Lewis, at the contractors, and between contractors and universities. In addition, the HOST Project is recognized for the value of focused as well as interdependent research when compared with generic, independent base R&T activities.

I want to say "thank you" to the HOST Project Team for another job well done in conducting this workshop. In particular, I want to thank the contractor speakers; the Subproject Managers for being session chairmen; my assistant, Bob Ensign; and Dr. Richard Ziegfeld from Sverdrup Technology for his editorial assistance. Finally, I want to express my sincere thanks to our Conference Coordinator, Laura Hill, for her exceptional dedication.

C - 6

BIBLIOGRAPHY

The following is a compilation of technical reports for activities supported by the HOST Project. The reports are separated into each of the six project disciplines along with a general category. They include contractor, university grantee, NASA Technical Memorandums, and professional society publications. In addition, reports that are considered to be pre-HOST (activities initiated just prior to the HOST Project that support the project's objective) are denoted by an asterisk (*).

Since the 1986 HOST Workshop Conference Publication appeared, this bibliography has been corrected in a few instances and has been updated. A more complete bibliography will follow in 1988 as an independent NASA Technical Memorandum.

INSTRUMENTATION

*1. Grant, H.P.; and Przybyszewski, J.S.: Thin Film Temperature Sensor. (PWA-5526-31, Pratt and Whitney Aircraft; NASA Contract NAS3-20831), NASA CR-159782, 1980.

*2. Grant, H.P.; Przybyszewski, J.S.; and Claing, R.G.: Turbine Blade Temperature Measurements Using Thin Film Temperature Sensors. (PWA-5604-31, Pratt and Whitney Aircraft; NASA Contract NAS3-20831), NASA CR-165201, 1981.

*3. Grant, H.P.; Przybyszewski, J.S.; Claing, R.G.; and Anderson, W.L.: Thin Film Temperature Sensors Phase III. (PWA-5708-26, Pratt and Whitney Aircraft; NASA Contract NAS3-22002), NASA CR-165476, 1982.

4. Atkinson, W.H.; and Strange, R.R.: Development of Advanced High-Temperature Heat Flux Sensors. (PWA-5723-27, Pratt and Whitney Aircraft; NASA Contract NAS3-22133), NASA CR-165618, 1982.

5. Elmore, D.L.; Robinson, W.W.; and Watkins, W.B.: Dynamic Gas Temperature Measurement System, Vol. I - Technical Efforts. (PWA/GPD-FR-17145 - Vol. I, Pratt and Whitney Aircraft; NASA Contract NAS3-23154), NASA CR-168267, 1983.

6. Purpura, P.T.: Dynamic Gas Temperature Measurement System, Vol. II - Operation and Program Manual. (PWA/GPD-FR-17145-Vol. II, Pratt and Whitney Aircraft; NASA Contract NAS3-23154), NASA CR-168267, 1983.

*7. Stetson, K.A.: Demonstration Test of Burner Liner Strain Measuring System. (R84926376-15, United Technologies Research Center; NASA Contract NAS3-23690), NASA CR-174743, 1984.

8. Seasholtz, R.G.; Oberle, L.G.; and Weikle, D.H.: Optimization of Fringe-Type Laser Anemometers for Turbine Engine Component Testing. AIAA Paper 84-1459, June 1984.

9. Atkinson, W.H.; Cyr, M.A.; and Strange, R.R.: Turbine Blade and Vane Heat Flux Sensor Development, Phase I. (PWA-5914-21, Pratt and Whitney Aircraft; NASA Contract NAS3-23529), NASA CR-168297, 1984.

10. Elmore, D.L.; and Watkins, W.B.: Further Development of the Dynamic Gas Temperature Measurement System. FR-18639, Pratt and Whitney, NAS3-24228, September 1984.

11. Morey, W.W.: Hot Section Viewing System. (R84925830-33, United Technologies Research Center; NASA Contract NAS3-23156), NASA CR-174773, 1984.

12. Hulse, C.O.; Bailey, R.S.; and Lemkey, F.D.: High Temperature Static Strain Gage Alloy Development Program. (R85915952-13, United Technologies Research Center; NASA Contract NAS3-23169), NASA CR-174833, 1985.

13. Hobart, H.F.: Evaluation Results of the 700 °C Chinese Strain Gauges. NASA TM-86973, 1985.

14. Atkinson, W.H.; Cyr, M.A.; and Strange, R.R.: Turbine Blade and Vane Heat Flux Sensor Development, Phase II. (PWA-5914-39, Pratt and Whitney Aircraft; NASA Contract NAS3-23529), NASA CR-174995, 1985.

15. Oberle, L.G.; and Seasholtz, R.G.: Filter Induced Errors in Laser Anemometer Measurements Using Counter Processors. NASA TM-87047, 1985.

16. Stetson, K.A.: Demonstration of Laser Speckle System on Burner Liner Cyclic Rig. (R86-927298-10, Pratt and Whitney Aircraft; NASA Contract NAS3-24615), NASA CR-179509, 1986.

17. Elmore, D.L.; Robinson, W.W.; and Watkins, W.B.: Further Development of the Dynamic Gas Temperature Measurement System, Volume I - Technical Efforts. (P/W/GPD-FR-19381-Vol-1, Pratt and Whitney Aircraft; NASA Contract NAS3-24228), NASA CR-179513-Vol-1, 1986.

18. Stocks, D.R.; and Elmore, D.L.: Further Development of the Dynamic Gas Temperature Measurement System, Vol. II - Computer Program User's Manual. (P/W/GPD-FR-19381-Vol-2, Pratt and Whitney Aircraft; NASA Contract NAS3-24228), NASA CR-179513-Vol-2, 1986.

19. Englund, D.R.: Research Instrumentation for Hot Section Components of Turbine Engines. NASA TM-88851, 1986

20. Hulse, C.O., et al.: High Temperature Static Strain Gage Development Contract. (R87-916527-1, Pratt and Whitney Aircraft; NASA Contract NAS3-23722), NASA CR-180811, 1987.

COMBUSTION

1. Sturgess, G.J.: Aerothermal-Modeling - Phase I, Task Report, Description of Aerothermal Model and Relation to Design System. PWA-5907-2, Pratt and Whitney Aircraft, NAS3-23524, August 1982.

2. Sturgess, G.J.: Aerothermal Modeling - Phase I, Task Report, Model Assessment Procedure. PWA-5907-3, Pratt and Whitney Aircraft, NAS3-23524, August 1982.

3. Holdeman, J.D.: Dilution Zone Mixing. Combustion Fundamentals Research, NASA CP-2268, 1982, pp. 65-76.

4. Srinivasan, R.; Berenfeld, A.; and Mongia, H.C.: Dilution Jet Mixing Program, Phase I Report. (GARRETT-21-4302, Garrett Turbine Engine Company; NASA Contract NAS3-22110), NASA CR-168031, 1982.

5. Holdeman, J.D. and Srinivasan, R.; and Berenfeld, A: Experiments in Dilution Jet Mixing. AIAA J., vol. 22, no. 10, Oct. 1983, pp. 1436-1443.

6. Holdeman, J.D.: Perspectives on the Mixing of a Row of Jets with a Confined Crossflow. AIAA Paper 83-1200, June 1983.

7. Sturgess, G.J.: Aerothermal Modeling Program - Phase I. (PWA-5907-19, Pratt and Whitney Aircraft; NASA Contract NAS3-23524), NASA CR-168202, 1983.

8. Srinivasan, R., et al: Executive Summary, Aerothermal Modeling Program - Phase I. (GARRETT-21-4766, Garrett Turbine Engine Company; NASA Contract NAS3-23523), NASA CR-174602, 1983.

9. Srinivasan, R., et al: Aerothermal Modeling Program - Phase I, Vol. I. (GARRETT-21-4742-1, Garrett Turbine Engine Company; NASA Contract NAS3-23523), NASA CR-168243-Vol. 1, 1983.

10. Srinivasan, R., et al: Aerothermal Modeling Program - Phase I, Vol. II. (GARRETT-21-4742-2, Garrett Turbine Engine Company; NASA Contract NAS3-23523), NASA CR-168243-Vol. 2, 1983.

11. Roback, R.; and Johnson, B.V.: Mass and Momentum Turbulent Transport Experiments with Confined Swirling Coaxial Jets. (R83915540-26, United Technology Research Center; NASA Contract NAS3-22771), NASA CR-168252, 1983.

12. Kenworthy, M.K.; Correa, S.M.; and Burrus, D.L.: Aerothermal Modeling, Executive Summary. NASA CR-168330, 1983.

13. Kenworthy, M.K.; Correa, S.M.; and Burrus, D.L.: Aerothermal Modeling - Phase I, Vol. I - Model Assessment. NASA CR-168296-Vol. 1, 1983.

14. Kenworthy, M.K.; Correa, S.M.; and Burrus, D.L.: Aerothermal Modeling - Phase I, Vol. II - Experimental Data. NASA CR-168296-Vol. 2, 1983.

15. Lilley, D.G., et al: Lateral Jet Injection Into Typical Combustor Flowfields. AIAA Paper 84-0374, Jan. 1984.

16. Srinivasan, R.; Coleman, E.; and Johnson, K.: Dilution Jet Mixing Program, Phase II. (GARRETT-21-4804, Garrett Turbine Engine Company; NASA Contract NAS3-22110), NASA CR-174624, 1984.

17. Holdeman, J.D.; and Srinivasan, R.: Modeling of Dilution Jet Flowfields, Combustion Fundamentals Research, NASA CP-2309, 1984, pp. 175-187.

18. Holdeman, J.D.; and Srinivasan, R.: On Modeling Dilution Jet Flowfields. AIAA Paper 84-1379, June 1984.

19. Holdeman, J.D.; Srinivasan, R.; and Berefeld, A.: Experiments in Dilution Jet Mixing. AIAA J., vol. 22, no. 10, Oct. 1984, pp. 1436-1443.

20. Johnson, B.V.; and Roback, R.: Turbulent Transport and Length Scale Measurement Experiments with Combined Coaxial Jets. (UTRC-R84915540-34, United Technologies Research Center; NASA Contract NAS3-22771), NASA CR-174831, 1984.

21. Johnson, B.V.; Roback, R.; and Bennett, J.C.: Scalar and Momentum Turbulent Transport Experiments with Swirling and Nonswirling Flows. Experimental Measurements and Techniques in Turbulent Reactive and Nonreactive Flows, ASME, 1984, pp. 107-119.

22. Lilley, D.G.: Swirling Flows in Typical Combustor Geometries. AIAA Paper 85-0148, 1985.

23. Ferrell, G.B.; Aoki, K.; and Lilley, D.G.: Flow Visualization of Lateral Jet Injection into Swirling Crossflow. AIAA Paper 85-0059, 1985.

24. Ferrell G.B.; and Lilley D.G.: Deflected Jet Experiments in a Turbulent Combustor Flowfield. NASA CR-174863, 1985.

25. Syed, S.A.; Chiappetta, L.M.; and Gosman, A.D.: Error Reduction Program. (PWA-5928-25, Pratt and Whitney Aircraft; NASA Contract NAS3-23686), NASA CR-174776, 1985.

26. Ferrell, G.B.; and Lilley, D.G.: Turbulence Measurements of Lateral Jet Injection into Confined Turbulent Crossflow. AIAA Paper 85-1102, 1985.

27. Holdeman, J.D., et al: Experiments in Dilution Jet Mixing: Effects of Multiple Rows and Non-circular Orifices. AIAA Paper 85-1104, June 1985.

28. Srinivasan, R., et al: Dilution Jet Mixing Program, Phase III. (GARRETT-21-5418, Garrett Turbine Engine Company; NASA Contract NAS3-22110), NASA CR-174884, 1985.

29. Holdeman, J.D.; and Srinivasan, R.: Modeling of Dilution Jet Flowfields. Propulsion Power, Vol. 2, No. 1, Jan.-Feb. 1986, pp. 4-10.

30. Ong, L.H.; and Lilley, D.G.: Measurements of a Single Lateral Jet Injected into Swirling Crossflow. NASA CR-175040, 1986.

31. McMurry, C.B.; and Lilley, D.G.: Experiments on Opposed Lateral Jets Injected into Swirling Crossflow. NASA CR-175041, 1986.

32. Srinivasan R.; and White C.: Dilution Jet Mixing Program, Supplementary Report. (GARRETT 21-4705, Garrett Turbine Engine Company; NASA Contract NAS3-22110), NASA CR-175043, 1986.

33. Holdeman J.D.; and Srinivasan, R.: Perspectives on Dilution Jet Mixing. AIAA Paper 86-1611, June 1986.

34. Lilley, D.G.: Lateral Jet Injection Into Typical Combustor Flowfields. NASA CR-3997, 1986.

35. Barron, D.A.: LDV Measurements in an Annular Combustor Model. M.S. Thesis, Purdue University, 1986.

36. Reynolds, R.; and White, C.: Transition Mixing Study. (G-21-5723, Garrett Turbine Engine Co.; NASA Contract (NAS3-24340), NASA CR-175062, 1986.

37. Srinivasan, R.; and Thorp, D.J.: Combustor Diffuser Interaction Program. (AFWAL-TR-86-2093, 1987.

38. McDonell, V.G.; Cameron, C.D.; and Samuelson, G.S.: Symmetry Assessment of a Gas Turbine Air-Assist Atomizers. AIAA Paper 87-2136, July 1987.

39. Mostafa, A.A., et al.: On the Evolution of Particle-Laden Jet Flows: A Theoretical and Experimental Study. AIAA Paper 87-2181, June 1987.

TURBINE HEAT TRANSFER

1. Florschuetz, L.W.; and Isoda, Y.: Flow Distributions and Discharge Coefficients for Jet Array Impingements with Initial Crossflow. ASME Paper 82-GT-156, Apr. 1982.

2. Florschuetz, L.W., et al: Jet Array Impingement Flow Distributions and Heat Transfer Characteristics - Effects of Initial Crossflow and Nonuniform Array Geometry - Gas Turbine Engine Component Cooling. NASA CR-3630, 1982.

3. Nealy, D.A., et al: Measurement of Heat Transfer Distribution Over the Surfaces of Highly Loaded Turbine Nozzle Guide Vanes. ASME Paper 83-GT-53, Mar. 1983.

4. Florschuetz, L.W.; Metzger, D.E.; and Su, C.C.: Heat Transfer Characteristics for Jet Array Impingement with Initial Crossflow. ASME Paper 83-GT-28, Mar. 1983.

5. Hylton, L.D., et al: Analytical and Experimental Evaluation of the Heat Transfer Distribution Over the Surfaces of Turbine Vanes. (EDR-11209 Allison Gas Turbine Division; NAS3-22761), NASA CR-168015, 1983.

6. Richards, D.R.; and Florschuetz, L.W.: Forced Convection Heat Transfer to Air/Water Vapor Mixtures. NASA CR-3769, 1984.

7. Nealy, D.A.; Mihelc, M.S; Hylton, L.D.; and Gladden, H.J.: Measurements of Heat Transfer Distribution Over the Surfaces of Highly Loaded Turbine Nozzle Guide Vanes. J. Eng. Gas Turbines Power, vol. 106, no. 1, Jan. 1984, pp. 144-158.

8. Florschuetz, L.W.; and Tseng, H.H.: Effect of Nonuniform Geometries on Flow Distributions and Heat Transfer Characteristics for Arrays of Impinging Jets. ASME Paper 84-GT-156, June 1984.

9. Vatsa, V.N.: A Three-Dimensional Boundary Layer Analysis Including Heat-Transfer and Blade-Rotation Effects. 3rd Symposium on Numerical and Physical Aspects of Aerodynamic Flows, T. Cebeci, ed., California State University, 1985, pp. 10-45 to 10-59.

10. Gladden, H.J.; Yeh, F.C.; and Fronek, D.L.: Heat Transfer Results and Operational Characteristics of the NASA Lewis Research Center Hot Section Cascade Test Facility. ASME Paper 85-GT-82, Mar. 1985.

11. Weinberg, B.C., et al: Calculations of Two- and Three-Dimensional Transonic Cascade Flow Fields Using the Navier-Stokes Equations. ASME Paper 85-GT-66, Mar. 1985.

12. Hippensteele, S.A.; Russel, L.M.; and Torres, F.J.: Local Heat-Transfer Measurements on a Large Scale-Model Turbine Blade Airfoil Using a Composite of a Heater Element and Liquid Crystals. ASME Paper 85-GT-59, Mar. 1985.

13. Florschuetz L.W.; and Su, C.C.: Recovery Effects on Heat Transfer Characteristics Within an Array of Impinging Jets. Arizona State University, NSG3-075, April 1985.

14. Turner, E.R., et al: Turbine Vane External Heat Transfer, Vol. I - Analytical and Experimental Evaluation of Surface Heat Transfer Distributions With Leading Edge Showerhead Film Cooling. (EDR-11984, Vol. 1, Allison Gas Turbine Division; NASA Contract NAS3-23695), NASA CR-174827, 1985.

15. Yang, R.J., et al: Turbine Vane External Heat Transfer, Vol. II - Numerical Solutions of the Navier-Stokes Equations for Two- and Three-Dimensional Turbine Cascades With Heat Transfer. (EDR-11984, Allison Gas Turbine Division; NASA Contract NAS3-23695), NASA CR-174828, 1985.

16. Gladden, H.J.; and Proctor, M.P.: Transient Technique for Measuring Heat Transfer Coefficients on Stator Airfoils in a Jet Engine Environment. AIAA Paper 85-1471, July 1985.

17. Anderson, O.L.; and Caplin, B.: User's Manual for Three Dimensional Boundary Layer (BL3-D) Code. (R85956834-1, United Technologies Research Center; NASA Contract NAS3-23716), NASA CR-174899, 1985.

18. Anderson, O.L.: Assessment of a 3-D Boundary Layer Analysis to Predict Heat Transfer and Flow Field in a Turbine Passage. (R85956834, United Technologies Research Center; NASA Contract NAS3-23716), NASA CR-174894, 1985.

19. Florschuetz, L.W.; and Su, C.C.: Heat Transfer Characteristics Within an Array of Impinging Jets. NASA CR-3936, 1985.

20. Anderson, O.L.: Calculation of Three-Dimensional Boundary Layers on Rotating Turbine Blades. Three Dimensional Flow Phenomena in Fluid Machinery, A. Hamed, J. Herring, and L. Povinello, eds., ASME, 1985, pp. 121-132.

21. Crawford, R.A., et al: Mean Velocity and Turbulence Measurements in a 90° Curved Duct With Thin Inlet Boundary Layer. (UTSI/85-08, Tennessee University Space Institute; NASA Contract NAS3-23278), NASA CR-174811, 1985.

22. Florschuetz, L.W.; and Metzger, D.E.: Effect of Initial Crossflow Temperature on Turbine Cooling With Jet Arrays. Arizona State University, NSG3-075.

23. Kopper, F.: Coolant Side Heat Transfer With Rotation. Pratt and Whitney Aircraft, NAS3-23691.

24. Dring, R.P.; Blair, M.F.; and Joslyn, H.D.: The Effects of Inlet Turbulence and Rotor Stator Interactions on the Aerodynamics and Heat Transfer of a Large-Scale Rotating Turbine Model. Vol. I, Final Report, NASA CR-179466, (United Technologies Research Center, NAS3-23717).

25. Dring, R.P.; Blair, M.F.; and Joslyn, H.D.: The Effects of Inlet Turbulence and Rotor Stator Interactions on the Aerodynamics and Heat Transfer of a Large-Scale Rotating Turbine Model. Vol. II, Heat Transfer Data Tabulation. 15% Axial Spacing. (UTRC-R86956480-2, United Technologies Research Center; NASA Contract NAS3-23717), NASA CR-179467, 1986.

26. Dring, R.P.; Blair, M.F.; and Joslyn, H.D.: The Effects of Inlet Turbulence and Rotor Stator Interactions on the Aerodynamics and Heat Transfer of a Large-Scale Rotating Turbine Model. Vol. III, Heat Transfer Data Tabulation. 65% Axial Spacing. (UTRC-R86956480-3, United Technologies Research Center; NASA Contract NAS3-23717), NASA CR-179468, 1986.

27. Dring, R.P.; Blair, M.F.; and Joslyn, H.D.: The Effects of Inlet Turbulence and Rotor/Stator Interactions on the Aerodynamics and Heat Transfer of a Large-Scale Rotating Turbine Model. Vol. IV, Aerodynamic Data Tabulation. NASA CR-179469, (United Technologies Research Center, NAS3-23717).

28. Chyu, M.K.; Metzger, D.E.; and Hwan, C.L.: Heat Transfer in Shrouded Rectangular Cavities. AIAA Paper 86-1327, June 1986.

STRUCTURAL ANALYSIS

1. Robinson, D.N.: Constitutive Relationships for Anisotropic High-Temperature Alloys. NASA TM-83437, 1983.

2. Wilson, R.B., et al: 3-D Inelastic Analysis Methods for Hot Section Components (Base Program), Turbine Blades, Turbine Vanes, and Combustor Liners. (PWA-5940-19, Pratt and Whitney Aircraft; NASA Contract NAS3-23697), NASA CR-174700, 1984.

3. Lindholm, U.S., et al: Constitutive Modeling for Isotropic Materials (HOST). (SWRI-7576, Southwest Research Institute; NASA Contract NAS3-23925), NASA CR-174718, 1984.

4. Maffeo, R.J.: Burner Liner Thermal/Structural Load Modeling. NASA CR-174892, 1984.

5. Rasmaswany, V.G.; Van Stone, R.H.; Dame, L.T.; and Laflen, J.H.: Constitutive Modeling for Isotropic Materials, Annual Report. NASA CR-17485, (General Electric Company, NAS3-23927), March 1985.

6. Ellis, J.R.; and Robinson D.N.: Some Advances in Experimentation Supporting Development of Viscoplastic Constitutive Models. NASA CR-174855, 1985.

7. McKnight, R.L.: Component-Specific Modeling. NASA CR-174765, 1985.

8. McKnight, R.L.: Component Specific Modeling. NASA CR-174925, 1985.

9. Robinson, D.N.: On Thermomechanical Testing in Support of Constitutive Equation Development for High-Temperature Alloys. NASA CR-174879, 1985.

10. Nagtegaal, J.C.; Nakazawa S.; and Wertheimer T.B.: 3-D Inelastic Analysis Methods for Turbine Engine Hot Section Components, Special Finite Element Models - Users Manual. MARC Corporation, May 1985.

11. Dias, J.B.; Nagtegaal, J.C.; Nakazawa S.; and Wertheimer, T.B.: Users' Manual (Version 2.1). MARC Corporation, May 1985.

12. Nonlinear Constitutive Relations for High Temperature Application, 1984. NASA CP-2369, 1985.

13. Lindholm, U.S., et al: Constitutive Modeling for Isotropic Materials, (HOST). (SWRI-7576/30, Southwest Research Institute; NASA Contract NAS3-23925), NASA CR-174980, 1985.

14. Hwang, S.Y.; and Kaufman, A.: On Local Total Strain Redistribution Using a Simplified Cyclic Inelastic Analysis Based on an Elastic Solution. AIAA Paper 85-1419, July 1985.

15. Kaufman A.; Laflen, J.H.; and Lindholm, U.S.: Unified Constitutive Material Models for Nonlinear Finite-Element Structural Analysis. AIAA Paper 85-1418, July 1985.

16. Robinson, D.N.: A Continuous Damage Model Based on Stepwise-Stress Creep Rupture Tests. NASA CR-174941, 1985.

17. Ellis, J.R.: Results of an Interlaboratory Fatigue Test Program Conducted on Alloy 800H at Room and Elevated Temperatures. NASA CR-174940, 1985.

18. Maffeo, R.: Burner Liner Thermal/Structural Load Modeling TRANCITS Program User's Manual. (R85AEB452, General Electric Company; NASA Contract NAS3-23272), NASA CR-174891, 1985.

19. Bartolotta, P.A.: Thermomechanical Cyclic Hardening Behavior of Hastelloy-X. NASA CR-174999, 1985.

20. Banerjee, P.K.; Snow D.W.; and Wilson R.B.: Stress Analysis of Gas Turbine Engine Structures Using the Boundary Element Method. Advanced Topics in Boundary Element Analysis, T.A. Cruse, A.B. Pifko, and H. Armer, eds., ASME, 1985, pp. 45-63.

21. Ellis, J.R.: An Experimental Study of Biaxial Yield in Modified 9Cr-1Mo Steel at Room Temperature. NASA CR-175012, 1985.

22. Nonlinear Constitutive Relations for High Temperature Applications. NASA CP-2271, 1983.

23. Dame, L.T.; and Stouffer, D.C.: Anisotropic Constitutive Model for Nickel Base Single Crystal Alloys: Development and Finite Element Implementation. NASA CR-175015, 1986.

24. Ramaswamy, V.G.: A Constitutive Model for the Inelastic Mutliaxial Cyclic Response of a Nickel Base Supperalloy Rene 80. NASA CR-3998, 1986.

25. Chan, K.S., et al.: Constitutive Modeling for Isotropic materials (HOST). (SWRI 06-7576, Southwest Research Institute; NASA Contract NAS3-23925), NASA CR-179522, 1986.

26. Nakazawa, S.: On 3-D Inelastic Analysis Methods for Hot Section Components: Vol. 1 - Special Finite Element Models. (PWA-5940-46-Vol-1, Pratt and Whitney Aircraft, NASA Contract NAS3-23697), NASA CR-179494, 1987.

27. Wilson, R.B.; and Banerjee, P.K.: 3-D Inelastic Analysis Methods for Hot Section Components, Vol. II - Advanced Special Functions Models. (PWA-5940-46-Vol-2, Pratt and Whitney Aircraft, NASA Contract NAS3-23697), NASA CR-179517, 1987.

FATIGUE and FRACTURE

*1. McKnight, R.L.; Laflen, J.H.; and Spamer, G.T.: Turbine Blade Tip Durability Analysis. (R81AEG372, General Electric Company; NASA Contract NAS3-22020), NASA CR-165268, 1981.

*2. Moreno, V.: Combustor Liner Durability Analysis. (PWA-5684-19, Pratt and Whitney Aircraft; NASA Contract NAS3-21836), NASA CR-165250, 1981.

*3. Walker, K.P.: Research Development Program for Nonlinear Structural Modeling with Advanced Time-Temperature Dependent Constitutive Relationships. (PWA-5700-50, Pratt and Whitney Aircraft; NASA Contract NAS3-22055), NASA CR-165533, 1981.

*4. Meyers, G.J.: Fracture Mechanics Criteria for Turbine Engine Hot Section Components. (PWA-5772-23, Pratt and Whitney Aircraft; NASA Contract NAS3-22550), NASA CR-167896, 1982.

*5. Domas, P.A., et al: Benchmark Notch Test for Life Prediction. (R82AEB358, General Electric Company; NASA Contract NAS3-22522), NASA CR-165571, 1982.

*6. Laflen, J.H.; and Cook, T.S.: Equivalent Damage - A Critical Assessment. (R82AEG533, General Electric Company; NASA Contract NAS3-22534), NASA CR-167874, 1982.

*7. McKnight, R.L., et al: Turbine Blade Nonlinear Structural and Life Analysis. J. Aircraft, vol. 20, no. 5, May 1983, p. 475-480.

8. Moreno, V.: Creep Fatigue Life Prediction for Engine Hot Section Materials (Isotropic). (PWA-5894-17, Pratt and Whitney Aircraft; NASA Contract NAS3-23288), NASA CR-168228, 1983.

*9. Sharpe, W.N., Jr.; and Ward, M.: Benchmark Cyclic Plastic Notch Strain Measurements. J. Eng. Mater. Technol., vol. 105, no. 4, Oct. 1983, pp. 235-241.

*10. Morena, V.: Development of a Simplified Analytical Method for Representing Material Cyclic Response. (PWA-5843-13, Pratt and Whitney Aircraft; NASA Contract NAS3-22821), NASA CR-168100, 1983.

*11. Moreno, V., et al: Nonlinear Structural and Life Analyses of a Combustor Liner. Comput. Struct., vol. 16, no. 1-4, 1983, pp. 509-515.

12. Liu, H.W.; and Oshida, Y.: Literature Survey on Oxidation and Fatigue Lives at Elevated Temperatures. NASA CR-174639, 1984.

13. Minzhong, Z.; and Liu, H.W.: Crack Tip Field and Fatigue Crack Growth in General Yielding and Low Cycle Fatigue. NASA CR-174686, 1984.

14. Kaufman, A.; and Halford, G.R.: Engine Cyclic Durability by Analysis and Material Testing. Engine Cyclic Durability by Analysis and Testing, AGARD CP-368, AGARD, France, 1984, pp.

15. Moreno, V.; Nissley, D.M.; and Liu, L.S.: Creep Fatigue Life Prediction for Engine Hot Section Materials (Isotropic). (PWA-5894-34, Pratt and Whitney Aircraft; NASA Contract NAS3-23288), NASA CR-174844, 1984.

16. Mauerer, G.; and Liu, H.W.: Morphological Study of Fatigue Crack Growth in the Near Threshold Region. Fatigue '84, C. J. Beevers, ed., Engineering Materials Advisory Services, West Midlands, England, 1984, pp. 297-306.

17. Kim, K.S.; and Orange, T.W.: A Review of Path-Independent Integrals in Elastic-Plastic Fracture Mechanics. Presented at the 18th National Symposium on Fracture Mechanics, June 24-27, 1985, Boulder, Colorado (to be published by ASTM in a Special Technical Publication).

18. Moreno, V., et al: Application of Two Creep Fatigue Life Models for the Prediction of Elevated Temperature Crack Initiation of a Nickel Base Alloy. AIAA Paper 85-1420, July 1985.

19. Kim, K.S.: A Review of Path-Independent Integrals in Elastic-Plastic Fracture Mechanics, Task 4. NASA CR-174956, 1985.

20. Yau J.F., et al: Elevated Temperature Crack Growth. NASA CR-174957, 1985.

21. Kaufman, A.; and Moreno, V.: Two Simplified Procedures for Estimating Cyclic Material Response From a Strain History. Nonlinear Constitutive Relations for High Temperature Applications, 1984, NASA CP-2369, 1984, pp. 201-219.

22. Liu, H.W.: Shear Fatigue Crack Growth: A Literature Survey. Fatigue Eng. Mater. Struct., vol. 8, no. 4, 1985, pp. 295-313.

23. Miner, M.V.; Gayda, J.; and Hebsur, M.G.: Creep-Fatigue Behavior of NiCoCrAlY Coated PWA 1480 Superalloy Crystals. NASA TM-87110, 1985.

24. Liu, H.W.; and Oshida, Y.: Grain Boundary Oxidation and Oxidation Accelerated Fatigue Crack Nucleation and Propagation. NASA CR-175050, 1986.

25. Minzhong, Z.; and Liu, H.W.: Fatigue Crack Growth Under General Yielding Cyclic-Loading. NASA CR-175049, 1986.

26. Linask, I., et al: Life Prediction and Constitutive Models for Engine Hot Section Anisotropic Materials Program. (PWA-5968-19, Pratt and Whitney Aircraft; NASA Contract NAS3-23939), NASA CR-174952, 1986.

27. Gayda, J.; Gabb, T.P.; and Miner, R.V.: The Low Cycle Fatigue Behavior of a Plasma-Sprayed Coating Material. Int. J. Fatigue, vol. 8, no. 4, Sept. 1986, pp. 217-223.

28. Hebsur, M.G.; and Miner, R.V.: High Temperature Tensile and Creep Behavior of Low Pressure Plasma Sprayed NiCoCrAlY Coating Alloy. Mater. Sci. Eng., vol. 83, No. 2, 1986, pp. 239-245.

29. Liu, H.W.; and Oshida, Y.: Grain Boundary Oxidation and Fatigue Crack Growth at Elevated Temperatures, NASA CR-179529, 1986.

30. Gabb, T.P.; Miner, R.V.; and Gayda, J.: The Tensile and Fatigue Deformation Structures in a Single Crystal Ni-Base Superalloy. Scr. Metall., vol. 20, no. 4, Apr. 1986, pp. 513-518.

31. Gabb, T.P.; and Welsch, G.E.: The Cyclic Stress-Strain Behavior of a Nickel-Base Superalloy at 650 °C. Scr. Metall., vol. 20, no. 7, July 1986, pp. 1049-1054.

32. Hebsur, M.G.; and Miner, R.V.: Stress Rupture and Creep Behavior of a Low Pressure Plasma Sprayed NiCoCrAlY Coating Alloy in Air and Vacuum, Thin Solid Films, to be published January 1987.

33. Kaufman, A., et al: Structural Analysis of Turbine Blades Using Unified Constitutive Models. NASA TM-88807, 1987.

34. Swanson, G.A., et al.: Life Prediction and Constitutive Models for Engine Hot Section Anisotropic Materials Program. (PWA-5968-19, Pratt and Whitney Aircraft, NASA Contract NAS3-23939), NASA CR-174952, 1986.

35. Nelson, R.S.; Schoendorf J.F.; and Lin, L.S. : Creep Fatigue Life Prediction for Engine Hot Section Materials (Isotropic). (PWA-5894-60, Pratt and Whitney Aircraft; NASA Contract NAS3-23288), NASA CR-179550, 1986.

36. Malik, S.N., et al.: Elevated Temperature Crack Growth. NASA CR-179601, 1987.

37. Swanson, G.A., et al.: Life Prediction and Constitutive Models for Engine Hot Section Anisotropic Materials Program. (PWA-5968-19, Pratt and Whitney Aircraft; NASA Contract NAS3-23939), NASA CR-174952, 1986.

38. Bartolotta, P.A.; and McGaw, M.A.: A High Temperature Fatigue and Structure Testing Facility. NASA TM-100151, 1987.

SURFACE PROTECTION

1. Rosner, D.E.; and Fernandez de la Mora, J.: Small Particle Transport Across Turbulent Non-Isothermal Boundary Layers. J. Eng. Power, vol. 104, no. 4, Oct. 1982, pp. 885-894.

2. Kohl, F.J.: Airfoil Deposition Model. Turbine Engine Hot Section Technology (HOST), NASA TM-83022, 1982, pp. 241-257.

3. Israel, R.; and Rosner, D.E.: Use of a Generalized Stokes Number to Determine the Aerodynamic Capture Efficiency of Non-Stokesian Particles from a Compressible Gas Flow. Aerosol Sci. Technol., vol. 2, no. 1, 1983, pp. 45-51.

4. Gokoglu, S.; and Rosner, D.E.: Windward Fraction of the Total Mass or Heat Transport for Flow Past a Circular Cylinder. Aerosol Sci. Technol., vol. 2, no. 4,, 1983, pp. 543-544.

5. Rosner, D.E.; Gunes, D.; and Nazih-Anous, N.: Aerodynamically-Driven Condensate Layer Thickness Distributions on Isothermal Cylindrical Surfaces. Chem. Eng. Commun., vol. 24, no. 4-6, Dec. 1983, pp. 275-287.

6. Gokoglu, S.; Israel, R.; and Rosner, D.E.: Rational Engineering Correlations of Diffusional and Inertial Particle Deposition Behavior in Non-Isothermal Forced Convection Environments. Fouling of Heat Exchanger Surfaces, Engineering Foundation, Inc., ed. R. Bryers, pp. 235-256, 1983.

7. Atkins, R.M.; and Rosner, D.E.: Experimental Studies of Salt/Ash Deposition Rates from Combustion Products Using Optical Techniques. Fouling and Slagging Resulting from Impurities in Combustion Gases, Engineering Foundation, Inc., ed. R. Bryers, pp. 469-492, 1983.

8. Stearns, C.A.; Kohl, F.J.; and Rosner, D.E.: Combustion System Processes Leading to Corrosive Deposits. High Temperature Corrosion, R.A. Rapp, ed., NACE-6, National Association of Corrosion Engineers, 1983, pp. 441-450.

9. Rosner, D.E.: Turbine Airfoil Deposition Models. Turbine Engine Hot Section Technology 1983, NASA CP-2289, 1983, pp. 233-240.

10. Gokoglu, S.A.: Deposition Model Verification. Turbine Engine Hot Section Technology 1983, NASA CP-2289, 1983, pp. 241-250.

11. Gokoglu, S.A.: Application of Vapor and Particle Deposition Theory to the Interpretation of Burner Rig Experiments, "Oxidation, Deposition and Hot Corrosion in Combustion Turbine Engines". 1983.

12. Gokoglu, S.A.; and Rosner, D.E.: Comparisons of Rational Engineering Correlations of Thermophoretically-Augmented Particle Mass Transfer with STAN5-Predictions for Developing Boundary Layers. NASA CR-168221, 1984.

13. Gokoglu, S.A.; Chen, B.K.; and Rosner, D.E.: Computer Program for the Calculation of Multicomponent Conventive Diffusion Deposition Rates from Chemically Frozen Boundary Layer Theory. NASA CR-168329, 1984.

14. Gokoglu, S.A.; and Rosner, D.E.: Engineering Correlations of Variable-Property Effects on Laminar Forced Convection Mass Transfer for Dilute Vapor Species and Small Particles in Air. NASA CR-168322, 1984.

15. Seshadri, K.; and Rosner, D.E.: Optical Methods and Results of Dew Point and Deposition Rate Measurements in Salt/Ash-Containing Combustion Gases-B_2O_3(1) Deposition Rates by Interference Methods and Comparisons with Theory. AICHE J., vol. 30, no. 2, Mar. 1984, pp. 187-196.

16. Gokoglu, S.A.; and Rosner, D.E.: Effect of Particulate Thermophoresis in Reducing the Fouling Rate Advantages of Effusion-Cooling. Int. J. Heat Fluid Flow, vol. 5, no. 1, Mar. 1984, pp. 37-41.

17. Gokoglu, S.A.; and Rosner, D.E.: Correlation of Thermophoretically-Modified Small Particle Diffusional Deposition Rates in Forced Convection Systems with Variable Properties, Transpiration Cooling and/or Viscous Dissipation. Int. J. Heat Mass Trans., vol. 27, no. 5, May 1984, pp. 639-646.

18. Gokoglu, S.A.; and Rosner, D.E.: Comparisons of Rational Engineering Correlations of Thermophoretically-Augmented Particle Mass Transfer with STAN5-Predictions for Developing Boundary Layers. ASME Paper 84-GT-158, June 1984.

19. Fryxell, R.E.: Effects of Surface Chemistry on Hot Corrosion Life. (R84AEB422, General Electric Company; NASA Contract NAS3-23926), NASA CR-174683, 1984.

*20. Miller, R.A.: Oxidation-Based Model for Thermal Barrier Coating Life. J. Ceram. Soc., vol. 67, no. 8, Aug. 1984, pp. 517-521.

21. Miller, R.A.; and Berndt, C.C.: Performance of Thermal Barrier Coatings in High Heat Flux Environments. Thin Solid Films, vol. 119, no. 2, 1984, pp. 195-202.

22. Berndt, C.C.; and Miller, R.A.: Mechanical Property Measurements of Plasma-Sprayed Thermal Barrier Coatings Subjected to Oxidation. Ceram. Eng. Sci. Proc., vol. 5, no. 7-8, July-Aug. 1984, pp. 479-490.

23. Berndt, C.C.: Acoustic Emission Evaluation of Plasma-Sprayed Thermal Barrier Coatings. J. Eng. Gas Turbines Power, vol. 107, no. 1, Jan. 1985, pp. 142-146.

24. Berndt, C.C.: Behavior of Plasma-Sprayed Coatings. Ultrastructure Processing of Ceramics, Glasses and Composites, L.L. Hench and D.R. Ulrich, eds., J. Wiley and Sons, 1984, pp. 524-534.

25. Berndt, C.C.: Fracture Toughness Tests on Plasma-Sprayed Coatings. Advances in Fracture Research, (Fractures '84), vol. 4, S. R. Valluri, et al., eds., Pergamon Press, 1984, pp. 2545-2552.

26. Berndt, C.C.; and Miller, R.A.: Failure Analysis of Plasma-Sprayed Thermal Barrier Coatings. Thin Solid Films, vol. 119, no. 2, 1984, pp. 173-184.

27. Gokoglu, S.A.: Experimental Verification of Vapor Deposition Model in Mach 0.3 Burner Rigs. Turbine Engine Hot Section Technology 1984, NASA CP-2339, 1984, pp. 110-122.

28. Fernandez de la Mora, J.; and Rosner, D.E.: Boundary Layer Effects on Particle Impaction and Capture. ASME Trans.-Journal of Fluids Engineering, 107, 1984.

29. Santoro, G.J., et al: Experimental and Theoretical Deposition Rates from Salt-Seeded Combustion Gases of a Mach 0.3 Burner Rig. NASA TP-2225, 1984.

30. Santoro, G.J., et al: Deposition of Na_2SO_4 from Salt-Seeded Combustion Gases of a High Velocity Burner Rig. NASA TM-83751, 1984.

31. Rosner, D.E.; and Kim, S.S.: Optical Experiments on Thermophoretically Augmented Submicron Particle Deposition from "Dusty" High Temperature Gas Flows. Chem. Eng. J., vol. 29, no. 3, Dec. 1984, pp. 147-157.

32. Rosner, D.E.: Turbine Airfoil Deposition Models. Turbine Engine Hot Section Technology 1984, CP-2339, 1984, pp. 101-109.

33. Rosner, D.E.: Non-Fickian Mass Transfer Across Combustion Gas Thermal Boundary Layers -- Power Production and Materials Processing Implications. Proceedings NSF Workshop for Interactive Thermal and Materials Sciences in Materials Processing, 1985.

34. Strangman, T.E.: Development of Thermomechanical Life Prediction Models for Thermal Barrier Coatings in Thermal Barrier Coatings Workshop Abstracts and Figures. Lewis Research Center, May 1985.

35. Fryxell, R.E.: Effects of Surface Chemistry on Hot Corrosion Life, (R85AEB307, General Electric Company; NASA Contract NAS3-23926), NASA CR-174915, 1985.

36. Neumann J.; and Strangman T.E.: Thermal Barrier Coating Life Prediction Model Development. NASA CR-175002, (Garrett Turbine Engine Company, NAS3-23945), September 1985.

37. Gokoglu, S.A.; and Santoro, G.J.: Experimental Verification of Vapor Deposition Rate Theory in High Velocity Burner Rigs. Turbine Engine Hot Section Technology 1985, NASA CP-2405, 1985, pp. 383-390.

38. Gokoglu, S.A.; and Santoro, G.J.: Determination of Convective Diffusion Heat/Mass Transfer Rates to Burner Rig Test Targets Comparable in Size to Cross-Stream Jet Diameter. ASME Paper 86-GT-68, June 1986.

39. Gokoglu, S.A.; and Rosner, D.E.: Viscous Dissipation Effects on Thermophoretically-Augmented Particle Transport Across Laminar Boundary Layers. Int. J. Heat Fluid Flow, vol. 6, no. 4., Dec. 1985, pp. 293-297.

40. Rosner, D.E.; and Nagarajan, R.: Transport-Induced Shifts in Condensate Dew-Point and Composition in Multicomponent Systems with Chemical Reaction. Chem. Eng. Sci., vol. 40, no. 2, 1985, pp. 177-186.

41. Gokoglu, S.A.; and Rosner, D.E.: Thermophoretically Enhanced Mass Transport Rates to Solid and Transpiration-Cooled Walls Across Turbulent (Law-of-the-Wall) Boundary Layers. Ind. Eng. Chem. Fundam., vol. 24, no. 2, May 1985, pp. 208-214.

42. Rosner, D.E.; and Nagarajan, R.: Turbine Airfoil Deposition Models and Their Hot Corrosion Implications. Turbine Engine Hot Section Technology 1985, NASA CP-2405, 1985, pp. 373-381.

43. Strangman, T.E.; and Neumann, J.: NASA CR-175002, (Garrett Turbine Engine Company), 1985.

44. Sheffler, K.D.; and DeMasi, J.T.: Thermal Barrier Coating Life Prediction Model Development. NASA CR-175087, 1985.

45. Hillery, R.V.; and Pilsner, B.H.: Thermal Barrier Coating Life Prediction Model. NASA CR-175010, 1985.

46. Gokoglu, S.A.; and Rosner, D.E.: Thermophoretically-Augmented Mass Transfer Rates to Solid Walls Across Laminar Boundary Layers. AIAA J., vol. 24, no. 1, Jan. 1986, pp. 172-179.

47. Gokoglu, S.A.; and Santoro, G.J.: Comparison of Theoretical and Experimental Sodium Sulfate Deposition Rates from Combustion Gases in a High Velocity Burner Rig, NASA TM-87287, 1986.

48. Rosner, D.E.; and Liang, B.S.: Laboratory Studies of the Deposition of Alkali Sulfate Vapors from Combustion Gases Using a Flash-Evaporation Technique. Chem. Eng. Commun., vol. 42, no. 1-3, 1986, pp. 171-196.

49. Liang, B.; and Rosner, D.E.: Laboratory Studies of the Deposition of Binary Alkali Sulfate Vapors from Salt-Seeded Combustion Gases Using a Flash-Evaporation Technique. AICHE Fall Meeting, Miami, Florida, 1986.

50. Liang, B.; and Rosner, D.E.: Simplification of Multi-Salt Dew Point Predictions Allowing for Salt/Combustion Product Chemical Reactions and Solution Non-Ideality. J. Electrochemical Society, 1986.

51. Rosner, D.E.; and Nagarajan, R.: Vapor Deposition and Condensate Flow on Combustion Turbine Blades: Theoretical Model to Predict/Understand Some Corrosion Rate Consequences of Molten Alkali Sulfate Deposition in the Field Laboratory. Int. J. Turbo Jet Engines, 1986.

52. Santoro, G.T.; and Gokoglu, S.A.: Experiments for the Determination of Convective Diffusion Heat/Mass Transfer Rates to Burner Rig Test Targets Comparable in Size to Jet Stream Diameter, NASA TM-87196, 1986.

53. Gokoglu, S.A.; and Rosner, D.E.: Prediction and Rational Correlation of Thermophoretically Reduced Particle Mass Transfer to Hot Surfaces Across Laminar or Turbulent Forced-Convection Gas Boundary Layers. Chem. Eng. Commun., vol. 44, no. 1-6, 1986, pp. 107-119.

54. Gokoglu, S.A.: Discussion of the Effect of Wall Suction and thermophoresis on Aerosol Particle Deposition from a Laminar Boundary Layer on a Flat Plate. Int. J. of Heat and Mass Transfer, 1986.

55. DeMasi, J.T.; and Sheffler, K.D.: Mechanisms of Thermal Barrier Coating Degradation and Failure. IBID.

56. Miller, R.A.: The Effect of Oxidation on the High Heat Flux Behavior of a Thermal Barrier Coating. IBID.

57. Duderstadt, E.C.; and Pilsner, B.H.: Effect of Bond Coat Creep and Oxidation. IBID.

58. Chang, G.C.; and Phucharoen, W.: Finite Element Analysis of Thermal Barrier Coatings. IBID.

59. DeMasi, J.T.: Thermal Barrier Coating Life Prediction Model Development. (Pratt and Whitney Aircraft; NASA Contract NAS3-23944), NASA CR-179508, 1986.

60. Hillery, R.V., et al.: Thermal Barrier Coating Life Prediction Model. (R86AEB511, General Electric Co.; NASA Contract NAS3-23943), NASA CR-179504, 1986.

61. Fryxell, R.E.; and Leese, G.E.: Effects of Surface Chemistry on Hot Corrosion Life. (R86AEB361, General Electric Co.; NASA Contract NAS3-23926), NASA CR-179471, 1986.

62. Strangman, T.E.; Neumann, J.; and Liu, A.: Thermal Barrier Coating Life-Prediction Model Development. (Garrett-21-5988; Garrett Turbine Engine Co.; NASA Contract NAS3-23945), NASA CR-179507, 1986.

GENERAL

*1. Dennis, A.J. and Cruse, T.A.: Cost Benefits from Improved Hot Section Life Prediction Technology. AIAA Paper 79-1154, June 1979.

2. Aircraft Engine Diagnostics. NASA CP-2190, 1981.

3. Turbine Engine Hot Section Technology (HOST). NASA TM-83022, 1982.

4. Turbine Engine Hot Section Technology 1983. NASA CP-2289, 1983.

5. Turbine Engine Hot Section Technology 1984. NASA CP-2339, 1984.

6. Turbine Engine Hot Section Technology 1985. NACA CR-2405, 1985.

7. Sokolowski, D.E. and Ensign, C.R.: Toward Improved Durability in Advanced Combustors and Turbines - Progress in the Prediction of Thermomechanical Loads. ASME Paper 86-GT-172, June 1986.

NASA
National Aeronautics and Space Administration

Report Documentation Page

1. Report No.	2. Government Accession No.	3. Recipient's Catalog No.
NASA CP-2493		

4. Title and Subtitle	5. Report Date
Turbine Engine Hot Section Technology—1987	October 1987
	6. Performing Organization Code

7. Author(s)	8. Performing Organization Report No.
	E-3745
	10. Work Unit No.
	533-04-11

9. Performing Organization Name and Address	11. Contract or Grant No.
National Aeronautics and Space Administration Lewis Research Center Cleveland, Ohio 44135-3191	
	13. Type of Report and Period Covered
	Conference Publication

12. Sponsoring Agency Name and Address	14. Sponsoring Agency Code
National Aeronautics and Space Administration Washington, D.C. 20546-0001	

15. Supplementary Notes

16. Abstract

On October 20 and 21, 1987, the Turbine Engine Hot Section Technology (HOST) Project of the NASA Lewis Research Center sponsored a workshop to discuss current research pertinent to engine durability problems. Presentations were made concerning the development of design analysis tools for combustor liners, turbine blades, and turbine vanes. Presentations were divided into six sessions: Instrumentation, Combustion, Turbine Heat Transfer, Structural Analysis, Fatigue and Fracture, and Surface Protection. The principal objective of each session was to disseminate research results to date. Topics discussed included modeling of thermal and fluid-flow phenomena, structural analysis, fatigue and fracture, surface protective coatings, constitutive behavior of materials, stress-strain response, and life-prediction methods. Researchers from industry, academia, and government presented results of their work sponsored by the HOST Project. This publication contains extended abstracts and visual material presented during the workshop.

17. Key Words (Suggested by Author(s))

Turbine Engine Hot Section Technology
HOST
Life prediction
Combustor liners
Turbine airfoils
Material behavior
Aircraft engines
Durability

Date for general release October 1989

STAR Category 39

19. Security Classif. (of this report)	20. Security Classif. (of this page)	21. No of pages	22. Price*
Unclassified	Unclassified	486	A21

NASA-Langley, 1987